USGS
science for a changing world

Huntington Beach Shoreline Contamination Investigation Phase III

Coastal Circulation and Transport Patterns: The Likelihood of OCSD's Plume Impacting the Huntington Beach Shoreline

Final Report

Open-File Report 04-1019

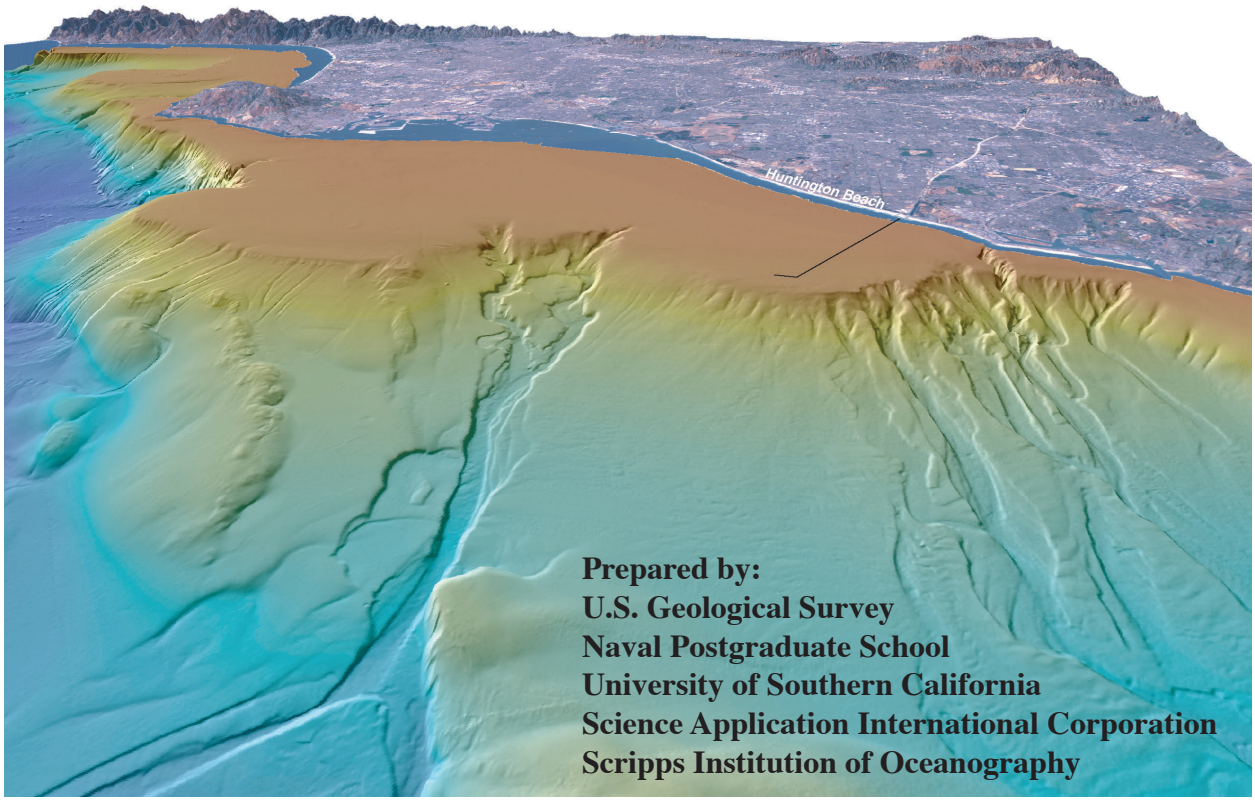

Prepared by:
U.S. Geological Survey
Naval Postgraduate School
University of Southern California
Science Application International Corporation
Scripps Institution of Oceanography

Prepared for Orange County Sanitation District

U.S. Department of the Interior
U.S. Geological Survey

HUNTINGTON BEACH SHORELINE CONTAMINATION INVESTIGATION, PHASE III

Coastal Circulation and Transport Patterns: The Likelihood of OCSD's Plume Impacting the Huntington Beach Shoreline

FINAL REPORT

Open-File Report 04-1019
2004

By

Marlene Noble and Jingping Xu, Editors

Authors:

Peter Hamilton, Scientific Application International Corporation, Raleigh, NC
Burton Jones, University of Southern California, Los Angeles, CA
John Largier, Scripps Institution of Oceanography, La Jolla, CA
Charles McGee, Orange County Sanitation District, Fountain Valley, CA
Marlene Noble, U.S. Geological Survey, Menlo Park, CA
Kevin Orzech, U.S. Geological Survey, Menlo Park, CA
George Robertson, Orange County Sanitation District, Fountain Valley, CA
Leslie Rosenfeld, Naval Postgraduate School, Monterey, CA
Jingping Xu, U.S. Geological Survey, Menlo Park, CA

TABLE OF CONTENTS

Acknowledgements

The editors and authors thank Joanne Ferreira, Marinna Martini, Jonathan Borden, Richard Rendigs, Kevin O'Toole, David Gonzales, Hal Williams, Fran Lightsom, Marla Stone, and the captain and crew of R/V Robert Gordon Sproul for preparing, deploying, and recovering the many types of instruments used in this project. Lori Hibbeler created the HTML document. Anne Gartner, Juliet Kinney, and Kevin Orzech helped to make the figures. We also would like to acknowledge the insightful reviews from the USC Sea Grant Panel: John Allen, Jack Barth, Walter Frick, Roger Fujioka, Trish Holden, Jesus Pineda, Cynthia Cdaback, and Judy Lemus. Anne Gartner proofread and formatted the report.

GLOSSARY

AB411	California Department of Health Services Health and Safety Code §115880 (Assembly Bill 411, Statutes of 1997, Chapter 765)
ADCP	Acoustic Doppler Current Profiler
ADV	Acoustic Doppler Velocimeter
Canonical day	Average day, obtained by averaging all values from the same time of day
CEOF	Complex empirical orthogonal function
CPD	Cycle per day
CTD	Conductivity-temperature-depth instrument system
Delaunay triangulation	A method for generating a grid of triangles from randomly spaced data points on a plane
Eigenvector	Spatial part of an EOF mode
Ekman layer	A layer of water at the top of the ocean in which the surface wind stress directly affects water motion
Ekman turning	Due to the earth's rotation, the wind-driven flow in the Ekman layer executes a spiral to the right (in the northern hemisphere) as depth increases
Enterococci	Subset of the fecal streptococci group of bacteria useful as indicators of fecal pollution and swimming-associated gastroenteritis, especially in marine waters
EOF	Empirical orthogonal function–a method to extract coherent signals from a spatial array
Fecal coliform	A subset of the total coliform group of bacteria that are more specific indicators of fecal pollution
FIB	Fecal indicator bacteria–collective term for total coliform, fecal coliform, and enterococci
Foreman tidal programs	Manuals for tidal current analysis and prediction
GMT	Greenwich Mean Time
Hodograph	A plot of the velocity of a particle as a function of time, with the velocity represented by the vector from the origin to a point on the hodograph
HB PIII	Huntington Beach Shoreline Contamination Investigation, Phase III
HHW	Higher high water
HLP	Hourly low-pass-filtered data
MEC	MEC Analytical Systems, Incorporated
MEM	Maximum Entropy Method
MF	Membrane filter analytical technique–one of the standard test methodologies used for daily permit-compliance testing for indicator bacteria
MGD	Million gallons per day
MLLW	Mean lower low water
MM	Monthly geometric mean standards of pollution, set by AB411
MPN	Most probable number of bacterial organisms per 100 mL–statistical estimate of the mean density of coliform bacteria in a sample

MTF	Multiple tube fermentation–a standard analytical technique used for daily permit-compliance testing for indicator bacteria, based on MPN
NaN	Not a Number–term assigned for unavailable or bad data points
NPDES	National Pollution Discharge Elimination System
NPS	Naval Postgraduate School
OCHCA	Orange County Health Care Agency
OCSD	Orange County Sanitation District
Plume Mapping/ Tracking SPS	One-year plume study using a towed, undulating underwater vehicle
POTW	Publicly owned treatment works
PST	Pacific Standard Time
RSB multiport diffuser	Roberts-Schneider-Baumgartner initial dilution model for submerged wastewater discharges
SAIC	Science Applications International Corporation
SIO	Scripps Institution of Oceanography
SPS	Strategic Process Study
SS	Single-sample standards
T-S	Temperature-salinity
Thermistor	Temperature recording device
Total coliform	Genera of bacteria from the family Enterobacteriaceae used to assess the sanitary quality of water
Towyo lines	Transects along which samples were collected.
TSS	Total suspended solids (particle dry weight retained on a 0.45 micron
TUV	Towed undulating vehicle
UCI Hypothesis	Combination of impact on shoreline by wastewater as a result of oceanographic processes such as internal waves and entrainment by thermal discharge from power plant

CHAPTER 1. INTRODUCTION AND BACKGROUND

George Robertson, Leslie Rosenfeld, Marlene Noble,
Peter Hamilton, Burton Jones, John Largier, and Jingping Xu

1.1. Project Overview

In July 1999, the Orange County Health Care Agency (OCHCA) began a series of beach closures in Huntington Beach, California (Figure 1-1), due to levels of total coliform, fecal coliform, and enterococci bacteria that exceeded newly applied beach sanitation AB411 standards (Table 1-1). (The actual implementation date for AB411 was July 27, 1999.) The OCHCA began closing beaches on July 3, 1999, because the level of contamination was thought to be of sewage origin, and was indicative of human sewage contamination. Since that time, surfzone bacterial levels from Orange County Sanitation District's (OCSD) monitoring stations located north of the Santa Ana River and, in particular, at sites near and adjacent to the AES Corporation's Huntington Beach power generation plant have continued to exceed the AB411 standards on some days during the summer. Beginning in 1999, many land, estuarine, and coastal ocean-based studies were conducted to identify the source or sources of the bacteria (Table 1-2). These investigations suggested that the elevated bacteria levels occurred primarily during late spring and summer and coincided with periods of maximum tidal range (i.e., spring tides). Grant et al. (2000) identified the offshore wastewater discharge from OCSD's outfall as a potential source for the observed shoreline contamination and hypothesized that this wastewater could be impacting the shoreline as the result of oceanographic processes such as internal waves, entrainment by the thermal discharge from the AES Corporation power plant, or a combination of both (i.e., the "UCI Hypothesis"). In the summer of 2001, an extensive coastal ocean measurement program was undertaken to determine if a significant amount of bacteria from the outfall was transported to the adjacent shoreline. This project was the Huntington Beach Shoreline Contamination Investigation, Phase III (HB PIII) of the Orange County Sanitation District's investigation of possible sources of the bacteria found on Huntington Beach. This report is a summary of the results of the Phase III investigations.

1.2. Orange County Sanitation District (OCSD) Operations

OCSD is the third largest southern California publicly owned treatment works (POTW). They continuously discharge treated wastewater from an ocean outfall located approximately 7 km offshore from Huntington Beach (Figure 1-2). At the time of this study the average daily discharge was almost $1x10^9$ L/day (234 MGD) of wastewater that represented an approximately 50:50 blend of advanced primary- and secondary-treated effluent to attain a minimum of 75% reduction in suspended solids concentrations (Figure 1-3).

The outfall design incorporates a 1-mile-long, 500-port diffuser located near mooring station HB12 (Figure 1-2) at a depth of 60 m in a typically stratified coastal environment. This diffuser allows for significant initial dilution of the wastewater plume as the effluent enters the coastal ocean. The minimum initial dilution of 180:1 (the ratio of ocean water to discharged wastewater) contained in OCSD's National Pollution Discharge Elimination System (NPDES) ocean discharge permit was based on modeling done by the California State Water Resources Control Board. Other near-field modeling by Stolzenbach and Hendricks (1997), MEC and Jones (2001), and TetraTech (2002) have demonstrated much higher initial dilutions (Figure 1-4).

1.3. Discharge Processes and Effluent Characteristics

1.3.1. Ocean Discharge Processes

Wastewater discharged through the diffuser ports form a "plume" that disperses in the receiving water environment and becomes progressively diluted with time and distance from the outfall. The rates of both the near-field or initial dilution and subsequent far-field reductions in effluent plume constituent concentrations have important permit compliance, environmental, and human health implications. Physical processes that affect mixing and dispersion of the plume are described briefly in this section. The information concerning the general design and function of the ocean outfall provides background information for the evaluations of impacts to receiving water quality.

Plume dispersion can be modeled as a two-step process: (1) "near-field" mixing, in which the buoyant plume rises and mixes with ambient seawater until it reaches its equilibrium density or rises to the sea surface; and (2) "far-field" dispersion by ambient currents with passive diffusion due to ambient turbulence (Figure 1-5). The buoyancy phase lasts on the order of minutes, while the passive dispersion phase lasts up to several days (Wu et al., 1994).

Effluent is discharged as a jet from each of the diffuser ports, with initial momentum due to hydrostatic pressure. The individual jets merge as a plume above the diffuser and rise due to buoyancy caused by the density difference between the effluent and ambient seawater. Regions above the diffuser, in which plume motions transition from a jet to a buoyant plume, are proportional to the momentum flux and buoyancy flux. During plume rise, effluent continues to mix with ambient seawater, diluting the plume constituents and increasing effluent density until it reaches equilibrium with ambient water or the sea surface. After reaching the surface or equilibrium density layer, the plume spreads horizontally, and further mixing with ambient seawater ceases above the bottom of the plume. When overlying waters are stratified because of changes with depth in density properties, the plume rises to the bottom of the pycnocline. The structure of buoyant plumes is dependent on ambient density stratification and current fields (Washburn et al., 1999).

Initial dilution refers to dilution from mixing between the plume and ambient seawater that occurs until the plume loses its initial momentum and reaches a density in equilibrium with the surrounding water. Dilution is defined as the reciprocal of the volume concentration, and is a function of location and time. From an engineering perspective, the design variables of primary importance in determining initial dilution are the overall length of the diffuser and depth of the discharge. The number of diffuser ports and port spacing are of secondary importance (Koh, 1983). OCSD's diffuser was designed to achieve an initial dilution of 148:1, although recent assessments based on hourly current velocity, receiving water temperature, and effluent flow data during June 15, 1999, through June 24, 2001, indicated an average flux-averaged dilution of 341:1 with an average depth of maximum plume concentration (i.e., minimum dilution) of 36 m below the sea surface (Table 1-3, Figure 1-6) (TetraTech, 2002).

The three primary factors affecting dispersion of the plume are density stratification, local current field, and turbulence levels. Far-field dispersion transports the plume, distorts the plume

shape, and promotes additional dilution due to small-scale turbulent mixing, shear dispersion, and horizontal mixing. Plume width increases while thickness decreases due to gravitational collapse (Washburn et al., 1999).

As initial plume momentum dissipates, effluent particles with densities greater than seawater sink, which contributes to separation of dissolved and particulate phases of the plume. The behavior and fate of the particulate fraction is important because the major fraction of metals, bacteria, and organic constituents are associated with small effluent particles (discussed below). Effluent particles sink at varying speeds and distances from the outfall, depending on their size, density, and depth-dependent velocities of horizontal and vertical currents. The median settling velocity of particulate matter in sewage is about 10^{-3} cm/sec, although rates vary widely (Csanady, 1983). Measurements of OCSD's effluent showed that approximately 10% of particles sank at a rate of 10^{-3} cm/sec, whereas the majority of particles appeared to be neutrally buoyant in seawater (SAIC et al., 2001).

The fundamental processes affecting the fate of effluent particles are settling, coagulation, and ingestion by organisms (Morel and Schiff, 1983). Settling of wastewater particles is related primarily to particle size and density, although this is a complex process due in part to the heterogeneity of final effluent, which may vary daily as well as seasonally (Baker et al., 1995), and the complex dynamic formation and dissolution of particle aggregations following discharge to the ocean. The importance of coagulation is related to particle density and turbulence of receiving waters. Generally, the effects of coagulation are minimal for wastewater with low particle concentrations because this reduces the probability of particle-to-particle contact. Consequently, settling rates typically are lower for more dilute particle concentrations. Conversely, higher turbulence levels increase the probability of particle interactions, and thus increase particle settling rates. Particle coagulation, biological consumption and repackaging, and aggregation with fine particles in the "flocculent" layer at the sediment-water interface are important processes that accelerate settling rates above those estimated from settling of individual particles alone (Stolzenbach et al., 1992).

1.3.2. Effluent Characteristics

Municipal wastewater is not homogenous but consists of a mixture of aqueous and particulate components with particles being complex mixtures of organic and inorganic solids. The complex composition of the discharged effluent affects the behavior, and ultimate fate and impact, once it enters receiving waters. Information concerning the size distributions, settling behavior, and contaminant concentrations of effluent particles has important implications for understanding the impacts of effluent discharges on receiving waters and predicting future impacts associated with changes in the effluent composition. SAIC et al. (2001) characterized the physical and chemical composition of OCSD's final effluent and the size distribution and settling behavior in seawater of effluent particles. These findings are summarized below.

Final effluent is considerably warmer and fresher than ambient receiving waters. Temperatures ranged from 23.1-27.1°C with an average of 25.1°C, while salinity averaged 2.25 psu and ranged from 1.21 to 2.59 psu. Total suspended solids (particle dry weight retained on a 0.45 micron filter) in the final whole effluent averaged 74.4 mg/L (Table 1-4). Mean and median

particle sizes in whole effluent averaged 0.0276 mm (27.6 microns) and 0.0168 mm (16.8 microns), respectively (Table 1-5), with a majority (85-90%) of the total TSS concentration represented by the three smallest particle size classes. Particle settling experiments showed that 2.8% of the particles settled to the bottom of the settling chamber within the first hour, 4.2% settled within six hours, 6.1% settled within 12 hours, and 7.9% settled within 24 hours. The cumulative particle recovery after 96 hours represented 12% of the initial particle mass. Bacteria were almost exclusively associated with the smallest effluent particles. Whole effluent samples contained an average of $2x10^7$ MPN/100 mL total coliform bacteria, $9.7x10^6$ MPN/100 mL fecal coliform bacteria, and $2.7x10^5$ MPN/100 mL enterococci bacteria. However, for most effluent constituents, the predicted changes to receiving waters associated with this discharge after initial dilution are relatively small (Table 1-6).

1.4. Huntington Beach Phase III (HB PIII) Hypotheses

The UCI Hypothesis and discussions about other potential cross-shelf transport mechanisms raised several important ocean process and transport questions which OCSD did not have sufficient data to address. The overall problem statement was that bacteria concentrations have periodically exceeded recreational water AB411 bacteria standards compliance limits and resulted in summertime beach closures or postings. The objectives for HB PIII were to (1) characterize the physical oceanographic processes involved in possible cross-shelf transport of the offshore wastewater plume to the vicinity of the AES Corporation thermal discharge outfall or other nearshore locations off Huntington Beach; (2) determine the potential for a causal link between bacteria in the offshore wastewater discharge and beach postings or closures; and (3) if possible, determine if the conditions during the summer of 2001 were similar to those of 1999 and other years with unusual surfzone bacteria levels.

OCSD, along with U.S. Geological Survey (USGS), Naval Postgraduate School (NPS), Scripps Institution of Oceanography (SIO), the University of Southern California (USC), Science Applications International Corporation (SAIC), and MEC Analytical Systems, Incorporated (MEC), developed and carried out a large-scale hydrographic and physical oceanographic study in the spring and summer of 2001, known as the Huntington Beach Shoreline Contamination Investigation, Phase III (HB PIII). As part of the study design phase, a Technical Advisory Committee (TAC) was established by OCSD to provide input from a wide range of groups, including other government agencies and non-government organizations, such as local environmental groups and private citizens. From these TAC meetings a series of hypotheses were developed for the study to test (Table 1-7).

1.4.1. Hypothesis Overview

To support the hypothesis posed by Grant et al. (2000), there would have to be a process or processes that meet the following conditions 1 and 2, as well as either 3 or 4: (1) rapid cross-shelf transport of the plume; (2) dilution and die-off rates of bacteria that are sufficiently low to prevent adequate dissipation of these indicators of the plume; (3) entrainment of the plume without significant dilution in the power plant thermal discharge; or (4) a mechanism for the direct transport of wastewater plume through the surfzone to the beach. Results from previous and ongoing OCSD monitoring have shown the following: (1) currents predominantly flow

parallel to isobaths (that is, either upcoast or downcoast); (2) there is some cross-shelf transport of the plume, but it has never been seen to impact the beach; (3) the wastewater plume is submerged from late spring through fall because it is trapped below the seasonal thermocline during these stratified periods; and (4) the extensive studies conducted during the summer of 1999 did not indicate any relationship between OCSD's discharge and surfzone bacteria seen at Huntington Beach.

Regarding Hypotheses B and C (Table 1-7), the TAC believed that these mechanisms are less likely to cause surfzone water-quality impairment than the mechanisms described in Hypothesis A. Therefore, it was not recommended that the study be designed explicitly to test these hypotheses. However, some data collected for testing Hypothesis A may be analyzed to provide limited testing of Hypotheses B and C.

1.5. Huntington Beach Phase III (HB PIII) Program Elements

The HB PIII study consisted of several integrated and complementary program elements that collected both temporal and spatial data to evaluate cross-shelf transport processes, including currents, wind, barotropic and baroclinic tides, internal waves, and upwelling. The study components included:

1) Current speed and direction, temperature, and conductivity measurements at multiple, fixed moorings;
2) Water sampling using hydrographic profiling and discrete measurements of specific water-quality parameters used to identify the wastewater plume;
3) Standard daily sampling and analysis of bacterial levels in the surfzone collected five days per week by OCSD and additional hourly sampling of surfzone bacteria during six hydrographic cruises conducted during spring tides; and
4) Near-field plume modeling.

In addition, historical and other concurrent data were used to evaluate any potential correlations between beach contamination events and concurrent meteorological and oceanographic conditions.

A description of the exact sites in the moored array, the hydrographic profiling program, and the bacterial sampling is given in Chapter 2. This section of the report also describes the methods used to process the data collected in this large, multidisciplinary program.

1.6. References

Baker, E.K., P.T. Harris, B. Kensett-Smith, D.F. Bagster, and D.M. Nobbs. 1995. Physical properties of sewage particles in seawater. Marine Pollution Bulletin v. 34, p. 247-252.

Csanady, G.T. 1983. Advection, diffusion, and particle settling. Chapter 5, in E.P. Myers and E.T. Harding (eds.), Disposal of municipal wastewater: Impacts on the coastal environment. MIT Sea Grant College Program III. MIT Technical Reports MITSG 83-33.

Grant, S., C. Webb, B. Sanders, A. Boehm, J. Kim, J. Redman, A. Chu, R. Morse, S. Jiang, N. Gardiner, and A. Brown. 2000. Huntington Beach Water Quality Investigation Phase II: An analysis of ocean surfzone, watershed, sediment and groundwater data collected from June 1998 through September 2000. Prepared for National Water Research Institute, County of Orange, Cities of Huntington Beach, Fountain Valley, Costa Mesa, Santa Ana, Newport Beach and Orange County Sanitation District.

Koh, R.C.Y. 1983. Delivery systems and initial dilution. Chapter 4, in E.P. Myers and E.T. Harding (eds.), Disposal of municipal wastewater: Impacts on the coastal environment. MIT Sea Grant College Program III. MIT Technical Reports MITSG 83-33.

MEC Analytical Systems, Inc., and B.H. Jones. 2001. Special study plume tracking, August 1999-September 2000. Prepared for the Orange County Sanitation District, Fountain Valley, California. Vols. 1-3.

Morel, F.M.M and S.L. Schiff. 1983. Geochemistry of municipal waste in coastal waters. Chapter 6, in E.P. Myers and E.T. Harding (eds.), Disposal of municipal wastewater: Impacts on the coastal environment. MIT Sea Grant College Program III. MIT Technical Reports MITSG 83-33.

Science Applications International Corporation (SAIC), MEC Analytical Systems, Inc., and CRG Marine Laboratories, Inc. 2001. Strategic process study: Final effluent characterization, Phase I. Prepared for Orange County Sanitation District (OCSD), Fountain Valley, California.

Stolzenbach, K.D., K.A. Newman, and C.S. Wong. 1992. Aggregation of fine particles at the sediment-water interface. Journal of Geophysical Research, v. 97, p. 17,889-17,898.

Stolzenbach, K. and T. Hendricks. 1997. Analysis of effluent plume transport. Report prepared for the Orange County Sanitation District. OCSD, Fountain Valley, California. 9 pp + Appendices.

TetraTech. 2002. Nearfield and farfield modeling of an ocean outfall wastewater discharge. Final Report prepared for the Orange County Sanitation District (OCSD), Fountain Valley, California, November 1, 2002. 50 p.

Washburn, L., S. Stone, and S. MacIntyre. 1999. Dispersion of produced water in a coastal environment and its biological implications. Continental Shelf Research, v. 19, p. 57-78.

Wu, Y., L. Washburn, and B.H. Jones. 1994. Buoyant plume dispersion in a coastal environment: evolving plume structure and dynamics. Continental Shelf Research, v. 14, p. 1001-1023.

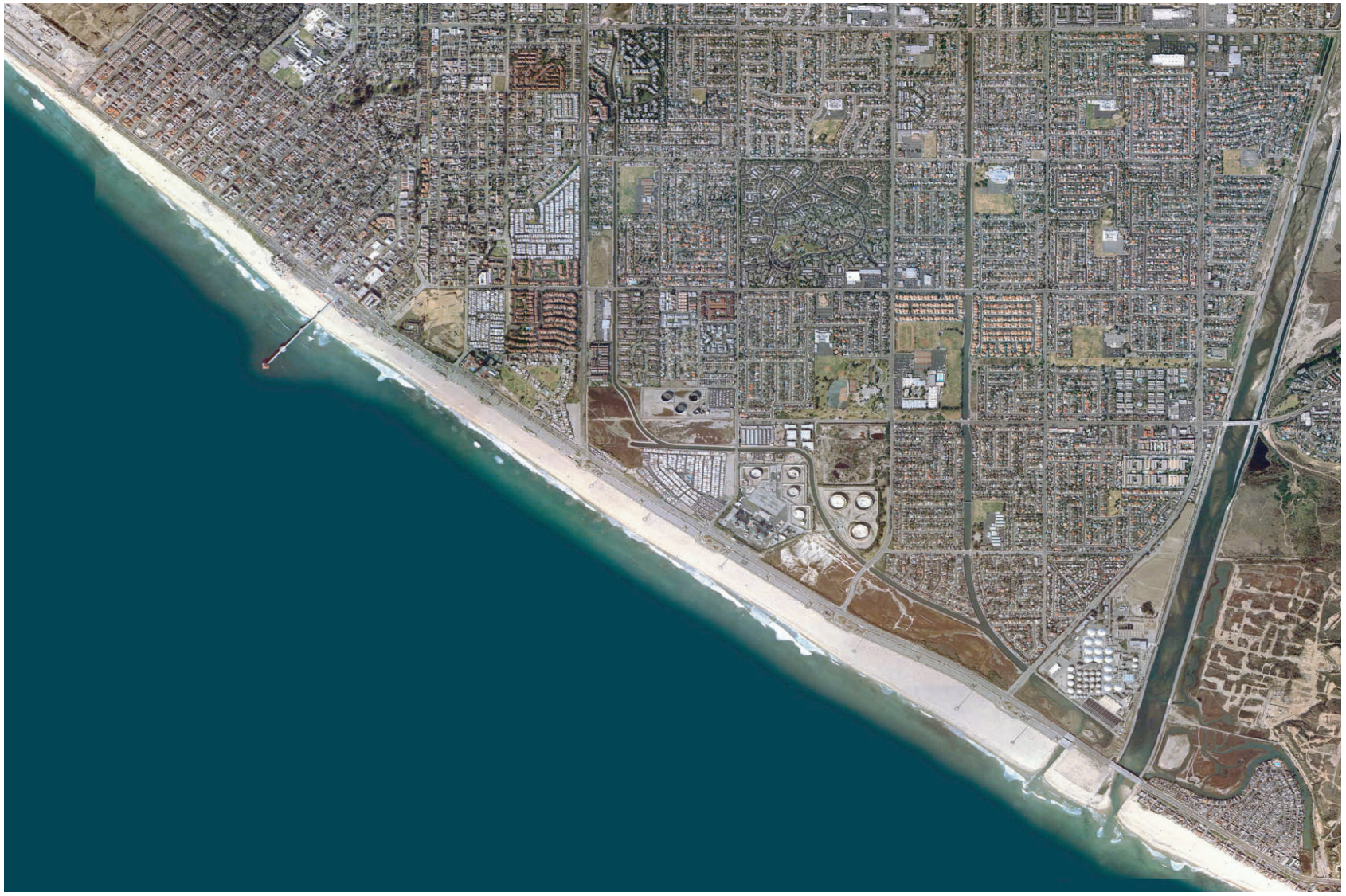

Figure 1-1. Area of beach postings and closures due to elevated bacterial measures. Huntington Beach, CA.

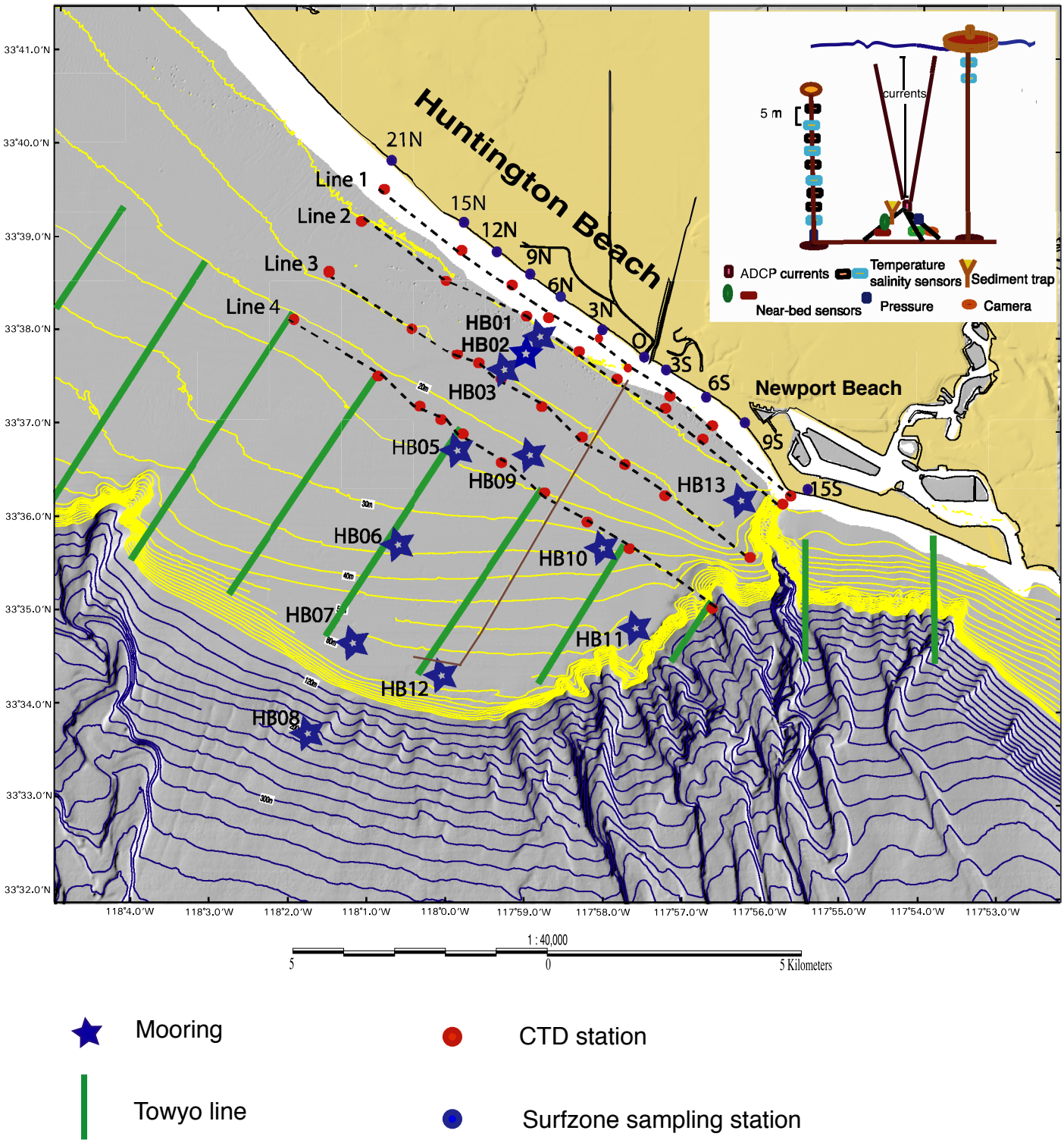

Figure 1-2. Map of the region, mooring sites, surfzone sampling stations, and instrumentations of a typical mooring (inset).

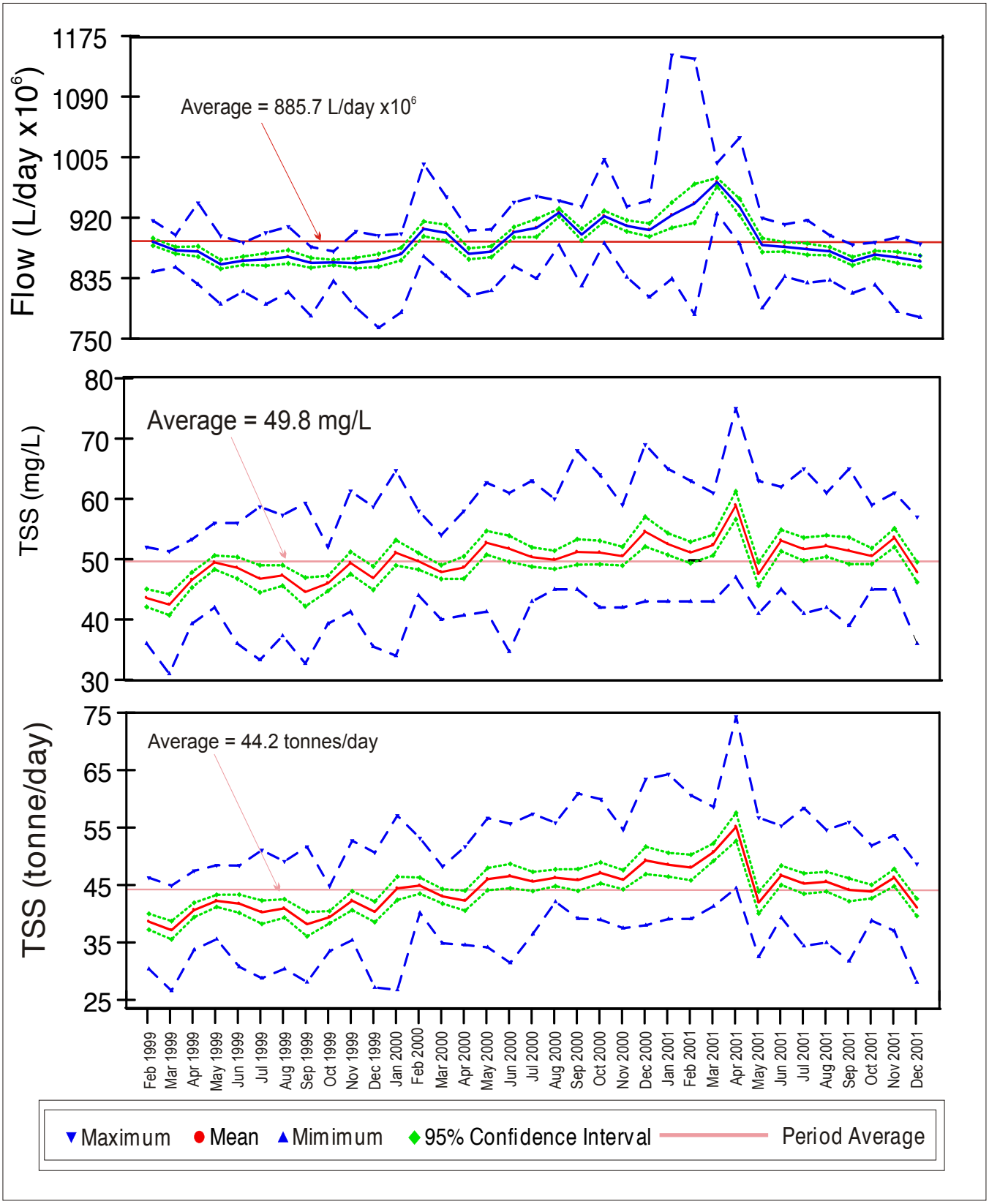

Figure 1-3. Trends in OCSD's effluent discharges to the San Pedro Shelf region. Monthly maximums, minimum averages and 95% confidence interval for February 1999 through December 2001.

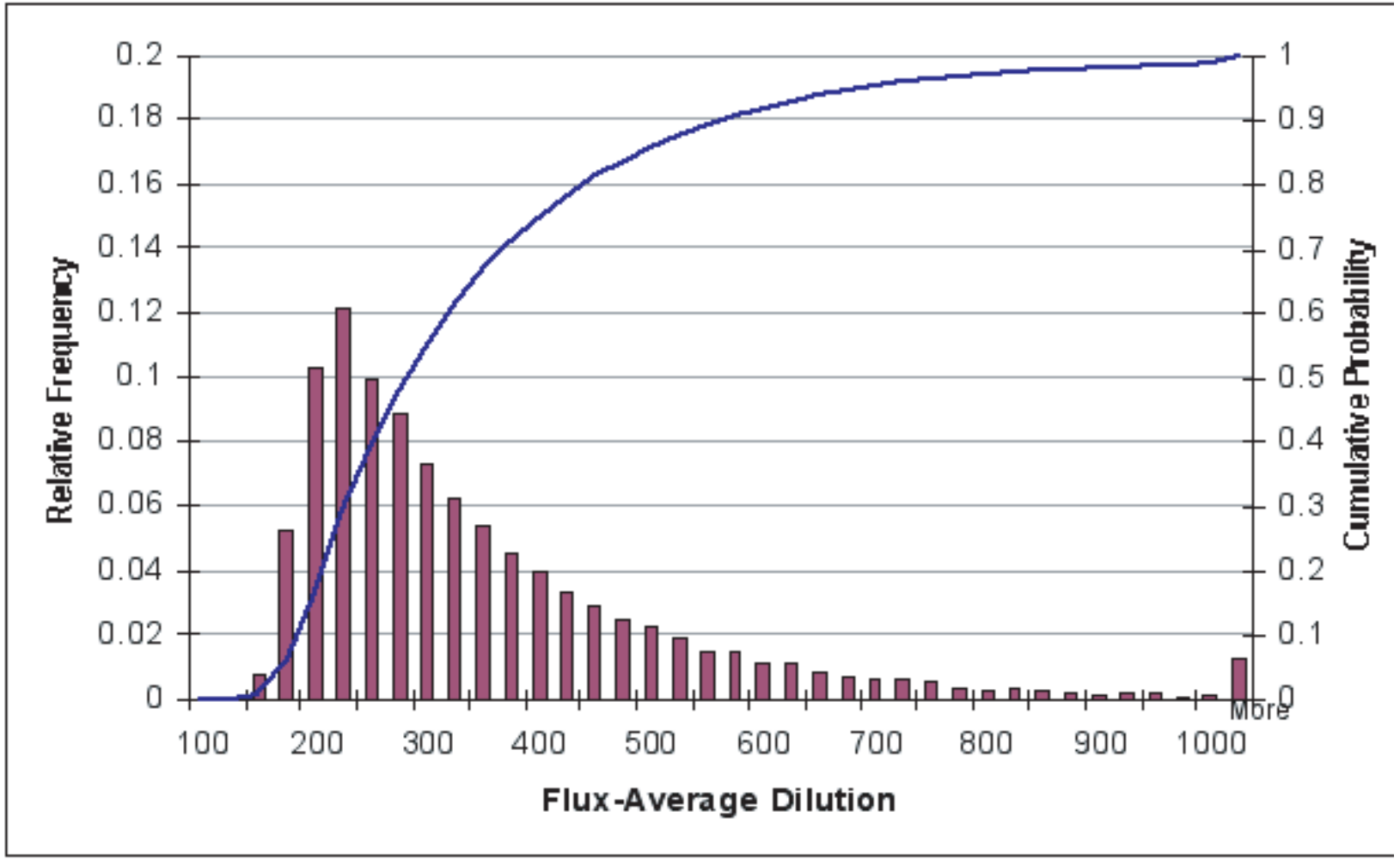

Figure 1-4. Histogram and cumulative distribution of flux-averaged dilution as predicted by visual plumes for the period of June 15, 1999, 0500, to June 24, 2001, 1100 GMT (Source: TetraTech 2002).

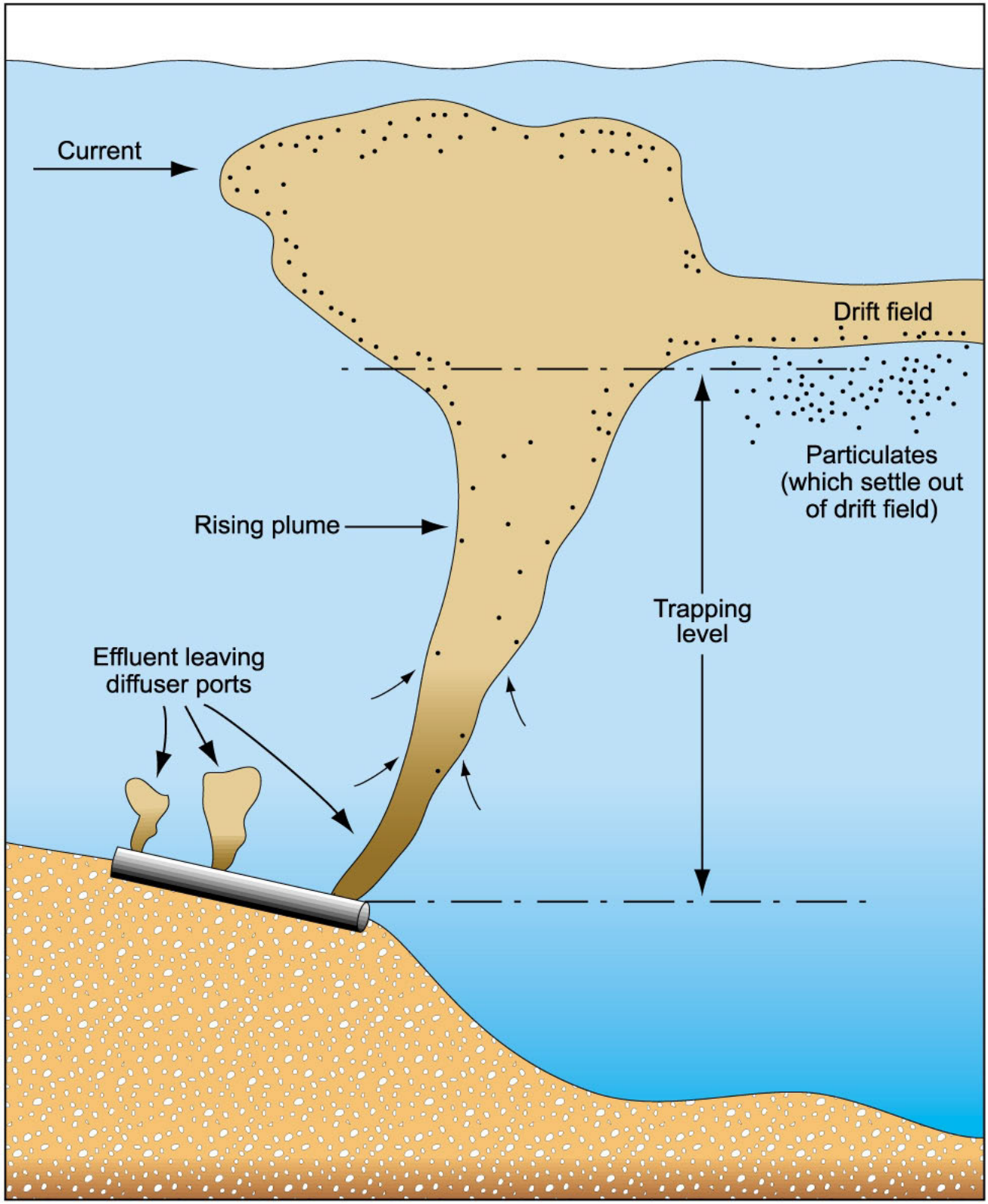

Figure 1-5. Initial waste field generated by marine outfall (Tetra Tech, 2000)

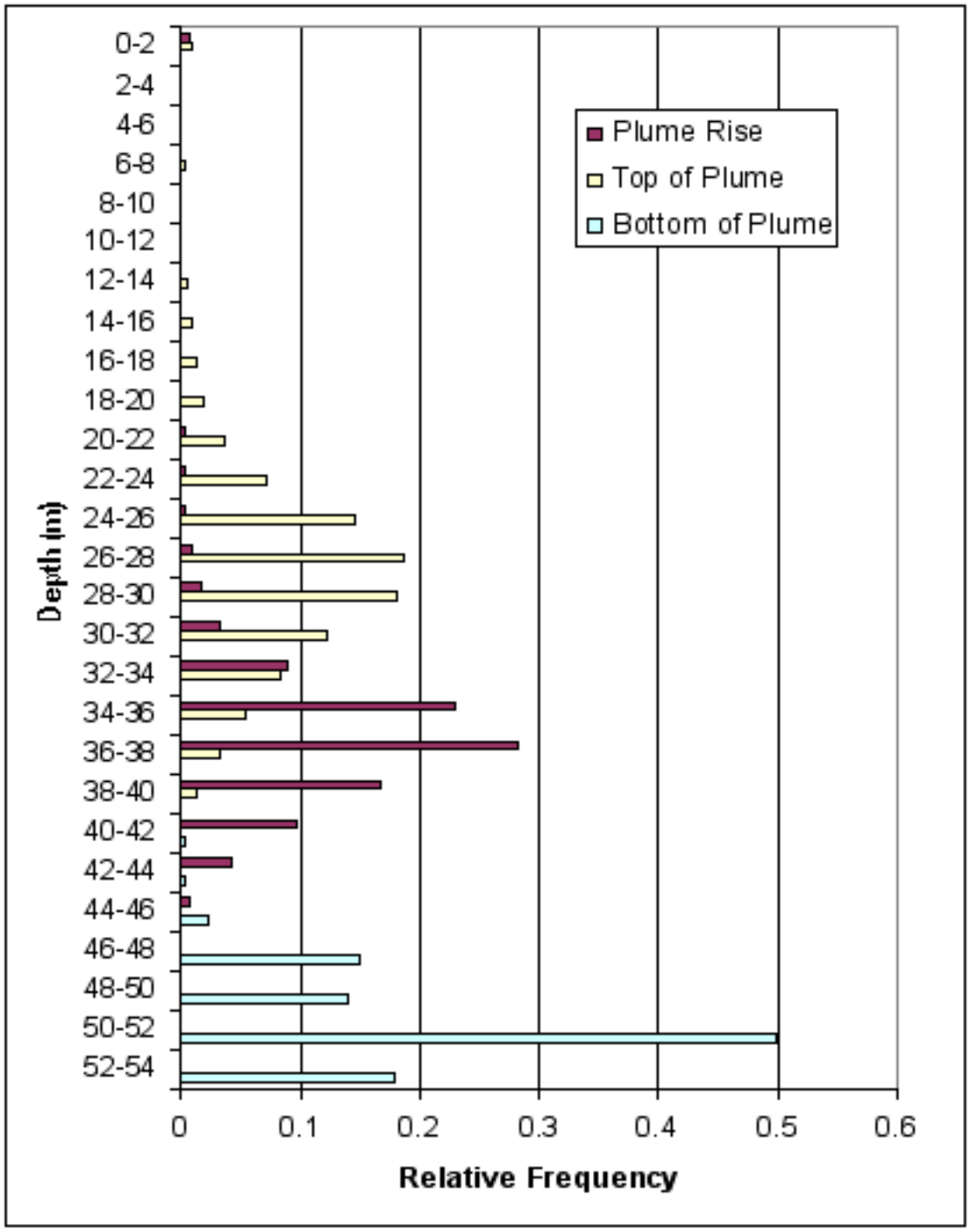

Figure 1-6. Histogram of depth of plume rise, top of plume, and bottom of plume as predicted by visual plumes for the period of June 15, 1999 0500 to June 24, 2001 1100 GMT (Source: TetraTech 2002).

Table 1-1. California Department of Health Services AB411 Objectives.

Measure	Single Sample Maximum Organisms per 100 mL	Geometric Monthly Mean Maximum Organisms per 100 mL
Total Coliform	10,000 1,000 (if Fecal/Total Ratio ≥0.1)	1,000
Fecal Coliform	400	200
Enterococci	104	35

Table 1-2. Summary of studies related to Huntington Beach shoreline contamination.

Study	Description	Purpose	Time Frame	Result
Picket Line	Microbiology samples taken along a transect parallel to shore ~1000 feet offshore.	Determine if the OCSD offshore discharge was coming onshore.	May, July and August 1999.	No samples with significantly elevated levels of bacteria. Higher values in the surfzone than along the picket line.
Closed circuit TV sewage infrastructure inspection	Inspection of OCSD, Huntington Beach and State Park sewer lines.	Identify breaks, joint offsets or significant root infiltration that could cause leakage.	June 30 to October 7, 1999	Identified breaks were repaired, with no effect on beach contamination levels.
Monitoring Wells	Groundwater sampled from five 30 to 60-foot wells via peristaltic pump.	Determine if there was a plume migrating to surf zone from Coast Trunk line or other facilities.	July 29-30, 1999	No contaminated samples were found.
Ground Penetrating Radar and Hydropunching	Near surface geology and groundwater was sampled.	Determine if the bedding around sewer lines, power plant lines, or local groundwater/ geological features were functioning as a transportation mechanism for bacterial contamination.	August 9-28, 1999	No contaminated samples were found.
Offshore triangle	Water samples were collected from sites along the beach, along the outfall pipe and at depth along three offshore transect lines.	Determine if the underground portion of the offshore OCSD outfall pipe was contributing to the beach contamination.	August 13, 1999	Offshore samples did not contain significantly elevated levels of bacteria.
Talbert Marsh (TM) and Santa Ana River (SAR) water quality and citrus studies	Microbiological and nutrient water samples collected from TM and outfall. Grapefruit and oranges were dropped at the ocean outlets of TM and SAR and tracked.	Determine if a transport mechanism to surf zone existed for the effluent water from TM and SAR.	August 30 and September 16, 1999.	Fruit washed ashore onto Huntington Beach in the areas of highest bacterial counts. The water quality results did not confirm the physical info from the citrus study.
TM and SAR overnight studies	Densities of indicator bacteria were measured at the outlets to TM and SAR at 30 min. intervals.	To determine whether bacteria Leave TM or SAR at low tides and enter the surf zone.	September 8-9, 1999	Inconclusive. High bacteria levels on the beach did not correlate with TM and SAR water.

Table 1-2, cont. Summary of studies related to Huntington Beach shoreline contamination.

Study	Description	Purpose	Time Frame	Result
Outfall Dye studies	Rhodamine dye was injected into the effluent and tracked.	Determine if the near-shore (buried) portion of the OCSD outfall pipe was leaking and to track the offshore plume.	September 30, 1999	No evidence of dye shoreward of the diffuser (offshore) portion of the pipe. Offshore plume was tracked moving down coast and shoreward.
OCSD Phase I Summary Report	Summarized the studies listed above and performed by OCSD during the Summer of 1999	Provide summary of the OCSD sanitary survey and related work to date.	December 1999	OCSD sewers were not leaking, outfall was not leaking, plume did not appear in the surfzone, and some local onshore contamination sources were pointed out.
UCI Talbert Marsh tidal transport study	Hydrology, bacteriology and Chemistry of water flowing in and out of TM was characterized.	Determine if the Talbert Watershed is a significant source of indicator bacteria to the near-shore area of Huntington Beach.	December 7-21, 1999	Pump station discharges increased the near-shore loading of total coliforms, but didn't explain all the contamination at the beach. TM also appeared to be a significant source of episodic near-shore loading of enterococci.
USC Sea Grant Huntington Beach Closure Investigation: Technical Review	An expert panel was convened by USC to review the 1999 OCSD investigation.	The panel was asked to address: 1) Were the proper studies done and were they correctly interpreted 2) What should the next set of studies consist of 3) What should be the longer-term research priories for future source investigations? 4) What lessons learned could be transferred to others?	Panel Verbally Reported in February 2000 with a final report in October 2000	The panel agreed with the OCSD study conclusion that the most likely source was land-based and that the areas sewer lines and offshore outfall had been effectively eliminated as a source. They also recommended using more source-tracking techniques and developing better onshore and offshore hydrodynamic models.

Table 1-2, cont. Summary of studies related to Huntington Beach shoreline contamination.

Study	Description	Purpose	Time Frame	Result
MEC: Huntington Beach Closure: Relationships Between High Counts of Bacteria on Huntington Beaches and Potential Sources	An OCSD consultant ran a series of statistical analyses (correlation study) on various available environmental factors for the summer of 1999. Based on the strongest correlations, four scenarios were hypothesized to account for the results.	To determine if statistics could reveal evidence of potential sources in the data that could not have been seen by just reviewing the data.	January 2000	Bacteria levels at the beach during High/Ebb tides and Low/Flood tides seem to have different contamination mechanisms. Variables that most correlated included: storm water pump station pump volumes, maximum tide, bird counts, shore currents, pycnocline depth and minimum tide levels.
UCI/Moffatt & Nichol/URS/Komex Huntington Beach Water Quality Investigation Phase II: An Analysis of Ocean, Surfzone, Watershed, Sediment and Groundwater Data Collected from June 1998 through September 2000	Investigation of contaminate transport by groundwater, long-shelf currents inside surfzone and onshore nuisance flows.	Evaluate transport efficacy of near-shore currents, evaluate utility of dry-weather diversion projects, and catalogue sources of indicator bacteria in the Talbert watershed.	December 15, 2000	No single contaminate source could be identified. Additional research on contribution of contaminants to surfzone by the Santa Ana River and potential interaction between the OCSD outfall and the AES power plant cooling water system.
OCSD On Shore Investigation July – October 2001	Investigate all potential on shore contamination sources in the Huntington Beach area.	Find on shore problems and fix them.	July – October 2001	A number of existing and suspected contamination sources were identified. Several potential sources were repaired during the project.

Table 1-2, cont. Summary of studies related to Huntington Beach shoreline contamination.

Study	Description	Purpose	Time Frame	Result
UCI Cross-Shelf Transport at Huntington Beach.	Analyses of current and temperature data from Huntington Beach shoreline and OCSD ocean outfall.	To determine if a correlation exists between the onshore and offshore water temperatures which may imply onshore movement of offshore cold water.	March 2002	Correlation exists between onshore and offshore cold water events. However, it's not clear where the on shore cold water came from since the circulation patterns, especially in the near-shore area are complex.. No evidence of shoreline contamination associated with correlation.
UCI Coastal Runoff Impacts Study (CRIS)	Measured flow and water quality at mouth the Santa Ana River, Talbert Marsh, Greenville-Banning Channel, and Newport Slough.	To evaluate sources and dynamics of pollution in the Santa Ana River Watershed and compare to Talbert Marsh Watershed.	June/July 2001	Fecal indicator bacteria generated locally from land-based sources. Fecal indicator viruses were associated with cold ocean water.
UCSB Association of Urban Runoff with Coastal Water Quality in Orange County, California	A temporal and spatial analysis of 2 years of data	To evaluate the relationship between storm events, urban runoff, and water quality.	Data collected from 1997 through 1999.	The primary source of North Orange County's coastal pollution is urban runoff discharge by the San Gabriel, and Santa Ana Rivers.
OCSD Expert Panel Review of Huntington Beach Investigations	To evaluate the scientific work completed to date.	Determine whether data collection and analysis were appropriate to answer the scientific questions about physical transport methods.	February 2002 through October/November 2002	Initial review supports investigator position that no connection could be made between the offshore wastewater plume and surfzone bacteria.

Table 1-2, cont. Summary of studies related to Huntington Beach shoreline contamination.

Study	Description	Purpose	Time Frame	Result
Huntington Beach Phase III Shoreline Contamination Investigation	Investigate hypothesis that the OCSD plume is impacting Huntington Beach shoreline.	To (1) measure physical oceanographic transport mechanisms exist and (2) determine shoreward transport of offshore plume.	June-October 2001	Transport mechanisms exist, but the data always showed a break between the offshore plume and shoreline bacteria. The 2001 elevated bacteria levels did not appear to be linked to the wastewater effluent discharges from the OCSD outfall

Table 1-3. Statistics of the time-series dilution modeling results (Source: TetraTech 2002).

	Flux-Averaged Dilution	Centerline Dilution	Depth Below Surface of Top of Plume (m)	Depth Below Surface of Plume Rise (m)	Depth Below Surface of Bottom of Plume (m)	Mixing Zone Length (m)
Mean	341	297	27.6	36.4	50.4	72
Median	284	247	27.9	36.7	51.3	59
Minimum	119	103	0	0	40.9	10
Maximum	2411	2097	41.6	45.9	54.0	745

Table 1-4. General physical and chemical properties of whole effluent (Source: SAIC et al. 2001).

Temp (°C)	DO (mg/L)	pH	Salinity	TSS (mg/L)	COD (mg/L)	NH_4 (mg/L)	TOC (mg/L)
25.1	1.52	7.2	2.25	74.4	188	72.0	19

Table 1-5. Average mean and median effluent particle sizes (mm) and proportion (%) by soil size categories for LASER particle size analysis (volume) of whole effluent (24 hour composite sample) (Source: SAIC et al. 2001).

Size		Proportion				
Mean Diameter (mm)	Median Diameter (mm)	Sand (0.25 – 1.0 mm)	Fine Sand (0.125 -0.25 mm)	Very Fine Sand (0.063 - 0.125 mm)	Silt (0.004 - 0.063 mm)	Clay (<0.004 mm)
0.0276	0.0168	0	0.3	14.2	74.7	10.9

Table 1-6. Summary of measurements (Source: SAIC et al. 2001) and predicted changes (compared to natural seawater at 60-m depths) from the wastewater discharge, following initial dilution of 180:1.

Parameter	Final Effluent (mean)	Approx. Natural	Predicted Change (assumes max. difference)
Temperature (°C)	25.1	9-12	Increase <0.1
Salinity (ppt)	2.25	33.5-34	Decrease <0.2
Dissolved Oxygen (mg/L)	1.52	4-6	Decrease <0.03
pH	7.2	7.4-7.9	Change l<0.003
Ammonium (mg/L)	72.0	<0.02	Increase <0.4
Total Coliform Bacteria (MPN/100 mL)	$2.0x10^7$	0	Increase ≤111,111
Fecal Coliform Bacteria (MPN/100 mL)	$9.7 x10^6$	0	Increase ≤53,889
Enterococci (CFU/100 mL)	$2.7 x10^5$	0	Increase ≤1,500

Table 1-7. Summary of hypotheses for the Huntington Beach Shoreline Contamination Investigation, Phase III. May-October 2001.

Hypothesis A – Subsurface Transport	
A.1	Oceanographic currents transport wastewater into the near-shore area off Huntington State Beach. • process is exacerbated during stratified periods and large spring tides. • thermocline traps plume at depth. • wastewater is transported cross-shelf by: (a) internal waves, particularly shoaling internal tides, and/or (b) wind induced baroclinic flow • alongshore and cross-shelf currents transport plume to "areas of vulnerability"
A.2	Wastewater is moved from near-shore area into surfzone by: (a) wave induced mixing, (b) power plant plume, (c) upwelling, and/or (d) internal tide/wave run-up
Hypothesis B – Surface Transport Hypothesis	
B.1	Wastewater surfaces offshore because of: (a) upwelling, (b) buoyant particles/grease balls, and/or (c) breaking internal waves.
B.2	Surface currents move wastewater to shore.
Hypothesis C – Sediment Transport Hypothesis	
C.1	Wastewater particles settle out of the plume and onto the ocean floor to create a reservoir of bacteria in the fine sediments.
C.2	There is a net shoreward transport of fine sediments by internal waves and surface waves
C.3	Resuspension of fine sediment under certain conditions brings particles to the shoreline

CHAPTER 2. METHODOLOGY

Peter Hamilton, Burton Jones, John Largier,
Marlene Noble, Leslie Rosenfeld, and Jingping Xu

2.1. Surfzone Bacteria Measurements

Three types of fecal indicator bacteria (FIB) were sampled: (1) total coliform (includes the genera *Escherichia, Citrobacter, Enterobacter,* and *Klebsiella*); (2) fecal coliform (includes the thermotolerant genera *Escherichia* and *Klebsiella*) or alternately *Escherichia coli*; and (3) enterococci (includes *Enterococcus faecalis, E. faecium, E. gallinarum*, and *E. avium*). It was estimated that *E. coli* represents roughly 90% of fecal coliform values, so *E. coli* densities were adjusted up by a factor of 1.1. These organisms are commonly found in the feces of humans and other warm-blooded animals. Although some strains are ubiquitous and not related to fecal pollution, their presence in water is used as an indication of fecal pollution and the possible presence of enteric pathogens. Epidemiological studies have indicated that swimming-associated gastroenteritis is directly related to the quality of bathing water. FIBs have been demonstrated to be valuable in determining the extent of fecal contamination in recreational surface waters, and their density in recreational water samples has been shown to have a predictive relationship with swimming-associated gastroenteritis at marine and fresh-water bathing beaches.

2.1.1. Sampling and Laboratory Methodology

Routine surfzone samples were collected in ankle-depth water 5 days/week, including one weekend day. Samples were generally collected between 0500 and 1000 PST, with sampling proceeding from the northernmost station to the southernmost. Based on 5 years of daily sampling at 24 Los Angeles area sites, Leecaster and Weisberg (2001) estimated that 70% of AB411 single-sample exceedances last only one day, and less than 10% last more than 3 days. Sampling five times per week, as OCSD does, probably misses about 20% of the total and fecal coliform exceedances.

During the six HB PIII hydrographic surveys, hourly surfzone samples were collected for analysis of FIB. This sampling began at 1200 PST on Day 1 of the surveys and concluded at 1200 PST on Day 3.

All FIB samples were collected in sterile 100 mL sample jars and stored on ice at a temperature of 4-10°C and transported to OCSD's laboratory within 6 hours. Sample analysis began as soon as possible after collection, but within 2 hours after its arrival at the laboratory. Detailed sample collection, preservation, and handling procedures are described in detail in OCSD (2001).

During this study OCSD used three methods to quantify coliform bacteria. For daily permit sampling, a multiple tube fermentation (MTF) test was done for total and fecal coliform bacteria. For the total coliform group this includes all aerobic and facultative anaerobic, gram-negative, non-spore forming, rod-shaped bacteria that ferment lactose within 48 ± 3 hours at an incubation temperature of 35.0 ± 0.5°C. For the fecal coliform group, this includes all aerobic and facultative anaerobic, gram-negative, non-spore forming, rod-shaped bacteria that ferment lactose within 24 ± 2 hours at an elevated incubation temperature of 44.5 ± 0.2°C. Results of MTF tests are reported in terms of the Most Probable Number (MPN) of organisms per 100 mL. The MPN is based on specific probability formulas, and is an estimate of the mean density of coliform bacteria in the sample (Table 2-1).

For the HB PIII project, OCSD used a chromogenic substrate coliform test, commonly known as Colilert-18®. The chromogenic substrate test utilizes defined substrate technology for the simultaneous detection of enzymes of total coliform bacteria and *E. coli* based upon both a color change to indicate the presence of total coliform bacteria, and fluorescence under ultraviolet light to indicate the presence of *E. coli*. Quantification is determined by the number of cells that test positive for either FIB and is reported as MPN/100 mL. Detailed laboratory and QA/QC methodology for both methods is contained in OCSD (2001). Some samples collected by the Orange County Health Department were analyzed using membrane filter (MF) technique.

An MF test method for enterococci in water is the standard test methodology used for OCSD's daily permit-compliance testing. The MF test method provides a direct count of bacteria in water based on the development of colonies on the surface of the membrane filter. For the HB PIII samples, OCSD used a chromogenic substrate coliform test, commonly known as Enterolert®. Detailed sample analysis procedures are described in OCSD (2001). The MF method was also used to determine fecal coliform concentrations in some of the samples.

Minimum and maximum detection limits vary depending on the method used, and the sample dilution. Minimum detection limits for total and fecal coliform are generally 10 or 20 MPN/100 mL, and 2 or 10 MPN/100 mL for enterococci. Maximum detection limit for fecal coliform is always 16,000 in this data set. The maximum detection limit for total coliform is most commonly at 16,000, but occasionally at other values (e.g., 24192, 2005). The most common maximum detection limit for enterococci is 400 MPN/100 mL, but sometimes values between 240 and 2005 are at the maximum detection limit.

Figure 2-1 shows the 95% confidence limits as a function of concentration for the MTF method and the Colilert® and Enterolert® methods. Noble et al. (2003) compared results from microbiological analyses of identical formulated samples carried out in 22 laboratories in southern California. They found no significant variation among the three methods described above, except that membrane filtration underestimates fecal coliform. They found that the variability was greatest for the MTF method, and that for all three measurement methods, intra-lab variability exceeded inter-lab variability. Table 2-2 adapted from Noble et al. (2003) shows the error bars around the AB411 single-sample standards (SS) determined from their study.

2.1.2. Interpretation of Microbiological Data

The interpretation of FIB analyses is complicated by the uncertainty in die-off rates of these bacteria and multiple sources of bacteria in the study area. In addition to the effects of dispersion and dilution, bacteria discharged into the environment do not behave in a conservative fashion. Fecal coliform bacteria are best adapted to living in a warm, dark, isotonic, pH-balanced environment with an abundance of food. Following discharge into environmental waters, bacteria levels begin to decline. Environmental factors such as salinity, heavy metals, sedimentation, coagulation and flocculation, solar radiation, nutrient deficiencies, predation, bacteriophages, algae, and bacterial toxins all impact the ultimate fate of the bacteria.

Numerous studies have been conducted examining the die-off rates of *E. coli*, the largest member of the fecal coliform group, in water. Of all the factors affecting survival, the two most important ones appear to be temperature and solar radiation, with cooler temperatures and low

solar radiation the most conducive to survival. Light is not as significant in extremely turbid waters, or once the coliform are deposited in the sediment. It is not clear, however, whether light only makes the organisms more susceptible to inactivation by any of the other factors. Because of the interaction of factors and geographic differences in these factors, there is no single die-off rate that can be universally applied to bacteria die-off. In general, though, the literature supports a time range for 90% of the *E. coli* to die off (T_{90}) to be as short as four to six hours to several days (Chamberlin and Mitchell, 1993).

The total and fecal coliform and enterococci concentrations measured in the surfzone between July 1, 1998, and December 31, 2001, provided by OCSD, were analyzed with respect to their temporal and spatial variability. Station locations are shown in Figures 2-2 and 2-3. The AB411 beach sanitation standards are listed in Table 1-1.

Several types of bacterial "events" were defined in order to reduce 3 FIBs times 18 stations into a few variables, and take advantage of spatial patterns appearing naturally in the data, which indicated that coliform contamination events were more localized and enterococci events more widespread (Figure 2-4). While the event definitions were formulated to ensure that all FIB concentrations exceeding AB411 standards at Huntington Beach were included, it turns out that, taken together, the three event types capture all but a handful of days on which there was an AB411 exceedance anywhere in the HB PIII data set. This approach also has the advantage that it allows treatment of the high temporal resolution sampling periods during the summer of 2001, in a manner consistent with no more than daily sampling during the remainder of 1998-2001. Furthermore, it avoids pitfalls associated with the minimum and maximum detection limits, which vary with the method and dilution used to determine bacteria concentration. Finally, by calculating sets of these events with both the AB411 SS as the triggering level, and the AB411 monthly geometric mean standards (MM) applied to single samples as the triggering level, it is demonstrated in Chapter 3 that the timing of the bacterial events is not highly sensitive to the choice of triggering level.

When total or fecal coliform exceeded AB411 standards at one or more of the stations between, and including stations 3N and 12N during a 24-hour period starting at 0000 PST and ending at 2359 PST, then it was designated that a type 1 event occurred that day. This was done using both the SS, and the MM applied to single samples.

- Total coliform > 10,000 MPN/100 mL (SS); 1,000 MPN/100 mL (MM)
- Total coliform > 1000 MPN/100 mL and total coliform/fecal coliform <10 (SS)
- Fecal coliform > 400 MPN/100 mL (SS); 200 MPN/100 mL (MM)

When, during a 24-hour period from 0000 PST to 2359 PST, enterococci exceeded AB411 standards [(104 MPN/100 mL (SS); 35 MPN/100 mL (MM)] at 3 or more of the numbered stations from 39S to 39N (SAR, TM, D2 AES not included), including at least one of stations 3N to 12N, inclusive, then it was designated that a type 2 event occurred that day. A third type of event was added to ensure that all days on which any of the SS were exceeded in the Huntington Beach area would be included in at least one type of event. A type 3 event was defined as

occurring on any day (PST) during which enterococci exceeded AB411 at any station between, and including stations 3N and 12N, on which there is not a type 1 or type 2 event.

Since there was hourly round-the-clock sampling done during the six hydrographic cruise survey periods during the HB PIII study, there was concern that those days could preferentially show up as having bacterial contamination events due to the nighttime and/or higher frequency sampling, so a surfzone bacterial data set subsampled to daily values was also created. If multiple samples were available for a station for a given PST day, the sample closest in time to that of the average sampling time for that station (calculated over May 1-October 31, 2001) was used. The event analysis described above was also carried out on this daily subsampled data set.

2.2. Hydrographic Measurements

Hydrographic studies were conducted for one 24-hour survey and five 48-hour surveys. Samples were collected at a 40-station sampling grid using a CTD (conductivity-temperature-depth) profiling system and also along 6 transects (labeled Towyo lines) using a towed undulating vehicle (TUV) (Figure 2-2). Onshore-offshore spacing between adjacent stations along the same transect was about 1 km, with about 2 km between adjacent stations in the alongshore direction (Figure 2-2). Surveys during the study period were conducted on May 21-22, June 19-21, July 5-7, July 19-21, August 19-21, and September 15-17, 2001. For each survey, sampling began and ended at 1200 PST.

2.2.1. Sampling Grid and Data Collection Practices

Measurements with a CTD profiling system were conducted using either a Sea-Bird Electronics SBE9-03/SBE 11 Deck Unit (SBE 9/11) or SBE 25 underwater unit equipped with Sea-Bird temperature and conductivity sensors, and a digiquartz pressure sensor according to OCSD standard operating procedure (OCSD, 2001/ECMSOP 1500). The WetLabs C-Star transmissometer and WetLabs Wet-Star chlorophyll fluorometer were powered by the CTD and logged through the CTD's analog-to-digital converter. Sea-Bird SEASOFT software was used to facilitate data acquisition, data display, and sensor calibration. Parameters measured using the profiling system include water temperature, conductivity, salinity, dissolved oxygen, pH, chlorophyll fluorescence, and light-beam transmission. Sensors on each CTD were precalibrated prior to field sampling. Once the CTD was deployed, it was lowered to 3 to 5 m where a 3-minute equilibration period was used at the first station and 90 seconds at subsequent stations. After equilibration, the CTD was brought back to the surface, then lowered to obtain the profile for the station. The CTDs were lowered to within 2 m of the bottom with a profiling rate of approximately 1.0 m/s, yielding a vertical resolution of about 12 cm, then gently lowered to set the rosette sampler on the bottom.

Discrete water samples for ammonium and FIBs were collected using a Sea-Bird Electronics Carousel Water Sampler (SBE 32/SBE 33) multi-bottle array at 1 m, at 5-m depth intervals throughout the water column, and at the bottom. These samples were taken during the upcast portion of the CTD cast (OCSD, 2001/SOP1501). Surface-water samples were collected at selected stations using a dip-pole.

Because of the intensive nature and duration of each sampling event, a considerable amount of coordination was required to get sampling equipment and crews on site, samples back to the laboratory, and laboratory staff to do the sample analysis. The offshore study area was divided into two subareas: downcoast CTD and upcoast CTD. Each sub-area was created so that sampling could be completed in a 4-hour time span. Each sub-area was sampled by a rotating schedule of three boats, which were managed to ensure that all of the sampling requirements were met and sampling crews and skippers were not fatigued. Tables 2-3a and 2-3b list the offshore sampling sequence and timing for each survey sub-area.

Four different CTDs were used in the offshore portion of this project. Data were captured at the highest rate possible with the various instruments. At the high end this meant that data were recorded at 24 scans per second. At the low end this meant that data was recorded at 8 scans per second. Initially, these data were processed using the software provided by the CTD manufacturer to apply small time offsets between different sensors due to delays in water reaching sensors through pumping systems, or to adjust for certain sensors with a response delay. Sea-Bird SEASOFT software was used to apply calibration/conversion functions to produce final engineering units from raw sensor signals. Data were processed according to OCSD SOP 1505.1. At this point ASCII data files containing all recorded data at each unique sampling location were generated.

To eliminate data from before and after the downcast, reduce what was a tremendous amount of data to a more manageable level, and to prepare a data set amenable to graphical and statistical analysis, a further data reduction process was completed in post-processing. This downcast portion initially includes all data at up to 24 scans per second, which at typical descent rates of 1 m/s could mean discrete readings at as close as 5 cm vertically.

2.2.2. Post-processing Methods

Data post-processing was accomplished by loading ASCII data into the Interactive Graphical Ocean Data Systems (IGODS) software. The process involves retaining a site's downcast data for the water column and identifying possible outliers based upon the difference between the downcast standard deviation and a five-point (midpoint is the evaluated datum) running average standard deviation. Datum was flagged if it exceeded the criteria limit for a measured parameter: temperature (0.5), salinity (0.3), dissolved oxygen (0.5), and transmissivity (0.5). The vertical profiles for each parameter were graphically and statistically evaluated looking for outlier points. These points were removed from the raw downcast data and documented in a text file that listed the points removed from each station. Upon removal, the cast was re-evaluated until all outliers were removed and the site's data was accepted. The outlier criteria were only guidelines, so points exceeding the limits were not automatically discarded and points below the limits were not automatically retained. The next data-reduction step was to produce a value at each integer 1-m depth interval. For each parameter the data were scanned to find the nearest data point in depth immediately above and below the integer depth and these two values were averaged together. After 1-m depth averaging was completed, missing data were recovered by examining the upcast data and using the appropriate depth value for any missing data. The final step was a review of the graphical representations of each parameter to determine whether further outlier removal was necessary. A minimal number of points were removed during this review.

2.2.3. Towed Undulating Vehicle (TUV) Measurements and Methods

This study also utilized a Guildline Minibat TUV equipped with a Sea-Bird 9/11 CTD and an in situ pump that pumped at a rate of 7 to 8 liters per minute using a vane pump with a graphite impeller attached to a well-pump motor. The water was pumped through a nylon tube running through the center of the tow cable to ship's deck and into the laboratory of the ship. In the laboratory the flow from the pump system ran through a Sea-Bird 25 CTD for measurement of temperature and conductivity.

Batch FIB samples were obtained from the flow stream and time-stamped with bar-code labels. The samples were placed on ice, kept in the dark, and transported back to OCSD's microbiology laboratory. A portion of the in situ pump flow stream was drawn continuously into a two-channel Technicon Autoanalyzer segmented flow system for analysis of nitrate and ammonium. Because nitrite was not measured separately, the nitrate measurement represented nitrate+nitrite. We assumed that nitrite was relatively low throughout the area and that the measurement represented predominantly nitrate, based on Mann and Lazier (1991) and Lalli and Parsons (1993).

Transit time of the water from the in situ pump on the tow fish to the laboratory was determined by comparing the salinity signals between the in situ CTD conductivity sensor and the laboratory CTD at the end of the flow tube. The transit time in the tube was the difference between the peaks in the two CTD salinity measurements. The approximate transit time was one minute. Samples taken from the in situ flow stream were aligned with the in situ measurements using the delay times from tow vehicle to the shipboard laboratory and additional lag times introduced by the Autoanalyzer. Once the delay times were accounted for, they were compared with other correlating variables for validation of the delay times. For example, nitrate is known to increase with depth so it is expected that the highest concentrations would be found in the deepest, densest water. Similarly, ammonium concentrations were compared with the salinity signal, expecting that the highest ammonium concentrations would be associated with the lowest salinities, especially near the outfall. In some cases small corrections to the delay times were made in order to compensate for the differences.

Mapping tracks were designed with a primary axis in the cross-shelf direction centered on the OCSD outfall diffuser. The TUV was towed at approximately 4 kts and undulated between the surface and 5 m above the bottom or about 70-100 m, depending on which was deeper.

2.2.4. Preparation of Three-dimensional Figures

To prepare three-dimensional volumetric images of the data sets, data from the CTD and Towyo transects for each survey were combined and interpolated to a three-dimensional grid using GMS software. Interpolations were done using an inverse distance-weighted algorithm that estimated the concentrations for each cell in the grid from the actual measurements. This interpolation provided three-dimensional curvilinear portrayals of surfaces. Only surfaces within the grid are shown. FIB concentrations were $\log_{10}$ transformed prior to interpolation, then backtransformed for display purposes. All other measures were interpolated based on the recorded values. For water-quality monitoring purposes, ammonium is usually reported in

concentrations of milligrams per liter (mg/L). Oceanographic concentrations are usually reported in microMolar (μM). One mg/L of ammonium (NH4) corresponds to 55.6 μM. Iso-surfaces (surfaces of constant concentration) were plotted for each measure at a concentration that portrayed the patterns of the measure on each sampling day. For all measures except salinity, the iso-surface encloses the volume with concentrations equal to or greater than the iso-surface concentration. Salinity iso-surfaces enclose volumes of equal or lesser salinity to display the freshwater signal of the wastewater plume.

2.2.5. Preparation of Two-Dimensional Transect Figures and Three-dimensional Curtain Plots

Contoured sections of the data from each CTD and Towyo transect were created using standard contouring tools available within Matlab™. After the track distances were calculated for the data set, the data were gridded to a standard contouring grid using a horizontal spacing of 0.4 km (400 m) and a vertical scale of 2 m. Matlab™ interpolates non-uniformly spaced data to a uniformly spaced grid using Delaunay triangulation. The physical and bio-optical variables were contoured in their linear units (i.e., no transformations were performed on the data before gridding and contouring). The bacteria data were transformed to $\log_{10}$(concentration) for each data point before the data were gridded. Where bacteria concentrations were below the detection limit (<10 MPN/100 mL), they were assigned a value of one. Therefore, in the contoured data figures contour lines less than "10" MPN/100 mL are below the detection limit. These gridded data were then used for the preparation of the curtain plots.

2.2.6. Temperature/Salinity Relationships and Salinity Anomaly

Salinity anomaly, as used here, has been developed by the USC Ocean Outfall Research Group. It is based on the idea that there are characteristic ambient water masses that are apparent in a temperature-salinity (T-S) diagram (Figure 2-5) and that the presence of effluent within the water column will cause a decrease in the salinity below ambient concentrations. Step one is to determine the lines that define the lower bound of salinity for the ambient water. The black lines in Figure 2-5 delineate the lower salinity boundary for the ambient seawater determined from the sections upcurrent and away from the outfall. The second step is to calculate $S_{amb}(T)$, the estimated ambient salinity based on the temperature for a given T-S data pair from the equations developed in the first step. The third step is to calculate the salinity anomaly (S_{anom}) which is calculated as the difference between the measured salinity (S_{meas}) and the estimated ambient salinity ($S_{amb}(T)$). Thus, $S_{anom} = S_{meas} - S_{amb}(T)$. The region where S_{anom} is less than -0.01 is shown in the vertical profile of salinity for Tow 9 from cruise 5 in Figure 2-6 with red circles indicating the regions of negative salinity anomaly. In this case there are clearly defined regions of low salinity anomaly. The effluent plume is indicated by the red circles below 30 m. Although surface runoff was evident in some of the tows for this cruise, no surface runoff was detected in this tow, and therefore there are no red circles in the nearsurface region. When both effluent plume and surface runoff plumes are present their vertical separation clearly indicates the different sources.

2.3. Nearfield Plume Modeling

For each survey we evaluated the nearfield plume characteristics using the "RSB" outfall plume model developed by Roberts, Snyder, and Baumgartner (1989a,b) and Roberts (1995). The plume was modeled at hourly intervals for a 10-day period centered on the hydrographic sampling period. The basic outfall characteristics used in the model are described in Table 2-4. The flow rate from the pipe was modeled as the hourly flow rate. Other parameters that were input to the model include the density profile and the current speed and direction. The density profile was calculated from the hourly temperature measurements from Mooring HB12, nearest to the outfall. Density was calculated from temperature based on an empirical temperature-density relationship developed during the Plume Mapping SPS (MEC, 2001) for the period between August 1999 and September 2000. The current speed and direction were calculated from the hourly current profiles throughout the sampling period. The average speed and direction for the currents between 30- and 55-m depth were used because this is the region of flow that directly affects the discharge from the outfall.

2.4. Moored Array

2.4.1. Water-column Measurements

An array of moorings was deployed at 12 sites across the shelf, in water depths from 10 to 205 m, for 4 months in the summer of 2001 (Figure 2-2). Related field activity identification numbers and their metadata url are as follows:

S-1-00-SC	http://walrus.wr.usgs.gov/infobank/s/s100sc/html/s-1-00-sc.meta.html
S-2-00-SC	http://walrus.wr.usgs.gov/infobank/s/s200sc/html/s-2-00-sc.meta.html
S-2-01-SC	http://walrus.wr.usgs.gov/infobank/s/s201sc/html/s-2-01-sc.meta.html
S-3-01-SC	http://walrus.wr.usgs.gov/infobank/s/s301sc/html/s-3-01-sc.meta.html
S-4-01-SC	http://walrus.wr.usgs.gov/infobank/s/s401sc/html/s-4-01-sc.meta.html

Each site hosted one or more moorings, and some sites included bottom tripods as well (Figures 2-7a-l). Most moorings were in the water from mid- or late June through mid-October. A set of moorings was deployed at 7 sites along the principle cross-shelf transect (HB01, HB02, HB03, HB05, HB06, HB07, HB08-mooring HB04 was never occupied because instrumentation was not received in time). The shallowest site in this array, HB01, was in 10 m of water between shore stations 3N and 6N. This site was also near the AES intake and outflow pipes. One site, HB07, was near the shelf break, 1.5 km upcoast of the center of the OCSD outfall. A single Acoustic Doppler Current Profiler (ADCP) was deployed at site HB08, which is on the slope in 205 m of water.

Three other sites (HB09, HB10, HB11) were aligned with the 15-m site at HB03, approximately 30° to the coastline (Figure 2-2). Because the shelf break turns toward the shoreline south of the outfall, this line was also approximately perpendicular to the local orientation of the shelf-break isobaths. The deepest site on the line, HB11, was in 55 m of water, near the edge of the shelf.

Two additional sites completed the shelf-wide array. HB12, near the shelf break, was very close to the OCSD outfall (Figure 2-2). This mooring was in the same location as one previously deployed in 1999/2000 for one year. HB13 was deployed upcoast of Newport Canyon in 15 m of water.

The mooring sites shared many common characteristics. Currents were measured at all but one location (HB02). At 7 of the 12 sites, currents were monitored over the entire water column by an upward-looking ADCP. Five of these ADCPs were deployed along the principle cross-shelf transect at HB03, HB05, HB06, HB07, and HB08 (Figures 2-7c, d, e, f, g). The other 2 ADCPs were deployed along the secondary cross-shelf transect at sites HB10 and HB11 (Figures 2-7i, j). Currents were monitored at the remaining sites, except HB02, by single-point current meters (Figures 2-7a, h, k, l). Most sites also measured temperature and salinity over the water column and at the bed. Ancillary measurements, such as water clarity, bottom pressure, resuspended sediments, near-bed currents from surface waves and photographs of the sea bed were measured at selected sites. Wind velocity and surface-wave characteristics were telemetered to shore from site HB07.

Current, temperature and salinity measurements were generally sampled every 2-5 minutes over the 4-month deployment period. In particular, most ADCPs on the shelf sampled at 3-minute intervals. Hence, internal waves with periods larger than 6 minutes were monitored at 5 of the 7 ADCP sites. The sampling interval for most single-point current meters over the shelf was 5 minutes. The slope currents were measured every 15 minutes. Joint temperature and salinity measurements were generally recorded every 2 minutes. Separate temperature measurements were generally recorded every 3-5 minutes. Detailed sampling intervals for each instrument is given in Tables 2-5a, b.

Most instruments recorded data for the full deployment period (Figures 2-8a,b,c). Near-bed current records were sporadic at HB01, but temperature, salinity, and pressure were recorded for the entire deployment.

A nearshore array of moorings was deployed in water depths shallower than 12 m after the principal array was in the water (Figure 2-9). Some instruments were deployed in July, others in August, and most remained in the water for a month or more (Figure 2-10). ADCPs were deployed inshore of HB01, near the AES Corporation outfall, and along a line upcoast of HB01 (Figure 2-9). Temperature chains and near-bed temperature sensors were deployed in this same general area. The sampling intervals for these instruments were generally less than 3 minutes. Except for one or two temperature sensors, most of these nearshore instruments had fairly good data return (Figure 2-10).

2.4.1.1. Naming Conventions

All records were assigned a unique ID and filename. These are listed in Tables 2-5a and 2-5b under “SAIC ID” and “Filename Prototype”, respectively. The IDs are of the form:

HBnm-#,

where HB (for Huntington Beach) is the program designator,

nm is the mooring number for the main array (e.g. 01, 02, ... 13), or
n = N for the nearshore array and m is the SIO mooring number, or
A, B, or C, if from the AES moorings, or
n = S for the SIO surf zone thermistors, or
n = M for the NPS meteorological buoy, and

is the position of the instrument on the mooring, counting down from the surface. In this scheme, the compound moorings of the main array (surface mooring, sub-surface mooring, and bottom tripod) are treated as a single mooring for the purpose of assigning the position number and IDs.

This report uses these IDs to identify instruments and data records. Often the mooring ID will be shortened to mooring number (e.g., mooring 3) or the "nm" part of the designator (e.g., N2 or N3). The IDs and filenames and their associated metadata (e.g., latitude, longitude, water depth, instrument depth, start and end dates, time intervals) are stored in a relational database system that is interfaced with SAIC's analysis system. The tables of the database allow efficient management and searching of the data records.

2.4.2. Wind and Wave Measurements

Winds and surface waves were measured from a surface buoy at HB07. Table 2-6 lists the instrumentation that was used. The meteorological data are 1-minute averages of 1 Hz measurements, although there were periodic small gaps, generally lasting less than 2 minutes. A uniform 1-minute time base was created and the data linearly interpolated onto that time base. Of the three sea-surface temperature instruments, only the bulk 1-m measurements were included in the final data set, since the interpretation of the IR surface temperature is not trivial and the floating thermistor went bad during the deployment. The sonic (Handar) and rotor-and-vane (RM Young) anemometers had very similar wind speeds, but the wind directions differed by about 15° when the winds were out of the WNW, with the sonic anemometer recording more northerly winds than the rotor-and-vane [i.e., if the sonic has winds from 290° (toward 110°), rotor-and-vane has winds from 275° (toward 95°)]. A post-deployment calibration of the buoy compass, used for both anemometers, was applied to both data sets. Data from the sonic anemometer were used for all the analyses in this report.

In order to compute surface-wave spectra, the north-south, east-west, and vertical buoy displacement time series were computed by rotating the measured buoy linear accelerations obtained from the three-dimensional motion sensor into the earth reference frame and then double integrating. Every fifth available data point (sampled at 10 Hz) was used in the wave-spectra computation, resulting in a 2-Hz sampling rate. One-dimensional wave-height spectra were obtained by computing FFTs from consecutive 256-point blocks of the vertical displacement time series. These 256-point wave height spectra were then averaged by frequency bins into approximately 1-hour spectra, from which time series of significant wave height and dominant wave direction and period were determined. Data were interpolated onto a uniform hourly time base, and 3-hour gaps that appeared every 70 hour were filled by linear interpolation.

Directional wave spectra, with directional resolution of 1°, and frequency resolution of 1/256 Hz, were computed from the earth-referenced north-south, east-west, and vertical displacement time series using the Maximum Entropy Method (MEM) described by Lygre and Krogstad (1986).

2.4.3. Near-bed Instruments and Methods

The instrumentation described in this section were designed for monitoring bottom boundary-layer dynamics, sediment suspension and transport, and morphology of the sea bed. They provided critical data in an attempt to answer the questions originated from one of the hypotheses: sediment transport (Chapters 1 and 8). Sediment traps collected particles for analyses of physical and chemical properties of the material. The initial processing of the sediment trap samples are still ongoing.

2.4.3.1. Acoustic Doppler Velocimeter (ADV)

Three ADVs (Sontek/YSI, San Diego) were deployed at sites HB05, HB07, and HB11 during the Phase III measurements. They were mounted on bottom tripods to measure three-dimensional (u, v, w) velocities at 65 cm above the bed. In addition, the ADV data loggers also recorded temperature, pressure, optical backscatter (OBS)/transmissometer data, and salinity/conductivity. Some of these sensors were external so they could be mounted at different locations on the tripods (Table 2-5a).

The ADVs were sampled in burst mode. A dual-burst-type sampling scheme was employed for all three ADVs:

	Sample Rate (Hz)	Sample Interval (sec)	Samples Per Burst
Burst Type 1	1	1200	20
Burst Type 2	2	3600	2048

Burst type 1 was designed for mean current measurement – it recorded 20 seconds of data every 20 minutes, from which 20-minute-averaged current time-series were generated. Burst type 2 was for wave measurement. The 17.1 minutes of data it logged at 2 Hz every hour were used to compute directional wave spectra. The data loggers on the ADVs started at 2001-6-13 07:51:03 (GMT) so the wave bursts are centered on the hour. A typical ADV data file had the following burst sequence:

Burst No.	Burst Type	Start Time
1	1	2001-6-13 07:51:03
2	2	2001-6-13 07:51:28
3	1	2001-6-13 08:11:03
4	1	2001-6-13 08:31:03
5	1	2001-6-13 08:51:03
6	2	2001-6-13 08:51:28
7	1	2001-6-13 09:11:03
8	1	2001-6-13 09:31:03

Five 3-minute averaged current data points were also calculated from the wave burst. The time records of these 3-minute averages lined up with the ADCPs, which were also sampled at a 3-minute interval. In the above example, the 3-minute averages were respectively centered on (2001-6-13) 08:54:00, 08:57:00, 09:00:00, 09:03:00, 09:06:00.

Burst-averaged data from burst type 1 and type 2 were created for the Phase III report. MATLAB™ routines developed inhouse were used to read the binary data from the ADV recorders, to convert to engineering units, to rotate velocities to the true North and East, to compute the statistics, and to write the data into NetCDF files. All time-series files were trimmed to contain in-water data only:

Site		Start Time	End Time	Total Length
HB05	Hourly	2001-6-14, 02:00:00	2001-10-12, 21:00:00	2900
	20-minute avg.	2001-6-14, 01:31:15	2001-10-12, 21:31:15	8700
HB07	Hourly	2001-6-13, 23:00:00	2001-10-30, 19:00:00	3333
	20-minute avg.	2001-6-13, 22:31:15	2001-10-30, 19:11:15	9999
HB11	Hourly	2001-6-13, 14:00:00	2001-9-12, 20:00:00	2191
	20-minute avg.	2001-6-13, 13:51:15	2001-9-12, 20:51:15	6573

The tripod at HB05 was recovered on June 15 2001; the tripods at HB07 and HB11 were recovered on October 31, 2001.

The ADV systems at sites HB05 and HB11 had problems during the deployment. For unknown reasons, the correlation level (an indicator that measures the data quality) signals from the three acoustic beams intermittently became very low, so the velocity data were very erratic. A MATLAB™ routine was written to clean these data records and to compute the statistics from only the good data. Not a Number (NaN) was assigned for all the bad data points. Also, the ADV at HB11 was apparently interrupted on September 12, 2001, and it started a different logging file. It was determined that the data from this second binary file were not usable, so only the data from the first logging file were provided in the report.

2.4.3.2. Video Cameras

Video cameras were mounted on the tripods at HB03, HB05, HB07, and HB11 to take footage of the sea bed. Digital 8 SONY Handycams were used at HB03 and HB11. Analog SONY Handycams were used at HB05 and HB07. The video cameras were customized with a controller board that determines the timing and length of the footage. All four controller boards had the same setting: they turned the camera and strobes on for taping for 15 seconds every 6 hours. The digital tape had a capacity of 90 minutes, and the analog tape had 180 minutes. The glass bottom of the cylinders that housed the cameras at the two shallow sites (HB03 and HB05) were covered by barnacles and other biological growth after one month or so. Images from the digital cameras appeared to have better quality.

2.5. Ancillary Data

2.5.1. Sea Level and Astronomical Data

Hourly (6-minute) sea-level data for Los Angeles (33°43.2'N., 118°16.3'W., station ID 9410660) for 1998-2001 (2001) were obtained through the National Ocean Service website (http://co-ops.nos.noaa.gov/). Sea levels are given as height in meters above mean lower low water (MLLW). While, technically, the term spring tide denotes the largest tidal range in a fortnightly (14-day) period, in order to assign a time unambiguously to each spring tide, the highest high water in a window of 10-20 days (9.4 days in one case) after the previous spring tide, with a neap tide in between, was picked as the date/time and height of "spring tide". Note that by using the actual sea level, rather than the phase of the moon, there is some variance in the time between "spring tides" due to meteorological effects, although on average it is 14.7 days, as would be expected.

Times of new and full moons and sunset and sunrise were obtained from the U.S. Naval Observatory website (http://mach.usno.navy.mil).

2.5.2. Airport Winds

Wind data, measured with a cup and vane system, were also obtained from the Automated Station Observing System (ASOS) from two nearby airports, Long Beach (LBH; 33° 48' 42" N, 118° 08' 47" W) and John Wayne (JWA; 33° 40' 48" N 117° 51' 59" W). The elevation of the ASOS station at LBH is 9.4 m above sea level, while the one at JWA is 16.5 m above sea level. Hourly wind speed and direction, based on 2-minute averages immediately preceding observation time, are recorded in increments of integer knots and 10°, respectively. The reported cutoff speed for ASOS is 2 kts, though the data here shows a minimum speed of 3 kts (anything less than that is recorded as 0 wind speed and 000 wind direction). If the wind direction varies by 60° or more during the 2-minute observation period, ASOS reports variable winds. Directions reported as variable were replaced with a null value, before low-pass filtering and subsequent analyses.

Wind data for 2001 from OCSD's plants 1 and 2 were also obtained and examined, but determined not to be of useable quality.

2.6. Data Quality and Processing Procedures and Analysis Methods

2.6.1. General Data Quality and Processing Procedures

The initial processing of data from the moored array, including extraction of data from the instrument, converting it to engineering units, and applying any necessary calibrations, were performed by the institution that owned the instruments, under the supervision of the appropriate principal investigator. Initial data quality inspections were performed by the principal investigators, and standard minimal cleanup of the data was performed in order to preserve the high temporal resolution of the data. This included flagging and removing suspect data points and interpolating short gaps of 1 or 2 points. Longer gaps were filled by special procedures discussed below. Current velocity records were corrected for magnetic variation at this stage.

After the initial data quality procedures, the data were transferred to SAIC and entered into the database management system. Data records resulting from multiple deployments at a single location and depth have been concatenated into continuous time series. Data gaps in these records, and other gaps resulting from a variety of causes, were less than 2 days in length, and were filled with data that are spectrally consistent with the rest of the record. In the case of ADCPs, an effort has been made to maintain the vertical coherence of the records. These records have been further cleaned up to remove spikes and obvious noise up to ~ 2 hours in length. The greatest amount of cleanup was needed for salinity and the near-surface bins of the ADCP velocity records.

Concatenation of bottom-pressure records was handled differently from the method described above, used for the other variables. Bottom-pressure data were averaged to 60 minutes, tidal analysis was performed, and the predicted tide was used to fill the gaps. Some minor leveling between deployments has been done for some records so that the deployment means are the same. Thus, the tidal phase is preserved across the gaps; however, the subtidal pressure is reduced to a linear trend across the gap.

The resulting concatenated, gap-filled records were then low-pass filtered to produce two sets of records–one retaining energy with periods longer than 3 hours, and one with energy at periods longer than 40 hours.

The 3-HLP filter uses a Lanzcos kernel with half-power point at 3 hours, and greater than 95% suppression at periods less than 1 hour. It removes 8 hours from the ends of the original time series. It is essentially equivalent to performing 1-hour averages of the original data. The 40-HLP filter suppresses fluctuations with periods less than 30 hours and removes 4 days from the ends of the 3-HLP series. The 3- and 40-HLP time series are decimated to time intervals of 1 and 6 hours, respectively.

The coordinate systems of the velocity and wind records were rotated so that the V-component (y-axis) is directed along the general trend of the isobaths. The directions were chosen by consensus of the PIs after considering the positions of the moorings, local isobath directions, and the principal axes of the velocity records. The rotations for each mooring that measured currents are given in Table 2-7. The conventions adopted are that positive, rotated U and V components are directed towards the shore and up-coast (towards the northwest), respectively.

The ADCPs used for the AES Corporation sites were deployed in magnetic frames. This was realized at the time and the bottom mounts were deployed so that the ADCP heads were aligned with magnetic north as determined by a diver-held compass. After retrieval, the correction to magnetic north of the transducer-head compass reading was applied to the velocity data by AES Corporation's contractors. Unfortunately, tide and wave action on the surface buoy, used to mark the deployment position, caused the bottom mounts to move and rotate so that the frame was no longer in its original orientation. The three frames were affected to differing degrees during their four deployments. Once the frames had moved substantially off magnetic north, the current directions were no longer accurate. Since the heading was recorded, the parts of the

records with headings close to zero degrees were extracted, and merged between deployments. Almost all of AES #3 (HBNC-7) and two substantial sections of AES #2 (HBNB-7) were useable. After processing, the 40-HLP records were compared with the nearby SIO ADCP #2 (HBN2-2). It was apparent that the AES #3 record was rotated anticlockwise relative to HBN2-2. Comparison of principal axes for the common period of overlap for the upper part of the water column indicates the differences were about 23°. This is close to twice the magnetic variation, indicating a possible error in applying this correction. Therefore, the AES #3 data has been rotated 23° anticlockwise, since it is nominally on the same isobath and only a short distance away from HBN2-2. The AES #2 data records did not need a correction. The AES temperature data from their thermistor strings were not considered reliable and have not been used for this study.

In shallow water, the 1- to 2-m range of the tide is a substantial proportion of the total water depth. Therefore, the ADCP velocity data, from the near-shore moorings (including valid AES ADCPs), have been processed to use a proportional surface following a vertical coordinate system. The ADCP measures velocities at fixed distances from the head, and thus at different stages of the tide a varying number of bins will have valid data. For time-series analysis, however, continuous time series are required with no gaps. Using fixed-depth levels, this restricts analysis to bins that are always valid (effectively 0.5- to 1-m below MLLW). Therefore, it is more useful, for shallow water instruments, to use a fixed number of depth levels, with the uppermost level tracking the sea surface, and the other levels, proportionally equally spaced between the surface bin and the (first) bin nearest the head. This is similar to the sigma vertical coordinate system used by many numerical hydrodynamic models. The number of depth levels chosen for this sigma coordinate scheme is the number of fixed-level measurement bins between the head and MLLW. The definition of the free surface is from nearby pressure gauges that are corrected to the MLLW datum by comparing with the Los Angeles Harbor tide gauge data. The 3- and 40-HLP files use the appropriately filtered pressure data.

The data returns, from all the moorings in the study, are given in Figures 2-8a, b, c, and Figure 2-10. The instrument IDs can be cross-referenced with Tables 2-5a,b for further details on the mooring platforms, sampling rates, etc.

2.6.2. Analysis Methods

2.6.2.1. Time Series

Standard techniques of time-series analysis are extensively used in this report. This section summarizes briefly these techniques and gives references to more detailed treatments found in the literature. It is assumed that the reader is familiar with basic statistics and the use of spectra for scalar and vector time series (Press et al., 1992; Priestley, 1981).

2.6.2.2. Tidal Analysis

Tidal analysis is the result of performing a least-square fit of the observed series to amplitudes and phases of specific frequencies that are derived from the motions of the sun and moon. The methods are given in Godin (1972) and the implementation for sea level and current records uses the programs written by Foreman (1977; 1978). The major constituents of interest

are grouped into two frequency bands, the semidiurnal (M_2, N_2, and S_2) and diurnal (K_1, P_1, and O_1). The amplitudes and phases of tidal currents are often represented as hodographs, where the velocity vector tip describes an ellipse as the vector rotates clockwise or anticlockwise with the period of the constituent. A good discussion of tidal analysis applied to oceanographic time series can be found in Foreman et al. (1995).

The barotropic tidal currents were calculated at sites where currents were measured with an ADCP (HB11, HB10, HB08, HB07, HB06, HB05, HB03 and HBN2), thus providing good vertical resolution. The currents in each 2-m bin were high-pass filtered to remove periods longer than 66 hours. The high-pass filtered currents at each site were then averaged over the entire water column. The amplitude of the barotropic tides were then calculated from the depth-averaged records at each site using the Foreman tidal analysis programs. The characteristics of the internal tidal currents were calculated from the high-pass-filtered ADCP records that had the depth-averaged barotropic tidal currents removed.

2.6.2.3. Complex Demodulation

Standard spectral and tidal analysis assumes that the time series are stationary. However, when the observations are substantially influenced by stochastic forcing mechanisms such as the wind, the amplitudes of the response can vary with time. Thus, it is often of interest to determine the time dependence of the amplitude of a well-defined frequency associated with the forcing. On the San Pedro shelf, sea breezes with a 24-hour period are a persistent feature of the atmospheric circulation that vary in strength from day to day. Complex demodulation is a technique to estimate the time-dependent amplitude and phase of a signal at a given frequency. It is most useful when the signal shows high energy in a narrow frequency band (e.g., diurnal, or 24-hour period). The method is given in Chapter 11 of Priestley (1981). The usual method is to remove a running mean from the 3-HLP series of length 2T, where T is the period of interest. The resulting complex demodulated series is then either averaged over the period 2T or low passed with a filter with greater than 95% suppression for periods shorter than 2T. For daily period motions, a four-day low-pass filter is often used. The filtering smoothes the often noisy amplitudes and phases of the complex demodulation at the expense of resolution in time. A least-squares algorithm (Emery and Thomson, 2001) was applied to compute the complex demodulation displayed in Figure 7-6.

2.6.2.4. Empirical Orthogonal Functions

Empirical orthogonal functions (EOF) are a method to extract coherent signals from a spatial array. EOF analysis is often called principal component analysis, and Preisendorfer (1988) has given a comprehensive treatise on the methods used in oceanography. The method decouples spatial variability, $e_n(x)$, from temporal variability, $A_n(t)$, and extracts statistical modes, ordered by the amount of the total variance of all the data that they can explain. The modes are orthogonal, and thus uncorrelated in time and space. Any time series in the spatial array is related to the modes by

$$U(x,t) = \Sigma_n A_n(t) \cdot e_n(x) , \qquad (2.1)$$

where n is summed over all the time series in the analysis. The input time series, U, are normally demeaned for the EOF analysis. If the time series, U, have different measurement units, then the usual practice is to normalize to unit variance. If U are all of the same type, then normalizing the input series is not necessary or even desirable. There are various rules for determining how many modes are significant, or differ from random noise (Preisendorfer, 1988; North et al., 1982). If a mode accounts for a large fraction of the total variance, and a reasonable proportion of the input series are correlated with the mode, then the mode is usually physically significant.

For time-domain analyses, described by (2.1), the input series are scalars. For velocity time series, the quantities in (2.1) are complex. This is called complex EOF analysis (CEOF), and it has the advantage that it does not artificially separate the along- and cross-shelf velocity modes. Since the eigenvectors and amplitudes in CEOF analysis are complex, they have both magnitude and direction. The orientation of the temporal amplitudes and spatial patterns are relative to an arbitrary reference. The usual practice, following Merrifield and Winant (1989), is to rotate the spatial pattern into the frame of the semi-major principal axis of the corresponding mode time series. In (2.1), either A or e can be normalized so that their variance is unity and the other quantity has the units of the input time series. The convention here is to normalize the amplitude time series.

The EOF analysis of (2.1) can also be used in frequency space, where A_n and U become functions of frequency (i.e., spectra). This is used where one wishes to analyze the spatial patterns for a process that has a response in a restricted frequency band. On the San Pedro Shelf, frequency domain EOF analysis is used for diurnal and semidiurnal band processes. The advantage of this type of an analysis is that phase relations of the measurements across the array are calculated for each mode, since the spatial eigenvector, e_n, is a complex function of frequency. Therefore, propagating waves are better described than with time domain analysis. Time lags are not accommodated by the time domain versions of (2.1).

2.7. References

Chamberlin, C.E. and R. Mitchell, 1993. A decay model for enteric bacteria in natural waters. Water Pollution Microbiology, John Wiley & Sons.

Emery, W.J. and R.E. Thomson, 2001. Data analysis methods in physical oceanography. Elsevier Science B.V., Amsterdam, The Netherlands.

Foreman, M.G.G., 1977. Manual for tidal heights analysis and prediction. Pacific Marine Science. Institute of Ocean Sciences, Patricia Bay, Sydney, B.C., Report 77-10, 97 p.

— 1978. Manual for tidal currents analysis and prediction. Pacific Marine Science. Institute of Ocean Sciences, Patricia Bay, Sydney, B.C., Report 78-6, 70 p.

Foreman, M.G.G., W.R Crawford, and R.F. Marsden, 1995. De-tiding: Theory and practice, in D.R. Lynch and A.M. Davies (eds.), Quantitative skill assessment for coastal numerical models. Coastal and Estuarine Studies, American Geophysical Union, Washington, D.C., v. 47, p. 203-240.

Godin, G., 1972. The analysis of tides. University of Toronto Press, Toronto, 264 p.

Lalli, C. M. and T.R. Parsons, 1993. Biological oceanography: an introduction. Pergamon Press, Oxford University Press, 301 p.

Leecaster, M.K. and S.B. Weisberg, 2001. Effect of sampling frequency on shoreline microbiology assessments. Marine Pollution Bulletin, v. 42, p. 1150-1154.

Lygre, A. and H.E. Krogstad, 1986. Maximum entropy estimation of the directional distribution in ocean wave spectra. Journal of Physical Oceanography, v. 16, p. 2052-2060.

Mann, K.H. and J.R.N. Lazier, 1991. Dynamics of marine ecosystems: biological-physical interactions in the ocean. Blackwell Science, Cambridge, Massachusetts, 466 p.

MEC (MEC Analytical Systems, Inc), 2001. Strategic Process Study, Plume tracking. June 1999 to Septemter 2000, Final Report, v. I – Executive Summary.

Merrifield, M.A., and C.D. Winant, 1989. Shelf circulation in the Gulf of California: A description of the variability. Journal of Geophysical Research, v. 94, p. 18133-18160.

Noble, R.T., S.B. Weisberg, M.K. Leecaster, C.D. McGee, K. Ritter, K.O. Walker, and P.M. Vainik, 2003. Comparison of beach bacterial water quality indicator measurement methods. Environmental Monitoring and Assessment. v. 81, p. 301-312.

North, G.R., T.L. Bell, R.F. Cahalan, and F.J. Moeng, 1982. Sampling errors in the estimation of empirical orthogonal functions. Mon. Weath. Rev., v. 110, p. 699-706.

Orange County Sanitation District (OCSD), 2001. Laboratory operating procedure method 9060.

Press, W.H., S.A. Teukolsky, W.T. Vetterling, and B.P. Flannery, 1992. Numerical recipes. Cambridge University Press, 2nd ed., 963 p.

Priesendorfer, R.W., 1988. Principal component analysis in meteorology and oceanography, in C.D. Mobley (ed.), Developments in atmospheric science. Elsevier, New York, v. 17, 425 p.

Priestley, M.B., 1981. Spectral analysis and time series. Academic Press, London, 890 p.

Roberts, P.J.W., 1995. Near-field modeling of the Mamala Bay outfalls. Water Science Technology, v. 32, p. 159-166.

Roberts, P.J.W., W.H. Snyder, and D.J. Baumgartner, 1989a. Ocean outfalls: I. Submerged wastefield formation. Journal of Hydraulic Engineering, ASCE, v. 115, p. 1-25.

——, 1989b. Ocean outfalls: II. Spatial evolution of submerged wastefield. Journal of Hydraulic Engineering, ASCE, v. 115, p. 26-48.

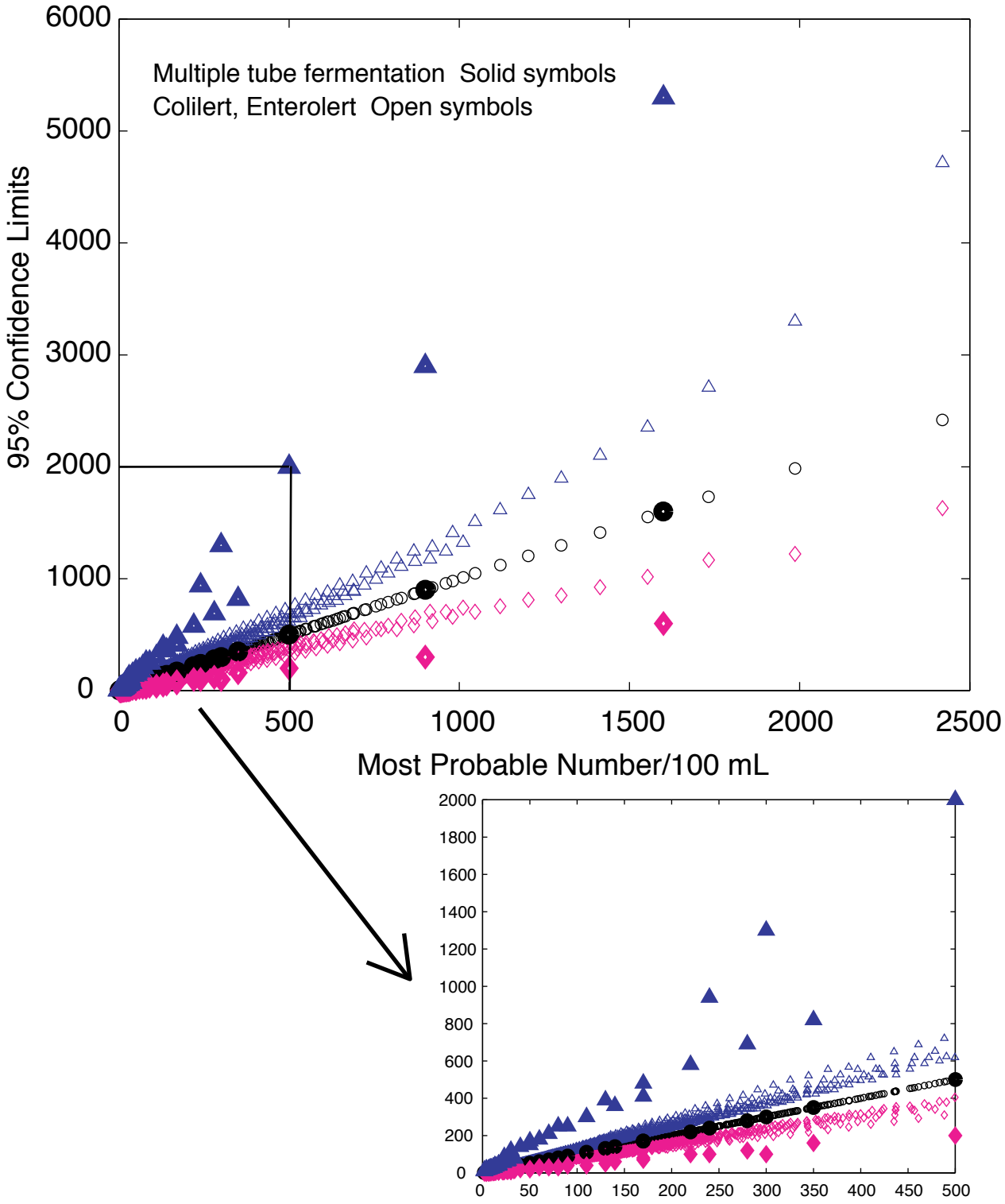

Figure 2-1. 95% confidence limits for the multiple tube fermentation (solid symbols) and chromogenic substrate methods (open symbols) are shown. Confidence limits are not a single valued function of most probable number, because a given value of most probable number may be arrived at by more than one combination of different size tubes or cells testing positive.

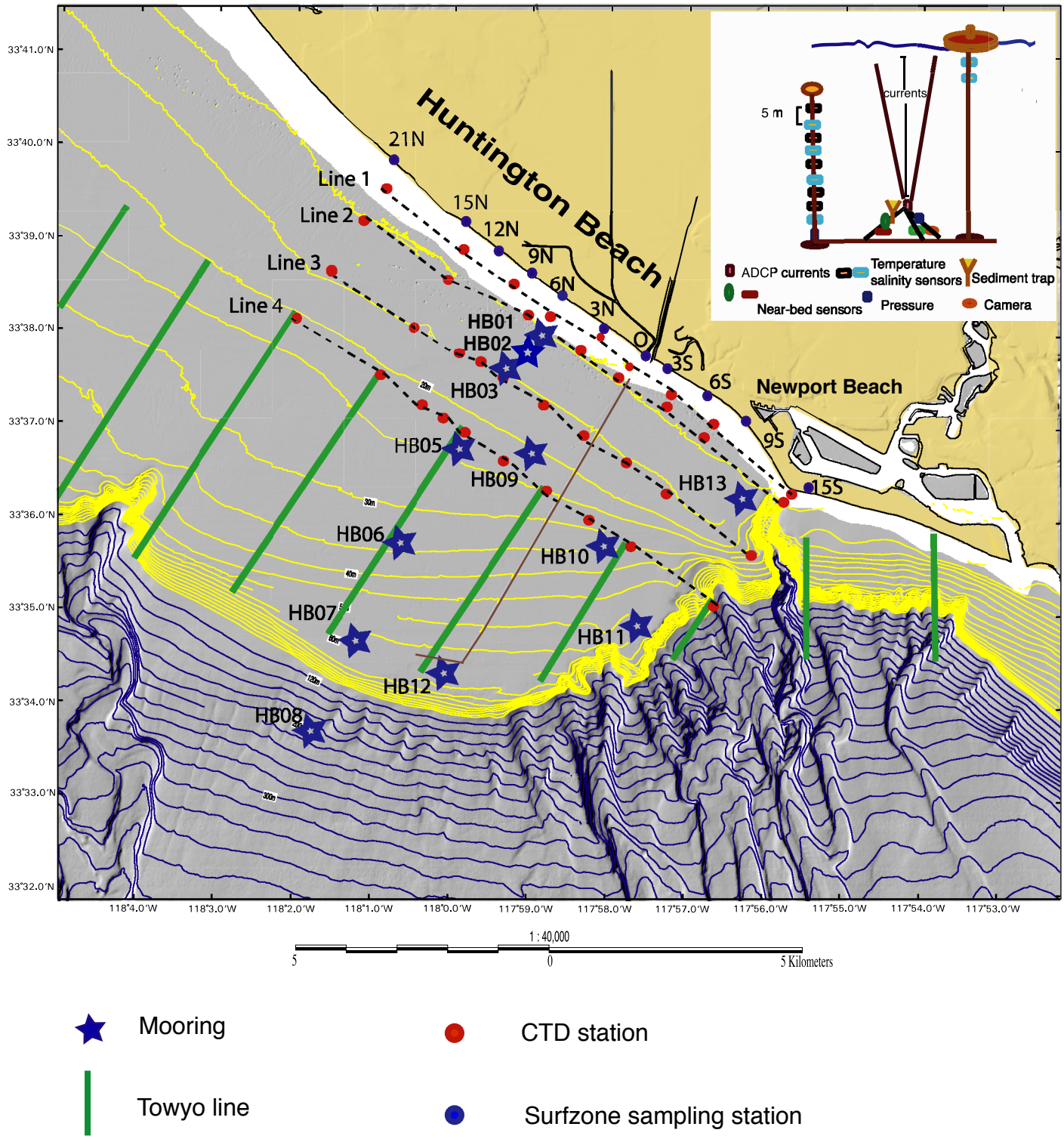

Figure 2-2. Map of the region, mooring sites, surfzone sampling stations, and instrumentations of a typical mooring (inset).

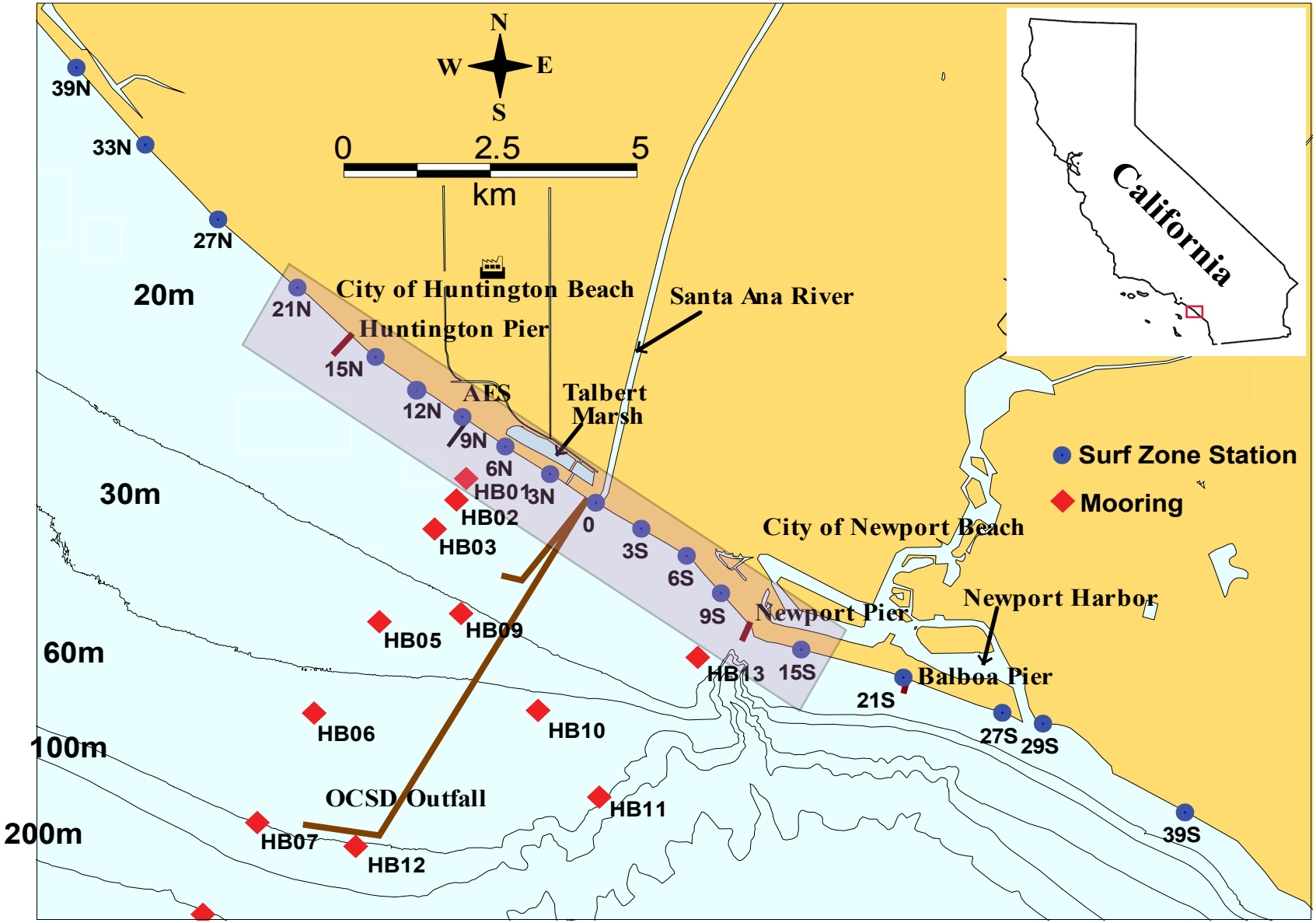

Figure 2-3. Map of the coastal zone surrounding Huntington Beach, California. The blue dots show the location of the surfzone sampling stations from 39N to 39S. The outfall is shown leaving the coast near station 0. The diffuser of the outfall is located near stations HB07 and HB12. Station 12S is located at Newport Pier.

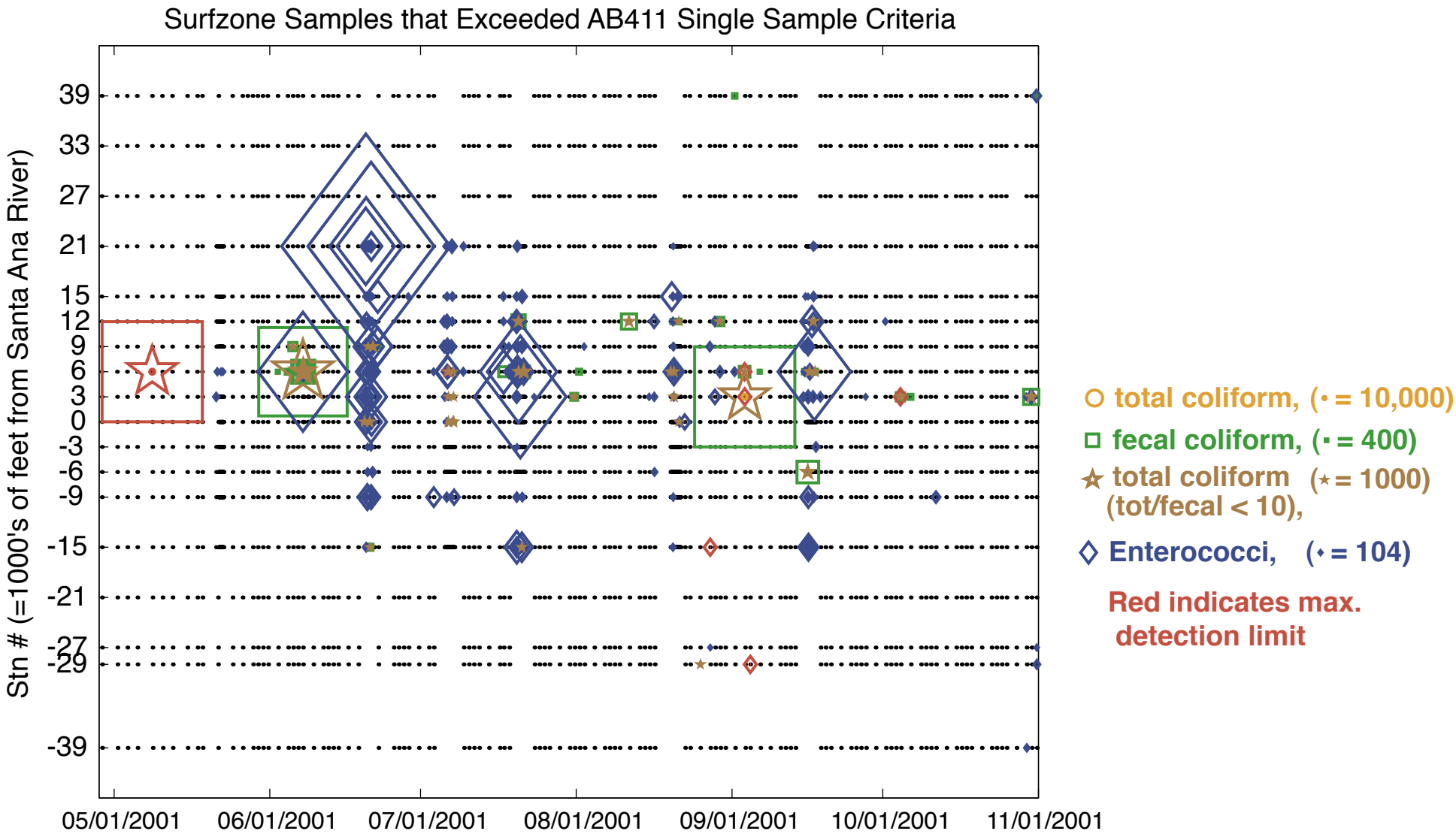

Figure 2-4. A black dot is plotted at each time (GMT) and location a sample was taken. Colored symbols are plotted at the time (GMT) and location of samples exceeding AB411 single sample standards. The size of the symbol is proportional to the ratio of the measured bacterial concentration to the AB411 criteria. The symbol size for a sample equal to the AB411 criteria is shown to the right of the indicator species in the legend.

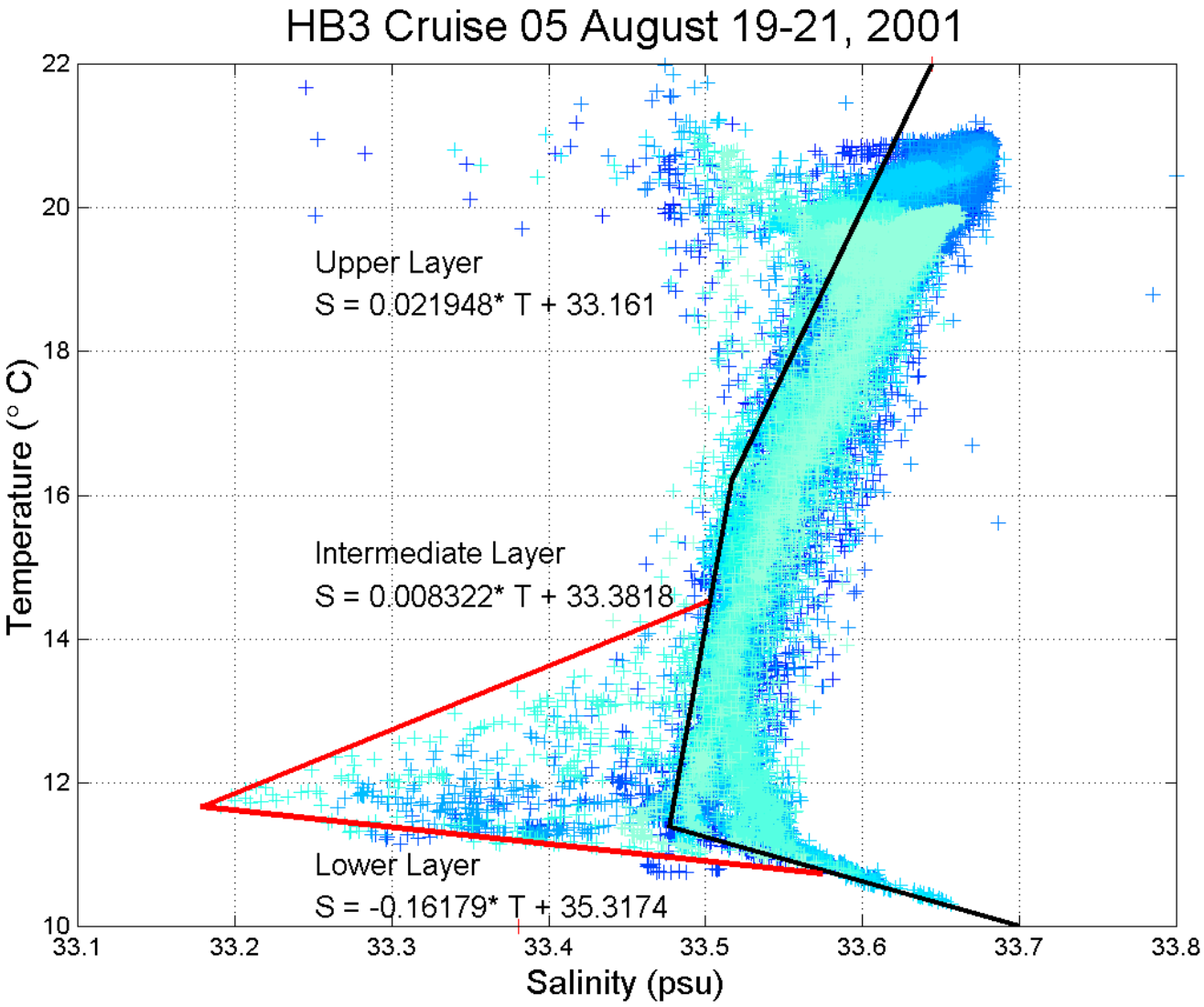

Figure 2-5. T-S plot for all of the Towyo transects for Cruise 5, August 19-21, 2001. Each color indicates a different tow. The black lines indicate the lower salinity boundary of the ambient T-S measured upcurrent from the OCSD outfall. In this case, upcurrent was upcoast from the outfall. The equations describe the lines in T-S space and are used to calculate the salinity anomaly. Values to the left of the ambient T-S lines are assumed to result from freshwater inputs. In this example, anomalously low salinities below 14.5∝C are due to the effluent plume and above 17∝C result from the influence of surface runoff into the coastal ocean.

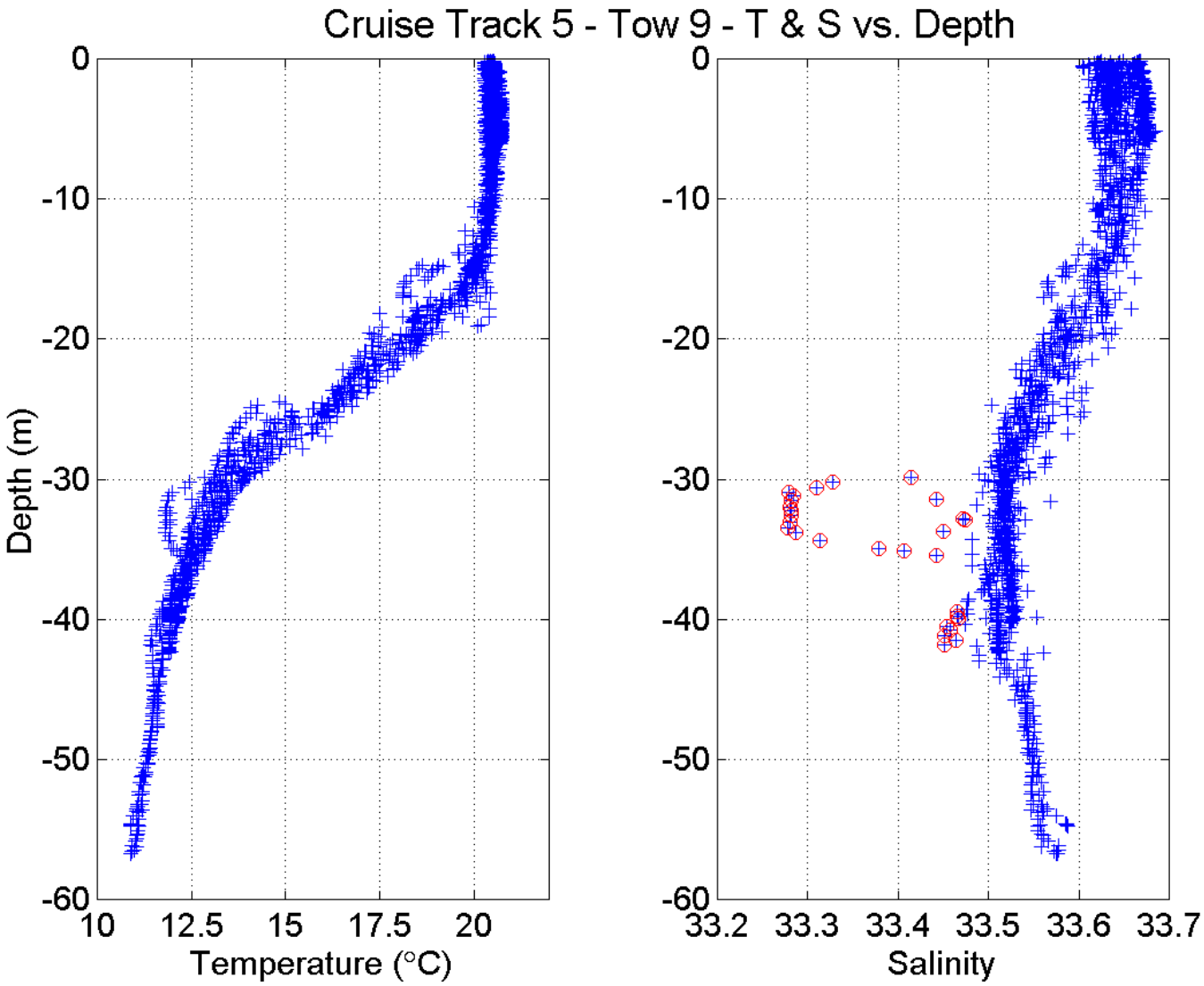

Figure 2-6. Vertical profiles of temperature and salinity for all of the one-second average data for Tow 9 from Cruise 5, a subset of the data shown in Figure 2-5. The red circles in the salinity profile indicate the measurements where the salinity anomaly is less than -0.01 psu (i.e., the measured salinity is more than 0.01 psu less than the predicted ambient salinity based on the T-S equation for this temperature region). Note that there are no salinity anomalies near surface indicating that in this particular tow there was no evidence of surface runoff in the upper layer.

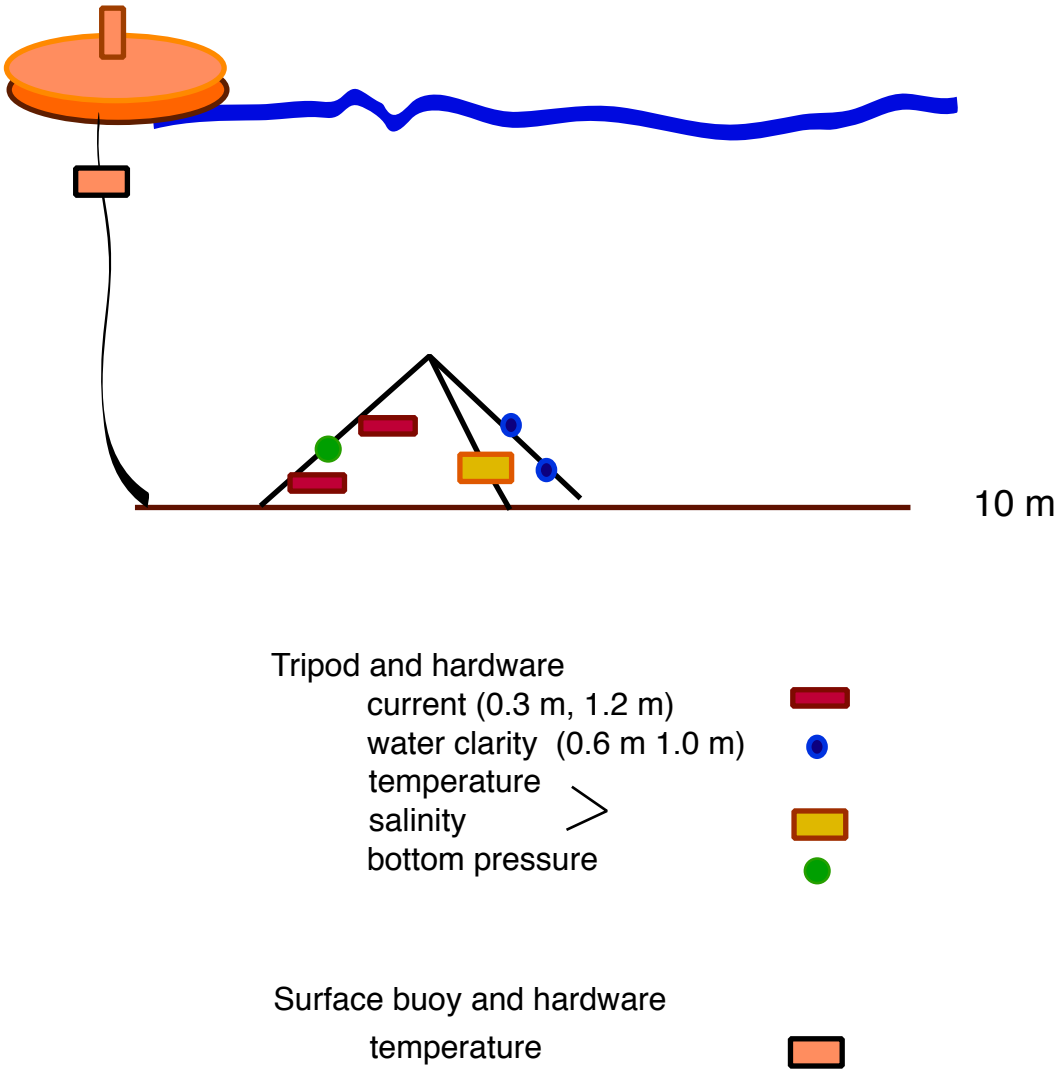

Figure 2-7a. Schematic of moorings deployed at site HB01.

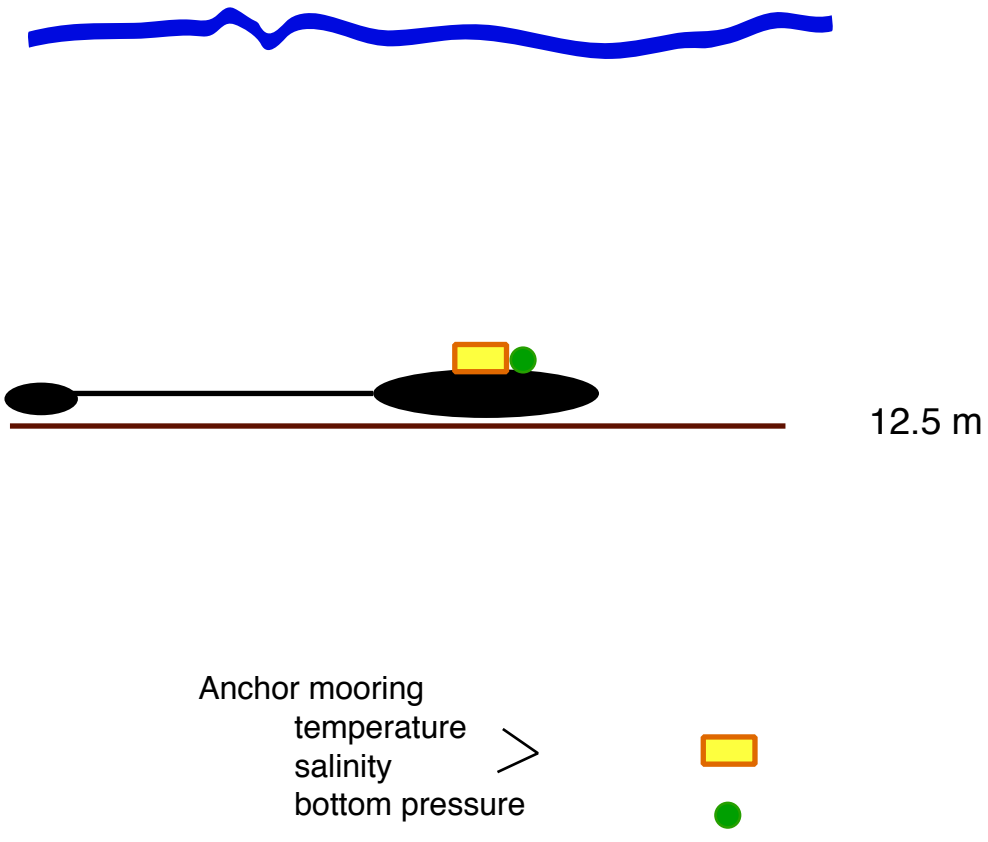

Figure 2-7b. Schematic of moorings at site HB02.

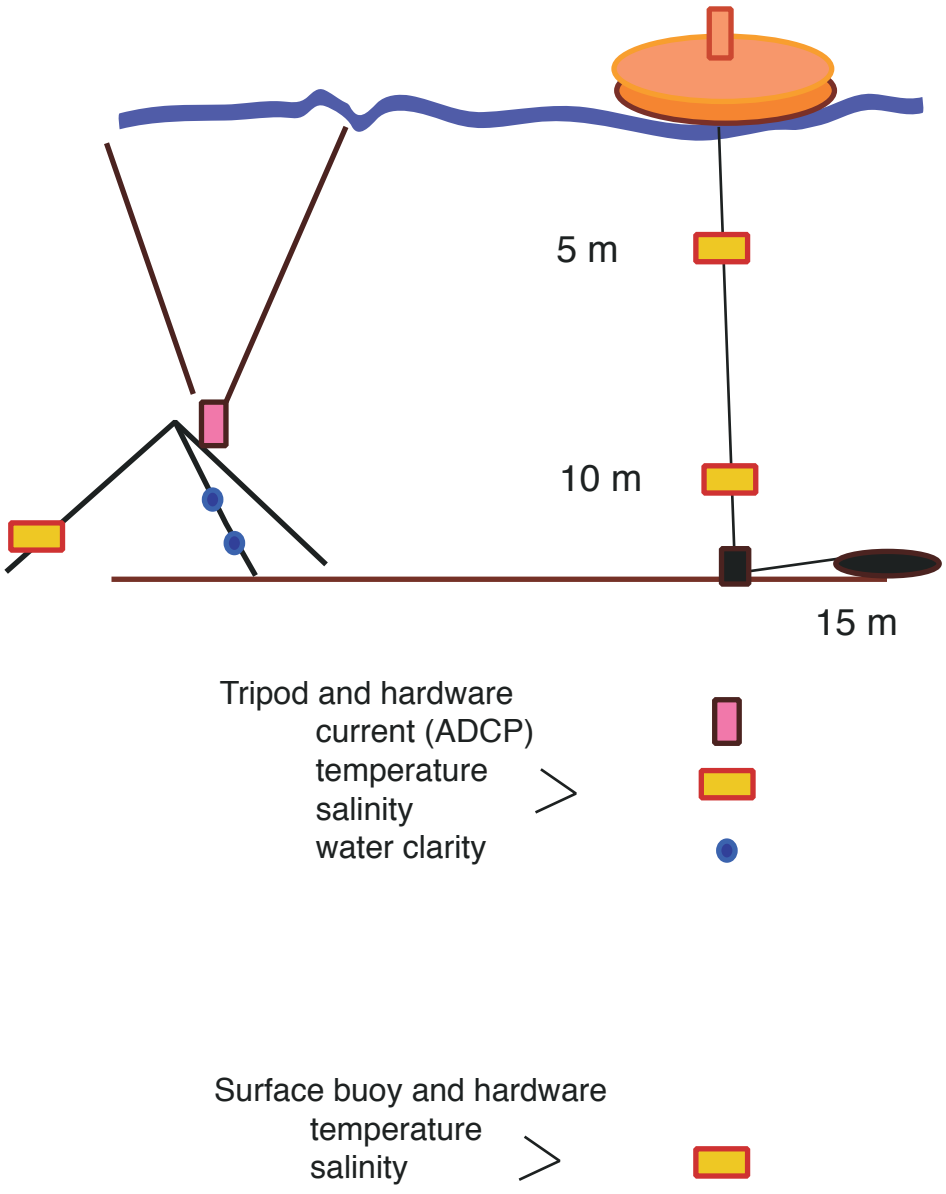

Figure 2-7c. Schematic of moorings at site HB03.

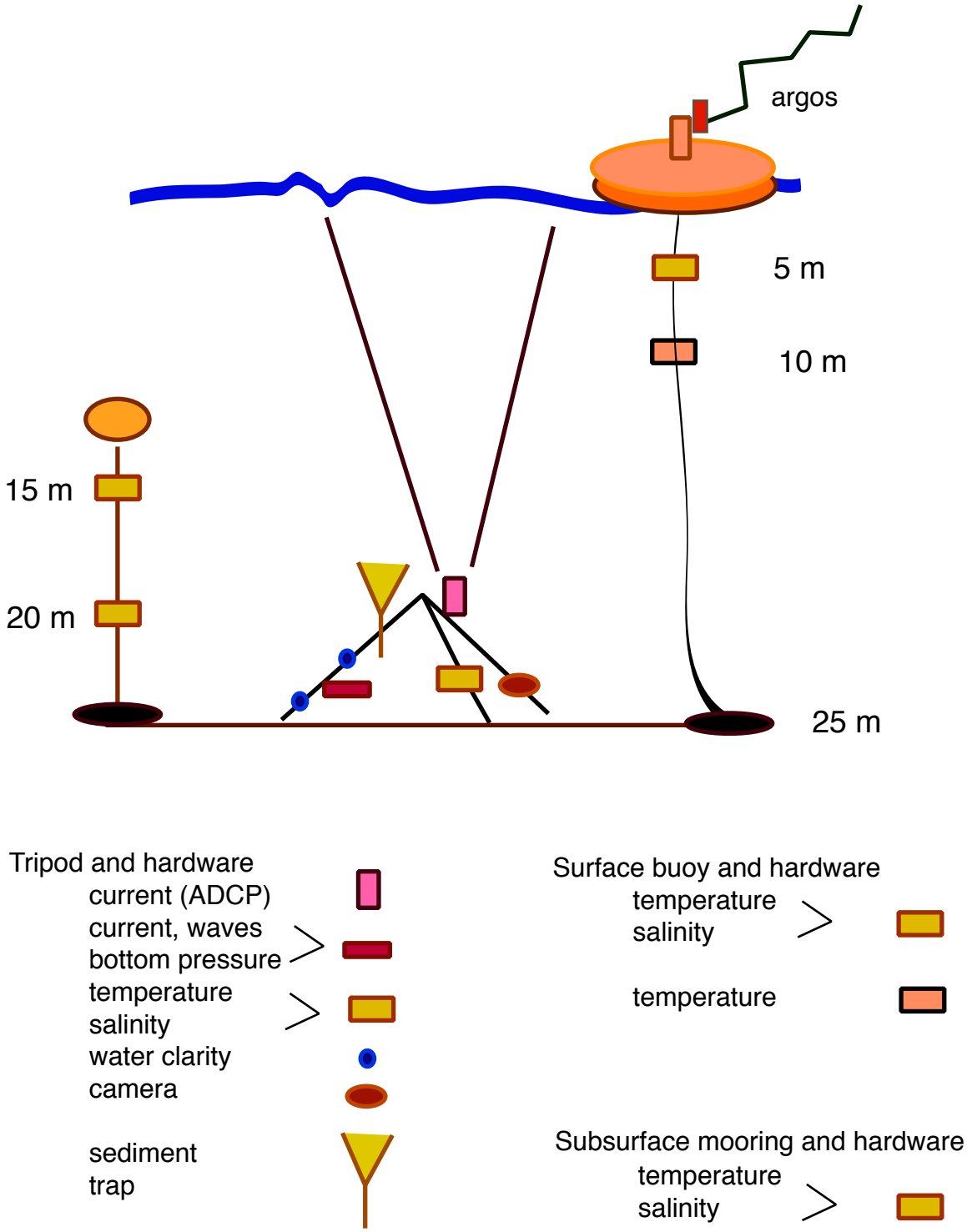

Figure 2-7d. Schematic of moorings at site HB05.

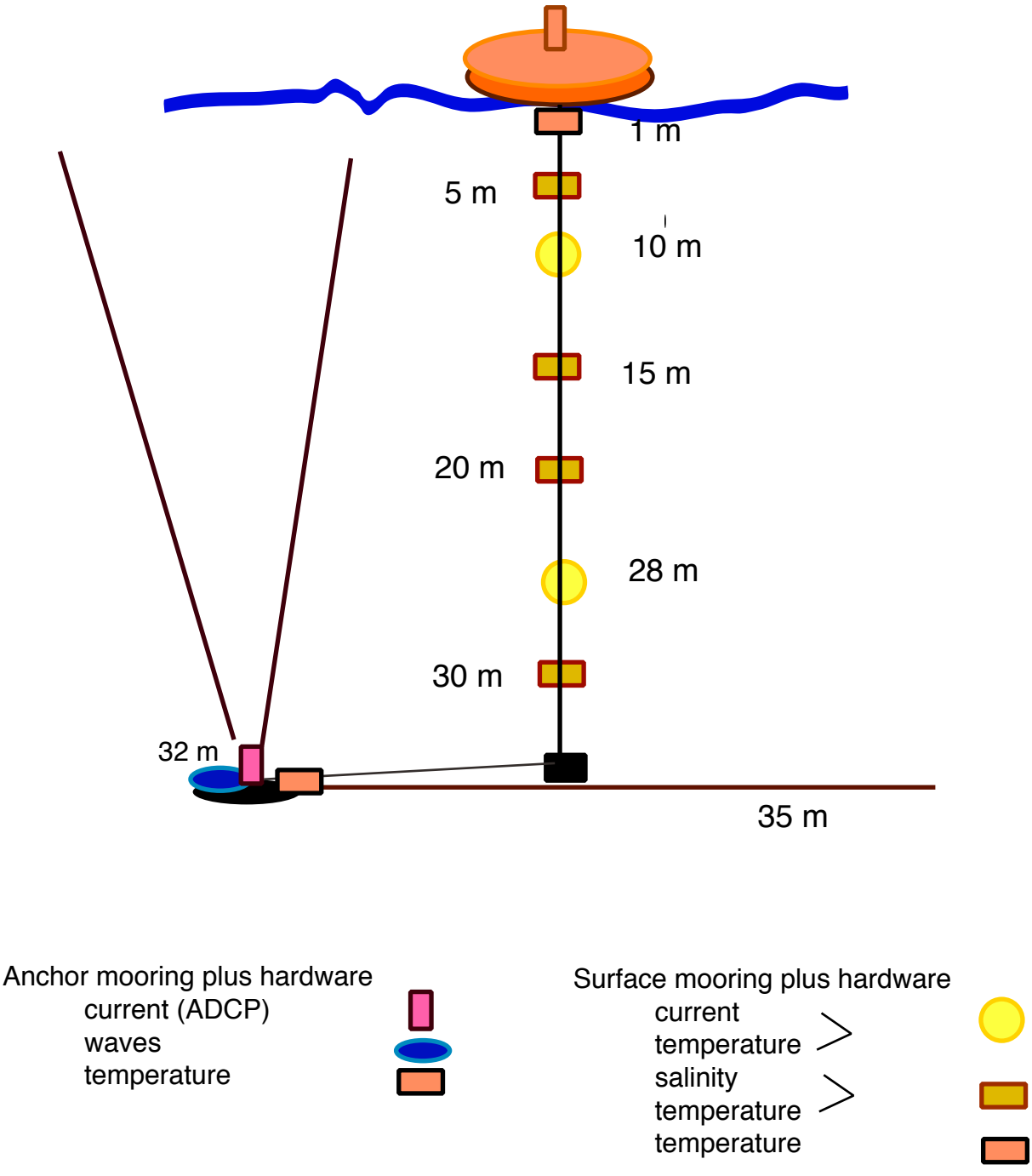

Figure 2-7e. Schematic of moorings at site HB06.

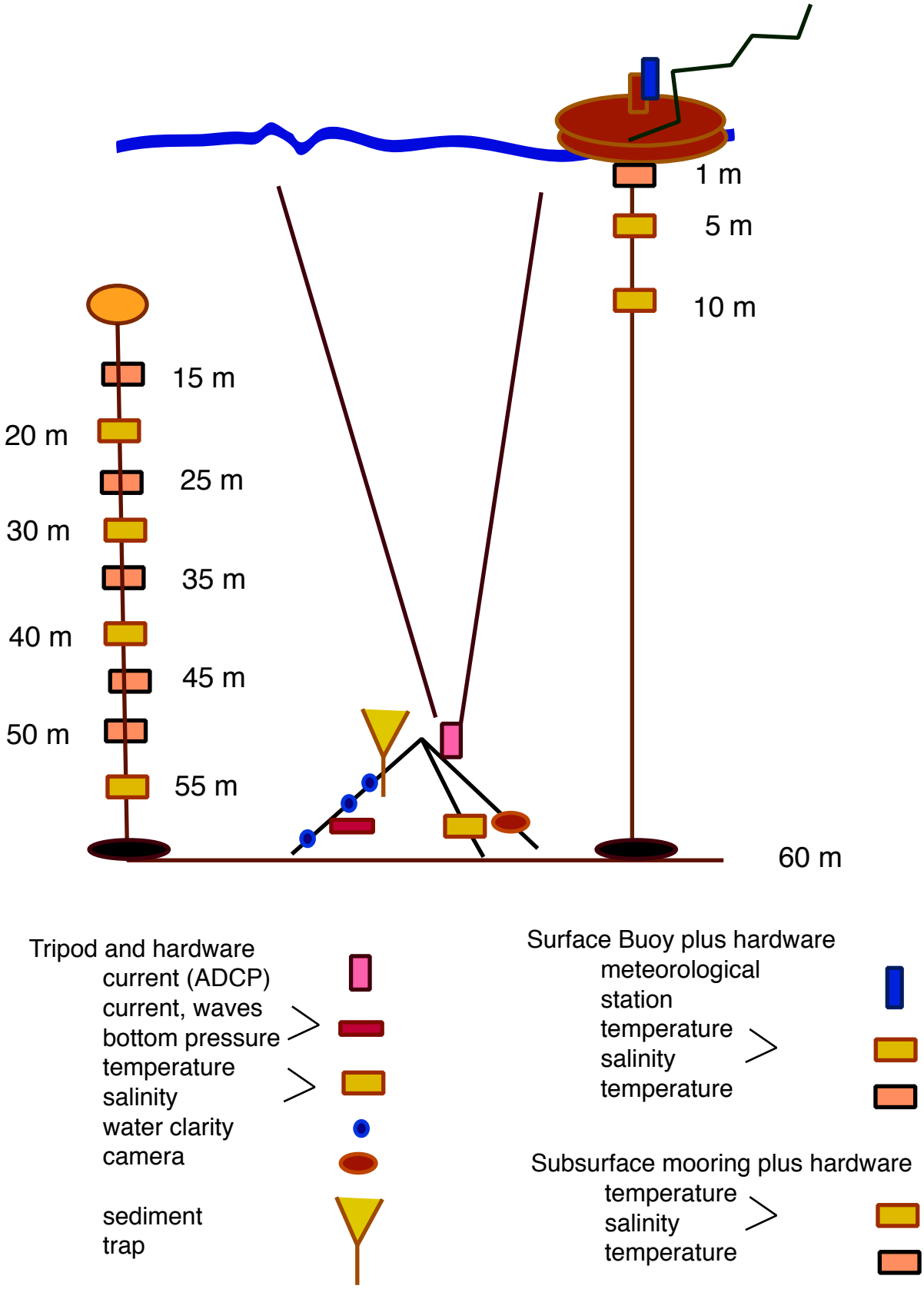

Figure 2-7f. Schematic of moorings at site HB07.

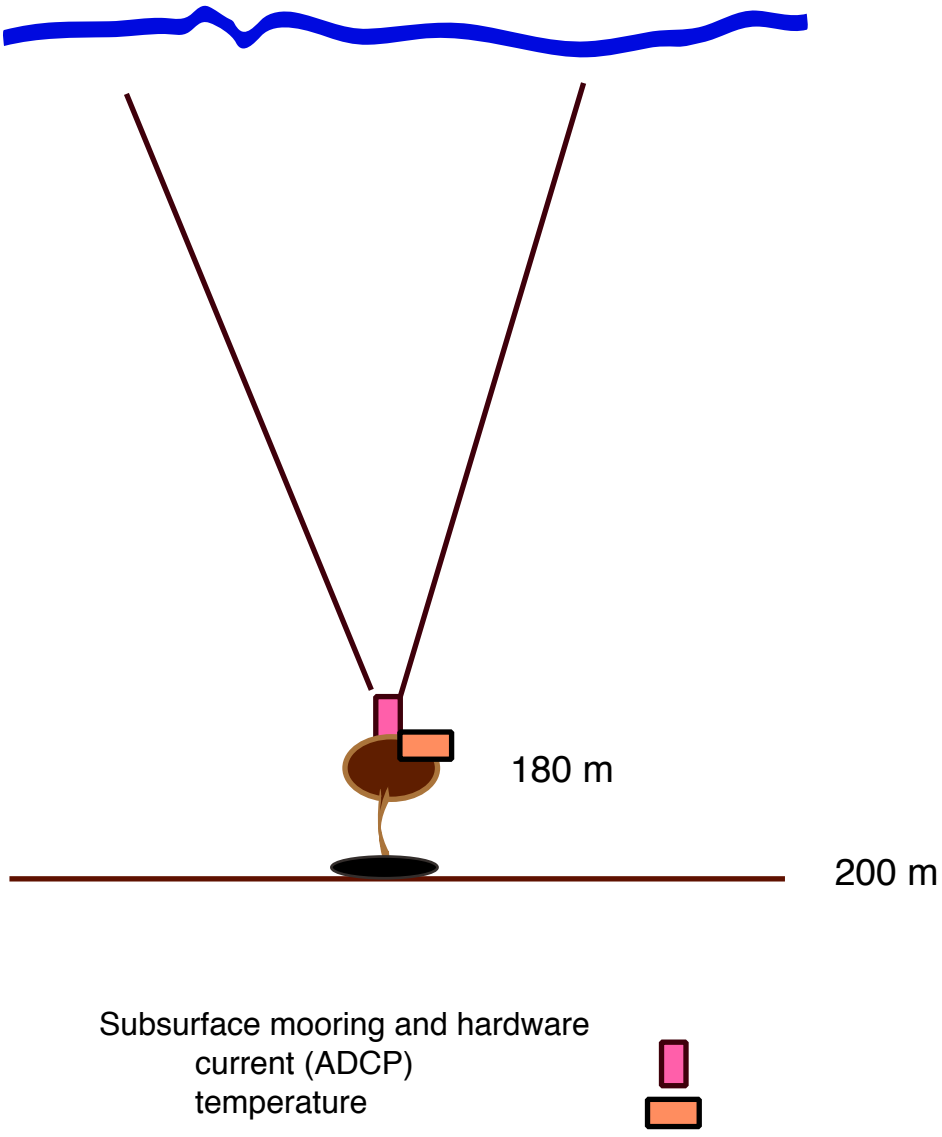

Figure 2-7g. Schematic of moorings at site HB08.

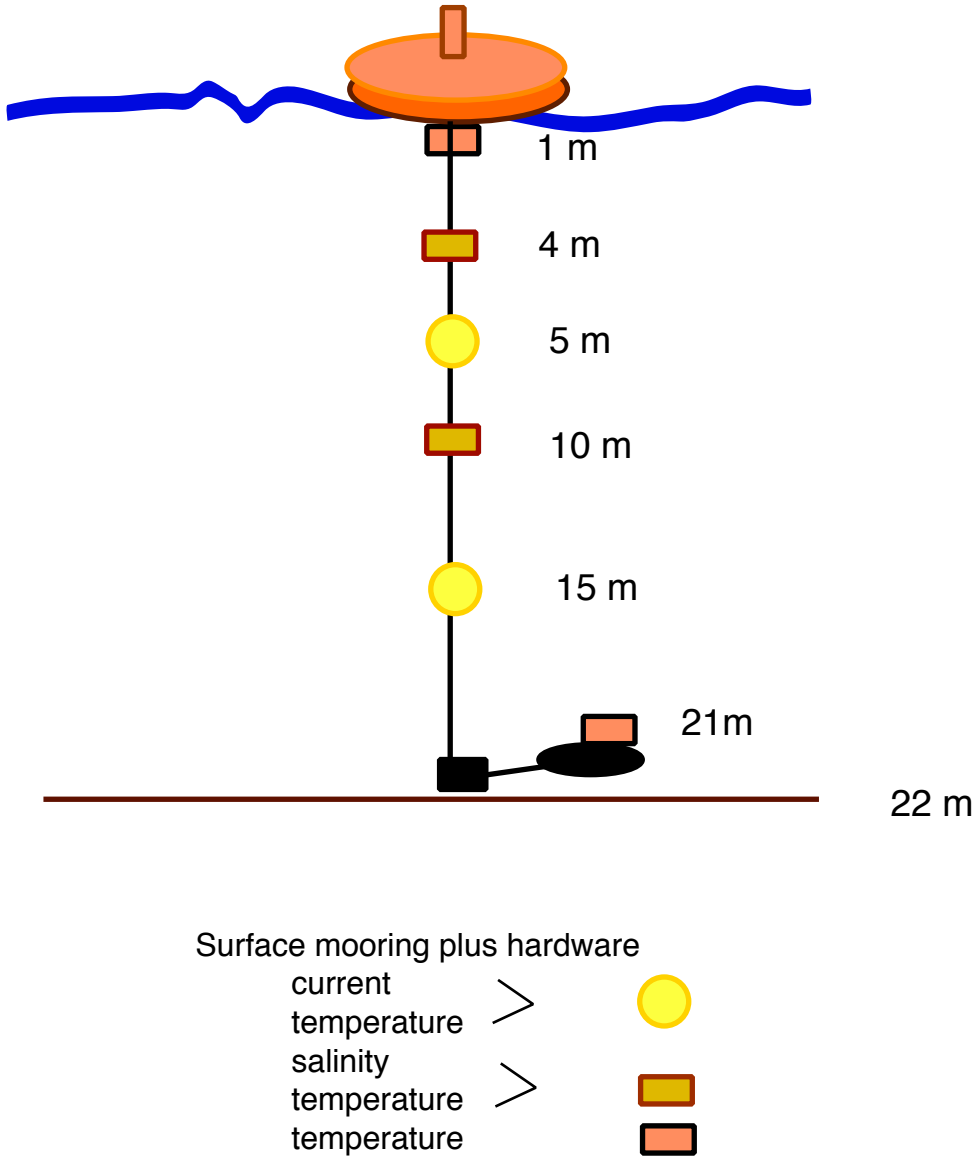

Figure 2-7h. Schematic of moorings at site HB09.

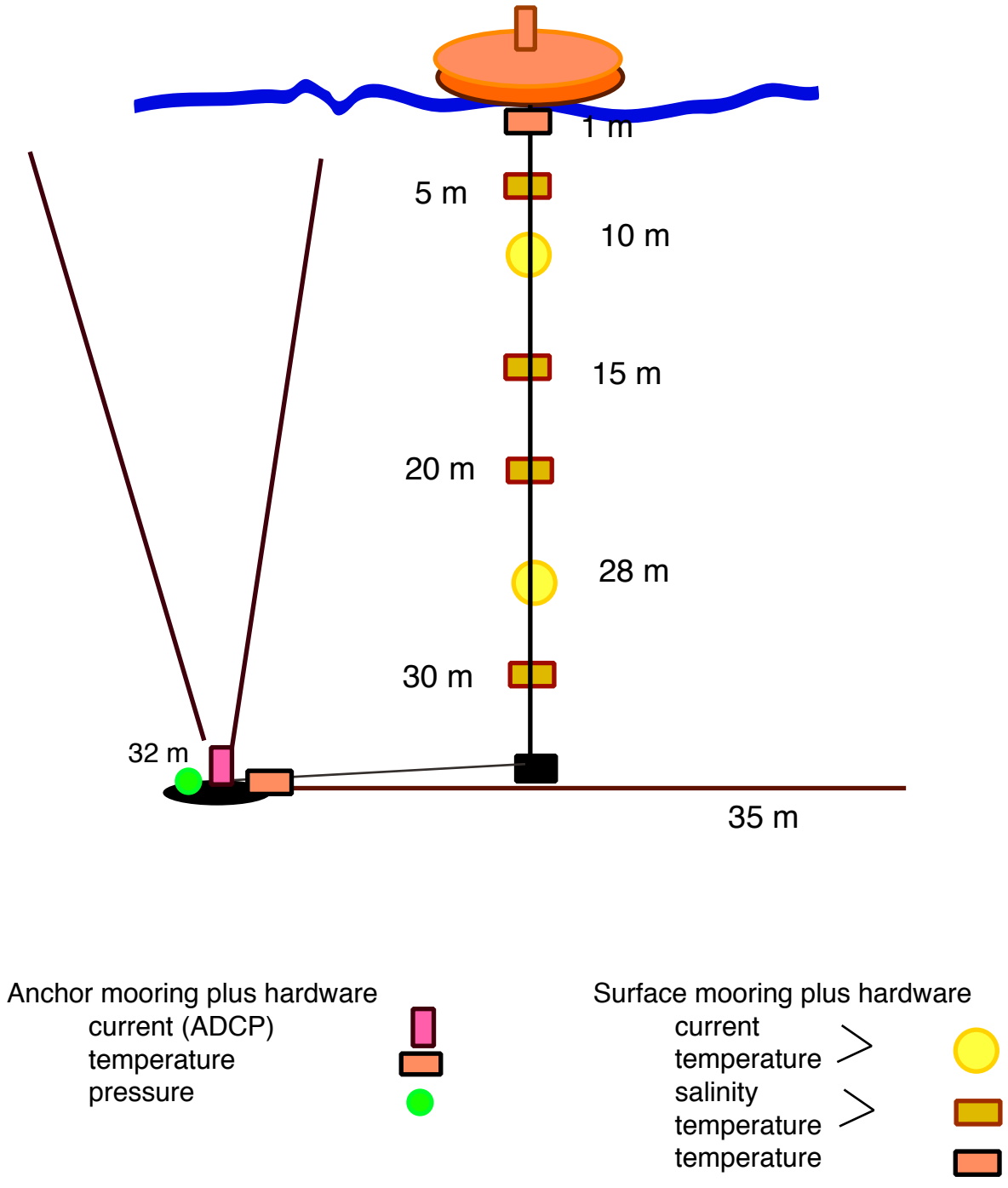

Figure 2-7i. Schematic of moorings at site HB10.

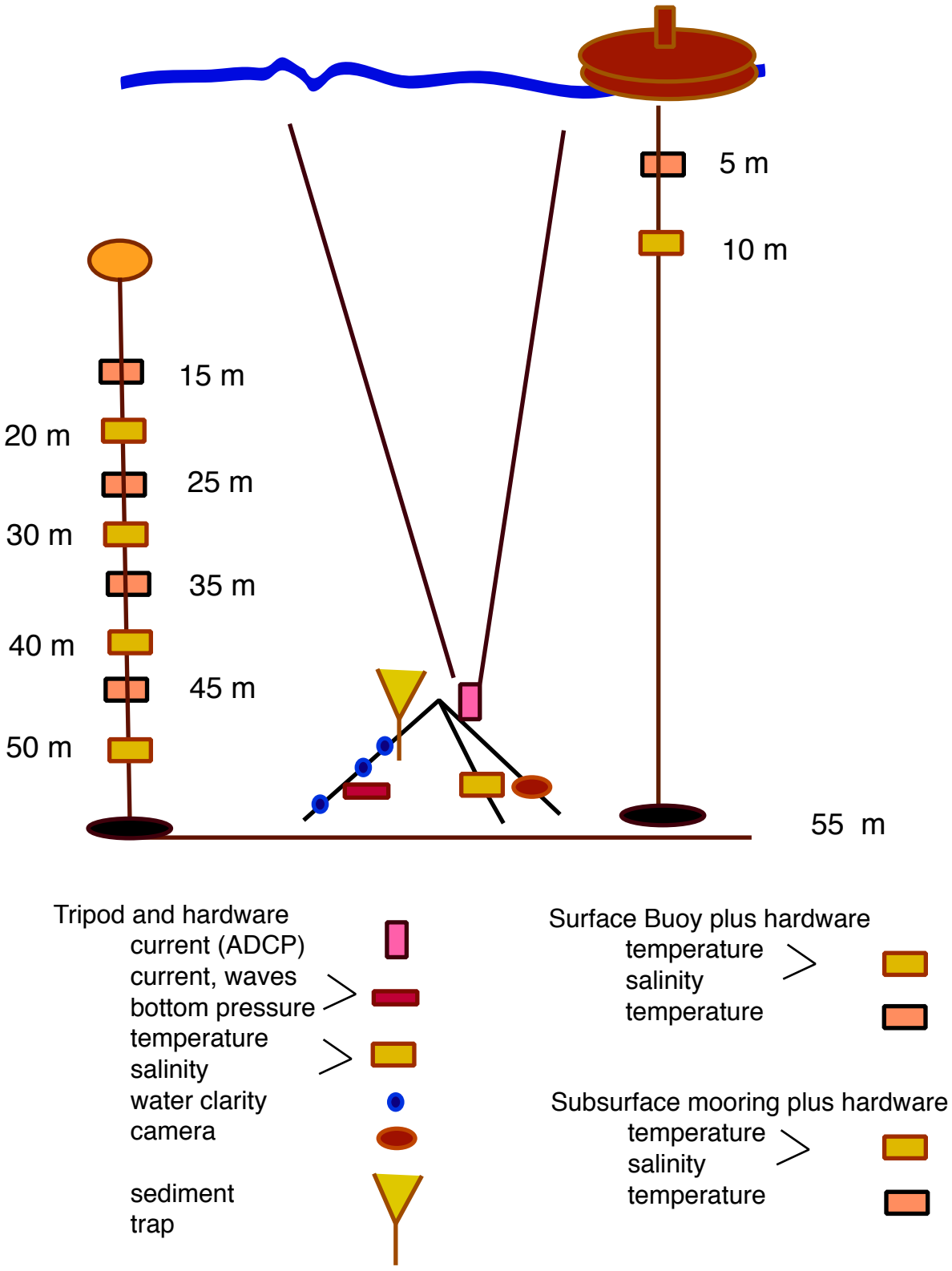

Figure 2-7j. Schematic of moorings at site HB11.

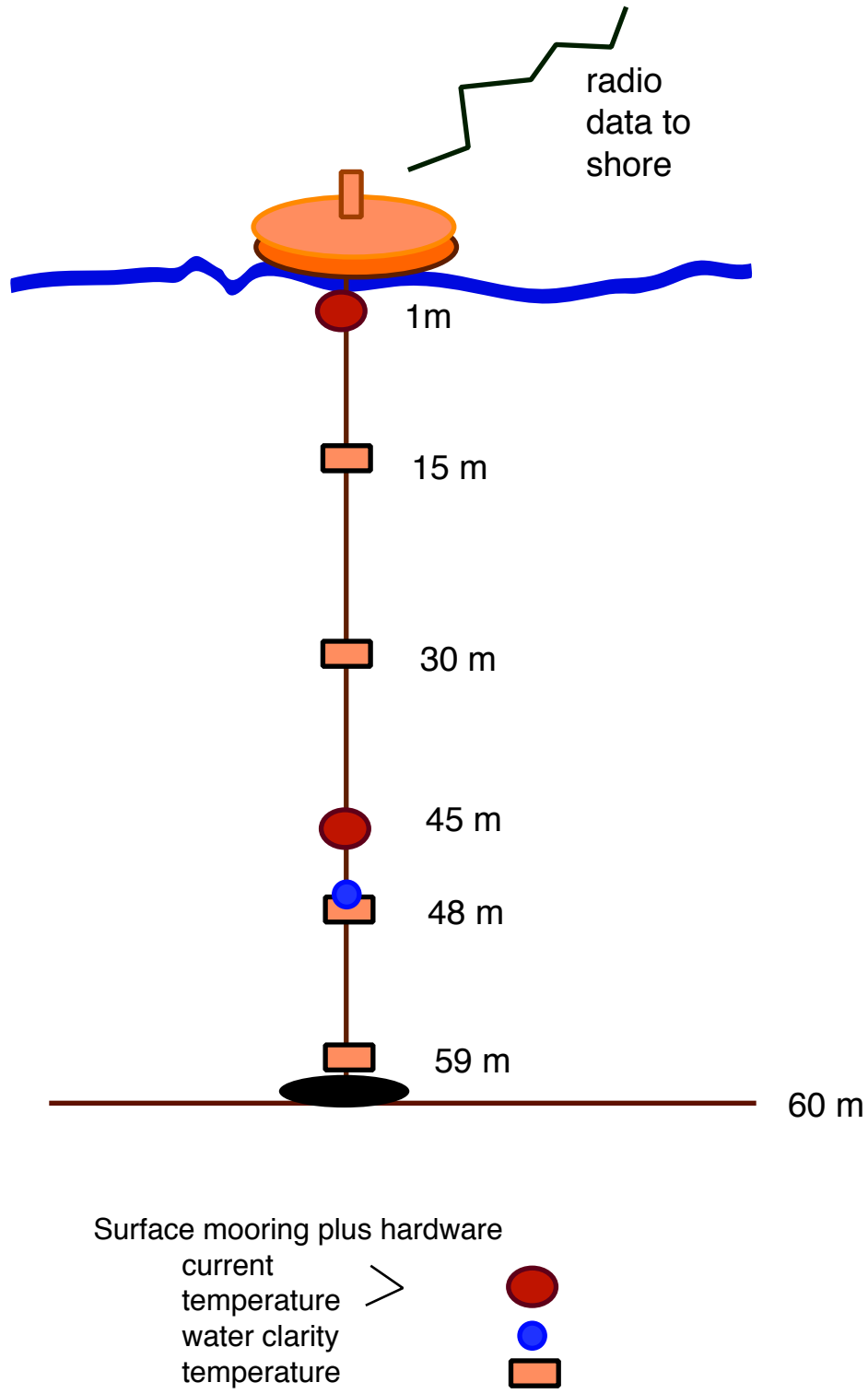

Figure 2-7k. Schematic of moorings at site HB12.

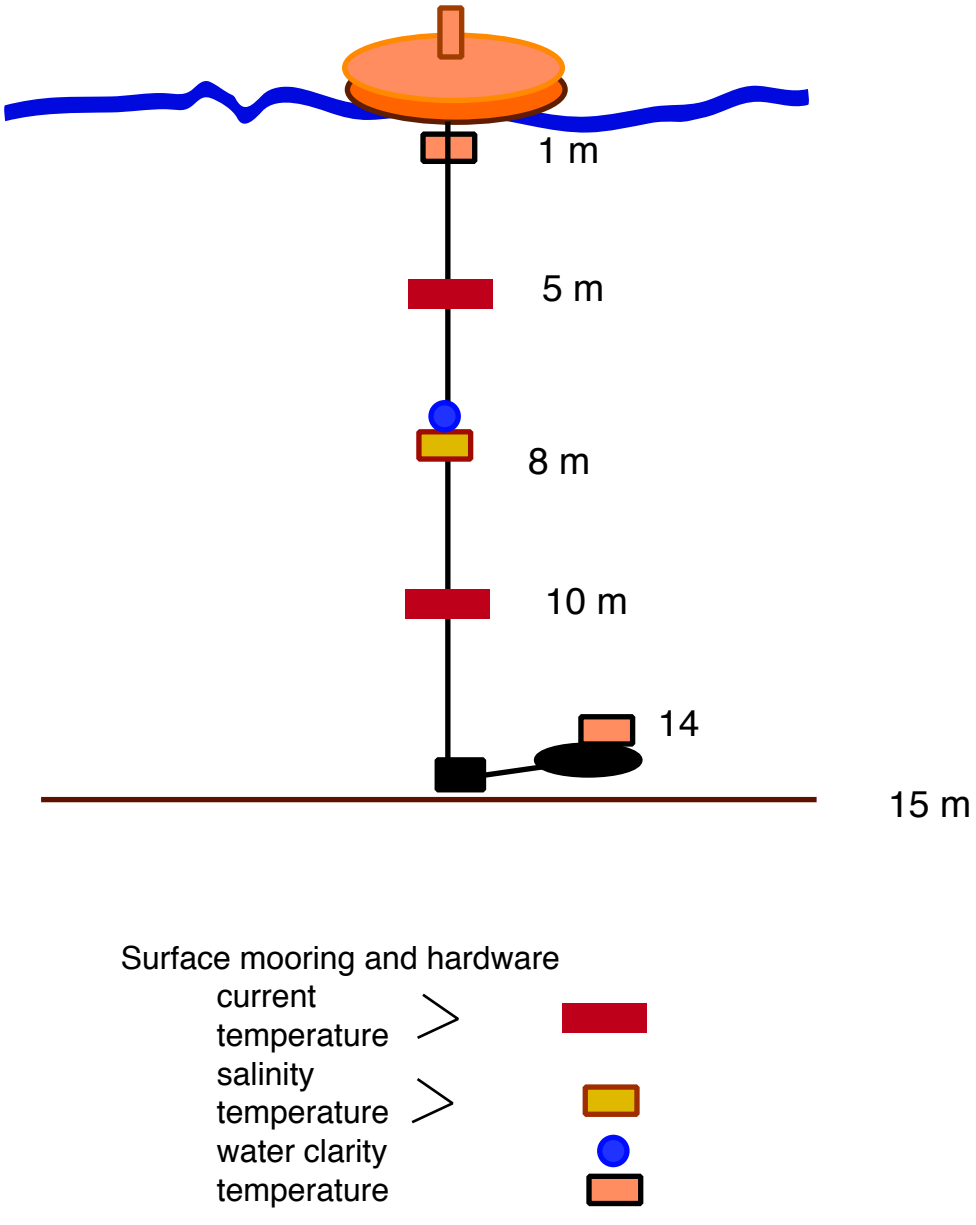

Figure 2-7l. Schematic of moorings at site HB13.

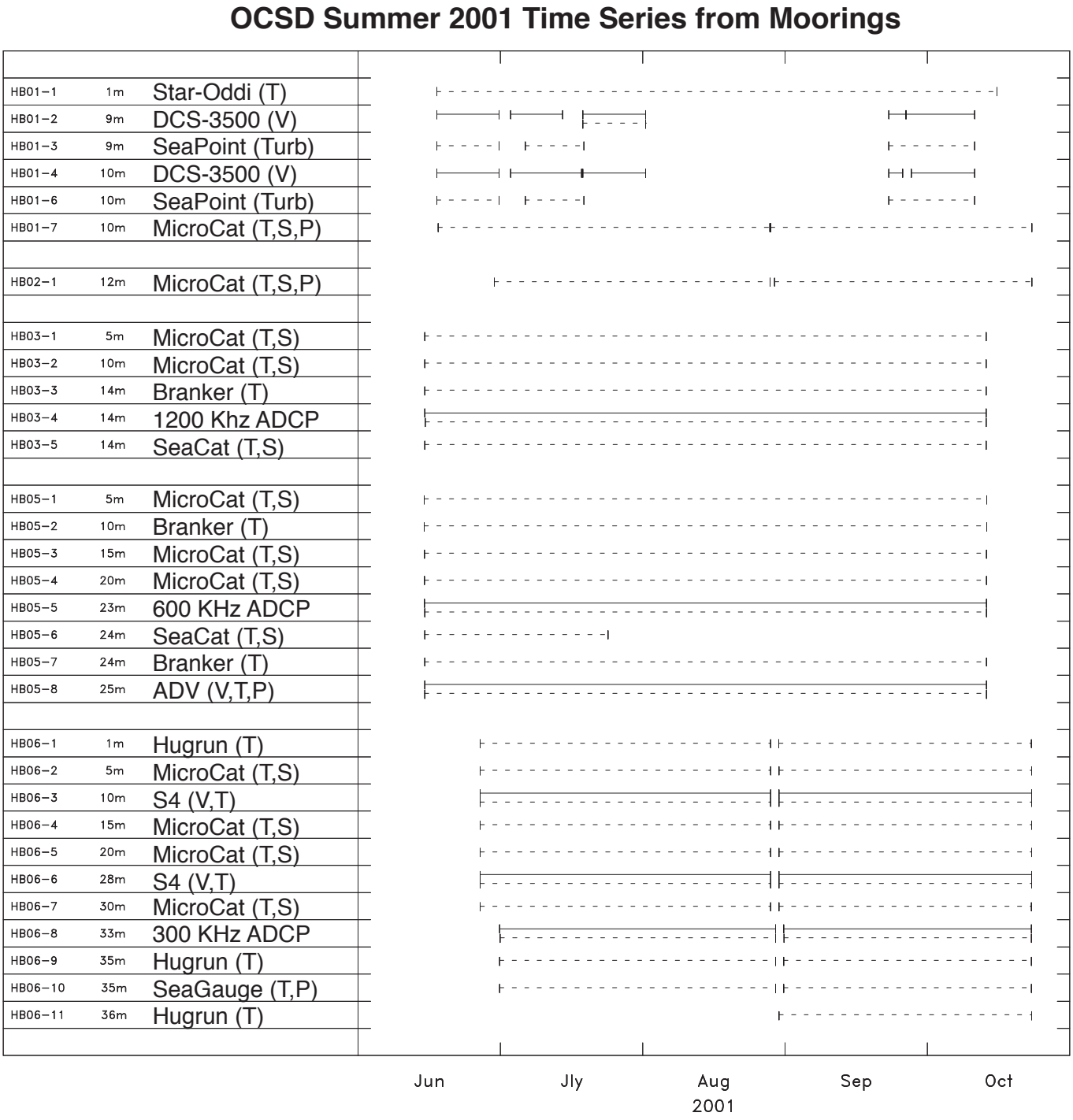

Figure 2-8a. Time lines of data return for moorings HB01 through HB06. Instrument depths are noted. Solid and dashed lines represent the returns for velocity and scalar variables, respectively.

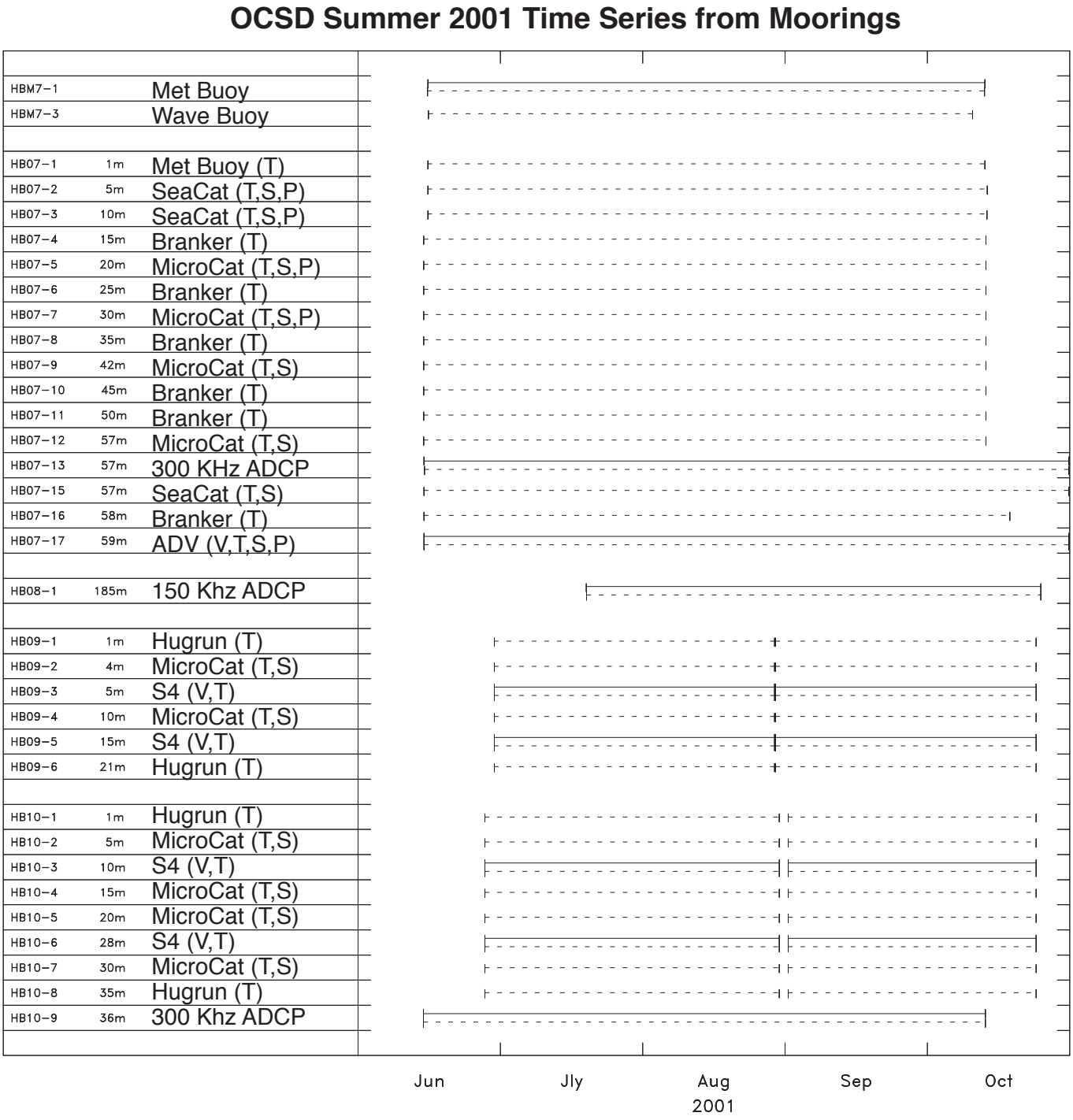

Figure 2-8b. Time lines of data return for moorings HB07 through HB10. Instrument depths are noted. Solid and dashed lines represent the returns for velocity and scalar variables, respectively.

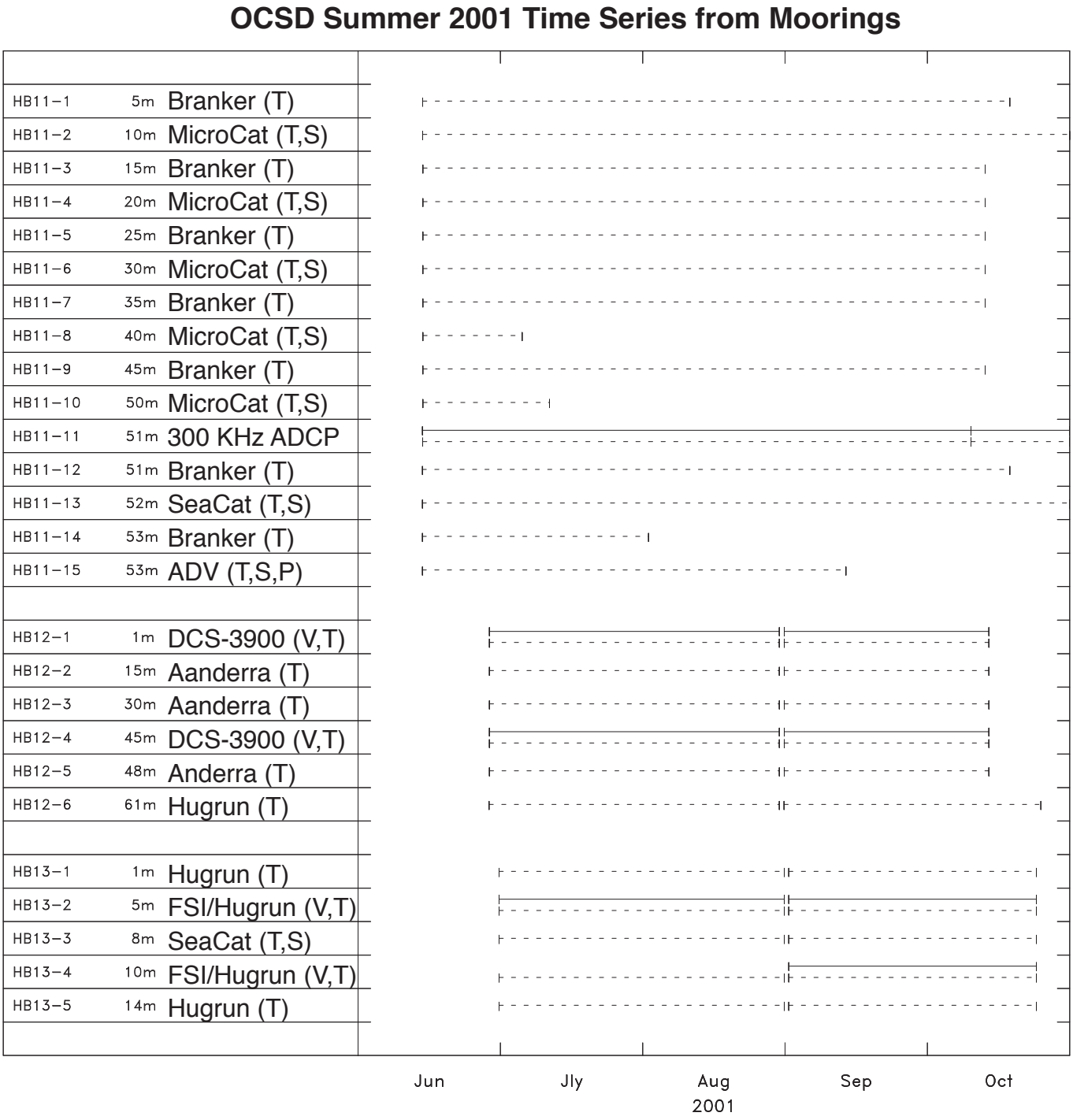

Figure 2-8c. Time lines of data return for moorings HB11 through HB13. Instrument depths are noted. Solid and dashed lines represent the returns for velocity and scalar variables, respectively.

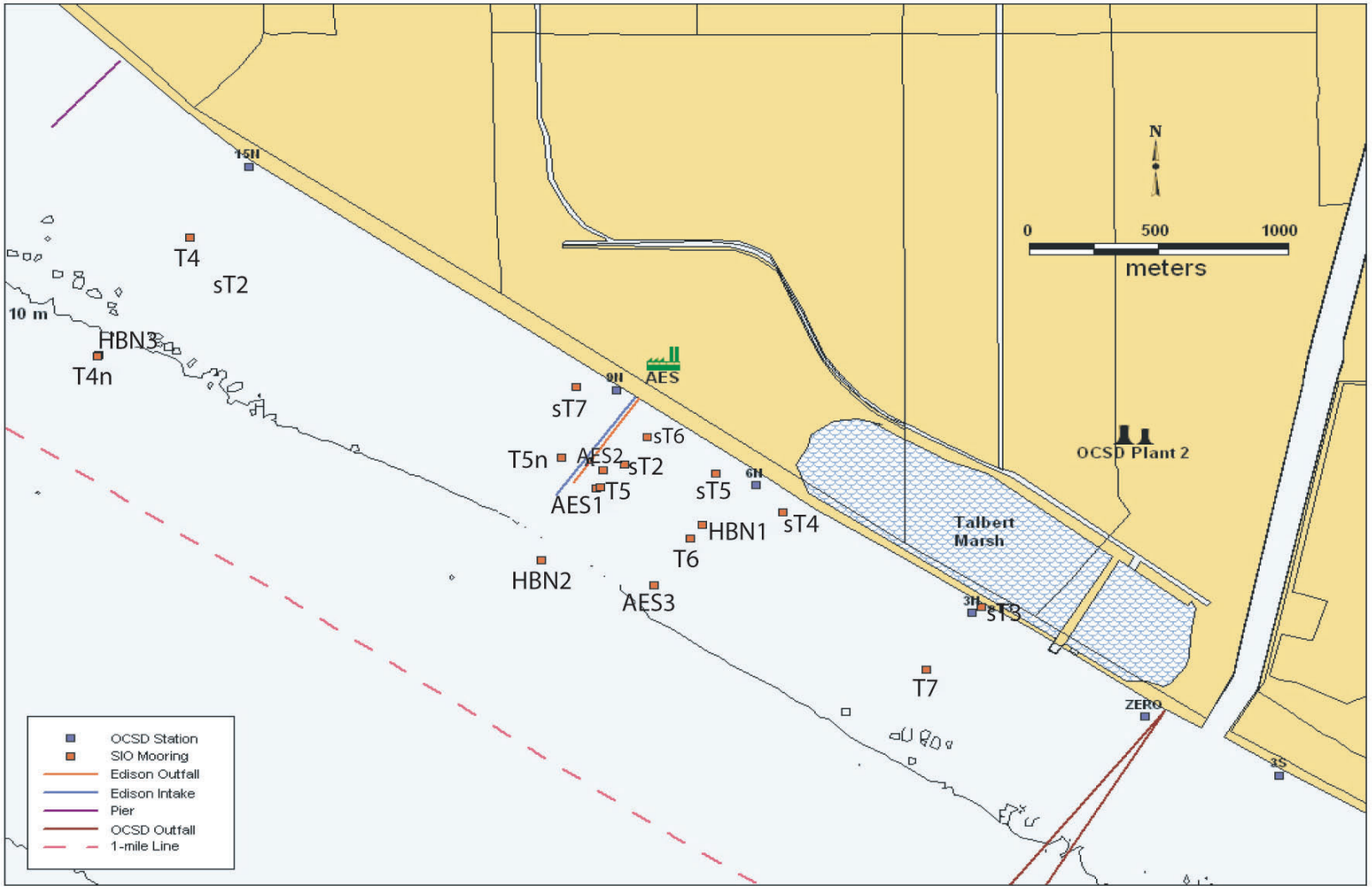

Figure 2-9. Location of nearshore moorings (red squares), beach sampling (blue squares), power plant intake (blue), and discharge (red), Talbert Marsh, and Santa Ana River.

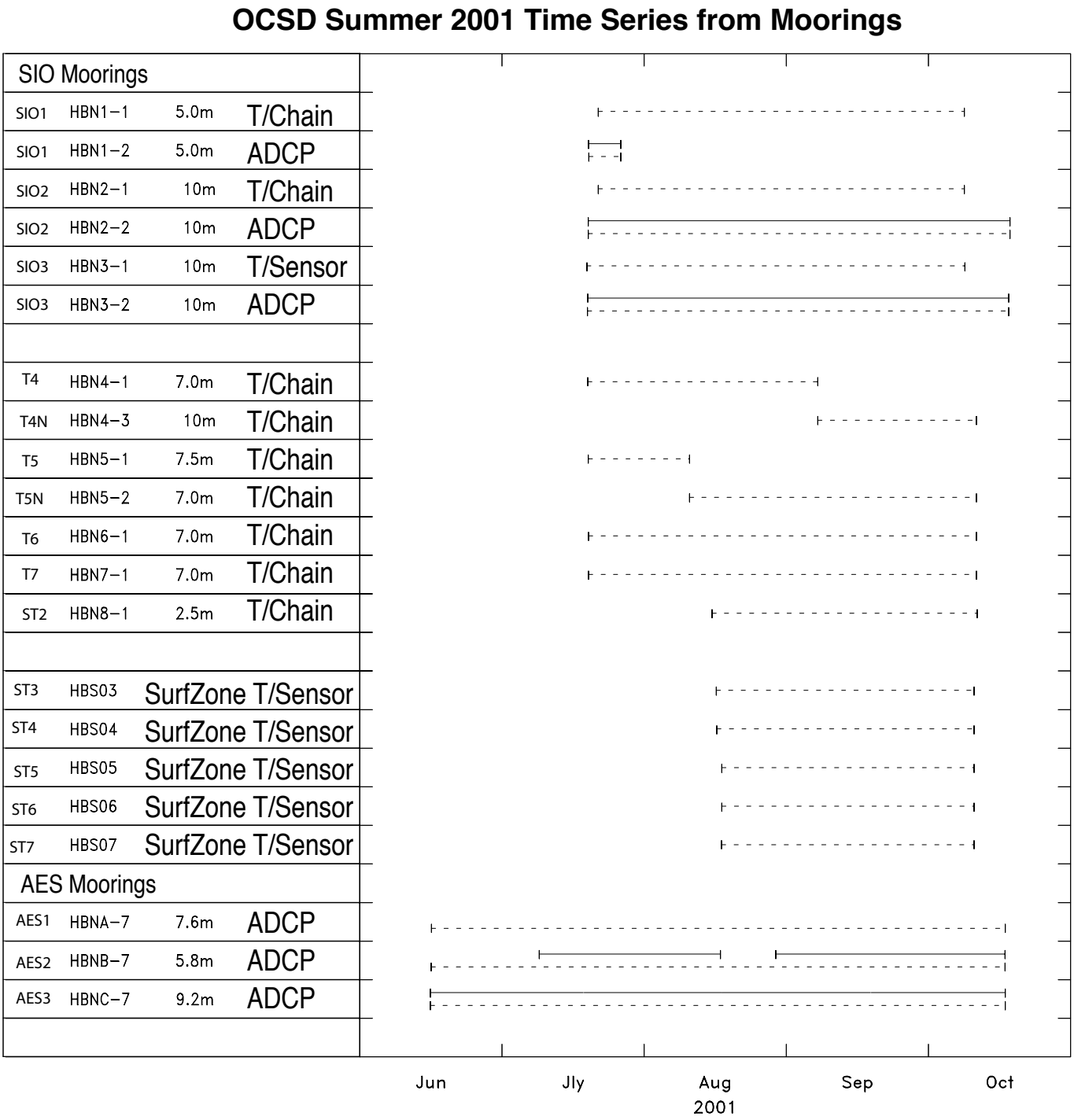

Figure 2-10. Time lines of data return for the near shore moorings deployed by SIO and AES. Instrument depths are noted. Solid and dashed lines represent the returns for velocity and scalar variables, respectively.

Table 2-1. MPN Index and 95% confidence limits for various combinations of positive results for Methods 9221B and 9221E: Multiple-Tube Fermentation Technique For Fecal Coliforms (EC Medium) and Standard Total Coliform Fermentation Technique where five tubes per dilution are used (10 mL, 1.0 mL and 0.1 mL sample portions).

Combination of Positive Tubes	MPN/ I00 mL	95% Confidence Limit		Combination of Positive Tubes	MPN/ 100 mL	95% Confidence Limits	
		Lower	Upper			Lower	Upper
0-0-0	<2	1.0	10	4-2-0	22	9.0	56
0-0-1	2	1.0	10	4-2-1	26	12	65
0-1-0	2	1.0	14	4-3-0	27	12	67
0-2-0	4			4-3-1	33	15	77
				4-4-0	34	16	80
1-0-0	2	1.0	11	5-0-0	23	9.0	86
1-0-1	4	1.0	15	5-0-1	30	10	110
1-1-0	4	1.0	15	5-0-2	40	20	140
1-1-1	6	2.0	18	5-1-0	30	10	120
1-2-0	6	2.0	18	5-1-1	50	20	150
				5-1-2	60	30	180
2-0-0	4	1.0	17	5-2-0	50	20	170
2-0-1	4	2.0	20	5-2-1	70	30	210
2-1-0	7	2.0	21	5-2-2	90	40	250
2-1-1	9	3.0	24	5-3-0	80	30	250
2-2-0	9	3.0	25	5-3-1	110	40	300
2-3-0	12	5.0	29	5-3-2	140	60	360
3-0-0	8	3.0	24	5-3-3	170	80	410
3-0-1	11	4.0	29	5-4-0	130	50	390
3-1-0	11	4.0	29	5-4-1	170	70	480
3-1-1	14	6.0	35	5-4-2	220	100	580
3-2-0	14	6.0	35	5-4-3	280	120	690
3-2-1	17	7.0	40	5-4-4	350	160	820
4-0-0	13	5.0	38	5-5-0	240	100	940
4-0-1	17	7.0	45	5-5-1	300	100	1300
4-1-0	17	7.0	46	5-5-2	500	200	2000
4-1-1	21	9.0	55	5-5-3	900	300	2900
4-1-2	26	12	63	5-5-4	1600	600	5300
				5-5-5	1600		

Table 2-2. Confidence limits around total coliform = 10,000; fecal coliform = 400; and enterococci = 104 are shown, based on a study intercomparing 22 labs (including OCSD) in southern California (Noble et al., 2003). Units are MPN/100 mL or cfu/100 mL. *Methods used by OCSD are italicized*. IDEXX is the company manufacturing the Colilert and Enterolert test methods.

Confidence Limits for Bacterial Water Quality Indicator Methods					
		Lower 95% CI	Lower 60% CI	Upper 60% CI	Upper 95% CI
Total coliform	*MTF*	*3482*	*5901*	*16946*	*28717*
	MF	7947	8915	11218	12583
	IDEXX	*4339*	*6587*	*15181*	*23048*
Fecal coliform	*MTF*	*122*	*221*	*724*	*1310*
	MF	*188*	*274*	*584*	*851*
	IDEXX	*164*	*256*	*625*	*976*
Enterococci	MTF	36	61	176	299
	MF	*70*	*86*	*126*	*153*
	IDEXX	*63*	*81*	*134*	*173*

Table 2-3a. Huntington Beach Phase III Offshore Water Quality Monitoring Stations**.**

Station	Line #	Latitude	Longitude	Depth	Comment
UPCOAST TRANSECTS					
2348	U1	33° 39.528'	118° 00.854'	10	
2349	U1	33° 39.190'	118° 01.135'	12	
2350	U1	33° 38.667'	118° 01.566'	16	
2351	U1	33° 38.151'	118° 02.001'	22	
2303	U2	33° 37.537'	118° 00.936'	22	
2302	U2	33° 38.053'	118° 00.495'	16	
2301	U2	33° 38.572'	118° 00.064'	11	
CUA	U2	33° 38.880'	117° 59.840'	7	
1A	U3	33° 38.510'	117° 59.240'	7	
2231	U3	33° 38.340'	117° 59.491'	11	
2232	U3	33° 37.788'	117° 59.939'	15	
2233	U3	33° 37.227'	118° 00.405'	22	
2D	U4	33° 37.073'	118° 00.137'	22	
2C	U4	33° 37.654'	117° 59.657'	16	
2B	U4	33° 38.190'	117° 59.060'	11	
2A	U4	33° 38.370'	117° 58.950'	6	
1G	U5	33° 38.160'	117° 58.740'	9	
2221	U5	33° 38.099'	117° 58.908'	11	
2222	U5	33° 37.522'	117° 59.374'	16	
2223	U5	33° 36.924'	117° 59.871'	23	
2224	U5	33° 36.035'	118° 00.608'	32	Parallel Cast
DOWNCOAST TRANSECTS					
DCD	D1	33° 36.263'	117° 55.674'	6	
2101	D1	33° 36.183'	117° 55.749'	11	
2102	D1	33° 35.631'	117° 56.206'	31	
2103	D1	33° 35.089'	117° 56.678'	110	
2183	D2	33° 35.701'	117° 57.744'	36	
2182	D2	33° 36.272'	117° 57.264'	17	
2181	D2	33° 36.877'	117° 56.752'	10	
DCC	D2	33° 37.002'	117° 56.663'	9	
DCB	D3	33° 37.311'	117° 57.201'	9	
2191	D3	33° 37.185'	117° 57.290'	10	
2192	D3	33° 36.594'	117° 57.778'	16	
2193	D3	33° 36.003'	117° 58.266'	29	
2203	D4	33° 36.313'	117° 58.810'	25	
2202	D4	33° 36.901'	117° 58.314'	17	
2201	D4	33° 37.493'	117° 57.831'	10	
DCA	D4	33° 37.628'	117° 57.733'	8	
DC	D5	33° 37.860'	117° 58.120'	8	
2211	D5	33° 37.801'	117° 58.368'	9	
2212	D5	33° 37.210'	117° 58.852'	16	
2213	D5	33° 36.619'	117° 59.343'	22	
2224	D5	33° 36.035'	118° 00.608'	32	Parallel Cast

Table 2-3b. Sampling and sample pickup sequence for offshore water quality sampling.

START	1200	1600	2000	2400	0400	0800	1200	1600	2000	2400	0400	0800	1200
JB	Upcoast Stations			Downcoast stations			Upcoast stations			Downcoast stations			
Early Bird			Upcoast Stations			Downcoast stations			Upcoast stations				
Westwind	Downcoast Stations				Upcoast stations			Downcoast stations			Upcoast stations		

Table 2-4. Parameters used in the nearfield plume model.

Model Fixed Parameters	Value
Effluent density	0.9972 g/cm^3
Port diameter	0.09 m
Discharge depth	54.6 m
Number of ports	503
Port spacing	7.31 m
Computed diffuser length	1828.3 m
Diffuser orientation to North	97.0 degrees

Table 2-5a. Instruments deployed in summer 2001 across the shelf off Huntington Beach.

Mooring ID	Location		Water Depth (m)	Instrument Type	Instrument Depth (m)	Variables Measured	Sampling Rate	Rotation Interval	Instrument Source	SAIC ID	Filename Prototype	USGS ID #
	Latitude	Longitude										
HB01	33°37.975'N	117°58.891'W	10.7	SeaPoint	0.38 AB	Turb	15 min	30 days	SAIC	HB01-6	SP16xc.D	
			(Bottom	DCS-3500	0.72 AB	V	15 min	30 days	SAIC	HB01-4	SP14xc.D	
			Mounted)	SeaPoint	1.52 AB	Turb	15 min	30 days	SAIC	HB01-3	SP13xc.D	
				DCS-3500	1.52 AB	V	15 min	30 days	SAIC	HB01-2	SP12xc.D	
	AB=Above Bottom		(NYD)	Ammonia	0.6 AB	Ammonia	TBD	30 days	USC	HB01-5	SP15xc.D	
	NYD = Not Yet Deployed			MicroCat	0.2 AB	T,S & Press	2 min	30 days	OCSD	HB01-7	SP17xc.D	
				Star-Oddi	1	T	2 min	120 days	SAIC	HB01-1	SP11xc.D	
HB02	33°37.764'N	117°58.998'W	12.8 Bottom Mounted	MicroCat	12.3	T,S & Press	2 min	60 days	SAIC	HB02-1	SP21xc.D	
HB03a	33°37.560'N	117°59.206'W	16	MicroCat	5	T, S	2 min	120 days	WH	HB03-1	SP31xc.D	6501
			Surface Mooring	MicroCat	10	T, S	2 min	120 days	WH	HB03-2	SP32xc.D	6502
HB03b	33°37.598'N	117°59.227'W	15	1200 kHz ADCP	1.3 AB	V,T	3 min	120 days	WH	HB03-4	SP34xc.D	6511
			Bottom	Sed. Trap	1.4 AB	Sed.,T on Pod	-	120 days	WH/Menlo	HB03-3	SP33xc.D	6513
			Mounted	SeaCat	1.0 AB	T,S,2 Obs	2.5 min	120 days	Menlo	HB03-5	SP35xc.D	6512
HB04	(Not Yet Deployed)		20	S4	14	V,Pressure	TBD	30 days	USC	HB04-1	SP41xc.D	
			S-Tether	Ammonia	17	Ammonia	TBD	30 days	USC	HB04-2	SP42xc.D	
HB05a	33°36.710'N	117°59.802'W	25	MicroCat	5	T,S	2 min	120 days	WH	HB05-1	SP51xc.D	6521
			Surface Mooring	Temp.	10	T	4 min	120 days	Menlo	HB05-2	SP52xc.D	6522
HB05b	33°36.719'N	117°59.704'W	25	MicroCat	15	T,S	2 min	120 days	WH	HB05-3	SP53xc.D	6541
			Subsurface Mooring	MicroCat	20	T,S	2 min	120 days	WH	HB05-4	SP54xc.D	6542
HB05c	33°36.745'N	117°59.822'W	25.5	600 kHz ADCP	2.3 AB	V,T	3 min	120 days	WH	HB05-5	SP55xc.D	6531
			Bottom	SeaCat	1.9 AB	T,S,Trans.	2.5 min	120 days	WH	HB05-6	SP56xc.D	6533
			Mounted	Sed. Trap	1.1 AB	Sed.	-	120 days	WH/Menlo			
				Camera	1.2AB	Photo, T on Pod	6 hrs	120 days	Menlo	HB05-7	SP57xc.D	6534
				ADV	0.8 AB	V,T,P,2 0bs	20 min/1 hr	120 days	Menlo	HB05-8	SP58xc.D	6532
HB06a	33°35.674'N	118°00.571'W	35.6	Hugrun	1	T	5 min	60 days	SAIC	HB06-1	SP61xc.D	
			Surface	MicroCat	5	T,S	1 min	60 days	OCSD	HB06-2	SP62xc.D	
			Mooring	S4	10	V, T	5 min	60 days	OCSD	HB06-3	SP63xc.D	
				MicroCat	15	T,S	1 min	60 days	OCSD	HB06-4	SP64xc.D	
				MicroCat	20	T,S	1 min	60 days	OCSD	HB06-5	SP65xc.D	
				S4	28	V,T	5 min	60 days	SAIC	HB06-6	SP66xc.D	
				MicroCat	30	T,S	1 min	60 days	OCSD	HB06-7	SP67xc.D	
				Hugrun	35.1	T	5 min	60 days	SAIC	HB06-11	SP6Bxc.D	

x = deployment # (1-4)
c = Data Type Code (C,T,M,etc.)

Table 2-5a, cont. Instruments deployed in summer 2001 across the shelf off Huntington Beach.

Mooring ID	Location		Water Depth (m)	Instrument Type	Instrument Depth (m)	Variables Measured	Sampling Rate	Rotation Interval	Instrument Source	SAIC ID	Filename Prototype	USGS ID #
	Latitude	Longitude										
HB06b	33°35.667'N	118°00.423'W	35.2	300 kHz ADCP	32.5	Vel,T	1 min	60 days	SAIC	HB06-8	SP68xc.D	
			S-Tether	Hugrun	34.6	T	5 min	60 days	SAIC	HB06-9	SP69xc.D	
				SeaGauge	34.8	Tide/Waves	15 min/6 hrs	60 days	SAIC	HB06-10	SP6Axc.D	
HB07a	33°34.593'N	118°01.256'W	60 Surface	Met Station	Surf	1 Wind,Atm_P, Rel_Hum,Air_T,SST	1 min	120 days	NPS	HBM7-1	SP7M1c.D	
				Wave Buoy	Surf	Sig_H, Dom_P,Dirn	60 min	120 days	NPS	HBM7-3	SP7M3c.D	
				Met Buoy	1	T	1min	120 days	NPS	HB07-1	SP71xc.D	
				SeaCat	5	T,S,P	6 min	120 days	NPS	HB07-2	SP72xc.D	
				SeaCat	10	T,S,P	6 min	120 days	NPS	HB07-3	SP73xc.D	
HB07b	33°34.606'N	118°01.156'W	62 Subsurface Mooring	Temp.	15	T	4 min	120 days	Menlo	HB07-4	SP74xc.D	6561
				MicroCat	20	T,S,P	2 min	120 days	NPS	HB07-5	SP75xc.D	
				Temp.	25	T	4 min	120 days	Menlo	HB07-6	SP76xc.D	6563
				MicroCat	30	T,S,P	2 min	120 days	NPS	HB07-7	SP77xc.D	
				Temp.	35	T	4 min	120 days	Menlo	HB07-8	SP78xc.D	6565
				MicroCat	40	T,S	2 min	120 days	WH	HB07-9	SP79xc.D	6566
				Temp.	45	T	4 min	120 days	Menlo	HB07-10	SP7Axc.D	6567
				Temp.	50	T	4 min	120 days	Menlo	HB07-11	SP7Bxc.D	6568
				MicroCat	55	T,S	2 min	120 days	WH	HB07-12	SP7Cxc.D	6569
HB07c	33°34.652'N	118°01.137'W	60 Bottom Mounted	300 kHz ADCP	3.1 AB	V,T	3 min	120 days	WH	HB07-13	SP7Dxc.D	6551
				SeaCat	2.5 AB	T,S,Trans.	5 min	120 days	WH	HB07-15	SP7Fxc.D	6554
				Sed., T on Pod	3.1 AB	Sed.	-	120 days	WH/Menlo	HB07-14	SP7Exc.D	6555
				Photo, T on Pod	1.7 AB	Photo	6 hrs	120 days	Menlo	HB07-16	SP7Gxc.D	6556
				ADV	?	V,T,P,Obs,Trans	20 min/1 hr	120 days	Menlo	HB07-17	SP7Hxc.D	6552
				PCADP	1.0 AB	Obs/Trans	?	120 days	?	HB07-18	SP7Ixc.D	6553
HB08	33°33.701'N	118°01.805'W	205 Subsurface Mooring	150 kHz ADCP in Flotation	185	V,T	15 mins	120 days	SAIC SAIC	HB08-1	SP81xc.D	
HB09	33°36.651'N	117°58.947'W	21.6 Surface Mooring	Hugrun	1	T	5 min	60 days	SAIC	HB09-1	SP91xc.D	
				MicroCat	4	T,S	1 min	60 days	SAIC	HB09-2	SP92xc.D	
				S4	5	V,T	5 min	60 days	OCSD	HB09-3	SP93xc.D	
				MicroCat	10	T,S	1 min	60 days	SAIC	HB09-4	SP94xc.D	
				S4	15	V,T	5 min	60 days	SAIC	HB09-5	SP95xc.D	
				Hugrun	21	T	5 min	60 days	SAIC	HB09-6	SP96xc.D	

Table 2-5a, cont. Instruments deployed in summer 2001 across the shelf off Huntington Beach.

Mooring ID	Location		Water Depth (m)	Instrument Type	Instrument Depth (m)	Variables Measured	Sampling Rate	Rotation Interval	Instrument Source	SAIC ID	Filename Prototype	USGS ID #
	Latitude	Longitude										
HB10a	33°35.700'N	117°58.097'W	35.2	Hugrun	1	T	5 min	60 days	SAIC	HB10-1	SPA1xc.D	
			Surface	MicroCat	5	T,S	1 min	60 days	OCSD	HB10-2	SPA2xc.D	
			Mooring	S4	10	V, T	5 min	60 days	OCSD	HB10-3	SPA3xc.D	
				MicroCat	15	T,S	1 min	60 days	OCSD	HB10-4	SPA4xc.D	
				MicroCat	20	T,S	1 min	60 days	OCSD	HB10-5	SPA5xc.D	
				S4	28	V,T	5 min	60 days	SAIC	HB10-6	SPA6xc.D	
				MicroCat	30	T,S	1 min	60 days	OCSD	HB10-7	SPA7xc.D	
				Hugrun	34.6	T	5 min	60 days	SAIC	HB10-8	SPA8xc.D	
HB10b	33°35.704'N	117°57.952'W	36 Bottom Mounted	300 kHz ADCP	35	V,T,P	6 min	120 days	NPS	HB10-9	SPA9xc.D	
HB11a	33°34.792'N	117°57.615'W	52	Temp.	5	T	4 min	120 days	Menlo	HB11-1	SPB1xc.D	6571
			Surface Mooring	MicroCat	10	T,S	2 min	120 days	WH	HB11-2	SPB2xc.D	6572
HB11b	33°34.784'N	117°57.660'W	55	Temp.	15	T	4 min	120 days	Menlo	HB11-3	SPB3xc.D	6591
			Subsurface	MicroCat	20	T,S	2 min	120 days	WH	HB11-4	SPB4xc.D	6592
			Mooring	Temp.	25	T	4 min	120 days	Menlo	HB11-5	SPB5xc.D	6593
				MicroCat	30	T,S	2 min	120 days	WH	HB11-6	SPB6xc.D	6594
				Temp.	35	T	4 min	120 days	Menlo	HB11-7	SPB7xc.D	6595
				MicroCat	40	T,S	2 min	120 days	WH	HB11-8	SPB8xc.D	6596
				Temp.	45	T	4 min	120 days	Menlo	HB11-9	SPB9xc.D	6597
				MicroCat	50	T,S	2 min	120 days	WH	HB11-10	SPBAxc.D	6598
HB11c	33°34.812'N	117°57.551'W	54	300 kHz ADCP	3.3 AB	V,T	3 min	120 days	WH	HB11-11	SPBBxc.D	6581
			Bottom	SeaCat	2.5 AB	T,S	5 min	120 days	WH	HB11-13	SPBDxc.D	6583
			Mounted	Sed. Trap	3.2 AB	Sed., T on Pod	-	120 days	WH/Menlo	HB11-12	SPBCxc.D	6584
				Camera	1.5 AB	Photo, T on Pod	6 hrs	120 days	Menlo	HB11-14	SPBExc.D	6585
				ADV	0.8 AB	V,T,P,Obs,Trans	20 min/1 hr	120 days	Menlo	HB11-15	SPBFxc.D	6582
HB12	33°34.366'N	118°00.112'W	61.6	DCS-3900	1	V,T	30 min	120 days	SAIC	HB12-1	SPC1xc.D	
			Surface	Therm	15	T	30 min	120 days	SAIC	HB12-2	SPC2xc.D	
			Mooring	Therm	30	T	30 min	120 days	SAIC	HB12-3	SPC3xc.D	
				DCS-3900	45	V,T	30 min	120 days	SAIC	HB12-4	SPC4xc.D	
				Therm/Turb	48	T, Turb	30 min	120 days	SAIC	HB12-5	SPC5xc.D	
				Hugrun	61	T	5 min	120 days	SAIC	HB12-6	SPC6xc.D	
HB13	33°36.220'N	117°56.331'W	14.7	Hugrun	1	T	5 min	60 days	SAIC	HB13-1	SPD1xc.D	
			Surface	FSI/Hugrun	5	V,T	10 min/5 min	60 days	SAIC	HB13-2	SPD2xc.D	
			Mooring	SeaCat/SeaPoint	8	T,S, Turb	2 min	60 days	SAIC	HB13-3	SPD3xc.D	
				FSI/Hugrun	10	V,T	10 min/5 min	60 days	SAIC	HB13-4	SPD4xc.D	
				Hugrun	14.2	T	5 min	60 days	SAIC	HB13-5	SPD5xc.D	

Table 2-5b. Nearshore instruments deployed in summer 2001.

Mooring ID	Location		Water Depth (m)	Instrument Type	Instrument Depth (m)	Variables Measured	Sampling Rate	Rotation Interval	Instrument Source	SAIC ID	Filename Prototype	Beach Station
	Latitude	Longitude										
HBN1	33°38.233'N	117°58.709'W	6	ADCP	6	V,T	1 min	90 days	SIO	HBN1-2	SN12xc.D	
				T/Chain	0-6	T	1 min	90 days	SIO	HBN1-1	SN11xc.D	
HBN2	33°38.147'N	117°59.113'W	11	ADCP	11	V,T	1 min	90 days	SIO	HBN2-2	SN22xc.D	
				T/Chain	0-11	T	1 min	90 days	SIO	HBN2-1	SN21xc.D	
HBN3	33°38.652'N	118°00.224'W	11	ADCP	11	V,T	1 min	90 days	SIO	HBN3-2	SN32xc.D	
				T/Chain	0-11	T	1 min	90 days	SIO	HBN3-1	SN31xc.D	
T4	33°38.940'N	117°59.992'W	7.5	T/Chain	0-7.5	T	30 secs	23 days	SIO	HBN4-1	SN41xc.D	
T5	33°38.326'N	117°58.963'W	8.1	T/Chain	0-8.1	T	30 secs	23 days	SIO	HBN5-1	SN51xc.D	
T6	33°38.201'N	117°58.738'W	7.7	T/Chain	0.7.7	T	30 secs	23 days	SIO	HBN6-1	SN61xc.D	
T7	33°37.877'N	117°58.148'W	7.7	T/Chain	0.7.7	T	30 secs	23 days	SIO	HBN7-1	SN71xc.D	
sT2	33°38.382'N	117°58.903'W	2.5	T/Chain	0-2.5	T	?	?	SIO	HBN8-1	SN81xc.D	
AES 01	33°38.322'N	117°58.974'W	12	T/Chain	1	T	3 min	30 days	AES	HBNA-1	SNA1xc.D	
	AES Power Plant Outfall Mooring			T/Chain	2	T	3 min	30 days	AES	HBNA-2	SNA2xc.D	
				T/Chain	4	T	3 min	30 days	AES	HBNA-3	SNA3xc.D	
				T/Chain	6	T	3 min	30 days	AES	HBNA-4	SNA4xc.D	
				T/Chain	8	T	3 min	30 days	AES	HBNA-5	SNA5xc.D	
				T/Chain	10	T	3 min	30 days	AES	HBNA-6	SNA6xc.D	
				ADCP	12	V/T	3 min	30 days	AES	HBNA-7	SNA7xc.D	
AES 02	33°38.367'N	117°58.957'W	9	T/Chain	1	T	3 min	30 days	AES	HBNB-1	SNB1xc.D	
	AES Power Plant Outfall Mooring			T/Chain	2	T	3 min	30 days	AES	HBNB-2	SNB2xc.D	
				T/Chain	4	T	3 min	30 days	AES	HBNB-3	SNB3xc.D	
				T/Chain	5	T	3 min	30 days	AES	HBNB-4	SNB4xc.D	
				T/Chain	6	T	3 min	30 days	AES	HBNB-5	SNB5xc.D	
				T/Chain	7	T	3 min	30 days	AES	HBNB-6	SNB6xc.D	
				ADCP	9	V/T	3 min	30 days	AES	HBNB-7	SNB7xc.D	
AES 03	33°38.086'N	117°58.829'W	12	T/Chain	1	T	3 min	30 days	AES	HBNC-1	SNC1xc.D	
	AES Power Plant Outfall Mooring			T/Chain	2	T	3 min	30 days	AES	HBNC-2	SNC2xc.D	
				T/Chain	4	T	3 min	30 days	AES	HBNC-3	SNC3xc.D	
				T/Chain	6	T	3 min	30 days	AES	HBNC-4	SNC4xc.D	
				T/Chain	8	T	3 min	30 days	AES	HBNC-5	SNC5xc.D	
				T/Chain	10	T	3 min	30 days	AES	HBNC-6	SNC6xc.D	
				ADCP	12	V/T	3 min	30 days	AES	HBNC-7	SNC7xc.D	
sT3	33°38.033'N	117°58.909'W	Surf Zone	Low-Res Therm	1	T	30 secs	22 days	SIO	HBS03	SS03xc.D	3N
sT4	33°38.264'N	117°58.508'W	Surf Zone	Low-Res Therm	1	T	30 secs	22 days	SIO	HBS04	SS04xc.D	6N
sT5	33°38.361'N	117°58.676'W	Surf Zone	Low-Res Therm	1	T	30 secs	22 days	SIO	HBS05	SS05xc.D	USGS
sT6	33°38.450'N	117°58.847'W	Surf Zone	Low-Res Therm	1	T	30 secs	22 days	SIO	HBS06	SS06xc.D	AES
sT7	33°38.572'N	117°59.026'W	Surf Zone	Low-Res Therm	1	T	30 secs	22 days	SIO	HBS07	SS07xc.D	9N
sT10	Station15N		Surf Zone	Low-Res Therm	?	T	?	?	SIO	HBS10	SS10xc.D	
sT11	Station 12N		Surf Zone	Low-Res Therm	?	T	?	?	SIO	HBS11	SS11xc.D	

Table 2-6. Meteorological and surface-wave instrumentation deployed on HBPIII HBM7 surface buoy.

Measured Parameters	Sensor Type	Manufacturer and Model	Height Above Surface
Wind Speed/Direction	Ultrasonic anemometer	Handar Model 425	4.84 m
Wind Speed/Direction	Propeller-vane anemometer	R. M. Young Wind Monitor Model 05106	3.97 m
Air Temperature	Pt 100 RTD	Rotronic MP101A	3.97 m
Relative Humidity	Rotronic Hygromer	Rotronic MP101A	3.97 m
Atmospheric Pressure	Barometer	A.I.R.	2.10 m
Sea Surface Temperature	IR Temperature Transducer	Everest Model 4000	2.40 m
Float Sea Temperature	Floating thermistor	NPS custom design	~ -1 cm
Bulk Sea Temperature	Hull thermistor	NPS custom design	-1.17 m
3-D Buoy Motion	Accelerometers & Rate gyros	Crossbow DMU-VGX	0.39 m
Buoy Heading	Magneto-Inductive Compass	Precision Navigation TCM-2	0.39 m

Table 2-7. Velocity Data Axis Rotations

Mooring ID	V-Component Direction (° True)
HB01	302
HB03	302
HB05	302
HB06	302
HB07	302
HB08	302
HB09	302
HB10	287
HB11	287
HB12	287
HB13	302
HBN1	301
HBN2	301
HBN3	301
HBNB	301
HBNC	301

CHAPTER 3. SURFZONE BACTERIA PATTERNS

Leslie Rosenfeld

3.1. Results from 3.5-year record: July 1, 1998–December 31, 2001

The total and fecal coliform and enterococci concentrations measured in the surfzone between July 1, 1998, and December 31, 2001, provided by OCSD, were analyzed with respect to their temporal and spatial variability. The methods used to collect and process these samples are described in Chapter 2. Station locations are shown in Figure 3-1.

15,909 samples from the numbered surfzone stations from 39,000 feet south of the Santa Ana River to 39,000 feet north of the Santa Ana River (including those sampled sporadically as well as those sampled regularly, but excluding Talbert Marsh and Santa Ana River) were analyzed for the three bacterial indicators. The distribution of samples by concentration is shown in Figures 3-2, 3-3, and 3-4 for total coliform, fecal coliform, and enterococci, respectively. Given what we know about the confidence limits on the bacterial concentration measurements, we attempted to group the measured concentration ranges into those which seemed very unlikely to have exceeded the AB411 single-sample standards (SS) (green), those which may or may not have actually exceeded AB411 SS (blue), and those which almost certainly did exceed SS (red). Total coliform is a little harder to interpret than the other two indicators, since there are two criteria, one involving a ratio to fecal coliform. Noble et al. (2003) only gives confidence limits for the total coliform = 10,000 standard. The blue bars make an attempt to include the total coliform = 1,000 standard, with the assumption that the ratio test is met. The majority of samples have bacterial concentrations less than, or equal to, the minimum detection limit (these percentages are listed in Figures 3-2, 3-3, and 3-4).

3.1.1. Relationship to Spring-Neap Tidal Cycle

Previous work (MEC, 2000; Grant et al., 2000) suggested that there was a relationship between the phase of the moon and the surfzone bacterial concentrations. Figure 3-5 shows measured Los Angeles sea level, "spring tides", and new and full moons for the HB PIII period. Averaged over 1998-2001, the spring-tide high water occurs 0.6 days after a new or full moon.

As described in Section 2.1.2, three types of surfzone bacteria event days were defined based on exceedance of AB411 standards (Table 1-1). Type 1 is based on total and fecal coliform in the stations 3N-12N region, type 2 on enterococci exceedances at multiple stations, and type 3 picks up any enterococci exceedances in the stations 3N-12N region which occur on days not already categorized as type 1 or 2 (Table 3-1).

These events are calculated using the daily subsampled data set (if multiple samples were available for a station for a given Pacific Standard Time (PST) day, the sample closest in time to that of the average sampling time for that station, calculated over May 1–October 31, 2001, was used) to minimize the prejudicial effect of the round-the-clock hourly sampling done for six 2-day periods only in 2001. Out of the 1280 days, of which 692 were sampled, type 1 events (red) occur on 148 days, type 2 events (blue) occur on 67 days, and type 3 events (orange) occur on 75 days (Figure 3-6). Without subsampling to no more than one sample per day per station, an additional 6 days qualifies as a type 1 event and an additional 10 days as a type 2 event. While throughout the 3.5-year record additional surfzone samples were occasionally taken in between those regularly collected at 3000-foot intervals, note that in 1999 this was done more often,

including in the stations 3N to 12N area. These contributed to a larger number of bacterial events, as defined here, relative to what would have been seen with only the regularly sampled stations.

If we consider individual samples, however, as opposed to days on which the previously defined events occur, we find that enterococci exceeds AB411 standards in many more samples than total and fecal coliform, as has been previously noted by Grant et al. (2000), and others. Out of a total of 14,866 surfzone samples (taken from the regularly sampled numbered stations, so that those sampled only sporadically or for short periods, as well as Talbert Marsh and Santa Ana River, are not included) taken during the 3.5-year period, 834 had enterococci concentrations greater than the AB411 SS, whereas only 292 had total or fecal coliform concentrations exceeding AB411 SS. 198 samples exceeded AB411 standards for both enterococci and coliform bacteria.

Further analysis was performed to quantify the relationship between tidal height (or range) and the occurrence of bacterial contamination in the surfzone. Each day in the 3.5-year record was classified by its proximity in time to the day on which spring tide, as defined in Section 2.5.1, occurred. The results reported below are for the bacterial events calculated using the full data set and AB411 SS. Results from calculations carried out using the data set subsampled to no more than daily are not significantly different. Figure 3-7 shows the percentage of days on which a type 1, type 2, or any type 1, 2, or 3, event occurs. There is a higher likelihood of a type 1 or 2 bacterial event occurring the day after the spring-tide high water than on any other day in the fortnightly cycle. Of all the days in a fortnightly cycle, the day that spring tide occurs has the greatest chance (60%) of experiencing an AB411 exceedance in the stations 3N-12N region. If we now take all of the bacterial events and classify what day they fall on relative to the spring tide, we find that about 50% of them occur within ± 2 days of the spring tide (Figure 3-8).

Finally, we also looked at the relationship between the height of the higher high water (HHW) each day and the probability of a bacterial event occurring. In this portion of the analysis we considered a simple logistic regression model. In this model, each day has a probability of having an event. Denote the probability of an event on day i by p_i. Then the logistic or "logit" model says:

$$\log(p_i/(1-p_i)) = \beta_0 + \beta_1 \, tide_i, \qquad (3.1)$$

where $tide_i$ is the height of the higher high tide on day i. We fit three separate models of this sort (one for each of event type 1 and 2, plus one in which the response was type 2 or type 3). In each case we found no added predictive power was gained by including a term quadratic in tide height, nor, not surprisingly, a term marking nearness to spring tide. Thus each model is of the form seen in Figure 3-9. In each case the tide height term is "statistically significant," indicating that the size of the effect we see in the model is such that it is very unlikely that an effect of that size would have arisen in the sample if in fact there were no such relationship in the population.

It is interesting to note that, in this area, the phases of the diurnal and semidiurnal tidal constituents are such that in recent years (1998-2001) the largest spring tides have fallen in the summer (May-August) and winter (December-February). It also turns out that the larger of the

two ebb tides (HHW to lower low water) during the summer spring tides falls at night, with the higher high tide at 0800–1000 PST. Given that the beat period resulting from the fortnightly cycle produced by the semidiurnal constituents M_2 and S_2 (14.77 days) and fortnightly cycle produced by the diurnal constituents O_1 and K_1 (13.66 days) is very nearly half a year (186.62 days), the timing of the largest spring tides relative to the annual cycle changes very little year to year.

3.2. HB PIII Temporal and Spatial Patterns: June–October 2001

The percentage of samples possibly exceeding the AB411 SS (blue plus red bars of Figures 3-2, 3-3, and 3-4) is not significantly different for the HB PIII period as opposed to the 1998-2001 period, except that there is a slightly higher percentage of enterococci with values >35 (22% vs. 17%) for the summer 2001 period, due to the nighttime sampling. Figures 3-10, 3-11, and 3-12 are contour plots of the logarithm of total coliform, fecal coliform, and enterococci concentrations, respectively, for the surfzone stations sampled during HB PIII. These are made using the daily subsampled data set. While the fortnightly pattern discussed earlier is evident in all three bacterial indicators, it is clearest in total coliform. Also, while all three indicator species show higher concentrations preferentially in a band between stations 3N and 12N, this is particularly true for fecal coliform. Occasionally, relatively high levels of enterococci (>300 MPN/100 mL) are found almost simultaneously all the way from stations 9S to 15N. Total coliform rarely exceeds 300 MPN/100 mL south of the Santa Ana River, but on one occasion (in mid-August) total coliform exceeds 200 MPN/100 mL from stations 15S to 12N.

The temporal relationship between various physical processes and surfzone bacterial concentrations high enough to trigger beach closures in accordance with AB411 standards was explored using bacterial "events" as defined in section 2.1.2. During the HB PIII study, almost every surfzone sample that exceeded an AB411 SS, fell on a day characterized as a type 1, 2, or 3 event, as seen in Figure 3-13. Hourly sea level, as measured at Los Angeles, is included in this figure to show graphically the preference for bacterial events occurring close to the time of spring tide, as discussed above.

In addition to calculating the events in terms of exceeding the AB411 SS, we also defined a set of events based on single samples exceeding the prescribed monthly geometric mean (MM) standards. We calculated events using the daily subsampled data set for both the single sample and monthly mean limits (Chapter 2). Figures 3-14 and 3-15 show these four sets of bacterial events. Using the lower monthly mean standard increases the number of days on which there are bacterial events, and using the data set subsampled to daily decreases the number of days on which there are events. Referring to Figure 3-14, it can be seen that if all the events (type 1 and/or 2 and 3) are considered together (i.e., all the colored dots), only one event (type 1 on ~July 11), calculated from the full data set using the monthly mean standard (row 3), occurs which is not contiguous with either an event, or an unsampled day next to an event, calculated using the SS with the full data set (row 1). If events are considered separately by type (Figure 3-15), two additional type 1 events defined by monthly mean appear that are not contiguous with SS type 1 events. They are, however, contiguous with type 3 events, and type 3 events occur by definition only on days when there is no type 1 or type 2 event, so a given day can swap between being a type 1 or 3, or a type 2 or 3, for the four-event data sets considered here. Figure 3-15

also illustrates that the large-scale enterococci events (type 2) are significantly reduced (there are fewer brown dots than red dots) when the daily subsampled, rather than the full, data set is used with the SS. Taken together, these figures reveal that, while the number of contiguous days during which bacterial concentrations exceed AB411 standards expands or contracts depending on whether the SS or monthly mean standard is applied and on whether all samples or the daily subsampled data is used, the timing of the events is essentially unchanged. In other words, if the Huntington Beach closures were based solely on single daytime samples, using either the AB411 SS or monthly mean standard, the length of the closures would vary, but the number of closures would not.

3.2.1. Temporal Relationship between High Bacterial Concentrations and Physical Phenomena

In an effort to relate the occurrence of bacterial concentrations exceeding AB411 standards to physical phenomena hypothesized to facilitate these events, the time series of bacterial events calculated with the SS and all data from June 14-October 9, 2001 (when the majority of the moorings were in the water) were used. In addition to the bacterial events, Figure 3-16 shows the days on which cold water was observed to be unusually close to shore, days on which the mid-shelf stratification was unusually weak, as well as the height of HHW and a characterization of the surface wave field for every day.

Cold water near shore was determined by two methods. In the first method, the temperature of the sewage outfall plume was determined by looking at the T/S distribution from the moorings in two-week increments from June 17 through October 15, 2001. The maximum temperature of the plume T/S anomaly was picked as an upper limit of the temperature of the plume, and this value was compared with the temperature time series at the nearshore moorings (HB01 and HB03). If the 10-m temperature at mooring HB01 was less than, or within 0.25ºC of, the warmest temperature in the sewage outfall plume, it was designated as a cold-water nearshore event. The result is the same whether mooring HB03 or HB01 is used. In the second method, the temperatures measured by the moorings along the main line were used to determine when the 12ºC isotherm was inshore of the 30-m isobath and the water at HB03 was cooler than 13ºC. The July 23-26 occurrence of cold water near shore, judged by both of these criteria, coincides with the largest cold-water sloshing event of the HB PIII project as identified by the 14ºC isotherm reaching 5 m, or higher, at the HBN2 site on the 11-m isobath.

Unusually weak stratification over the mid-shelf was also identified by two methods. One criteria specified that the water column at HB03 be well-mixed from top to bottom. The other criteria identified days with reduced stratification by specifying that the temperature difference, at any time during the day, between thermistors at two out of three moorings (listed below) be less than the mean temperature difference minus two standard deviations of the temperature difference. The calculation was carried out using the hourly low-pass-filtered (3-hour cut-off) data. The moorings, thermistors, and temperature differences used are as follows:

HB01: surface to 10 m, $\Delta T < 0.41°C$

HB03: 5 to 15 m, $\Delta T < 0.70°C$
HB05: 5 to 20 m, $\Delta T < 1.06°C$

The hourly surface-wave directional spectra were averaged into daily spectra. These were examined by eye and characterized as consisting of southerly swell, westerly wind waves, southerly wind waves, a combination of the above, or no waves. An example of each is shown in Figures 3-17a, b. 55% of days with a bacterial event (of any of the previously defined types) coincided with southerly swell, while 45% of days with a bacterial event occurred on days with either no waves to speak of, or westerly wind waves alone. These are nearly identical to the percentages of all days in the study period with (54%) and without (46%) southerly swell, thus indicating that bacterial events did not occur preferentially during southerly swell. Considering each of the three event types separately, type 1 (58%) and type 3 (50%) events occur in concert with southerly swell in close to the same proportions as southerly swell occurs in general (54%), while type 2 bacterial events have a slight bias towards southerly swell, with 75% of them occurring on southerly swell days.

Other than large tidal ranges (i.e., spring tides), the only other physical variable pictured in Figure 3-16 that co-occurs with bacterial events more often than not is the occurrence of reduced stratification in the nearshore zone. Four out of five of those occurrences (each set of contiguous days is considered as an occurrence) coincide with type 1 events. However, during these events the plume is below the warm unstratified water, and is maintained offshore. Evidence for the internal tide swash into the nearshore zone, hypothesized to facilitate transport of sewage plume bacteria to shore, is greatest during July 23-26. The only exceedance of the AB411 SS in the Huntington Beach area on these days was a single sample taken at 3N on July 23 with a measured enterococci concentration of 110 MPN/100 mL. Even if you consider the lower monthly mean standard, the only additional exceedances are an enterococci value of 60 at station 6N and fecal coliform equal to 220 at station 12N on July 23. The timing of the cold swashes and the surfzone sampling at stations 3N–12N (Table 3-2) was such that the samples could have captured high bacterial concentrations if they were brought in to shore together with the cold water.

3.2.2. Hourly Round-the-clock Sampling during Cruise Periods/Spring Tides

During the six cruise periods, scheduled to coincide with the occurrence of spring tides, samples were taken for bacteriological analysis in the surfzone at stations 15S to 21N every hour for 48 hours (with the exception of the first cruise in May when the hourly sampling was done for only 36 hours, with one several-hour break).

Consistent with the results of Boehm et al. (2002) for data from May 2000, contour plots of these data show a strong day-night cycle in all three fecal indicator bacteria, with the highest values occurring at night. Figures 3-18, 3-19, and 3-20 show this for the cruise in early July. While there are similarities in the spatial patterns for all three indicators, there are also differences. The higher concentrations tend to be found north of the Santa Ana River, but when there are elevated levels south of the Santa Ana River, they occur to some degree in all three indicators (e.g., 2000-2300 PDT July 19 and 2100-2200 PDT July 20) (Figures 3-21, 3-22, and 3-23). The highest values of total coliform tend to occur at station 0 (next to the mouth of the

Santa Ana River), and there is some suggestion of upcoast (northwestward propagation) from there, with a speed of about 30 cm/s (Figures 3-18 and 3-21). Fecal coliform values generally peak at station 6N (Figures 3-19, 3-22, and 3-24), while enterococci values tend to be high not only at station 6N, but also at the southern end of the range (Figures 3-20, 3-23, and 3-25) and occasionally at the northern end (Figure 3-26). Enterococci have a minimum from stations 6S to 0. These patterns also hold for the daily subsampled data shown in Figures 3-10, 3-11, and 3-12.

The onset of elevated total coliform values at station 0 occurs between about 1200 and 0300 (Figures 3-18, 3-21, and 3-27), shortly prior to the nighttime low tide (0300-0600) (Table 3-3). Since the time of low tide varies so little among the six intensive sampling periods, it is impossible to say based on this alone whether the timing of the elevated bacteria levels is related to the phase of the semidiurnal tidal cycle, the diurnal light cycle, or both. Bacterial concentrations are not generally elevated near the daytime low tide, the higher low tide of the two, except as noted below.

On the few occasions when there are high values of coliform in the middle of the day (e.g., ~1330 PDT on June 19 and 20 and ~1500 PDT on July 6) (Figures 3-27, 3-28, and 3-18, respectively), enterococci values are only slightly elevated (Figure 3-25), if at all, while at night all three indicators show notably higher concentrations. Note that these midday increases in bacteria level have their maxima at station 0 for all three indicators, and occur close to the time of the higher low tide (1354 PDT on June 19, 1318 PDT on June 20, and 1542 PDT on July 6).

When the timing of samples exceeding the AB411 SS is examined in these hourly data, they also occur predominantly at night, particularly for enterococci which has the lowest standard. Boehm et al. (2002) noted that enterococci falls below detection limits earlier in the day than total and fecal coliform. Enterococci exceedances, wherever they occur, do so overwhelmingly between sunset and sunrise (Figures 3-29, 3-30, and 3-31). As previously stated, however, this time period also coincides closely with the time between HHW and lower low water. Note, however, that the onset of enterococci exceedances precedes both the high tide (the start of the ebb tidal flow) and the sudden drop in near-bottom nearshore temperature (e.g., nights of July 19 and 20) (Figure 3-31). This could indicate that the day-night cycle in enterococci is more strongly influenced by sunlight-induced die-off than by tidal influence on either a landward or seaward source. The coliform exceedances, however, do not show this strong relationship to the day-night cycle, nor does such a pattern appear when a cut-off even lower than the AB411 SS is used for visualization (Figures 3-32, 3-33, and 3-34). The predominance of high coliform values near the time of low tide is evident, however.

The surfzone bacteria data for stations 3N-12N for the whole HB PIII period show no significant relationship with sample temperature. The relationship with time of day is due solely to the sampling strategy in this mostly once per day data set. There is a weak inverse correspondence between bottom pressure (equivalent to sea level for this purpose) and total and fecal coliform. When the hourly data from the six intensive sampling periods is examined together, however, the relationships between bacteria and sea-level height, time of day, and phase of semidiurnal tide that were pointed out for the individual high-resolution sampling periods becomes more obvious.

Figure 3-35 shows the concentration of all three fecal indicator bacteria at all stations, 15S to 21N, for all hourly data from the six cruise periods plotted as a function of time of day. Again we see that enterococci values rebound as soon as the sun sets, while coliform values don't rise until later in the evening, and don't reach values as high as seen in the early morning. When the same surfzone bacterial data is plotted versus sea level (Figure 3-36), we see that coliform values are highest (with a few exceptions) when sea level is low, whereas enterococci have no obvious relationship to sea level. The total coliform peak that is seen 5-10 hours after HHW at station 0 (Figure 3-37) also occurs north of the Santa Ana River (represented by station 6N here), while the weaker peak 15-20 hours after HHW only appears at station 0, perhaps indicating die-off or dilution to the background levels before the source waters are advected past station 6N. Fecal coliform shows a pronounced peak at station 6N, but not at station 0, 6-10 hours after HHW. The enterococci pattern is quite different from total and fecal coliform.

These results suggest that coliform levels are controlled more by phase of the tide, and enterococci by time of day. However, due to the fact that all the hourly sampling in this study was separated by about two weeks so that the larger ebb always fell at night, we can not definitively separate the two effects. Also, without reliable information as to the die-off rate of the different bacterial indicators under the prevailing temperature and salinity conditions, we cannot say how that influences the temporal patterns.

Taken together, however, these results suggest that tidal flow out of the Santa Ana River may be a source of high bacteria concentration, particularly for total coliform. There is also some indication that there may be a local source of bacterial contamination, particularly high in fecal coliform, near station 6N. Enterococci appear to have multiple sources, and exhibit a particularly pronounced day-night cycle. Boehm et al. (2002) suggested that the most likely answer to the question "Why is the surf zone so rapidly re-supplied with indicator bacteria after the sun goes down?" is that there is a continuous supply of indicator bacteria to the surfzone. These data would support that suggestion for enterococci. Grant et al. (2001), also using May 2000 data, identified the Talbert Marsh as a net source of enterococci and characterized the temporal variability of enterococci concentration in terms of flood vs. ebb tides, but did not look at the influence of time of day.

3.3. References

Boehm, A.B. et al., 2002. Decadal and shorter period variability of surf zone water quality at Huntington Beach, California. Environmental Science and Technology, v. 36, p. 3885-3892.

Grant, S.B. et al., 2001. Generation of *Enterococci* bacteria in a coastal saltwater marsh and its impact on surf zone water quality. Environmental Science and Technology, v. 35, p. 2407-2416.

Grant, S.B. et al., 2000. Huntington Beach Water Quality Investigation Phase II: An analysis of ocean, surf zone, watershed, sediment and groundwater data collected from June 1998 through September 2000. Final Report.

MEC, 2000. Huntington Beach closure: relationships between high counts of bacteria on Huntington Beaches and potential sources. Final Report.

Noble, R.T. et al., 2003. Comparison of beach bacterial water quality indicator measurement methods. Environmental Monitoring and Assessment, v. 81, p. 301-312.

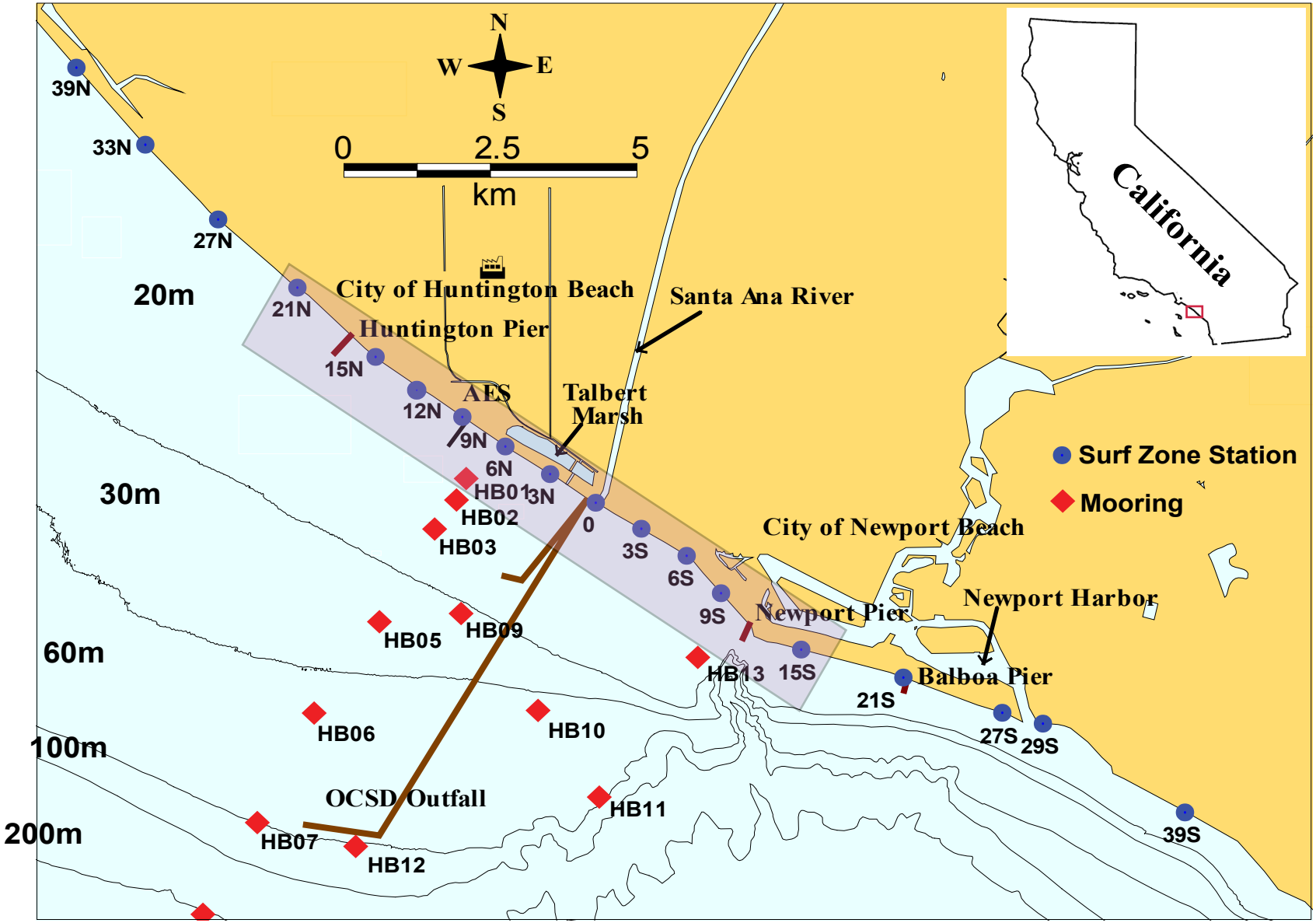

Figure 3-1. Map of the coastal zone surrounding Huntington Beach, California. The blue dots show the location of the surfzone sampling stations from 39N to 39S. The outfall is shown leaving the coast near station 0. The diffuser of the outfall is located near stations HB07 and HB12. Station 12S is located at Newport Pier.

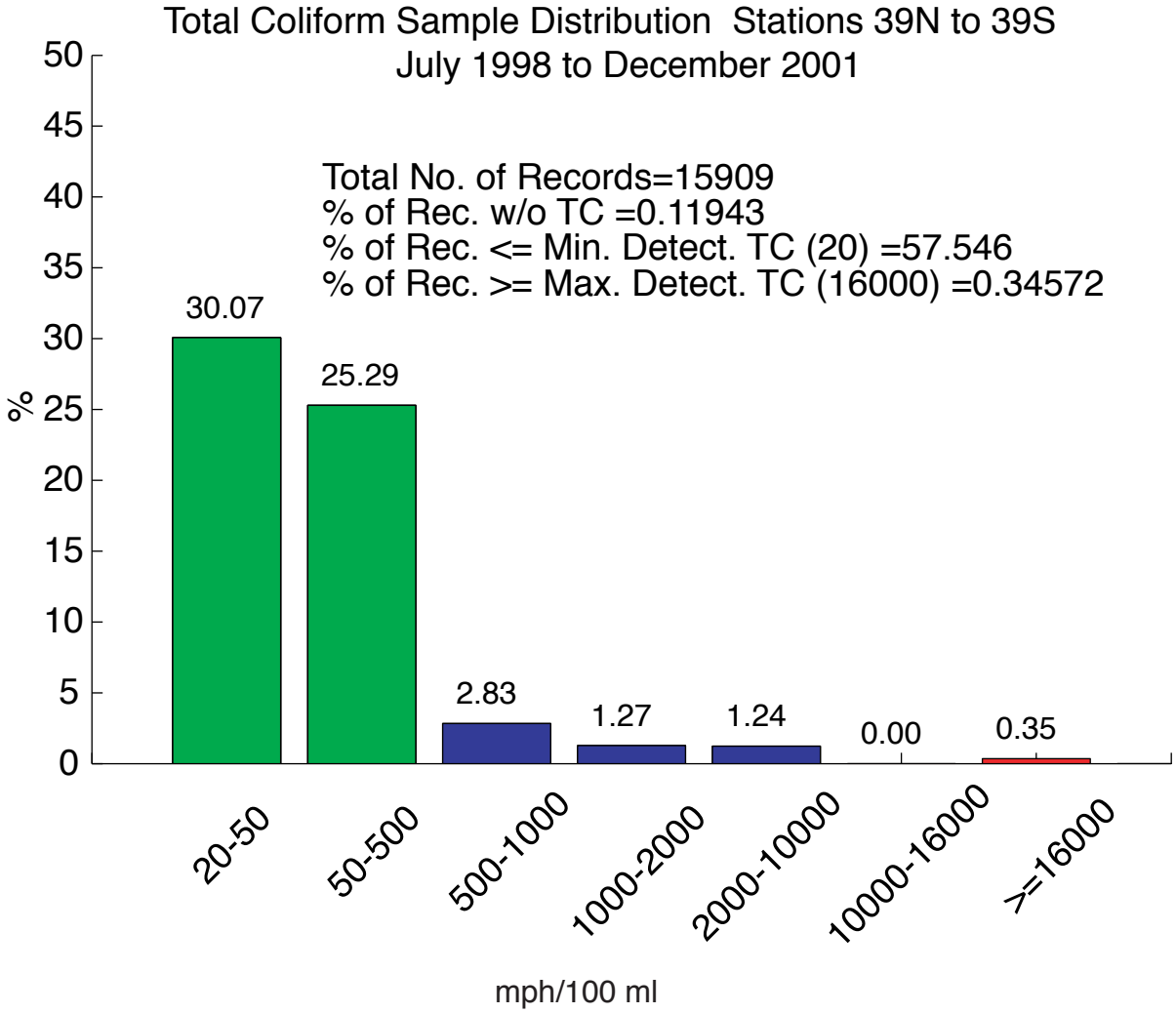

Figure 3-2. Percent of samples falling within each concentration range is indicated. Only records with concentrations not marked as being at the minimum detectable limit are included in the histogram. The percent less than, or equal to, the common minimum detection limit, whether marked by < or not, is shown in the text in the figure. The sum of the percentages represented by the bars plus the percent of records <= the common minimum detection limit (20) may exceed 100, since values of 20, if not marked as being at the minimum detection limit, are counted in two categories. Records at the maximum detection limit are included in the histogram. The measured concentration ranges are loosely grouped into those which seemed very unlikely to have exceeded the AB411 single-sample standard (green), those which may or may not have actually exceeded AB411 single-sample standards (blue), and those which almost certainly did exceed the standards (red). Since there are two indicators for total coliform, one involving a ratio to fecal coliform, the blue bars make an attempt to include the total coliform = 1,000 standard, with the assumption that the ratio test is met.

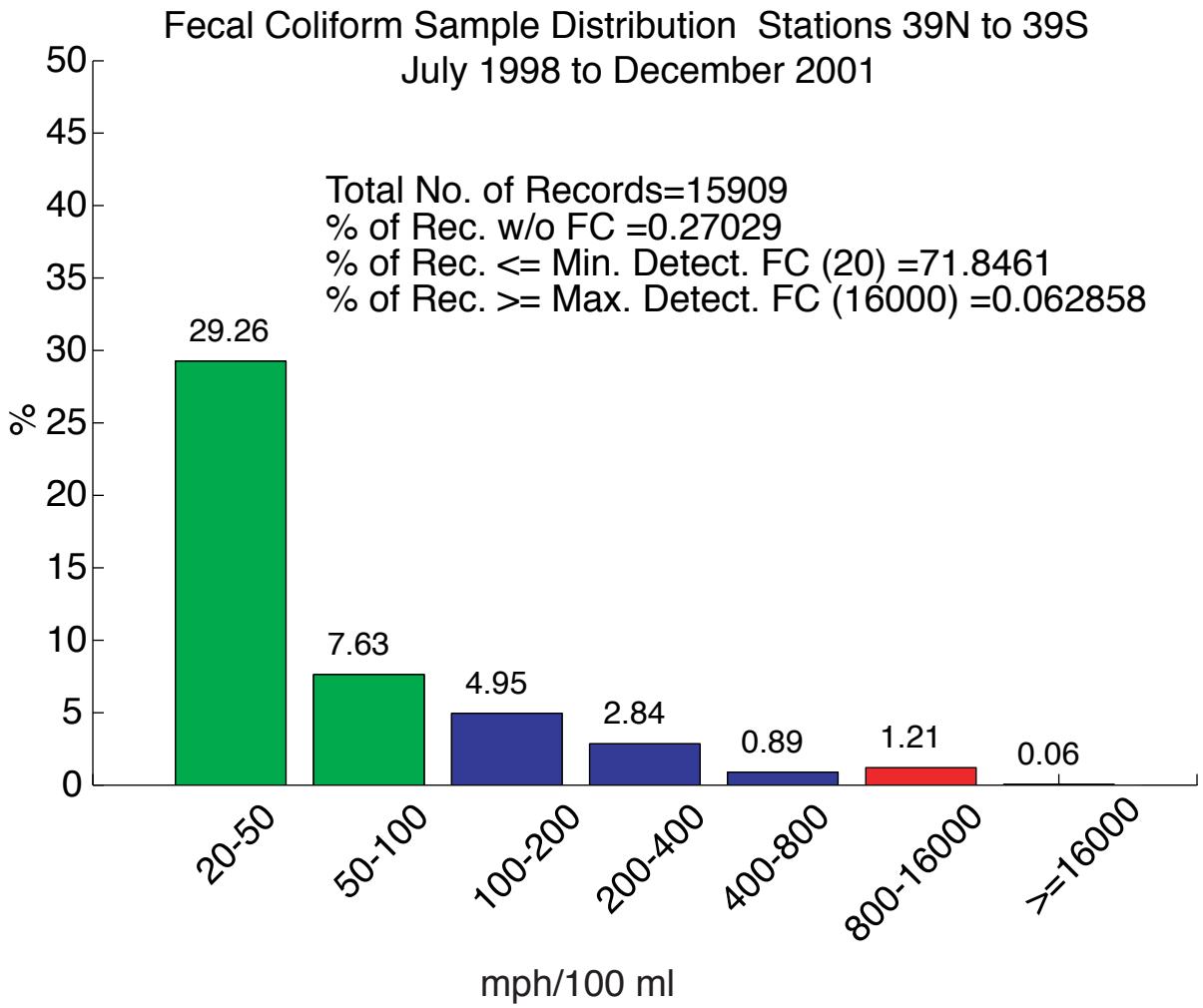

Figure 3-3. Percent of samples falling within each concentration range is indicated. Only records with concentrations not marked as being at the minimum detectable limit are included in the histogram. The percent less than, or equal to, the common minimum detection limit, whether marked by < or not, is shown in the text in the figure. The sum of the percentages represented by the bars plus the percent of records <= the common minimum detection limit (20) may exceed 100, since values of 20, if not marked as being at the minimum detection limit, are counted in two categories. Records at the maximum detection limit are included in the histogram. The measured concentration ranges are loosely grouped into those which seemed very unlikely to have exceeded the AB411 single-sample standards (green), those which may or may not have actually exceeded AB411 single sample-standards (blue), and those which almost certainly did exceed the standards (red).

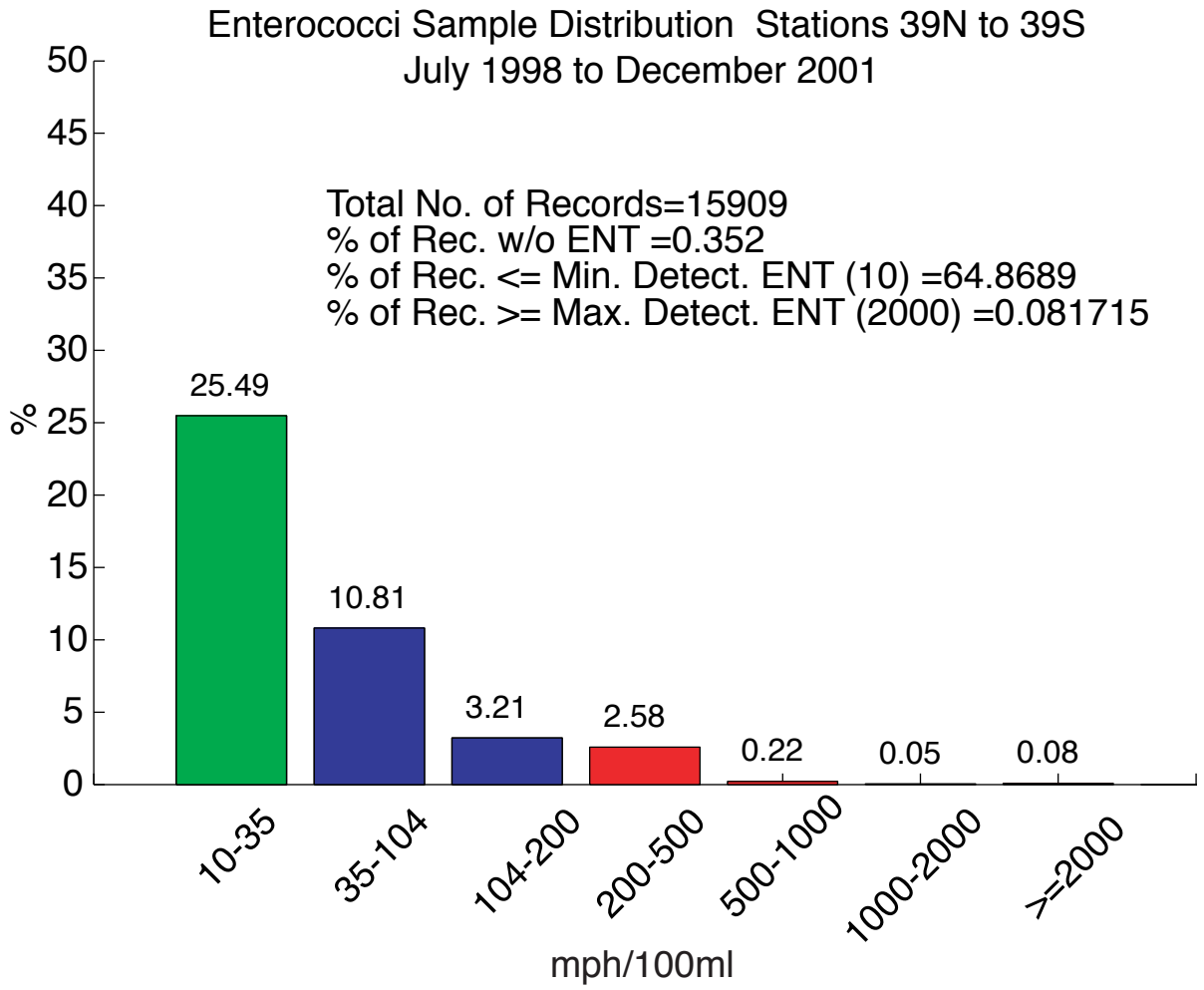

Figure 3-4. Percent of samples falling within each concentration range is indicated. Only records with concentrations not marked as being at the minimum detectable limit are included in the histogram. The percent less than, or equal to, the common minimum detection limit, whether marked by < or not, is shown in the text in the figure. The sum of the percentages represented by the bars plus the percent of records <= the common minimum detection limit (10) may exceed 100, since values of 10, if not marked as being at the minimum detection limit, are counted in two categories. Records at the maximum detection limit are included in the histogram. The measured concentration ranges are loosely grouped into those which seemed very unlikely to have exceeded the AB411 single-sample standards (green), those which may or may not have actually exceeded AB411 single-sample standards (blue), and those which almost certainly did exceed the standards (red).

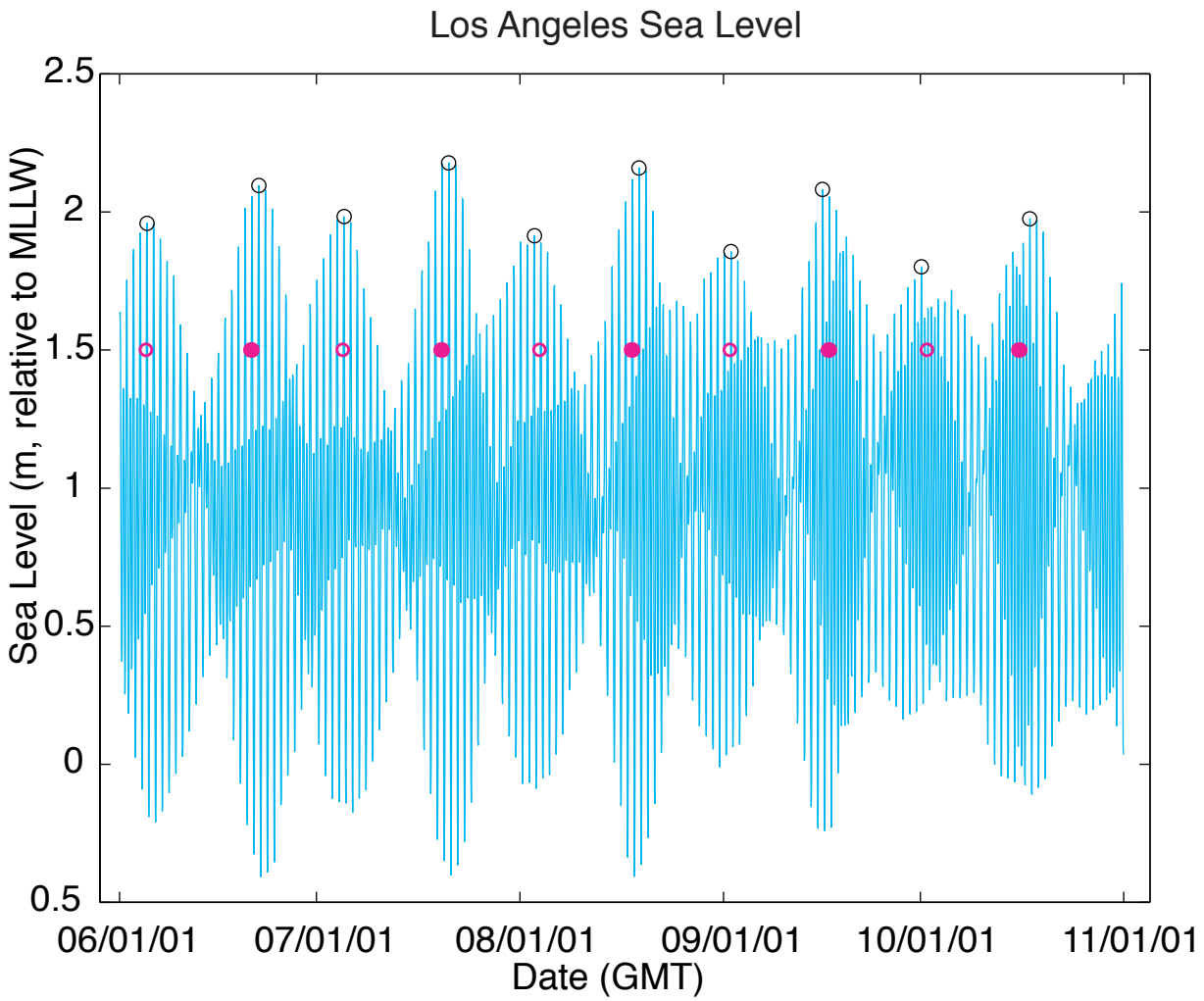

Figure 3-5. Hourly sea level, relative to mean lower low water, measured at Los Angeles, spring tides (black circles), and new (solid magenta circles) and full (open magenta circles) moons for the HB PIII period.

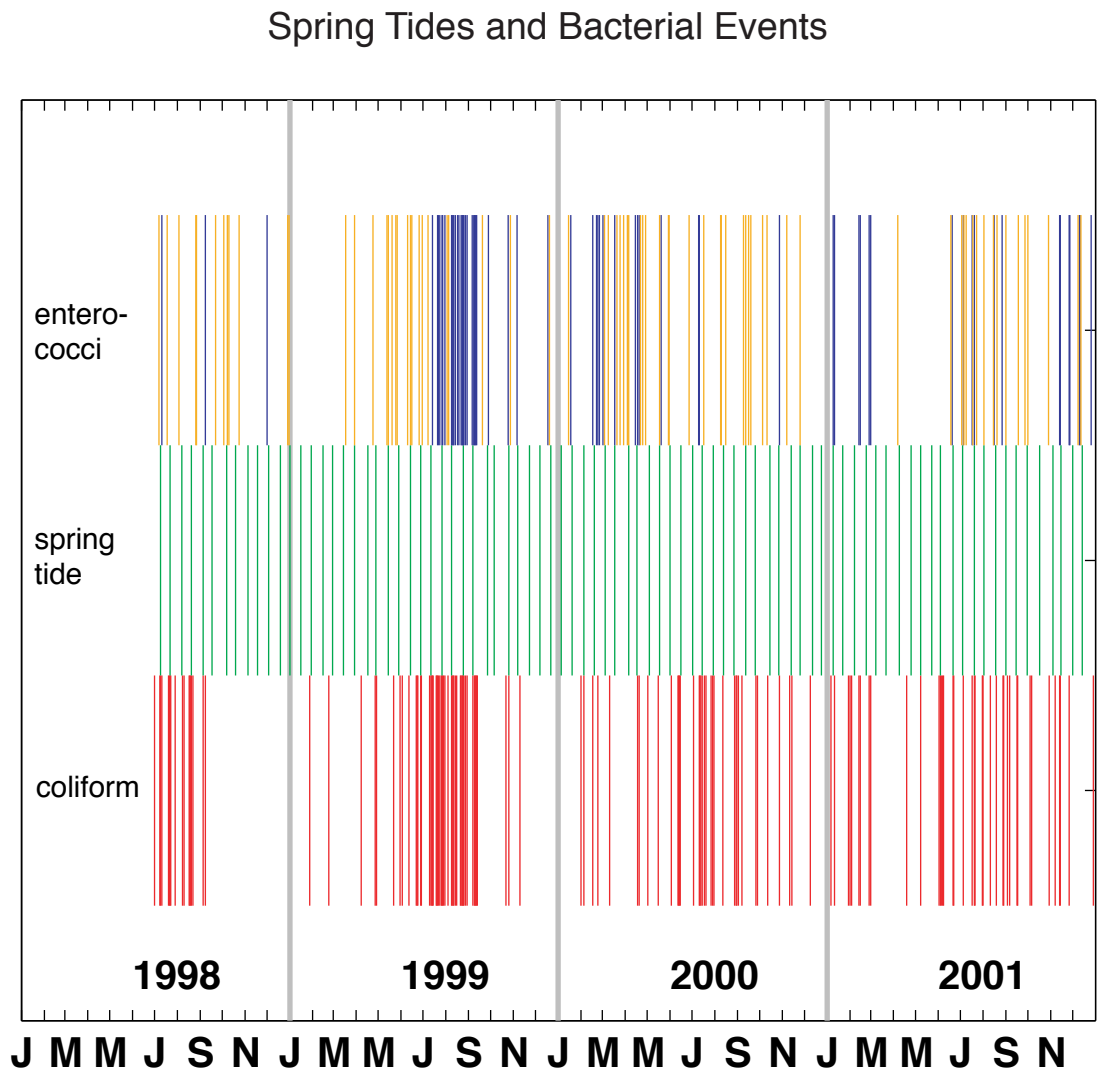

Figure 3-6. Days on which type 1 bacterial events (total or fecal coliform exceeds AB411 standards at any of stations 3N-12N) occur are shown as red lines in the bottom row; type 2 events (enterococci exceeds AB411 standards at 3 or more stations including one of 3N-12N) as blue lines in the top row; and type 3 events (enterococci exceeds AB411 at any 3N-12N station, on which there is not a type 1 or type 2 event) as orange lines in the top row. These events are calculated using the single-sample standards and the daily subsampled data set. The green lines in the middle row indicate the days on which spring tide occurred.

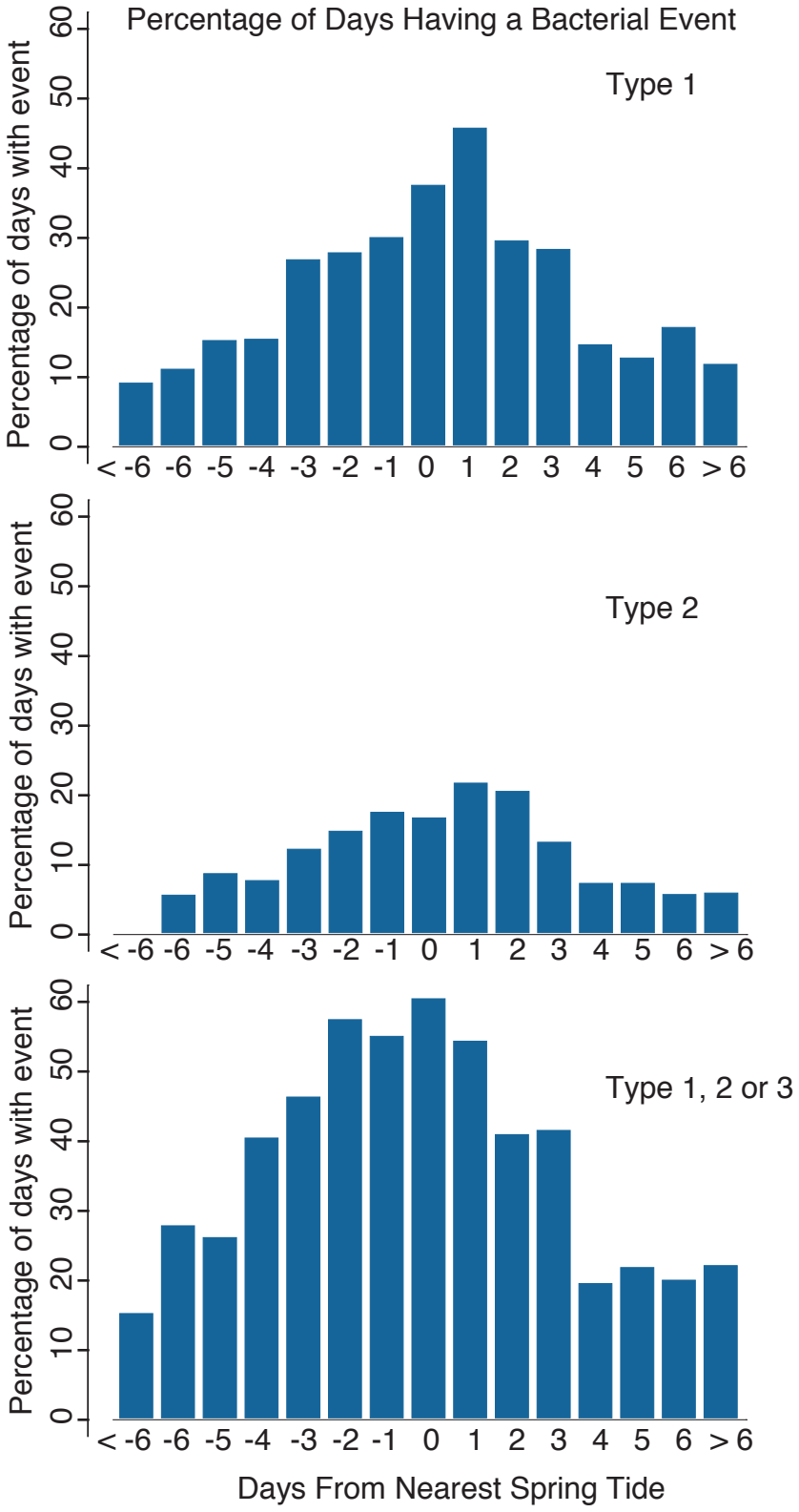

Figure 3-7. Days during 7/98-12/01 are classified by proximity to spring tide, and the percentage of each type of day on which bacterial events occurs is plotted. Negative numbers denote days preceding spring tides; positive numbers follow. If a day was equidistant from the two nearest spring tides, the positive value was chosen.

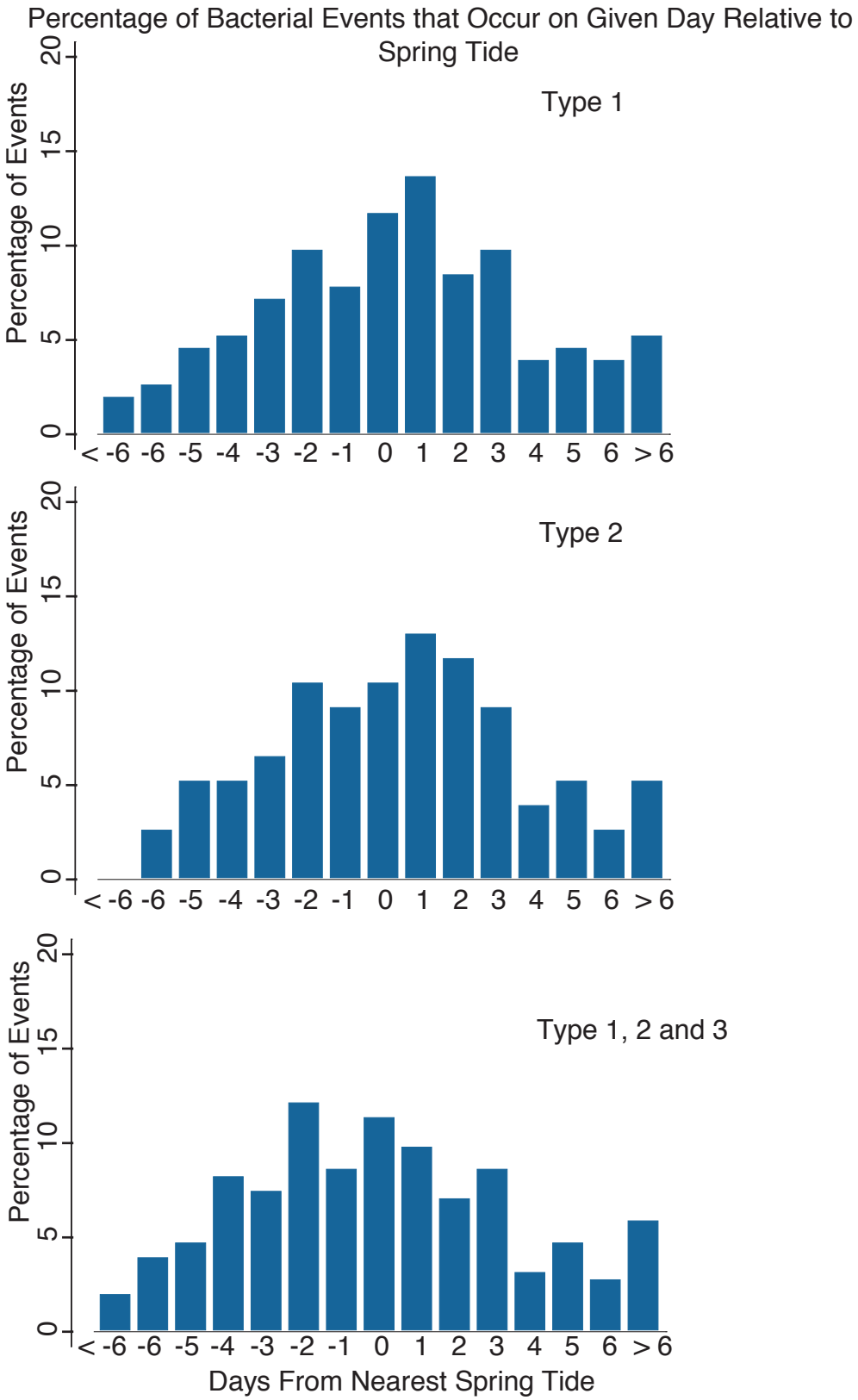

Figure 3-8. The distribution of events (summing to 100%) by day relative to spring tide is shown. Negative numbers denote days preceding spring tides; positive numbers follow. If a day was equidistant from the two nearest spring tides, the positive value was chosen.

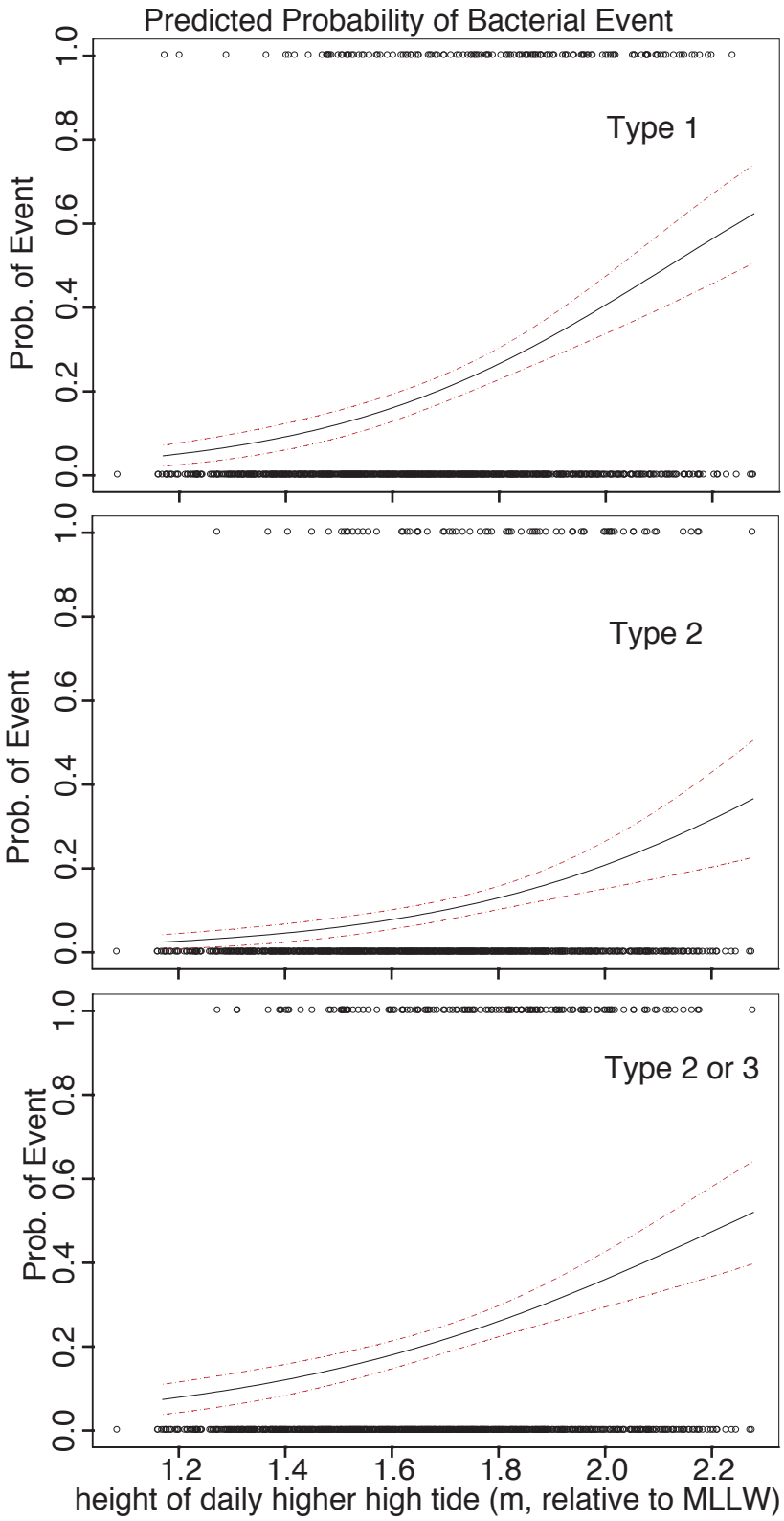

Figure 3-9. The open circles plotted at 1 or 0 on the y axis indicate event or no event versus height of higher high water on the x axis. The solid line shows the predicted probability, as a function of tide height. The two dotted red lines on either side give estimated 95% confidence levels for the probabilities at each point.

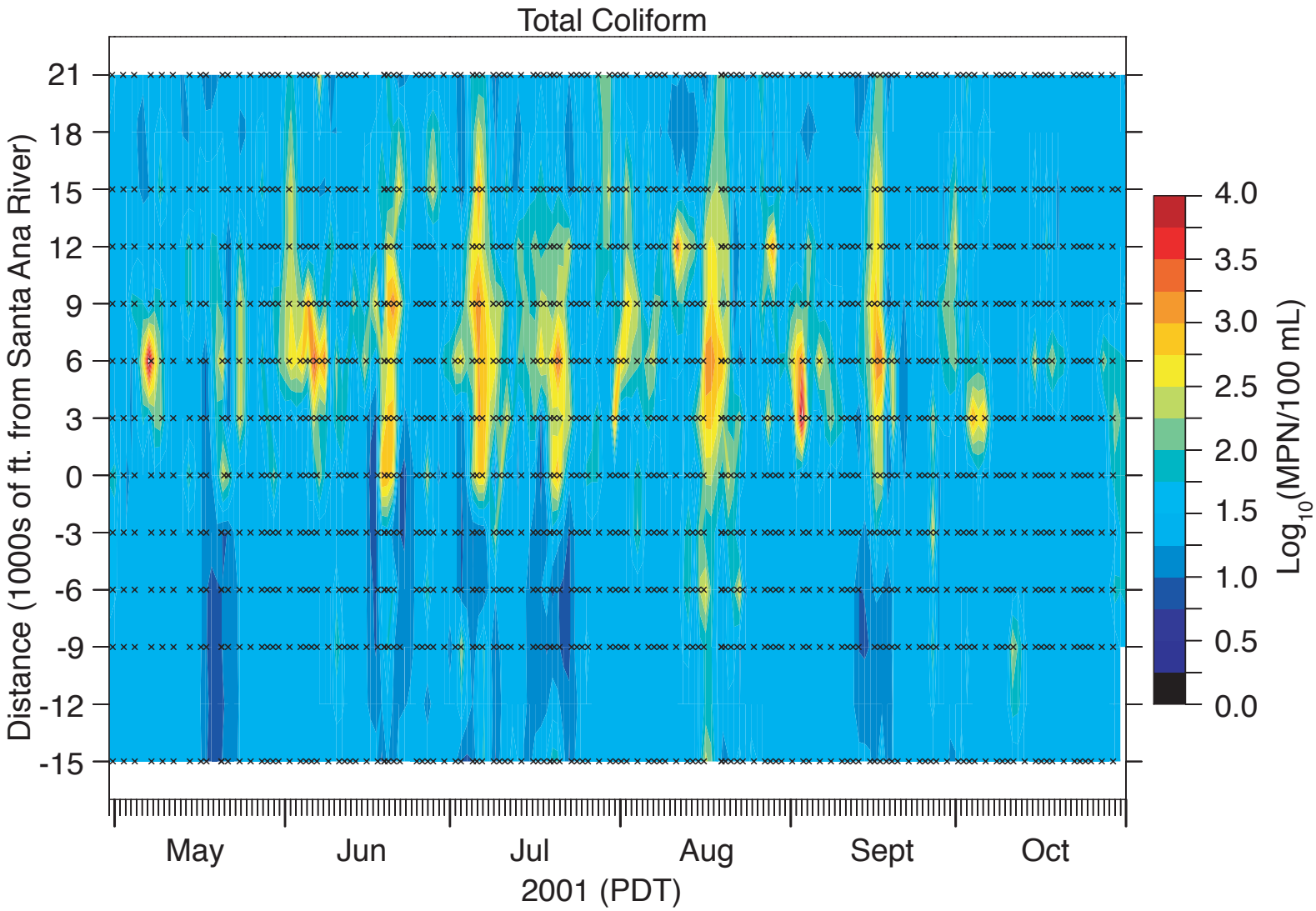

Figure 3-10. Log_{10} of total coliform concentration (MPN/100 mL) is plotted versus time and distance alongshore. The data set subsampled to no more than daily values was used. X's indicate the day and location of each sample. Data is contoured with PlotPlus on a 180 x 13 grid (time and distance, respectively) using cay=5 and nrng=2. The cay value determines the interpolation scheme. Cay=0 means Laplacian interpolation is used. As cay is increased, spline interpolation predominates over Laplacian. For pure spline interpolation cay=infinity. Grid points are set to "undefined", and not used, if farther than nrng away from the nearest data point.

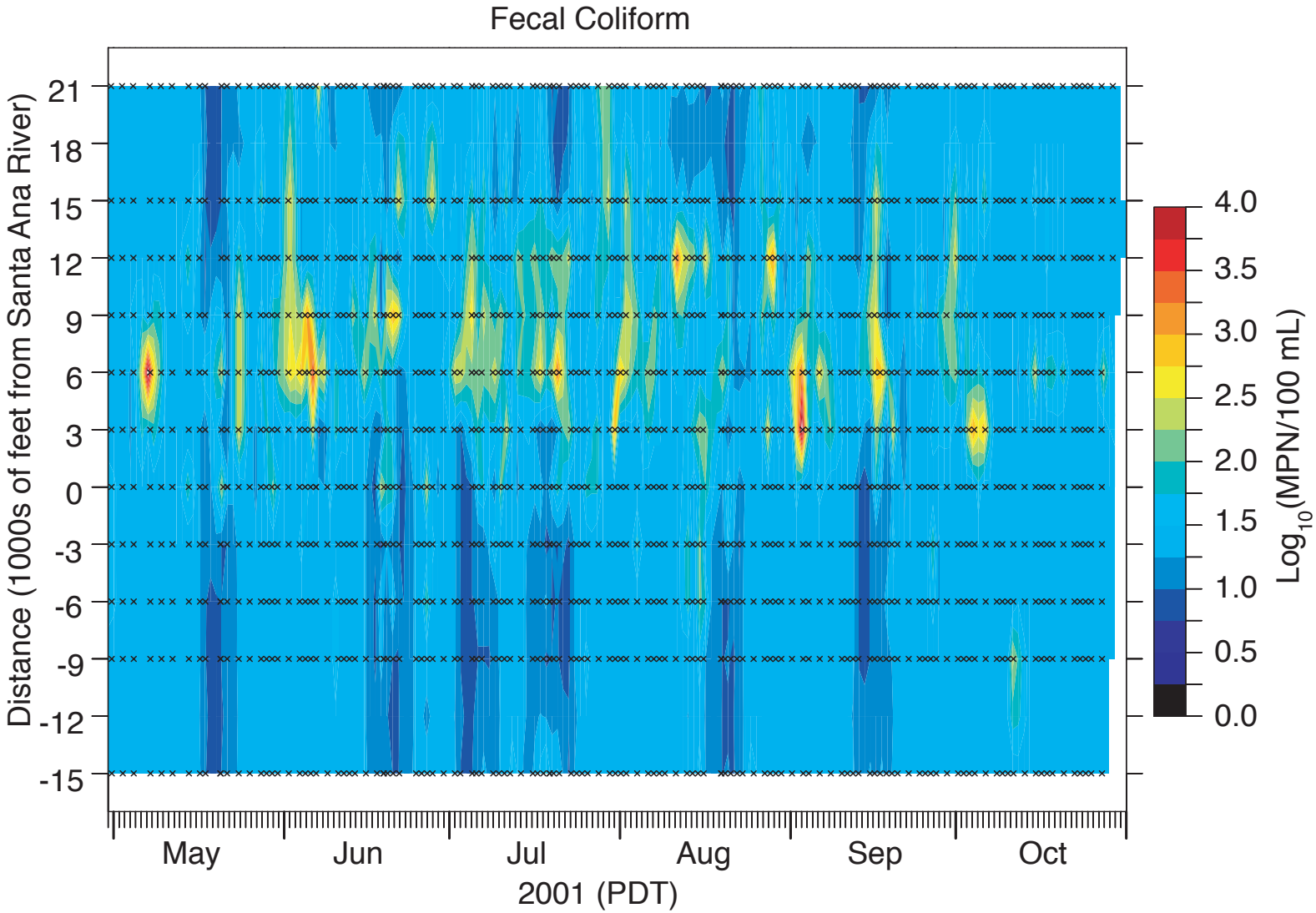

Figure 3-11. Log_{10} of fecal coliform concentration (MPN/100 mL) is plotted versus time and distance alongshore. The data set subsampled to no more than daily values was used. X's indicate the day and location of each sample. Data is contoured with PlotPlus on a 180 x 13 grid (time and distance, respectively) using cay=5 and nrng=2. The cay value determines the interpolation scheme. Cay=0 means Laplacian interpolation is used. As cay is increased, spline interpolation predominates over Laplacian. For pure spline interpolation cay=infinity. Grid points are set to "undefined", and not used, if farther than nrng away from the nearest data point.

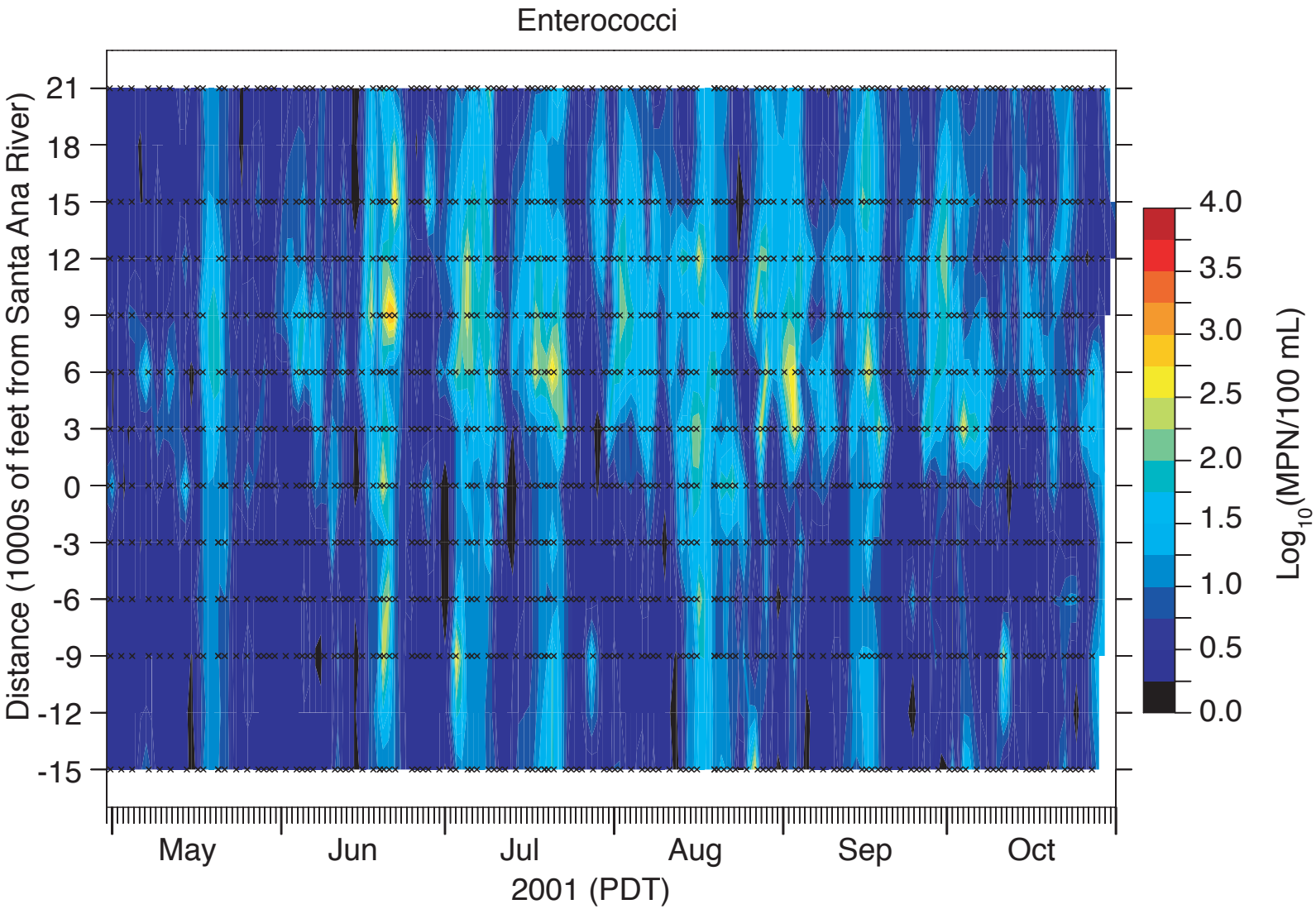

Figure 3-12. Log_{10} of enterococci concentration (MPN/100 mL) is plotted versus time and distance alongshore. The data set subsampled to no more than daily values was used. X's indicate the day and location of each sample. Data is contoured with PlotPlus on a 180 x 13 grid (time and distance, respectively) using cay=5 and nrng=2. The cay value determines the interpolation scheme. Cay=0 means Laplacian interpolation is used. As cay is increased, spline interpolation predominates over Laplacian. For pure spline interpolation cay=infinity. Grid points are set to "undefined", and not used, if farther than nrng away from the nearest data point.

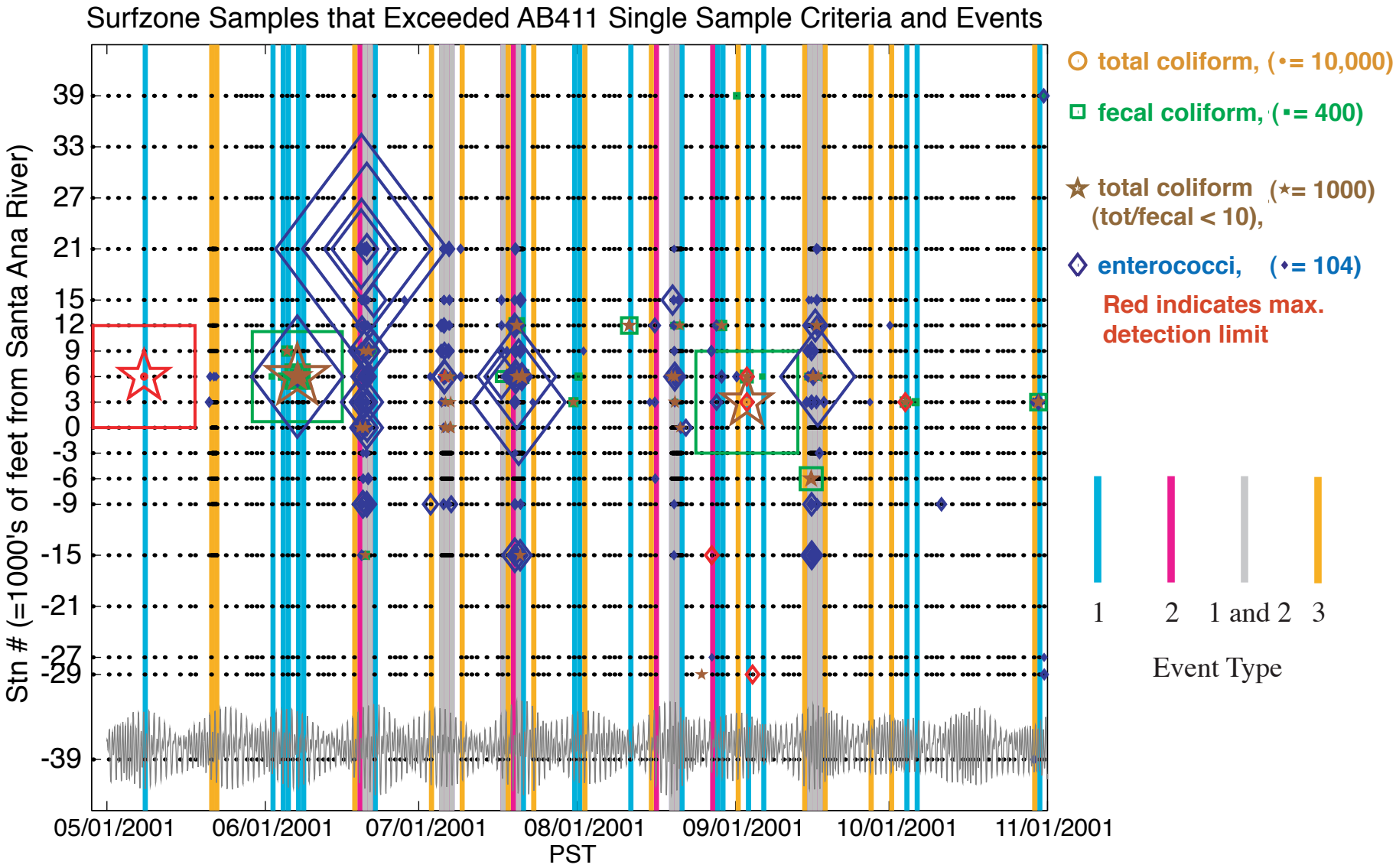

Figure 3-13. The vertical bars indicate days on which bacterial events occurred, blue=type 1, magenta=type 2, gray=types 1 and 2, gold= type 3. Sea level measured at Los Angeles is shown at the bottom of the figure. A black dot is plotted at each time and location a sample was taken. Colored symbols are plotted at the time and location of samples exceeding AB411 single-sample standards. The size of the symbol is proportional to the ratio of the measured bacterial concentration to the AB411 criteria. The symbol size for a sample equal to the AB411 criteria is shown to the right of the indicator species in the legend.

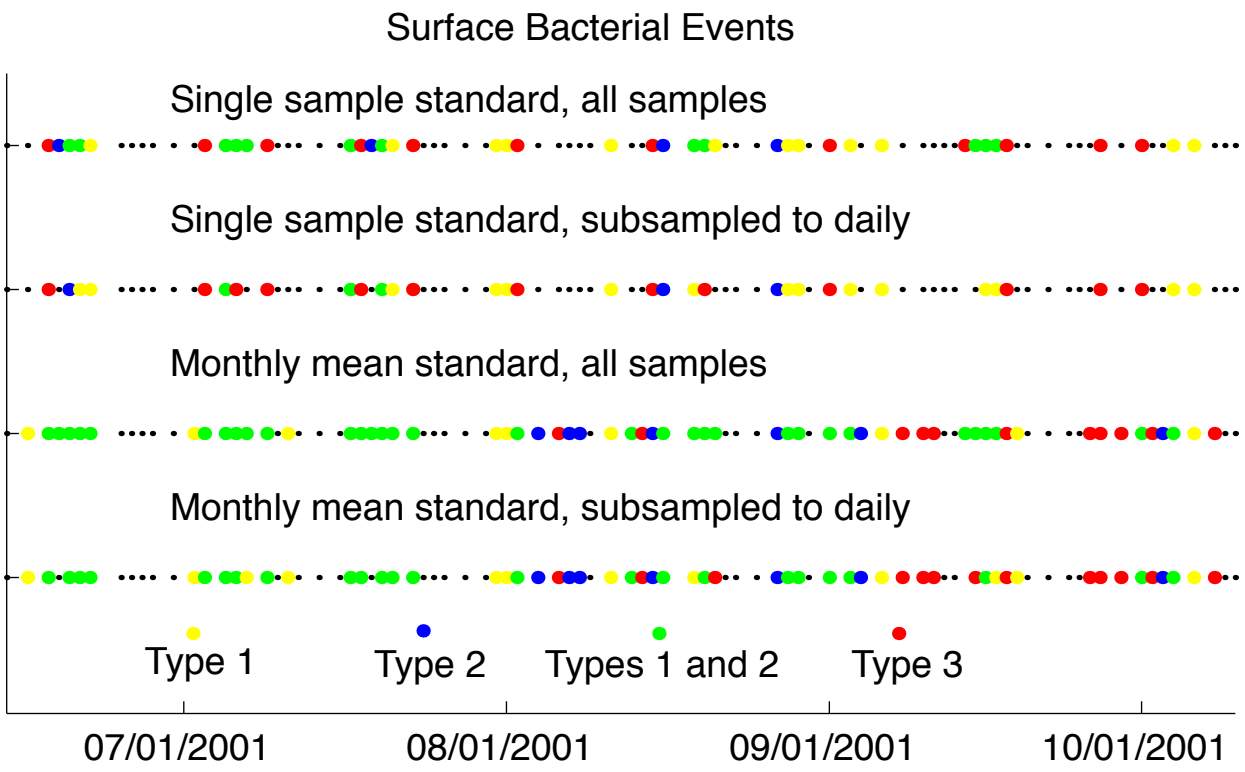

Figure 3-14. Colored dots indicate days on which surfzone bacterial events occurred during HB PIII; black dots indicate days on which samples were taken, but no event occurred. Yellow=type 1; blue=type 2; green=types 1 and 2; red=type 3. Events were defined for both the full data set (rows 1 and 3), and the set subsampled to no more than daily (rows 2 and 4), using both the single-sample standards (rows 1 and 2) and the monthly geometric mean standards applied to single samples (rows 3 and 4).

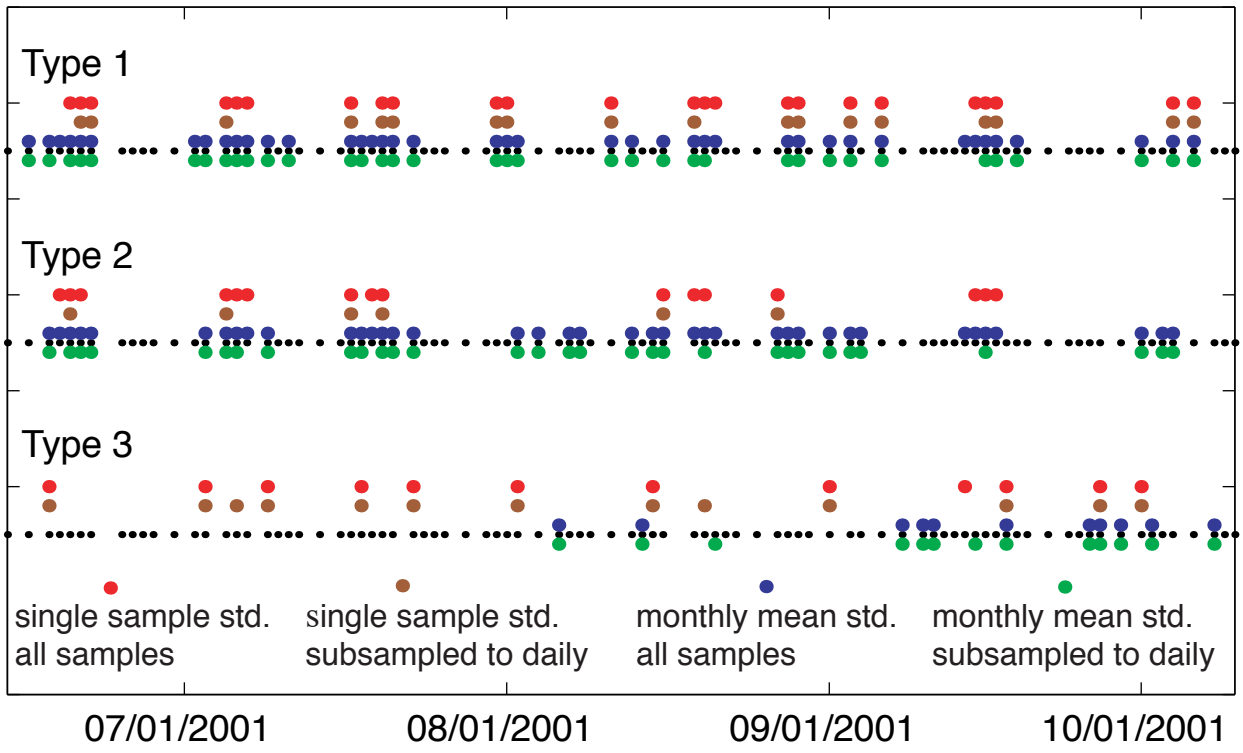

Figure 3-l5. The bacterial events shown in Figure 3-13 are included here in an alternate display. Events are grouped by type: type 1 on top, type 2 in the middle, and type 3 on the bottom. Red=single sample standard, all samples; brown=single-sample standard, subsampled to daily; blue=monthly mean standard, all samples; green= monthly geometric mean standard, subsampled to daily; black=days on which samples were taken.

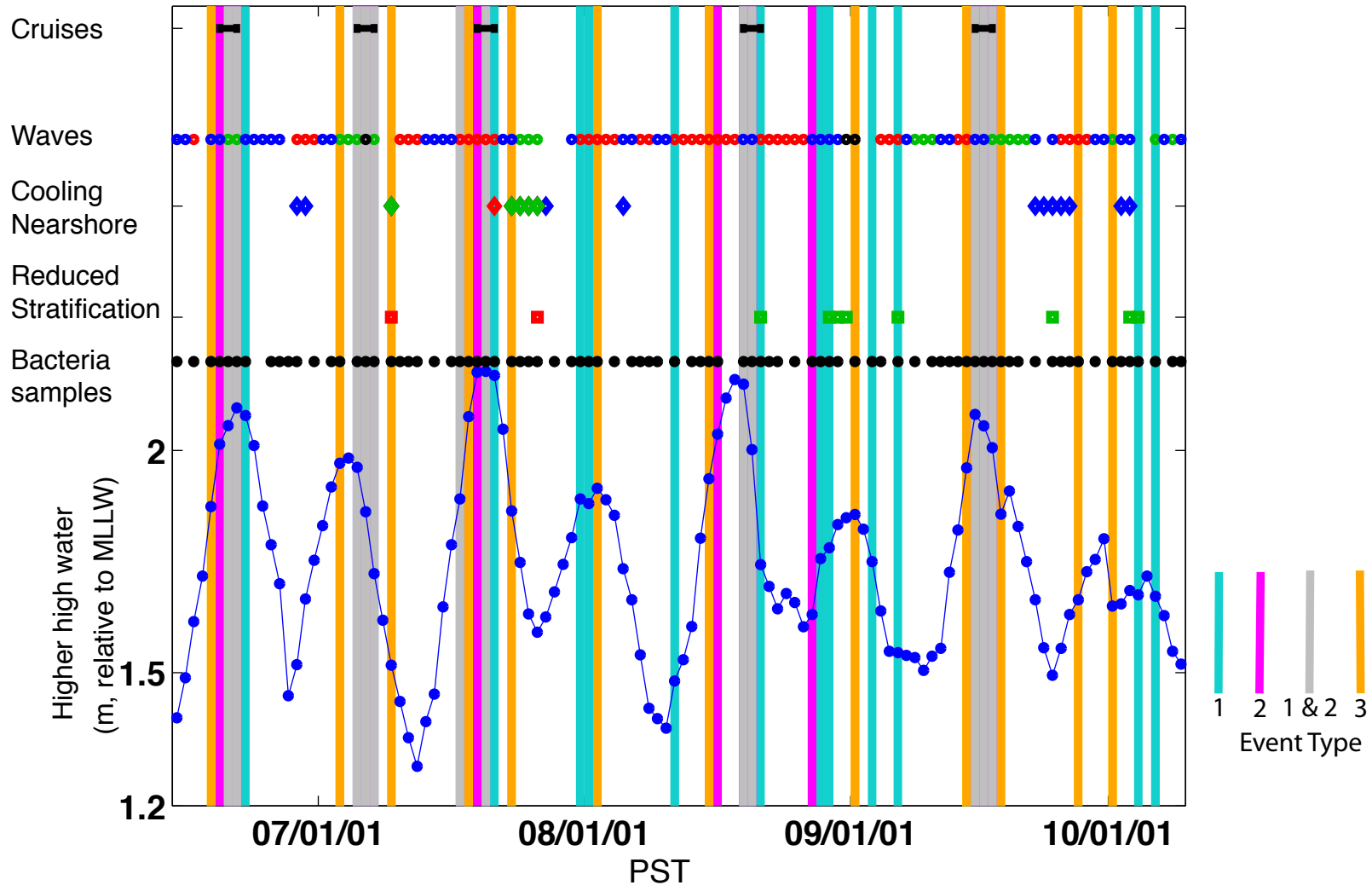

Figure 3-16. Days on which bacterial events occur (vertical bars: blue=type 1, magenta=type 2, gray= types 1 and 2, gold=type 3) are shown together with cruise days, during which round-the-clock surfzone bacterial sampling was done (row 1: ▬); characterization of that day's wave spectra (row 2: ○ westerly wind waves, ○ southerly swell, ○ westerly wind waves + southerly swell, ● short period southerly waves + southerly swell, no dot = no measurable waves); occurrence of cold water nearshore (row 3: ♦ 12 °C inshore of 30m, ♦ HB01 temperature < maximum plume temperature, ♦ both); and occurrence of reduced stratification (row 4: ■ HB03 mixed, ■ reduced stratification at HB01-HB05). Black dots in row 5 indicate whether bacterial samples were taken that day. The day's higher high water as measured at Los Angeles is shown at the bottom.

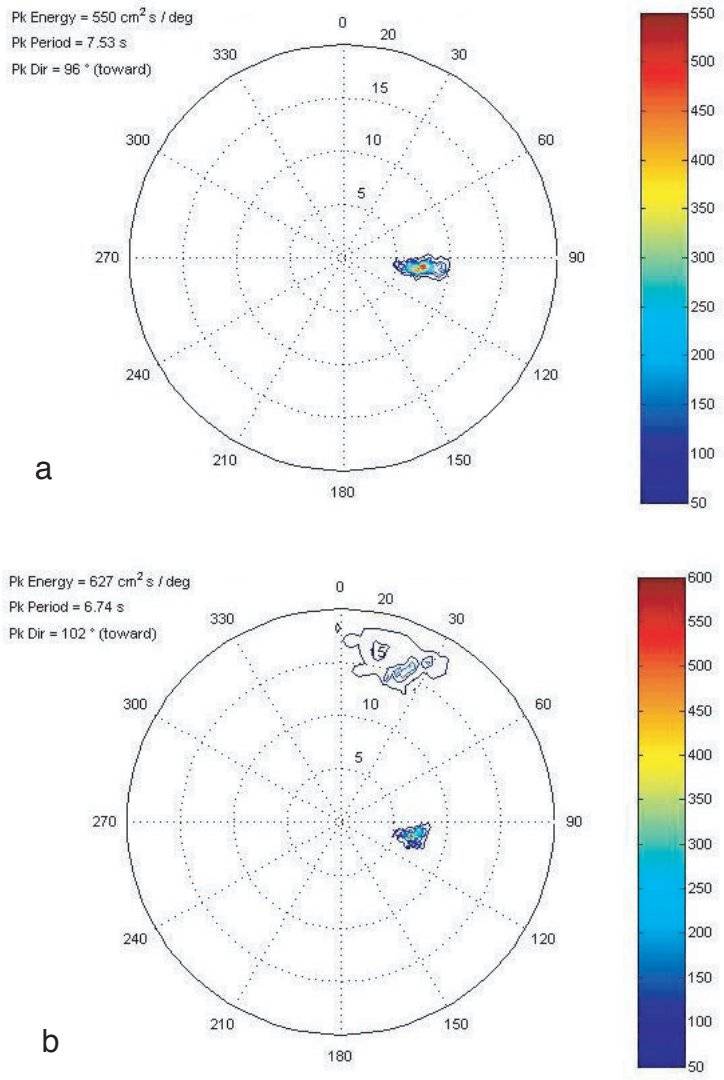

Figure 3-17a. One-day average directional surface wave spectra measured at HB07 are shown for each of two days. a) June 29, 2001: westerly wind waves, b) July 13, 2001: southerly swell plus westerly wind waves. Contours are in units of cm^2/Hz/deg.

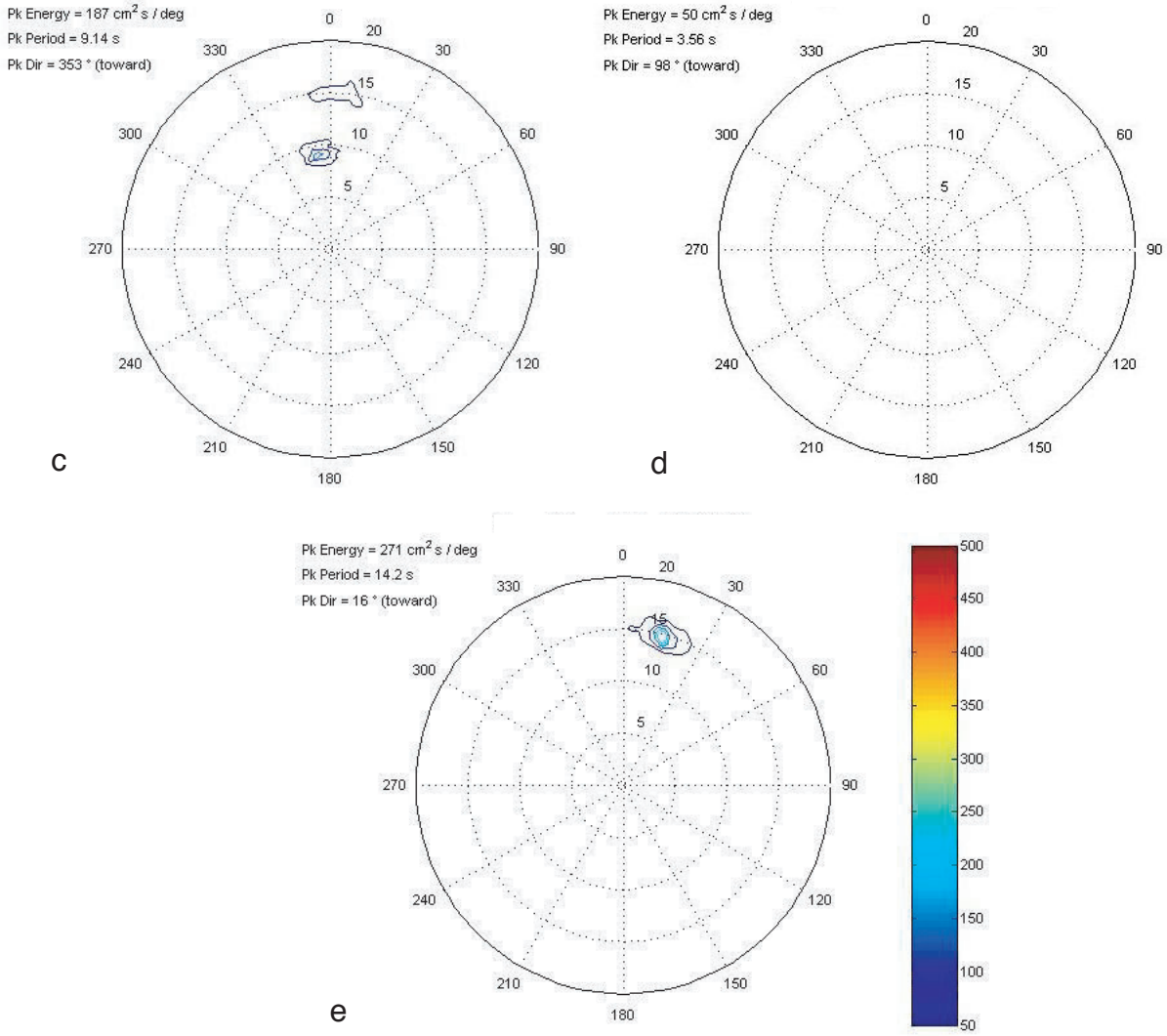

Figure 3-17b. One-day average directional surface wave spectra measured at HB07 are shown for each of three days: c) August 31, 2001: southerly swell plus southerly wind waves (or shorter period swell), d) September 2, 2001: no measurable waves, and e) September 20, 2001: southerly swell. Contours are in units of cm^2/Hz/deg.

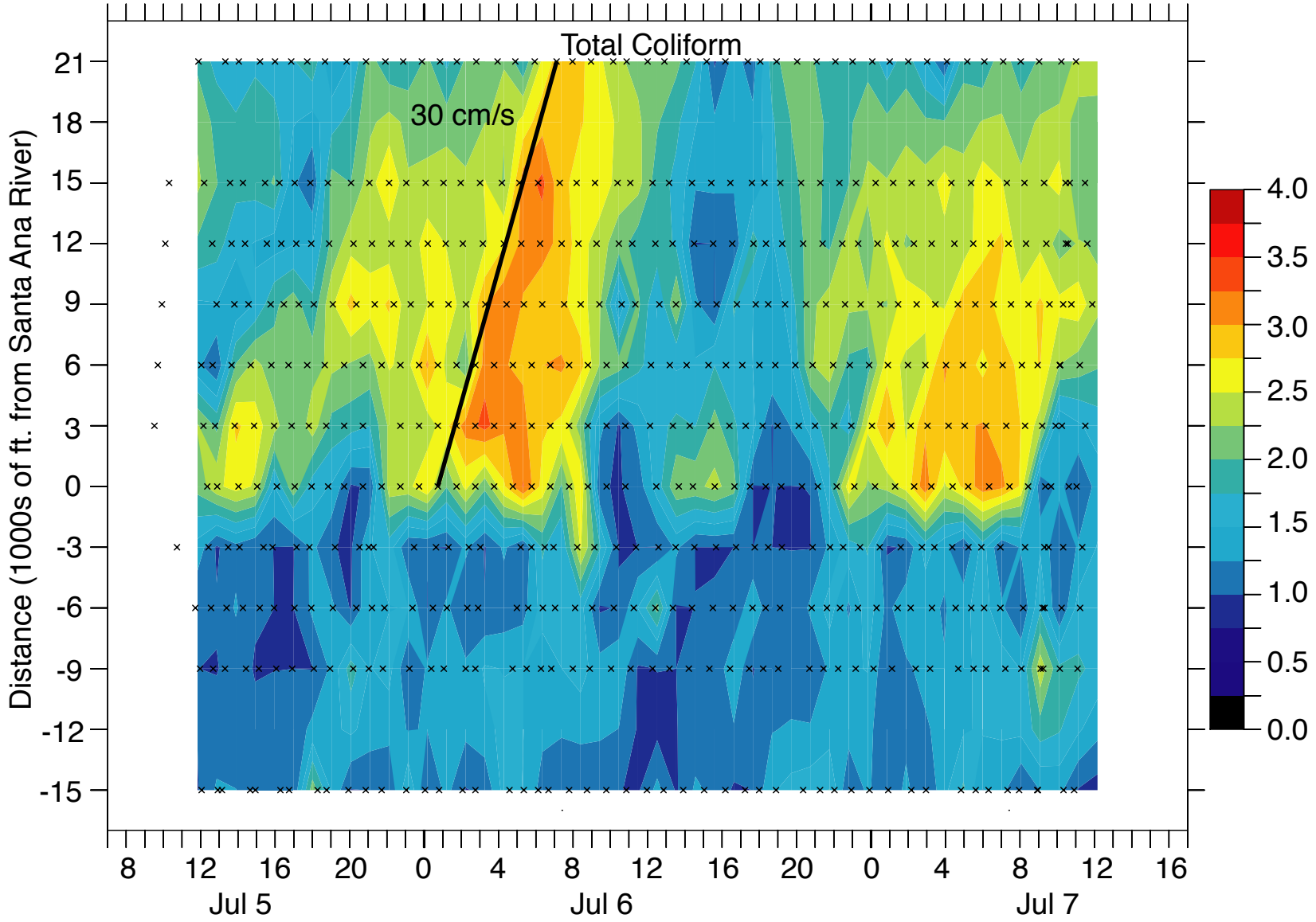

Figure 3-18. The $\log_{10}$ of total coliform concentration (MPN/100 mL) is plotted versus local time and distance alongshore. Black x's indicate the time and location of each sample. Data is contoured on a 48 by 13 grid (time and distance, respectively) using cay=5 and nrng=2. Time is Pacific Daylight Time (PDT).

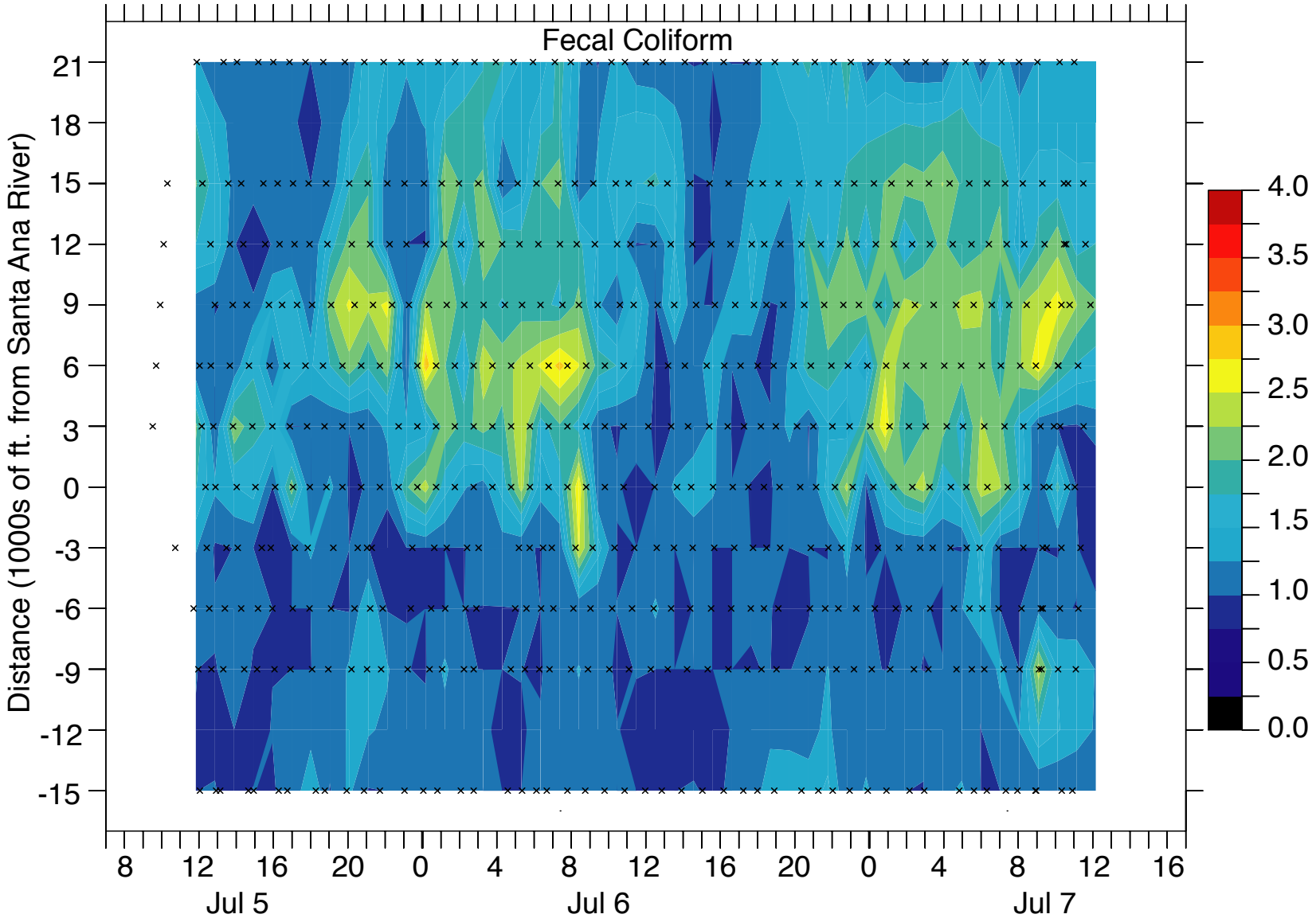

Figure 3-19. The $\log_{10}$ of fecal coliform concentration (MPN/100 mL) is plotted versus local time and distance alongshore. Black x's indicate the time and location of each sample. Data is contoured on a 48 by 13 grid (time and distance, respectively) using cay=5 and nrng=2. Time is Pacific Daylight Time (PDT).

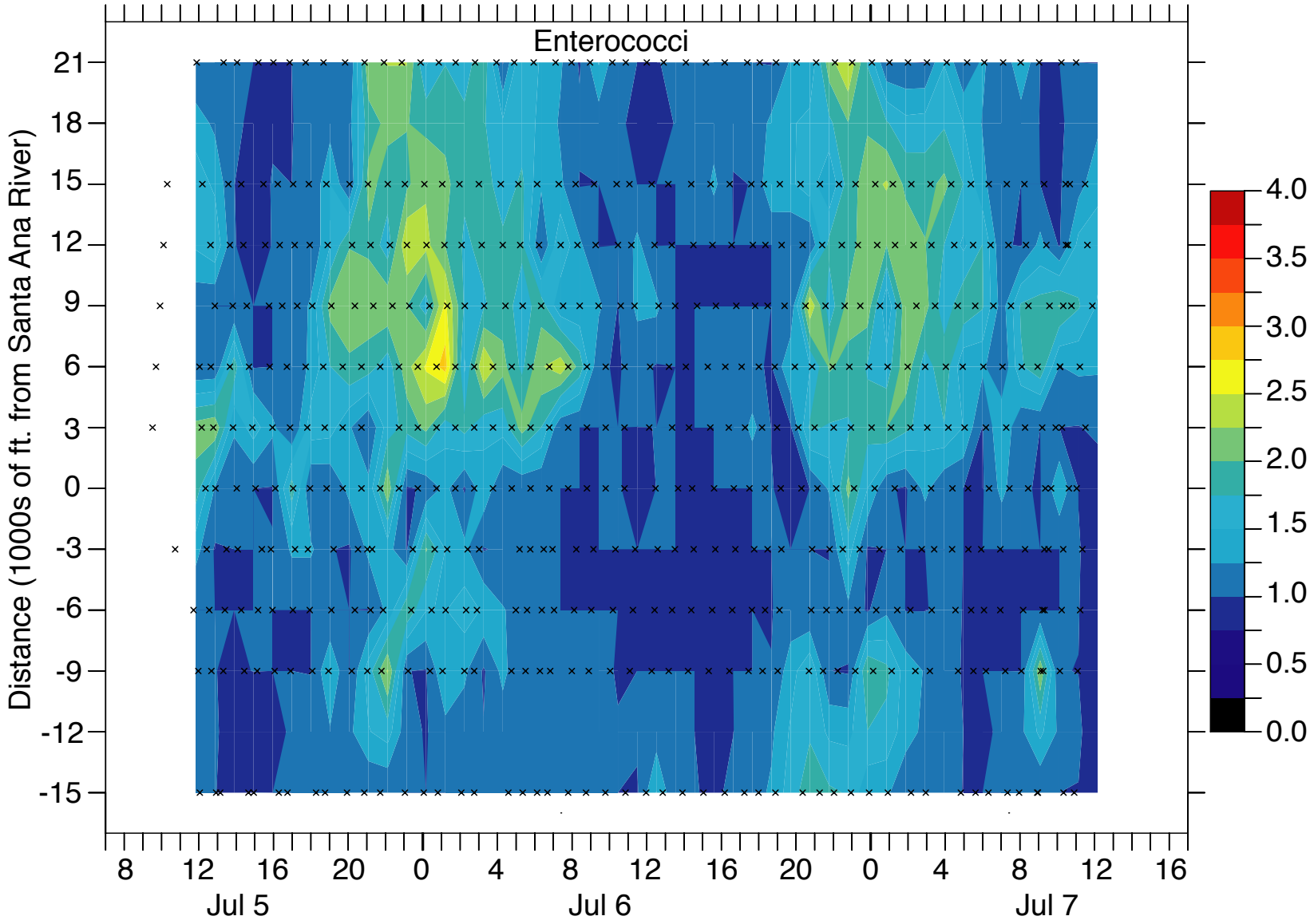

Figure 3-20. The $\log_{10}$ of enterococci concentration (MPN/100 mL) is plotted versus local time and distance alongshore. Black x's indicate the time and location of each sample. Data is contoured on a 48 by 13 grid (time and distance, respectively) using cay=5 and nrng=2. Time is Pacific Daylight Time (PDT).

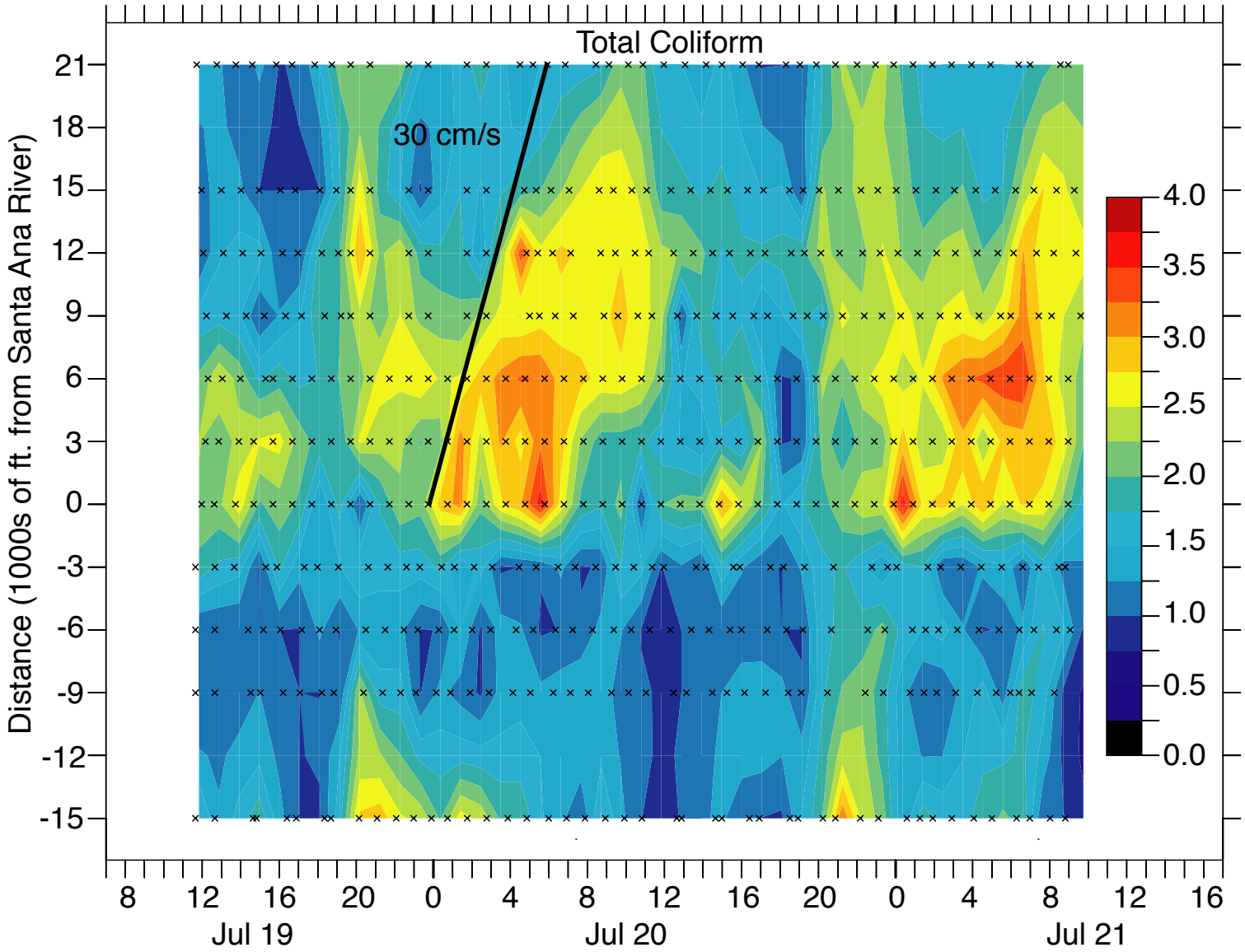

Figure 3-21. The $\log_{10}$ of total coliform concentration (MPN/100 mL) is plotted versus local time and distance alongshore. Black x's indicate the time and location of each sample. Data is contoured on a 48 by 13 grid (time and distance, respectively) using cay=5 and nrng=2. Time is Pacific Daylight Time (PDT).

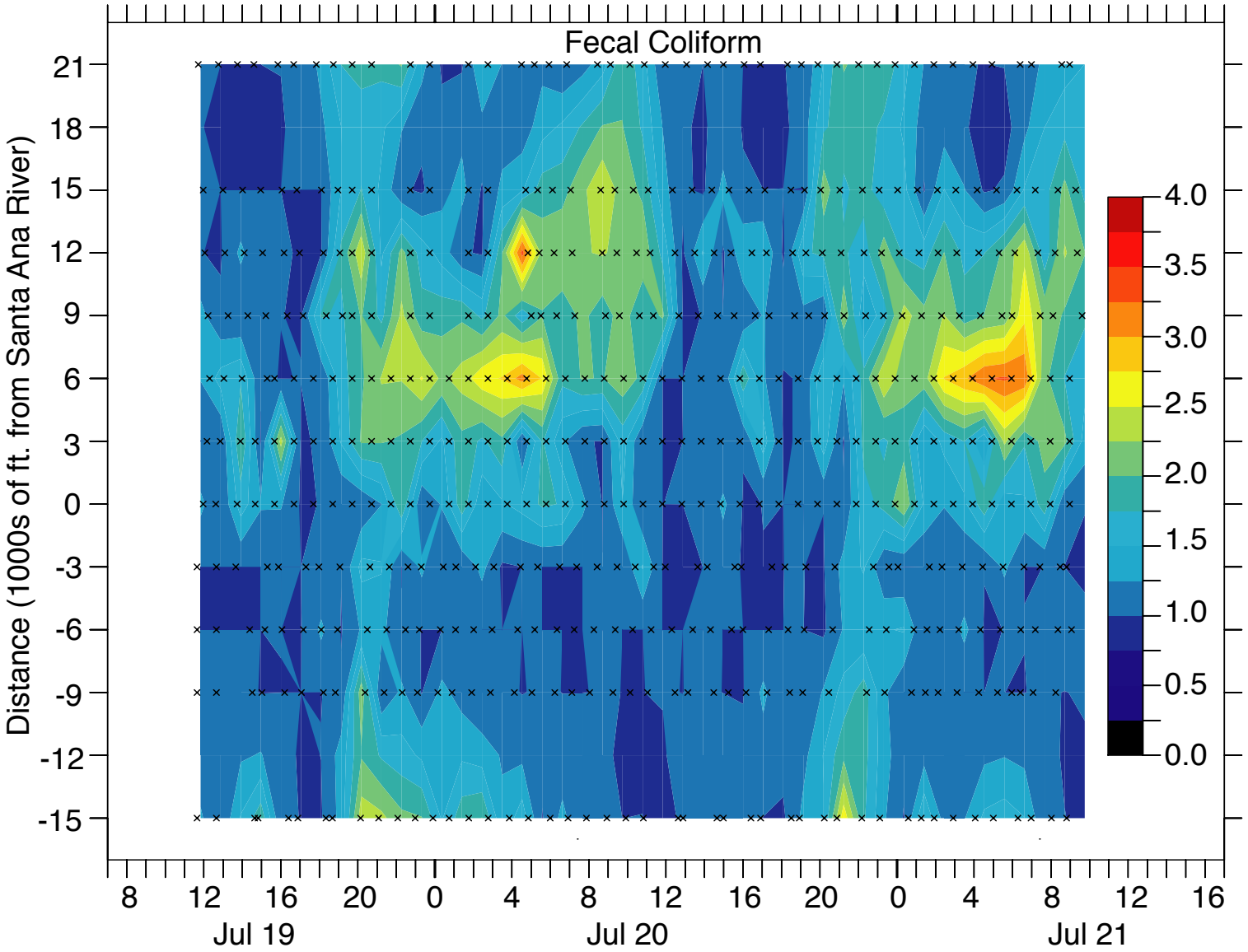

Figure 3-22. The $\log_{10}$ of fecal coliform concentration (MPN/100 mL) is plotted versus local time and distance alongshore. Black x's indicate the time and location of each sample. Data is contoured on a 48 by 13 grid (time and distance, respectively) using cay=5 and nrng=2. Time is Pacific Daylight Time (PDT).

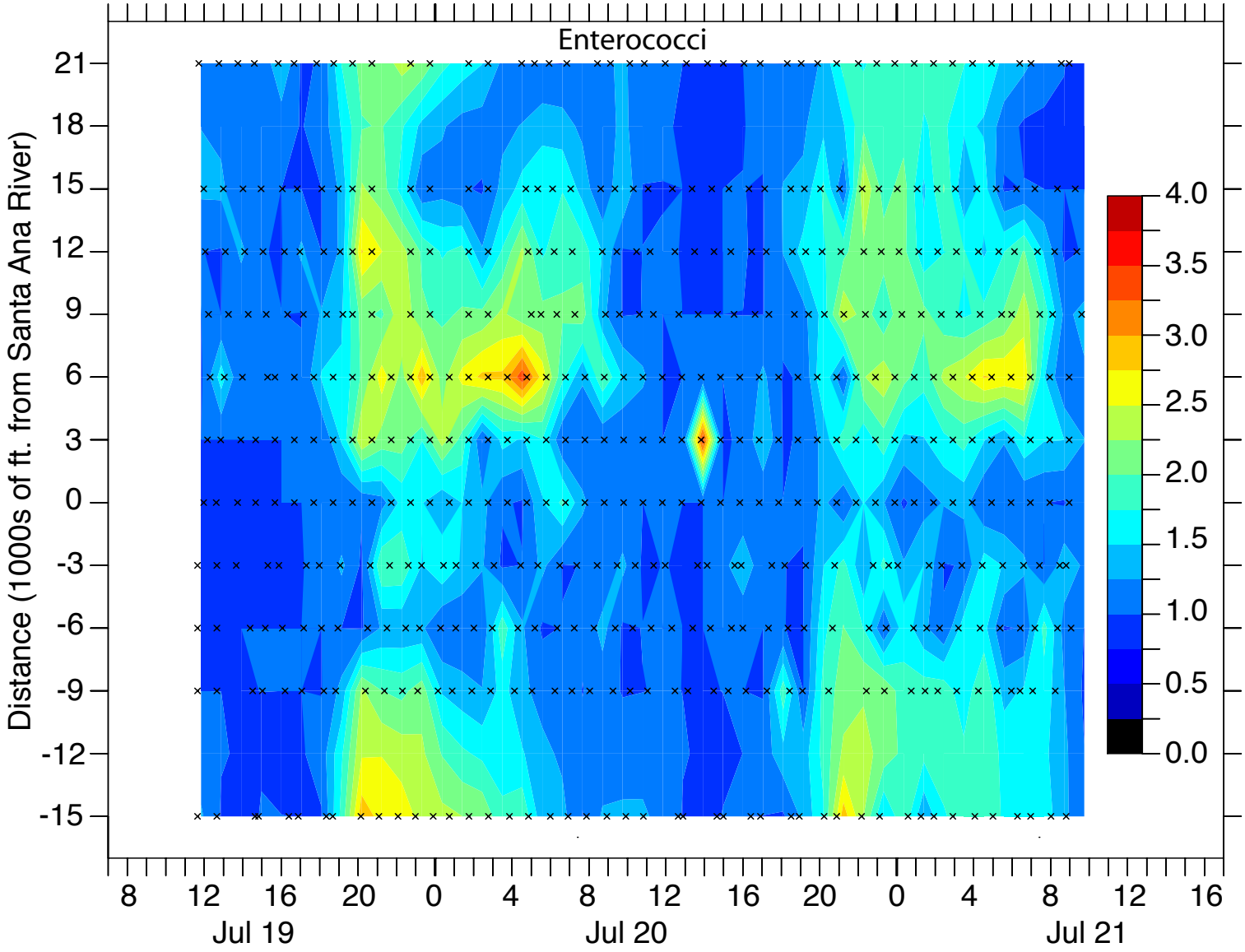

Figure 3-23. The $\log_{10}$ of enterococci concentration (MPN/100 mL) is plotted versus local time and distance alongshore. Black x's indicate the time and location of each sample. Data is contoured on a 48 by 13 grid (time and distance, respectively) using cay=5 and nrng=2. Time is Pacific Daylight Time (PDT).

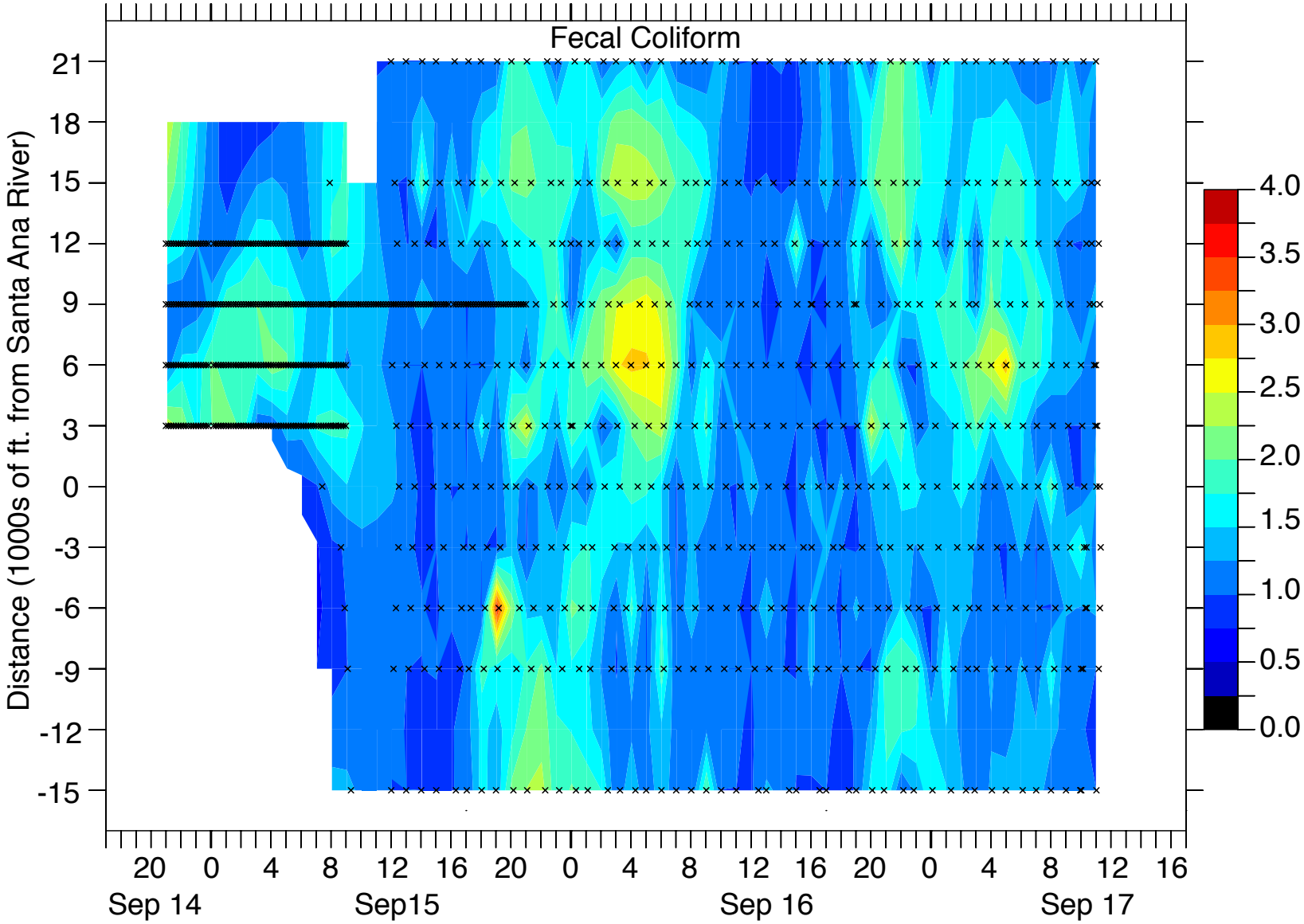

Figure 3-24. The $\log_{10}$ of fecal coliform concentration (MPN/100 mL) is plotted versus local time and distance alongshore. Black x's indicate the time and location of each sample. Data is contoured on a 48 by 13 grid (time and distance, respectively) using cay=5 and nrng=2. Time is Pacific Daylight Time (PDT).

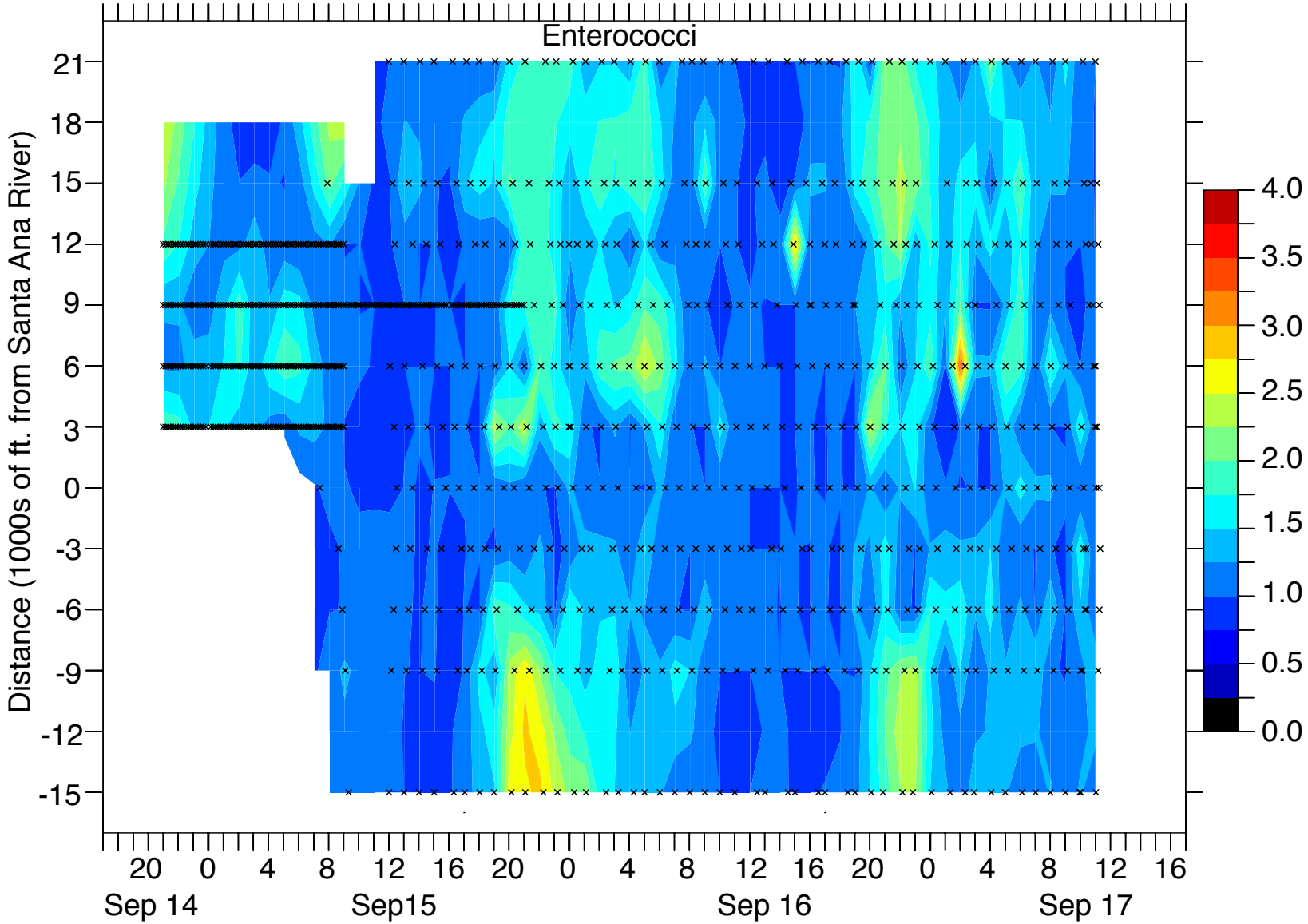

Figure 3-25. The $\log_{10}$ of enterococci concentration (MPN/100 mL) is plotted versus local time and distance alongshore. Black x's indicate the time and location of each sample. Data is contoured on a 48 by 13 grid (time and distance, respectively) using cay=5 and nrng=2. Time is Pacific Daylight Time (PDT). .

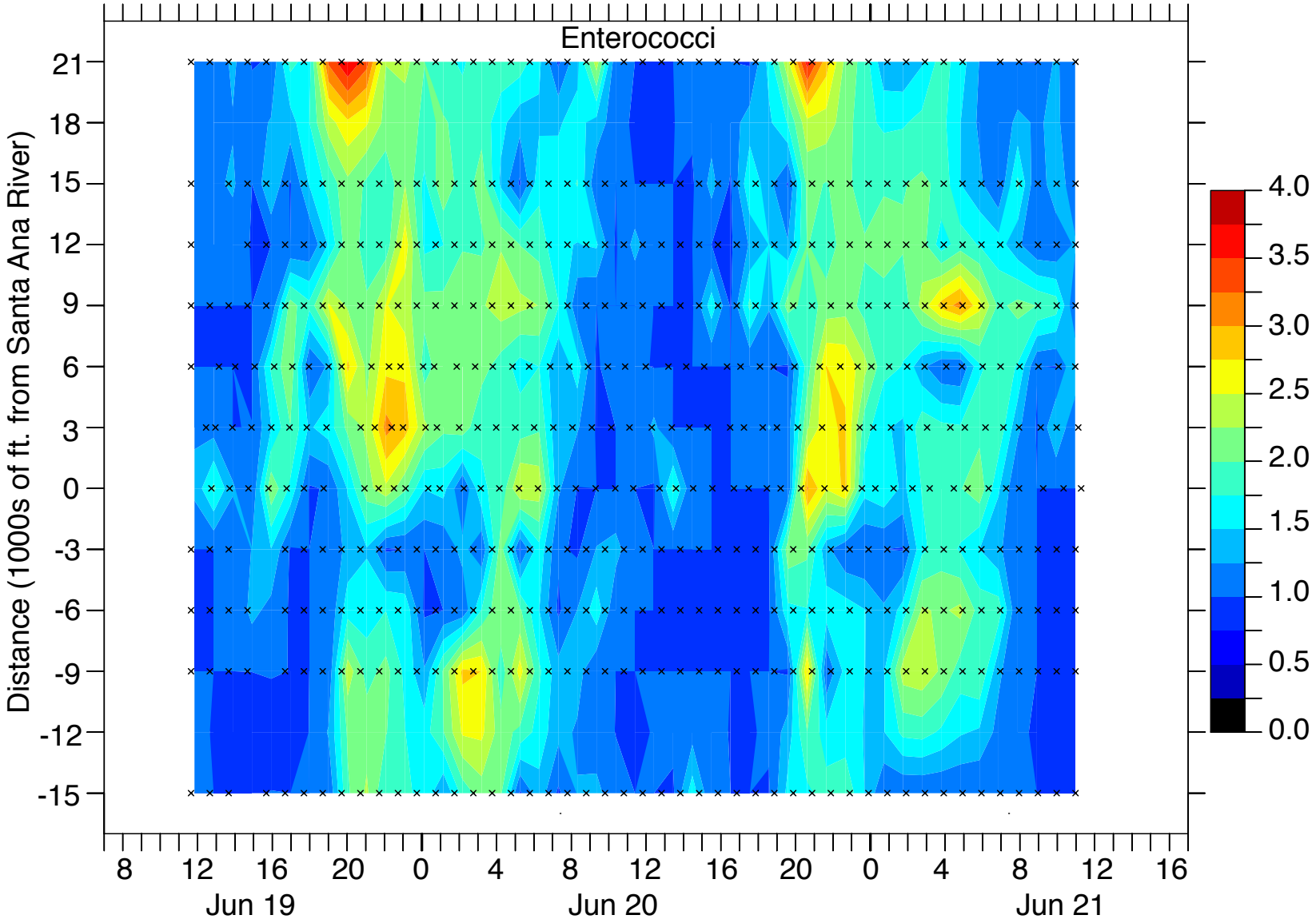

Figure 3-26. The $\log_{10}$ of enterococci concentration (MPN/100 mL) is plotted versus local time and distance alongshore. Black x's indicate the time and location of each sample. Data is contoured on a 48 by 13 grid (time and distance, respectively) using cay=5 and nrng=2. Time is Pacific Daylight Time (PDT).

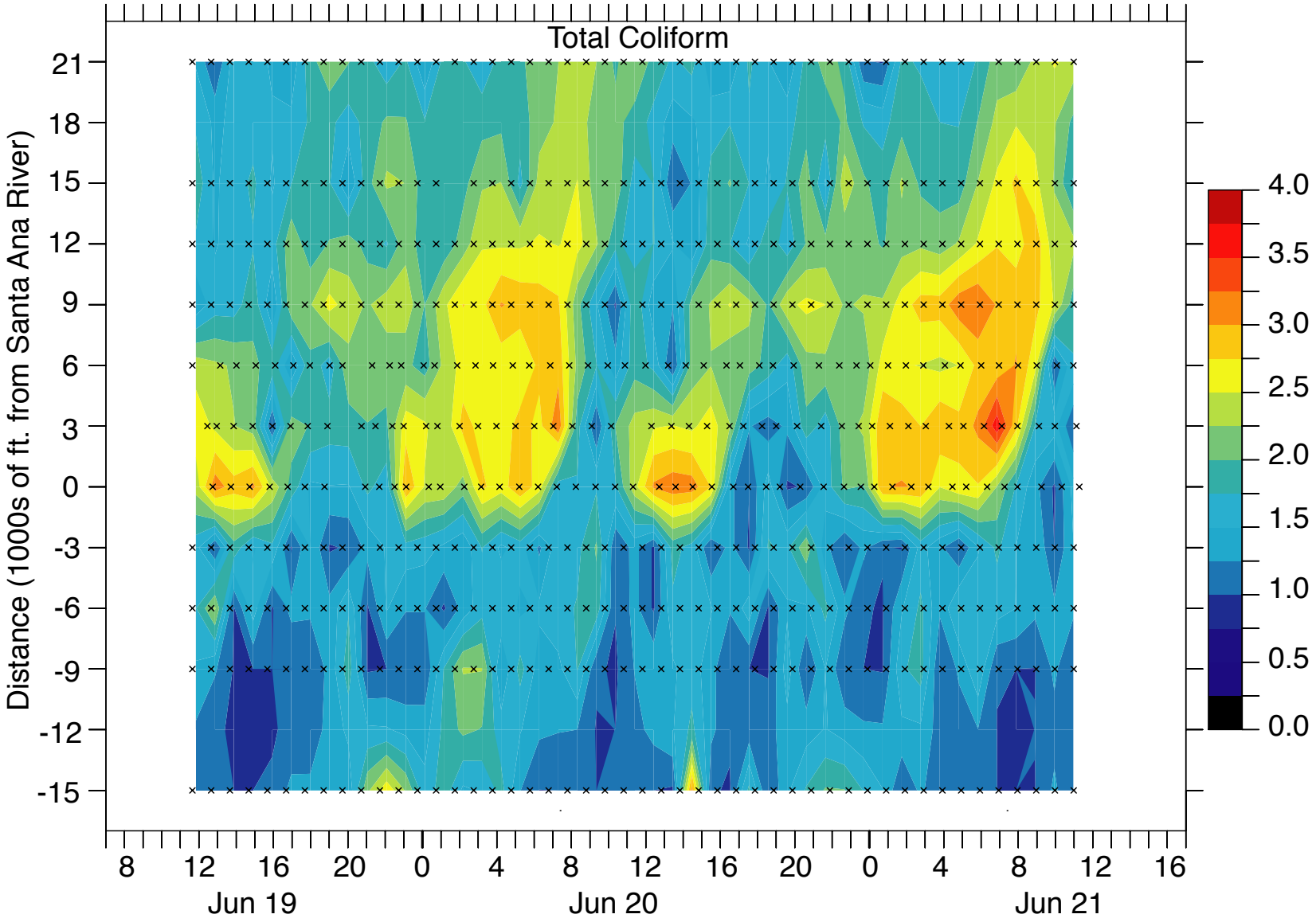

Figure 3-27. The $\log_{10}$ of total coliform concentration (MPN/100 mL) is plotted versus local time and distance alongshore. Black x's indicate the time and location of each sample. Data is contoured on a 48 by 13 grid (time and distance, respectively) using cay=5 and nrng=2. Time is Pacific Daylight Time (PDT).

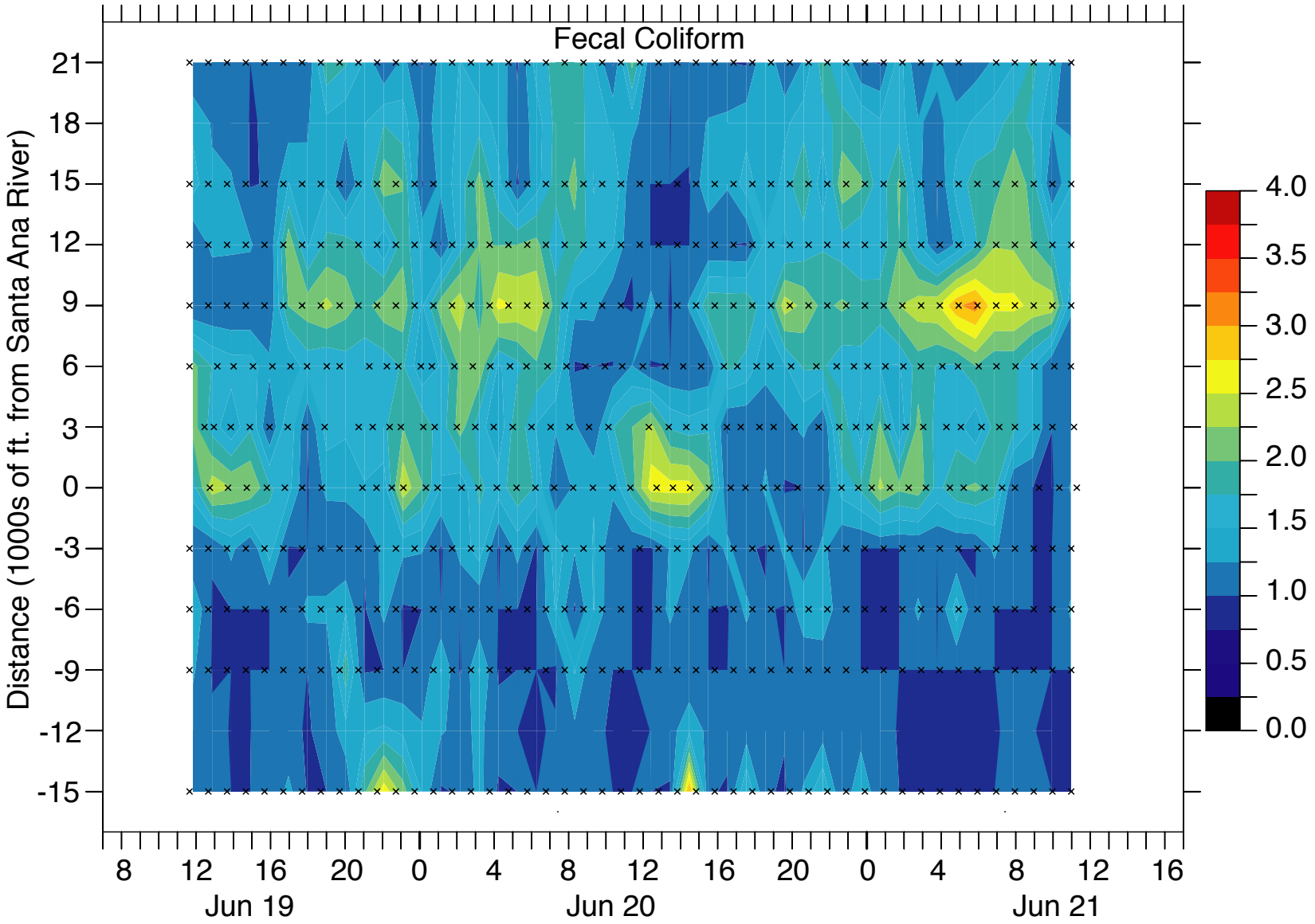

Figure 3-28. The $\log_{10}$ of fecal coliform concentration (MPN/100 mL) is plotted versus local time and distance alongshore. Black x's indicate the time and location of each sample. Data is contoured on a 48 by 13 grid (time and distance, respectively) using cay=5 and nrng=2. Time is Pacific Daylight Time (PDT).

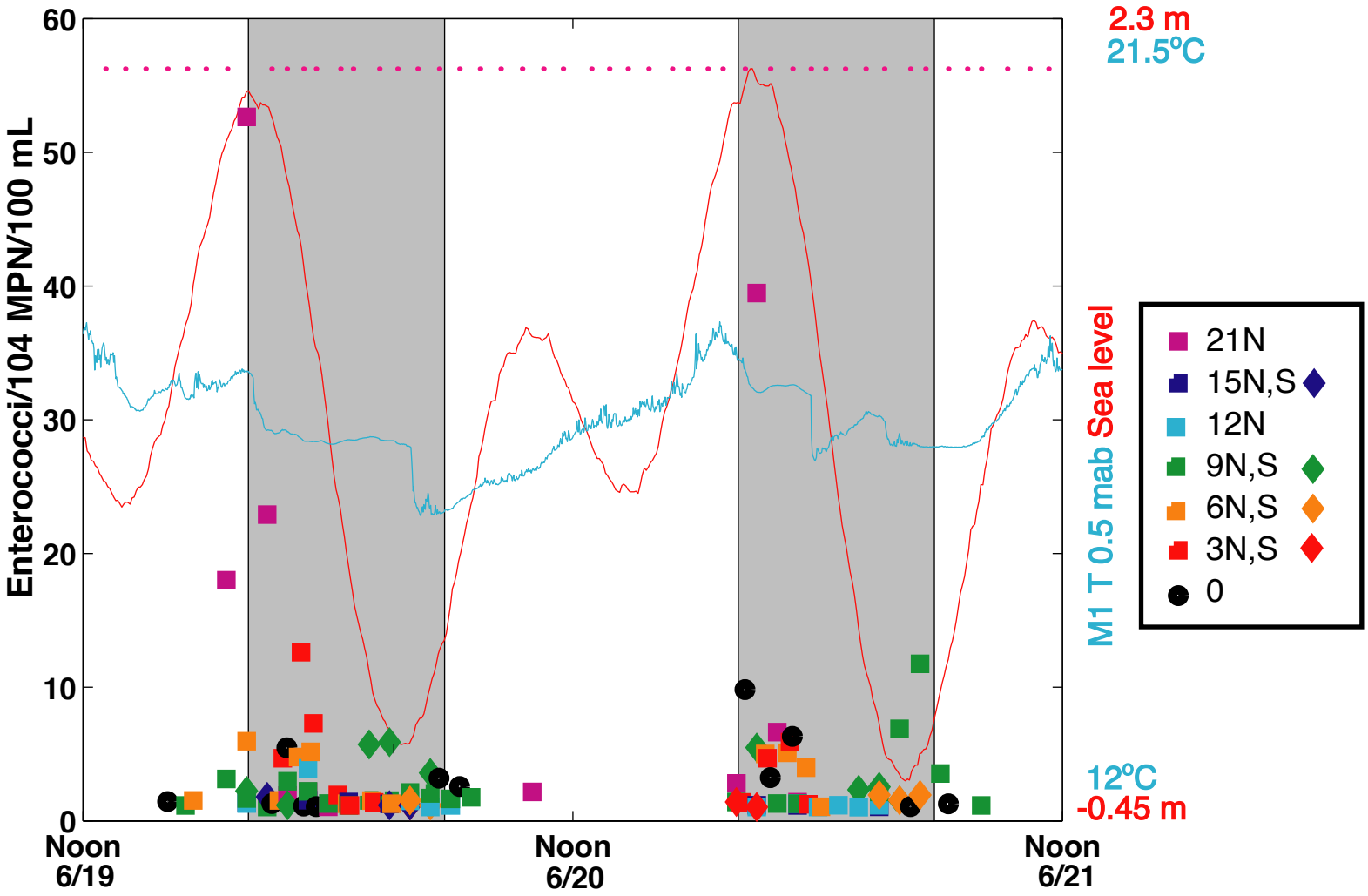

Figure 3-29. The ratio of enterococci concentrations to the AB411 single-sample standard at stations 15S to 21N for the second intensive sampling period is plotted together with sampling times at station 0 (pink dots), Los Angeles sea level (red line), and temperature 0.5 m above bottom at HB01 (blue line). Only samples exceeding 104 MPN/100 mL are shown here. A local time reference is used.

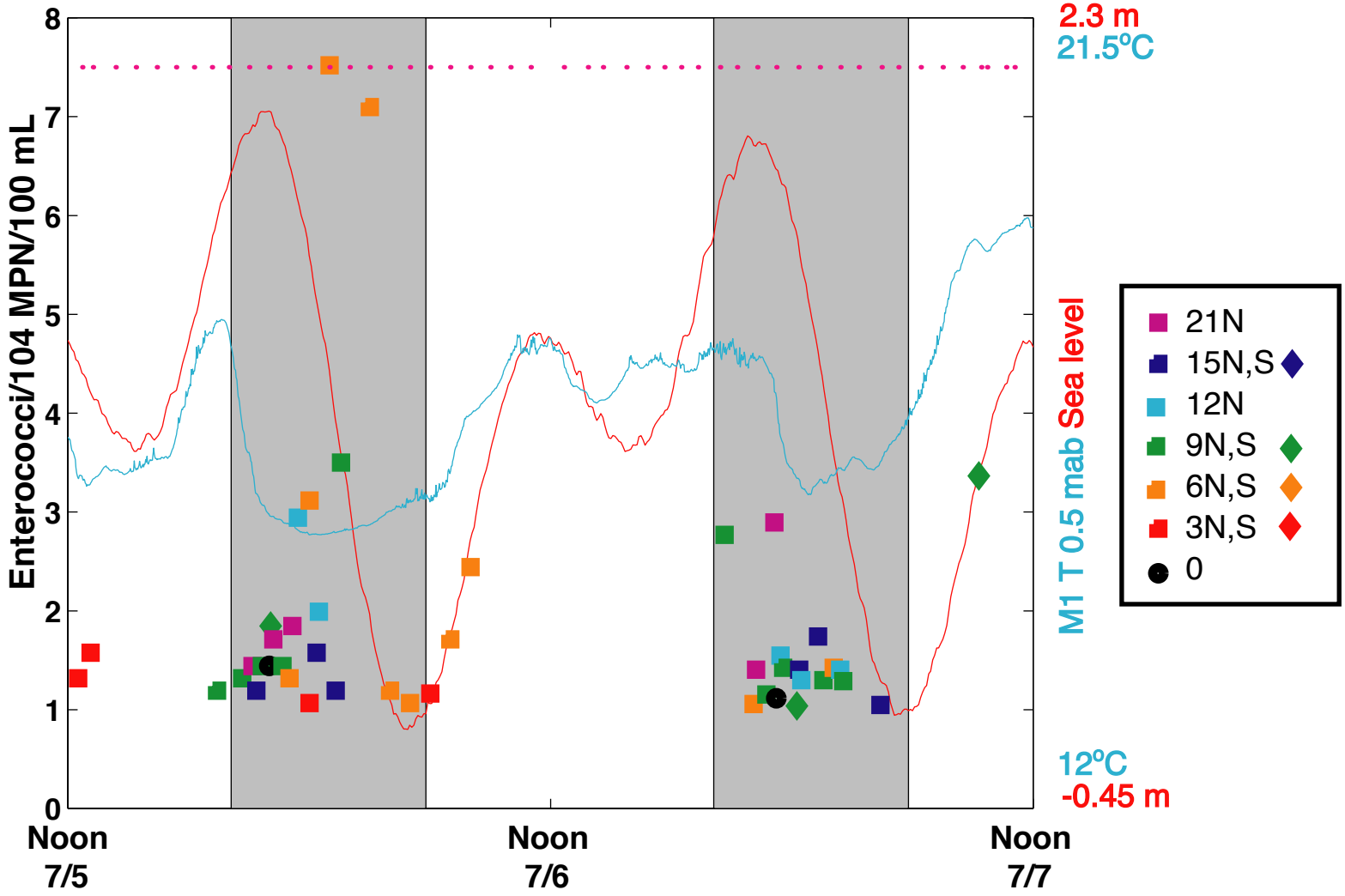

Figure 3-30. The ratio of enterococci concentrations to the AB411 single-sample standard at stations 15S to 21N for the third intensive sampling period is plotted together with sampling times at station 0 (pink dots), Los Angeles sea level (red line), and temperature 0.5 m above bottom at HB01 (blue line). Only samples exceeding 104 MPN/100 mL are shown here. A local time reference is used. Note the change in vertical scale for the bacterial concentration ratio.

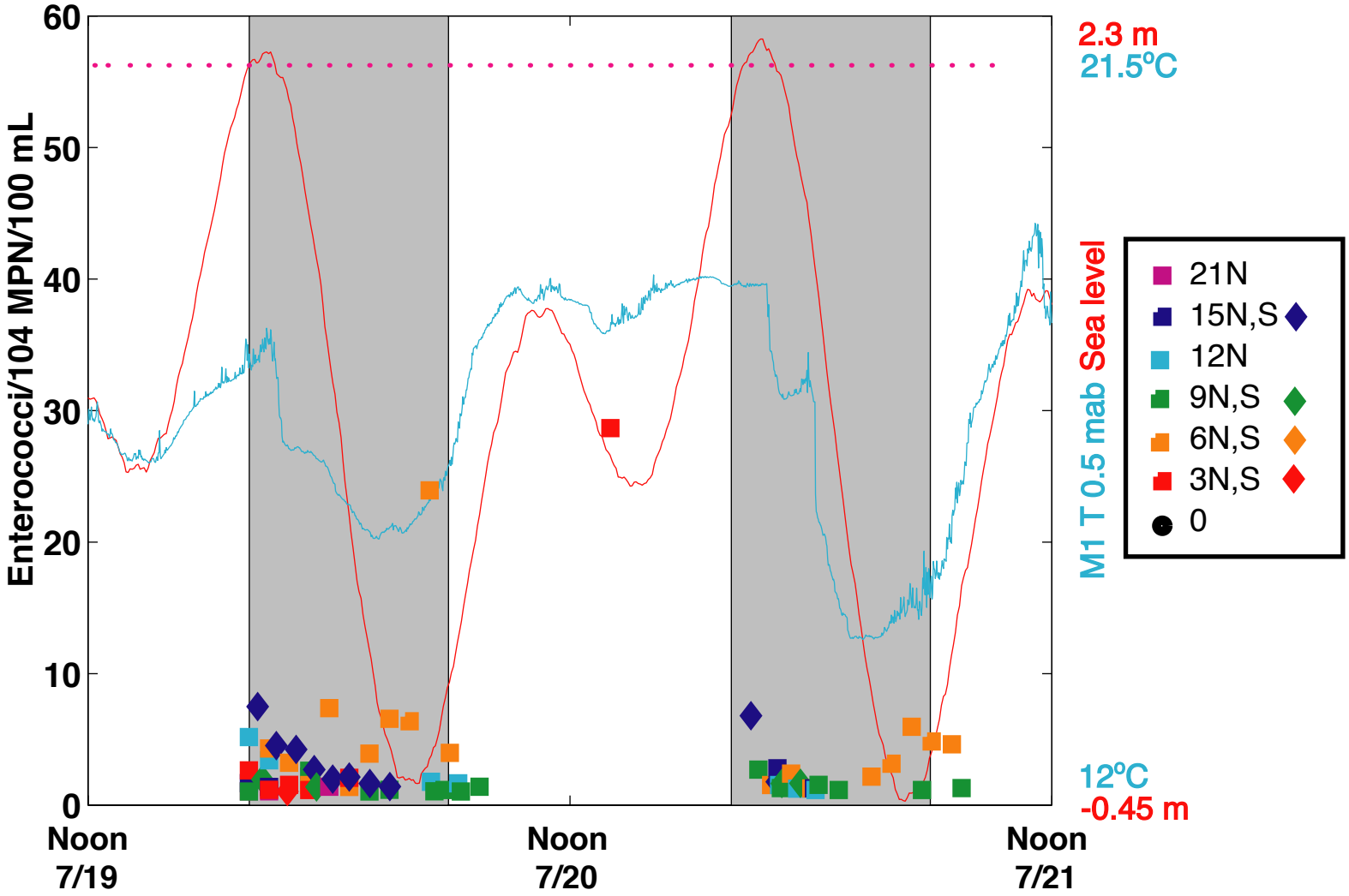

Figure 3-31. The ratio of enterococci concentrations to the AB411 single-sample standard at stations 15S to 21N for the fourth intensive sampling period is plotted together with sampling times at station 0 (pink dots), Los Angeles sea level (red line), and temperature 0.5 m above bottom at HB01 (blue line). Only samples exceeding 104 MPN/100 mL are shown here. A local time reference is used.

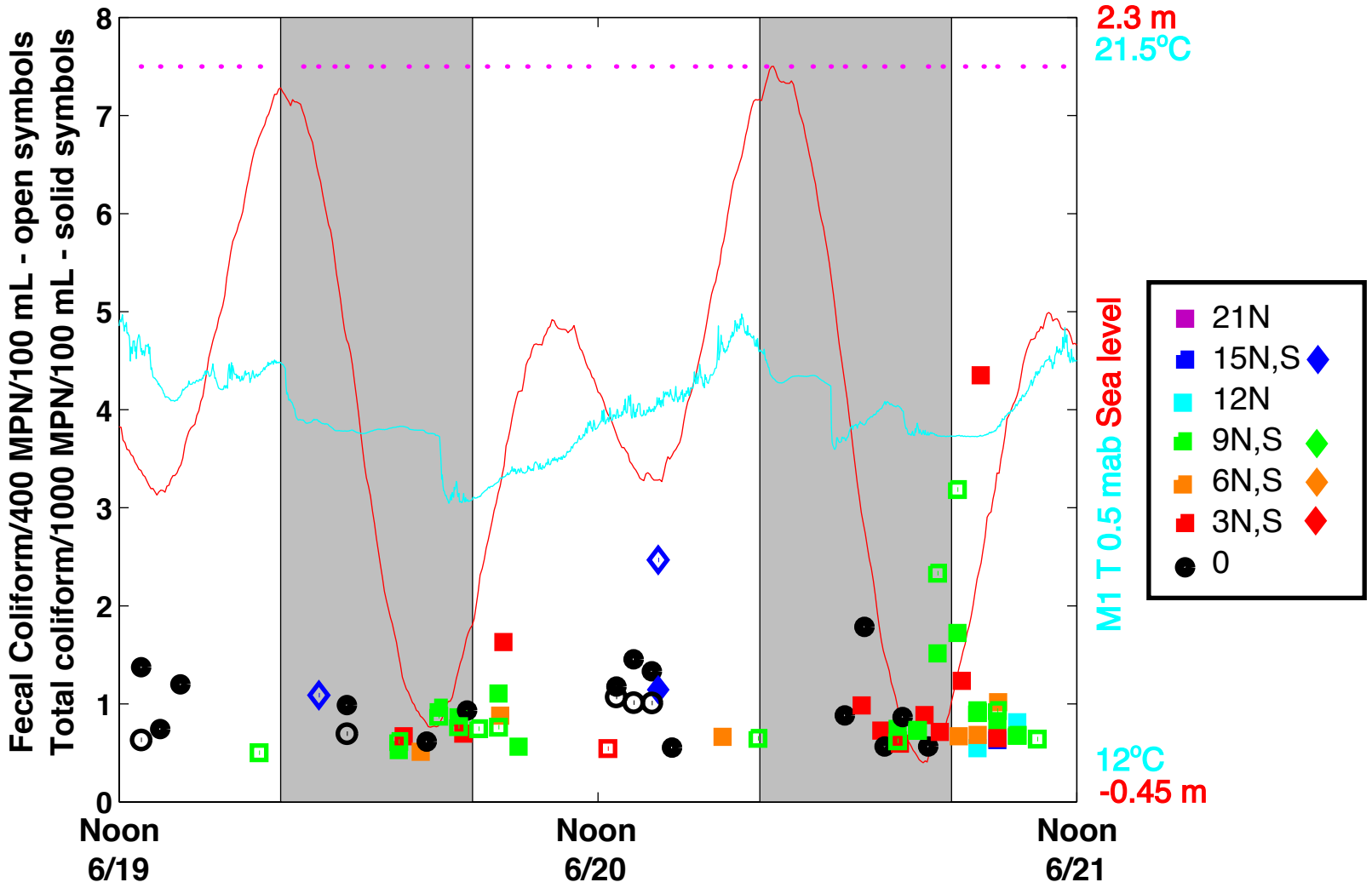

Figure 3-32. The ratio of total and fecal coliform concentrations to their respective AB411 single-sample standards* at stations 15S to 21N for the second intensive sampling period is plotted together with sampling times at station 0 (pink dots), Los Angeles sea level (red line), and temperature 0.5 m above bottom at HB01 (blue line). Only samples with ratios exceeding 0.5 are shown here. A local time reference is used.

*Note that not all samples with total coliform >1000 MPN/100 mL exceed AB411 standards, as the total/fecal coliform ratio may not be <10.

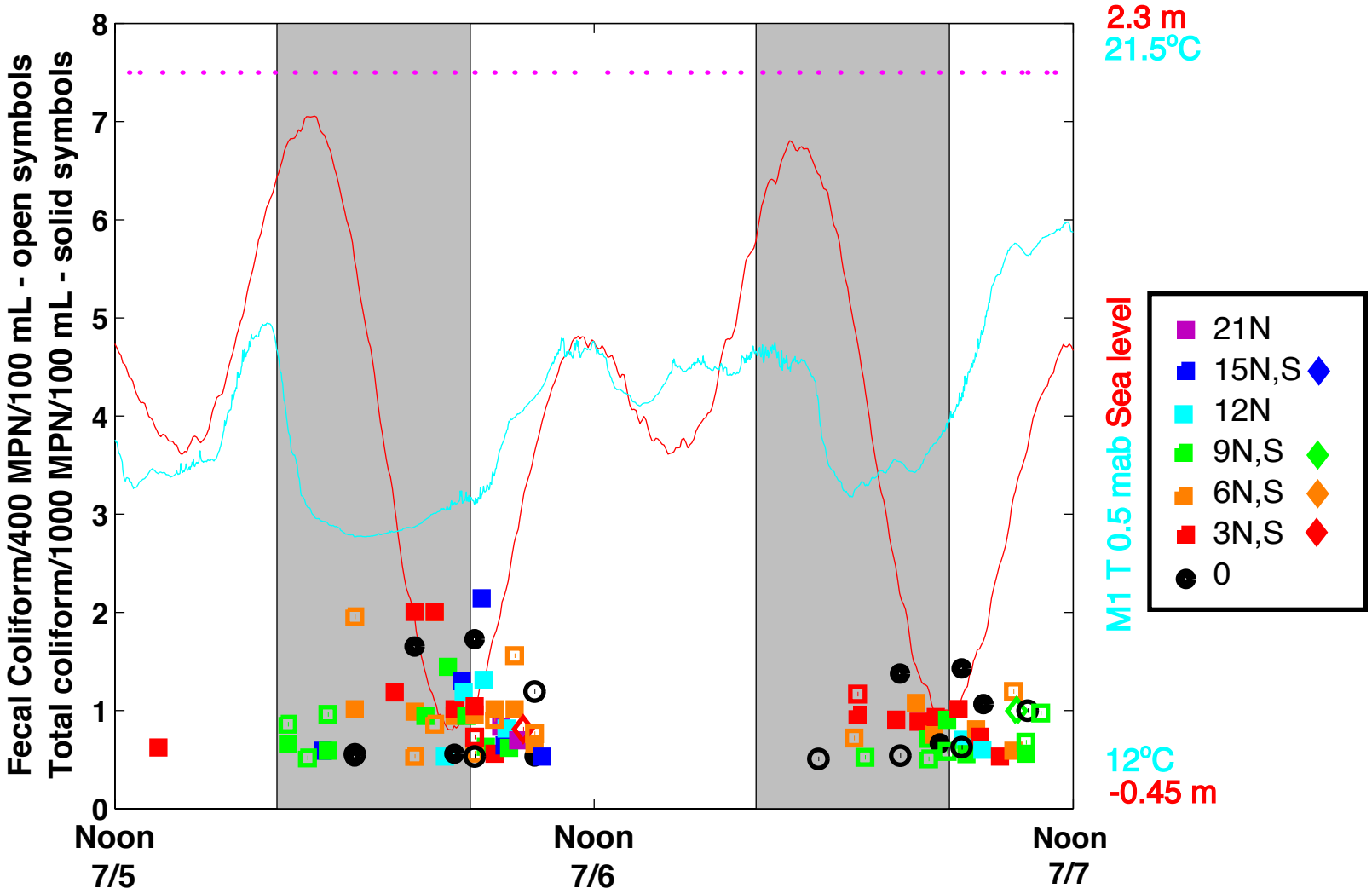

Figure 3-33. The ratio of total and fecal coliform concentrations to their respective AB411 single-sample standards* at stations 15S to 21N for the third intensive sampling period is plotted together with sampling times at station 0 (pink dots), Los Angeles sea level (red line), and temperature 0.5 m above bottom at HB01 (blue line). Only samples with ratios exceeding 0.5 are shown here. A local time reference is used.

*Note that not all samples with total coliform >1000 MPN/100 mL exceed AB411 standards, as the total/fecal coliform ratio may not be <10.

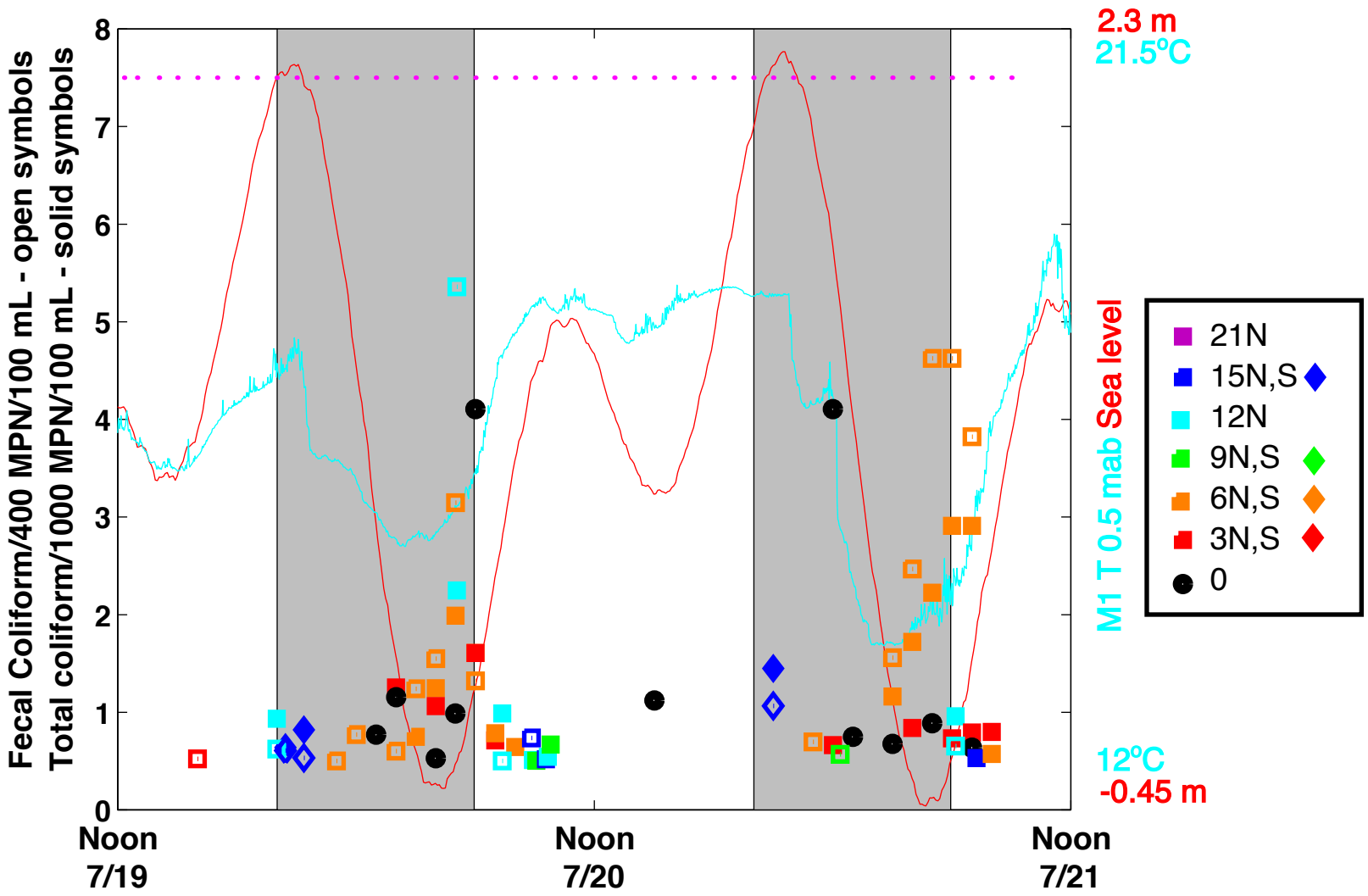

Figure 3-34. The ratio of total and fecal coliform concentrations to their respective AB411 single-sample standards* at stations 15S to 21N for the fourth intensive sampling period is plotted together with sampling times at station 0 (pink dots), Los Angeles sea level (red line), and temperature 0.5 m above bottom at HB01 (blue line). Only samples with ratios exceeding 0.5 are shown here. A local time reference is used.

*Note that not all samples with total coliform >1000 MPN/100 mL exceed AB411 standards, as the total/fecal coliform ratio may not be <10.

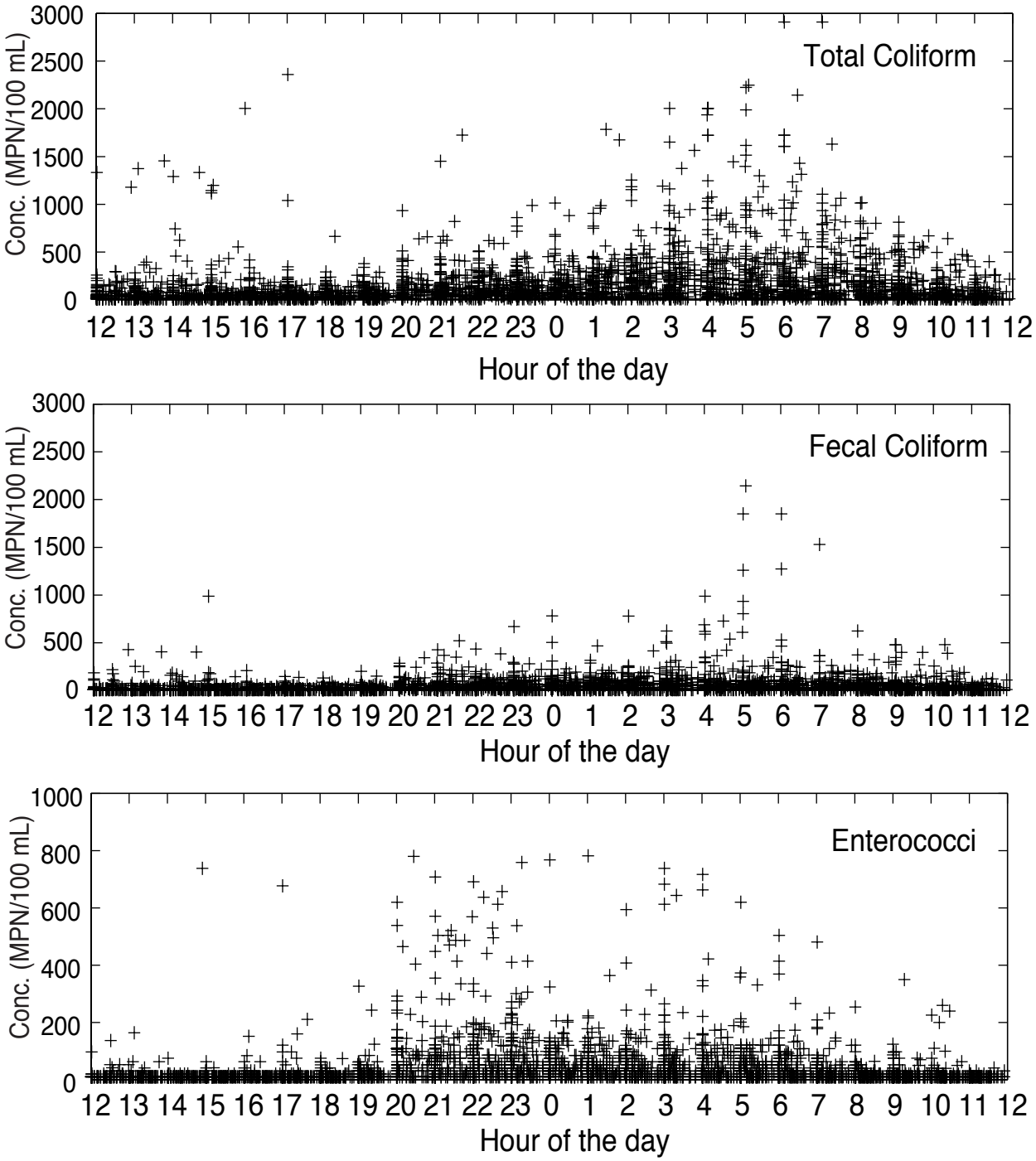

Figure 3-35. Concentrations of fecal indicator bacteria at all stations 15S to 21N for all hourly data from the six cruise periods are plotted versus time of day using a 24-hour clock. Three total coliform, one fecal coliform, and nine enterococci samples had concentrations greater than the maximum values plotted in this figure.

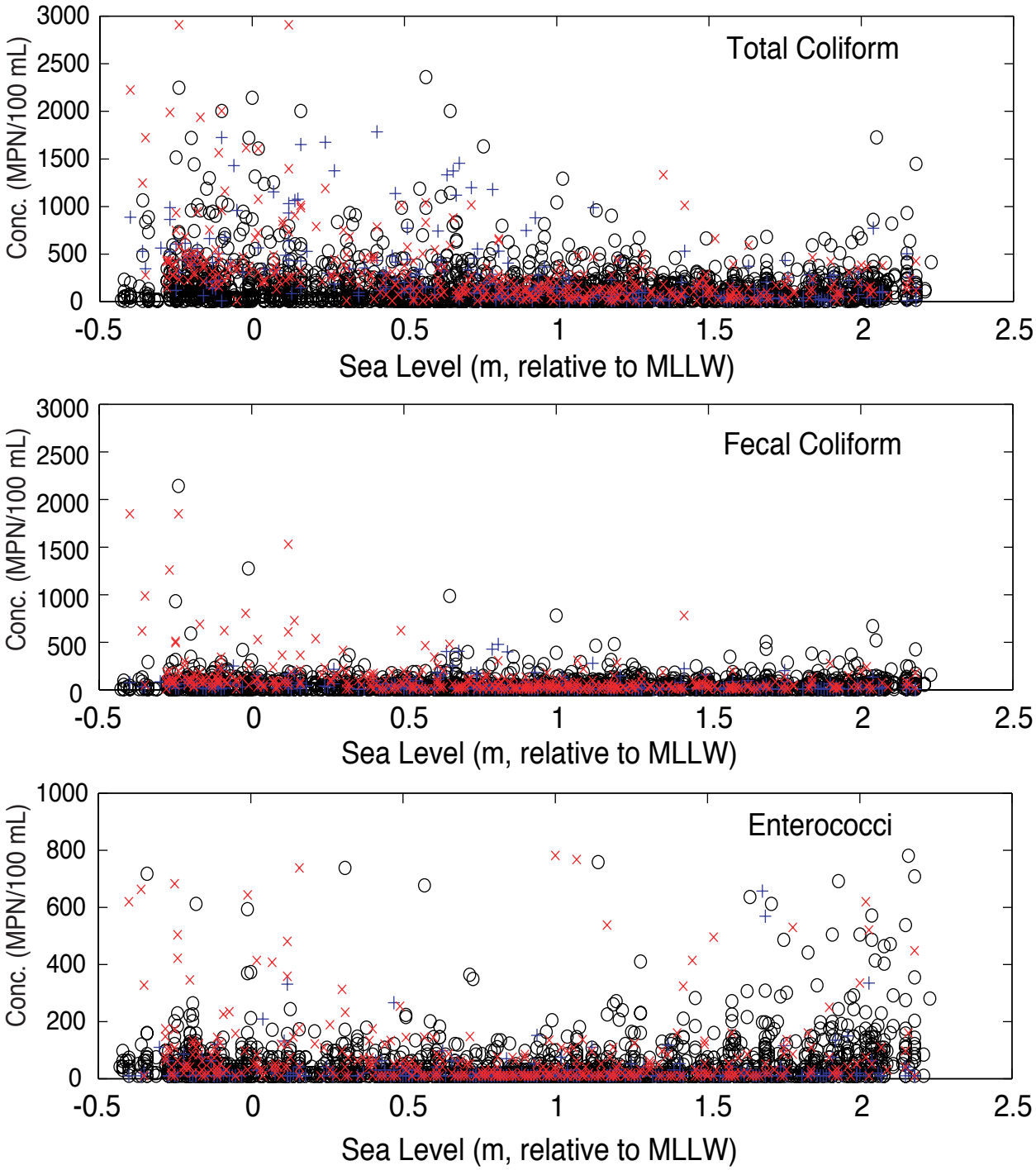

Figure 3-36. The same surfzone bacterial data as shown in figure 3-34 is plotted versus sea level measured in Los Angeles. Values measured at station 6N are shown as red x's, those measured at station 0 as blue +'s, all other stations are black o's.

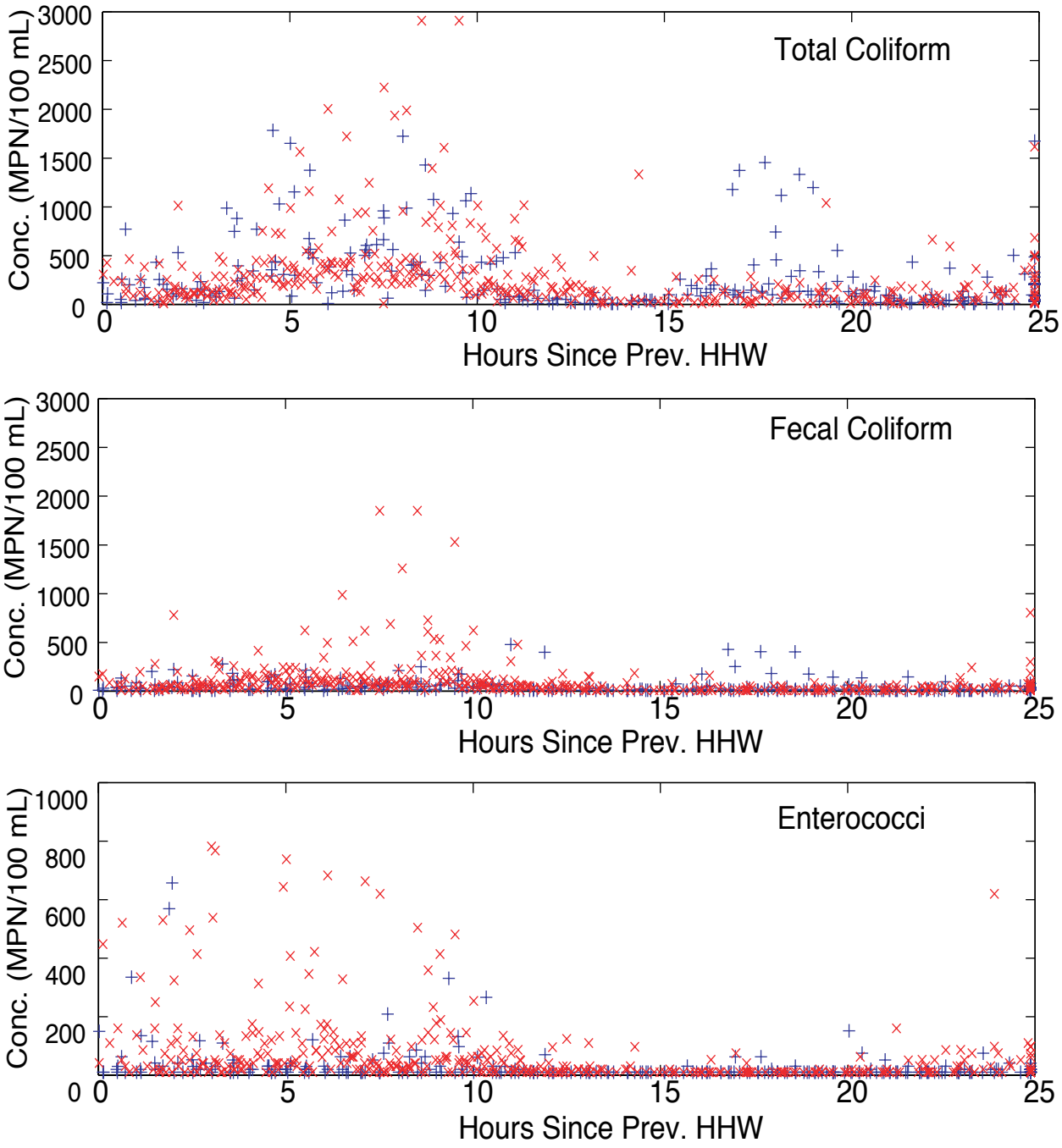

Figure 3-37. Concentrations of fecal indicator bacteria at stations 0 (blue +'s) and 6N (red x's) for all hourly data from the six cruise periods are plotted versus time since the previous higher high water as measured at Los Angeles. Two total coliform, no fecal coliform and three enterococci samples had concentrations greater than the maximum values plotted on the figure.

Table 3.1. Surfzone bacteria event definitions.

Type 1	Total or fecal coliform exceeds AB411 standards at stations 3N, 6N, 9N, or 12N in a given PST day
Type 2	Enterococci exceeds AB411 standards at 3 or more stations including at least one of 3N, 6N, 9N, or 12N and excluding TM, SAR, D2, AESA and AESB, during a given PST day
Type 3	Enterococci exceeds AB411 standards at station 3N, 6N, 9N, or 12N during a given PST day on which there is not a type 1 or type 2 event

Table 3-2. The timing of the cold surges, defined as the 13° isotherm being shoreward of the 20-m isobath, is shown together with Huntington Beach surfzone sample times.

Date	Cold Surge Time (PST)	Station 3N-12N Sample Times (PST)
7/23/01	0200 – 0700	0725 – 0755
7/24/01	0100 – 0900	0635 – 0710
7/25/01	0300 – 0600	0630 – 0705
7/26/01	0200 – 0700	0630 – 0705

Table 3-3. Times of lower low water during the six cruise/intensive sampling periods.

Date (2001)	Time (PDT)
21 May	0300
22 May	0330
20 June	0336
21 June	0418
06 July	0454
07 July	0506
20 July	0424
21 July	0442
20 August	0442
21 August	0548
16 September	0330
17 September	0400

CHAPTER 4. SUBTIDAL CIRCULATION PATHWAYS

Peter Hamilton

4.1. Low-Frequency Flows in the Summer of 2001

4.1.1. Historical Flow Patterns

Previous studies have shown that the subtidal flow on the San Pedro shelf is dominated by sustained strong alongshore currents that are unrelated to the local winds (Hamilton et al., 2001). Characteristic periods range from about 10 to 30 days with downcoast (i.e., towards San Diego) and upcoast currents strongly sheared vertically and more depth independent, respectively. In the summer of 1999, downcoast flows dominated surface currents on the outer shelf near the outfall, where the vertical shears often allow upcoast flows in the lower water column. Thus, the plume can be dispersed in both the up- and downcoast directions with similar probability. On the 15-m isobath, the 1999 study showed that the flows were similar to the outer shelf, but had less magnitude. It was concluded that the subtidal flows were remotely forced, probably by the current regime over the San Pedro slope. The origin of the strong downcoast flows in summer and at other times of the year is not known, and is opposite to the view that the slope regions of the southern California bight are dominated by the poleward flows of the Southern California Eddy, the recirculation limb of the southward flowing California Current system (Hickey, 1992).

The present study allows the investigation of the patterns of current flow from the outer shelf to nearshore regions of the San Pedro Shelf with coverage of the middle part of the shelf that has not hitherto been available. Besides the dominant influence of the low-frequency currents on the dispersion of outfall plume, the flow regime controls the distribution of the temperature and salinity fields across the shelf that in turn modulate the higher frequency internal tide and sea-breeze-forced flows. Subtidal changes in nearshore temperatures are directly related to the distribution of low-frequency flows across the width of the shelf.

This section discusses the basic statistical characteristics of the subtidal current and temperature fields, the geostrophic balance of the alongshore currents, and the time-variable changes in the flow patterns through empirical orthogonal function (EOF) analysis. The ability of the subtidal current field to transport material across the shelf is evaluated.

4.1.2. Basic Statistics

Basic statistics for the velocity and temperature 40-hour low-pass-filtered (40-HLP) time series were calculated for the longest common period that accommodated most of the nearshore and main-array moorings (Figures 4-1 and 4-2). Calculations were made for means of the along- and cross-shore velocities and the standard deviations along the major and minor principal axes directions. The directions, relative to true north, of the major principal axes were also calculated. The results are given as vertical section plots for the main and south transects in Figures 4-3 and 4-4, respectively. The most important features are the strong downcoast, surface-intensified, alongshore flows. Mooring HB06 has the highest near-surface means and variances in the alongshore direction. These means and variances decrease with depth and towards shallow water. Corresponding to the mean downcoast flows, the mean isotherms slope up towards the coast, which is consistent with geostrophic balance of the alongshore vertical shears with the cross-shelf density gradients. The cross-shore velocity means suggest onshore flow at depth with offshore flow in the surface layer. These mean cross-shore flows, however, have large

uncertainties because the alongshore currents have much larger magnitudes than the cross-shore, and, thus, small changes in the direction of the axis can have large effects on the calculated values. The minor axis standard deviations show the same pattern as those for the major axis, with decreases towards the coast and with depth. The direction of the principal axes shows a relatively rapid change between upper and lower layers where the directions are quite constant. This is exaggerated in the plots because the axis chosen for the direction switches quadrants. However, even if the same quadrant is used there is a still a significant change across the layers of between 10 and 30°. The section plots suggest that if the thin layer where the axis direction changes represents the separation between upper and lower layers, then the lower layer is below about 20 to 30 m, but extends into the nearshore where it is very thin. As will be discussed in subsequent sections, this is consistent with the behavior of the higher frequency components of the circulation.

The main difference in the south transect statistics (Figure 4-4) is that, compared to the main transect, there is more deep, upcoast mean flow at the outer shelf moorings (HB11 and HB10) than at the main transect (HB07 and HB06; Figure 4-3). This is reflected in the downslope of the lower-layer mean 12 and 13°C isotherms towards the coast. Poleward mean flow is clearly observed over the slope (HB08) below about 50 m (Figure 4-5). The largest poleward flows occur at about 100 to 120 m depth, which is below the depth of the shelf break (~60 m). These deep currents are part of the poleward undercurrent that is a persistent feature of slope circulation along the U.S. west coast. These poleward flows have a seasonal signal and can surface in the winter and spring (Hickey, 1992). Short-term (~10 days) surfacing of the poleward flow occurs in the summer of 2001, causing upcoast flow at all depths over the middle and outer shelf.

Another view of the subtidal statistics is given by the mean current and standard deviation ellipses for the near-surface and lower layers (Figure 4-6). The near-surface means are generally comparable or greater than the along-shelf fluctuations that show the persistence and strength of the downcoast currents. The directions of the near-surface major axes and mean current vectors tend to parallel the coast and show little influence of the changing isobath directions on the outer shelf. The lower-layer means, on the other hand, are less than the major axis standard deviations, except at 100-m depth over the slope. The means remain downcoast in the nearshore and become upcoast seaward of the 30-m isobath. As noted before, the lower-layer upcoast means are larger, east of the main transect where the isobaths turn eastward and the shelf width narrows. Thus, it appears that in the upper part of the slope, poleward undercurrent overruns the outer part of the shelf after it encounters the slope to the west side of the Newport Canyon. Variances in the lower layer are considerably smaller than in the near-surface layer (Figure 4-6). The map view of the change in principal axis direction between the upper and lower layers is given in Figure 4-7. The degree of rotation increases from inner to outer shelf, and the rotations are larger on the south than the main transect. The lower-layer current fluctuations on the middle and outer shelf follow the trend of the isobaths, indicating that topography is controlling the flows, while the upper-layers are more parallel to the coastline. The anticlockwise rotation of the axes, with depth, is consistent with Ekman turning, and up- and down-welling cross-shelf flows, forced by alongshore down- and upcoast current fluctuations, respectively. This is even true in the shallow water where the isobaths and the coastline are in the same direction (HBN2 and HBN3).

4.1.3. The Influence of Alongshore Currents on Nearshore Cold Water Intrusions

The persistent alongshore downcoast currents are consistent with the upsloping of isotherms towards the coast through geostrophy or the thermal wind relation (Pond and Pickard, 1978). Thus, the raising of the isotherms near the shore and the consequent occurrence of colder water should be closely related to the strength of the downcoast currents. Similarly, the lowering of isotherms on the inner shelf and the occurrence of warmer water deeper in the water column should accompany upcoast current events. To test the degree that the thermal wind relation holds, the cross-shelf temperature differences are compared with alongshore currents between pairs of moorings on the main transect. Figure 4-8 shows the temperature gradients at mid-depth between alternate moorings and the alongshore velocities at moorings in between for middle shelf. There is a clear relation between the velocity and temperature difference curves as the correlation coefficients (R) confirm. Particularly noteworthy is the correspondence between the positive temperature differences (warmer inshore) and the reversal of the currents to upcoast.

At HB03 (Figure 4-9), the correlation between the temperature difference from HB01 to HB05 and the near-surface currents is even higher than offshore. The current fluctuations at HB03 are relatively stronger at shorter periods than further offshore and the fluctuations are not always similar to those at moorings 5 and 6. Similarly, there are differences in the temperature gradients between HB01 and HB05 and those further offshore. This indicates the temperature gradients are not uniform across the shelf, and the inner shelf has some differences in response when compared to the middle and outer shelf. This will influence the occurrence of colder water in the nearshore regions, and will be explored in more detail in the next section. At the shallowest, 10-m mooring (HBNC), the currents are clearly similar to the flows at HB03 on the 15-m isobath, but they have no relation to the local temperature gradients between HBN6 and HB01. The distance between these two stations is only 0.5 km and near-surface temperatures were used. Therefore, the calculations could be less precise than with moorings further apart. However, it seems that the thermal wind balance breaks down in the nearshore, probably because of mixing and boundary layer effects.

4.1.4. Characteristic Circulation Patterns

To find the dominant spatial and temporal patterns in the subtidal currents, complex empirical orthogonal function (CEOF) analysis was used for the longest common period. CEOF analysis does not separate out the U (cross-shelf) and V (along-shelf) components of the velocity vectors so that they are not separately weighted in the covariance matrix. This accounts for the large differences in cross- and alongshelf variances without discounting their connections. This can occur in EOF analyses where the U and V components are treated as separate variables. The approach in this study follows the analysis methods used in Munchow and Chant (2000). The mean vectors were removed from each velocity record on all available moorings. Because the moorings had different degrees of vertical resolution, the number of velocity positions that were used at each ADCP mooring was made proportional to the number of whole degree isotherms present in the mean temperature profile at each site (Figures 4-3 and 4-4). This resulted in using velocity bins at ~4-m and ~2-m intervals on the outer and inner shelf moorings, respectively. Thus, for the CEOF analysis, the number of velocity positions used at each mooring was roughly

weighted according to water depth and stratification. The moorings are fairly evenly spaced so no weighting by the area that an individual record represents was used. As in Munchow and Chant (2000), the spatial eigenvectors show the variance accounted for at each position by the mode. In CEOF analysis the direction of mode eigenvector is arbitrary, therefore to facilitate physical interpretation, the eigenvectors are rotated into the principal axis coordinates of the corresponding complex amplitude time series (Merrifield and Winant, 1989). The rotated amplitude time series were also normalized to unit variance.

The mean vectors and the complex eigenvector components for the first two modes are given in Figures 4-10 and 4-11, respectively. Because the eigenvector components represent the fluctuations about the means, approximately 50% of the time the spatial patterns will be reversed. Therefore, adding and subtracting the mode eigenvectors to the means can be used to construct characteristic flow patterns. However, since the means are strongly downcoast, upcoast flows occur for only relatively short periods over most of the shelf. The mean vectors show the same patterns as discussed above with the poleward undercurrent present at depth on the slope and outer shelf (Figure 4-10). Mode 1 fluctuations are all in the same direction and fairly uniform across the shelf and slope waters above ~60 m. There is some decrease in magnitude towards the shore and with depth. Thus, this mode has a similar pattern to the distribution of major axis velocity variance in Figures 4-3 and 4-4, and indicates that up- and downcoast flows, relative to the mean currents, occur quite uniformly across the shelf and the upper slope above the shelf break. The second significant mode shows maximum response at the inshore moorings HBN2, HBN3, HB03, and HB13. At the 10-m isobath moorings, the second mode response has larger amplitude than the first mode, and since the modes are uncorrelated, this indicates that nearshore is dominated by fluctuations of a different character to the middle and outer shelf. The second mode also has a significant response in the opposite direction to the nearshore at deeper depths, extending into the core of the undercurrent, over the slope. This seems to indicate that fluctuations of the undercurrent, which are largely uncorrelated with the shallower layers over the slope and outer shelf, are coherent with nearshore fluctuations of the opposite sign. Therefore, increasing poleward flow at depth over the slope corresponds to increasing downcoast flows in shallow water near the coast. Dynamical explanations of this phenomenon have not yet been made. Similar connections between oppositely directed fluctuations at the outer shelf and the nearshore (15-m isobath) were found by Hamilton et al. (2001) in the analysis of the Phase II current data (June 1999 to June 2000). In that study, the reversed flow pattern was not so prominent, because no very shallow moorings were deployed.

The common period is from the end of July to the beginning of October. The coldest water was present in the nearshore in July, and, therefore, another CEOF analysis of the flow patterns that included the July period was performed. This long-period CEOF analysis excluded the slope mooring (HB08) and the nearshore SIO moorings (HBN2 and HBN3), replacing them with the 10-m AES ADCP mooring at HBNC. The mean currents for the long period are given in Figure 4-10 and only show minor differences with the shorter common period means for the same moorings. The first two modes, from the long-period analysis, account for similar percentages of the total variances as those from the common period (Figure 4-12). The first mode has the same pattern as Figure 4-11, with the vectors all in the same direction and a

decrease in the amplitudes with depth and towards the nearshore. The second mode, again, has its largest amplitudes in the nearshore (HBNC and HB03) and indications of a correlation with reversed vectors on the outer shelf (HB07). This is very similar to mode 2 for the common period, and indicates that this mode is a robust feature of the circulation. In Figure 4-13, the component amplitudes and coherence squared of the velocities with the mode are shown for two moorings extracted from the complete analysis. The latter is equivalent to the fractional variance explained by a mode for a particular measurement position. According to Figure 4-12, HB06 and HBNC are strongly dominated by modes 1 and 2, respectively. The coherence squared in Figure 4-13 also shows that more than half the observed variance at the nearshore mooring HBNC is explained by mode 2, and nearly all the observed variance at HB06 is explained by mode 1. This implies that the nearshore current fluctuations are somewhat decoupled from the circulations on the middle and outer shelf (Figures 4-8 and 4-9). This also implies that the behavior of the amplitude time series of the two modes can be used to characterize different regimes in the cross-shelf current and temperature fields that occurred during the summer 2001 experiment.

The normalized amplitude time series of the modes from the long-period analysis are given in Figure 4-14. Mode 1 is characterized by relatively long periods of sustained flows with both up and downcoast fluctuations, whilst mode 2 has generally shorter periods. This figure compares the mode 1 time series with the 5-m depth velocities (mean removed) at HB06, which are almost totally explained by this mode. It can be seen that the observed fluctuations are well characterized by this mode. Similarly, mode 2 is compared with the 2-m depth velocities at HBNC, and again this mode accounts for most of the observed fluctuations. Since the modes are uncorrelated, the distinction between the nearshore subtidal currents and the majority of the flows over the shelf appears to be valid.

Hamilton et al. (2001) and Hickey (1992) could find very little evidence of relationship of the alongshore shelf currents to the local wind in San Pedro and Santa Monica Bays. At periods longer than a day, local winds at the coast tend to be weak and variable. This study deployed a meteorological buoy at the shelf break (HB07) that showed persistent downcoast winds modulated by a strong sea-breeze signal (Chapter 6). The kinetic energy spectra, in variance preserving form, of the wind from the meteorological buoy and the normalized complex mode amplitudes (Figure 4-15) show that mode 2 and the wind have a similar peak at about 7 to 9 day periods. The major peak for mode 1 is at about 15 days where the wind has little energy. The difference in the characteristic periods of the mode fluctuations is visually apparent in Figure 4-14. The coherence squared of the wind alongshore component with the V components of the modes (Figure 4-15) show that mode 1 is not significantly correlated, but mode 2 is correlated at periods longer than 5 days with a lag of about 12 to 18 hours. Thus, it appears that the nearshore currents, associated with mode 2, are forced by local alongshore winds over the shelf, but the majority of the subtidal flow fluctuations over the middle and outer shelf are unrelated to the local winds. Unfortunately, there are no reliable wind measurements in the nearshore zone, so it is not known how the winds at the beach differ from those at the shelf break.

Figure 4-14 also shows time series of the estimated offshore position, along the main transect, of the 14°C isotherm where it intersects the bottom. The 14°C isotherm characterizes the lower thermocline, and is associated with the equilibrium depth of the top of the plume, immediately after discharge from the outfall. The large shoreward excursions of this isotherm in July are accompanied by strong (mode 1) downcoast flows. Similarly, the cold event at the end of September was preceded by strong downcoast flow. When mode 1 switches to upcoast at the beginning of August, the isotherm moves offshore, consistent with thermal wind and the leveling and depression of the isotherms. Therefore, based on the directions of the fluctuating mode amplitudes, four periods have been selected (Table 4-1) where the density field across the shelf could be expected to have different average characteristics. These periods, separated by the vertical lines in Figure 4-14, have been selected with tidal and sea-breeze analysis in mind, because the characteristics of the internal tide and sea-breeze-forced flows are modified by changing low-frequency density fields.

The main transect mean temperature fields for each period in Table 4-1 are given in Figure 4-16. These fields should be examined along with the current mode time series in Figure 4-14. Thus, in period 1, enhanced downcoast flows over most of the shelf result in up-sloped isotherms over most of the transect. In period 2, at the beginning of August, the upcoast mode 1 is consistent with the leveling of the isotherms and increased stratification above the thermocline. The down-slope of the deeper isotherms shows that there is upcoast flow at depth (Figure 4-8). In the latter half of August (period 3), mode 1 is weakly downcoast, or upcoast, towards the end of the period, and mode 2 is upcoast. This results in a mean temperature field that has fairly level isotherms. The thermocline has deepened and surface layer has become less stratified, presumably because of larger scale seasonal changes. In the last period, both modes 1 and 2 are downcoast, and therefore reinforce each other. This results in the mean temperature field having the largest up-slope of the isotherms of any of the previous periods. The surface layer in the offshore waters remains only weakly stratified.

Large-scale changes in the temperature distribution across the shelf, over periods of two to four weeks, have been qualitatively related to the behavior of the current modes. It might be expected that the temperature fluctuations can be closely related to the velocity-mode time series. However, the offshore distance of the 14°C isotherm, plotted in Figure 4-14, is not significantly correlated with either velocity mode, and this suggests that more than one process is influencing this signal. To investigate this further, a time-domain EOF analysis was performed just using the 40-HLP temperature records (with means removed) from the main transect. The record lengths were exactly the same as for the CEOF analysis of the velocities. The amplitudes of the eigenvectors of the first two modes are given in Figure 4-17. The first mode amplitudes are all positive with maxima at the depths of the thermocline (10 to 25 m). This can be interpreted as changes in the depth of the thermocline that are imposed on the shelf by the larger southern California Bight circulation processes. This effect is amplified across the shelf so that the largest amplitudes of this mode are in the nearshore at stations with between 10- and 20-m water depth. Mode 2 amplitudes are of both signs with the node at about 10-m depth. This can be interpreted as being caused by tilting of the isotherms, such that when temperatures increase below 20 m in

the offshore, there is a corresponding decrease in the nearshore and in the surface layer (and vice versa). Maximum amplitudes of both temperature modes occur in the nearshore.

The time series of the amplitudes of the temperature modes are given in the top panel of Figure 4-14. It can be seen that mode 2 is closely related to the velocity mode 1, such that downcoast flows correspond to positive temperature amplitudes, and therefore, increasing tilts to the isotherms. The mode 1 temperature amplitudes seem to represent the external effects on the shelf, and it can be seen that the time series of the offshore distance of the 14°C isotherm is a combination of both modes. Thus, mode 1 is responsible for the general warming through the month of August. The correlation (R) of the mode 2 temperatures with the velocity mode 1 time series is -0.78, and shows the inverse relation of the tilting isotherm mode with the primary mode of the middle and outer shelf velocity fluctuations that is dynamically consistent with the thermal wind relation. There are no other significant correlations of the temperature and velocity modes, and this implies that the nearshore velocity mode 2 has little influence on appearance of cold water at the coast, though it is clear that there are times when mode 2 can reinforce mode 1. For example, in period 4, the reinforcing downcoast modes produce stronger isotherm tilts. This does not apparently apply throughout the summer. The maximum amplitudes of the mode 2 currents also occur close to shore where thermal wind breaks down (Figure 4-9), and, therefore, it should not be expected that mode 2 velocities be closely related to cross-shelf temperature gradients.

4.1.5. Discussion

The analysis of the spatial patterns and time evolution of the current and temperature modes have produced some new information on the dominant modes of variability of the subtidal circulation on the San Pedro shelf. Important features are the separation of the alongshore flow into uncorrelated shelf and nearshore modes. The nearshore currents are closely related to the alongshore wind fluctuations over the shelf. The majority of the shelf current fluctuations are not directly forced by local winds but appear to be part of larger-scale California Bight circulation processes that are not well characterized. The shelf mode is correlated with the up and down tilts of the isotherms through thermal wind, but the temperature field also is strongly controlled by external processes that impose isotherm depth changes across the width of the shelf. Both these processes can move colder water into the nearshore.

Cross-shelf transport processes appear to be complex. Changing positions of isotherms implies cross-shelf circulations arising from changes in the alongshore currents through “geostrophic adjustment” and current-induced upwelling. The former is likely transitory, and the latter, because of the downcoast mean flow, is likely to result in very small cross-shelf transports. The limited current measurements in the bottom boundary layer generally show small means and weak subtidal fluctuations, and there is little evidence of cross-shelf flows in a distinct bottom Ekman layer. The on- and offshore excursions of the 14°C isotherm (Figure 4-14) show that the maximum displacement over a day is about 2 km, which results in a cross-shelf transport velocity of 2.3 cm/s. This kind of transport is difficult to extract from the current measurements when the alongshore currents have magnitudes of 10 to 20 cm/s. An attempt was made to

calculate the cross-shelf transport velocity in the lower layer, using the area under the 14°C isotherm on the main transect, using:

$$U = 1/h * dA/dt \qquad (4.1)$$

where A = the cross-sectional area under the 14°C isotherm;

h = the lower layer depth between 14°C and the bottom at mooring HB07;

U = the cross-shelf transport between 14°C and the bottom.

This assumes that 14°C is an impermeable surface and that the cross-shelf transport is uniform in the alongshore direction. The calculated U was compared with the same quantity estimated from the ADCP at HB07, but no significant correlation was found for several estimations using different coordinate axes for the observations (e.g., the minor principal axis, isobath coordinates, etc.). This seems to indicate that cross-shelf subtidal transport is a three-dimensional process.

In the nearshore, the wind-forced (mode 2) currents imply onshore transport in the lower layer and offshore in the upper layer for downcoast directed winds. However, because of the shallow depths (~<10 m), the top and bottom Ekman layers merge and the cross-shelf transports are suppressed. Only very small transport velocities (<1 cm/s) are expected from this process. Therefore, subtidal cross-shelf transport is very difficult to quantify, and, as will be discussed in later sections, sea-breeze- and internal-tide-forced cross-shelf transports have larger magnitudes and may be more effective at short-term movement of material across the shelf. The best guide to subtidal cross-shelf transport appears to be the on- and offshore excursions of the isotherms.

4.2. Typical Diffusion Time on the Shelf

Surveys of the outfall plume (Chapter 10) have shown that the distribution of material can be quite patchy with areas of relatively higher concentrations interspersed with lower concentration regions. This is a quite common occurrence for pollutant discharges into the ocean and results from stirring by the sheared currents and turbulent mixing (Eckart, 1948). The time- and space-dependent current field stretches and distorts the plume and may separate the plume into patches. Turbulent mixing processes act most effectively to smooth large concentration gradients created by the current shears. Eckart's famous analogy was of stirring cream into a coffee cup. It is useful to make rough estimates of how long such a large separated patch or "rogue blob" may be expected to exist with concentrations substantially above background. This rough estimate of the dispersal time assumes that a section of the plume with the typical widths and heights of the established plume has become detached from the main discharge.

It is assumed that the initial cloud is a patch of plume water with volume = $\pi\, l_0^2 d/4$, where $l_0 \sim 10$ m is the horizontal diameter, and $d \sim 5$ m is the depth of the cloud. Typical maximum concentrations of sewage, after initial mixing by the outfall discharges, are about 200 mg/L. Background concentrations of particles in the coastal ocean, away from bottom boundary layers, are generally less than 10 mg/L. Assuming that a dilution of 50:1 is required and vertical

diffusion is negligible, then the diameter that this dilution achieves is given by $L^2 = 50\ l_0^2$, thus L ~ 70 m. The resulting standard deviation, $\sigma = L/3 \sim 23$ m, and the relation between σ and the elapsed diffusion time, t, is (Csanady, 1973):

$$\sigma^2 = 4\ K\ t$$

Representative values of K from the Okubo diffusion diagram or dye diffusion studies in coastal waters, for 10 to 100 m horizontal scales, are 0.01 to 0.1 m^2/s (10^2 - 10^3 cm^2/s). This gives a diffusion time, t ~ 220 to 22 minutes (i.e., between 0.5 and 4 hr).

A dilution of 500:1 gives a range of diffusion times of 4 to 40 hours. The shorter time is probably more relevant because K increases with length scale. Therefore, a large rogue blob of the plume would be expected to disperse to background levels in less than 6 hours or about half a tidal cycle.

4.3. Transport Patterns: Summer 1999 versus 2001

From June 1999 to June 2000, SAIC deployed and maintained four current meter moorings and a number of bottom-mounted thermistors on the San Pedro shelf in the vicinity of the outfall. Three conventional moorings, with two current meters and two thermistors, were deployed on the 15-m isobath between the Newport Canyon and the approximate position of HB03. The offshore mooring was in the same position as HB12 and consisted of a real-time surface mooring with current measurements at 1- and 45-m depth and temperature measurements at 5 m depth, and an associated bottom mounted ADCP. These measurements have been discussed in Hamilton et al. (2001). Comparison of these measurements with the present experiment allows a limited assessment of the inter-annual variability of the circulation. The summer of 1999 was noted for extensive bacterial contamination (Chapter 3), and, therefore, it is of interest to see if the circulation differed substantially from that of the summer of 2001.

The 40-HLP current vectors and temperature records from instruments in essentially the same positions on the 60-m isobath (moorings P and HB12) and on the 15-m isobath (moorings Q and HB03 in 1999 and 2001, respectively) are shown in Figure 4-18. In 2001, the outer shelf currents are stronger than in 1999, but with fewer major upcoast reversals. In the upper layer, the temperatures are generally cooler in 1999. From the middle of August through September, the outer-shelf upper layer was substantially cooler in 1999 compared to 2001. On the other hand, the bottom waters were generally warmer and this indicates that the outer shelf was less stratified, particularly in August and September, in 1999 than in 2001. In the nearshore, comparing the two years, mooring Q, at 10-m depth, was warmer in early July, but was substantially cooler (similar to P) in the second half of the summer. Thus, for most of the summer, there was less of a cross-shelf temperature gradient with weaker up-tilts of the isotherms towards shore than in 2001. This is consistent with the relatively weaker fluctuating flows at Q in 1999, than at HB03 in 2001. Therefore, despite being relatively colder in July 1999, the 14°C isotherm does not penetrate quite as far into the coast as in July 2001. This is shown in the top panel of Figure 4-18 where the position of the isotherm in 1999 is estimated using the 15-m mooring (R) and the bottom thermistors (U, V, W, X and P) deployed along the

cross-shelf path of the outfall pipe. Resolution, above 5-m depth and nearshore, is not as good as in 2001. In August and September 1999, the cooler water offshore, relative to the warmer water in 2001, does allow the 14°C isotherm to penetrate much closer to the coast than in the same period in 2001, and, thus, sub-thermocline water would have had a more direct connection with the nearshore, similar to the earlier summer.

Basic statistics of the time series presented in Figure 4-18 are given in Table 4-2. The same length 99-day, 40-HLP time series are used for all the statistics. The statistics for 1999 are given in red, and the U and V velocity components are across- and along-shelf, respectively. At the surface, the 2001 data show much larger downcoast mean flows with temperatures 1.5 to 2°C warmer than in 1999. In the lower layer, the 1999 data show higher variances with temperatures about 0.5°C warmer than in 2001. Therefore, at plume depths, the dispersion of material should be greater in 1999 than in 2001. In the nearshore, the larger means and higher variances of the currents in 2001 are quite clear. Since the analysis of Chapter 6 indicates that on the 15-m isobath the flows are partially accounted for by local winds, it is possible that offshore downcoast winds were weaker in 1999 compared to 2001. Unfortunately, wind measurements were not taken on the outer shelf in the summer of 1999, and this speculation cannot be confirmed. Table 4-2 also shows the statistics of the depths below the surface of the top and middle of the plume, calculated from the RSB initial dilution model for outfall diffusers. The middle of the plume corresponds to the depth of minimum dilution. A description of the use of this model for the 1999 period is given in SAIC (2002), and the model was applied in exactly the same way for the summer of 2001. The mean and minimum depths are about 2 and 5 m higher, respectively, in the water column in 1999 as compared to 2001. Since the currents at plume depths are more energetic in the earlier period, the higher rise heights are primarily caused by weaker stratification below the thermocline.

The summer of 1999 had colder water, less energetic currents on the inner shelf, was less stratified, and had more energetic flows at plume depth near the outfall, when compared to the summer of 2001. The consequences for pollutant dispersion from the outfall were that, in 2001 the plume was generally higher in the water column, and was probably more dispersed by the offshore flows in 1999 versus 2001. The generally colder conditions in 1999 means that sub-thermocline water was more often in contact with the nearshore, and any plume material reaching the 15-m isobath would be less likely to be flushed because of the weaker alongshore currents.

4.4. References

Csanady, G.T., 1973. Turbulent diffusion in the environment. Reidel, Holland, 248 p.

Eckart, C., 1948. An analysis of stirring and mixing processes in incompressible fluids. Journal of Marine Research, v. 7, p. 265-275.

Hamilton, P., J.J. Singer, E. Waddell, and G. Robertson, 2001. Circulation processes on the San Pedro Shelf. Proceeding, MTS 2001 Conference, Nov. 2001, Honolulu, Hawaii, 8 p.

Hickey, B.M., 1992. Circulation over the Santa Monica-San Pedro basin and shelf. Pro. Oceanography, v. 30, p. 37-115.

Merrifield, M.A. and C.D. Winant, 1989. Shelf circulation in the Gulf of California: A description of the variability. Journal of Geophysical Research, v. 94, p. 18133-18160.

Munchow, A. and R.J. Chant, 2000. Kinematics of inner shelf motions during the summer stratified season off New Jersey. Journal of Physical Oceanography, v. 30, p. 247-268.

Pond, S. and G.L. Pickard, 1978. Introductory dynamic oceanography. Pergamon Press, Oxford, 241 p.

SAIC, 2002. Strategic Process Study #1: Plume tracking–plume modeling. Final Report prepared for Orange County Sanitation District (OCSD), Fountain Valley, CA.

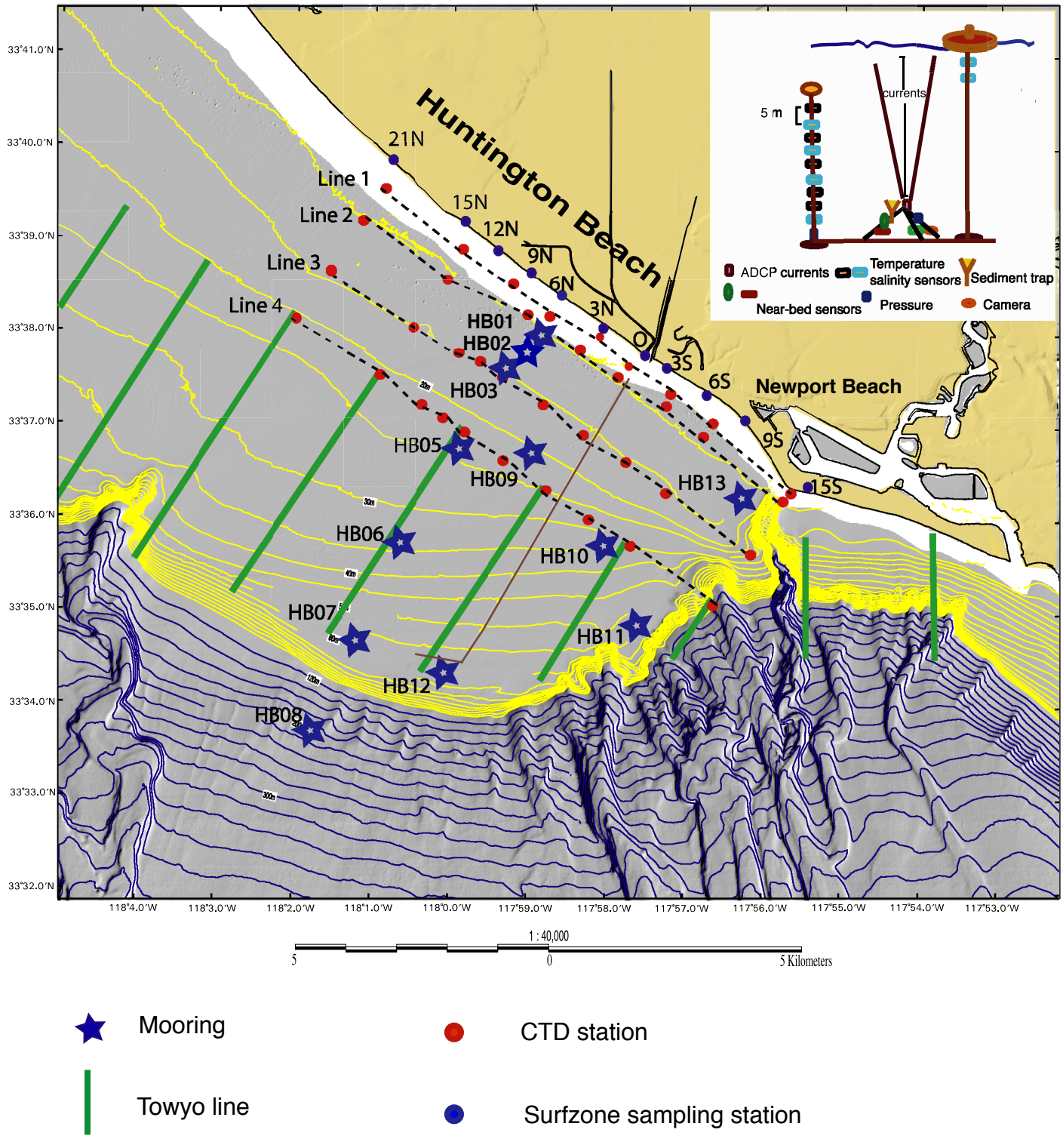

Figure 4-1. Map of the region, mooring sites, surfzone sampling stations, and instrumentations of a typical mooring (inset).

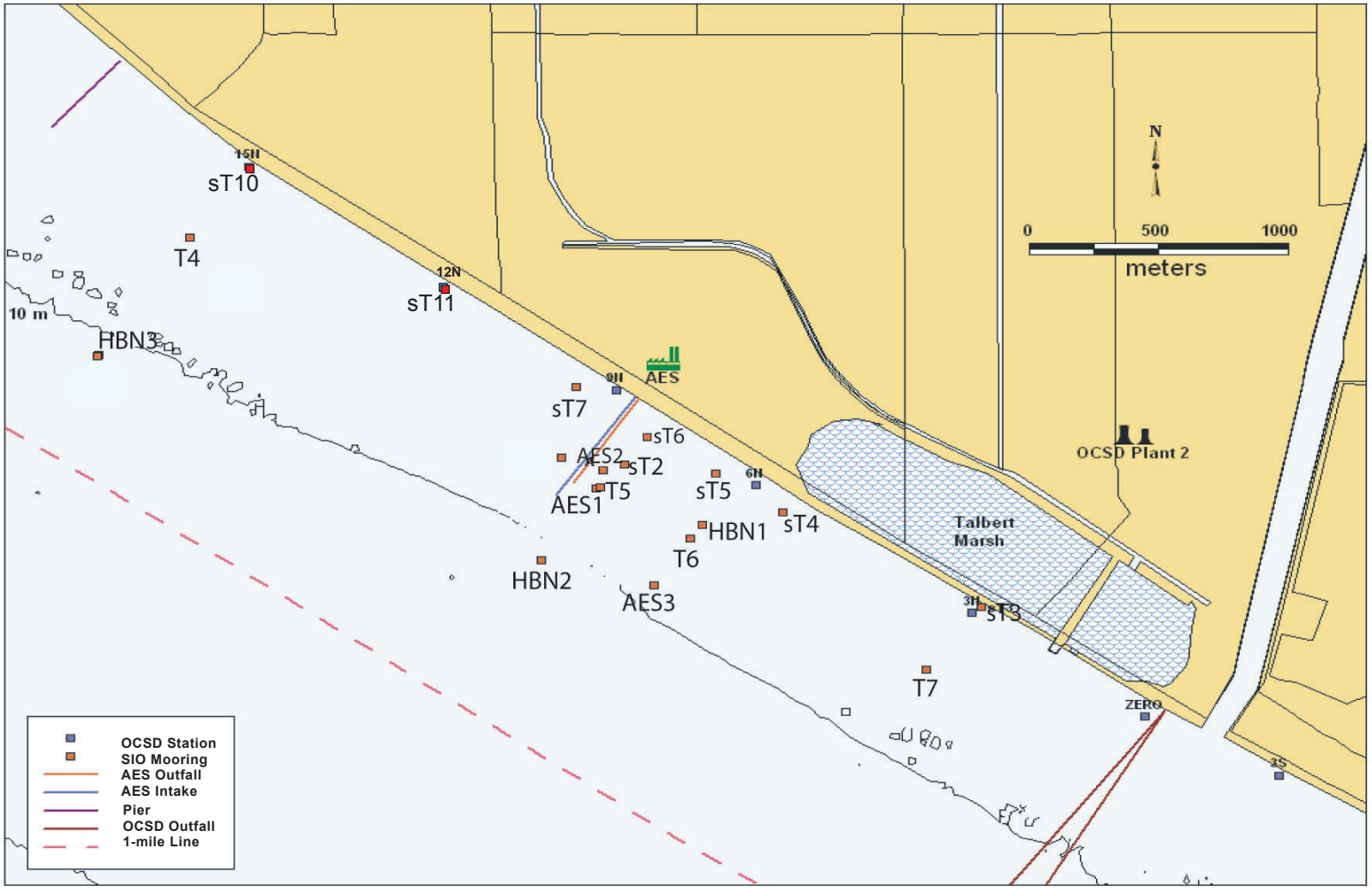

Figure 4-2. Location of nearshore moorings (red squares), beach sampling (blue squares), power plant intake (blue), and discharge (red), Talbert Marsh, and Santa Ana River.

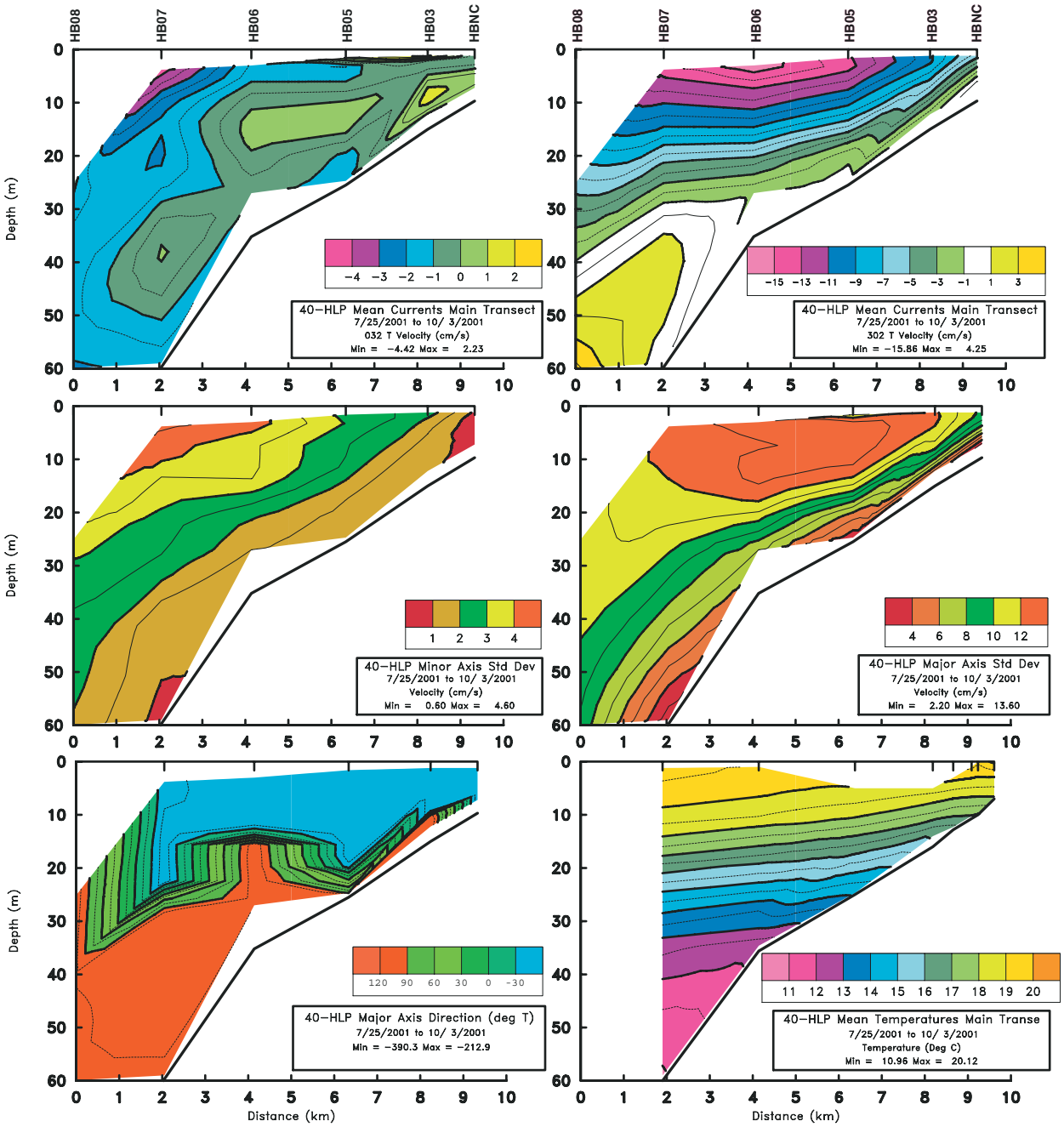

Figure 4-3. 40-HLP statistics for (left to right, followed by top to bottom) mean cross- and alongshelf velocities, standard deviations of velocities along minor and major axes, directions of the major axes, and the mean temperature field for the main transect.

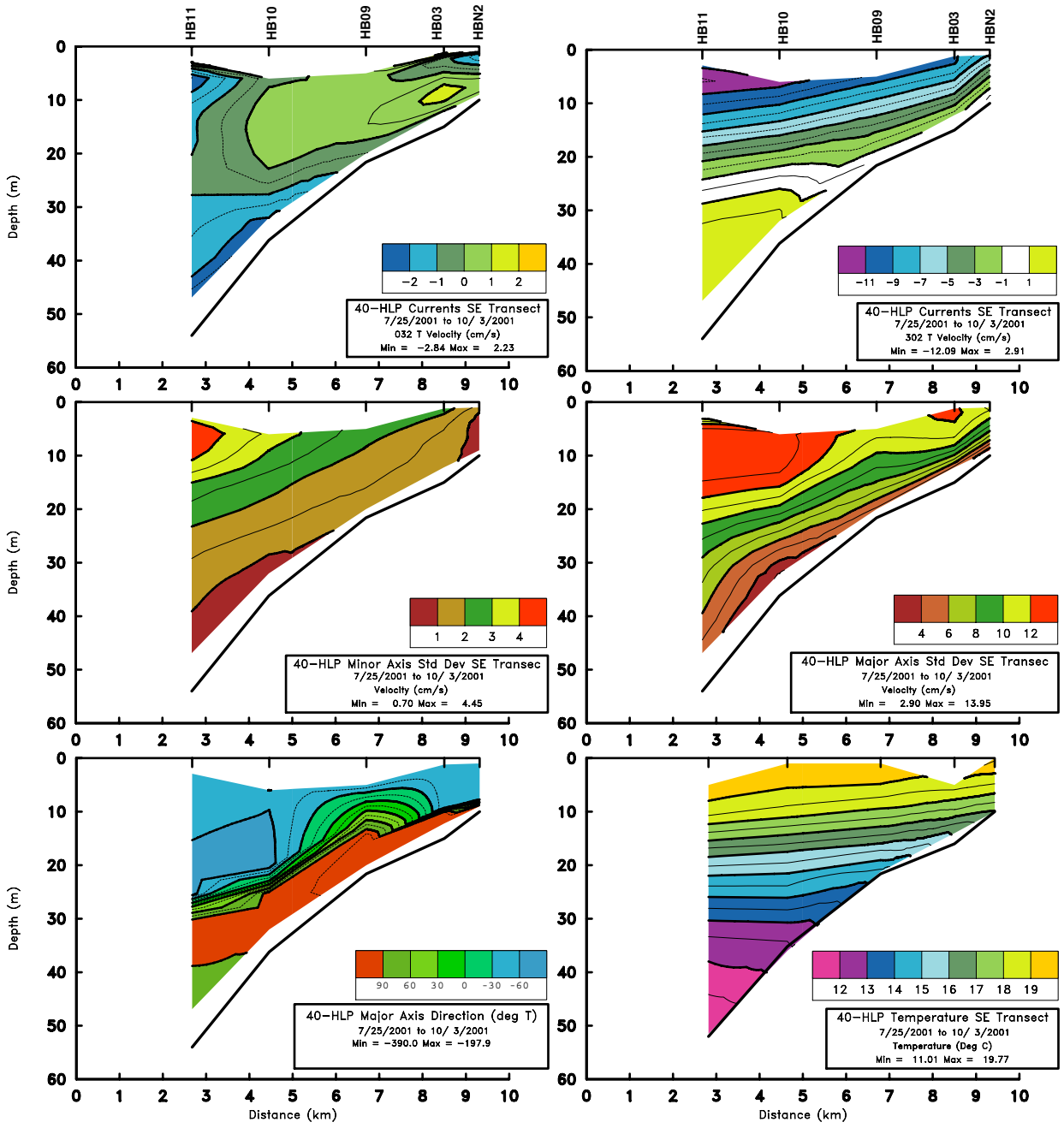

Figure 4-4. 40-HLP statistics for (left to right, followed by top to bottom) mean cross- and along-shelf velocities, standard deviations of velocities along minor and major axes, directions of the major axes, and the mean temperature field for the south transect.

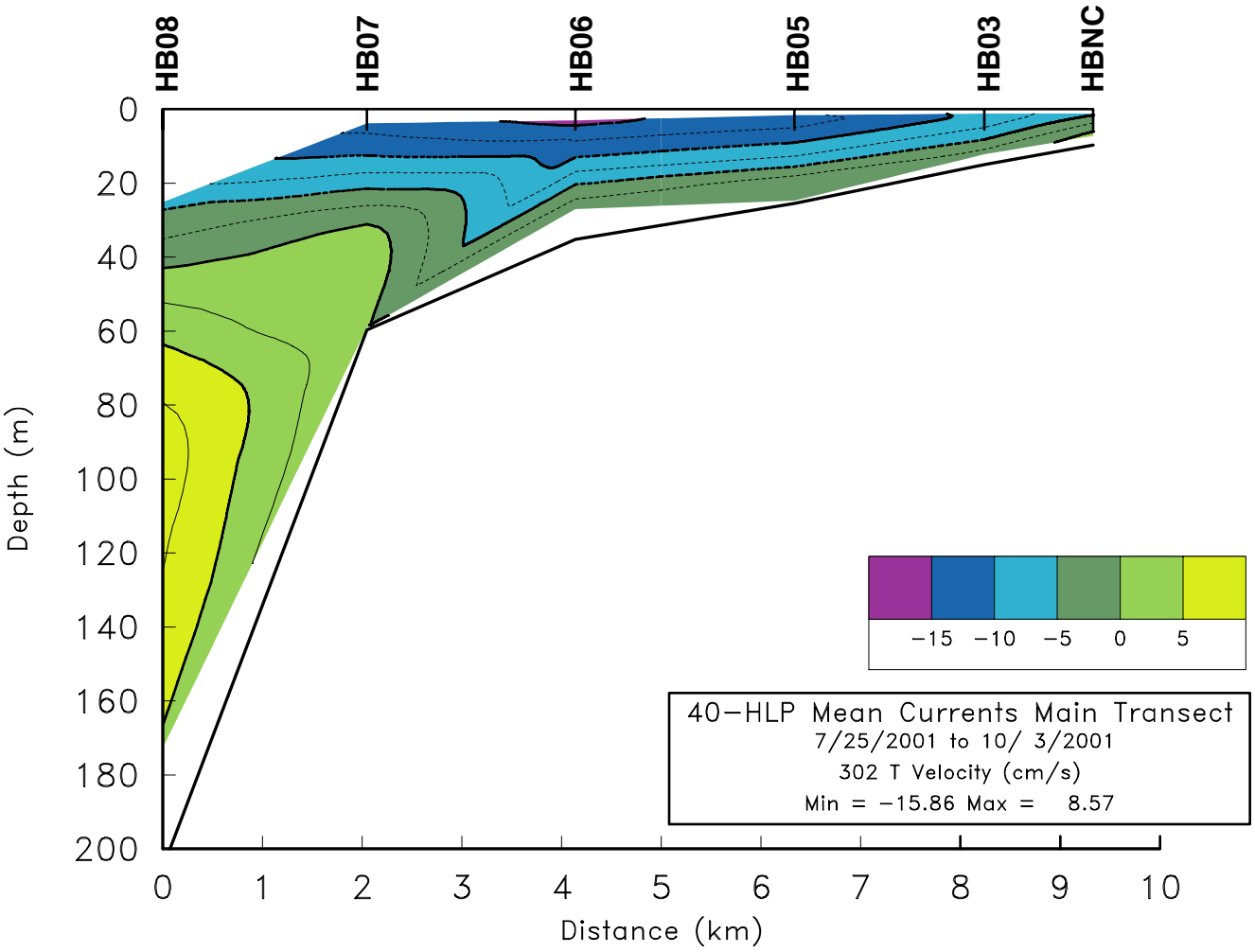

Figure 4-5. 40-HLP mean alongshore (V-component) currents, including the full depth of the slope mooring HB08.

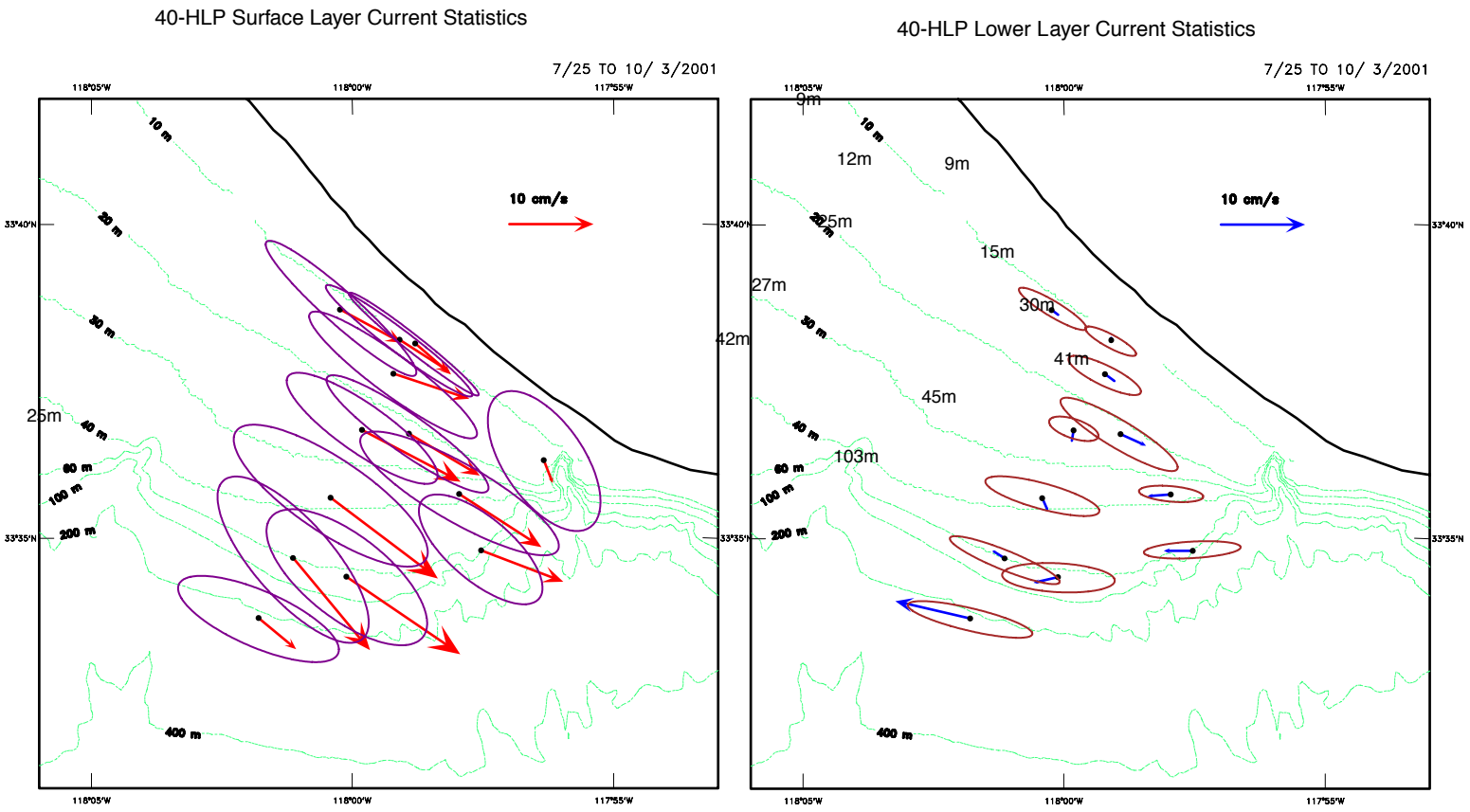

Figure 4-6. Surface layer (1 to 6 m, except over the slope) and bottom layer (depths indicated) mean and standard deviation ellipses for 40-HLP velocity data.

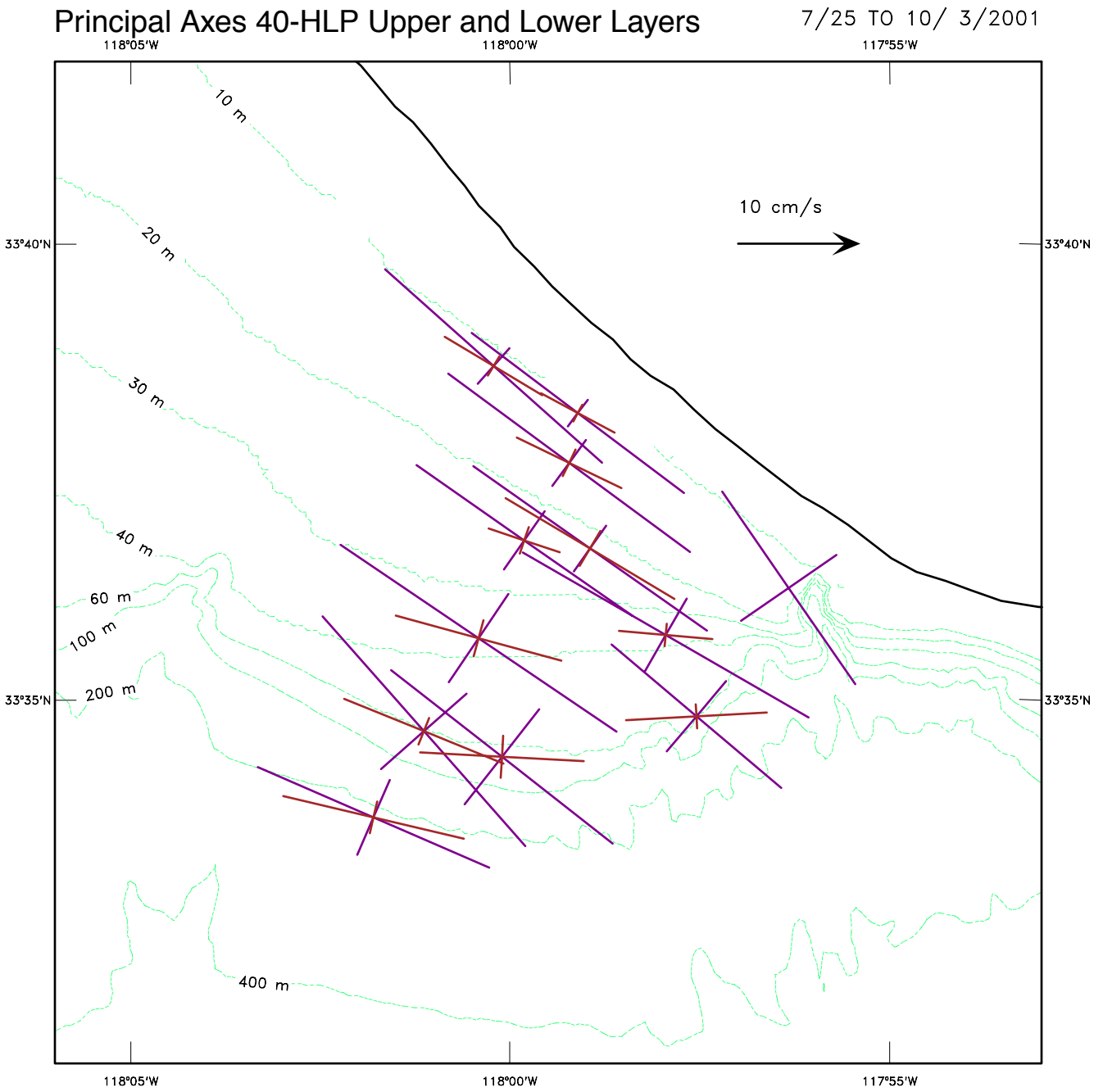

Figure 4-7. Principal axis directions from 40-HLP velocity data for the upper (purple) and lower (brown) layers. The lower-layer instrument depths are the same as in Figure 4-6.

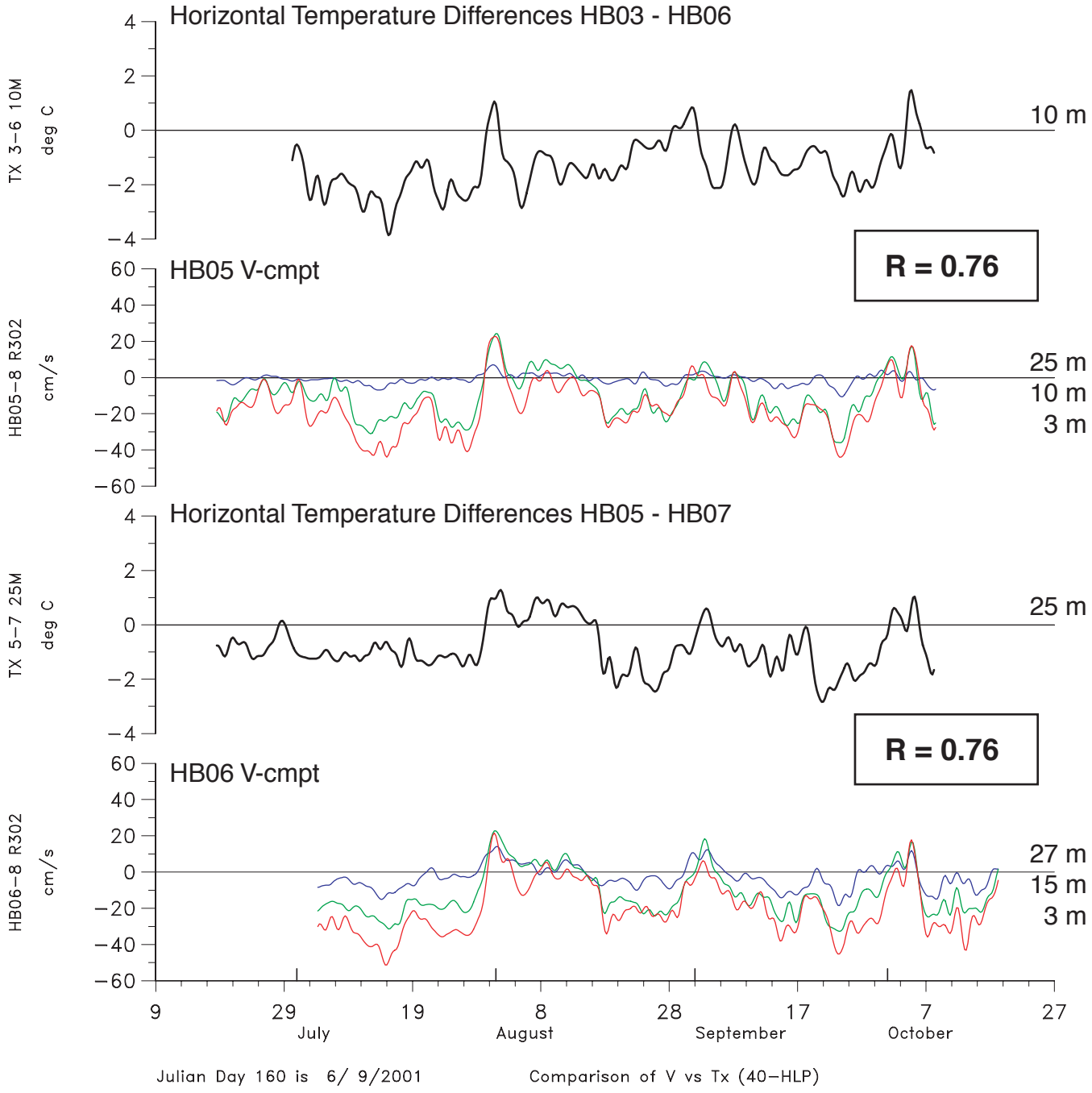

Figure 4-8. Comparison of the along-isobath component (V) of 40-HLP currents with horizontal temperature differences between moorings onshore and offshore of the current measurements on the middle shelf. Correlation coefficient, R, is between the temperature differences and the 3-m velocity component.

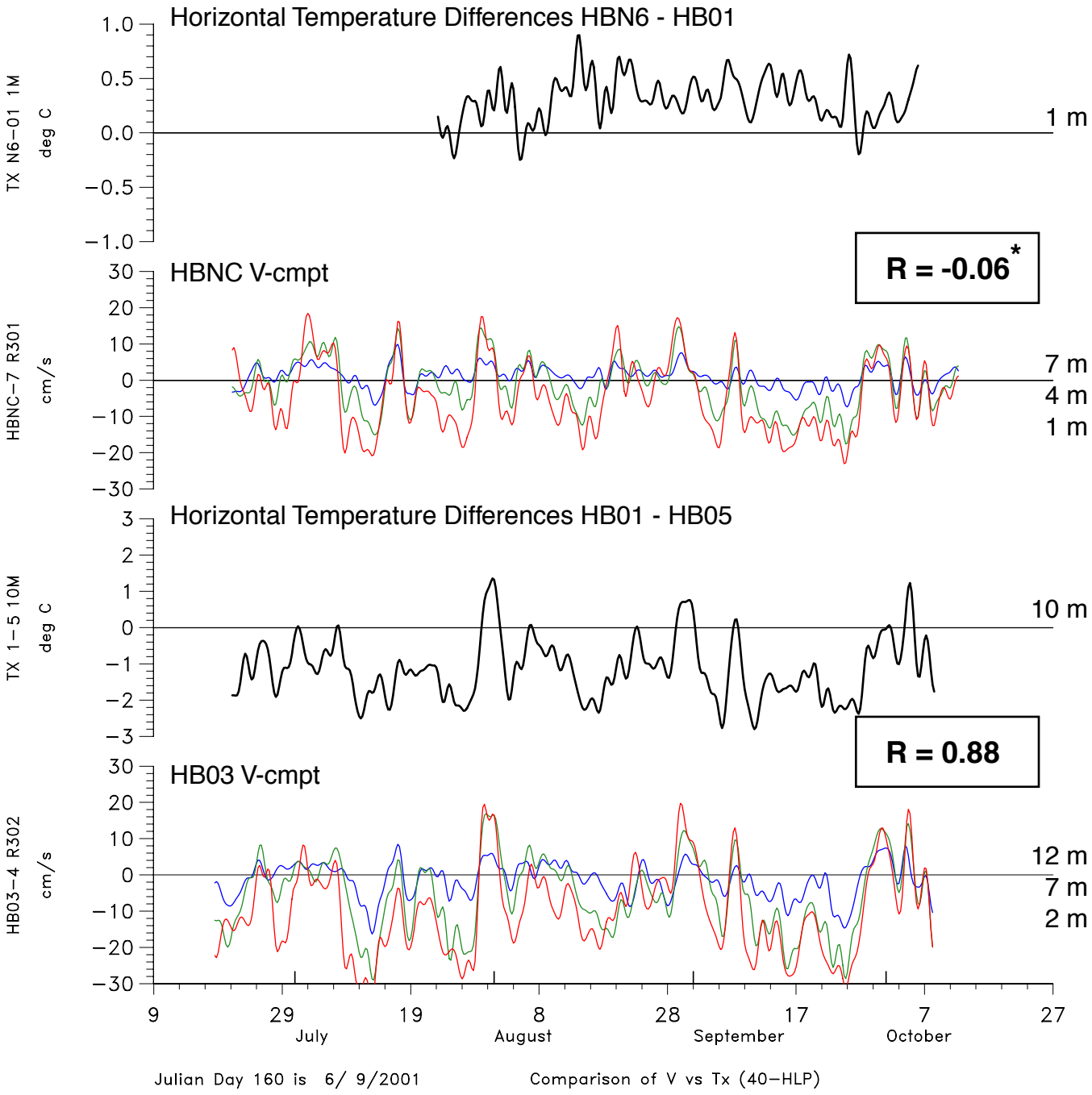

Figure 4-9. Comparison of the along-isobath component (V) of 40-HLP currents with horizontal temperature differences between moorings onshore and offshore of the current measurements on the inner shelf. Correlation coefficient, R, is between the temperature differences and the 1- and 2-m velocity component. R* value is not significant.

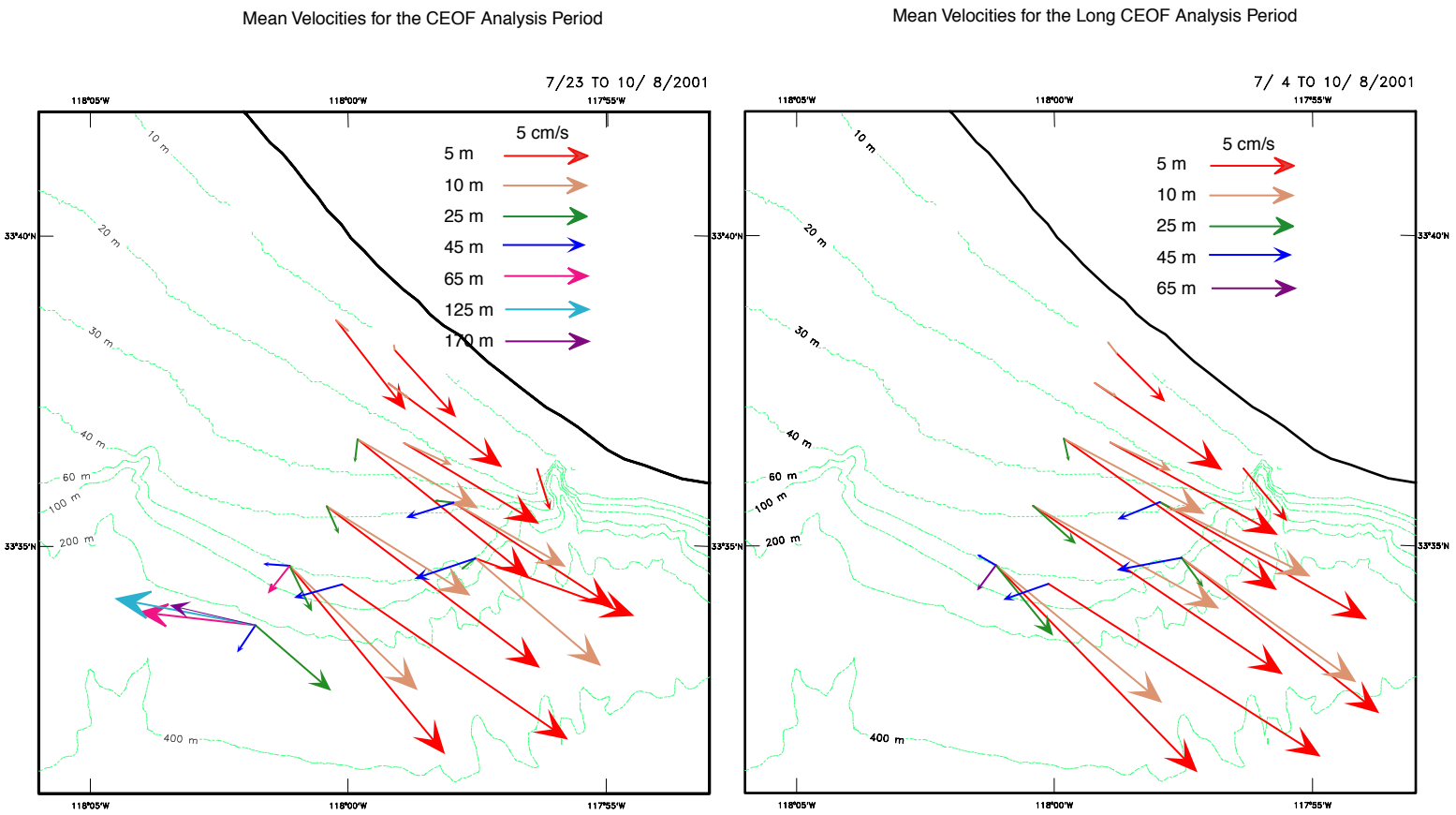

Figure 4-10. Mean subtidal velocity vectors at the indicated depths for the common (left panel) and long (right panel) periods, respectively.

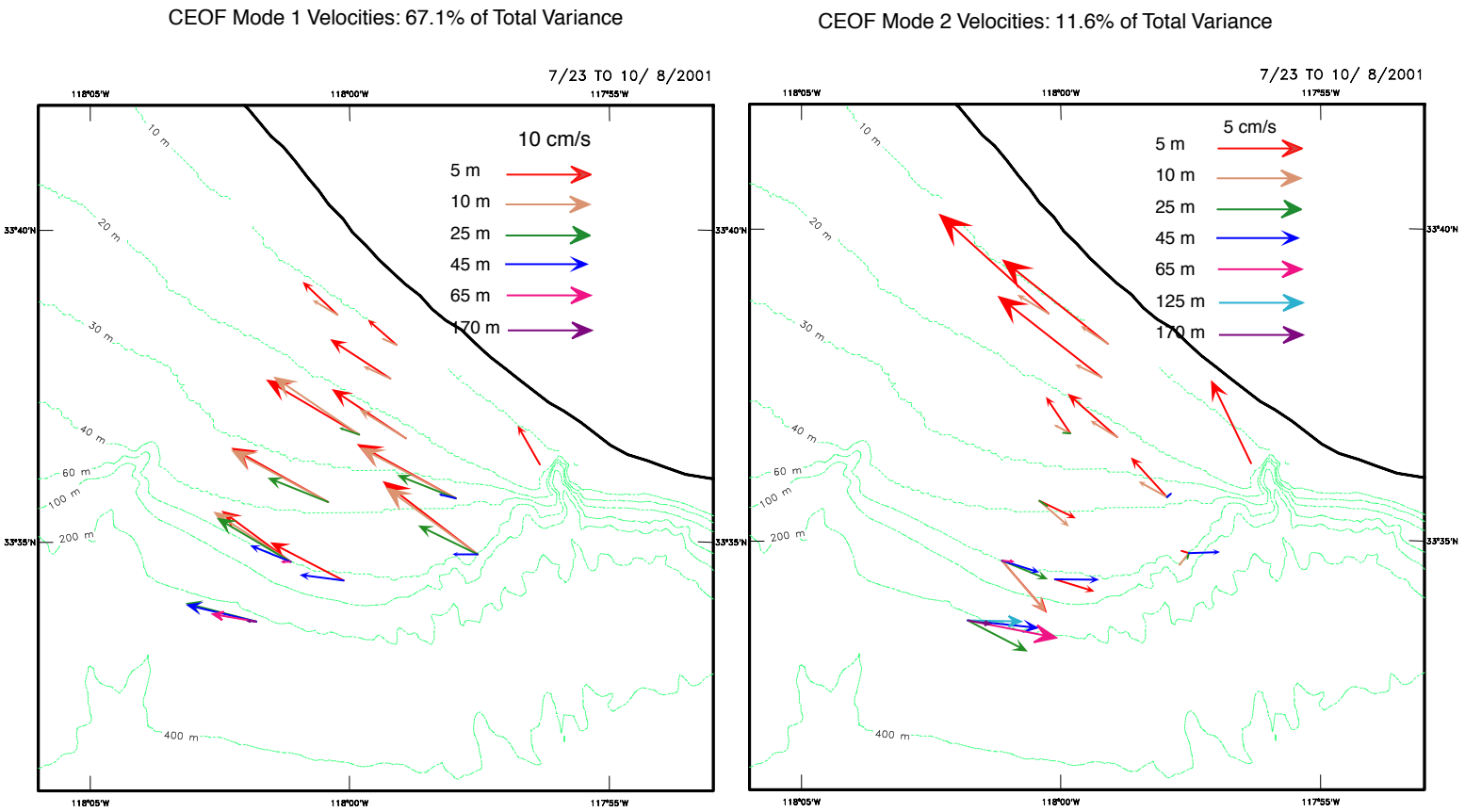

Figure 4-11. Eigenvector components at the indicated depths for CEOF modes 1 and 2 using the common period. Note the change in the velocity scales.

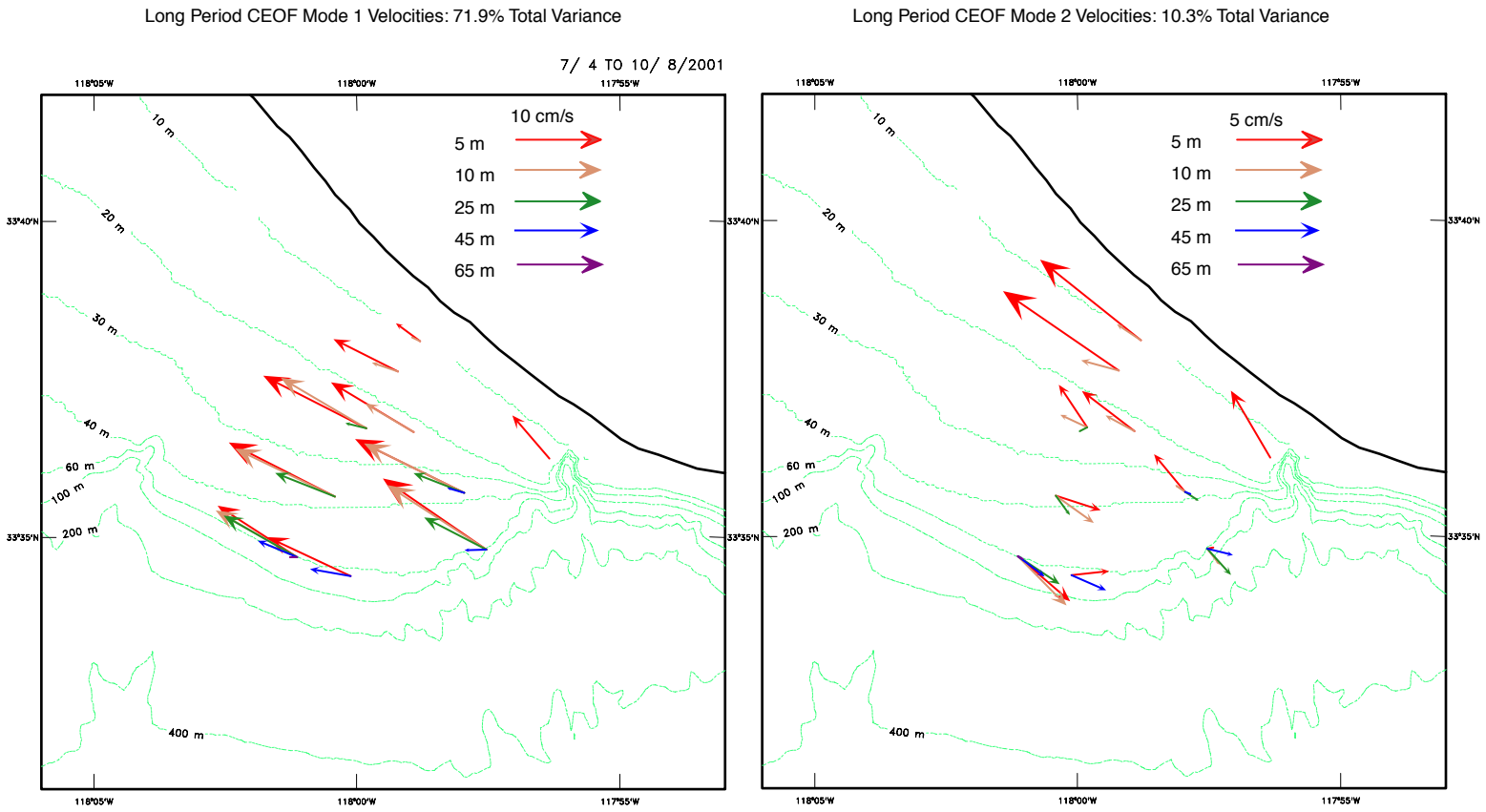

Figure 4-12. Eigenvector components at the indicated depths for CEOF modes 1 and 2 using the long period. Note the change in the velocity scales.

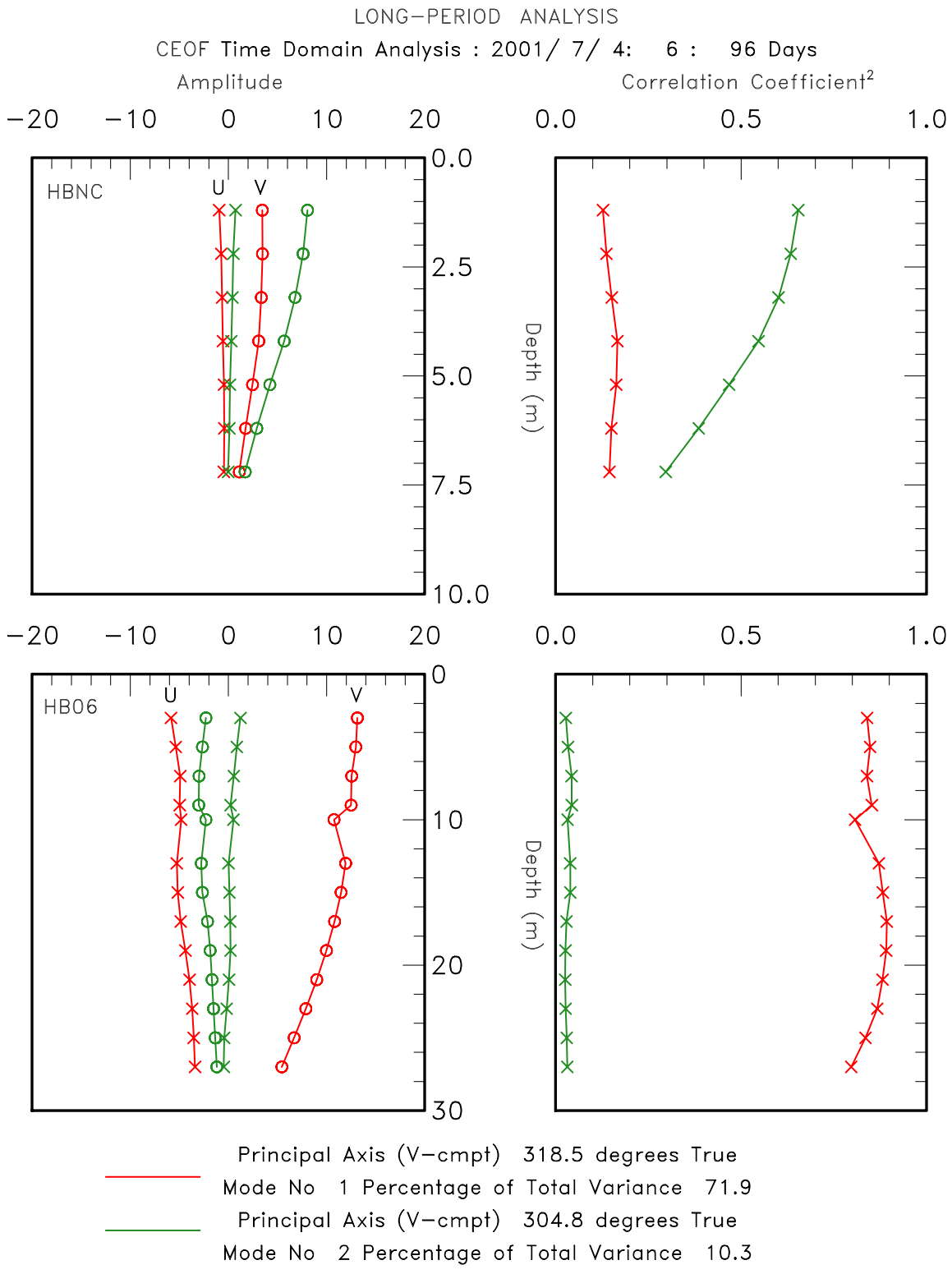

Figure 4-13. Amplitude of the U (cross-shore) and V (alongshore) components (left panels) and the coherence squared of the station with the mode (right panels) from the long-period CEOF analysis for moorings HBNC (top) and HB06 (bottom). Modes 1 and 2 are red and green, respectively.

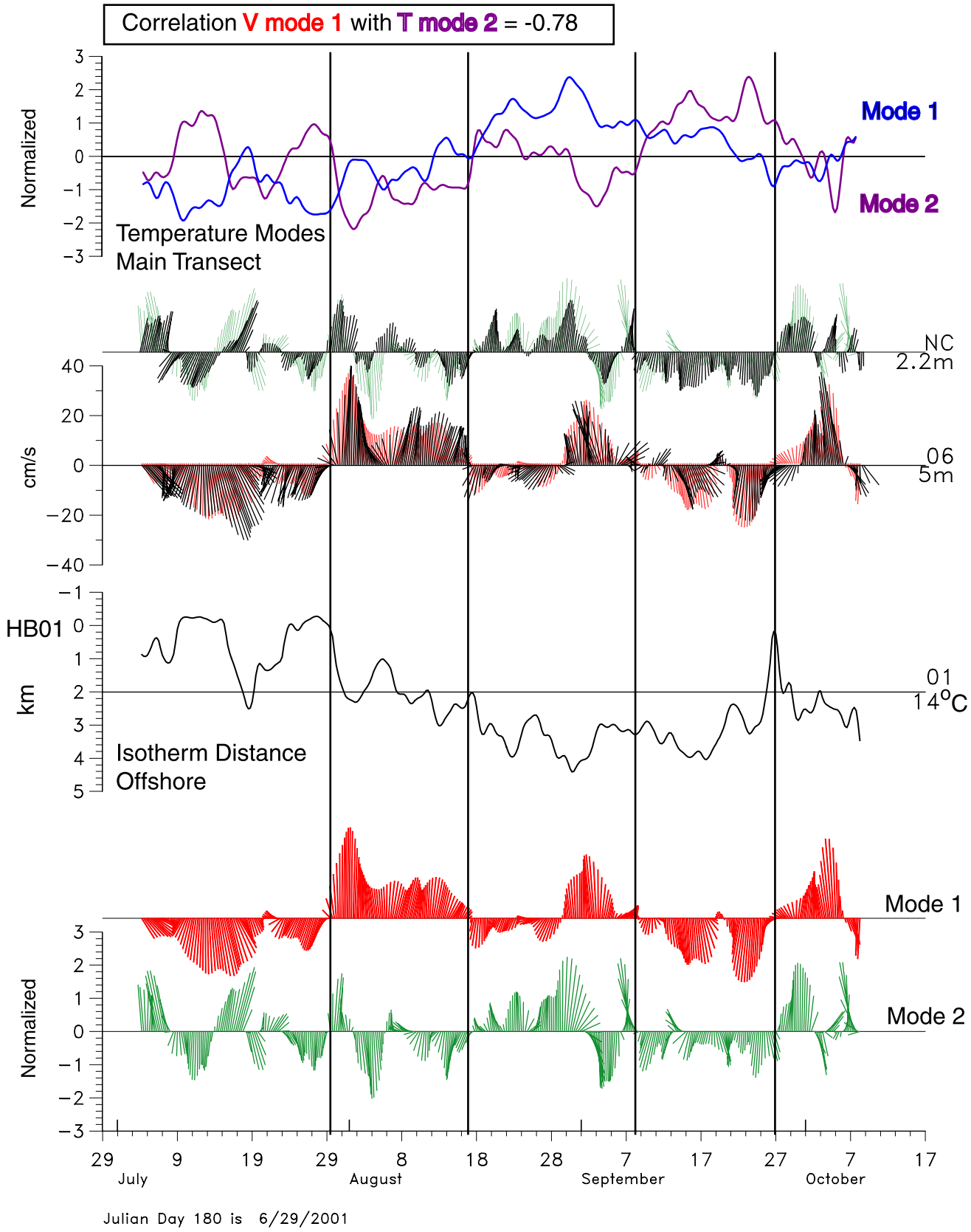

Figure 4-14. Time series of the normalized mode 1 (red) and 2 (green) amplitudes (lower two panels) from the long-period CEOF analysis of velocities. These are overlaid on the demeaned current vectors (black sticks) from moorings HB06 (5 m) and HBNC (2 m). The third panel from the bottom shows the distance offshore, along the main transect (wrt HB01) of the 14°C isotherm where it intersects the bottom. The top panel shows the time series of mode amplitudes from the main transect EOF analysis of temperatures.

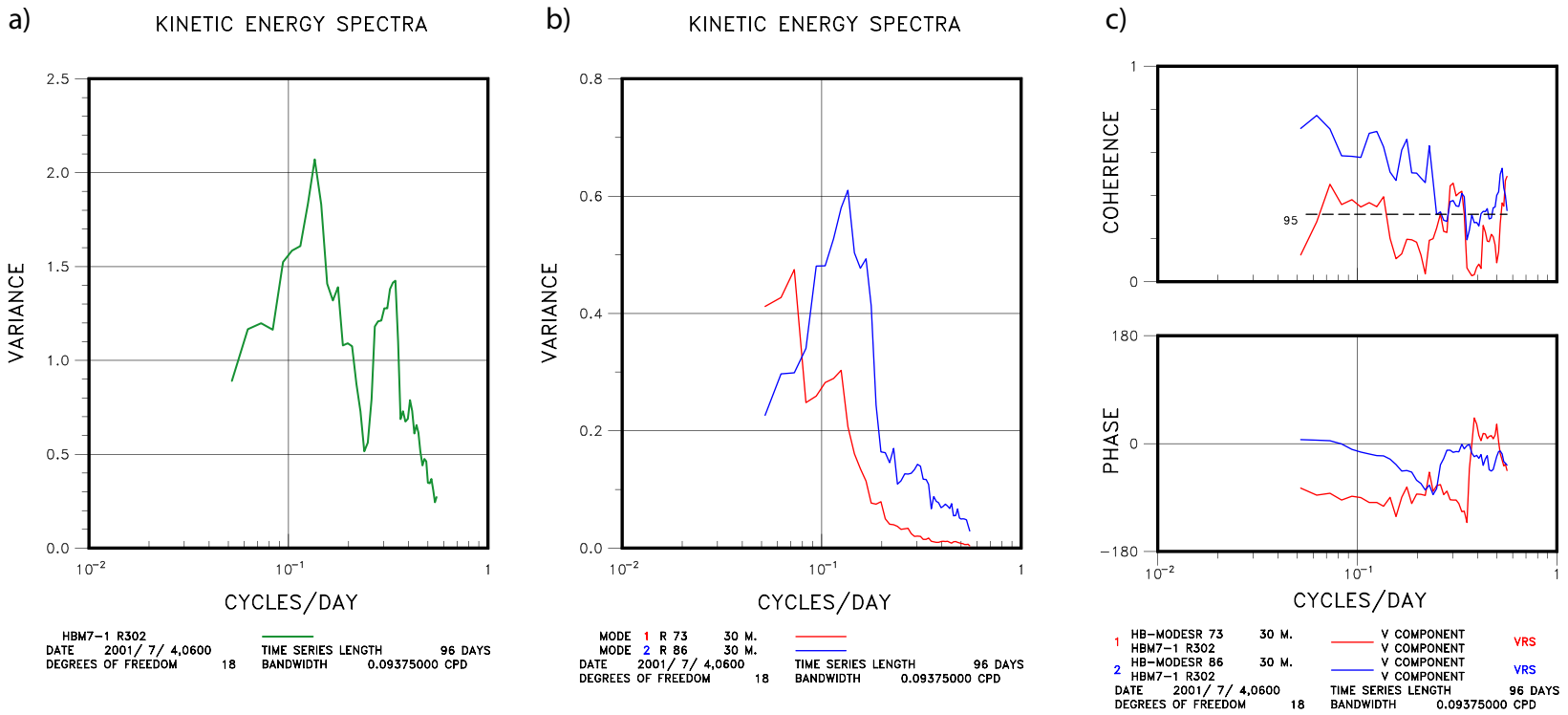

Figure 4-15. Kinetic energy spectra of the wind at HB07(a), and of the long-period CEOF modes 1 (red) and 2 (blue), and coherence squared and phase differences between the V-components of modes 1 and 2 with the V-component of the wind.

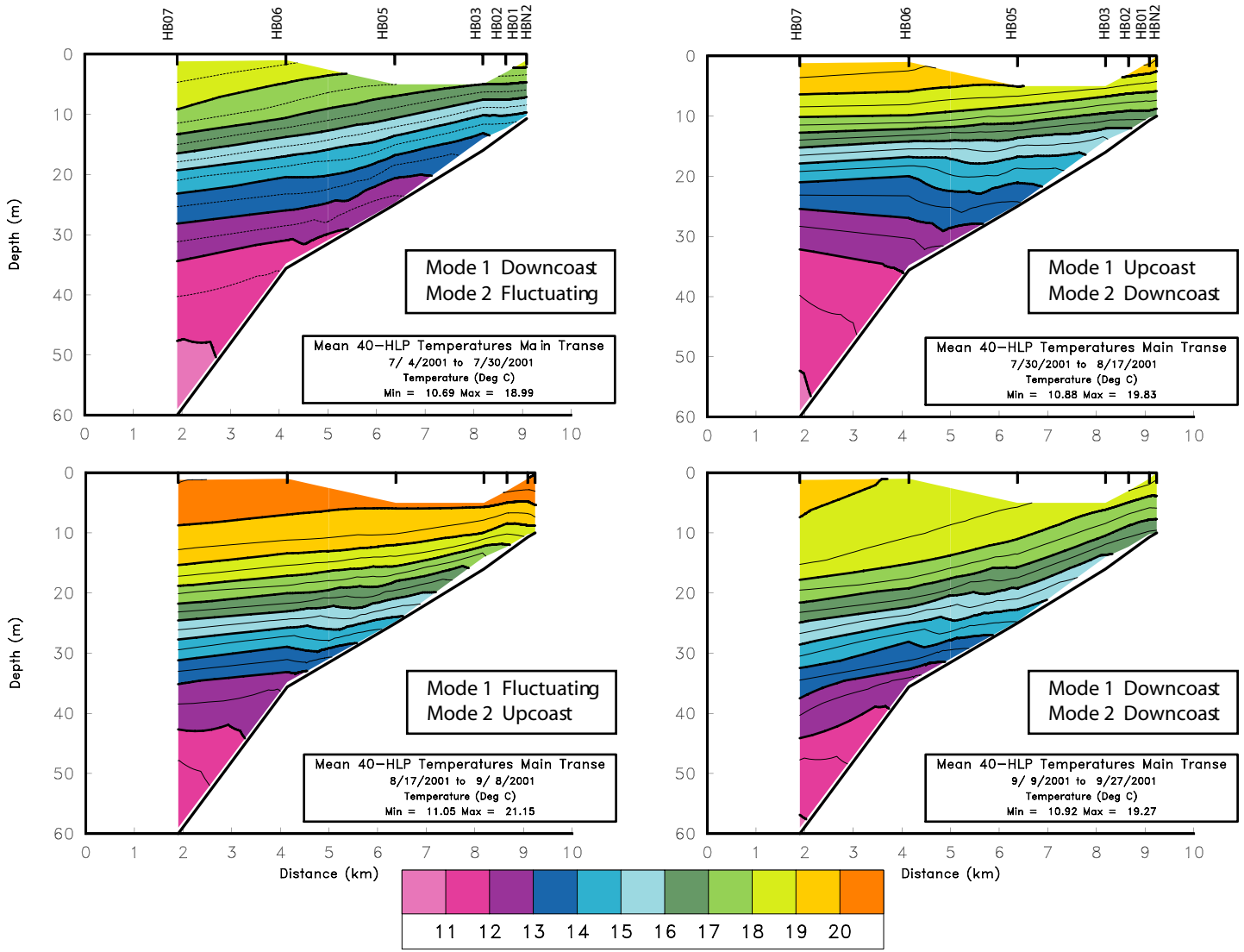

Figure 4-16. Mean temperature fields, from 40-HLP main transect data, for the four periods defined in Table 4-1.

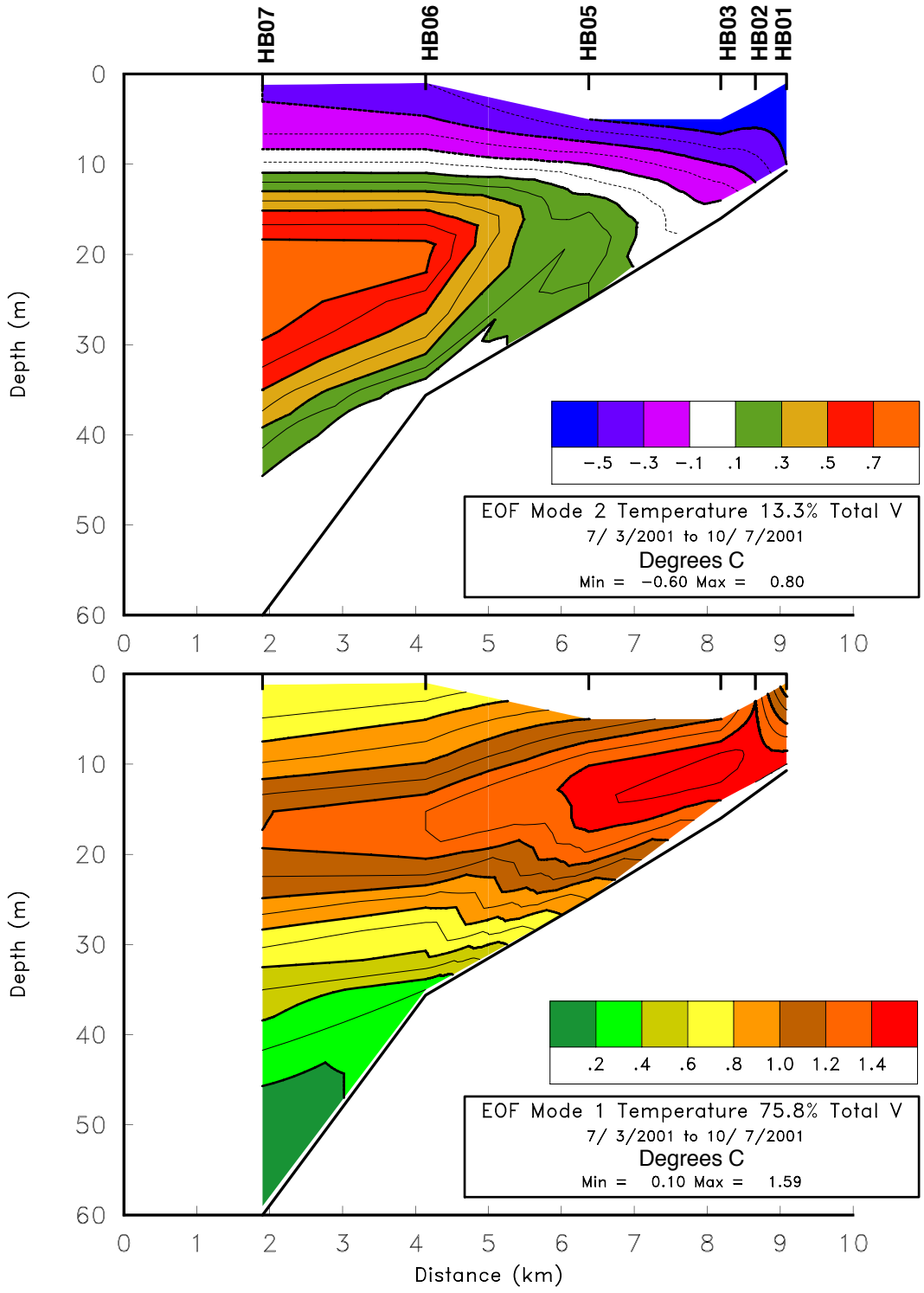

Figure 4-17. Eigenvector amplitudes for modes 1 (lower) and 2 (upper) from an EOF analysis of subtidal temperature data on the main transect.

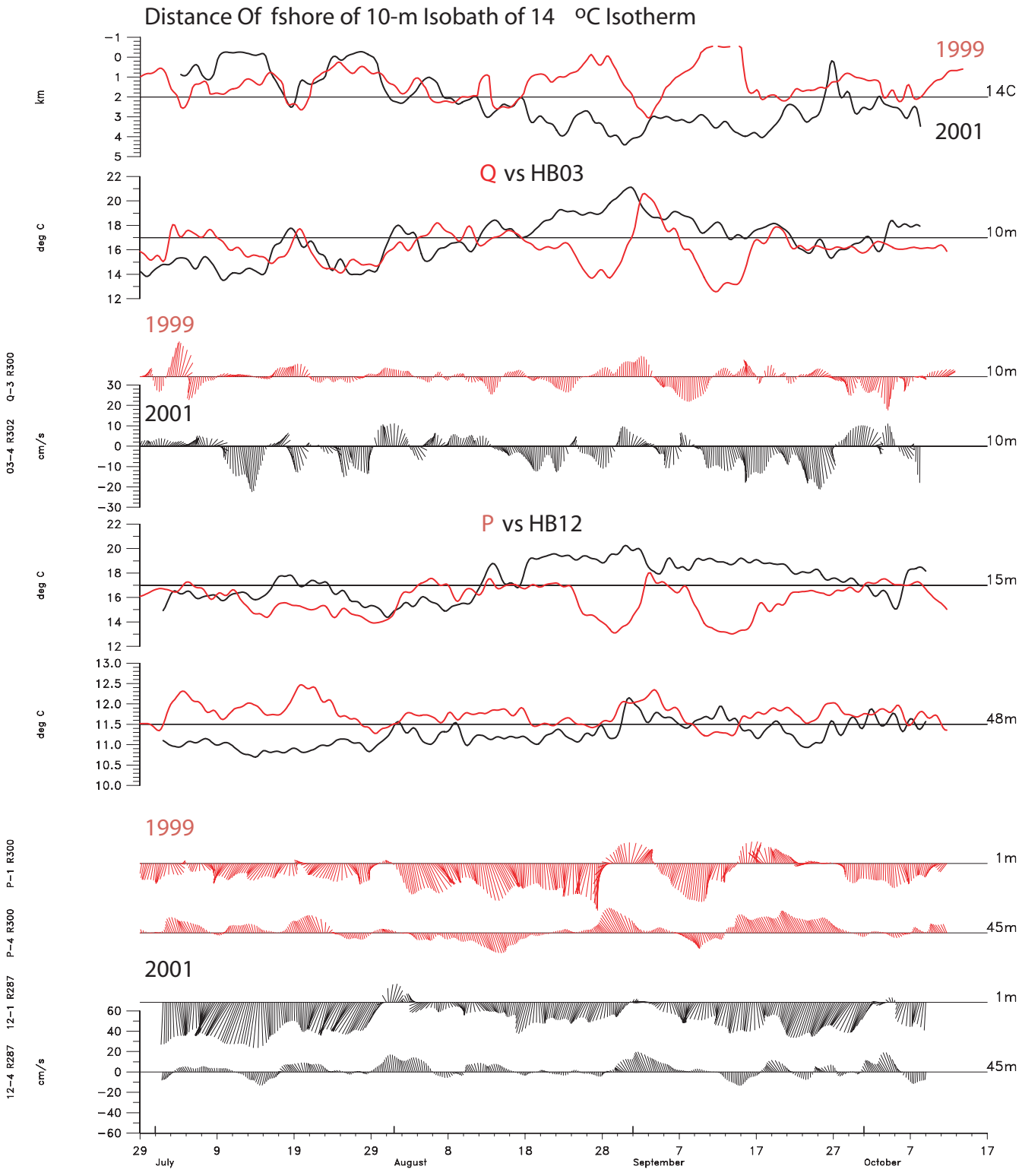

Figure 4-18. Comparison of 40-HLP velocity and temperature time series from the same mooring positions for the summers of 2001 (black lines) and 1999 (red lines). The top panel shows the distance offshore relative to the 10-m isobath where the 14°C isotherm intersects the bottom. In 1999 and 2001, the main transect and along the outfall pipe, respectively, are the sections used.

Table 4-1. Analysis Period Definitions

Period	Dates	Mode 1	Mode 2
1	July 4 – July 30	Strong Downcoast	Fluctuating
2	July 30 – Aug17	Upcoast	Downcoast
3	Aug 17 – Sep 9	Fluctuating	Upcoast
4	Sep 9 – Sep 27	Downcoast	Downcoast

Table 4-2. Comparison of Basic Statistics for 1999 and 2001 Summers

ID	Depth (m)	Cmpt	Units	Mean	Maximum	Minimum	Variance
HB12-1 R287	1	U	cm/s	-5.01	7.723	-20.879	6.373
		V	cm/s	-19.082	17.937	-44.428	12.075
OC-P-1 R300	1	U	cm/s	-0.626	19.237	-13.329	6.213
		V	cm/s	-12.361	21.345	-46.053	13.846
HB12-2	15	T	°C	17.411	20.254	14.385	2.207
OC-P-2	15	T	°C	15.829	18.007	13.019	1.265
HB12-4 R287	45	U	cm/s	-1.728	2.610	-8.577	2.219
		V	cm/s	+2.187	19.618	-13.348	6.711
OC-P-4 R300	45	U	cm/s	-1.225	7.422	-12.403	4.104
		V	cm/s	+2.597	24.244	-19.603	8.944
HB12-5	48	T	°C	11.258	12.148	10.696	0.298
OC-P-5	48	T	°C	11.757	12.471	11.212	0.257
HB03-4 R302	10.2	U	cm/s	+1.226	5.894	-2.092	1.524
		V	cm/s	-3.122	11.060	-22.382	7.590
OC-Q-3 R300	10	U	cm/s	+0.592	4.185	-3.27	1.216
		V	cm/s	-0.481	17.116	-16.393	4.983
HB03-2	10	T	°C	16.902	21.122	13.503	1.710
OC-Q-3	10	T	°C	16.150	20.613	12.562	1.401
Diffuser Plume Parameters from Nearfield Outfall Model							
Plume Top Depth		Z	m	31.1	42.5	22.2	7.39
		Z	m	27.9	40.6	15.1	6.46
Plume Center Depth (Minimum Dilution)		Z	m	38.9	46.5	32.9	3.31
		Z	m	36.7	45.2	28.1	2.90

CHAPTER 5. NEWPORT CANYON TRANSPORT PATHWAY

Kevin Orzech and Marlene Noble

5.1. Hypothesis

Occasionally, subtidal currents over the outer shelf flow downcoast toward the southeast. Usually, if current speeds are not too strong, these subtidal flows follow isobaths transporting water over the same depths on the shelf. Because the edge of the shelf downcoast of the outfall pipe bends sharply toward the coast, these downcoast subtidal currents may carry suspended materials including bacteria from the plume toward the coast and into Newport Canyon (Figure 5-1). If this contaminated effluent from the plume is upwelled or transported out of Newport Canyon by some oceanographic process and the nearshore currents are also directed upcoast, then a hypothetical pathway exists between the outfall and Huntington Beach.

For this investigation, we used subtidal data from the current meters at moorings along the hypothetical pathway (moorings HB07, HB11, HB13, and HB03) to determine if and when the hypothetical pathway does in fact exist. We compared current speeds at the top, middle, and bottom plume depths along the shelf edge to determine the percentage of time that currents were downcoast and when the pathway was possibly open.

5.2. Methods to Determine When the Pathway Was Open

To define possible contamination events, currents must flow in directions that are along the pathway toward Huntington Beach and flows must persist long enough to carry the water from the outfall along the entire pathway to the nearshore region off Huntington Beach. Six necessary conditions were defined to evaluate this (the first four are shown in Figure 5-1):

1) Currents at HB07 flowed downcoast for a sufficient time to transport water from the outfall to HB11 (5.5 km). Here we assume that the currents always follow isobaths until they reach Newport Canyon, although it is known that downcoast currents do occasionally flow onto the slope when the shelf-break isobaths turn toward the northeast.

2) Once the hypothetical water particles and suspended materials reached HB11, the downcoast currents at that site must have lasted long enough for the suspended material to enter Newport Canyon (3.5 km from HB11).

3) Once in the canyon, the hypothetical plume water was assumed to upwell near HB13. Upcoast alongshore currents at that site need to flow for a long enough period to carry the suspended material to the nearshore region off the Santa Ana River (3.5 km from the canyon).

4) A contamination *window first opened* when the hypothetical plume water first reached the Santa Ana River and at the same time currents at HB03 flowed upcoast, effectively carrying the water along the nearshore region off Huntington Beach (2.5 km from the river to HB03).

5) The hypothetical *window remained open* as long as currents at each of the moorings continued to flow along the pathway toward Huntington Beach.

6) The hypothetical *window closed* soon after currents reversed direction at any of the moorings along the pathway. At this point the pathway was no longer intact and the source of contamination was cut off. We assumed that the potentially contaminated water remaining in the system at the time of reversal would also flow to the beach, provided currents at moorings past the point of cut-off flowed in the direction of Huntington Beach. Actual window closure times were calculated based on this assumption and on when currents would transport remaining hypothetical effluent to HB03.

For the first two legs of transport, currents at three discrete depths along the shelf edge (HB07 at 30 m, 38 m, and 50 m, and HB11 at 30 m, 38 m, and 48 m) were evaluated to determine the fate of contaminated water from the top, core and bottom of the plume. The plume near the shelf edge lies on average from 29 m to about 50 m below the surface (Chapter 10). Currents over these depths often vary in speed and direction in large part because the California undercurrent spills up onto the shelf and carries the deepest shelf waters upcoast while shallower waters flow downcoast.

All rates and distances of transport were calculated by overplotting the current-velocity time-series data and integrating under these curves. Figure 5-2 shows an example of these curves for a period that met the six conditions of transport. Here, a window of hypothetical contamination begins on July 2 and ends on July 4 GMT when possibly contaminated water from the outfall could have been in the nearshore region off Huntington Beach.

Three assumptions bias the results toward defining more contamination events than may actually occur. First, we assumed downcoast currents at the shelf break always hugged the shelf edge and transported water and suspended materials toward the canyon; this ignores the fact that it is known that downcoast currents do occasionally flow onto the slope when the shelf-break isobaths turn toward the northeast. Second, water within Newport Canyon was assumed to always upwell onto the shelf. Upwelling occurred only intermittently within the canyon as shown by the hydrographic surveys (Chapter 10). Last, we assumed sufficient cross-shore transport mechanisms were always available to bring contaminated water ashore from the nearshore region. Typically, alongshore flow predominates in nearshore environments.

5.3. Results

Currents over the shelf were large enough in duration and velocity to transport plume water from the outfall into Newport Canyon eight times during the summer of 2001 (Tables 5-1a, b, c). Upcoast flow in the nearshore was persistent enough to bring plume water to the nearshore by Huntington Beach four of these times for water near the top of the plume and two of these times for water near the core and base of the plume. During the other times currents flowed downcoast at the nearshore moorings, denying the possibility of transport of effluent upcoast to the beach. For the October 17 event, the upcoast flow rates at HB13 were substituted for HB03 data that were not recorded.

5.3.1. Comparison Between Canyon Events and Beach Contamination Events

No windows of hypothetical beach contamination for both the core and bottom of the plume coincided with beach bacteria events. Only one beach contamination day (July 7) corresponded with flow of upper plume water along the canyon pathway. The specific contamination on the beach was a moderate-sized enterococci and total coliform event from stations 0 to 15N (Chapter 3; Figure 2-2) that spanned three days (July 5 to 7). Note that surfzone bacteria samples were not collected on every day that a window of hypothetical contamination was open. For example, during the window from July 1 to 4 sampling occurred on only two days (Tables 5-1a, b, c).

To account for the possible inaccuracies in representing current speeds along the pathway from discrete mooring sites that were stationed a few km apart, the time windows were broadened by one day on each end of the windows. No more events resulted from the expanded windows at core and bottom plume depths. One more beach contamination event coincided with an expanded window for the upper plume waters. This was an isolated type 1 event at station 3N on July 31. Also, the expanded window around the July 7 event included July 6–another day with beach contamination above AB411 levels.

5.4. Discussion

Minor if any causal association existed between the pathway and beach contamination events during summer 2001. The pathway was open for 4-7% of the days in the study period for the actual and expanded windows, respectively (Figure 5-3). The actual and expanded windows were associated with only 1 to 3 of the 42 days when either a type 1, 2 or 3 contamination event occurred during the study period from June to October 2001.

The most concentrated effluent commonly lies at about 39-m water depth near the shelf edge. Water at this depth could possibly be transported from the outfall along the canyon pathway to the beach two times. No events coincided with these open windows. No more events resulted from the expanded windows at core and bottom plume depths, indicating that the most concentrated plume water did not come to shore via the pathway in any significant amount, if at all. The edges of the plume contain the least concentrated effluent because the contamination diffuses more readily into the surrounding seawater. Therefore the events defined in this study represent times when the least contaminated plume water may have reached Huntington Beach.

The hypothetical beach contamination on July 7 from the canyon pathway is unlikely to produce the beach-wide event at that time. This event was spread across most of Huntington Beach for three days at relatively moderate to high levels of contamination. It is not likely that water from the top of the plume contains this level of concentrated pollution. Also, HB13 currents flowed strongly downcoast until the morning of July 6. This implies that the period of contamination was caused by a source that was polluting the beach for a day prior to the arrival of any possible effluent from the canyon. This event also had high enterococci counts. As shown in Chapter 3, enterococci have been associated with sunlight-induced die-off during the day. This suggests that events that span more than one day require a source that supplies contamination to the beach at least daily if not continuously. Another source must be responsible for most if not all of the contamination during this event.

Possible contamination from the canyon on July 31 was relevant after the original window was expanded one day. The event was isolated and small. The sampling coincided with the last few hours of the expanded window of upper plume water reaching the beach. This type 1 event occurred also on August 1, suggesting that another source is responsible for the contamination.

5.4.1. General Flow Patterns for Alongshore Currents near the Outfall

During summer 2001, currents at the top of the plume obtained magnitudes strong enough to reach Huntington Beach via the hypothesized canyon pathway over twice as often as did water from the core and bottom of the plume (155 hours vs. 67 hours). Current histograms for moorings at the shelf edge revealed that currents at lower and middle plume depths on average flowed upcoast while water near the top of the plume flowed downcoast (Figures 5-4a, b, c). Note that the largest mean upcoast currents occurred near the bed while water near the top of the plume usually flowed downcoast. The effect was most strongly seen at HB11 where mean speeds of over 3 cm/s upcoast were obtained at the core and bottom plume depths (at 39 m and 47 m). The strength of upcoast flow with depth decreases from HB12 to HB07.

Hamilton (Chapter 4) also showed that the deepest currents over the outer shelf did not flow downcoast on average unlike the currents in the mid to upper water column (Chapter 4; Figure 4-8). For example, mean currents at HB11 at 45 m flowed almost due west on average, away from the canyon.

The California undercurrent likely played a primary role in retarding the flow of core and bottom plume water into Newport Canyon during the summer. The undercurrent flows along the continental slope upcoast and poleward toward and around the San Pedro Bay shelf. It is the dominant current that flows over the slope on the west margin of North America (Pierce et al, 1996). It has been shown to reach speeds as high as 50 cm/s with a mean speed of about 24 cm/s (Noble and Ramp, 2000; Pierce et al., 1996). Pierce et al. (2000) and Barth et al. (2000) also showed that the undercurrent meanders onshore and offshore at promontories off the Northern California coast and that this flow interacts with shelf currents and the deeper California Current.

Where the slope orientation changes abruptly southwest of Newport Canyon the undercurrent spills onto the shelf and cuts the shelf corner, adding an upcoast component to the flow in the deepest shelf waters. This may result in a shearing of the plume-depth water that transports the deepest waters upcoast away from Newport Canyon. The undercurrent would first come onto the shelf near HB11, where the shelf bends. At HB12 and HB07 the mean flow near the bed was upcoast but weaker than HB11. This was probably due to movement of the undercurrent back toward the slope.

This upcoast flow of deeper waters may be more pronounced during summer. Histogram plots for winter 2002, summer 1999, and winter 2000 reveal that upcoast mean flow is stronger during summer for both years of data (Figures 5-5a, b and 5-6a, b). Winter currents in both years at the top and core of the plume flowed dominantly downcoast. This indicates that plume water could reach the canyon more often in winter months. The SAIC 1999 mooring is located near

the summer 2001 HB12 site. These results corroborate Chelton's work (1984) that showed maximum speeds of the undercurrent occurred in late summer to early fall off central California.

5.5. Conclusions

The hypothetical pathway of beach contamination via Newport Canyon is known to exist in part; during hydrographic and plume tracking surveys, plume water was measured in Newport Canyon inshore, but not above the canyon rim or alongshore north of the canyon (Chapter 10 and MEC, 2001). Our measurements show that the pathway does exist, but it is rarely intact (5% of the summer 2001). Also, when the pathway was open it coincided with beach contamination events during only 1 of the 4 open-window periods. Therefore, the pathway is an insubstantial source of beach pollution, if at all. The California undercurrent is partially responsible; when the current spills onto the shelf the deepest plume water near the shelf edge is forced upcoast away from the canyon, and probably more so in summer than in winter.

5.6. References

Barth, J.A., S.D. Pierce, and R.L. Smith, 2000. A separating coastal upwelling jet at Cape Blanco, Oregon, and its connection to the California Current System. Deep-Sea Research II v. 47, p. 783-810.

Chelton, D.B., 1984. Seasonal variablility of alongshore geostrophic velocity off central California. Journal of Geophysical Research, v. 89 (C3), p. 3473-3486.

MEC (MEC Analytical Systems, Inc), 2001. Strategic Process Study, Plume Tracking. June 1999 to September 2000. Final Report, Vol. I: Executive Summary.

Noble, M.A. and S.R. Ramp, 2000. Subtidal currents over the central California slope: evidence for offshore veering of the undercurrent and for direct, wind-driven slope currents. Deep-Sea Research II, v. 47, p. 871-906.

Pierce, S. D., R.L. Smith, and P.M. Kosro, 1996. Observations of the poleward undercurrent along the eastern boundary of the mid-latitude Pacific. Transactions, American Geophysical Union, EOS 77 (46), F345.

Pierce, S. D., R.L. Smith, P.M. Kosro, J.A. Barth, and D.C. Wilson, 2000. Continuity of the poleward undercurrent along the eastern boundary of the mid-latitude north Pacific. Deep-Sea Research II, v. 45, p. 811-829.

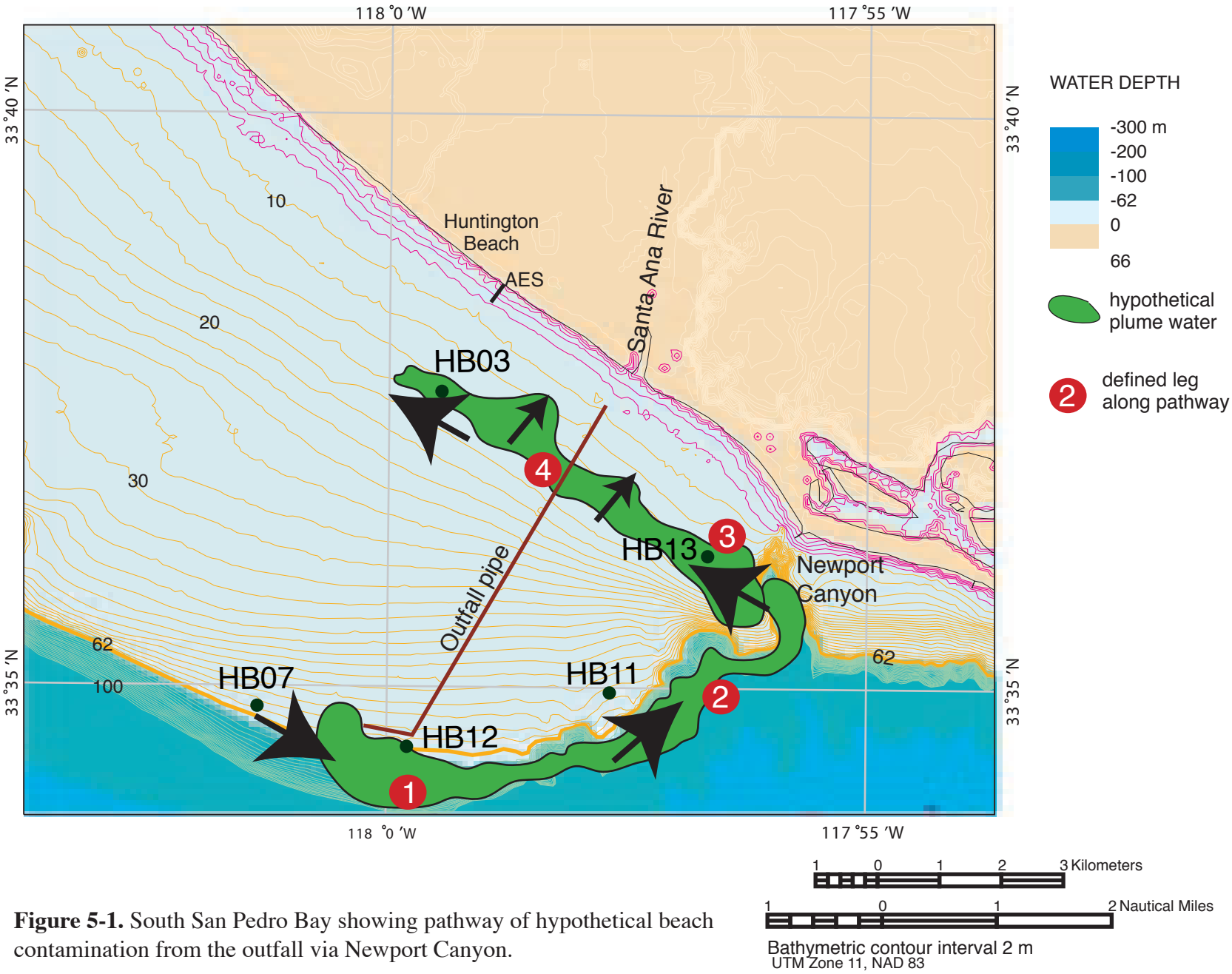

Figure 5-1. South San Pedro Bay showing pathway of hypothetical beach contamination from the outfall via Newport Canyon.

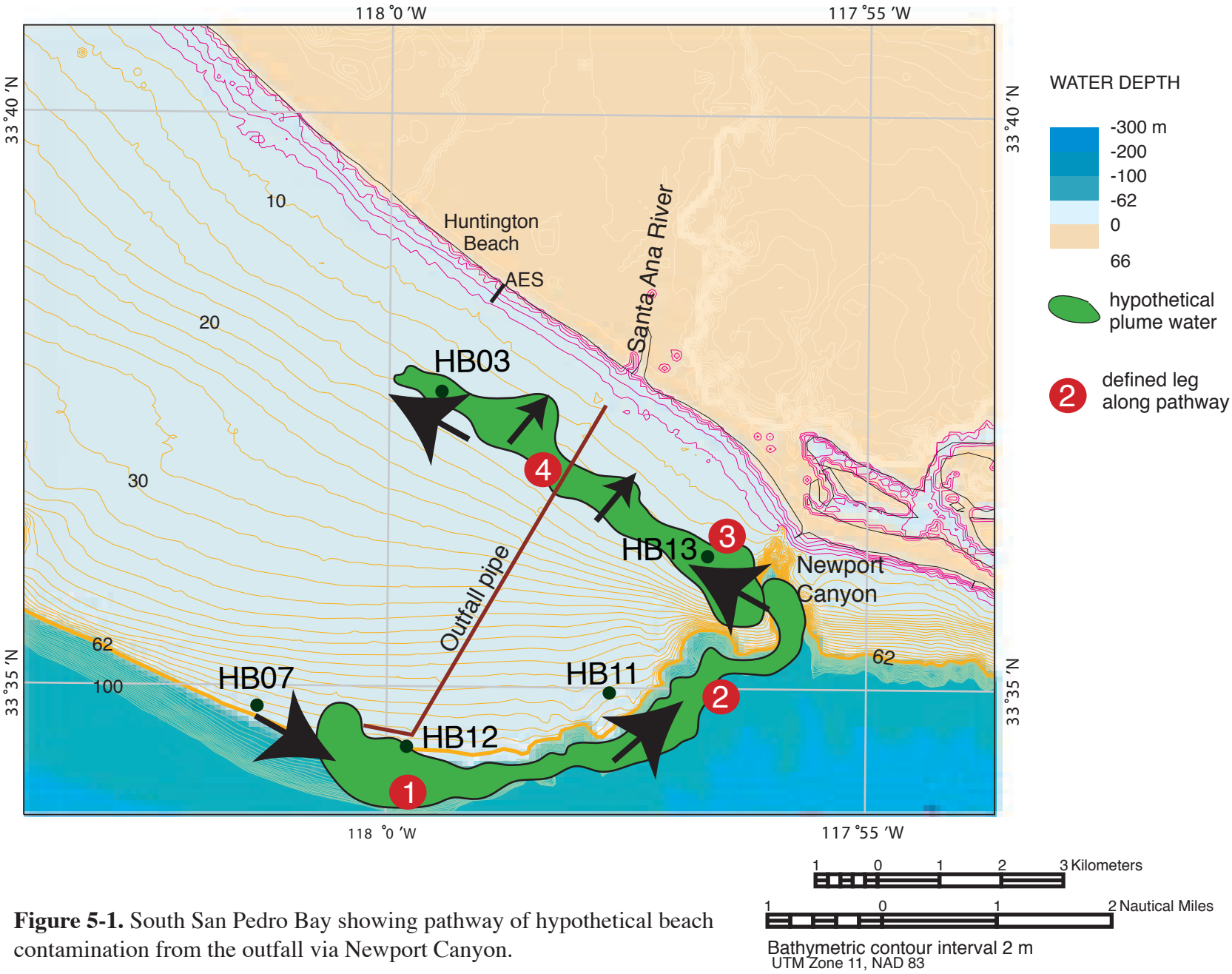

Figure 5-1. South San Pedro Bay showing pathway of hypothetical beach contamination from the outfall via Newport Canyon.

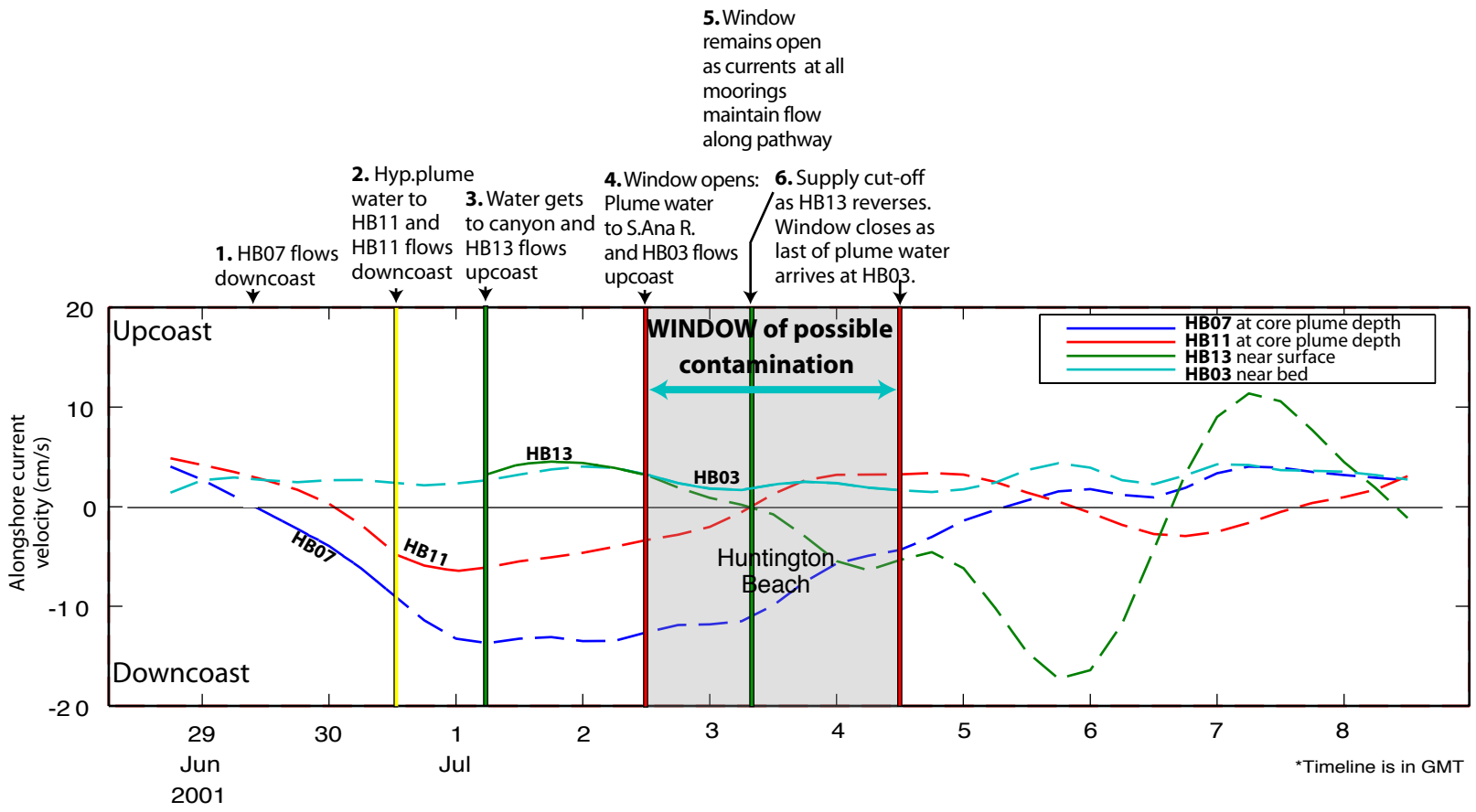

Figure 5-2. Alongshore current velocity curves for a hypothetical contamination event from the Newport Canyon pathway showing the six conditions to define an event. Solid sections of colored lines show the velocities and mooring used per leg of transport to determine whether hypothetical plume water reached Huntington Beach to intially open the window.

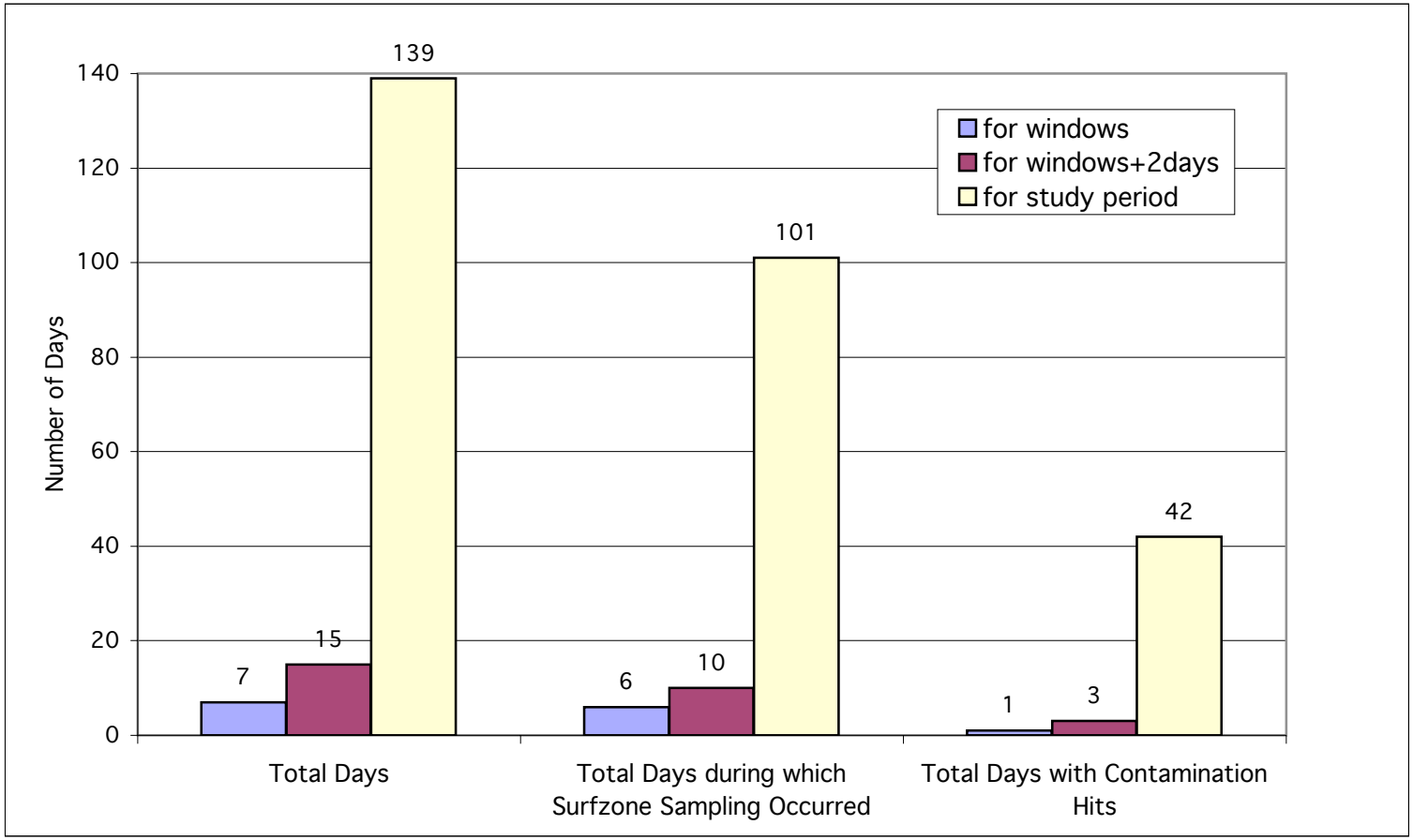

Figure 5-3. The chart shows comparisons of statistics for window and study-wide dates. Yellow bars reveal the number of days during the study period for various statistics. Blue and red bars show number of days during open windows and expanded windows respectively. A window day was counted if the window time included any of the standard sample period time from 6:00 am to 10:00 am (PDT) for that day. The far left set of bars shows there were 7 and 15 days that windows and expanded windows were open in the 139-day study period. The middle set of bars shows that of the 101 days that surfzone bacteria sampling occurred, windows and expanded windows were open for 6 and 10 of those days respectively. The far right set of bars shows that Huntington Beach was contaminated above AB411 standards by type 1, 2, or 3 events (Chapter 3) for 42 days of the study period. One and three of these days occurred at a time when the canyon pathway windows and expanded windows were open.

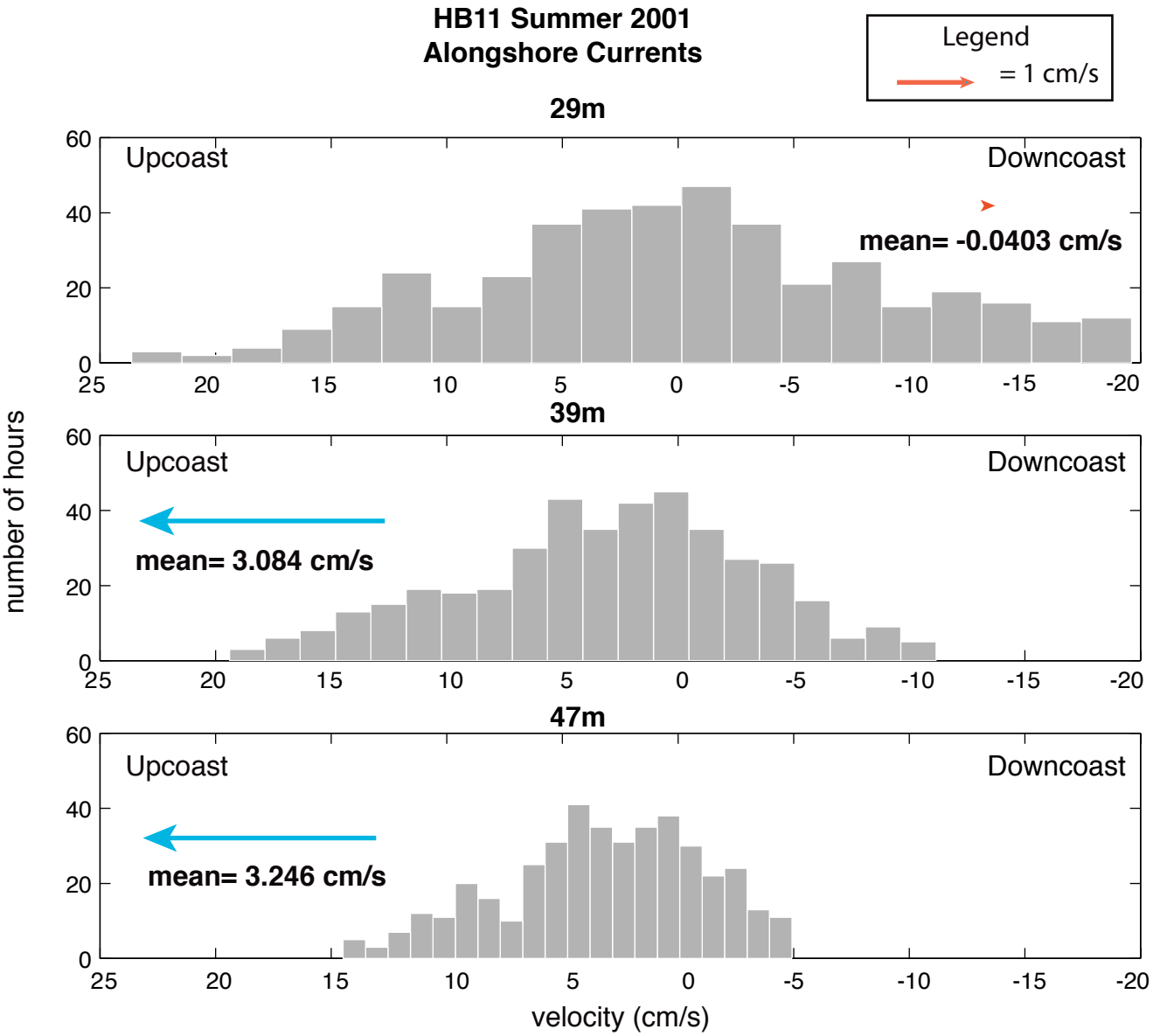

Figure 5-4a. Histograms of low-pass-filtered alongshore currents at HB11 for summer 2001 at upper, core and bottom plume depths.

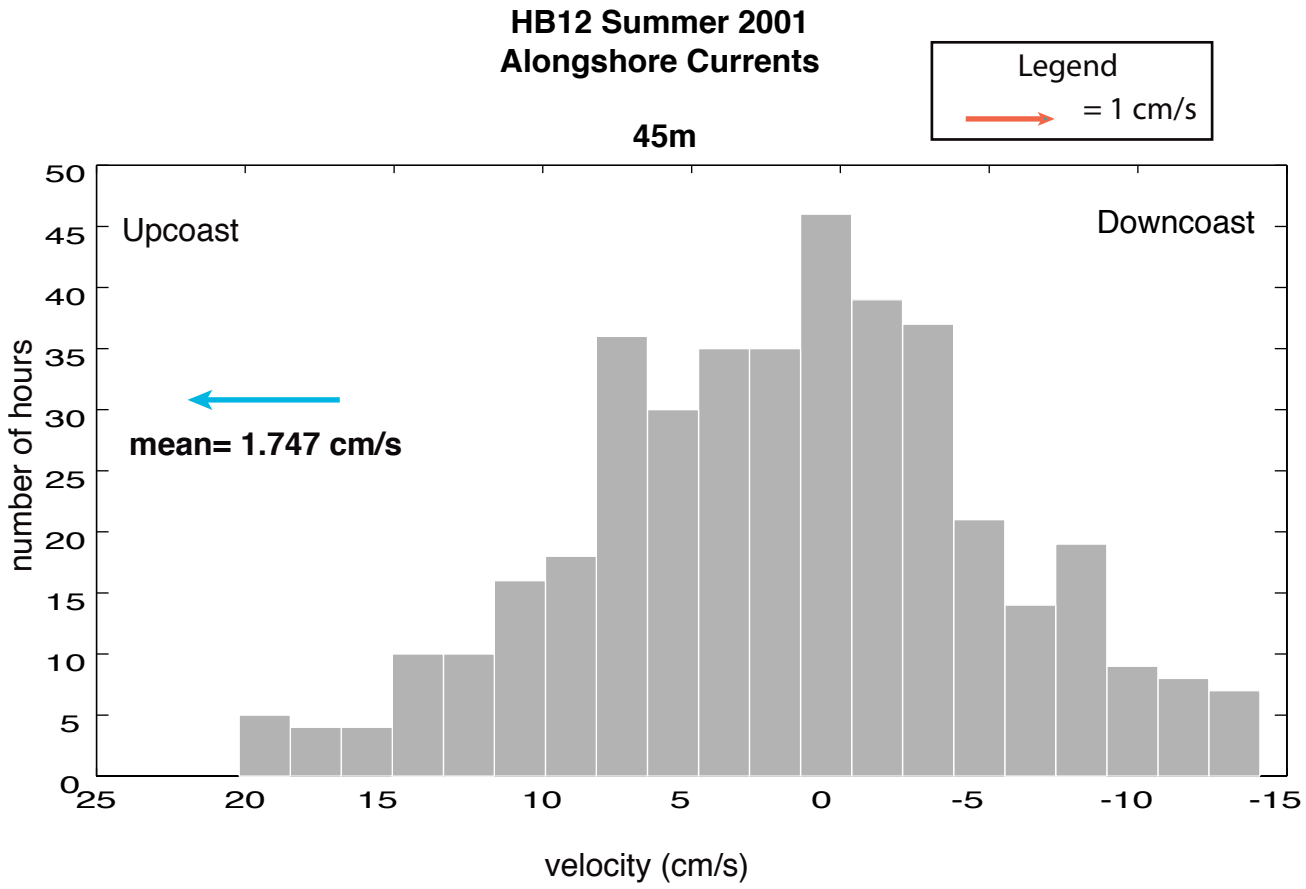

Figure 5-4b. Histograms of low-pass-filtered alongshore currents at HB12 for summer 2001 at 45 m.

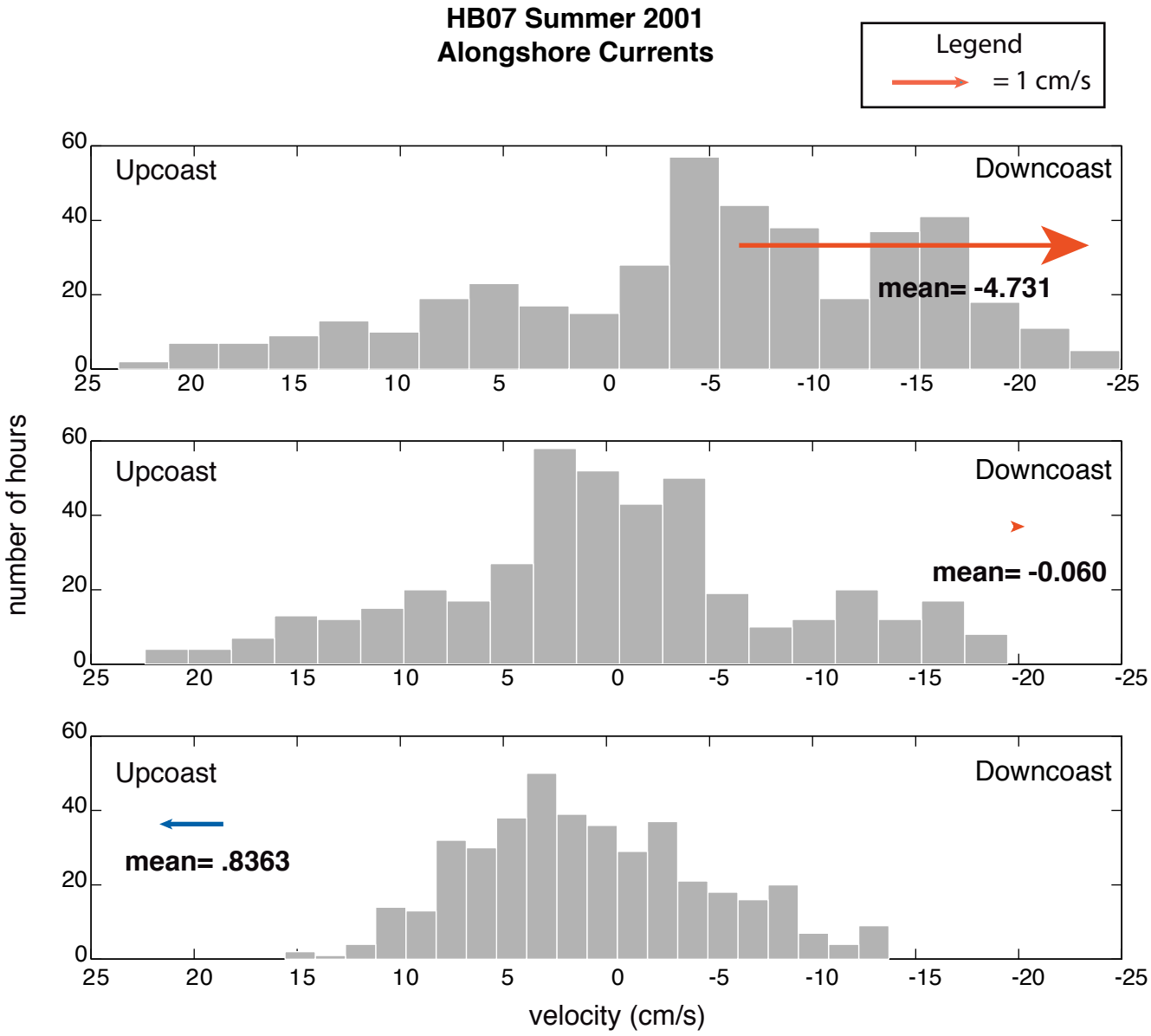

Figure 5-4c. Histograms of low-pass-filtered alongshore currents at HB07 for summer 2001 at upper, core and bottom plume depths.

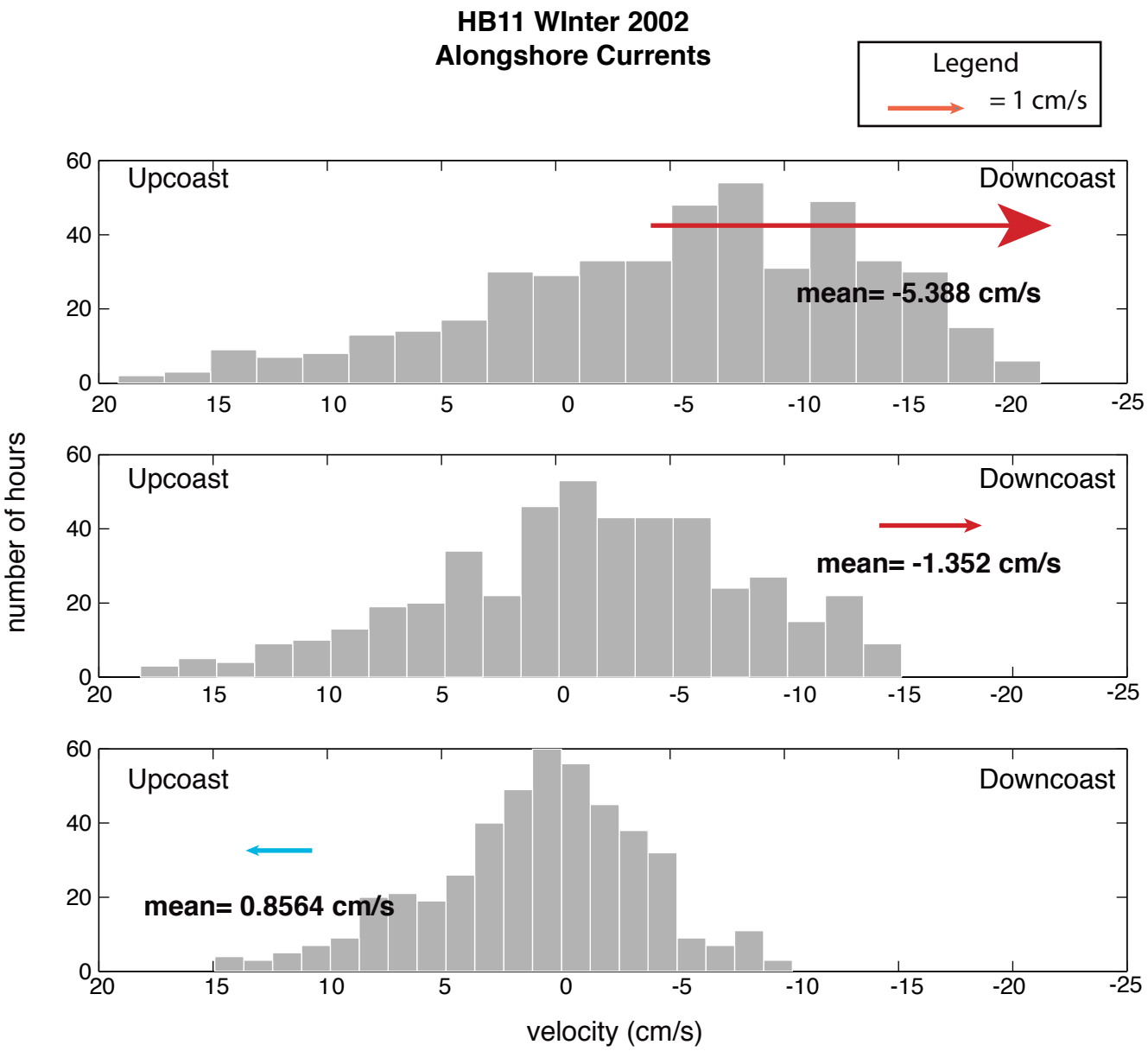

Figure 5-5a. Histograms of low-pass-filtered alongshore currents at HB11 for winter 2002 at upper, core and bottom plume depths.

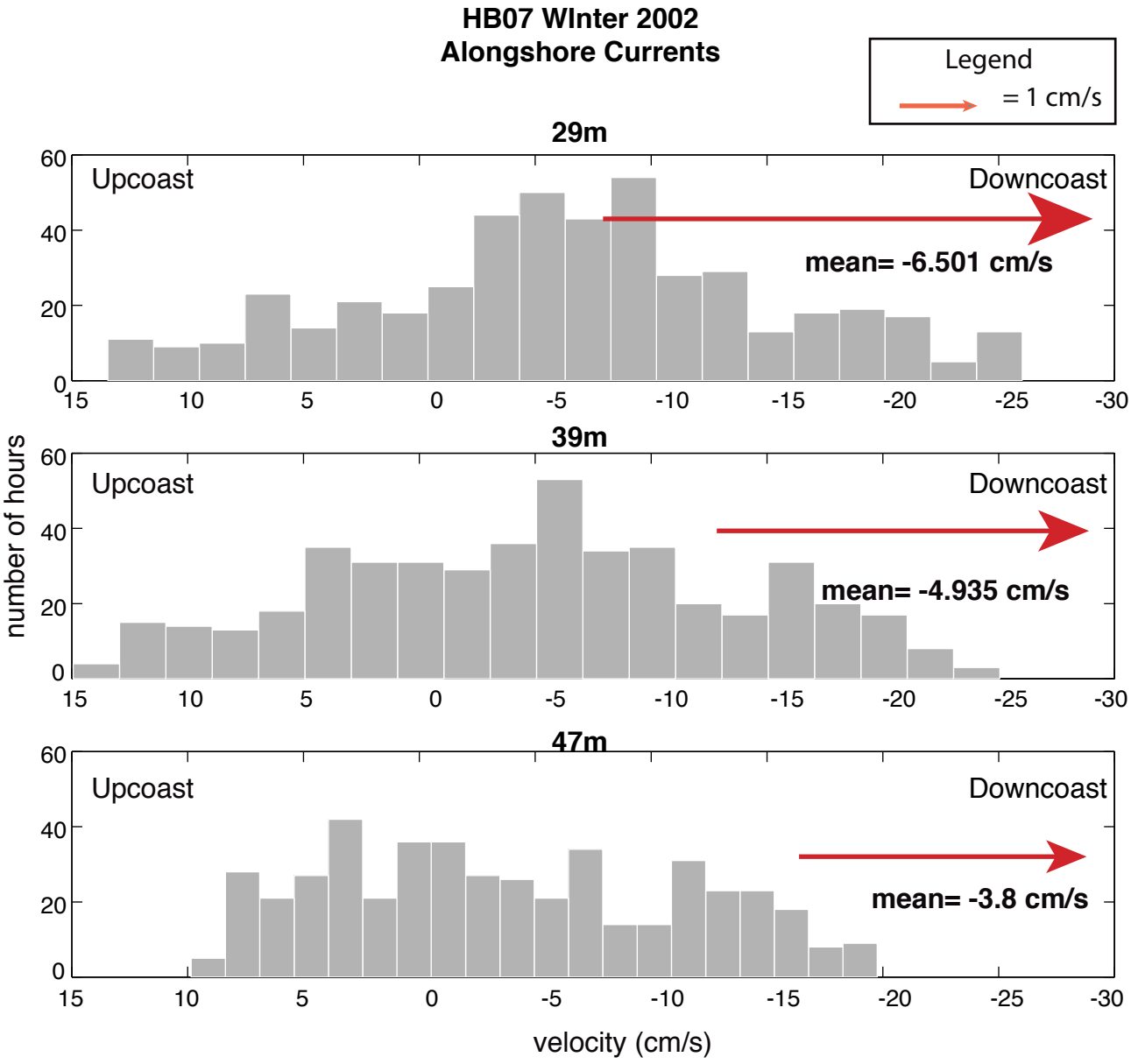

Figure 5-5b. Histograms of low-pass-filtered alongshore currents at HB07 for winter 2002 at upper, core and bottom plume depths.

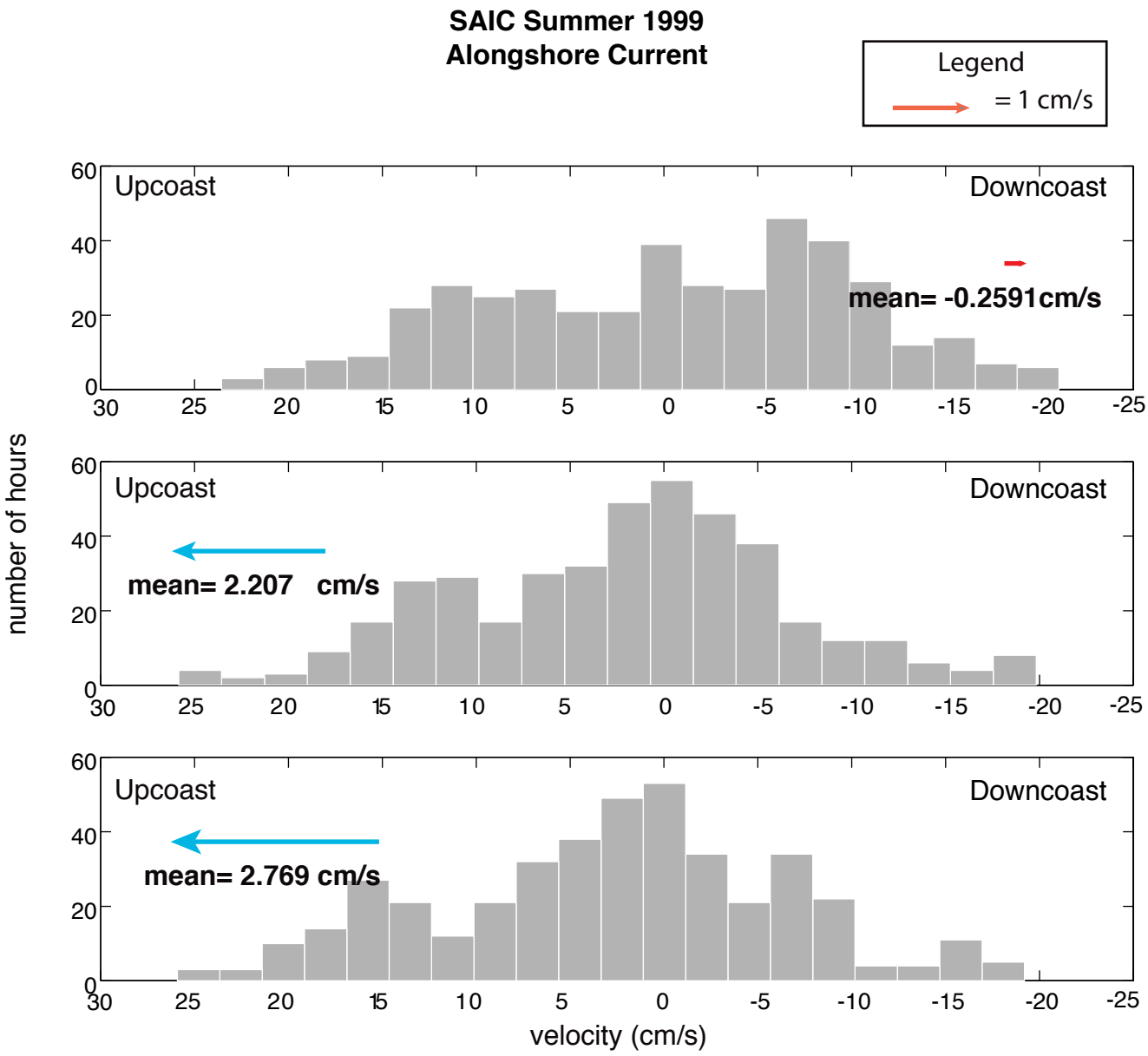

Figure 5-6a. Histograms of low-pass-filtered alongshore currents at SAIC site for summer 1999 at upper, core and bottom plume depths.

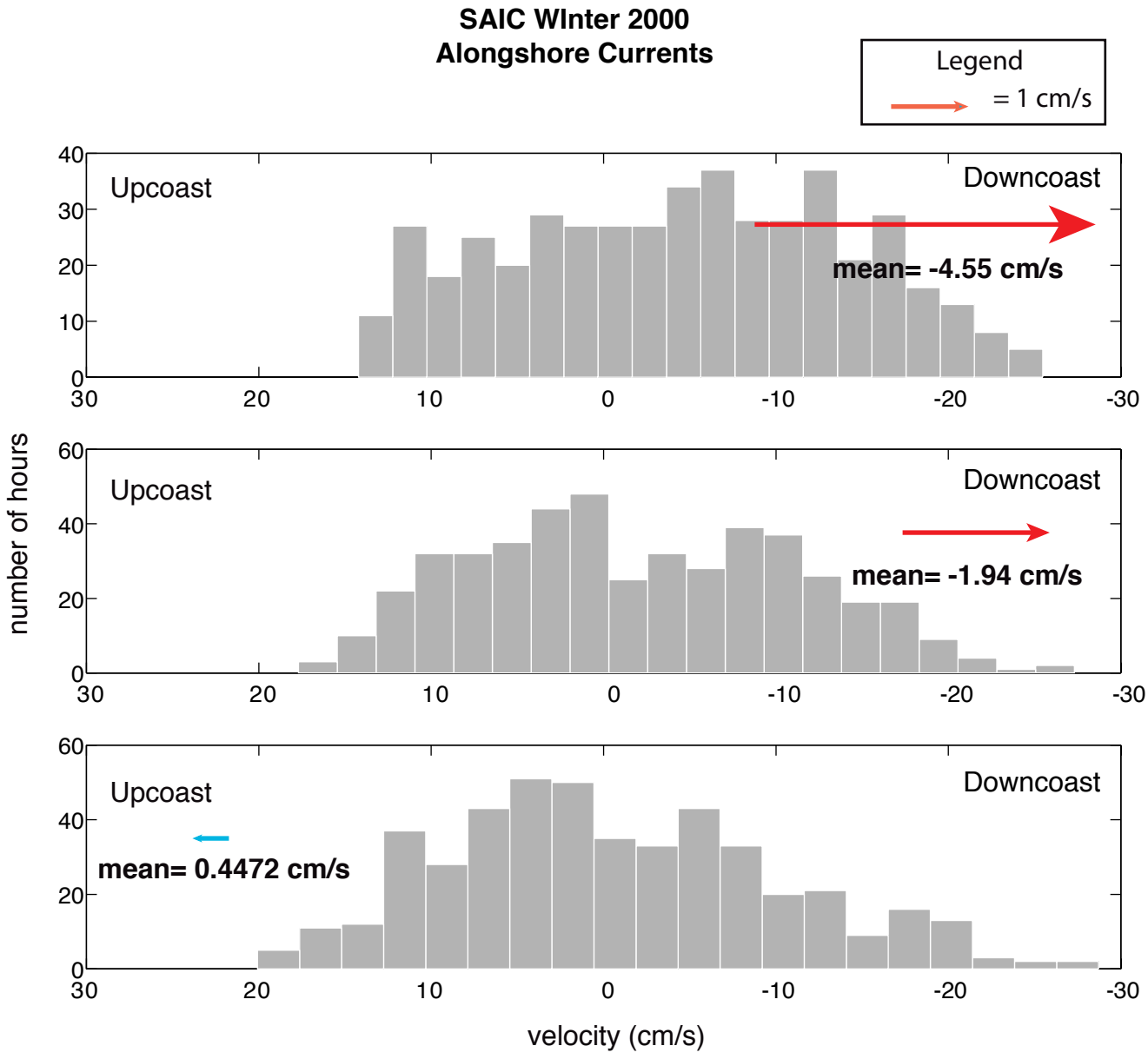

Figure 5-6b. Histograms of low-pass-filtered alongshore currents at the SAIC site for winter 2000 at upper, core and bottom plume depths.

Table 5-1a. Summary of times and events of possible Huntington Beach contamination via the Newport Canyon pathway. Top of the plume (30 m). Times are PDT.

Possible event**	How far effluent may travel	Hypothetical Contamination Window				Total window hours	Bacteria samples during window	AB411 event during window	Bacteria samples during window +/- one day	AB411 event in window +/- one day
		Start Day	Start time	End day	End time					
1	To Hunt.Beach	1-Jul	19:00	4-Jul	6:00	62	2	No	2	No
2	To Hunt.Beach	6-Jul	21:00	9-Jul	0:00	52	1	YES	3	YES
3	To Hunt.Beach	29-Jul	13:00	30-Jul	12:00	23	1	No	2	YES
4	To Canyon Only	na	na	na	na	na	na	na	na	na
5	To Canyon Only	na	na	na	na	na	na	na	na	na
6	To Canyon Only	na	na	na	na	na	na	na	na	na
7	To Canyon Only	na	na	na	na	na	na	na	na	na
8	To Hunt.Beach	17-Oct	9:00	19-Oct	3:00	18	2	No	3	No

Table 5-1b. Summary of times and events of possible Huntington Beach contamination via the Newport Canyon pathway. Core of the plume (38 m). Times are PDT.

Possible event**	How far effluent may travel	Hypothetical Contamination Window				Total window hours	Bacteria samples during window	AB411 event during window	Bacteria samples during window +/- one day	AB411 event in window +/- one day
		Start Day	Start time	End day	End time					
1	To Hunt.Beach	2-Jul	3:00	4-Jul	4:00	49	2	No	2	No
2	Not to Canyon	na	na	na	na	na	na	na	na	na
3	Not to Canyon	na	na	na	na	na	na	na	na	na
4	Not to Canyon	na	na	na	na	na	na	na	na	na
5	To Canyon Only	na	na	na	na	na	na	na	na	na
6	Not to Canyon	na	na	na	na	na	na	na	na	na
7	To Canyon Only	na	na	na	na	na	na	na	na	na
8	To Hunt.Beach	17-Oct	9:00	19-Oct	3:00	18	2	No	3	No

Table 5-1c. Summary of times and events of possible Huntington Beach contamination via the Newport Canyon pathway. Bottom of the plume (58 m). Times are PDT.

Possible event**	How far effluent may travel	Hypothetical Contamination Window				Total window hours	Bacteria samples during window	AB411 event during window	Bacteria samples during window +/- one day	AB411 event in window +/- one day
		Start Day	Start time	End day	End time					
1	**To Hunt.Beach**	**2-Jul**	**6:00**	**4-Jul**	**4:00**	**46**	**2**	**No**	**2**	**No**
2	Not to Canyon	na	na	na	na	na	na	na	na	na
3	**To Hunt.Beach**	**29-Jul**	**13:00**	**30-Jul**	**4:00**	**15**	**0**	**na**	**2**	**No**
4	Not to Canyon	na	na	na	na	na	na	na	na	na
5A	Not to Canyon	na	na	na	na	na	na	na	na	na
5B	To Canyon Only	na	na	na	na	na	na	na	na	na
6	Not to Canyon	na	na	na	na	na	na	na	na	na
7	Not to Canyon	na	na	na	na	na	na	na	na	na
8	Not to Canyon	na	na	na	na	na	na	na	na	na

na = not applicable

**Events are times when HB07 and HB11 flowed downcoast and coincided with or immediately followed times when HB13 and HB03 flowed upcoast.

Event	Start date	End date
1	29-Jun	4-Jul
2	5-Jul	9-Jul
3	26-Jul	30-Jul
4	6-Sep	9-Sep
5	5-Oct	8-Oct
6	8-Oct	11-Oct
7	13-Oct	14-Oct
8	15-Oct	19-Oct

CHAPTER 6. SEA BREEZE

Peter Hamilton

6.1. Introduction

In the analysis of the Phase II measurements (Hamilton et al., 2001), large-magnitude rotary currents were observed on the outer shelf through the upper 30 m of the water column. The signal period was exactly 24 hours, and because the surface tide at this period (S_1) is very small and the 24-hour period is longer than the local inertial period (21.7 hours), the motions were attributed to direct forcing by the sea breeze. Freely propagating internal waves only exist for periods shorter than the inertial period, $2\pi/f$, where f is the Coriolis parameter. The sea breeze in the southern California Bight is a persistent feature of the coastal atmosphere throughout the year, with the strongest winds occurring in the summer. Winds from the meteorological buoy (HB07) at the shelf break and two local airports (Orange County (John Wayne) and Long Beach) are given in Figure 6-1 for July and August. John Wayne Airport winds are from a site about 9 km from the shoreline, directly inshore from the mouth of the Santa Ana River. The Long Beach site is about 30 km WNW of John Wayne Airport, and about 4.5 km from the shoreline, with an east-west direction in this part of San Pedro Bay. Station locations for instruments are shown in Figures 6-2, with additional stations shown in Figure 6-3.

Sea breezes normally arise from differential heating between the land and coastal sea, and the landward wind, which is at maximum in the late afternoon, is perpendicular to the coastline and drives a density current that moves cool moist marine air over the land (Simpson, 1995). The wind components at John Wayne Airport clearly show the dominance of the cross-shoreline flows with maximum onshore winds in the afternoon (Figure 6-1). (Note that the time zone of the series is GMT so 7 hours need to be subtracted to get local (PDT) time). Wind measurements at Plant #2 close to the beach were not reliable, because of sensor problems during this study. However, wind measurements at Plant #2 in the summer of 2002 show that the daily beach winds are primarily directed across the shoreline, as afternoon beach goers may verify (Largier, personal communication). The cross-shore wind component at the buoy (HB07) is similar to that at John Wayne Airport, except with diminished magnitudes. The alongshore wind, however, is the larger component, and the maximum downcoast winds generally occur 1 or 2 hours later than the onshore component peak. Beardsley et al. (1987) discuss the occurrence of daily alongshore wind fluctuations off the northern California coast, and show that they are not caused by normal sea breezes but rather by a daily modulation of the marine layer inversion, partly caused by the barrier of the coastal mountains. The maximum downcoast daily winds occur in mid-afternoon off northern California, and the cross-shore winds are either very weak or not present. This is clearly not the case off Huntington Beach because of the late afternoon maximum of the strong sea-breeze system that is unimpeded by the low relief of the Los Angeles coastal region. Therefore, the dynamics of the sea breeze that produces strong daily alongshore winds on the outer shelf are not clear at present. It is speculated that modulations of the height of the marine layer by the sea-breeze system may be responsible. The coincidence of the daily atmospheric pressure minimum with the maximum alongshore wind could support this.

The wind record at Long Beach Airport shows both cross-shore and alongshore components. The alongshore component is in phase with the alongshore component at the buoy (Figure 6-1). However, the Long Beach station is situated where the coastline curves

and it may be influenced by the topography of the Palos Verde coastal hills just to the north. It does indicate that fluctuating daily alongshore winds may occur over most of the San Pedro shelf.

The regular character of the daily sea-breeze winds is evident from Figure 6-1. There are few studies of the coastal ocean response to daily period winds. An exception is Rosenfeld (1988), who described the surface-intensified daily currents on the northern California shelf. The distribution of current amplitudes in the surface mixed layer, with depth and distance offshore, was attributed to direct forcing by the daily alongshore winds. A difference with the San Pedro currents, described subsequently, is that the northern California measurements showed only small phase changes with depth, whereas on the San Pedro shelf, the phase changes are large (Hamilton et al., 2001). This has important implications for cross-shelf transports in the upper layers.

Lerczak et al. (2001) discuss the generation of diurnal period internal waves off Mission Beach, California. They attribute the observed daily current fluctuations to propagating internal waves forced by the sea breeze. Their observations have similarities to the San Pedro currents in that the current vectors rotate clockwise and decay with depth. However, the Mission Beach diurnal currents were more intermittent than for San Pedro, and extended to the bottom in water depths of 70 m or more. San Pedro diurnal currents are generally negligible below 30 m. The arguments for the existence of propagating internal waves require that the effective Coriolis parameter be decreased by anticyclonic vorticity of the low-frequency current field so that the effective inertial period is longer than 24 hours. The effective local inertial frequency, f_e, is given by Mooers, 1975.

$$f_e^2 = f (f + \zeta) \qquad (6.1)$$

where ζ is the relative vorticity of the flow. In coastal regions, ζ is usually approximated by dV/dx, the cross-shelf gradient of the alongshore component of the current. Off Mission Beach changes in f_e account for the intermittency of the observed wave field as the background currents change (Lerczak et al., 2001). Mission Beach is further south than San Pedro, and, thus, relatively small decreases in effective f, (~8%) allow the propagation of internal waves.

The ratio ζ/f was calculated by least-square fitting a plane to the east and north gradients of the velocity components, at a depth of 5 m, using multiple moorings. The method is similar to that used by Chereskin et al. (2000) for a spatial array of moored instruments. For the outer and inner shelf, moorings HB05, HB06, HB07, HB09, HB10 and HB11, and HB03, HB05, HB09, and HBNC, respectively, were used. The results are very similar to just estimating dV/dx between moorings HB05 and HB07, and HBNC and HB05, respectively. If the ratio ζ/f is less than -0.18, then freely propagating 24-hour-period internal waves are dynamically possible. Above this value, the waves are evanescent. The resulting time series are given in Figure 6-4, along with amplitudes of the diurnal period currents and wind, at HB06, HB03, and the HB07 buoy, respectively. The diurnal amplitudes are calculated by complex demodulation with a 4-day filter and 2-day running means removed. On the inner shelf, apart from a couple of events, f_e is greater than 1 cpd, yet the diurnal current

amplitudes are quite large throughout the summer until the beginning of October. Wind amplitudes also remain fairly constant separated by short calm periods. On the outer shelf, f_e falls below 1 cpd in July and in the second half of September. The diurnal current amplitudes at HB06 show some relative increases during these periods and the event between July 10 and 19 corresponds to a period of calm winds. Thus, there is some evidence that diurnal internal waves could exist on occasion and perhaps enhance the directly forced daily current fluctuations. However, for the majority of the summer and almost always on the inner shelf, f_e is greater than 1 cpd, yet vigorous diurnal current fluctuations are persistent. Therefore, the generation and maintenance of surface-layer diurnal currents for the San Pedro shelf seems to be more complex than by propagation of internal waves, as is the case further south where the continental shelf is narrow (Lerczak et al., 2001).

6.2. Diurnal Period Current and Temperature Fluctuations

The depth profiles of current velocity for each ADCP mooring were analyzed for the diurnal frequency band using EOFs. The longest common period of 84 days that included the near-shore moorings was used for the spectra. The profiles of amplitude and phase for the main transect moorings HB07, HB05, HB03, and HBN2 are given in Figure 6-5. At the outer moorings, the U and V amplitudes are about equal and V leads U by approximately 90°, which indicates that the current vectors rotate clockwise through 360° every 24 hours. The amplitude profiles show two maxima, separated by a minimum. The first maximum is at or near the surface and the second between 15 and 20 m, with the minimum at about 5 to 10-m depth. Below about 30 m at HB07, the diurnal amplitudes become very small. The other noteworthy feature of the depth profiles is the 180° phase difference between the upper and lower maxima. The upper and lower amplitude maxima and the 180° phase shift also apply to the cross-shelf (U) component at the inner shelf moorings HB03 and HBN2. The depth change of phase for the U components is particularly rapid at the 5- to 10-m depth of the amplitude minima for HB05, HB03, and HBN2. The upper and lower maxima also decrease in magnitude from the shelf break to the near shore, as expected, because there is no volume flux through the shoreline. The implications of these results indicate that when the surface sea-breeze-driven current is towards shore, there is an offshore flow at about 10- to 20-m depth, which only extends down to about 30 m, and vice versa. This implies, through continuity, that there is a daily cycle of up and down vertical velocities, which have a maximum at between 5 and 10 m, and occur across the shelf, but are probably most intense on the inner shelf. Thus, the sea-breeze-forced flows are a mechanism where material at about 20- to 30-m depth could be transported across the shelf, and upwelled into the surface layer, and vice versa.

Cross-shelf fluctuations of velocity are the dominant influence on the temperature field, and, therefore, it is expected that the observed temperature fluctuations in the upper 20 m and nearshore will be predominantly diurnal. Figure 6-6 shows a short period of the 5-, 10-. and 15-m temperature records from the main transect, along with winds and sea level. At the nearshore moorings, HBN2 and HB03, the temperature data have a clear daily signal with the coldest water occurring when winds are slack in the early hours of the morning. Moreover, the largest amplitude fluctuations occur at the 5-m level corresponding to the minimum in cross-shelf velocity amplitudes at these sites. Similarly, at HB05, the largest amplitude of the temperature fluctuations is at 10 m, which is also the depth of the minimum cross-shelf

velocity amplitude. At the latter station, there is a little more evidence of semidiurnal fluctuations, but the majority of the record still has a diurnal character. How much the daily heating and cooling cycle influences these temperature records is not yet clear, but because the maximum amplitude fluctuations are subsurface rather than at the surface points to a strong influence from cross-shelf advection. The air temperature record at the buoy (Figure 6-1) shows relatively small 1 to 2°C day-night fluctuations, and generally the subsurface fluctuations exceed this range and are unlikely to be accounted for by surface-heat fluxes. At the shelf-break mooring, HB07, the 15-m level shows more of a semidiurnal tidal character. This level, at this time, is in the thermocline and the fluctuations seem to be more in character with the internal M_2 tide. This is analyzed in Chapter 7. The 5-m level has weak fluctuations, and this reflects the level temperature surfaces in the upper water column at the shelf break (Figure 4-16) and the lack of sea-breeze-forced vertical velocities. Vertical velocity fluctuations are only likely to be important where the sea-breeze-forced currents interact with the seabed in shallower water.

The depth distribution of diurnal period amplitudes and phases of the U component indicate that, at any instant, the onshore-offshore flows cancel out. Thus, the diurnal depth-mean cross-shelf velocities are very small (<1 cm/s) and can be accounted for by the diurnal astronomical tide. This is also true for the along-shelf (V) component at the shelf break, but on the inner shelf, the top to bottom phase difference for V is small (~30 to 60°) and linear with depth (Figure 6-5). The V amplitudes also decrease linearly with depth, which is not the behavior expected of purely tidal flow at diurnal periods. Therefore, it appears that the alongshore diurnal velocities are also influenced by the wind, even though the sea breeze is predominantly cross-shore at the beach. It is, therefore, difficult to separate out the diurnal tide from the sea-breeze currents in the nearshore.

An EOF analysis for the diurnal frequency band was used to characterize the surface current patterns and their relationship to the wind (Figure 6-7). Because phase can change quite rapidly with depth, only the current records that were closest to the surface were used, and because wind and currents have different units, the cross spectra were normalized. The surface currents and winds are almost in phase, with the currents lagging by less than one hour. Thus, when the sea breeze is strongly downcoast at the buoy and simultaneously landward at John Wayne Airport (Figure 6-1), the surface currents across the shelf are also downcoast. Maximum offshore flow at the surface then occurs about 6 hours later (~2300 PDT), and maximum onshore flow about 18 hours later (~1100 PDT). The situation is reversed for the lower layer (10- to 20-m depth), where maximum on- and offshore currents occur around 2300 and 1100 (PDT), respectively. The occurrence of nearshore cold water in the early hours of the morning is consistent with maximum subsurface onshore flows occurring a few hours earlier with upwelling of colder water into the near surface. The close matching of the current phase at HBN2 and HBN3 with the offshore surface currents, where diurnal astronomical tidal currents are weak, supports the notion that these nearshore, along-shelf diurnal currents are primarily wind driven. The current hodographs are roughly circular on the outer shelf, becoming more elliptical with the major axis directed along-shelf in the nearshore, as was pointed out previously in the discussion of the velocity components. The other important point to be made is that these are fluctuations with substantial magnitudes,

even in shallow water. They have comparable magnitudes at the surface to the subtidal flows (Figure 4-6).

6.3. Variability of the Cross-shelf Sea Breeze Circulations

The cross-shelf structure of the sea-breeze-forced currents has been analyzed using the longest possible time series (July 20 to October 12). In Chapter 4, it was shown that the subtidal circulation changes the structure of the cross-shelf temperature fields and strongly influences the presence of colder water in the near shore. Since the diurnal fluctuations are modulations on the longer time-scale changes, the analysis of the cross-shelf diurnal period transport uses the same four periods that were defined by the low-frequency current modes. The mean temperature sections for the four periods are given in Figure 4-16; these fields are subtracted from the temperature records for each period before input into the diurnal frequency domain EOF analysis. The onshore-offshore displacements of the 14, 16 and 18°C isotherms for the four periods are given in Figures 6-8 and 6-9. In these plots, if the isotherm moves further offshore than 3 km from HB01 (i.e., HB05), then this water is below the depth where the diurnal currents are significant. In period 1, the coldest water nearshore (isotherms closest to shore) occurs at neap tide, when tidal period oscillations of the isotherms are very small, despite strong diurnal winds. This appears to be coincidence since it does not hold in the following periods. It is possible that strong uptilting of the isotherms because of large downcoast subtidal flows (Figure 4-14), generates a surface front that inhibits cross-shelf, upper-layer fluxes at these times. When oscillations appear, they are clearly diurnal, despite the spring tides, with the coldest water occurring at the time of minimum sea-breeze winds. In period 2, the upper-layer mean temperature field has fairly level isotherms and this is reflected in the spreading of the depths and positions of the isotherms in Figure 6-8. Again the isotherm fluctuations are dominated by diurnal fluctuations with some semidiurnal influence on the 14°C isotherm. The changing mixtures of semidiurnal and diurnal influences with depth can cause interesting behavior. For example, between July 30 and August 2, the 14 and 16°C isotherm positions generally move in opposite directions (Figure 6-8). The oscillations have similar characteristics in period 3 (Figure 6-9), except that, as the 14°C isotherm moves deeper, the semidiurnal fluctuations become more prominent. This period has times when the sea breeze reduces in strength (August 18-21, and August 28-September 1). Coincidently, the amplitudes of the diurnal fluctuations of temperature and cross-isobath current are reduced and the semidiurnal fluctuations become more prominent. The fourth period occurs while the subtidal isotherms are quite strongly tilted up towards the coast, though the thermocline is much deeper than in period 1. However, similar to parts of period 1, period 4 fluctuations are relatively weak, though apparently not related to the neap tide.

Frequency-domain EOF analyses were performed for the diurnal period band using all the temperature records for each of the four periods. A subset of the velocity records, using the same positions as the subtidal analyses (Chapter 4), but excluding any records below 60 m on HB08, were used for separate EOF analyses. The subset of the results for the main transect are shown in Figures 6-10 through 6-13 where the first modes from the temperature and the cross-shelf (U) velocity component are displayed as contoured cross-sections. Note that the U and V component velocities were part of the same velocity analysis, but the V components are not shown. The first modes explain between 67 and 85% of the total

variance of all the records included in these analyses. The results for period 1 (Figure 6-10) show maximum amplitude temperature fluctuations occur on the inner shelf centered on about 10-m depth. The amplitudes become very small below 30 m for both temperature and velocity and the phase contours are horizontal. The U-component amplitudes show the double maxima at all stations, with the upper concentrated close to the surface and the lower at about 15 m on the outer shelf and becoming shallower as the water depth shoals. Cross-shelf velocity amplitudes decrease towards the shore. Phase differences between the near surface and the bottom, or 25 m, whichever is less, are approximately 180°, showing that the flows at the depths of the maxima are in opposition. This cross-shelf distribution of diurnal velocity components explains the large temperature amplitudes on the inner shelf because of enhanced vertical velocities required by continuity. Horizontal advection of temperature could also contribute to the large nearshore amplitudes because of the cross-shelf temperature gradients in the upper layer, established by the background flows. It is noted that in Figure 6-10, temperature measurements at HB01 are from surface and bottom only so it is possible that larger mid-depth temperature amplitudes are present in shallower water than indicated by the contours. Vertical phase differences for temperature are not large over the depth range of significant cross-shore velocities, and this is also consistent with direct pumping of the isotherms. The same general patterns hold for the other three periods; however, there are some significant differences in magnitudes and the details of the cross-shelf amplitudes and phases.

In period 2 (Figure 6-11), the amplitudes are less than in period 1 and the subsurface U-component maximum is not as well defined in the offshore stations. In this case, with more nearshore temperature measurements available, the maximum in temperature amplitudes extends to at least the 10-m isobath. In period 3 (Figure 6-12), the subsurface maximum in the U components is reestablished, but at deeper depths than in period 1. Temperature amplitudes are small; however, in this period the upper layers are only weakly stratified (Figure 4-16). The higher temperature amplitudes extend further offshore than in the earlier periods and this appears to be a consequence of the deeper penetration depth of the sea-breeze-forced cross-shelf flows. The same trend is continued in period 4 (Figure 6-13), where the subsurface maximum in cross-shelf velocity has moved deeper and the upper layer stratification is further reduced in the offshore. The temperature amplitude maximum has also moved further offshore, indicating that the region where vertical velocities are important is deeper, and has been displaced offshore to between HB05 and HB03. The increasing depth of the subsurface maximum at the outer shelf stations through periods 2, 3, and 4 indicate that upper-layer stratification may have an important role in limiting the penetration depth of the sea-breeze-forced flows. The depth of the subsurface return flows, in turn, determines the region of the inner shelf where vertical transport becomes important. These differences are illustrated in Figure 6-14 where the U- and V- component amplitudes for HB06 are plotted as profiles. The deepening trend, for periods 2, 3 and 4, is clear for both the U and V component. For period 1, the U-component subsurface maximum is slightly shallower than period 2; however, the V-component maximum is as deep as period 4. Surface maxima show a factor two range with period 2 having the smallest value and period 1 the largest. However, at moorings HB03 and HBN2, period 2 amplitudes are the largest for the four periods (Figure 6-14). This may be a consequence of period 2 having more level isotherms than the other periods so that there is less inhibition by surface, cross-shelf density

gradients. HB03 and HBN2 cross-shelf components show the surface and bottom maxima, and the HBN2 along-shelf component linearly decreases with depth for all four periods, similar to the individual mooring analyses given in the previous section. Therefore, the cross-shelf response of the flow field to sea-breeze winds appears to be quite complex, even though the basic flow patterns are quite consistent over the summer. The continuity arguments for enhanced vertical transport on the inner shelf in water depths of 10 to 25 m do not depend on the existence of stratification, and, therefore, could be considered independent of any other internal wave activity.

To examine the coherence between the wind and the surface currents, EOF analyses of these records were performed for each of the four periods. The results are given in Figures 6-15 and 6-16. The relative phases between the wind and current fluctuations are approximately the same for all periods. Comparing the first two periods, the wind fluctuations at the buoy have very similar alongshore magnitudes, with period 1 having slightly larger cross-shore magnitudes. There is, however, quite a substantial difference in the current hodographs over most of the shelf, except for the nearshore at HBN2 and HBN3. A difference between periods 1 and 2 is that the anticyclonic vorticity of the low-frequency flows allows freely propagating internal waves on the outer shelf for substantial parts of period 1, but not in period 2 (Figure 6-4). The presence of propagating waves could enhance the response to the wind and allow the energy to penetrate deeper in the water column as is observed for period 1. Period 3 has less wind energy than period 2, but the current fluctuations are similar or slightly larger. In period 4 (Figure 6-16), the wind fluctuations are similar to period 2, and the current hodographs remain similar to period 3, except in the nearshore where they are again enhanced. Thus, despite relatively constant sea breezes, the response of the currents can have different magnitudes, depending on whether internal waves can propagate, and the stratification of the upper layers that can change the depth profile of the fluctuation amplitudes. It will probably require a model study to sort out the importance of the various influences on the sea-breeze circulation.

Though diurnal period fluctuations have been observed in coastal seas, this is probably the first study where the mechanisms and contributions to cross-shelf transport processes have been comprehensively described and quantified. The importance of sea-breeze-forced flows to nearshore transport processes has probably been underestimated for this region.

6.4 References

Beardsley, R.C., C.E. Dorman, C.A. Friehe, L.K. Rosenfeld, and C.D. Winant, 1987. Local atmospheric forcing during the Coastal Ocean Dynamics Experiment: 1, A description of the marine boundary layer and atmospheric conditions over a northern California upwelling region. Journal of Geophysical Research, v. 92, p. 1467-1488.

Chereskin, T.K., M.Y. Morris, P.P. Niiler, P.M. Kosro, R.L. Smith, S.R. Ramp, C.A. Collins, and D.L. Musgrave, 2000. Spatial and temporal characteristics of the mesoscale circulation of the California Current for eddy-resolving moored and shipboard measurements. Journal of Geophysical Research, v. 105(C1), p. 1245

Hamilton, P., J.J. Singer, E. Waddell, and G. Robertson, 2001. Circulation processes on the San Pedro shelf. Proceeding: MTS 2001 Conference, November, 2001, Honolulu, Hawaii, 8 p.

Largier, John. Personal communication.

Lerczak, J.A., M.C. Hendershott, and C.D. Winant, 2001. Observations and modeling of coastal internal waves driven by a diurnal sea breeze. Journal of Geophysical Research, v. 106, p. 19715-19730.

Mooers, C.N.K., 1975. Several effects of a baroclinic current on the cross-stream propagation of inertial-internal waves. Geophysical Fluid Dynamics, v. 6, p. 245-275.

Rosenfeld, L.K., 1988. Diurnal period wind stress and current fluctuations over the continental shelf off northern California. Journal of Geophysical Research, v. 93, p. 2257-2276.

Simpson, J.E., 1995. Sea-breeze and local winds. Cambridge University Press, 234 p.

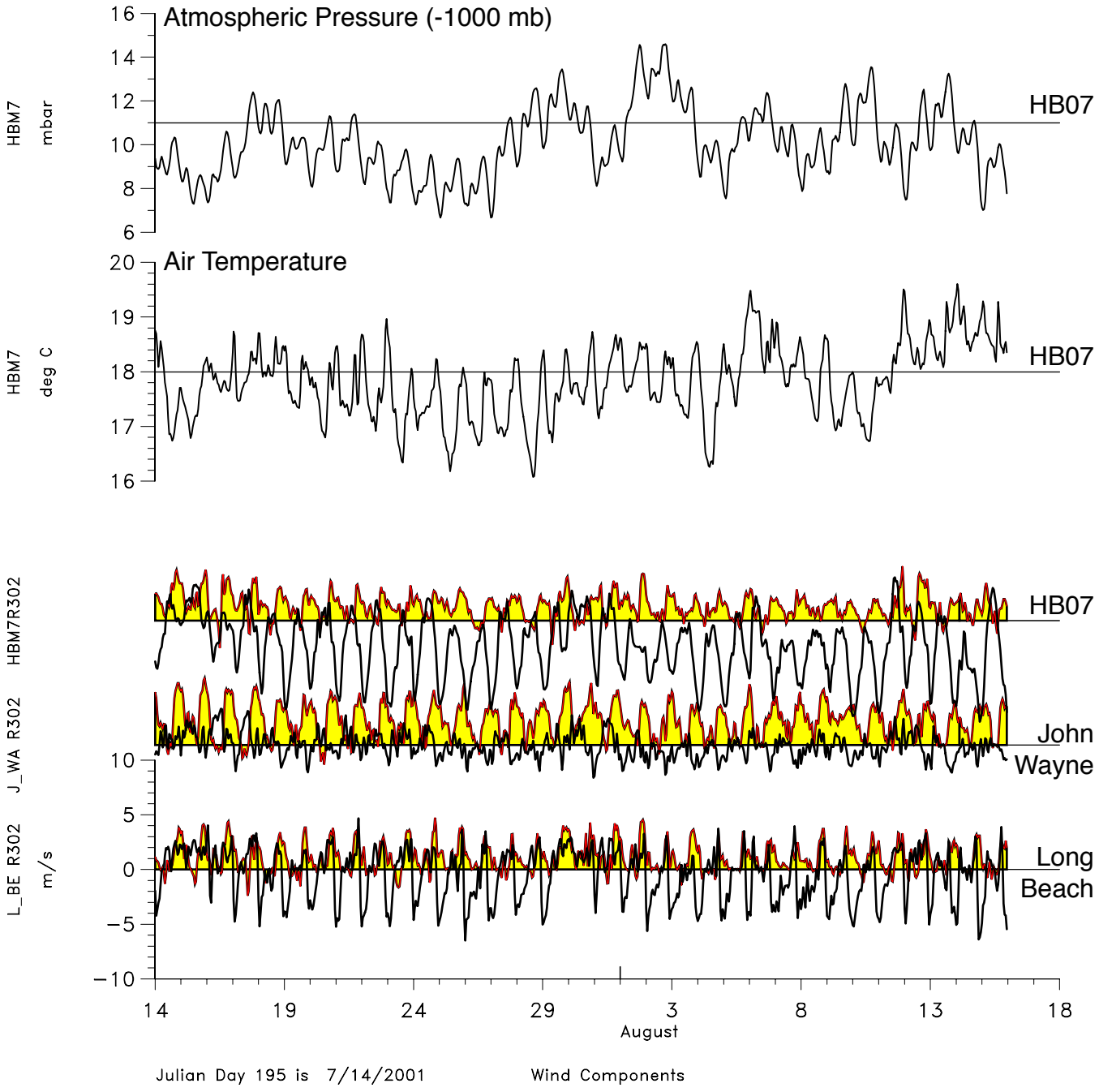

Figure 6-1. Alongshore (302ºT) [black line] and cross-shore (032ºT) [red line with yellow shading] wind components at the indicated meteorological buoy and airports. Wind components use the oceanographic convention of direction towards. Top two panels show air temperature and atmospheric pressure at the meteorological buoy (HB07). Ticks on the time axis are at 0000 GMT for each day.

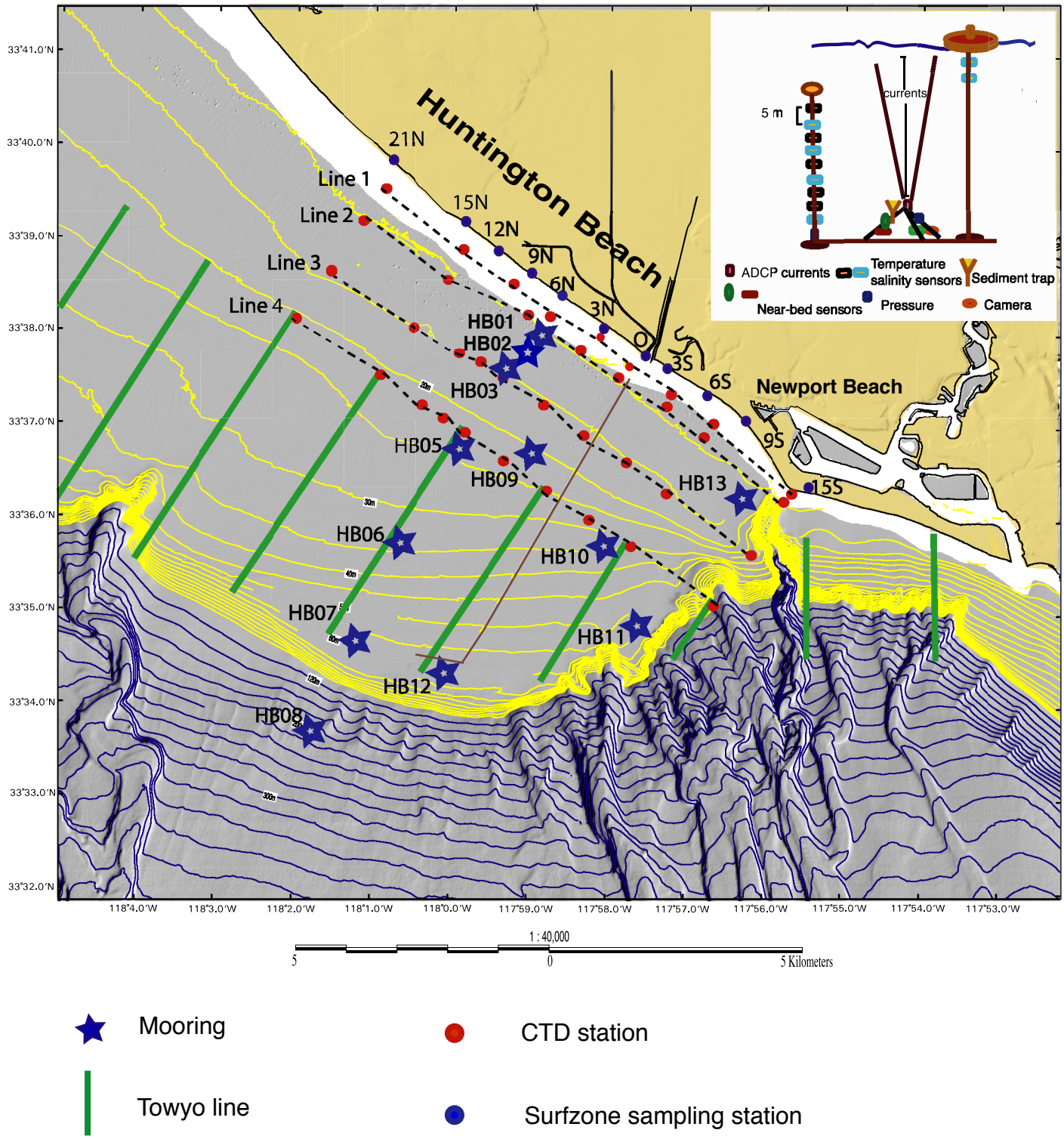

Figure 6-2. Map of the region, mooring sites, surfzone sampling stations, and instrumentations of a typical mooring (inset).

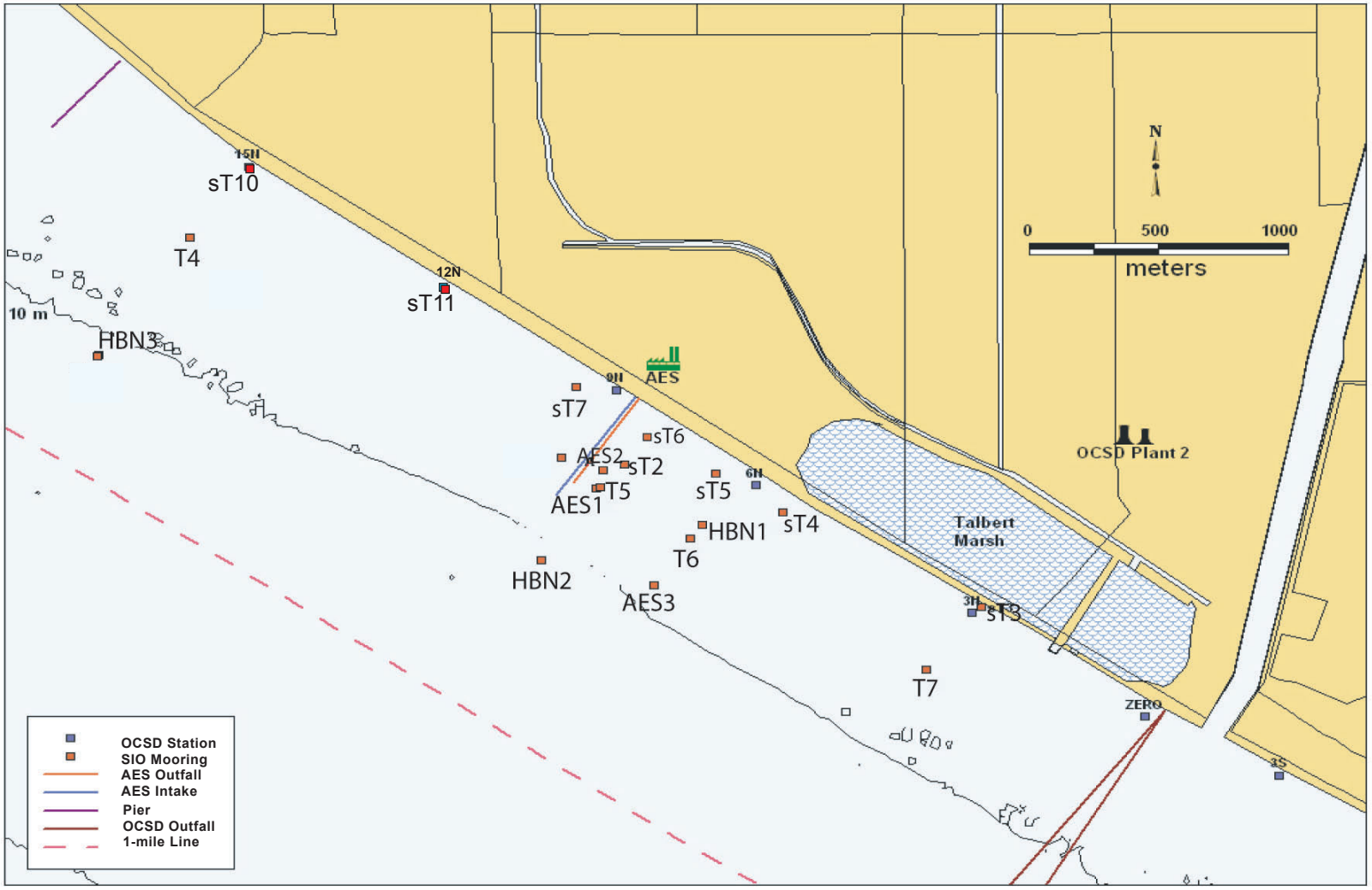

Figure 6-3. Location of nearshore moorings (red squares), beach sampling (blue squares), power plant intake (blue), and discharge (red), Talbert Marsh, and Santa Ana River.

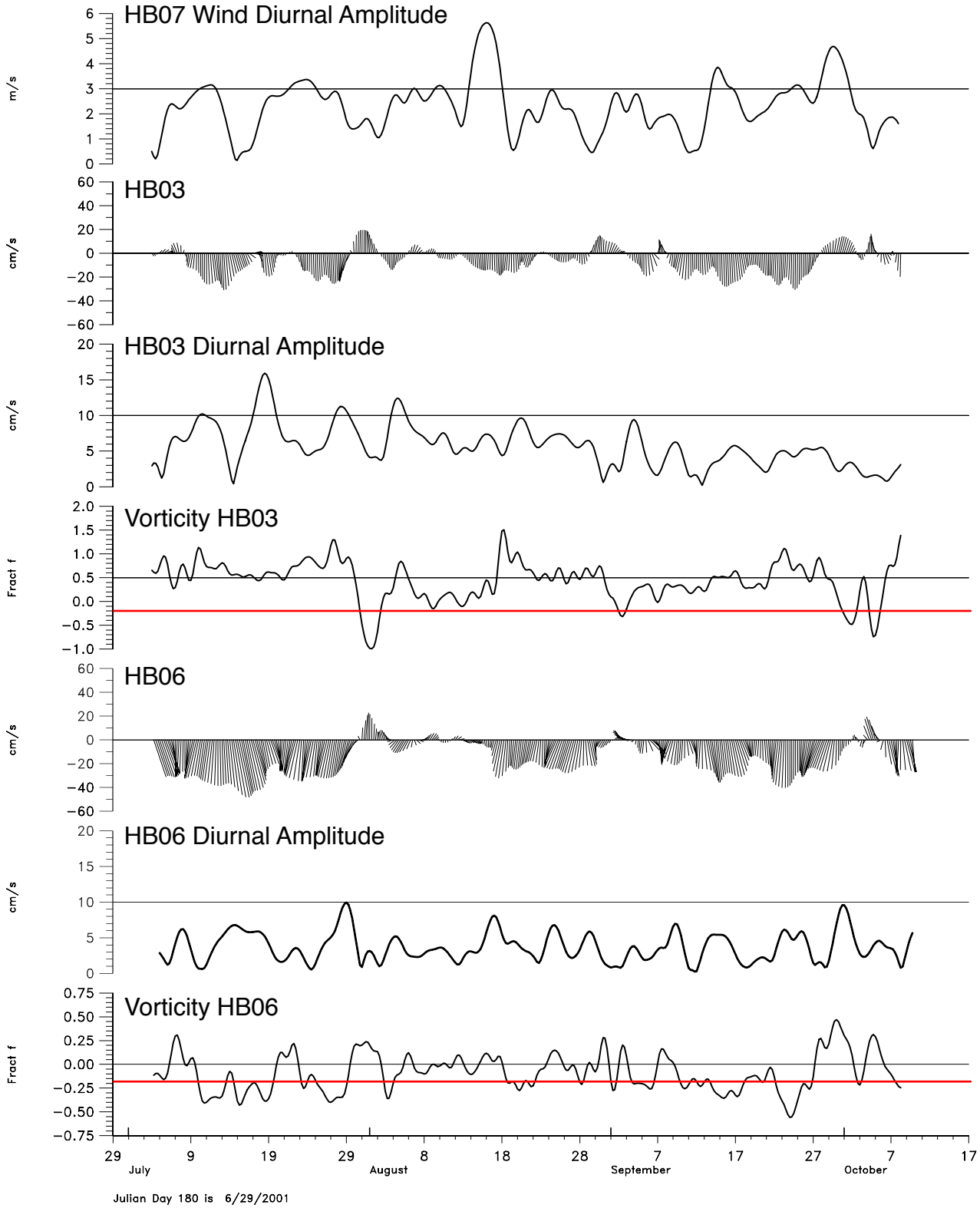

Figure 6-4. Time series of relative vorticity (normalized by f), diurnal current amplitude, and 40-HLP current vectors at 5-m depth for the indicated stations. The red lines denote the value for ζ/f below which diurnal internal waves can propagate. The top panel shows the amplitude of the diurnal wind at the HB07 buoy.

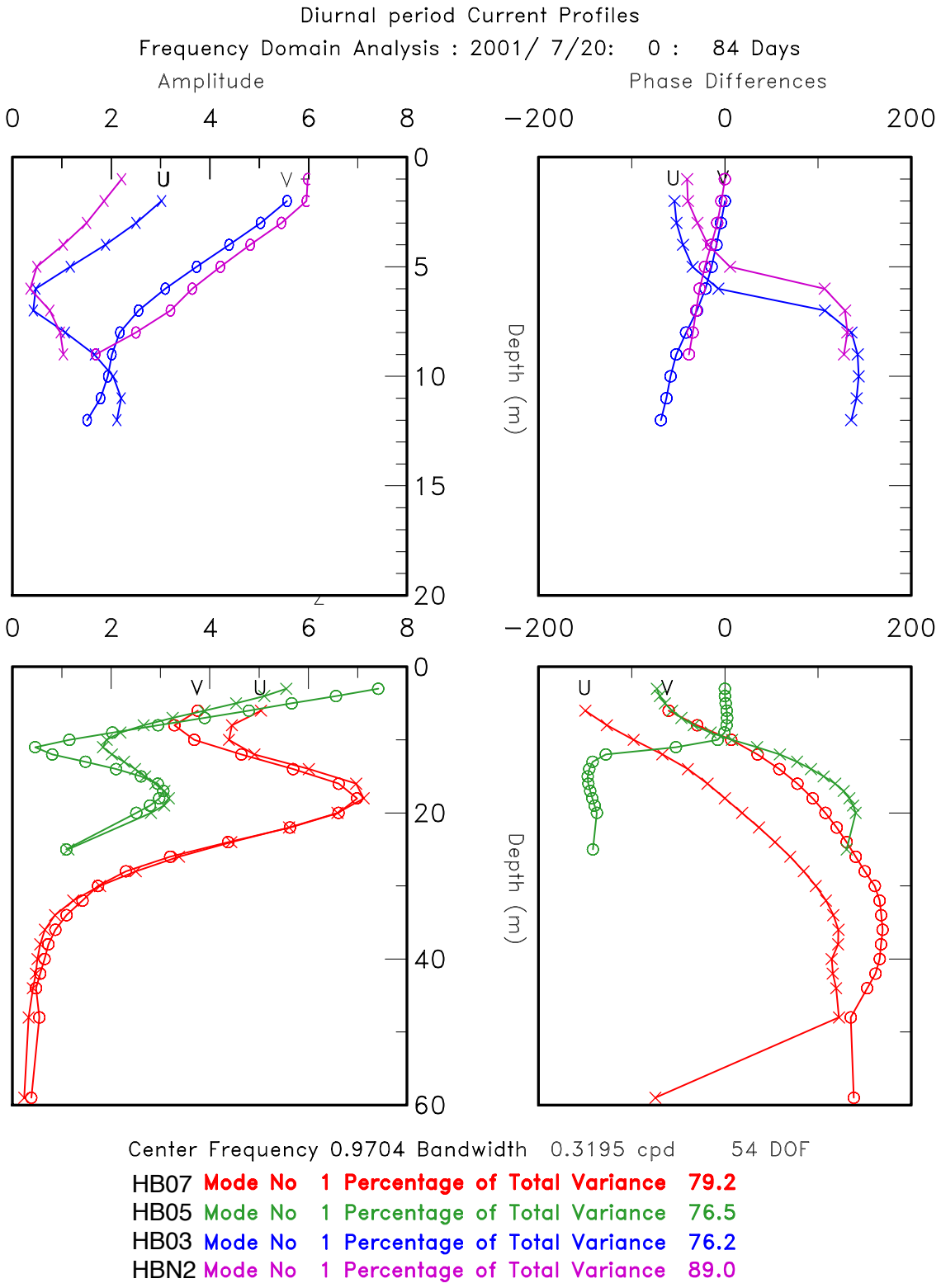

Figure 6-5. Depth profiles of cross- (U) and alongshore (V) velocities from a frequency domain EOF analysis of diurnal period currents for the indicated moorings.

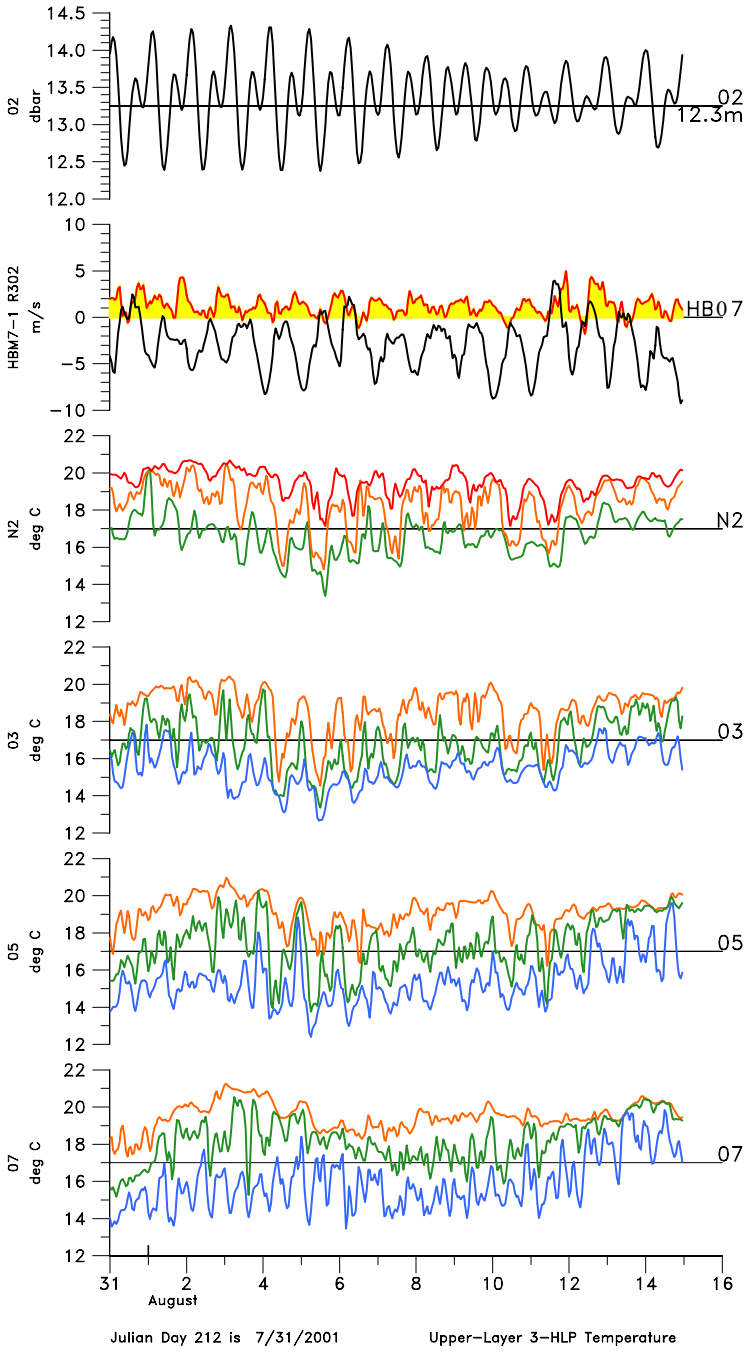

Figure 6-6. Upper layer 3-HLP temperature records from the indicated moorings (bottom 4 panels). Depths are 0.5 m (red), 5 m (orange), 10 m (green) and 15 m (blue). Top two panels are tidal bottom pressure and HB07 buoy winds (black line - alongshore; red with yellow shading - across-shore). Ticks on the time axis are at 0000 GMT for each day.

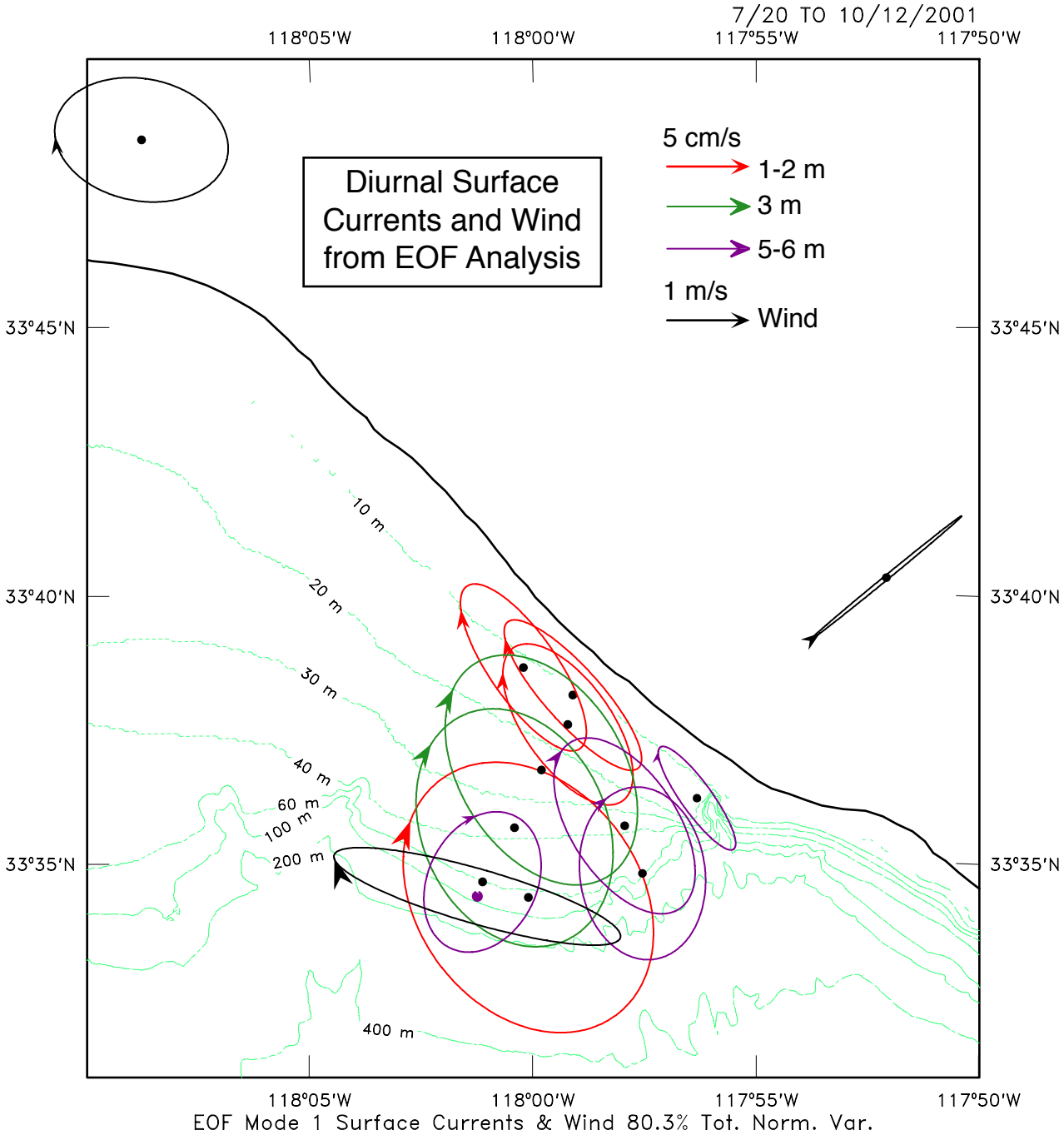

Figure 6-7. Velocity hodographs for near-surface currents and wind from an EOF analysis of diurnal period motions for the indicated period. Arrowheads denote relative phase.

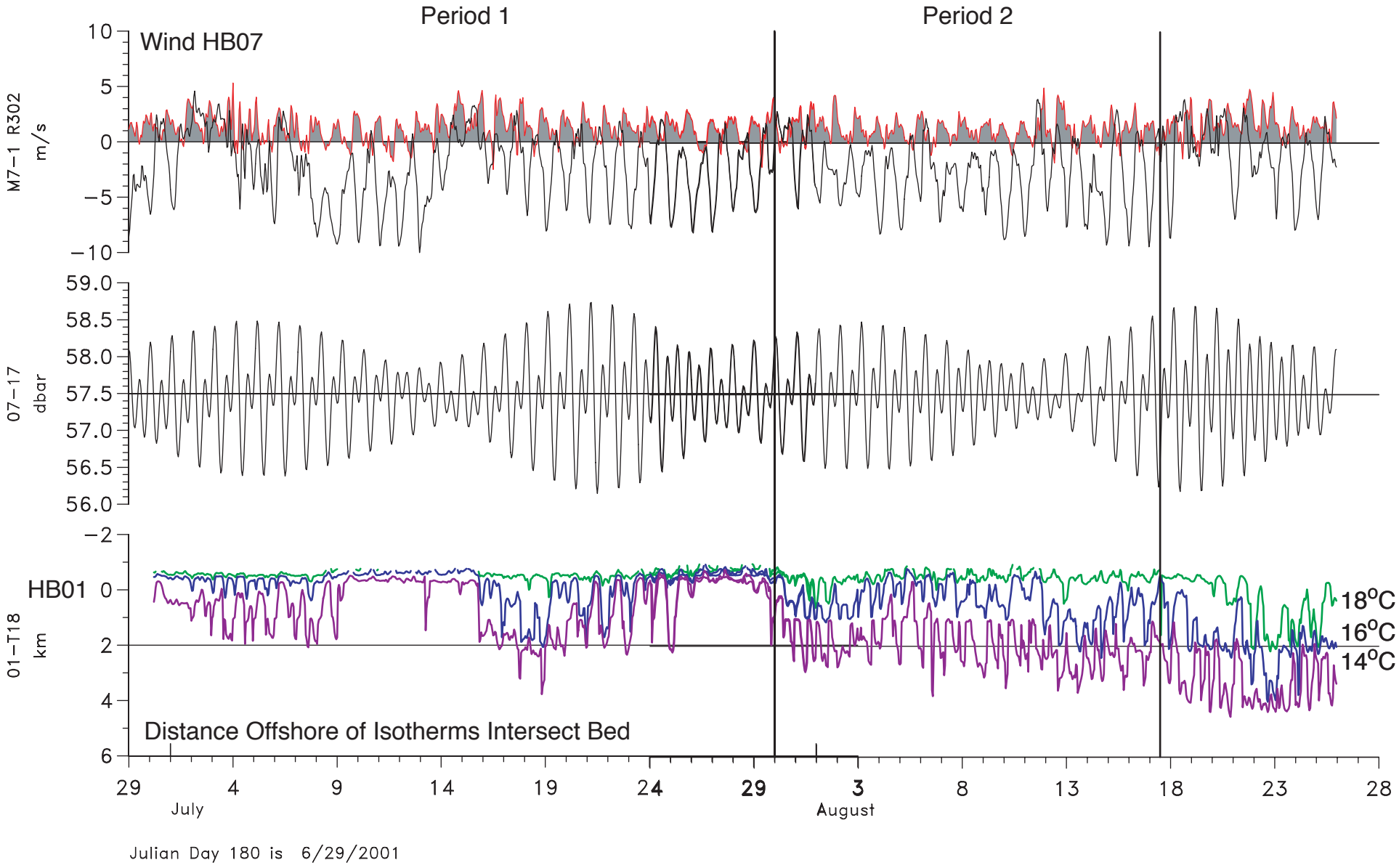

Figure 6-8. 3-HLP time series for analysis periods 1 and 2 of the offshore distance from HB01, along the main transect of the indicated isotherms where they intersect the bed. No line indicates the isotherm has surfaced. The middle panel is sea-level (bottom pressure) from HB07, and the top panel the along- (solid line) and across-shelf (red line shaded) wind components from HB07. Ticks on the time axis are at 0000 GMT for each day.

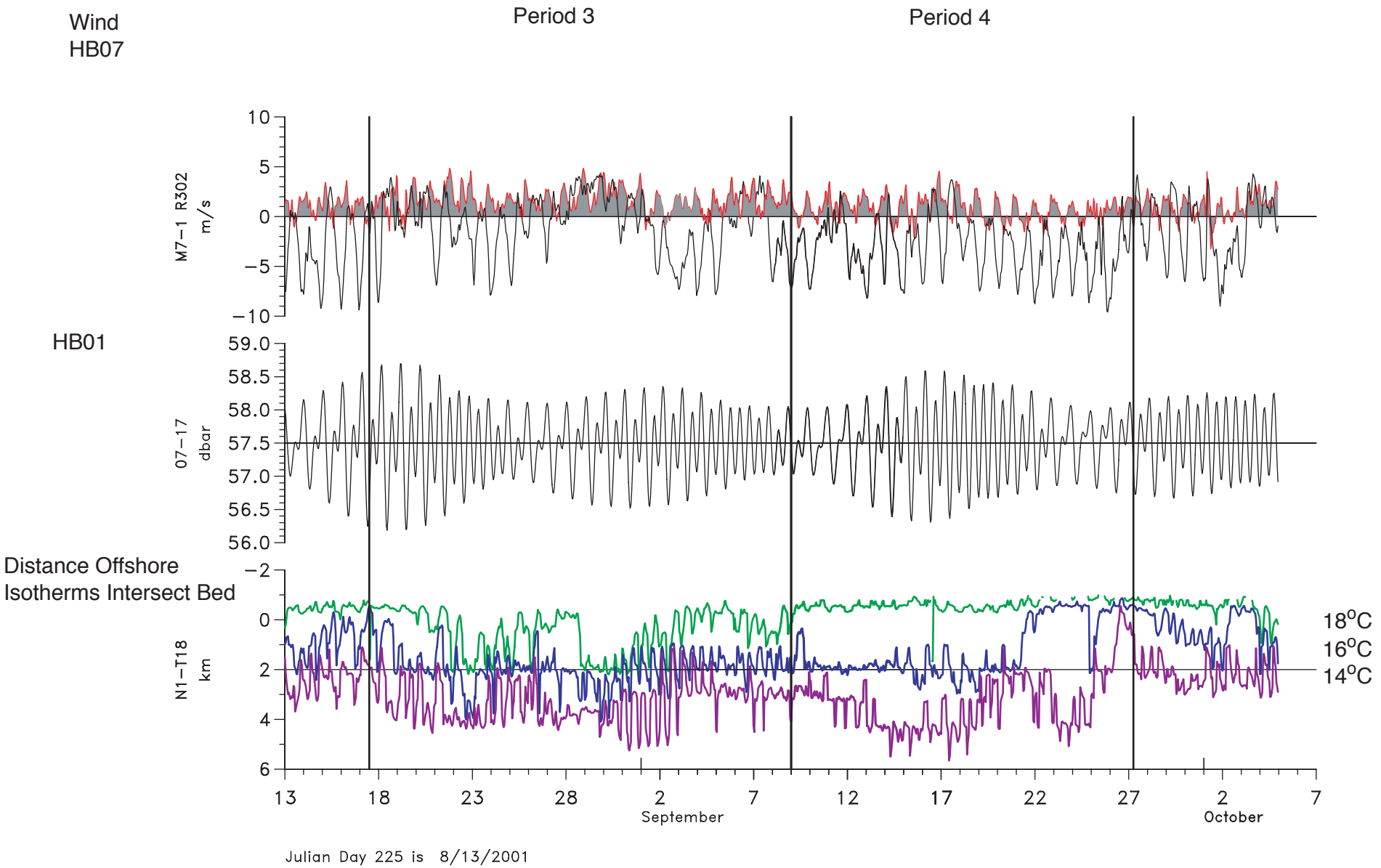

Figure 6-9. 3-HLP time series, for analysis periods 3 and 4, of the offshore distance from HB01 along the main transect of the indicated isotherms where they intersect the bed. No line indicates the isotherm has surfaced. The middle panel is sea-level (bottom pressure) from HB07, and the top panel the along- (solid line) and across-shelf (red line shaded) wind components from HB07. Ticks on the time axis are at 0000 GMT for each day.

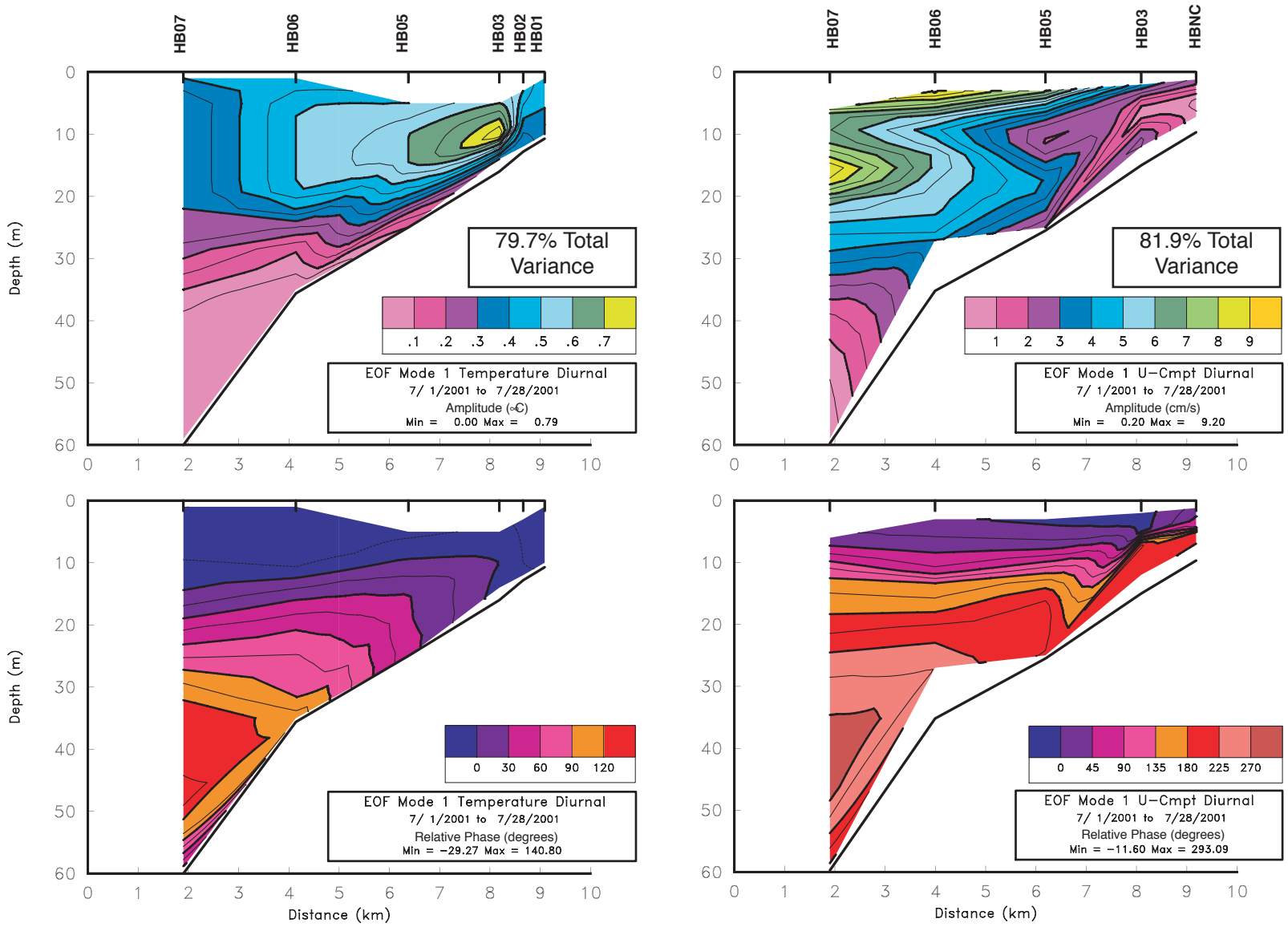

Figure 6-10. Amplitude (top) and phase (bottom) from a diurnal period EOF analysis of temperature (left) and velocity (cross-shelf (U) component shown on the right) for period 1. The first mode from both analyses are shown, and the percent of total variance accounted for by the modes indicated.

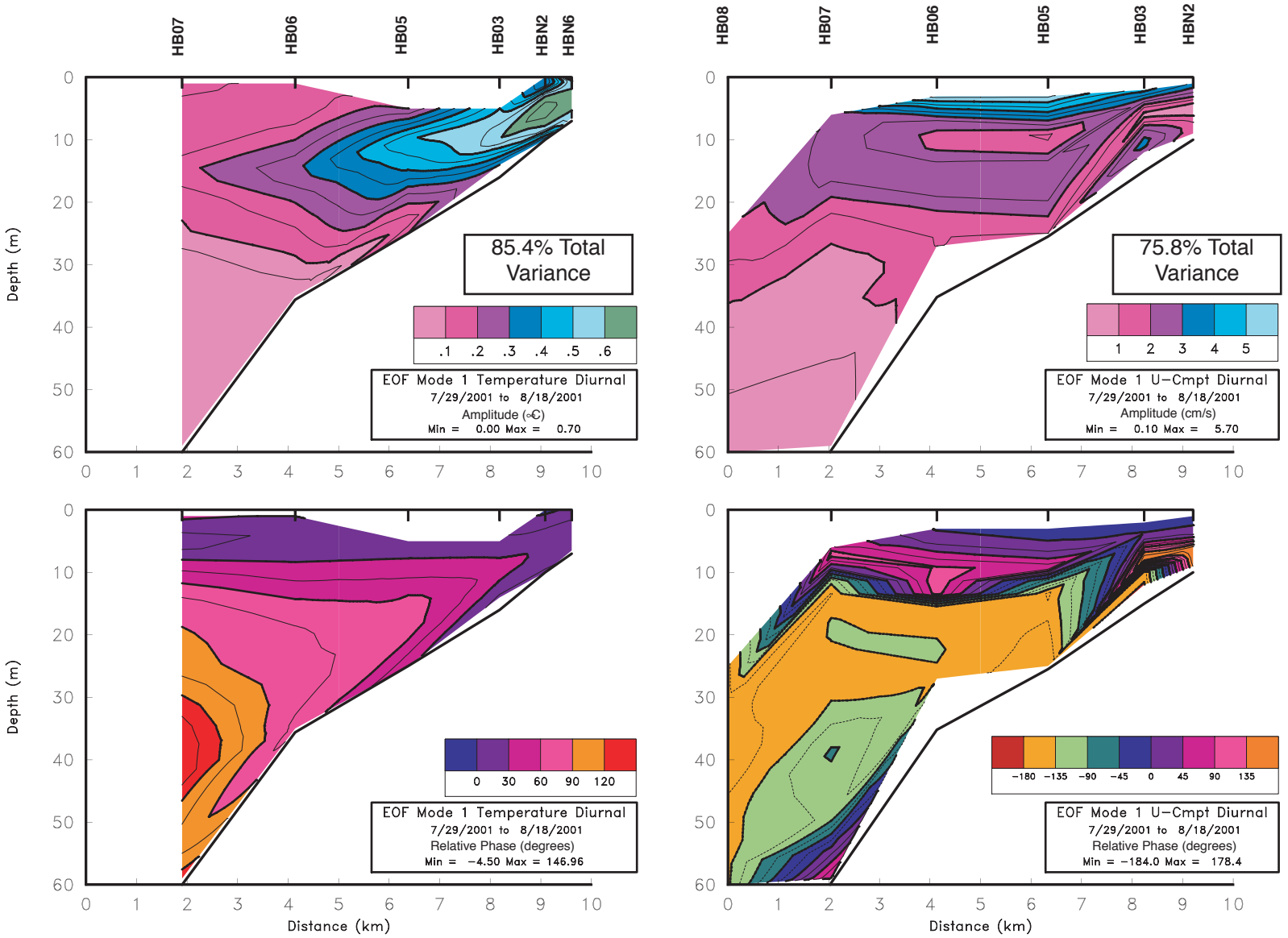

Figure 6-11. Amplitude (top) and phase (bottom) from a diurnal period EOF analysis of temperature (left) and velocity (cross-shelf (U) component shown on the right) for period 2. The first mode from both analyses are shown, and the percent of total variance accounted for by the modes indicated.

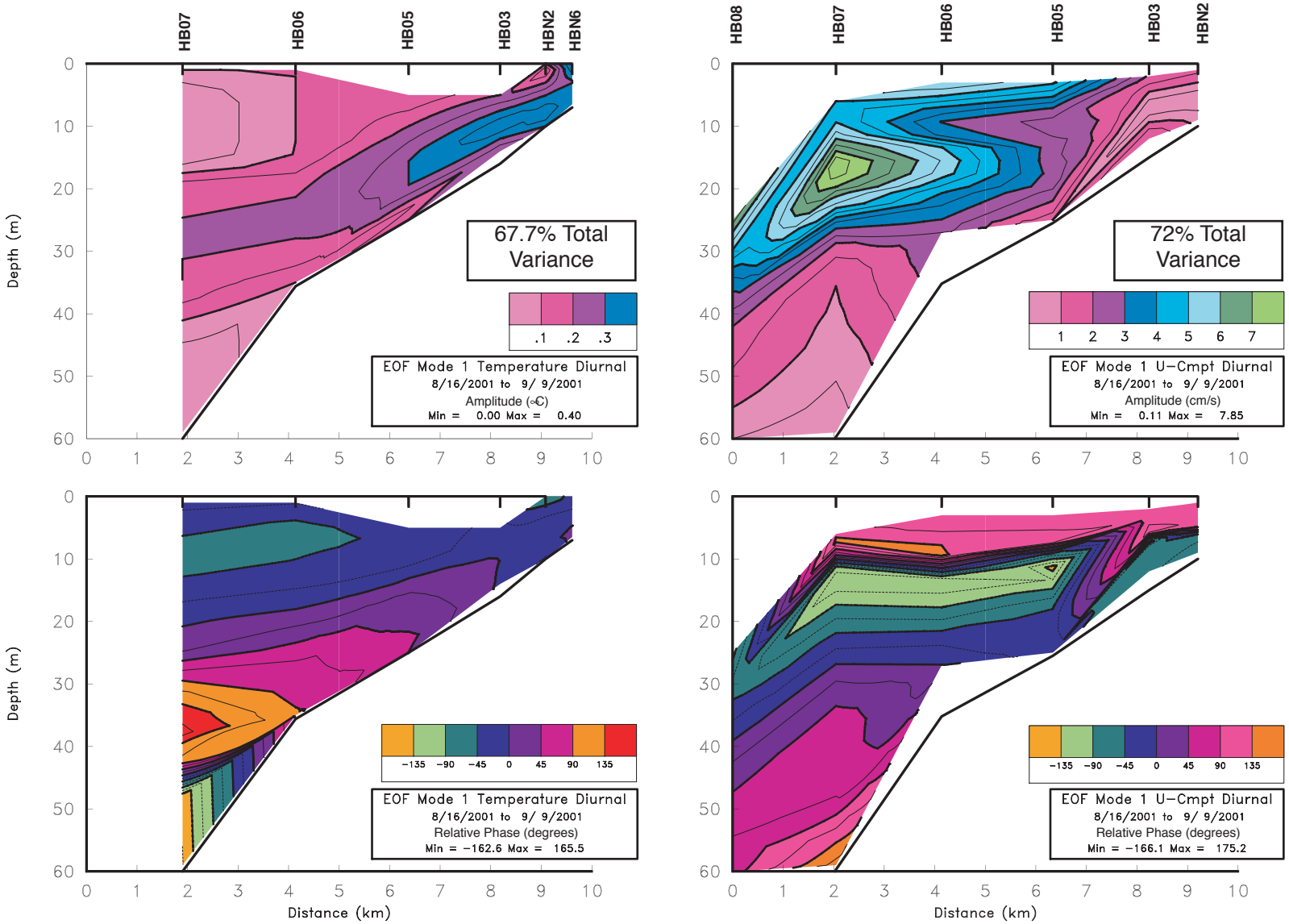

Figure 6-12. Amplitude (top) and phase (bottom) from a diurnal period EOF analysis of temperature (left) and velocity (cross-shelf (U) component shown on the right) for period 3. The first mode from both analyses are shown, and the percent of total variance accounted for by the modes indicated.

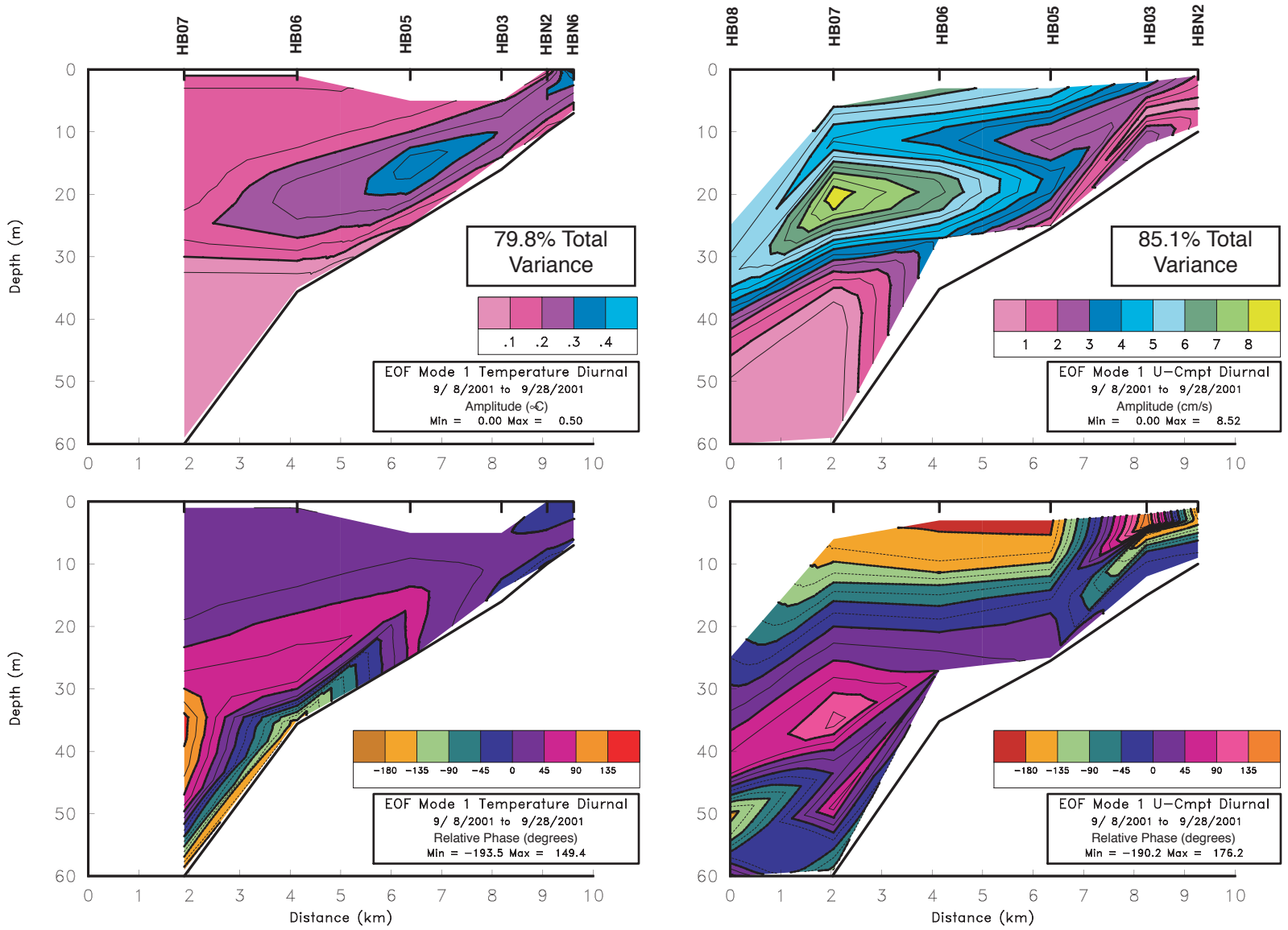

Figure 6-13. Amplitude (top) and phase (bottom) from a diurnal period EOF analysis of temperature (left) and velocity (cross-shelf (U) component shown on the right) for period 4. The first mode from both analyses are shown, and the percent of total variance accounted for by the modes indicated.

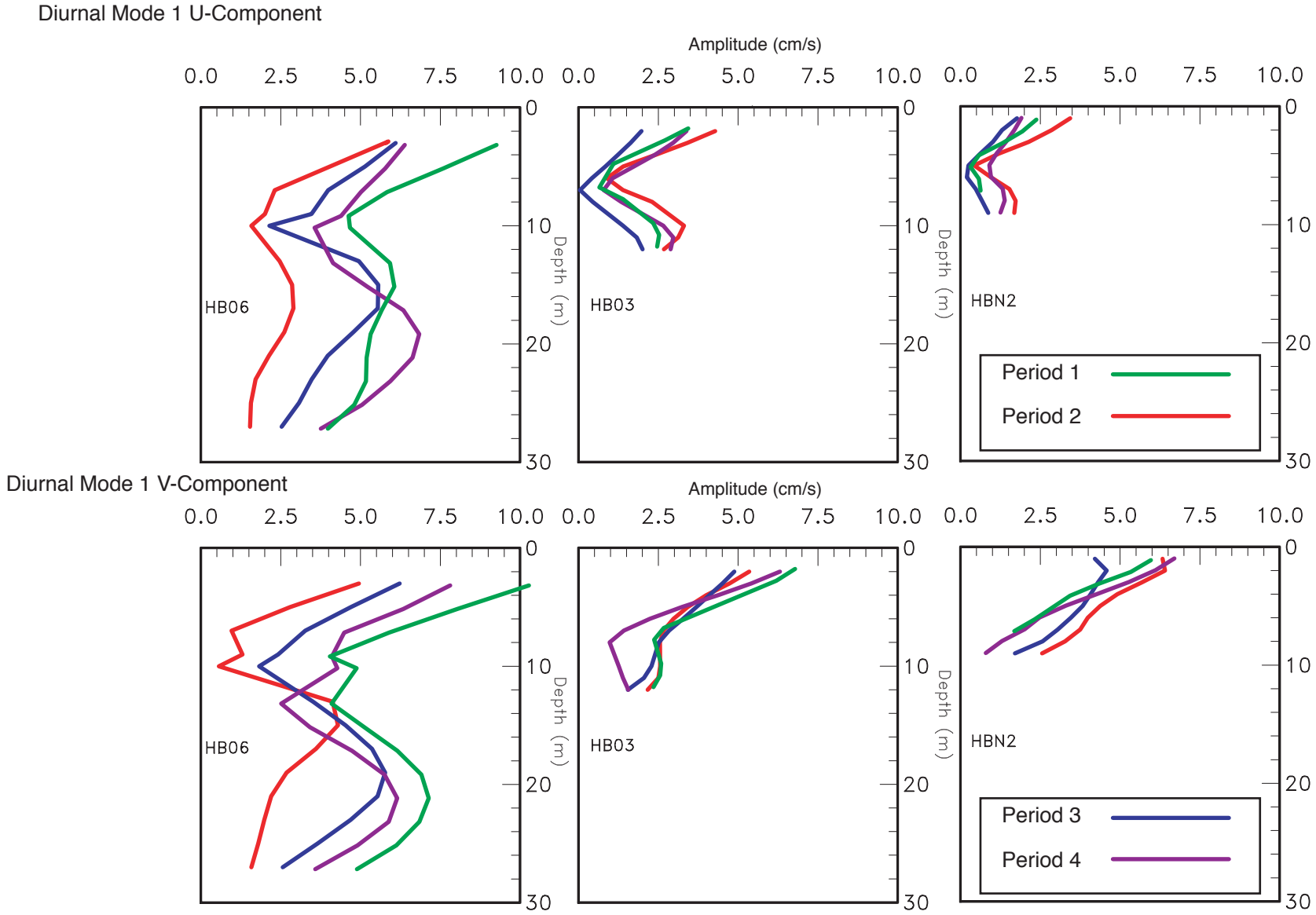

Figure 6-14. Cross- (U) and along-shelf (V) velocity component amplitudes for the four periods. Selected depth profiles for the indicated moorings of mode 1 from the diurnal frequency band EOF analyses are shown.

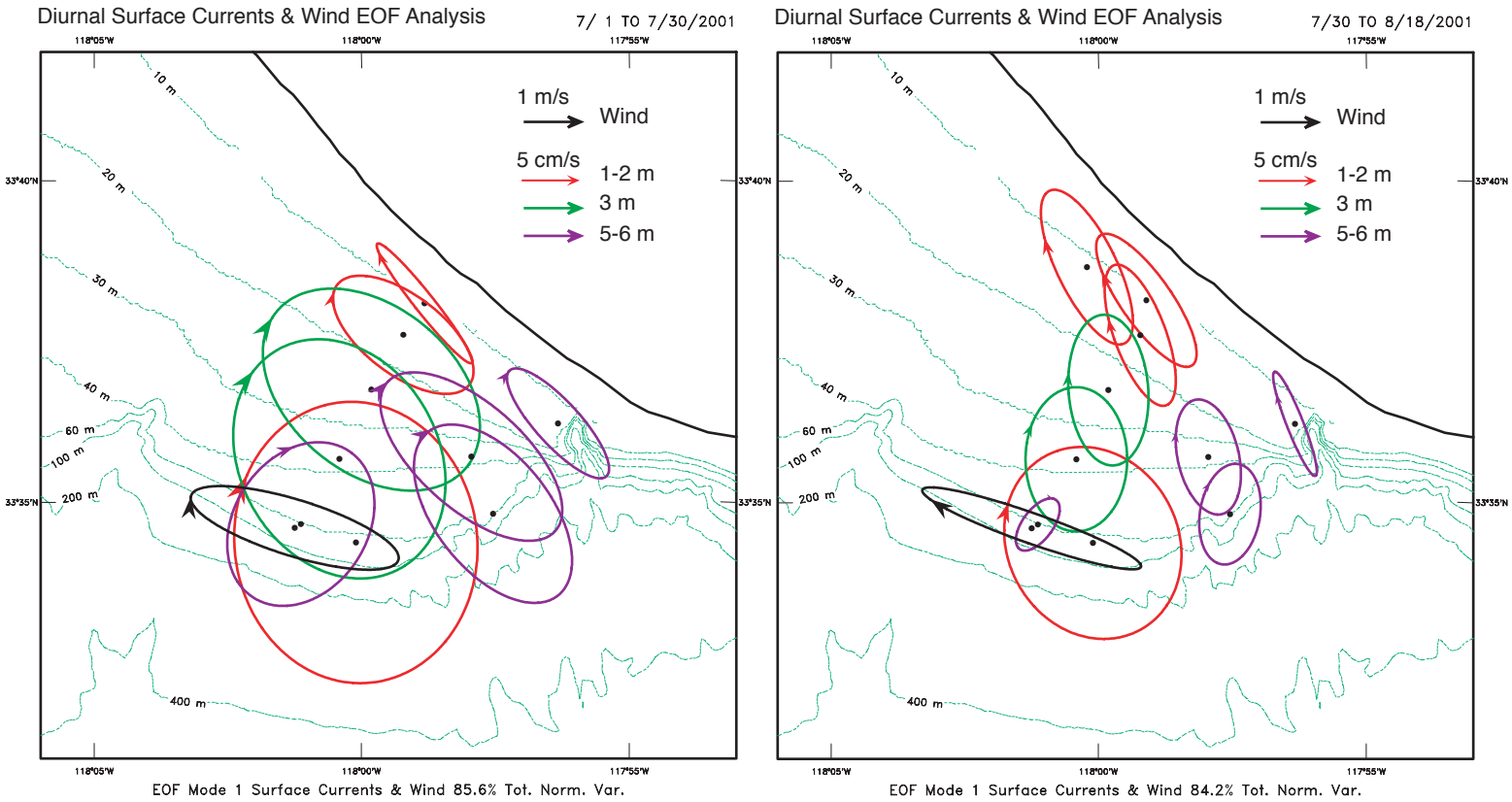

Figure 6-15. Velocity hodographs for near-surface currents and HB07 buoy winds from an EOF analysis of diurnal period motions for period 1 (left panel) and 2 (right panel). Arrowheads denote relative phase.

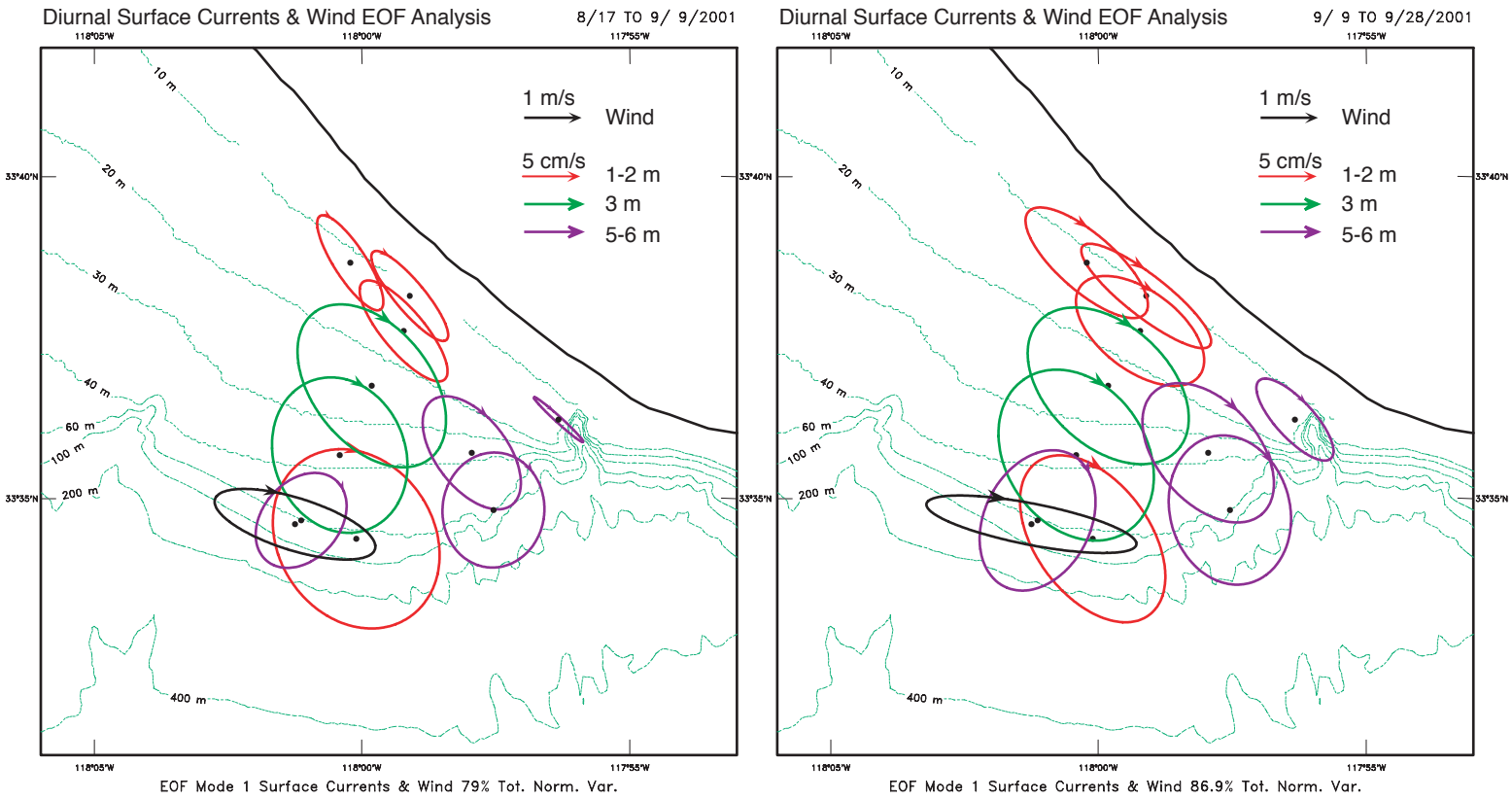

Figure 6-16. Velocity hodographs for near-surface currents and HB07 buoy winds from an EOF analysis of diurnal period motions for period 3 (left panel) and 4 (right panel). Arrowheads denote relative phase.

CHAPTER 7. TIDAL TRANSPORT PATHWAYS

Marlene Noble and Peter Hamilton

7.1. Introduction

Pulses of cool water occasionally appear 1-2 km offshore of Huntington Beach during the summer months (SAIC, 2001; Boehm et al., 2002). The pulses usually move cool water into and out of the nearshore region once or twice a day for periods of several days. Because the cool-water pulses sometimes have temperatures similar to that of the offshore effluent plume, it was hypothesized that semidiurnal internal tidal currents carried water from the offshore effluent plume across the shelf. The shoaling of these internal tidal currents could then carry the effluent into the nearshore region (Figure 7-1). In an effort to decide whether either diurnal or semidiurnal tidal currents could effectively transport the effluent plume across the shelf in the summer of 2001, we determined the characteristics of the persistent barotropic and the more intermittent baroclinic, or internal, semidiurnal tidal currents for the region. The characteristics of sheared diurnal currents, which are predominantly forced by sea breezes, are characterized here and in Chapter 6. As discussed in the previous chapter, cross-shelf diurnal fluctuations are, for the most part, not internal waves, and, thus, less effective at displacing the thermocline. However, if the semidiurnal internal tide raises the thermocline into the nearshore, directly forced diurnal currents may "push" the colder water further inshore (Section 6.6).

7.2. Barotropic Tides

Barotropic tides are characterized by a pronounced deflection of the sea surface. There was a nearly uniform deflection of sea level over the middle and outer shelf (Table 7-1). Sea-level oscillations at the semidiurnal frequencies were about 50 cm for the M_2 and 20 cm for the S_2 tidal constituents. The ratio between the M_2 and S_2 amplitudes was 2.5. This is near the predicted astronomical ratio of 2.1 (Godin, 1972). There was no significant phase difference between these two tidal constituents. There were no direct measurements of pressure at the coast, but sea-level deflections within Los Angeles Harbor were 51 and 20 cm for M_2 and S_2, respectively. This is within the range of measurements offshore. Sea-level deflections at the two diurnal frequencies were smaller than at the semidiurnal frequencies, nearly 21 and 33 cm across the shelf for the O_1 and K_1 constituents, respectively. The phase difference between these two constituents was around 20°, with O_1 leading.

The beat frequency between the two semidiurnal constituents has a period of 14.8 days. About every two weeks, the M_2 and S_2 deflections reinforce each other and sea-level deflections have amplitudes of 70 cm. About 7 days later, the amplitude is reduced to 30 cm. This is the spring-neap cycle in sea level. For the diurnal tidal constituents, the beat frequency is 13.7 days. In July, the larger sea-level deflections caused by the individual diurnal and semidiurnal beat frequencies reinforce each other (Figure 7-2). Hence, the highest highs and lowest lows in tidal sea-level oscillations occur in July off Huntington Beach. The repeat cycle between the two-beat frequencies is 182.6 days, exactly one half of a year. Hence, Huntington Beach will have the largest extremes in sea level in July and again in January for the foreseeable future.

Barotropic tidal currents are expected to have constant amplitude and phase over the water column, providing the measurement site is outside the bottom frictional boundary

layer. In order to estimate the barotropic tidal currents at sites where currents were measured with an ADCP (sites HB11, HB10, HB08, HB07, HB06, HB05, HB03, and HBN2), the currents in each 2-m bin were high-pass-filtered to remove periods longer than 66 hours. The high-pass-filtered currents at each site were then averaged over the entire water column. The amplitude of the barotropic tides was then calculated from the depth-averaged records at each site using the Foreman tidal analysis programs (Foreman, 1977, 1978).

The barotropic diurnal and semidiurnal currents are energetic components of the spectrum for both along- and cross-shelf currents (Figure 7-3a,b). The barotropic semidiurnal currents are more energetic than barotropic diurnal currents. At the semidiurnal frequency, the along-shelf currents are more energetic than the cross-shelf currents, with the largest spectral peaks found over the middle and inner shelf. The semidiurnal cross-shelf currents decrease between the middle- and inner-shelf sites. This is expected because the coast (the coastal wall) imposes a zero cross-flow condition at the shore. The along-shelf currents also dominate the diurnal frequency band. The strongest diurnal currents are found over the inner shelf. The cross-shore currents account for only a minor portion of energy in the diurnal band.

The tidal currents have strong oscillatory motions which result in little net movement over a tidal cycle. An ellipse (Figures 7-4a-g) can describe the speed and direction of the tidal currents over a tidal cycle. The current vectors trace out an ellipse, showing which direction the current is flowing at any phase of the tide.

The strongest currents flow parallel to the long axis of the ellipse. The length of the major axis represents the strength of the flow. For semidiurnal tides, the currents 3 hours later are weaker and flow parallel to the ellipse's minor axis. Six hours later, the currents again flow parallel to the long axis of the ellipse, but in the opposite direction of the flow 6 hours prior. About 12.42 hours later, the currents return to their original direction and speed.

On the outer shelf, barotropic semidiurnal tidal current ellipses are aligned halfway between the along- and cross-shelf directions (Figure 7-4a). Current speeds along the major axis of the M_2 tidal ellipses range between 2-3 cm/s over the outer shelf (Table 7-2). The S_2 constituent is usually less than 1 cm/s. Semidiurnal tidal currents increase slightly in amplitude in shallower water depths. Currents along the major axis of the tidal ellipse can reach 5 cm/s over the middle and inner shelf. But the most notable characteristic is that the barotropic semidiurnal tidal ellipses tend to be aligned parallel to the coast in the shallowest water depths (Figure 7-4a).

The barotropic diurnal tides are weaker than the semidiurnal currents, with speeds on the outer shelf of 2 cm/s or smaller (Table 7-2). However, they share the same characteristics as the barotropic semidiurnal tides. Current amplitudes increase towards the shore and tidal current ellipses tend to be aligned with the local isobaths (Figure 7-4b).

7.3. Semidiurnal Internal Tidal Currents

The characteristics of the average amplitude of the internal tidal currents were calculated from the high-pass-filtered ADCP records that had the depth-averaged barotropic tidal constituents removed. Variance-preserving spectra of these records show that the internal tides account for a varying percentage of the semidiurnal tidal energy over the water column (Figure 7-5a-d). The energy in the semidiurnal surface tides at HB07 is slightly larger than the near-surface internal tidal currents there. However, it is the cross-shore, rather than the along-shore, component that has the largest internal tidal energy, suggesting the internal tidal ellipses are more oriented perpendicular to the isobaths. The energy in the surface and near-bottom internal tides are similar; surface internal tides are only slightly more energetic than internal tides near the bed.

More precise characteristics for the average internal tidal ellipses were calculated at each ADCP bin using the Foreman tidal programs. The semidiurnal internal tides had the expected structure with depth; surface currents were approximately 180° out of phase with bottom currents, even in water depths of 10 m (Table 7-3a,b). The semidiurnal internal tidal current amplitudes were smaller than the barotropic amplitudes, with speeds along the major axis less than 3 cm/s. However, the orientation of the major axis of the semidiurnal internal tidal ellipse was approximately 90° to that of the barotropic (Figure 7-4c,d). The strongest semidiurnal internal tides flowed toward or away from the shoreline both near the surface and at the bed.

The semidiurnal internal tidal currents did not have constant amplitude over the summer months. They can be larger or smaller than their average amplitude for periods of days to weeks. A complex demodulation of the energy in the cross-shore semidiurnal internal tidal band shows that the near-surface tidal currents were strong in early July (Figure 7-6). Cross-shore internal tidal currents can have speeds over 10 cm/s near the end of July and are enhanced for several days in August and September. It is interesting to note that the energetic cross-shore semidiurnal tidal currents did not occur during spring tides, as measured by the pressure sensors. In particular, Energetic internal tides were mainly absent from the inner shelf site in the latter portion of the measurement program. As discussed in Chapter 4, this is probably because of the deepening of the thermocline in August and September that leaves the nearshore less stratified than in early July. The patterns are a little more consistent over the outer shelf where maximum internal tidal currents occur at 4-10 days after maximum spring surface tides.

7.4. Vertically-Sheared Diurnal Tidal Currents

The near-surface currents in the diurnal tidal band are dominated by wind forcing, as discussed in Chapter 6. In order to look more closely at the vertically sheared portion of the diurnal band currents, their characteristics were calculated from the high-pass-filtered ADCP records that had the depth-averaged barotropic tidal constituents removed. Because the K_1 frequency is very close to 1 cycle per day and the daily wind-forced currents are strongest nearer the surface, this analysis is likely to show the strong influence of sea-breeze currents that are not of astronomical origin.

Over the outer shelf, the K_1-sheared currents were largest within 10 m of the surface, with amplitudes of 8-10 cm/s over the outer and mid shelf. More moderate amplitudes, with speeds of 2-4 cm/s, were found within 10-30 m of the surface (Table 7-3c). Near-surface ellipses had moderately circular shapes. Bottom speeds near the shelf break were 1-2 cm/s. As one approached the coastline, near-surface amplitudes remained large over the mid shelf, but near-bottom currents increased as the water depth decreased. Near-bottom currents had nearly the same amplitudes as found in similar water depths at the shelf break. Closer to the coast, the near-surface and near-bottom current ellipses had similar amplitudes and ellipse orientations (Table 7-3c, Figure 7-4e). At the shallowest sites, sheared diurnal ellipses were orientated slightly more along the isobaths.

The sheared current in the O_1 tidal band was much weaker than in the K_1 band (Table 7-3d, Figure 7-4f). Near-surface current speeds over the outer shelf were 1-3 cm/s. Otherwise sheared current characteristics were similar to those in the K_1 band. Near-surface currents were larger than those near the bed over the outer shelf (Table 7-3d, Figure 7-4f). Near-surface and near-bed currents were closer in amplitude in the shallow water near the coast.

7.5. Cross-Shore Transport by Tidal Currents

7.5.1. Event Analysis of Energetic Cross-Shore Tidal Current Pulses

If one assumes that cross-shore currents of the 4 major tidal constituents off Huntington Beach are in phase and reinforce each other, they can flow across the shelf with speeds of 5-8 cm/s below the thermocline on the outer shelf. Water can be transported onshore by this flood tide 0.7 to 1.1 km, which is less than 1/6 of the shelf width. Subsequently, as the tidal currents ebb, the average tidal currents will carry the water about the same distance offshore. On the inner shelf, barotropic tidal currents flow parallel to shore. It is the internal tidal currents, with average cross-shore currents of 2-3 cm/s, that transport water and suspended material toward the coast. Clearly, the average tidal currents will not move suspended effluent material from where it is discharged at the shelf break to the nearshore in a few days or a few tidal cycles.

However, semidiurnal internal tides have larger than average amplitudes for periods of days to a week. During the summer of 2001, the largest cross-shore internal tidal currents occurred in late July (Figure 7-6). A closer examination of this energetic period shows that the pulses have a pronounced mixed tidal signal. That is, every other tidal current pulse can be noticeably larger than the preceding pulse. The effect is compounded if daily wind forcing reinforces the larger of the two pulses. Internal tidal-current speeds near the bed were larger than 10 cm/s. During this same period, cold water was found nearshore. Water colder than 12°C, which is normally found at the shelf break at depths equivalent to that of the core of the effluent discharge plume, is found offshore of Huntington Beach in water depths less than 30 m (Table 7-4).

The large semidiurnal pulses in early and late July and late September show that water cooler than 13°C reaches the 10- and 15-m isobaths (Figure 7-7). It appears that internal tidal pulses, combined with other forcing, can move cool water from below the thermocline

toward the coast. A closer examination of a typical large pulse during a 7-hour period (slightly more than half a tidal cycle) shows that 12°C water migrated about 4 km across the shelf, from 40- to about 20-m water depths (Figure 7-8a,b). Simultaneously, warm surface waters were displaced offshore. About 6 hours later, the cool water moved back offshore and the warm surface waters returned. This pattern repeated itself in the late-night hours for several days. An analysis of the events, combined with the temperature and salinity properties of the water particles and an indication of where the isotherms intersect the seabed, indicates that over a tidal period nearshore cooler water probably advected from no further away than mid-shelf. In addition, the cooler water in the very nearshore region may have been subthermocline, not bottom water, mixed to the surface by the strong internal tidal pulses as they shoaled in water depths of 15 m. It should be noted that water and suspended materials near the shelf break were transported along, as well as across, the shelf. The alongshore currents in the internal tidal pulses had speeds of 10-30 cm/s. Hence, water and suspended materials from the shelf break were displaced up or down coast as they moved toward or away from the beach.

7.5.2. Cross-shelf Displacements of the 14°C Isotherm at Tidal Periods

The large cross-shore tidal pulses discussed above occasionally move water as cold as 12°C (which represents the core of the effluent plume) from the outer shelf into water depths shallower than 30 m (Table 7-4). We can also track the movement of the 14°C isotherm across the shelf at tidal periods for most of the record. Because 14°C water is nearly the same temperature as water at the top of the plume, one can use this isotherm to estimate cross-shore excursions of this portion of plume water.

If, as discussed above, the semidiurnal internal tide is the primary forcing mechanism for the on and offshore displacements of bottom colder water, there should be a direct relation between the tidal-period cross-shelf current fluctuations and the isotherm displacements. This has been studied by calculating the cross-shelf current component (averaged over the portion of the water column beween the 14°C isotherm and the bottom) on the outer shelf that is required to account for the displacements of the 14°C isotherm. This isotherm is representative of the lower thermocline, and is found at about 30-m depth in July, though it deepens with the thermocline through August and September. The 14°C isotherm is approximated as an impermeable surface, and the implicit assumption is that the tidal cross-shelf flow regime is uniform in the along-shelf direction. The relations between the cross-sectional area, along the main transect and below the 14°C surface, and the depth-mean current component is given by the equation in Section 4.1.5. The method of calculation is the same as discussed in that section except that 3-HLP isotherm depths are used. The results of calculations of U, the cross-shelf transport between 14°C and the bottom at HB07, derived from the rate of change of the cross-sectional area, are given in Figure 7-9, where the cross-sectional area and the onshore position of the 14°C surface where it intersects the bottom, are also given. U is compared to the mean cross-shore component of velocity at HB07, where the ADCP depth bins and the bottom current meter are averaged between the position of the 14°C isotherm and the bottom. The highest correlation was found when the component direction was taken as the minor principal axis direction for the lower layer (Chapter 4), i.e., approximately normal to the local isobaths. It

can be seen that the calculated transport velocity and the observed mean current component correspond quite closely, both in the amplitudes of the fluctuations and their phasing.

Both the calculated and observed velocities in Figure 7-9 are predominantly semidiurnal. However, the offshore position of the 14°C isotherm has diurnal as well as semidiurnal signals, particularly in July when the isotherm is closest to the coast. Later in the record, as the isotherm moves deeper and out of the influence of the sea breeze, semidiurnal fluctuations dominate isotherm fluctuations. In July, there are times when the isotherm position is virtually stationary (e.g., at neap tides around July 14 and 29), but the cross-sectional area still has large fluctuations. This implies that, during these periods, the cross-shore semidiurnal lower-layer transports are strongly attenuated on the inner shelf. There are also periods (July 20-27 and August 3-8) where the daily inequality in the semidiurnal current amplitudes produces a more diurnal signal in the area, and even more so in the isotherm position. This appears to be because the smaller amplitude cross-shelf current fluctuations do not proportionally perturb the surface as much as the larger. This is a consequence of the diurnal inequality of the semidiurnal tide. However, these predominantly diurnal fluctuations of the 14°C isotherm position occur when it is present in the nearshore, and therefore may be also influenced by the sea-breeze-forced cross-shelf flows.

The mixtures of diurnal and semidiurnal signals in Figure 7-9 are presented as variance preserving spectra where equal areas under the curve represent equal contributions to the variance (Figure 7-10). The offshore position spectra and the upper-layer cross-shelf currents at HB07 show strong variances in the diurnal and semidiurnal bands, but the lower-layer velocity components, both observed and calculated, are strongly semidiurnal. The arguments of Chapter 6 suggest that the diurnal fluctuations in the upper-layer cross-shelf currents are forced by the sea breeze. We expect that the actual amplitude of the diurnal fluctuation in these currents is much smaller than the measured because the maximum amplitude of the sea-breeze-forced current fluctuations is at the surface, which is not well captured by the ADCP. This current is not measured and therefore can't cancel the oppositely directed diurnal fluctuations found just above the 14°C isotherm.

The coherence squared between the calculated and observed velocity components are well above the 95% significance level for both diurnal and semidiurnal frequency bands with only small phase differences (Figure 7-10). The energy in the diurnal band is, however, small. For the isotherm position, where the diurnal energy is substantial, the coherence squared with the observed velocity component is less significant in this band indicating other factors are influencing this signal. However, the coherence squared in the semidiurnal band, for these two series, is again well above the 95% significance level. This confirms the dominant internal tide forcing of the lower layer and the onshore excursions of sub-thermocline water.

7.6. Conceptual Model of Tidal Period Circulation

The preceding sections have shown that for periods shorter than about 30 hours shelf circulation processes are a complex mixture of sea-breeze-forced flows with a 24-hour period and internal tide propagation with predominantly semidiurnal periods. These

processes strongly influence the cross-shelf current fluctuations, and, therefore, dominate the tidal-period temperature fluctuations because cross-shelf density gradients are much larger than along-shelf gradients. In the along-shelf direction, the barotropic tide is also an important contribution to the current fluctuations. In this section, a conceptual description of the cross-shelf circulation processes at diurnal and semidiurnal periods is attempted, since these current fluctuations strongly affect the short-term transport of pollutants across the shelf into the nearshore.

The sea-breeze-forced flows are confined to layers above 30 m, and consist of surface currents that are in phase with the wind fluctuations and subsurface flows between 10- and 20-m depth that flow in the opposite direction. In the cross-shelf direction, this creates a two-layer flow system, and because the amplitudes decrease from the outer shelf towards the shore, it was surmised that vertical velocity fluctuations become important where these flows encounter the sloping seabed. The temperature fluctuations fit this model with predominantly diurnal fluctuations in the upper layer, with maximum amplitudes occurring in water depths of 10 to 20 m and at depths corresponding to the interface between the oppositely directed cross-shelf flows. The depth of penetration of sea-breeze-forced flows varies with the degree of stratification in the upper layers and the horizontal shears of the subtidal currents. The latter affects whether or not diurnal-period internal waves can propagate. If internal waves can freely propagate, the energy of the flows tends to be higher and penetration depths deeper for similar winds than when the diurnal flows are directly forced.

In contrast to the daily period currents in the upper layer, cross-shelf velocities at tidal periods in the lower layer are dominated by the internal semidiurnal tide. Barotropic semidiurnal tidal currents are present, but they are primarily directed along the trend of the isobaths (Figure 7-4g). Therefore, temperature fluctuations on the outer shelf and below 30 m are predominantly semidiurnal. Using the 14°C isotherm as a surrogate for the lower thermocline and the interface between the upper and lower layers, it was shown that the onshore-offshore excursions of this isotherm could be reasonably accounted for by the fluctuations of lower-layer cross-shelf velocities at the shelf break. Moreover, the semidiurnal temperature fluctuations were approximately out of phase between the shelf break and the nearshore. This means that when the 14°C isotherm moves downward at the shelf break, it moves further onshore and to a shallower position where it intersects with the bottom in the nearshore. Thus, the lower layer appears to slosh backwards and forwards across the shelf, forced by the cross-shelf internal tide. The fluctuations of the inshore edge of the 14°C isotherm often have a diurnal, rather than a semidiurnal, character. It is not clear whether this is caused by a non-linear response to the lower-layer cross-shelf velocity fluctuations, which can have a diurnal inequality similar to the surface tide, or whether, when the lower layer penetrates into the nearshore, it is assisted or taken over by the sea-breeze-forced flows.

A sketch of the sea-breeze and semidiurnal internal-tide-forced cross-shelf flow fluctuations is given in Figure 7-11. This is based on the above analysis and sketches the movements of the isotherms. Since the upper and lower layers have different dominant periodicities, there will be times when the sea-breeze-forced currents below ~10 m, on the

inner shelf, may assist or inhibit the onshore slosh of sub-thermocline water toward the shore. This simplified picture of the cross-shelf tidal-period circulation processes is modified by seasonal changes in the depth of the thermocline and its degree of slope, caused by the thermal wind balance with the subtidal along-shore currents. When the thermocline deepens, as it does in August, compared to July, then the lower-layer sloshing is less likely to penetrate into the nearshore, and, because of this, the fluctuations of the inshore edge of the 14°C isotherm will have a more semidiurnal character.

7.7. Relationships Between Cross-Shore Tidal Current Pulses and the Exceedance of AB411 Standards in the Surfzone

In an effort to relate the appearance of the most energetic cross-shore tidal current pulses to the occurrence of bacterial concentrations exceeding AB411 standards at the beach, a time series of cool, nearshore events was constructed. A cool event occurred when the energetic cross-shore current pulses brought water colder than 12°C into 30-m water depth (Table 7-4) or colder than 13°C into 15-m water depth. A cool event also occurred when the nearshore temperature was as cold or colder than the temperature at the top of the offshore effluent plume, irrespective of a transport pathway (Figure 7-7). The July 23-26 cooling events, as judged by both of these criteria, were the largest cooling events in the summer of 2001.

The series of cool events (Figure 7-12) was compared to the dates when types 1, 2 and/or 3 contamination events were found along the local beaches. Most of the nearshore cooling events did not coincide with significant contamination events. Only 3 of the 17 cooling events occurred on days when AB411 standards were exceeded in the surfzone. Most of the large cooling events at the end of July happened after a nearly weeklong beach contamination event. In addition, the strongest internal tides did not tend to occur during spring tides (Figure 7-6), which historically is the most likely time the beach is contaminated.

7.8. References

Boehm, A.B., B.F. Sanders, and C.D. Winant, 2002. Cross-shelf transport at Huntington Beach; Implications for the fate of sewage discharged through an offshore ocean outfall. Environmental Science and Technology, v. 36(9), p. 1899-1906.

Foreman, M.G.G., 1977. Manual for tidal heights analysis and prediction. Institute of Ocean Sciences, Patricia Bay, Sydney, British Columbia, Pacific Marine Science Report 77-10, 97 p.

——, 1978. Manual for tidal currents analysis and prediction. Institute of Ocean Sciences, Patricia Bay, Sydney, British Columbia, Pacific Marine Sciences Report 78-6, 70 p.

Godin, G., 1972. The analysis of tides. University of Toronto Press, Toronto, 264 p.

Hamilton, P., J.J. Singer, E. Waddell, and G. Robertson, 2001. Circulation processes on the San Pedro Shelf. Proceeding, MTS 2001 Conference, November 2001, Honolulu, Hawaii, 8 p.

SAIC, 2001, Strategic Process Study: I, Plume tracking-ocean currents. Final report prepared for Orange County Sanitation District, 61 p.

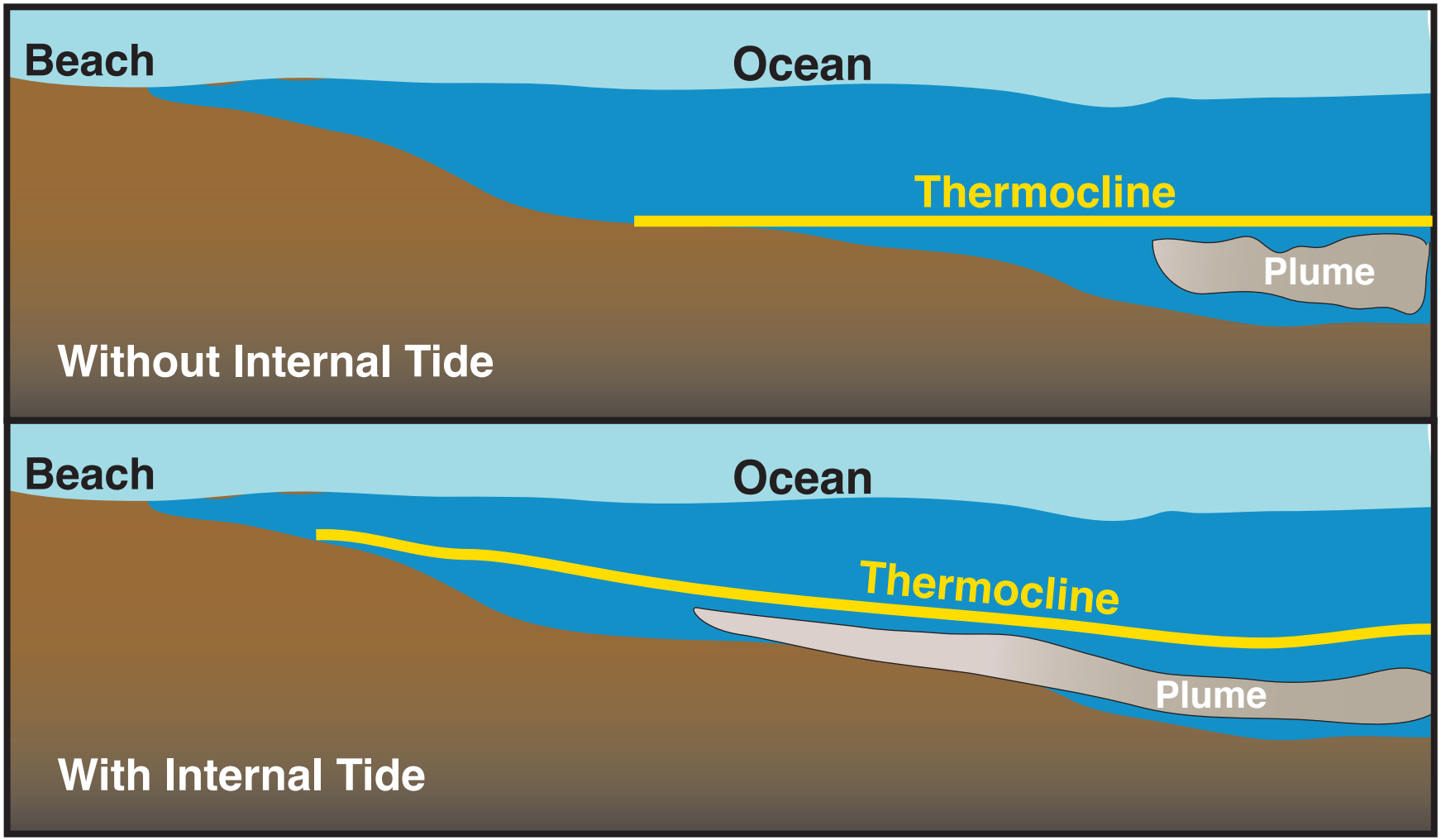

Figure 7-1. Schematic of cross-shore transport of the plume from the outfall by internal tidal currents.

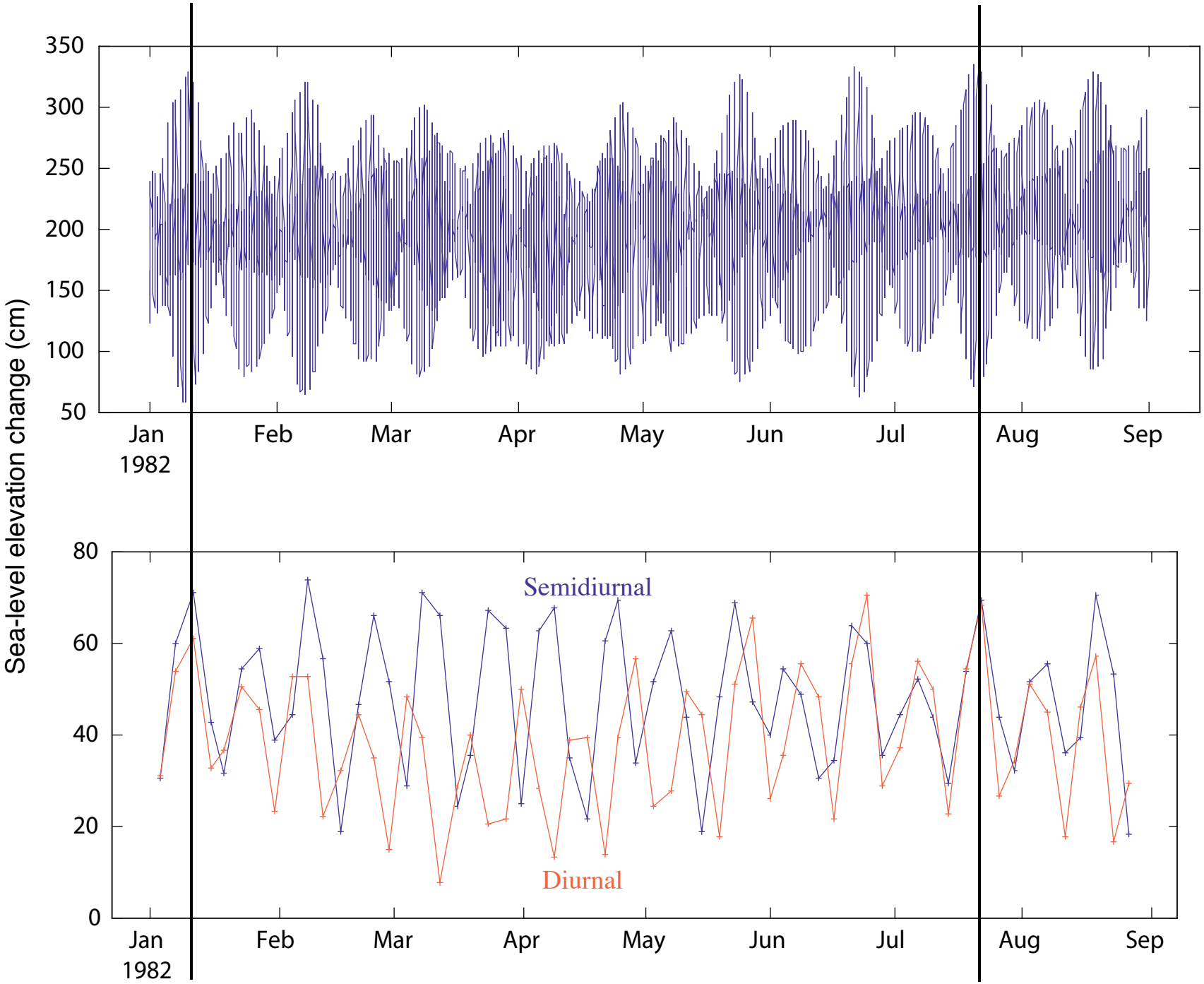

Figure 7-2. Sea level at Los Angeles Harbor (top) and off Huntington Beach, CA, for diurnal and semidiurnal periods (bottom) showing six months beat frequency between the Spring-Neap and Tropic Equatorial cycles.

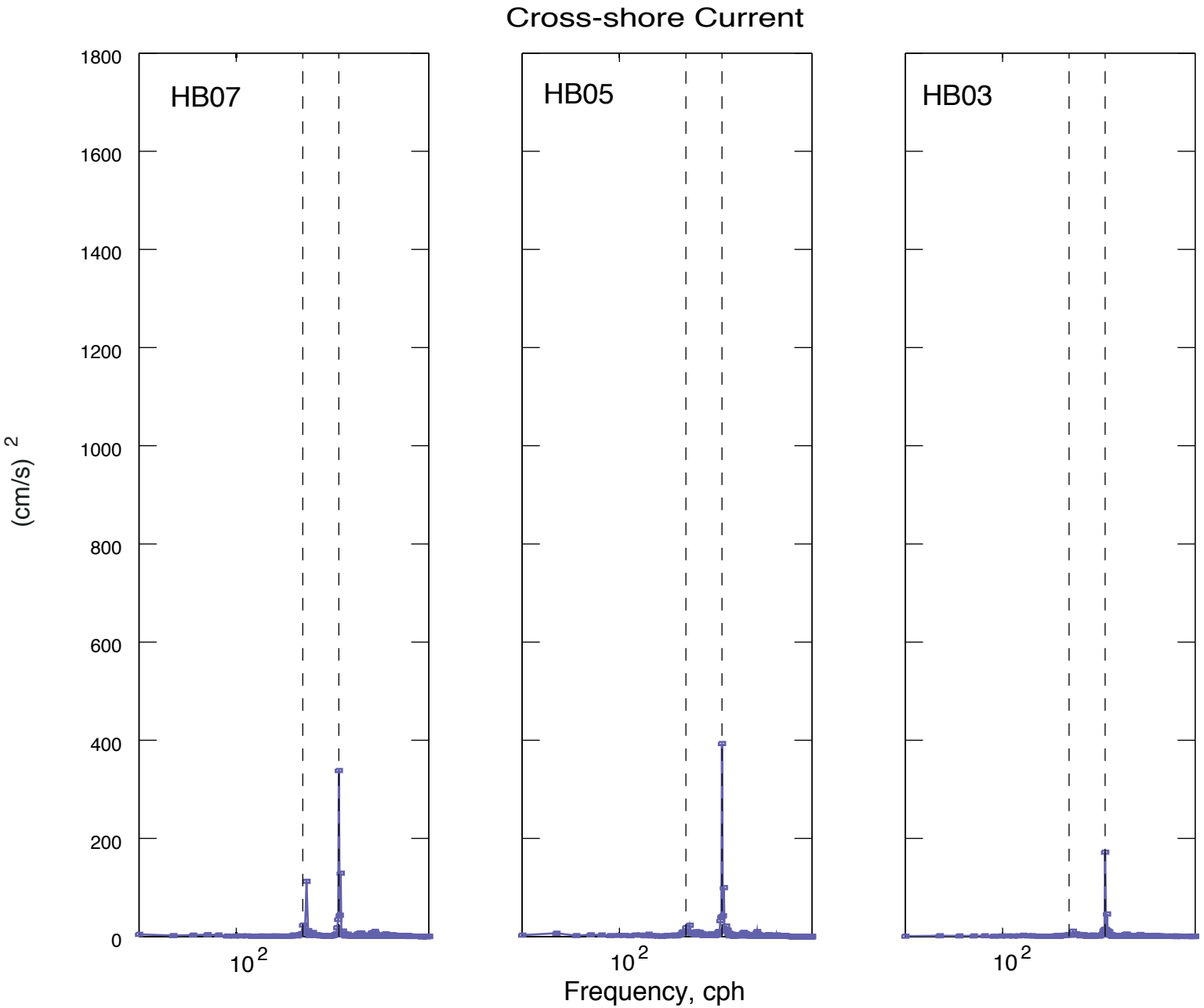

Figure 7-3a. Cross-shore variance-preserving spectra of the depth-averaged along- and cross-shore currents at sites HB07, HB05, and HB03. The subtidal currents have not been removed from these records. The vertical dashed lines in each spectra denote the diurnal and semidiurnal tidal bands.

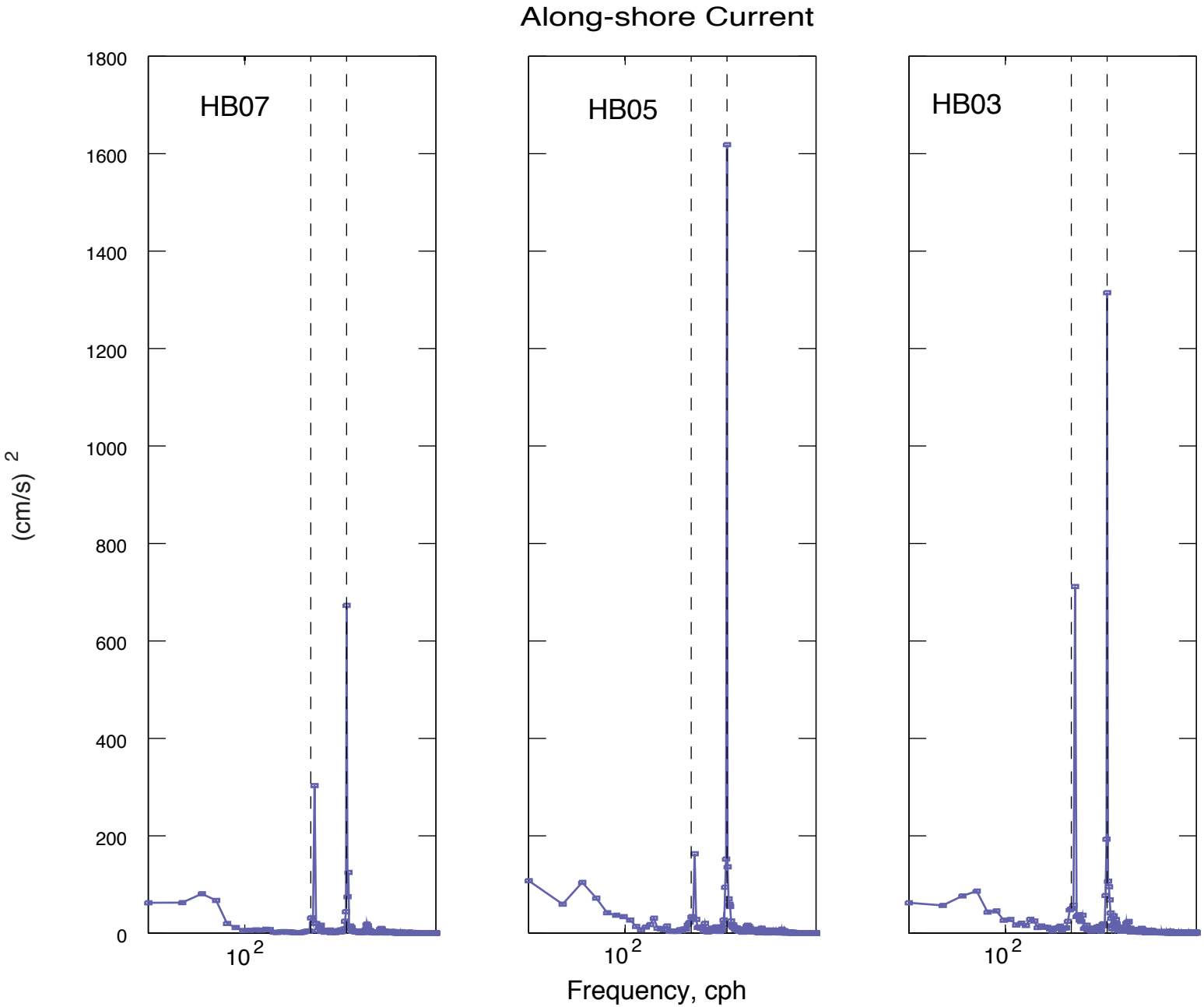

Figure 7-3b. Alongshore variance-preserving spectra of the depth-averaged along- and cross-shore currents at sites HB07, HB05, and HB03. The subtidal currents have not been removed from these records. The vertical dashed lines in each spectra denote the diurnal and semidiurnal tidal bands.

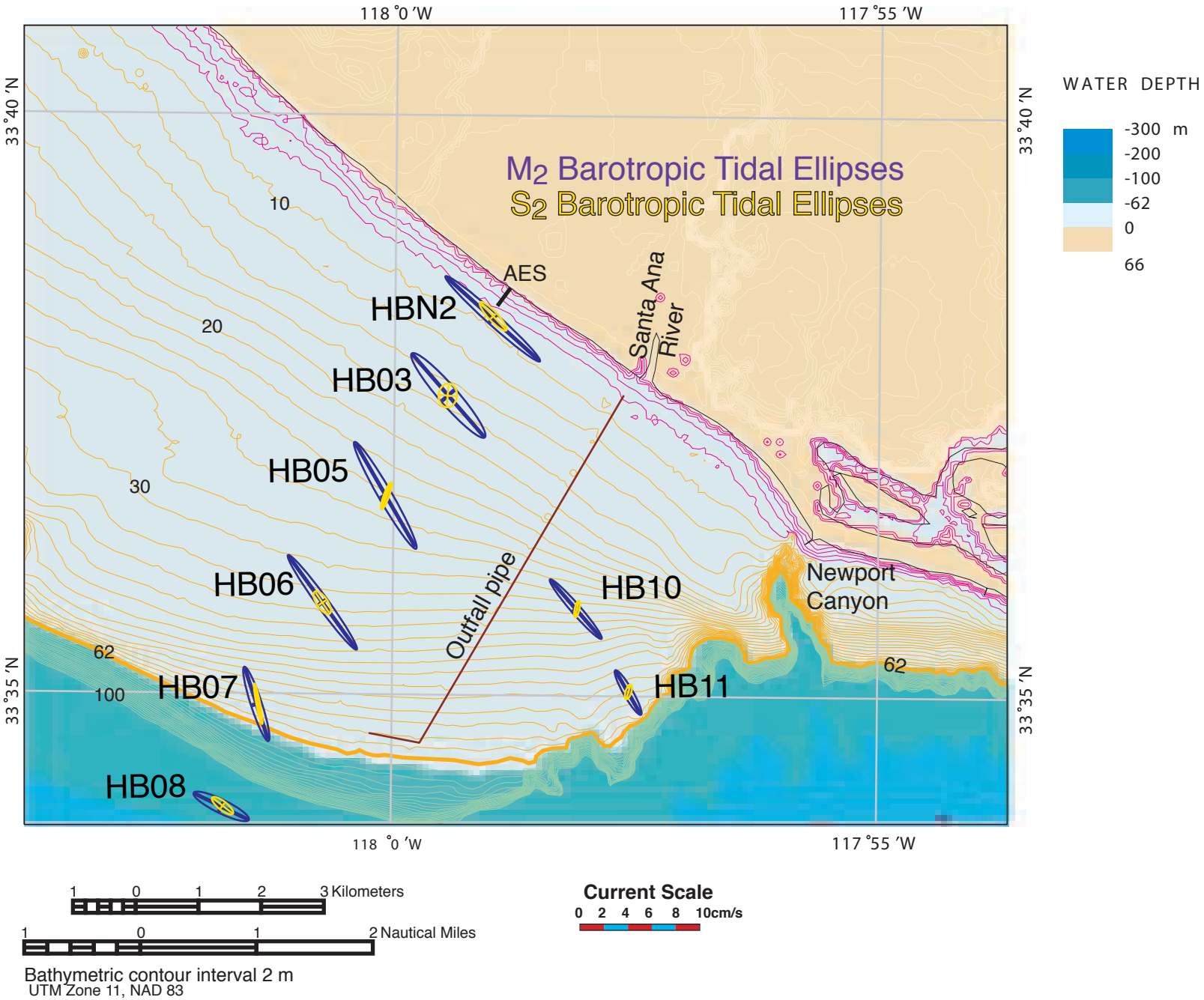

Figure 7-4a. Barotropic semidiurnal tidal current ellipses off Huntington Beach, CA, from June to October 2001.

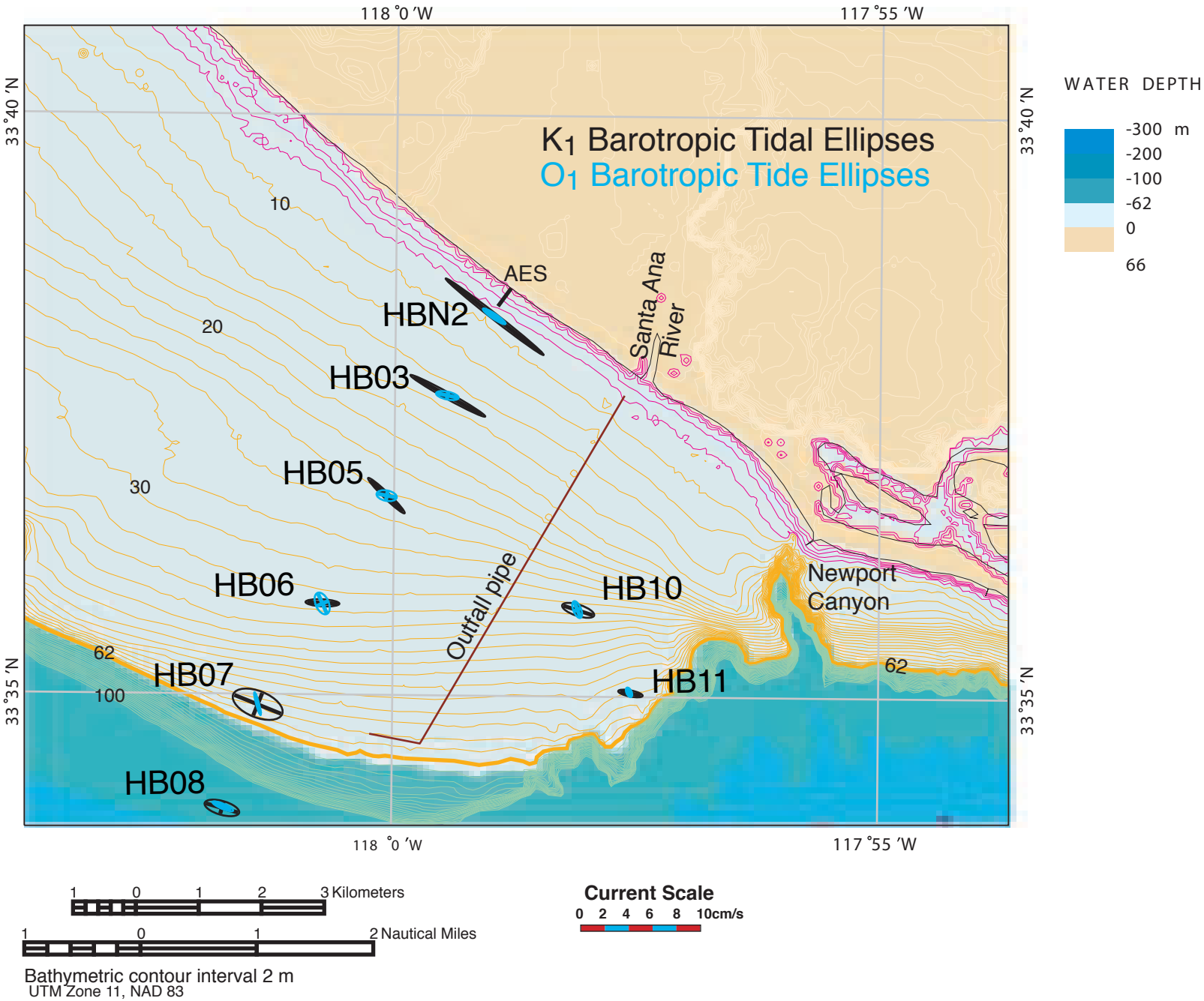

Figure 7-4b. Barotropic diurnal tidal current ellipses in off Huntington Beach, CA, from June to October 2001.

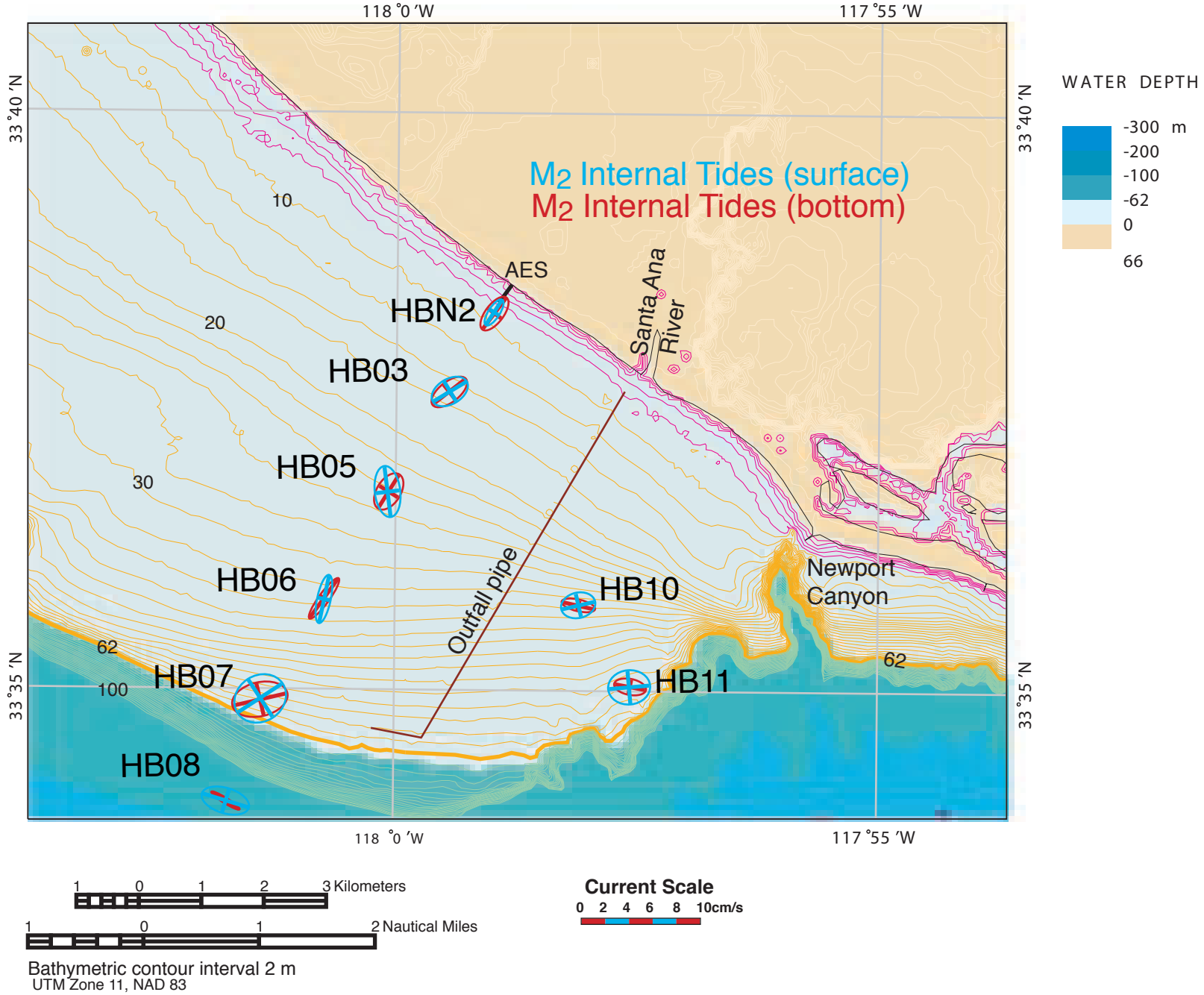

Figure 7-4c. Near-surface and near-bottom M_2 internal tidal ellipses off Huntington Beach, CA, from June to October 2001.

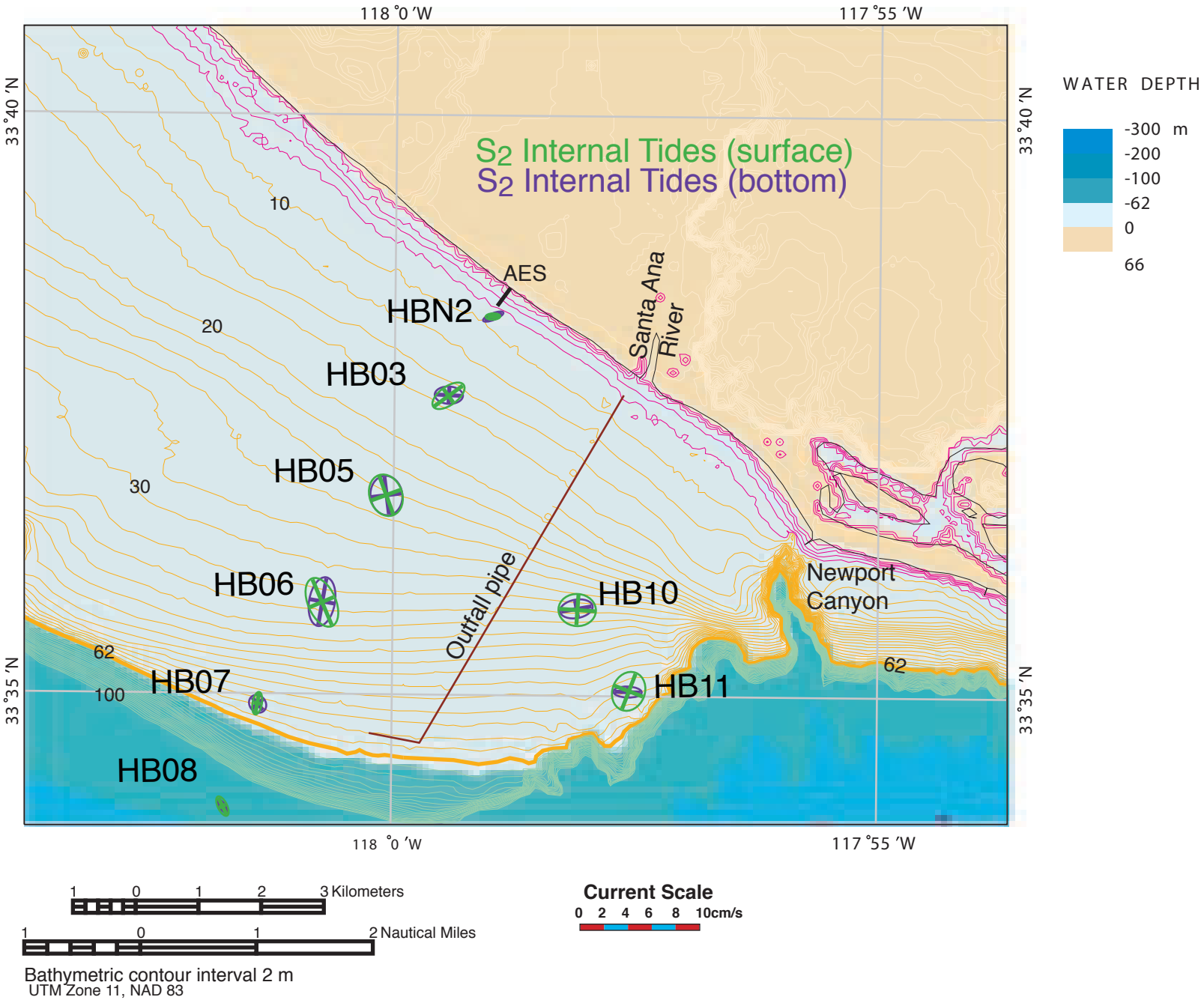

Figure 7-4d. Near-surface and near-bottom S_2 internal tidal ellipses off Huntington Beach, CA, from June to October 2001.

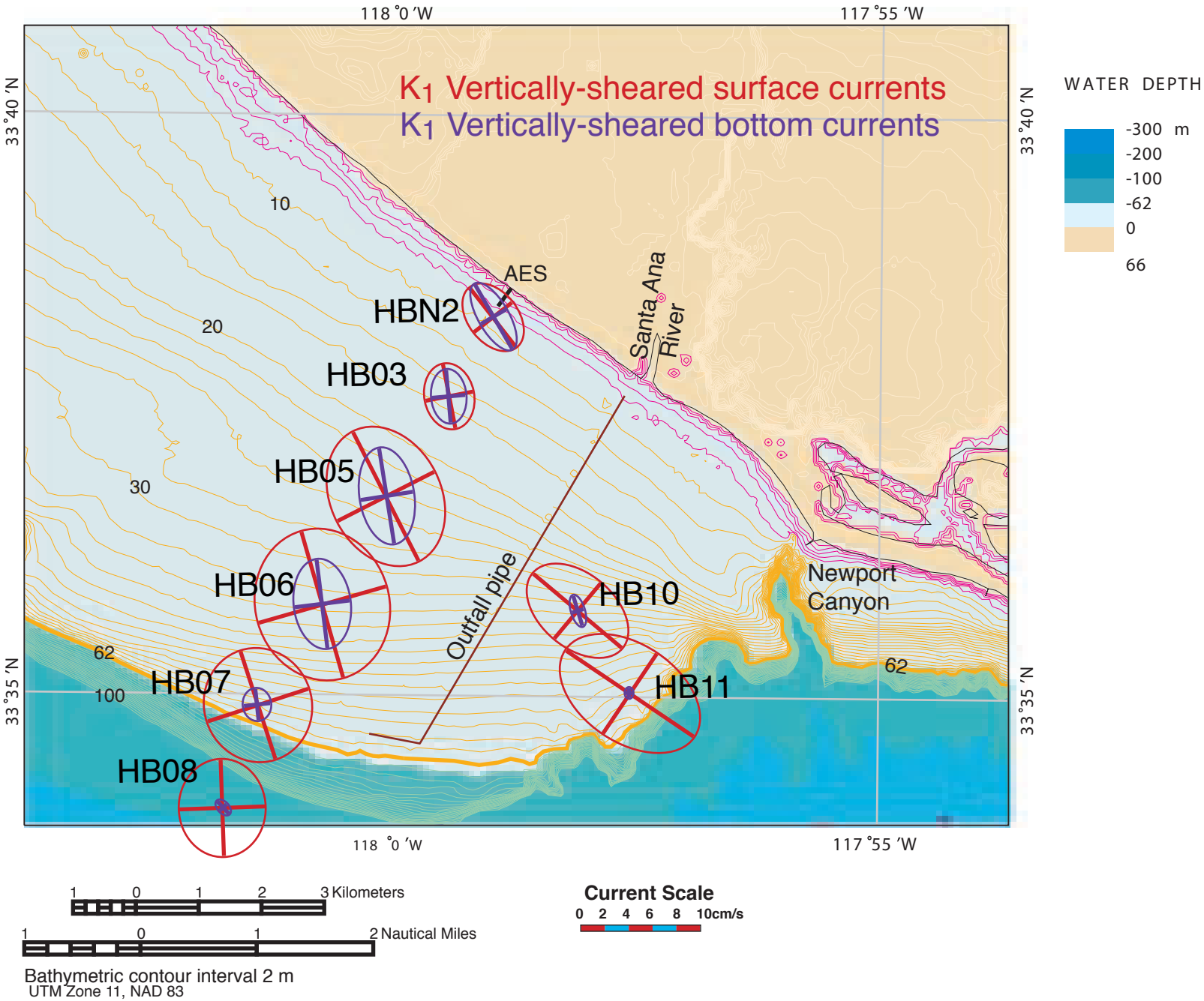

Figure 7-4e. Vertically-sheared tidal current ellipses at the surface and near the bed in the K_1 frequency band off Huntington Beach, CA, from June to October 2001.

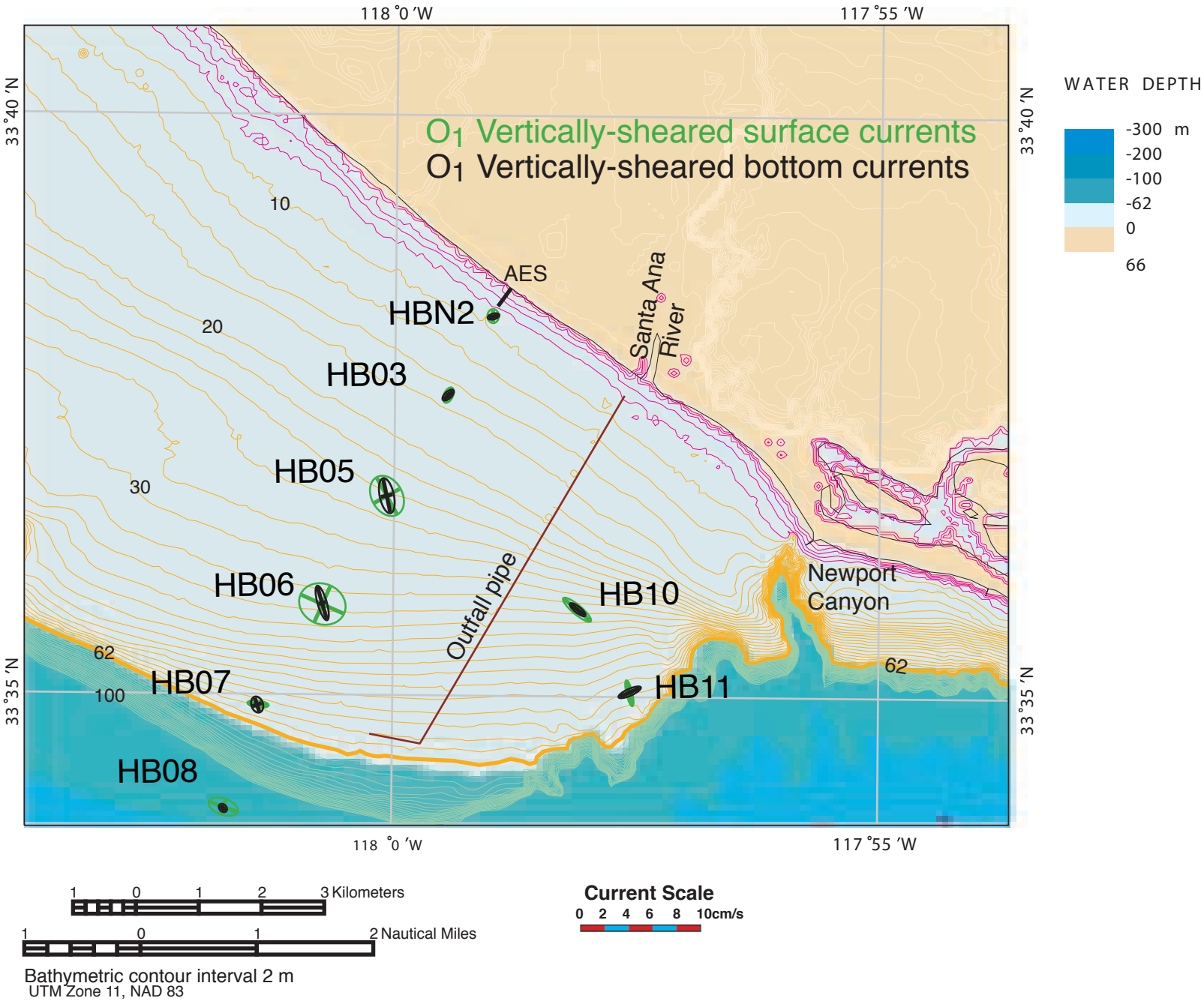

Figure 7-4f. Vertically-sheared tidal current ellipses at the surface and near the bed in the O_1 frequency band off Huntington Beach, CA, from June to October 2001.

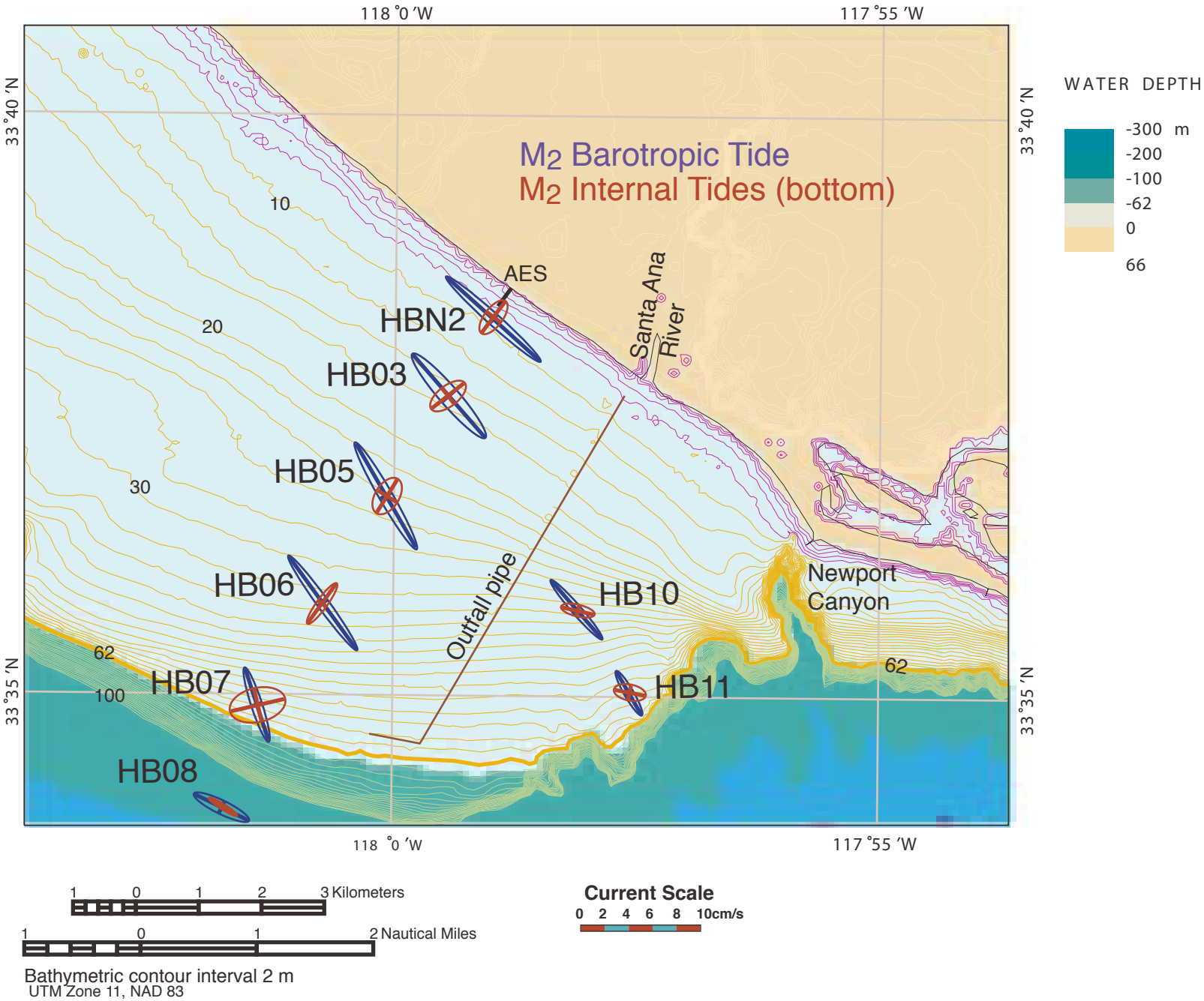

Figure 7-4g. M_2 barotropic and internal tidal ellipses off Huntington Beach, CA, from June to October 2001.

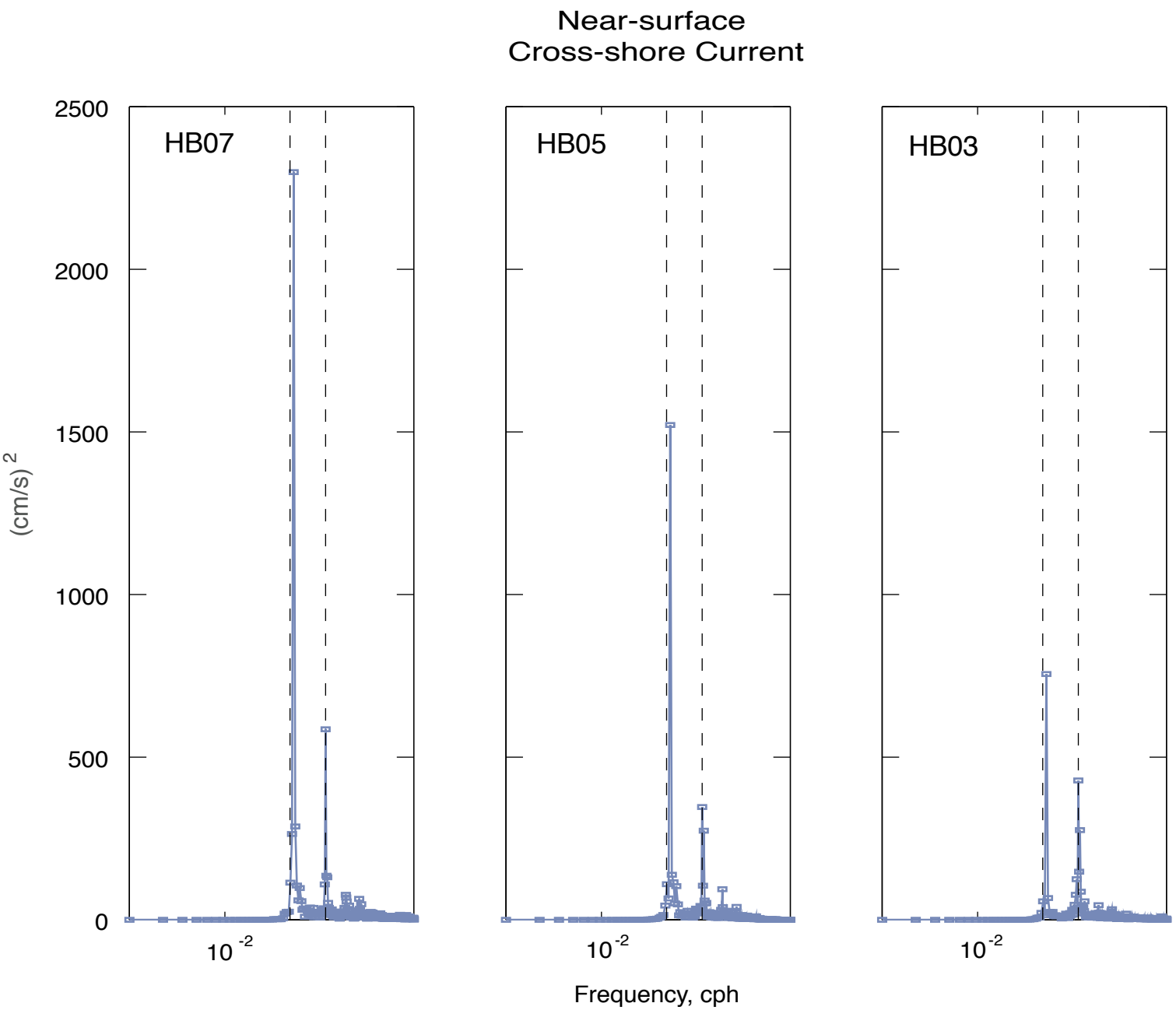

Figure 7-5a. Cross-shore variance preserving spectra for near-surface semidiurnal internal tides and vertically-sheared currents in the diurnal tidal band. Subtidal and barotropic tidal currents have been removed from the spectra. The vertical dashed lines in the spectra denote the diurnal and semidiurnal tidal bands.

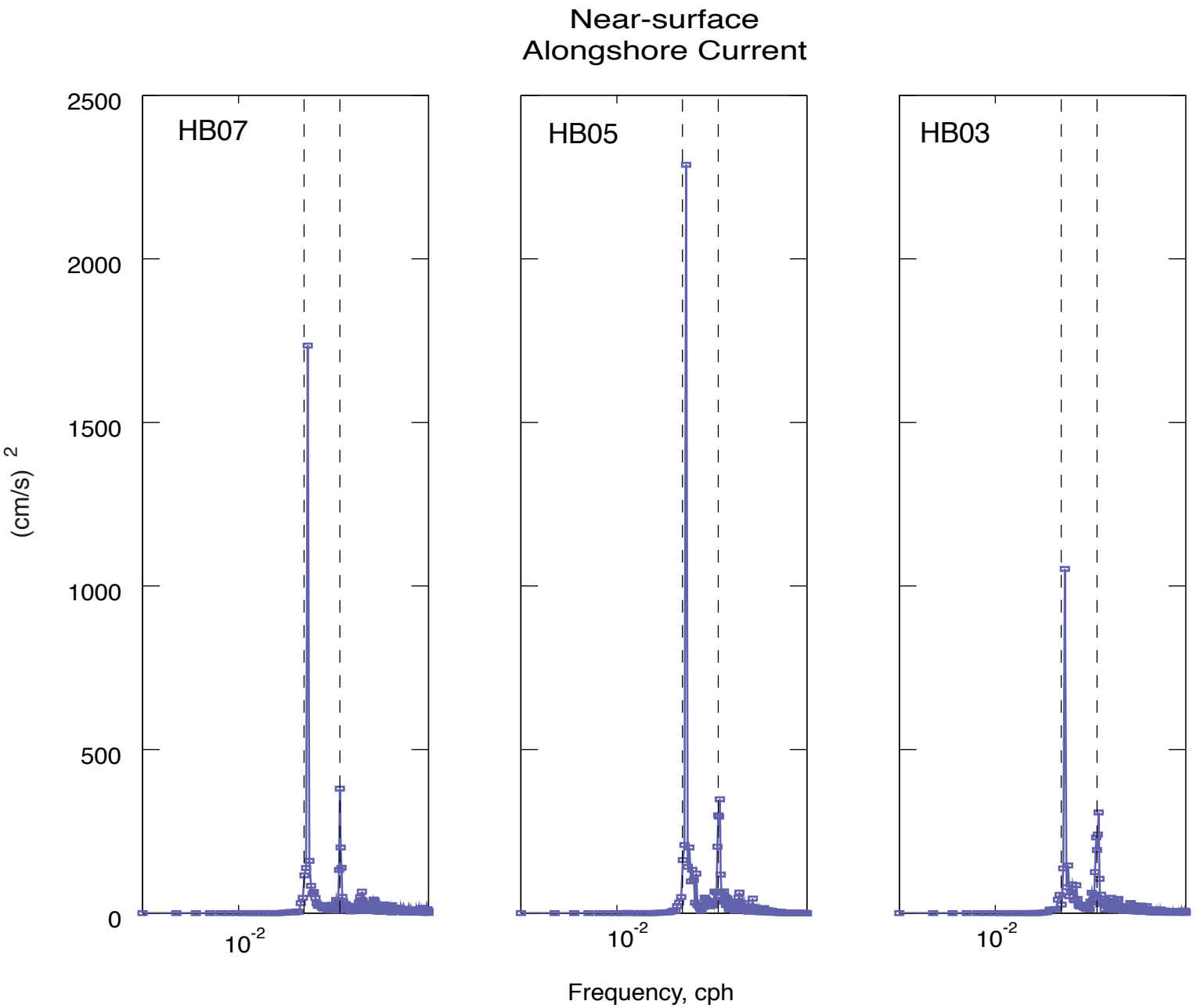

Figure 7-5b. Same as for Figure 7-5a, but for near-surface, alongshore data.

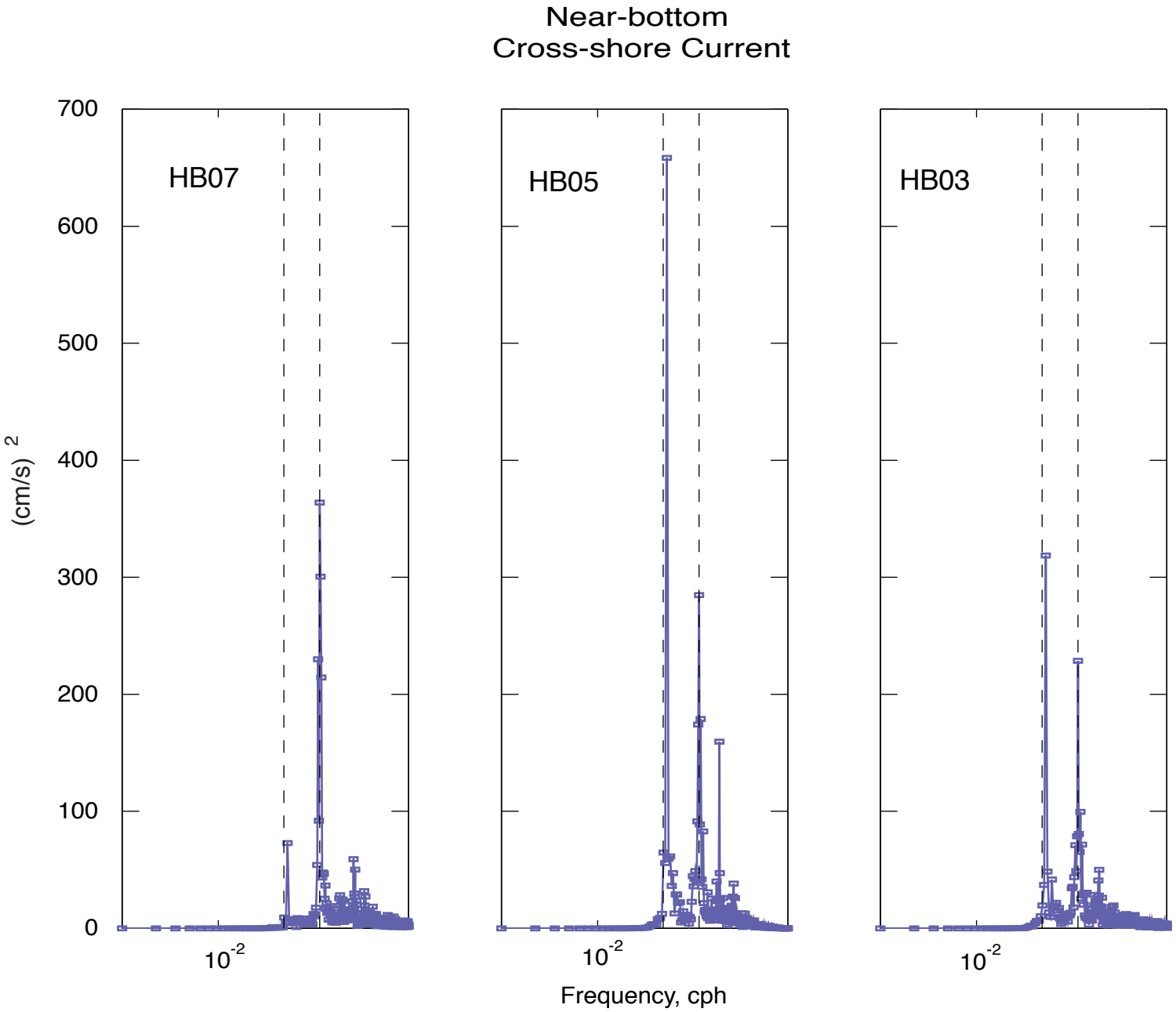

Figure 7-5c. Same as for Figure 7-5a, but for near-bottom, cross-shore data.

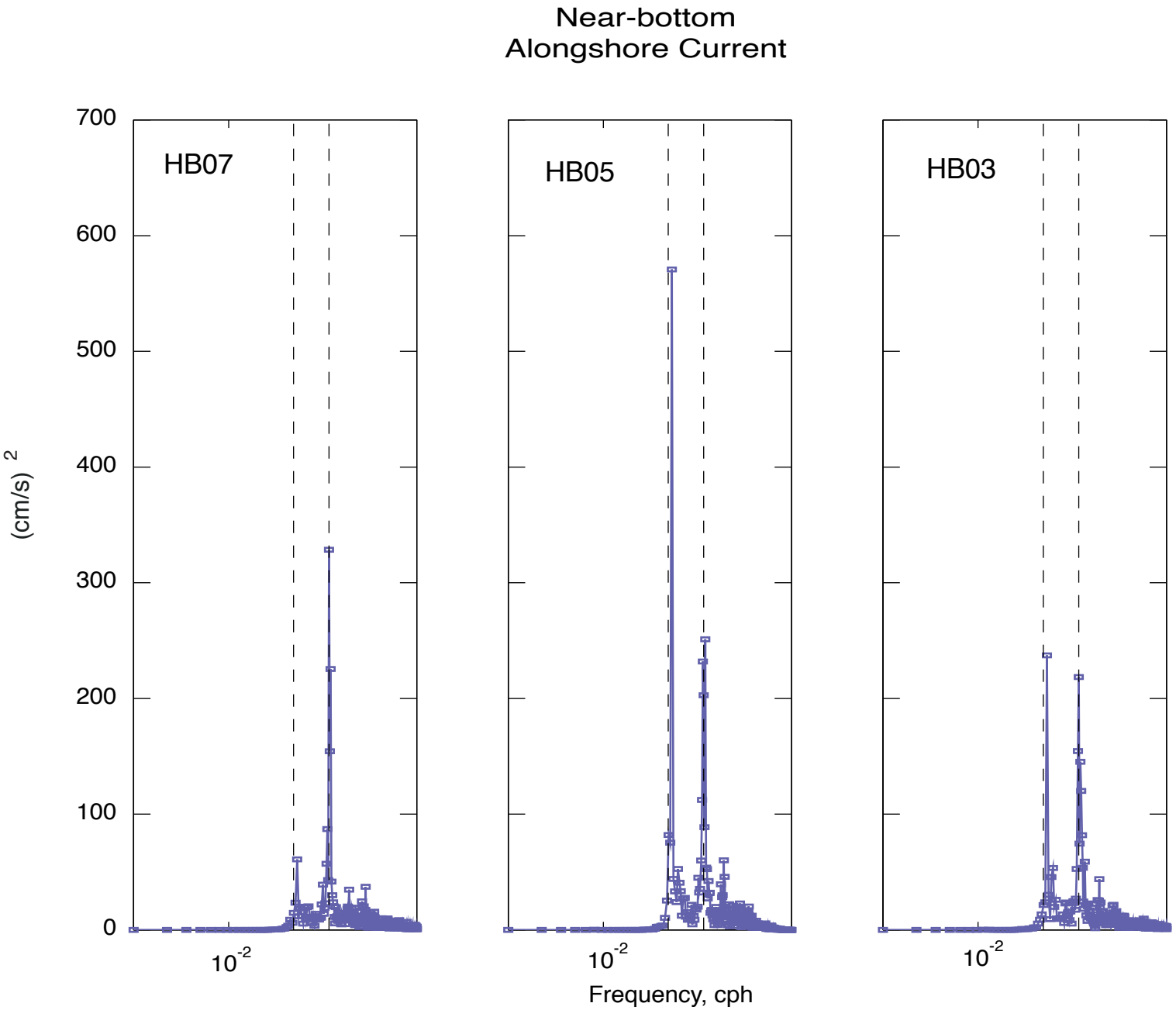

Figure 7-5d. Same as for Figure 7-5a, but for near-bottom, alongshore data.

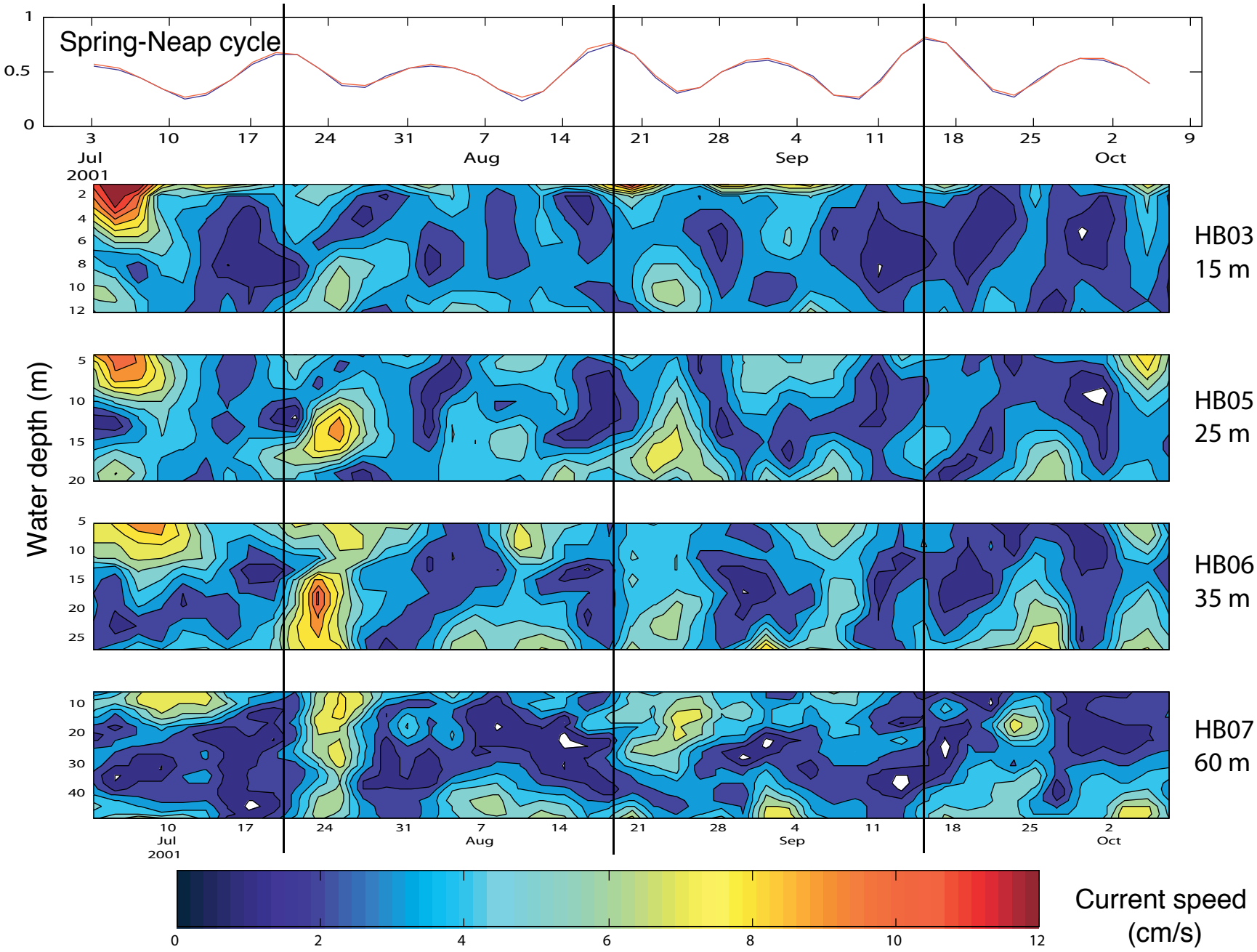

Figure 7-6. A complex demodulation of the cross-shore semidiurnal internal tidal currents using a 4-day window. Current amplitudes with depth and time are depicted at sites HB03, HB05, HB06, and HB07. The complex demodulation was also run on sea level, which shows a pronounced Spring-Neap cycle.

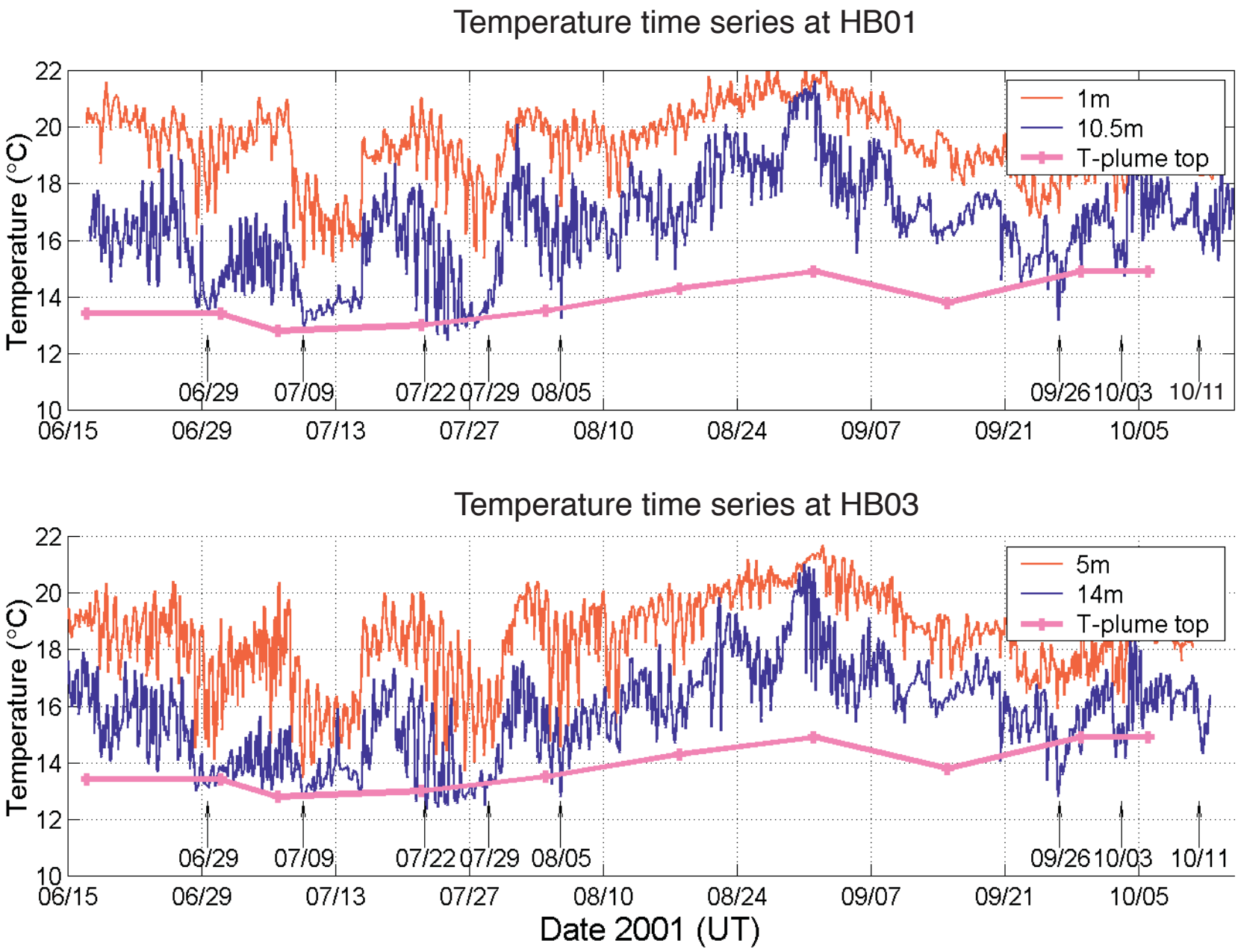

Figure 7-7. Comparison of nearshore water and offshore plume temperatures. In early and late July and late September, 13°C water reaches the 10-m and 15-m isobaths (HB01 and HB03 respectively).

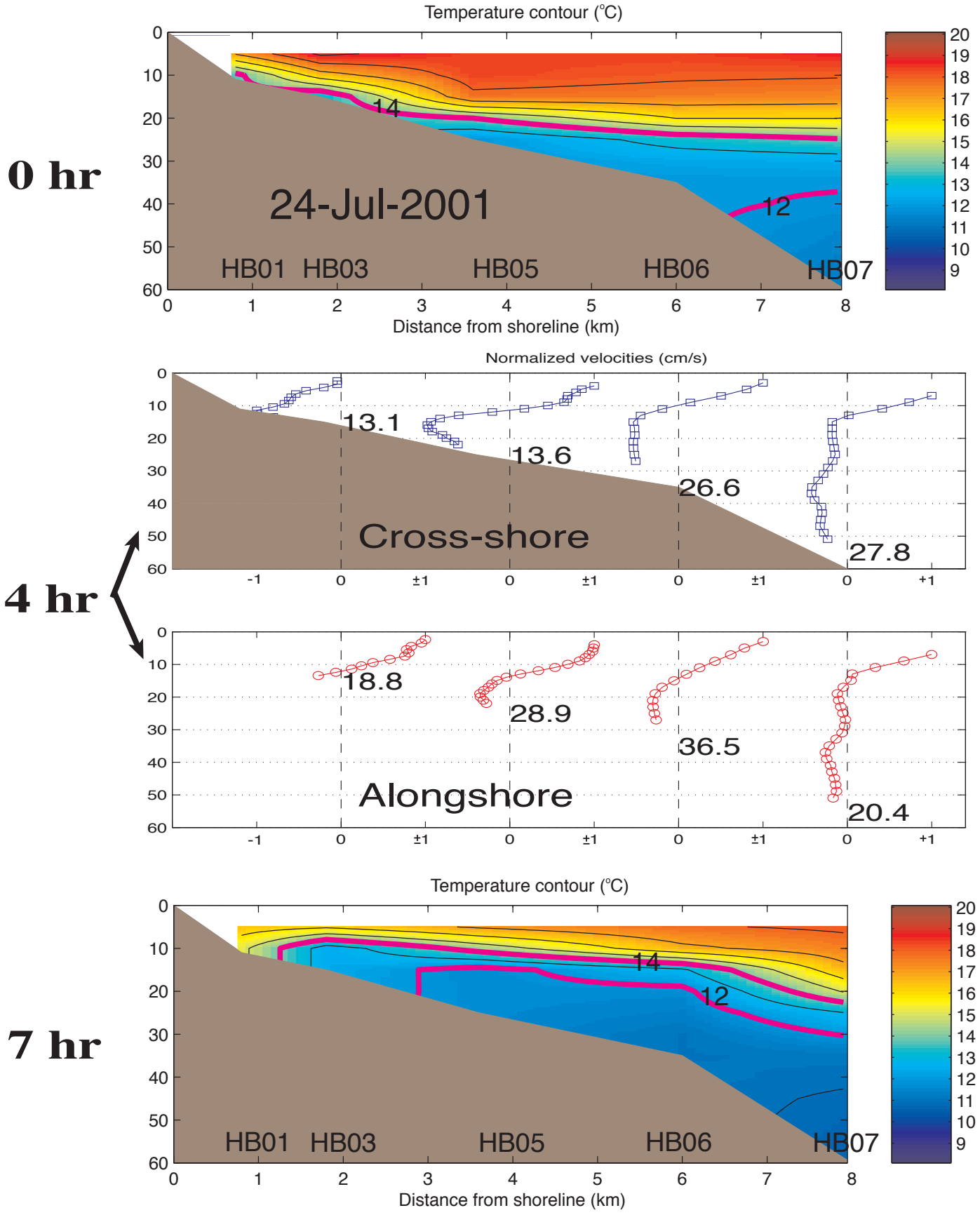

Figure 7-8a. Temperature and current profiles for the rising period of a cold-pulse event on July 24.

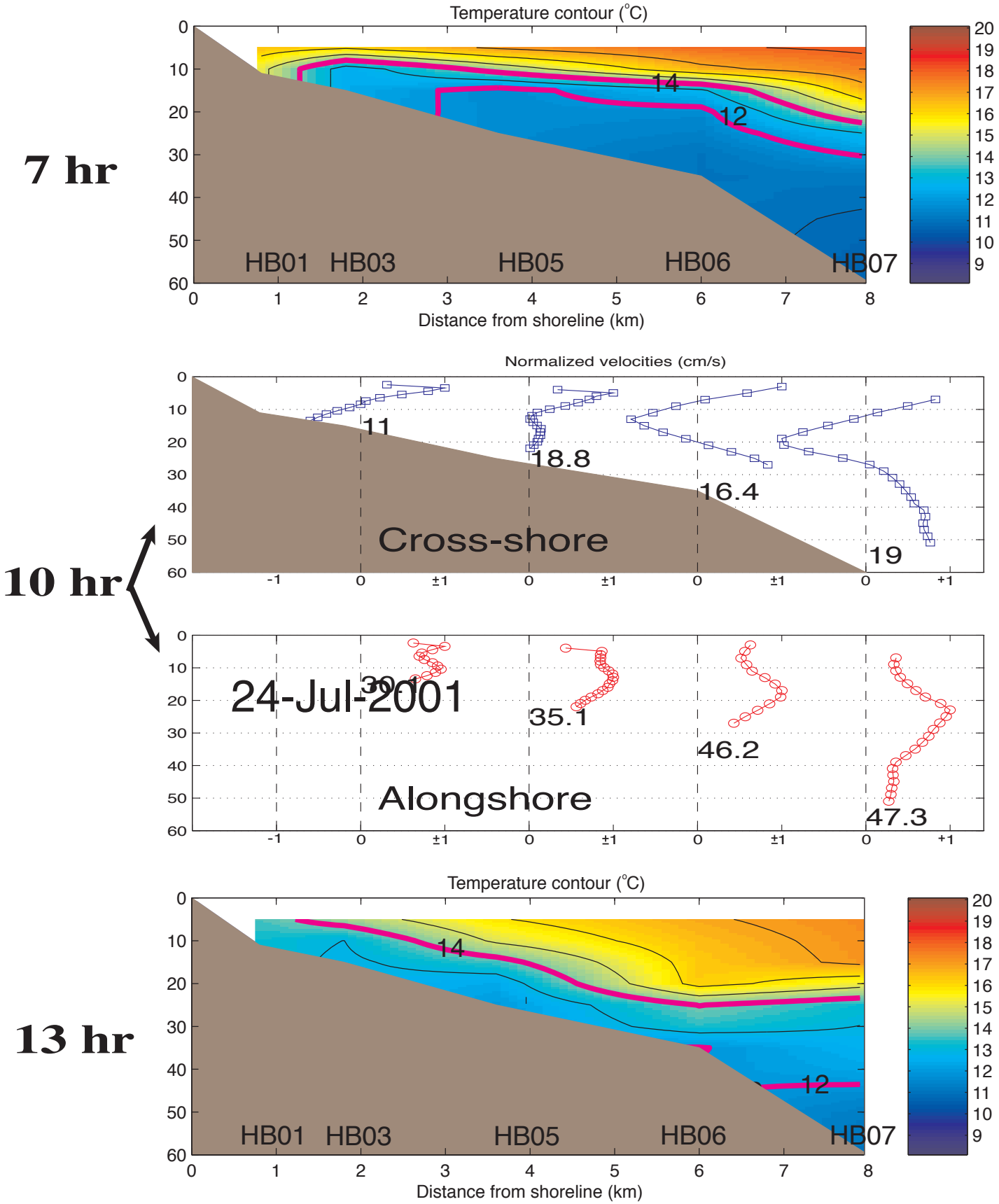

Figure 7-8b. Temperature and current profiles for the falling period of a cold-pulse event on July 24.

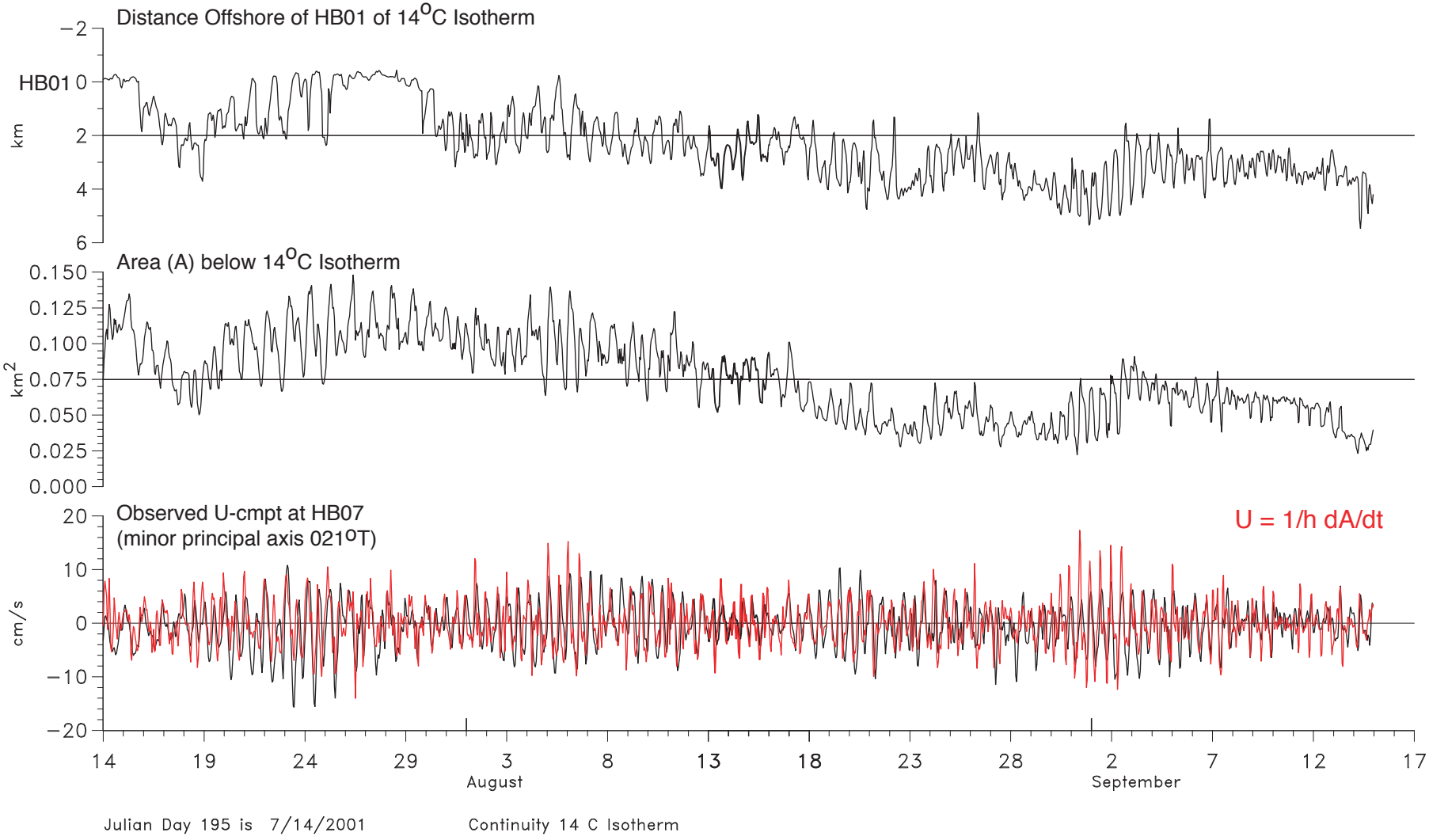

Figure 7-9. 3-HLP time series derived from the depths of the 14°C isotherm for main transect moorings. Top panel: The distance offshore, relative to HB01, of the 14°C isotherm where it intersects the seabed. Middle panel: The area under the 14°C isotherm between HB07 and the shore. Bottom panel: The observed minor principal axis velocity component (U), averaged between the 14°C isotherm and the bottom (black line), and the cross-shelf component derived from A by equation 4.1 (red line).

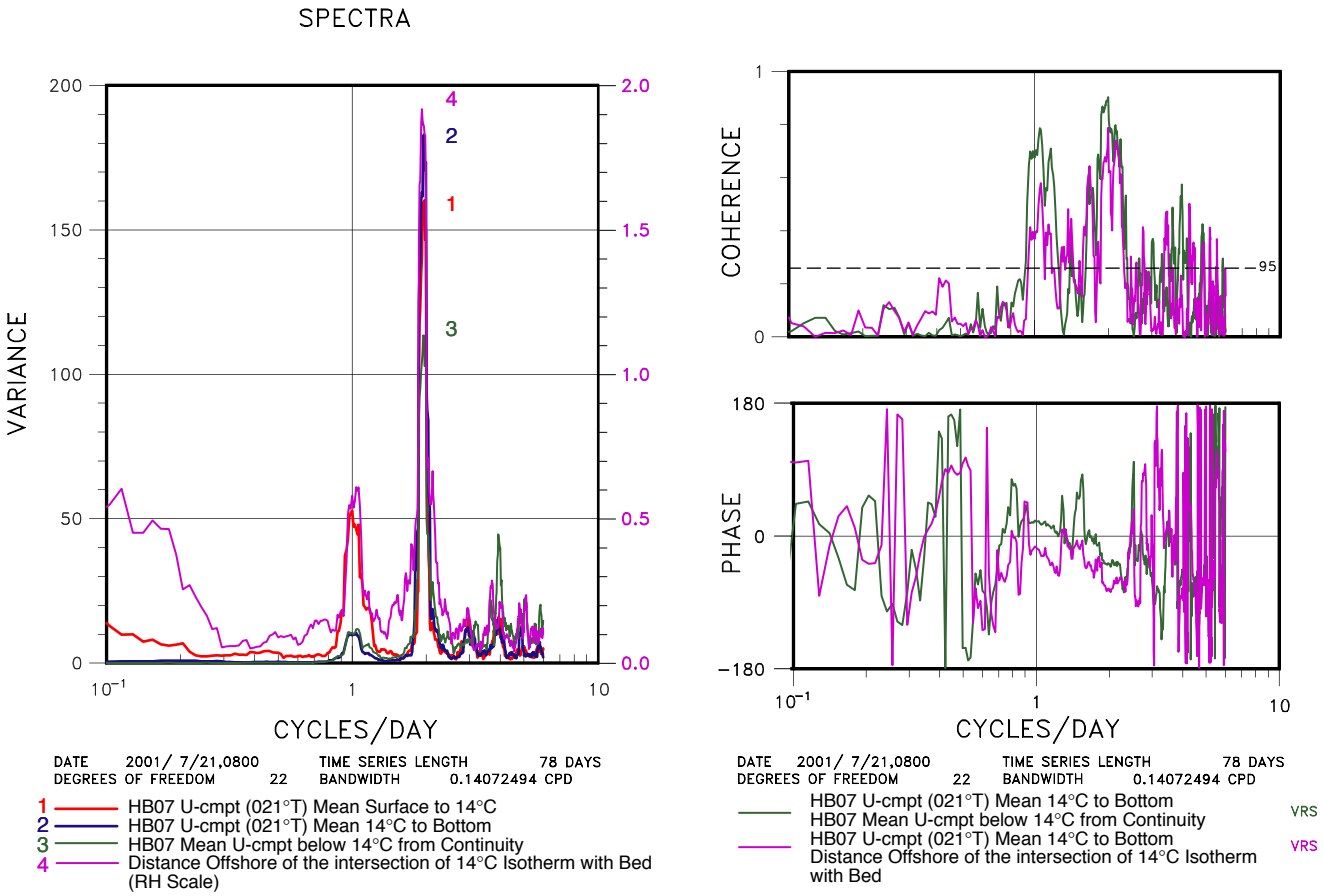

Figure 7-10. Variance preserving spectra (left panel) for the indicated time series. Continuity derived U component uses equation 4.1. Right panels show coherence squared and phase differences for the indicated pairs of time series. The 95% significance level is given by the horizontal dashed line.

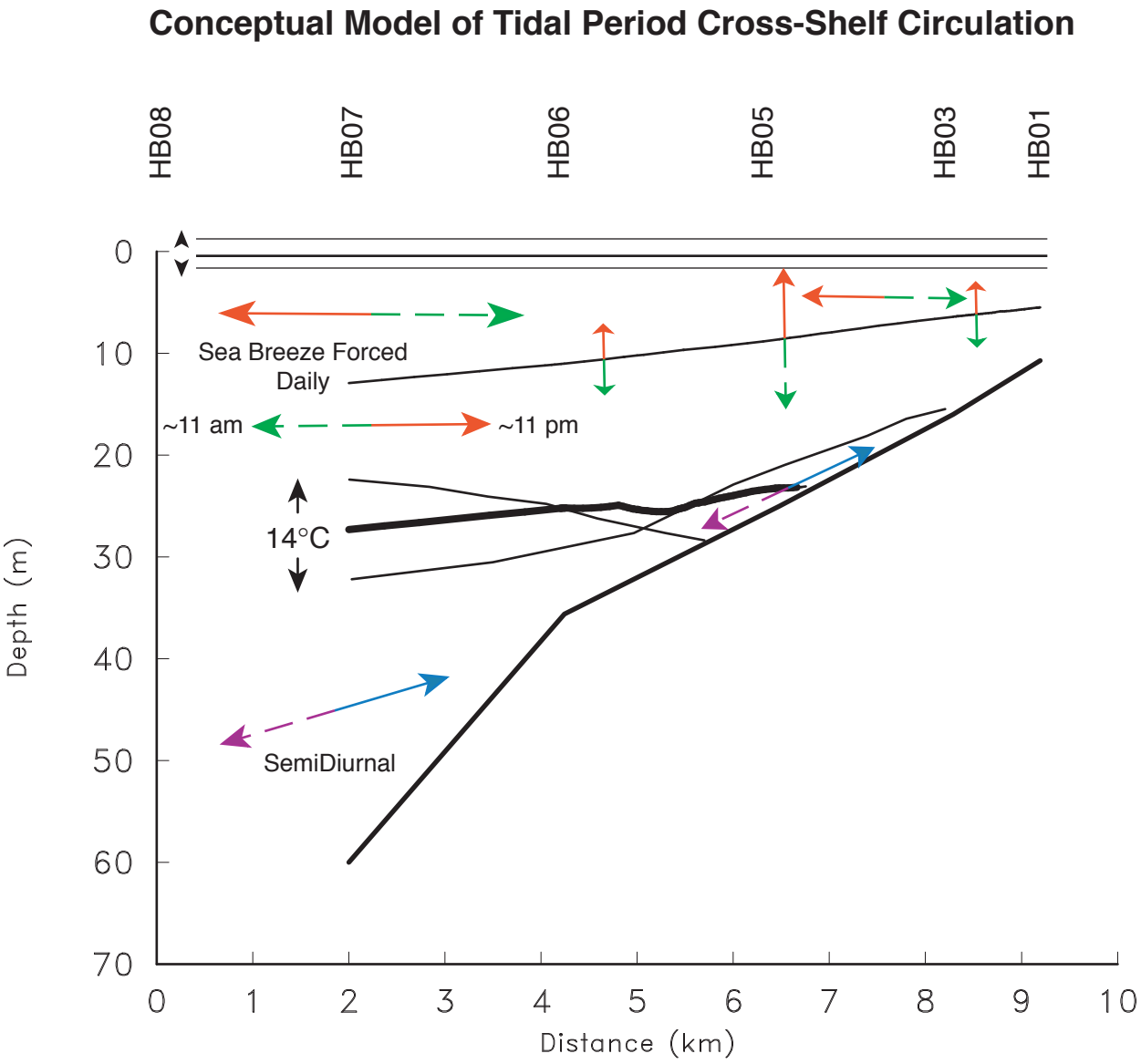

Figure 7-11. Conceptual model of the cross-shelf current and temperature fluctuations caused by the sea breeze and semidiurnal tide. Solid and dashed arrows represent maximum velocities a half-cycle apart. Red and green, and blue and purple arrows, are 24- and 12.42-hour oscillations, respectively.

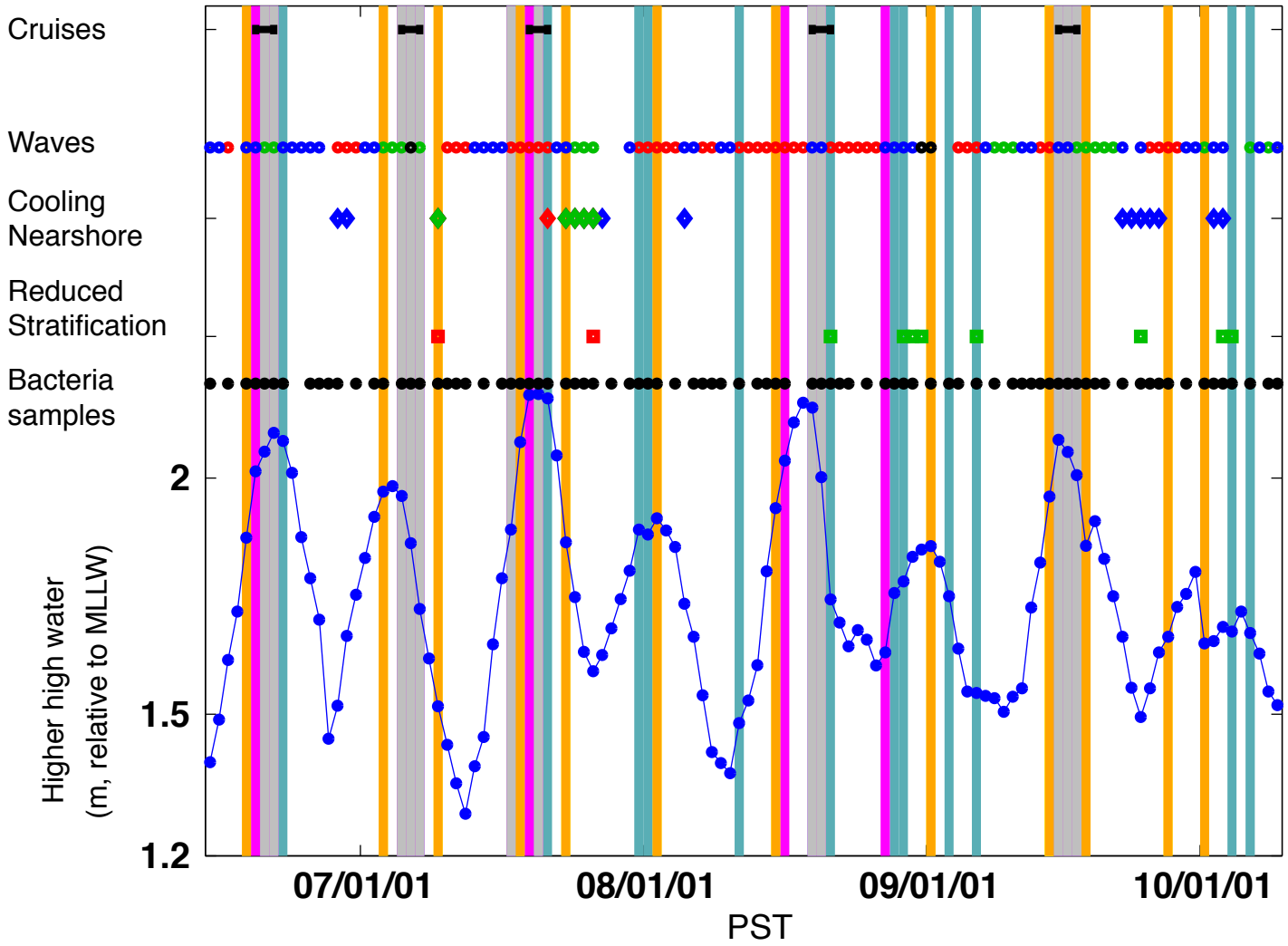

Figure 7.12. Days on which bacterial events occur (vertical bars: blue/green=type 1, purple=type 2, gray= types 1 and 2, orange=type 3) are shown together with cruise days (row 1: black bars); characterization of that day's wave spectra (row 2: red=westerly wind waves, green=southerly swell, blue=westerly wind waves + southerly swell, black=short period southerly waves + southerly swell, no dot =no measurable waves); occurrence of cold water nearshore (row 3: red= 12 deg C inshore of 30m, blue =HB01 temperature < maximum plume temperature, green=both); and occurrence of reduced stratification (row 4: red=HB03 mixed, green=reduced stratification at HB01-HB05). Black dots in row 5 indicate whether bacterial samples were taken that day. The day's higher high water as measured at Los Angeles is shown at the bottom.

Table 7.1. Sea level deflections and phases for the four principal tidal constituents across the mid- and outer shelf off. Huntington Beach within Los Angeles Harbor.

Deflections					
Tidal constituent	HB07 (cm)	HB11 (cm)	HB05 (cm)	HB10 (cm)	Los Angeles (cm)
O_1	21	22	21	21	22
K_1	32	37	33	33	34
M_2	51	50	50	49	51
S_2	21	18	20	20	20
Phases					
O_1	181	180	180	191	193
K_1	200	204	202	216	214
M_2	120	120	120	143	147
S_2	117	124	120	145	144

Table 7-2. Barotropic tides off Huntington Beach. The tidal characteristics are calculated for the period between June and October 2001. Inclination is in degrees from cross-shore. Phase is defined so that the major axis of the tidal ellipse has a positive cross-shelf component.

Mooring/ Tide	Major Amplit. (cm/s)	Minor Amplit. (cm/s)	Inclination (degrees)	Phase (degrees)
HBN2				
O_1	1.0	0.2	88	9
K_1	4.9	0.1	84	96
M_2	5.2	0.4	80	39
S_2	1.5	0.3	75	59
HB03				
O_1	0.9	0.3	-70	175
K_1	3.3	0.1	-87	266
M_2	4.6	0.7	73	51
S_2	0.9	0.7	27	70
HB05				
O_1	0.8	0.4	-69	190
K_1	1.9	0.1	78	85
M_2	5.0	0.5	62	50
S_2	1.1	0.0	12	53
HB06				
O_1	0.9	0.5	56	77
K_1	1.3	0.2	-61	344
M_2	4.8	0.5	68	63
S_2	1.0	0.4	66	102
HB07				
O_1	0.8	0.1	47	94
K_1	2.1	1.0	-80	5
M_2	3.2	0.2	50	64
S_2	1.6	0.1	43	85
HB08				
O_1	0.8	0.2	-81	308
K_1	1.4	0.5	-75	7
M_2	2.5	0.5	-84	290
S_2	1.0	0.3	84	122
HB10				
O_1	0.7	0.3	64	31
K_1	1.3	0.4	89	113
M_2	3.2	0.3	58	50
S_2	0.6	0.1	5	15
HB11				
O_1	0.4	0.2	67	52
K_1	0.9	0.1	-84	348
M_2	2.1	0.7	48	61
S_2	0.7	0.1	0	57

Table 7-3a. Characteristics of the M_2 internal tides with depth along the main cross-shore line of the array. Current characteristics were calculated between June and October, 2001. Inclination is in degrees from cross-shore. Phase is defined so that the major axis of the tidal ellipse has a positive cross-shelf component.

HBN2 (10m)

Depth (m)	Major Amplitude (cm/s)	Minor Amplitude (cm/s)	Inclination (degrees)	Phase (degrees)
0.0	1.4	0.5	-8	20
1.0	1.2	0.4	-1	52
2.0	1.0	0.4	-7	59
3.0	0.7	0.2	-15	66
4.0	0.5	0.1	-17	70
5.0	0.1	0.1	-3	111
6.0	0.5	0.1	-26	234
7.5	1.2	0.5	-12	232
8.0	1.5	0.7	-8	233
9.0	2.0	0.6	8	232

HB03 (15m)

Depth (m)	Major Amplitude (cm/s)	Minor Amplitude (cm/s)	Inclination (degrees)	Phase (degrees)
3.5	2.4	1.3	-11	9
4.5	1.9	1.1	-21	23
5.5	1.6	1.0	-27	31
6.5	1.3	0.7	-25	31
7.5	0.9	0.4	-21	31
8.5	0.4	0.0	-3	38
9.5	0.4	0.2	81	82
10.5	0.8	0.6	-51	228
11.5	1.3	0.8	-32	216
12.5	1.7	0.9	-20	209
13.5	2.1	0.5	-9	205

HB05 (25m)

Depth (m)	Major Amplitude (cm/s)	Minor Amplitude (cm/s)	Inclination (degrees)	Phase (degrees)
6	2.5	1.2	41	269
8	1.9	1.0	39	269
10	1.4	0.8	33	264
12	0.6	0.4	-19	281
14	0.7	0.2	78	92
16	1.2	0.4	52	78
18	1.6	0.8	41	82
20	1.6	1.0	17	97
22	1.5	0.6	-24	118

Table 7-3a, cont. M_2 internal tides.

HB06 (35m)

Depth (m)	Major Amplitude (cm/s)	Minor Amplitude (cm/s)	Inclination (degrees)	Phase (degrees)
3	2.2	0.7	21	232
5	2.0	0.5	20	224
7	1.8	0.3	16	224
9	1.6	0.3	8	225
13	0.8	0.1	-9	233
15	0.4	0.3	-54	239
17	0.9	0.1	43	15
19	1.1	0.0	36	32
21	1.3	0.2	28	50
23	1.5	0.2	15	62
25	2.0	0.4	-3	64
27	2.5	0.6	-15	59

HB07 (60m)

Depth (m)	Major Amplitude (cm/s)	Minor Amplitude (cm/s)	Inclination (degrees)	Phase (degrees)
7	2.5	1.3	-18	187
9	2.5	1.2	-22	184
13	2.2	0.7	-26	184
17	1.6	0.4	-42	197
21	1.3	0.1	-56	227
25	1.1	0.3	-58	244
29	1.0	0.0	-74	272
33	0.6	0.0	-61	320
37	1.0	0.3	-57	16
41	1.5	0.5	-46	36
45	2.2	1.0	-44	44
49	2.4	1.4	-45	38

Table 7-3b. Same as Table 7-3a, but for S_2 internal tides.

HBN2 (10m)

Depth (m)	Major Amplitude (cm/s)	Minor Amplitude (cm/s)	Inclination (degrees)	Phase (degrees)
0.0	0.5	0.4	-56	331
1.0	0.5	0.1	-56	22
2.0	0.5	0.0	-59	71
3.0	0.5	0.0	-39	115
4.0	0.5	0.1	-40	130
5.0	0.5	0.4	-63	170
6.0	0.5	0.3	84	32
7.5	0.3	0.0	-58	253
8.0	0.6	0.1	-36	280
9.0	1.0	0.3	-12	285

HB03 (15m)

Depth (m)	Major Amplitude (cm/s)	Minor Amplitude (cm/s)	Inclination (degrees)	Phase (degrees)
3.5	1.8	0.7	-23	355
4.5	1.2	0.7	-22	13
5.5	0.9	0.7	-55	63
6.5	0.9	0.4	-74	95
7.5	0.7	0.2	-69	107
8.5	0.5	0.1	-51	120
9.5	0.3	0.3	-9	127
10.5	0.5	0.3	79	81
11.5	0.8	0.5	-77	264
12.5	1.1	0.7	-60	266
13.5	1.3	0.9	-38	258

HB05 (25m)

Depth (m)	Major Amplitude (cm/s)	Minor Amplitude (cm/s)	Inclination (degrees)	Phase (degrees)
6	2.1	1.6	46	289
8	1.8	1.1	55	286
10	1.3	0.8	44	298
12	0.7	0.4	6	334
14	0.2	0.1	52	76
16	0.8	0.5	46	116
18	1.4	0.9	41	123
20	1.6	1.3	39	120
22	1.6	1.3	30	128

Table 7-3b, cont. S_2 internal tides.

HB06 (35m)

Depth (m)	Major Amplitude (cm/s)	Minor Amplitude (cm/s)	Inclination (degrees)	Phase (degrees)
3	2.2	1.2	57	292
5	2.2	1.0	58	292
7	1.9	0.9	45	296
9	1.5	0.6	25	301
13	1.0	0.3	-28	296
15	0.9	0.4	-72	309
17	0.8	0.3	68	137
19	0.9	0.4	48	125
21	1.1	0.6	44	116
23	1.5	0.8	33	116
25	1.8	1.0	22	119
27	2.1	1.2	18	112

HB07 (60m)

Depth (m)	Major Amplitude (cm/s)	Minor Amplitude (cm/s)	Inclination (degrees)	Phase (degrees)
7	1.1	0.5	53	289
9	0.8	0.1	29	289
13	0.8	0.3	-26	253
17	1.0	0.7	-63	264
21	0.6	0.3	48	142
25	0.5	0.1	59	157
29	0.3	0.1	33	154
33	0.4	0.0	-1	127
37	0.4	0.2	5	83
41	0.5	0.4	25	18
45	0.6	0.5	72	310
49	0.9	0.8	70	304

Table 7-3c. Same as Table 7-3a, but for K_1 sheared diurnal tides.

HBN2 (10m)

Depth (m)	Major Amplitude (cm/s)	Minor Amplitude (cm/s)	Inclination (degrees)	Phase (degrees)
0.0	3.5	-2.4	74	67
1.0	3.3	-2.3	75	72
2.0	2.2	-1.0	59	82
3.0	1.0	-0.1	47	90
4.0	0.5	0.3	40	94
5.0	1.0	-0.6	-79	213
6.0	1.7	-1.1	60	255
7.5	2.4	-1.2	55	264
8.0	2.7	-1.2	59	266
9.0	3.4	-1.2	65	270

HB03 (15m)

Depth (m)	Major Amplitude (cm/s)	Minor Amplitude (cm/s)	Inclination (degrees)	Phase (degrees)
3.5	4.7	-3.6	54	76
4.5	3.8	-2.9	48	79
5.5	2.9	-2.0	42	81
6.5	1.9	-1.1	38	78
7.5	0.9	-0.4	30	73
8.5	0.3	-0.1	-44	211
9.5	1.0	-0.7	56	249
10.5	1.7	-1.1	42	256
11.5	2.1	-1.3	36	260
12.5	2.3	-1.5	35	263
13.5	2.5	-1.4	43	263

HB05 (25m)

Depth (m)	Major Amplitude (cm/s)	Minor Amplitude (cm/s)	Inclination (degrees)	Phase (degrees)
6	7.1	-5.5	65	51
8	5.0	-3.5	55	52
10	2.9	-1.7	46	47
12	1.3	-0.5	18	27
14	1.5	-1.1	-40	355
16	2.5	-1.9	71	223
18	3.5	-2.2	55	227
20	4.0	-2.3	44	230
22	3.9	-2.0	38	233

Table 7-3c, cont. K_1 sheared diurnal tides.

HB06 (35m)

Depth (m)	Major Amplitude (cm/s)	Minor Amplitude (cm/s)	Inclination (degrees)	Phase (degrees)
3	10.0	-8.2	73	60
5	7.3	-6.5	59	65
7	5.0	-4.5	39	71
9	3.6	-3.0	58	26
13	3.6	-3.0	6	359
15	4.0	-3.4	-10	351
17	4.2	-3.9	-28	348
19	4.3	-4.0	71	230
21	4.4	-3.6	54	230
23	4.3	-3.1	46	224
25	3.8	-2.5	40	218
27	3.2	-1.8	36	211

HB07 (60m)

Depth (m)	Major Amplitude (cm/s)	Minor Amplitude (cm/s)	Inclination (degrees)	Phase (degrees)
5	7.9	-7.0	27	81
9	6.1	-5.6	29	65
13	3.7	-3.3	80	324
17	3.9	-2.9	25	314
21	4.4	-3.2	-13	314
25	3.0	-2.7	1	265
29	2.2	-1.5	19	208
33	1.8	-1.2	24	167
37	1.6	-1.0	28	139
41	1.5	-0.9	24	128
45	1.4	-1.0	22	125
49	1.3	-1.1	40	105

Table 7-3d. Same as Table 7-3a, but for O_1 sheared diurnal tides.

HBN2 (10m)

Depth (m)	Major Amplitude (cm/s)	Minor Amplitude (cm/s)	Inclination (degrees)	Phase (degrees)
0.0	0.9	-0.5	165	151
1.0	0.6	-0.4	10	316
2.0	0.4	-0.3	94	240
3.0	0.2	0.0	142	213
4.0	0.2	0.1	28	92
5.0	0.4	-0.1	45	112
6.0	0.4	-0.3	30	118
7.5	0.5	-0.2	133	7
8.0	0.5	-0.1	133	6
9.0	0.3	0.0	149	19

HB03 (15m)

Depth (m)	Major Amplitude (cm/s)	Minor Amplitude (cm/s)	Inclination (degrees)	Phase (degrees)
3.5	1.2	-0.3	3	329
4.5	0.8	-0.3	9	322
5.5	0.6	-0.3	12	311
6.5	0.4	-0.2	0	311
7.5	0.2	-0.1	-34	322
8.5	0.2	0.0	-82	307
9.5	0.3	-0.1	49	107
10.5	0.4	-0.2	12	124
11.5	0.5	-0.2	-9	137
12.5	0.5	-0.2	-17	144
13.5	0.4	-0.2	-15	152

HB05 (25m)

Depth (m)	Major Amplitude (cm/s)	Minor Amplitude (cm/s)	Inclination (degrees)	Phase (degrees)
6	1.9	-1.5	60	263
8	1.5	-0.9	62	253
10	1.1	-0.4	54	256
12	0.7	0.0	39	248
14	0.5	-0.1	-27	214
16	0.9	-0.6	80	61
18	1.5	-0.6	53	72
20	1.5	-0.5	43	81
22	1.1	-0.4	47	86

Table 7-3d, cont. O_1 sheared diurnal tides.

HB06 (35m)

Depth (m)	Major Amplitude (cm/s)	Minor Amplitude (cm/s)	Inclination (degrees)	Phase (degrees)
3	2.7	-2.6	8	312
5	2.3	-2.0	-78	33
7	1.8	-1.3	-85	33
9	1.3	-0.5	65	232
13	1.1	0.2	-6	191
15	1.4	-0.2	-28	182
17	1.6	-0.6	-48	188
19	1.5	-0.9	-80	208
21	1.7	-0.8	67	54
23	1.6	-0.6	52	69
25	1.5	-0.3	44	81
27	1.1	-0.1	45	89

HB07 (60m)

Depth (m)	Major Amplitude (cm/s)	Minor Amplitude (cm/s)	Inclination (degrees)	Phase (degrees)
5	1.3	-1.2	-48	352
9	1.0	-0.6	-77	26
13	0.5	0.2	-27	160
17	1.4	-0.2	-38	182
21	1.5	-0.7	-64	195
25	1.3	-0.4	56	40
29	0.9	0.0	21	37
33	0.5	0.1	-42	12
37	0.7	-0.2	-74	2
41	0.8	-0.5	-79	8
45	0.7	-0.5	83	205
49	0.6	-0.4	47	248

Table 7-4. Cold surge events in the summer of 2001. Table shows all periods when water cooler than 12°C reaches the 30-m or shallower isobath and water cooler than 13°C is found at HB03 (15-m isobath). These cool-water pulses have tidal frequencies and retreat offshore after coming onshore.

Date	Shallowest isobath for 12°C water (m)	Time when 12°C water was close to shore
July 9	28	1000-1300
July 21	25	0800-0900
July 23	25	0900-1000
July 24	25	0900
July 25	30	1000-1300
July 26	30	0800-1300

CHAPTER 8. SEDIMENT RESUSPENSION AND TRANSPORT NEAR THE OCSD OUTFALL

Jingping Xu

8.1. Introduction

One of the hypotheses in the Huntington Beach Phase III study is that sediment transport could be a mechanism that brings outfall bacteria to the beach. When bottom shear stress due to surface waves, internal waves, shelf currents, or the combination of these forces exceeds a critical value, which is mainly determined by the grain size, the bed sediment, as well as particle-bound bacteria, could be resuspended into the water column. Cross-shelf transport mechanisms (Chapters 5, 6, and 7) could then bring the suspended particles to the shore. It is not clear how bacteria are partitioned between water-borne and particle-bound after being discharged from the OCSD outfall diffuser. We assume that a certain percentage of discharged bacteria are absorbed to sediment particles and then deposited on the sea floor in the vicinity of the outfall diffuser. In this chapter, we explore the possibility of sediment resuspension in the vicinity of the OCSD outfall by calculating the bed shear stress from the measured data of surface waves and near-bed currents.

8.2. Surface waves and near-bed currents

Surface waves and winds were measured from a meteorological buoy at HB07 (Chapter 2). Hourly wind speed, wave period, and significant wave heights are plotted in Figure 8-1. It shows a typical southern California summer condition with calm wave climate and daily sea breeze weather pattern. During the four-month long deployment, significant wave height rarely reached 1.0 m, and the vast majority was between 0.6 and 0.7 m. The surface waves fall into two distinct groups, in terms of wave period and wave direction (Figure 8-2). The majority are short-period waves (5-10 seconds) that are mainly from the west, exhibit a daily cycle, and are presumably generated by the daily westerly sea breeze. There is a high correlation between the diurnal oscillation in the wind speed and wave height (Figure 8-1), and between the directions of wind and these short-period waves (Figure 8-3). The second wave group is the long-period (14-18 seconds) swells from the south. These swells are generally created by distant storms that can be as far as 8000 km away (Xu and Noble, 2003). Typically these swells are less energetic than the locally generated wind waves (Figure 8-2).

The near-bed current was measured with an Acoustic Doppler Velocimeter (ADV) located 60 cm above the sea floor. To obtain a record of low-frequency currents (not due to waves), an hourly-averaged record was generated by averaging 2048 data points sampled at 2 Hz (Figure 8-4). The hourly current showed magnitudes ranging from 0 to 19 cm/s, but mostly between 2 and 10 cm/s. In 70-m water depth (HB07) this current was unlikely to be wind-driven; this is evidenced by the higher frequency variability of the current as compared with the wind (Figures 8-4 and 8-5). In the spectral domain, while the diurnal band dominates the wind energy due to the daily breeze, the near-bed current was predominantly semidiurnal. This semidiurnal tidal current in the bottom boundary layer was stronger in the cross-shelf direction, in contrast to the mainly along-isobath subtidal current in the bottom boundary layer at this site (Figure 8-6).

8.3. Bed shear stress

The hourly data of wave heights, wave periods and near-bed current velocities described in the previous section were used to calculate bed shear stresses, τ_{cw}, using a simple quadratic equation (Nielsen, 1992):

$$\tau_{cw} = \rho u_{*cw}^2 \qquad (8.1)$$

where τ_{cw} is bed shear stress due to combined waves and currents, ρ (=1027 kg/m^3) is the sea-water density and u_{*cw} is the combined shear velocity:

$$u_{*cw} = \sqrt{u_{*c}^2 + u_{*w}^2} \qquad (8.2)$$

where u_{*c} and u_{*w} are shear stresses due to currents and waves, respectively. The shear velocities can be estimated using quadratic formula:

$$\begin{aligned} \tau_w &= 0.5\rho f_w u_b^2 = \rho u_{*w}^2 \\ \tau_c &= \rho C_D u_c^2 = \rho u_{*c}^2 \end{aligned} \qquad (8.3)$$

therefore

(8.4)

u_b is the near-bed orbital velocity that is calculated from the heights and periods of the surface waves. u_c is the hourly mean current measured at 60 cm above the bed. f_w is friction factor associated with waves, and can be calculated using an explicit formula (Swart, 1974):

$$f_w = \exp\left(5.213\left(\frac{2.5d_0}{A_b}\right)^{0.194} - 5.9777\right) \qquad (8\text{-}5)$$

where d_0 is the median grain size at HB07 (100 micron), and A_b is the near-bed orbital semi-excursion. The current friction factor, $C_{D,}$, is estimated using an iterative routine described in (Grant and Madsen, 1979).

8.4. Sediment resuspension near OCSD outfall

The estimated bed shear stress (Figure 8-7) intermittently surpassed the critical shear stress of 0.5 dyne/cm^2 (Gardner, 1989) and caused resuspension of the fine material (very fine sand and silt) from the bed. Some estimated shear stresses were even occasionally higher than a more conservative critical value of 1.0 dyne/cm^2 reported in the literature (Maa et al., 1993). These resuspension events, and therefore the validity of the estimated values of bed shear stress, are also confirmed by both the water clarity data and video footage. In the first video footage during June 25-26, 2001, the concentration of suspended particles was clearly higher than in the video footage from previous days, although most features on the bottom were not eroded. In the video footage during July 26-27, 2001, the particle concentration grew higher and there was obvious erosion of the bedforms.

Figure 8-7 shows no apparent correlation between resuspension and beach contamination events, although a few beach contamination events do coincide with or immediately follow periods of high shear stress (e.g., beach events on July 19-22, July 5-8, August 10-11, August

28-30, September 4, September 15-17, and October 4-6). Whether the resuspended sediments can be brought to the nearshore and then on to the beach depends on the sediment properties (e.g., settling velocity), changes in sediment-bacteria associations, and shelf circulation patterns that are controlled by oceanographic processes described in other sections of this report. If bacteria are mixed into the sub-thermocline layer, the resulting transport problem is similar to that of whether the sub-thermocline wastewater plume waters can be transported onshore quickly enough (e.g., by internal waves).

Bed shear stress was also estimated at a site (HBN2) in 10 m of water depth (Figure 8-8). The current speed was from the first bin of an ADCP measurement at this site. There was no wave measurement at HBN2; therefore the wave height and period from the HB07 site were used. Based on linear wave theory (e.g., Dean and Dalrymple, 1991), long-period swells have slightly higher wave height in 10 m of water depth than in 60 m water depth, while short-period wind-waves have slightly lower wave height in 10 m than in 60 m of water depth. For a deep-water swell of 14-second period and 0.6-m height (Figure 8-1), its wave height in 10 m of water depth is ~10% greater than in 60 m of water depth. For a deep-water wave of 7-second period and 1.0-m height, its wave height in 10 m water depth is ~8% less than in 60 m water depth. Figure 8-8 clearly shows that the bed shear stress in the 10-m site was almost consistently greater than 1.0 dyne/cm^2 (the heavy dotted horizontal line)–the upper limit of critical value for fine material. Even the 80% of the estimated value (the lighter dotted line), which adequately accounts for the lower wave height at the 10-m site for short-period wind waves, is much greater than the critical shear stress. This indicates that fine material (silt and fine sand) are mostly in suspension in 10 m of water depth. If particle-bound bacteria are on these fine particles by preference, due to their higher absorbing power, the bacteria themselves will also be in suspension most of the time.

8.5. Summary

Sediment resuspension was occasionally observed near the OCSD outfall during the four-month deployment, mainly in high wind-wave events. These resuspension events, however, were not correlated with beach bacteria contamination. In 10 m of water depth, fine sediments were almost consistently in suspension due to high bed shear stress. Therefore, even the particle-bound bacteria should also be mostly in suspension.

8.6. References

Dean, R.G. and R.A. Dalrymple, 1991. Water wave mechanics for engineers and scientists. World Scientific Publishing, Singapore, 353 p.

Gardner, W.D., 1989. Periodic resuspension in Baltimore Canyon by focusing of internal waves. Journal of Geophysical Research, v. 94, p. 18185-18194

Maa, J.P.-Y., L.D. Wright, C.-H. Lee, and T.W. Shannon, 1993. VIMS sea carousel: a field instrument for studying sediment transport. Marine Geology, v. 115, p. 271-287.

Grant, W.D. and O.S. Madsen, 1979. Combined wave and current interaction with a rough bottom. Journal of Geophysical Research, v. 84, p. 1797-1808.

Nielsen, P., 1992. Coastal bottom boundary layers and sediment transport. World Scientific Publishing, Singapore, 324 p.

Swart, D.H., 1974. Offshore sediment transport and equilibrium beach profiles. Delft Hydraulics Laboratory Publication, No. 131.

Xu, J.P. and M.A. Noble, 2003. Tracking storm origins from RDI ADCP measurements. 50th EPOC conference, Catalina Island, CA, September 24-27, 2003.

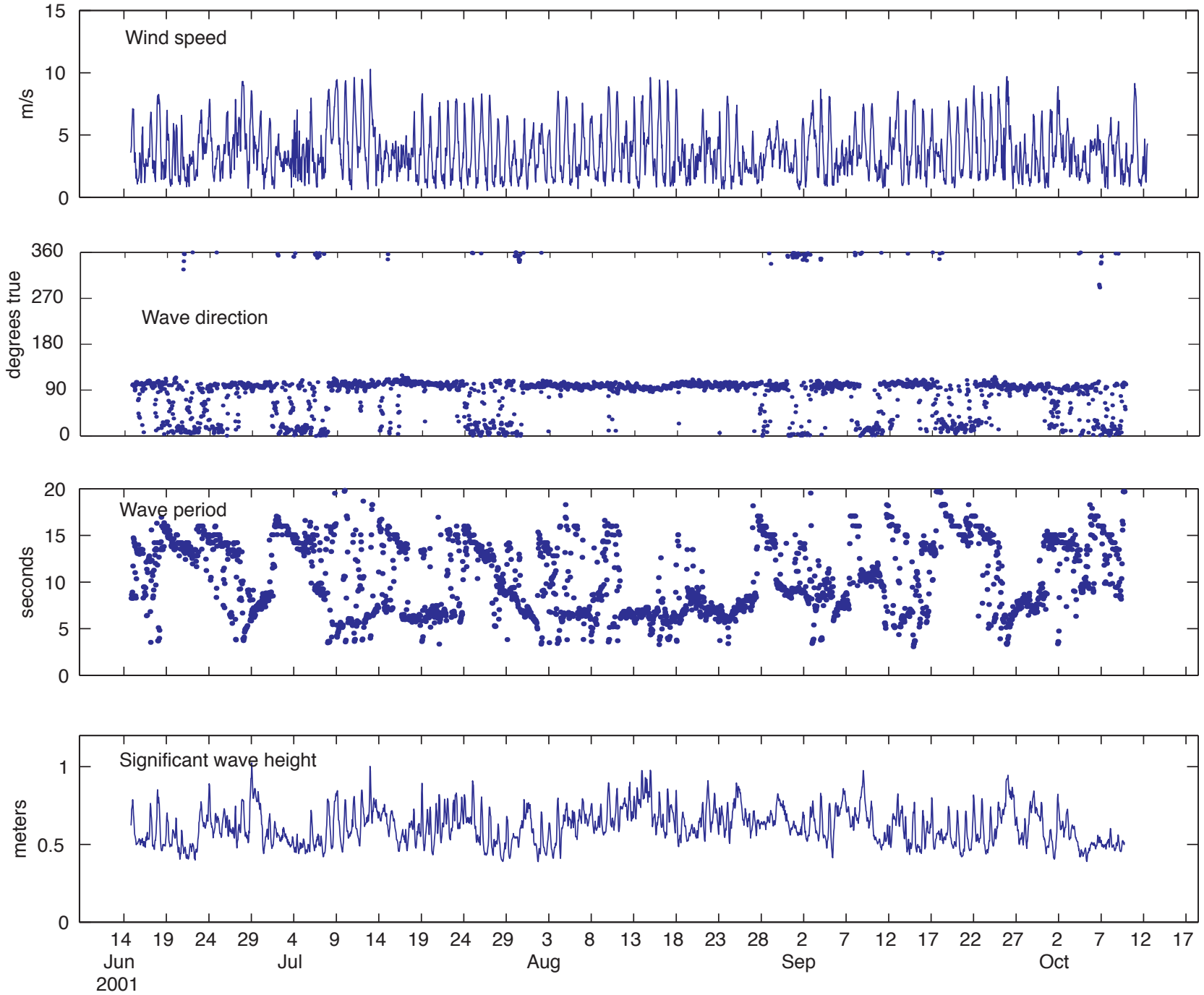

Figure 8-1. Hourly averaged time-series of wind speed, wave direction, wave period, and significant wave height. The data were collected on a meteorological buoy deployed at HB07.

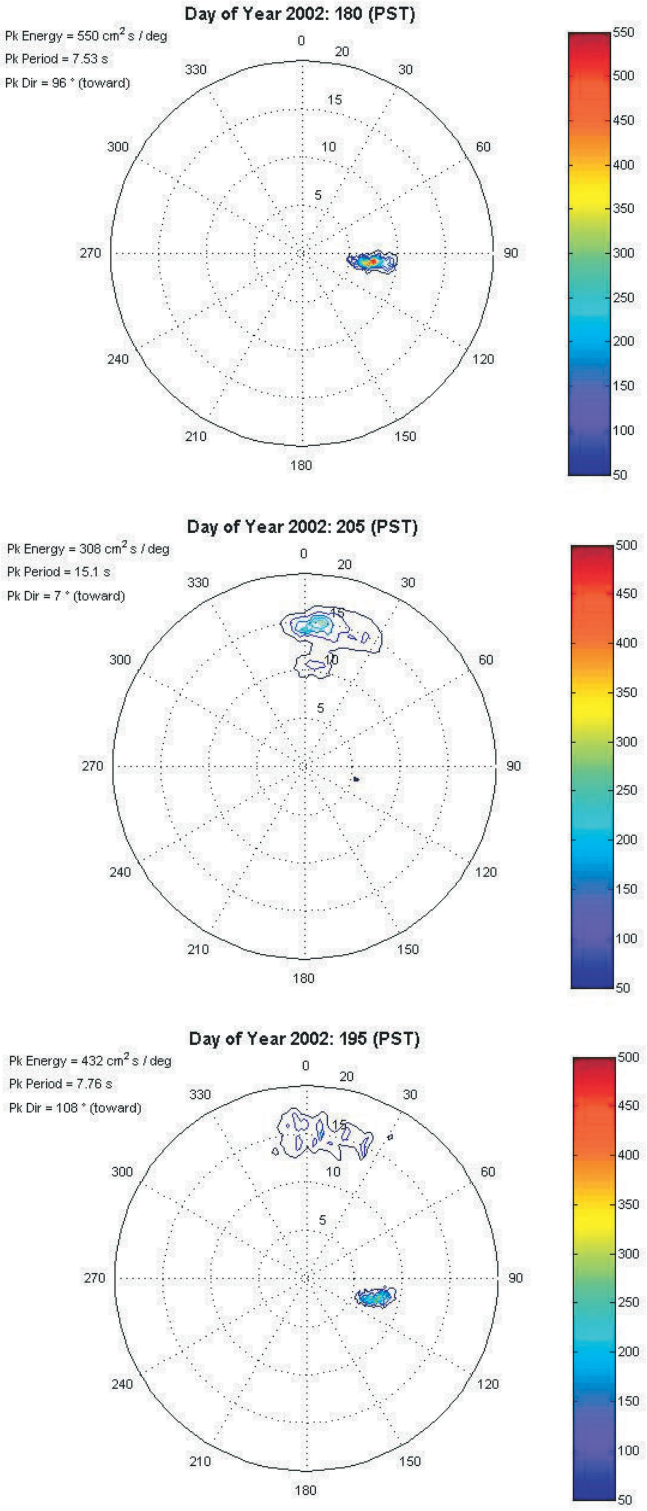

Figure 8-2. Directional wave spectra showing westerly wind waves (top), southerly swells (middle), and mixed (bottom) wave conditions. Westerly wind waves were predominant during the deployment. The data were collected on a meteorological buoy deployed at HB07.

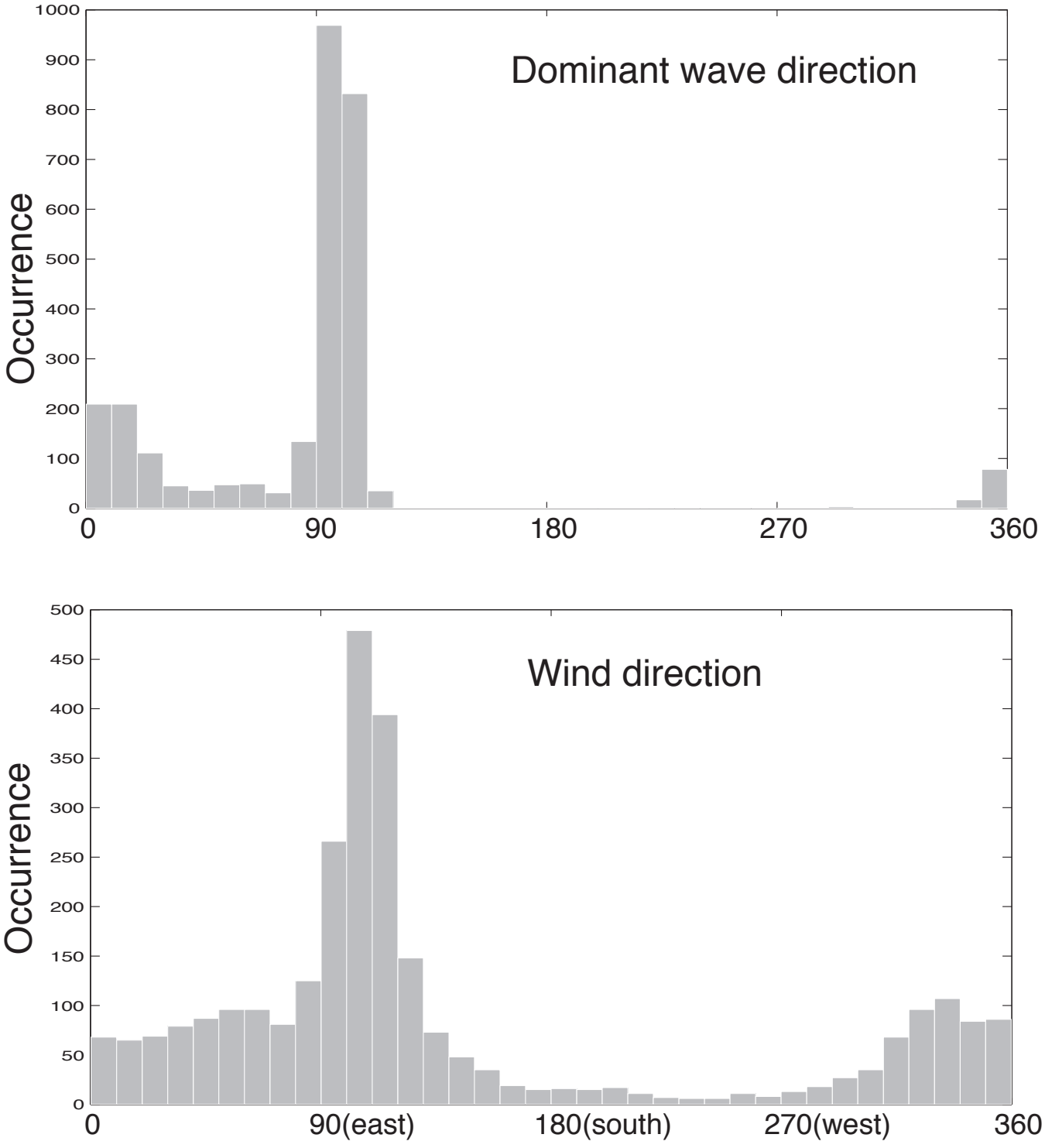

Figure 8-3. Histograms of wave direction (top) and wind direction (bottom). Wind direction is presented in oceanographic convention, i.e., blow toward. The data were collected on a meteorological buoy deployed at HB07.

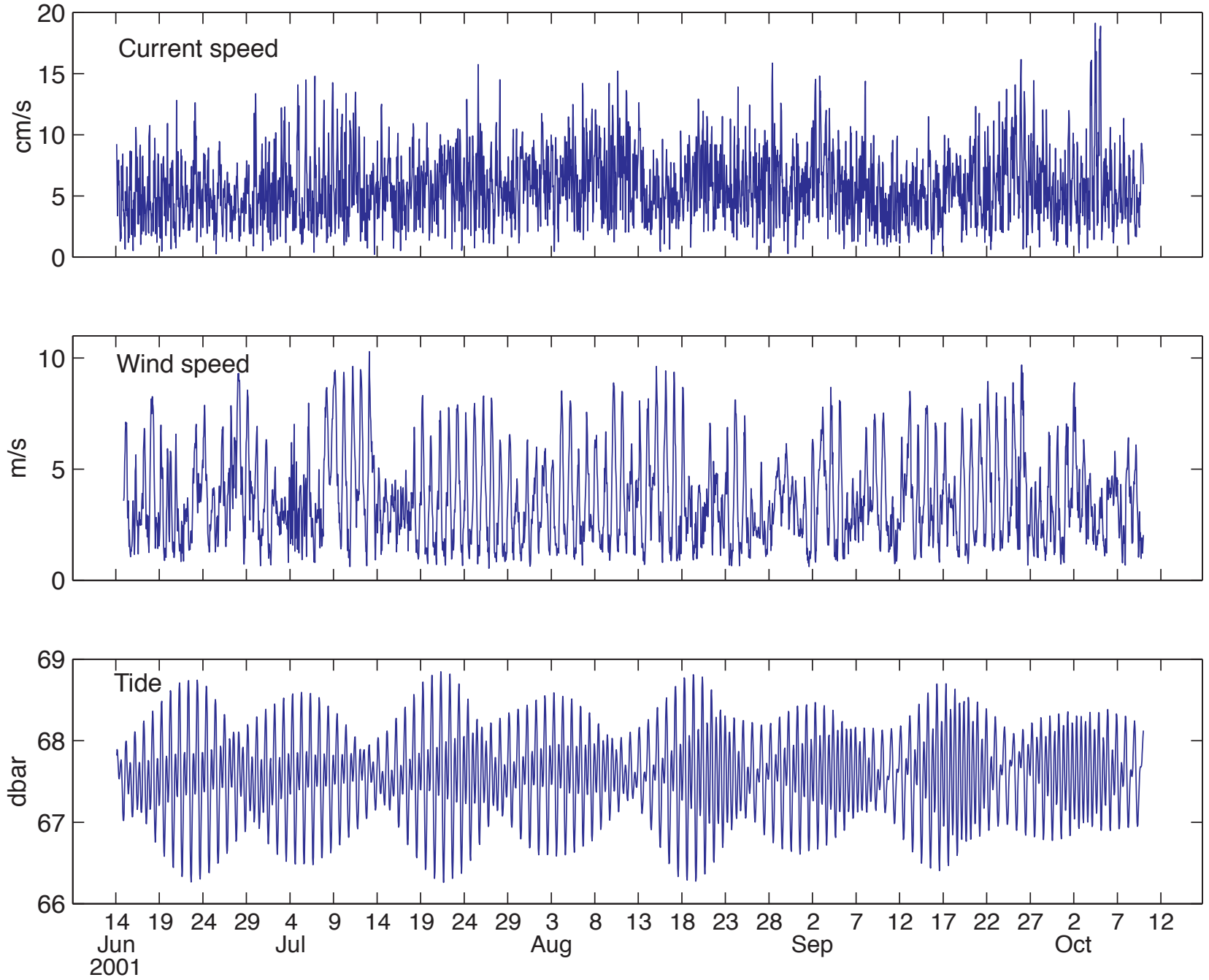

Figure 8-4. Hourly-averaged time-series of current speed (top), wind speed (middle), and tide (bottom). The wind data were collected on a meteorological buoy deployed at HB07. The current and tide (pressure) were measured from a tripod at HB07.

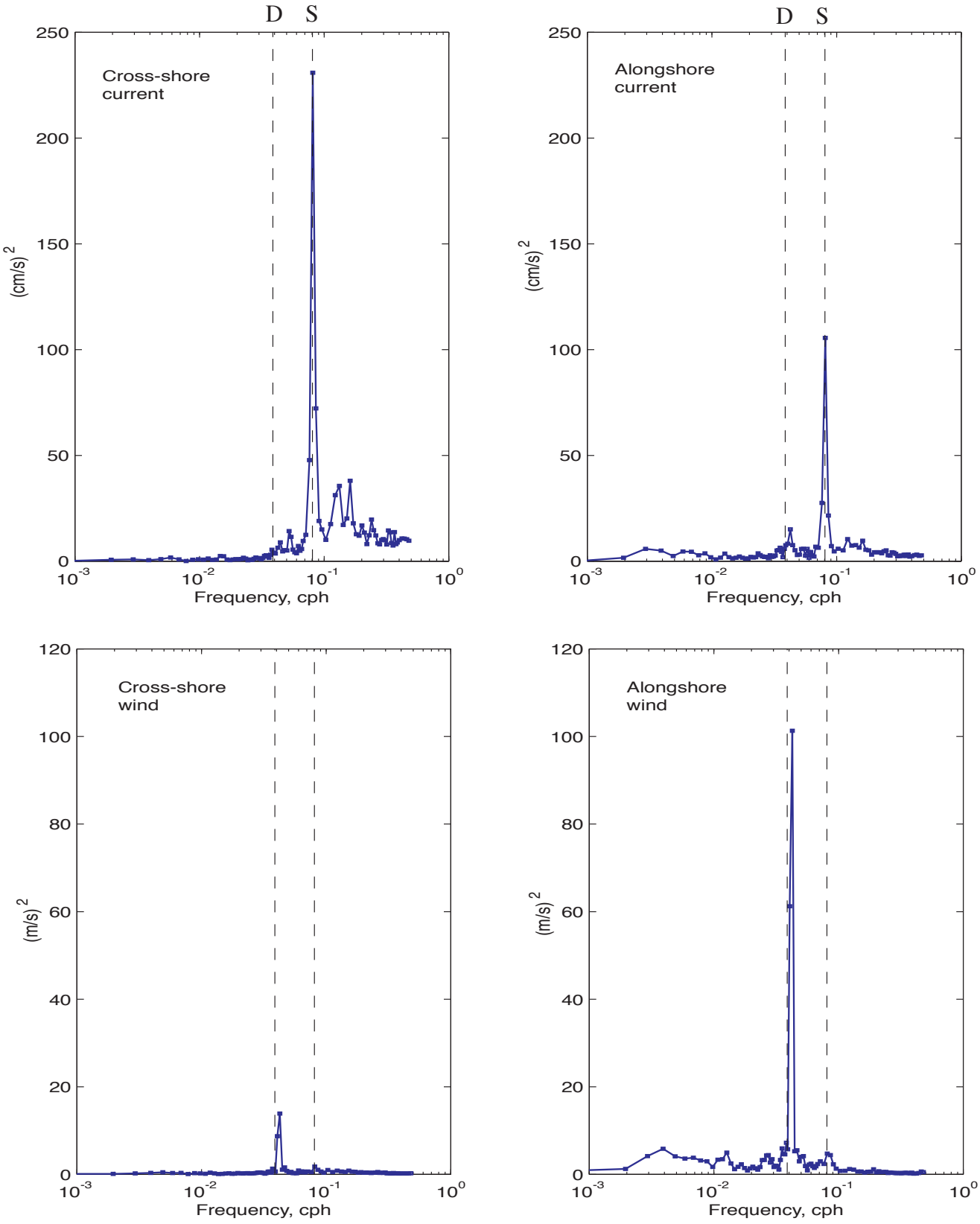

Figure 8-5. Energy spectra of near-bed current (top) and wind (bottom) at HB07. While the wind is mainly diurnal (daily sea breeze) the near-bed current is semidiurnal dominated. The two dashed lines represent the frequencies of diurnal (D) and semidiurnal (S).

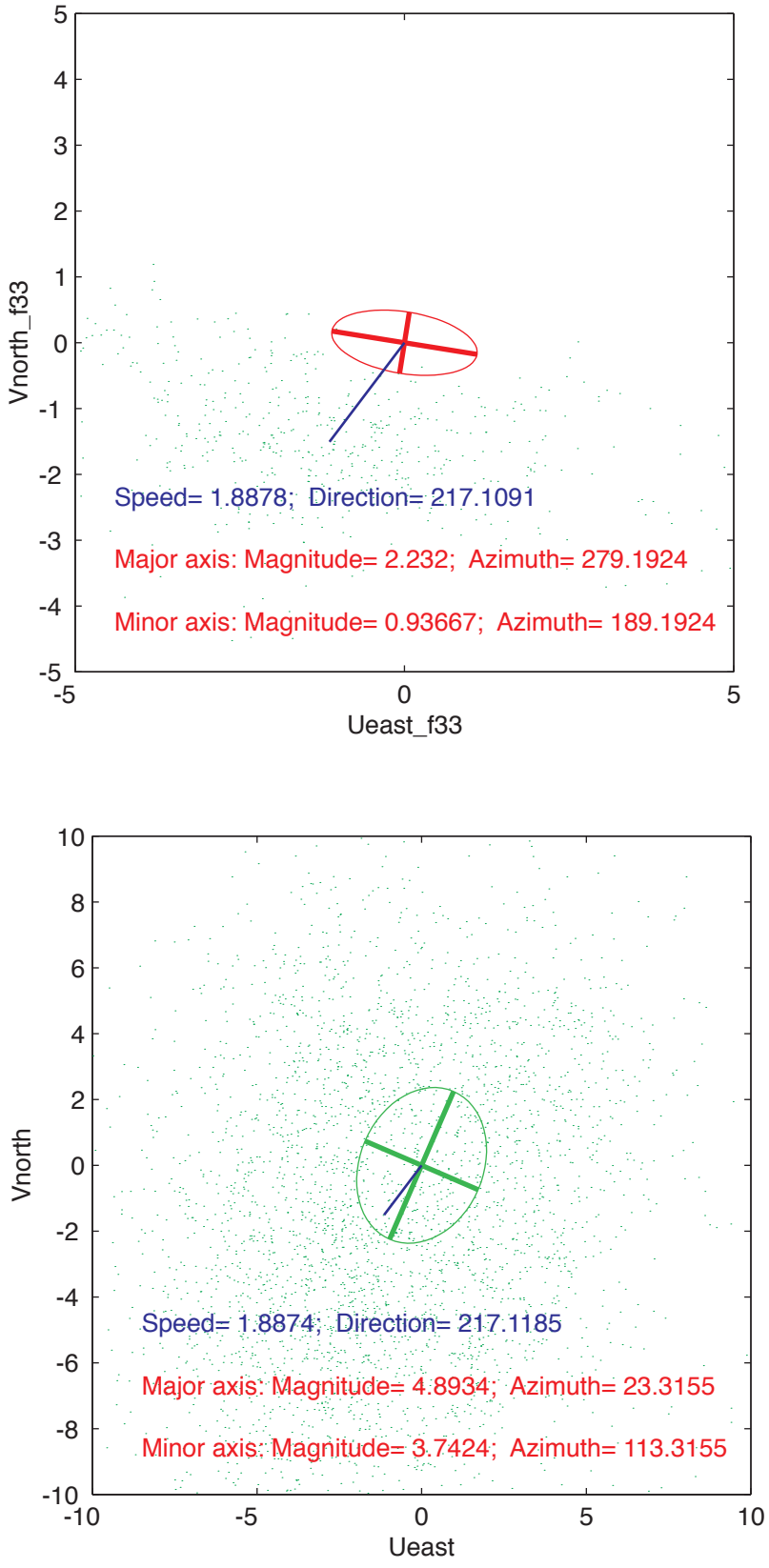

Figure 8-6. Scatter plots of low-pass-filtered (top) and hourly-averaged (bottom) near-bed current measured 60 cm above bed at HB07. While the low-pass-filtered subtidal current clearly follows the isobath at the shelf break, the hourly current shows a major axis that is cross-shelf oriented.

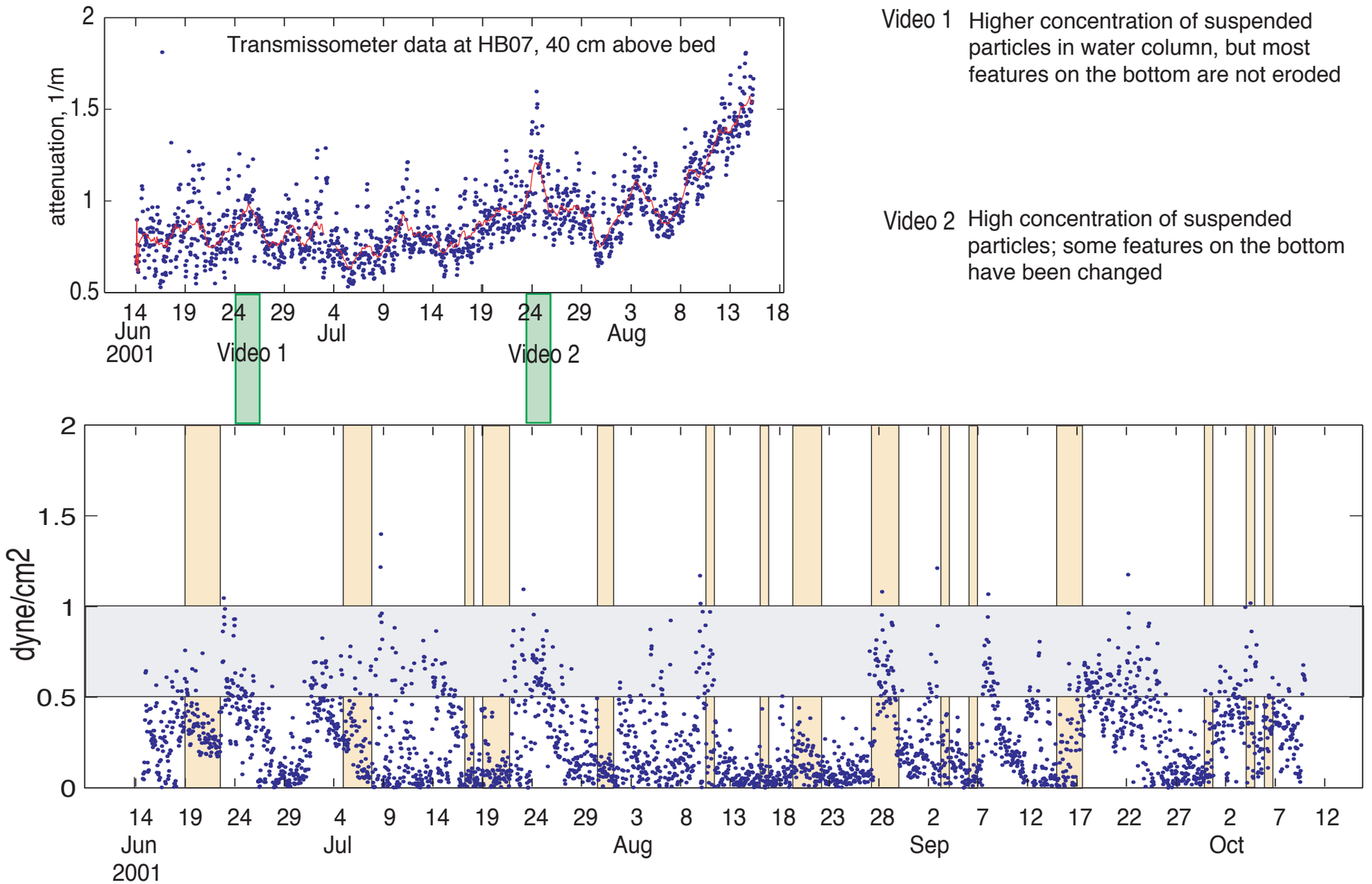

Figure 8-7. Time-series of water clarity (top panel, red line is low-pass-filtered) and estimated bedshear stress (bottom panel). The transmissometer was fouled after early August. The vertical bands in the bottom panel designate the beach contamination events. Shear stress values within or above the horizontal band are able to resuspend very fine sands and silts.

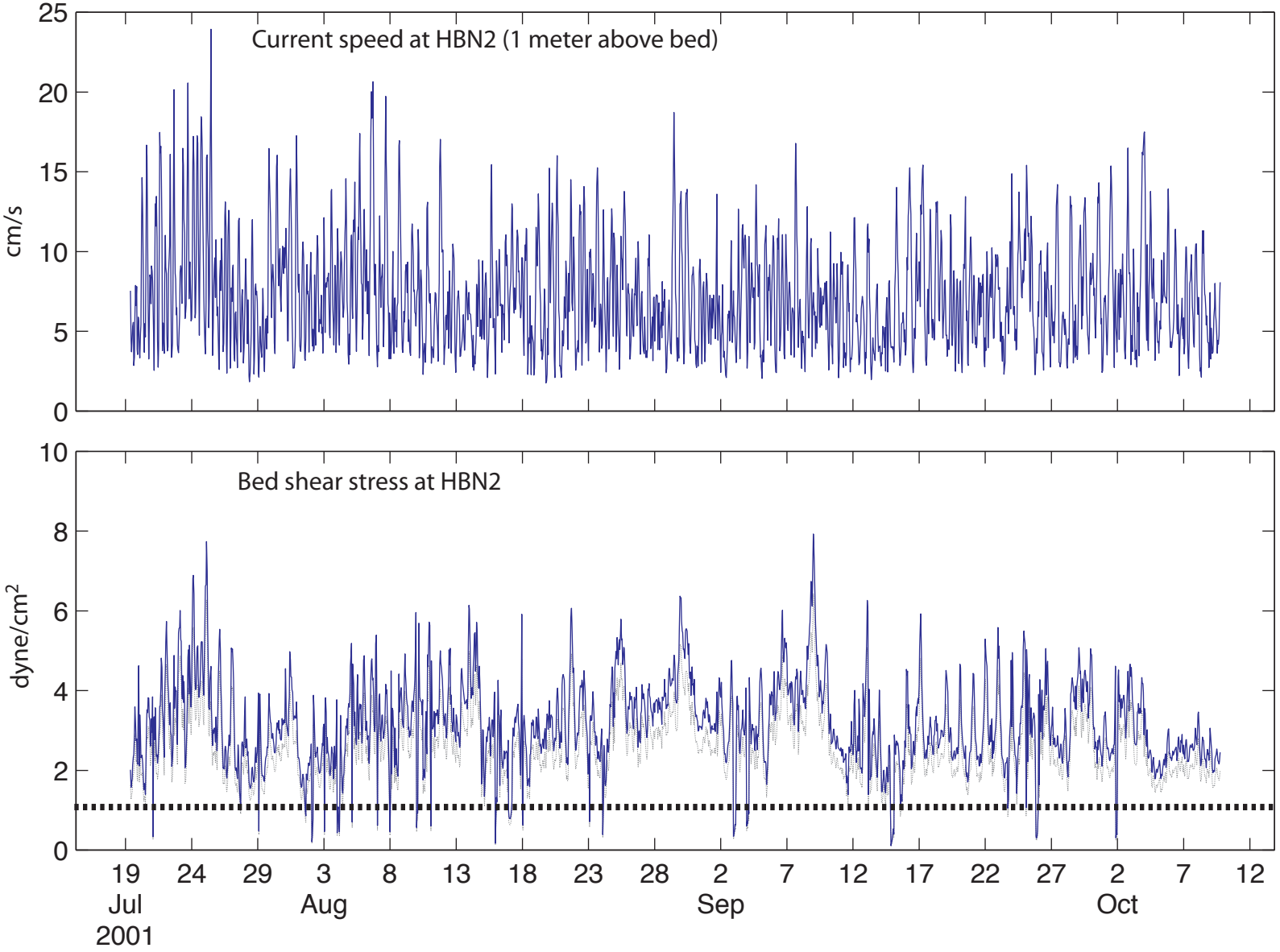

Figure 8-8. Hourly time-series of current speed (top panel) and calculated bed shear stress (bottom panel) at the HBN2 site (10-m water depth). The lighter line is 80% of calculated shear stress value. The horizontal, thick dotted line is the upper limit of critical shear stress (1.0 dyne/cm^2).

CHAPTER 9. NEARSHORE CIRCULATION AND TRANSPORT PATHWAYS

John Largier

9.1. Introduction

This chapter addresses the circulation in the nearshore and the possibilities for outfall-contaminated water to be transported into the surfzone (Figure 9-1). The previous chapters have addressed patterns and processes over the shelf in the vicinity of the outfall and inshore over the shelf. In addition to being transported from the outfall on the outer shelf to the nearshore, wastewater plume waters need to be transported through the nearshore and into the surfzone before their bacterial load will be detected at the beach sampling stations and before associated pathogens will pose a threat to the health of swimmers and surfers. In this study, the "nearshore" is understood as that region where the water depth is less than the thermocline depth over the shelf–so that, in the absence of thermocline motions, the water would be weakly stratified and uniformly warm. By this definition, the nearshore off Huntington Beach typically extends out to about 15-20 m in summer and a bit deeper during the fall. Cross-shore transport within the surfzone and across the breaker line was not addressed directly in this study.

In spite of the massive effort in sampling fecal indicator bacteria off Huntington Beach in 2001, the intensity of sampling of bacteria away from the shoreline is inadequate to address patterns and processes that exhibit small space and time scales (this is particularly true in the nearshore where space and time scales are smallest). The approach of investigating onshore transport of cold waters, adopted here, is based on the observation that the wastewater plume is mixed into cold sub-thermocline waters and trapped beneath the thermocline (Chapter 10). Model and observations indicate that the mixed wastewater plume is at temperatures below 14°C. As nearshore waters are much warmer in summer and fall (18-24°C) (Figure 9-2), the presence of cold water nearshore indicates onshore transport of sub-thermocline water and the possibility of plume waters being transported into the nearshore.

The approach in this chapter, then, is to investigate when and where and how often such cold water is observed in the nearshore and to identify and characterize the transport processes, including possible mixing and dilution enroute. This addresses the possibility of wastewater being carried through the nearshore and into the surfzone, but it does not address whether there were any such events. The latter issue is addressed in Chapter 3, where an attempt is made to link observed bacteria events along the shoreline with cold-water transport events.

There are two primary reasons why one does not expect to see this sub-thermocline cold water moving into the nearshore on a more regular basis.

(1) Polarization: Currents directed perpendicular to the shore get weaker as one approaches the shore, going to zero at the shoreline (unless they are very short-lived, such as waves, or very localized, such as rip currents). Horizontal excursions of cold water are thus short, being limited by the strength and duration of onshore currents.

(2) Potential energy: Substantial energy is required to lift the dense cold water up from below the thermocline to the surface. The vertical excursions of sub-thermocline water are thus limited by the energy available (relative to the depth and strength of the thermocline/pycnocline). No potential energy is required to move cold water inshore to the depth where the thermocline intersects the bottom (e.g., 20 m), irrespective of how close this

is to shore, but substantial potential energy is required to raise this cold water up as it intrudes into the nearshore, irrespective of the horizontal excursion from the 20-m isobath to the surfzone.

Where cold water enters the nearshore and surfzone over an extended length of the beach, it does so through onshore flow of cold water. However, as one approaches the shoreline, the strength of cross-shore transport weakens, primarily because it is not possible to move water through this coastal boundary. This is clearly seen in spectra of depth-averaged current velocities from nearshore moorings (Figure 9-3a) and in the orientation of barotropic tidal ellipses (Chapter 7), and is further discussed by Carrillo et al (2004). While depth-averaged cross-shore and alongshore currents at HB07 exhibit similar strength for periods up to 2-3 days, cross-shore tidal and diurnal currents at HB05 and HB03 are about half the strength of alongshore currents, and inshore at HBN2 tidal-diurnal cross-shore currents are several times weaker than alongshore. Inshore of 10 m, cross-shore tidal currents are very weak (about 1 cm/s, e.g., at AES2) corresponding to horizontal excursions of order 0.5 km and 1 km for semidiurnal and diurnal tides, respectively. Inshore of 10 m, only short-lived depth-averaged cross-shore currents (periods of a few hours or less) are as strong as alongshore currents. However, stronger cross-shore currents are observed nearshore in the presence of stratification, where vertical shear allows surface water to flow in one direction while near-bottom water flows in the opposite direction, with no net transport into the coast. This can be seen in spectra of current shear (Figure 9-3a). For all moorings offshore of 10 m, cross-shore and alongshore current shear is comparable in the tidal-diurnal band and at higher frequencies, although cross-shore flows are a bit stronger in the internal wave band (particularly nearshore). But, closest inshore at AES2, even sheared cross-shore flows are much weaker than alongshore flows, due to the shallowness of the water column (which limits vertical shear), in addition to the proximity of the shoreline. A summary of the relative weakening of cross-shore flow nearshore (i.e., polarization) is given in Figure 9-3b. In the nearshore, alongshore currents are stronger and more persistent.

Stratification is thus key to allowing cross-shore transport in the nearshore, and cold water will generally be transported into the nearshore as a near-bottom intrusion, with concurrent offshore flow near-surface. This intrusion of cold water actually creates or strengthens the stratification in a water column that would have been isothermal or weakly stratified. The presence of strong thermal stratification and the associated cross-shore shear flows in the nearshore are thus largely due to near-bottom intrusions of colder water. These intrusions are primarily associated with three processes that extend from offshore into the nearshore:

- internal tides (Chapter 7),
- wind-driven daily oscillations (Chapter 6), and
- subtidal upwelling effects (Chapter 4).

In addition to shoreward intrusions of cold water through natural processes driven by tidal or wind forcing, human activity may be important in the form of the cooling water pumped into and discharged from the Huntington Beach power plant. The power plant draws in cool near-bottom ocean water at an intake on the 8-m isobath and discharges heated water at an outfall on the 6.5-m isobath (Figure 9-4). The water discharged is warmer than the surface ocean water and thus

rises to the surface and forms a thermal plume floating on the ambient ocean water. This thermal plume spreads radially from the discharge point and may easily enter the surfzone as well as being easily moved by winds, e.g., onshore by afternoon sea breezes. Thus, the cooling water system offers a way to lift up cold water (that may be contaminated) as well as allowing an onshore shear flow.

9.2. Cold-water Intrusions into the Nearshore

The presence of cold water at the 15-m mooring HB03 has been explained in terms of subtidal upwelling (Chapter 4), onshore movement of near-bottom water due to the daily sea-breeze wind cycle (Chapter 6), and onshore movement of near-bottom water due to internal tides (Chapter 7). These time scales of cold-water intrusion are evident in Figure 9-2 and in spectra of near-bottom temperatures in the nearshore (Figure 9-5a). An example of subtidal intrusion was observed between September 10 and 17, when colder temperatures persisted in the nearshore for several days, concurrent with a general uplift of the thermocline over the whole shelf (Chapter 4). At other times, nearshore water was warm, and cold-water intrusions were brief, occurring once or twice a day. However, in the nearshore the diurnal signal was most evident (Figure 9-2), with only brief periods where the semidiurnal signal was strong (e.g., at HBN2 on September 3-4). The increasing importance of diurnal fluctuations near-surface and nearshore is also illustrated in Figure 9-5b. Semidiurnal fluctuations are strongest on the thermocline, being weak above the thermocline, whereas diurnal fluctuations are strong in the thermocline and throughout the surface layer, specifically nearshore.

In Chapter 4 subtidal flow and associated cooling of the shelf is described. These subtidal upwelling events also flood the nearshore with cooler water (for example, in Figures 4-14, 6-8, and 6-9); one can see the concurrence of cool periods at HB01 (10-m isobath) with cool periods offshore. The minimum temperatures in the nearshore during these persistent cool periods is much the same as the minimum temperatures associated with tidal-diurnal cold-water intrusions and the absence of stratification results in weak tidal-diurnal variability during these periods. These events take a few days to set up the cold nearshore temperatures, as deeper water is slowly advected onshore. Further, it is shown in Chapter 4 that these subtidal cold events are associated with periods of southward flow over the shelf. So, while the shelf is inundated in cold water and the 14^{o}C isotherm may reach the nearshore (Figure 4-14), this cold water has typically come from further north.

Short-lived intrusions of cold water occur diurnally and semidiurnally in the nearshore (Figures 9-2 and 9-5b), with low temperatures being observed for a few hours before the cold water drains back down to thermocline depths and the nearshore is again filled with warmer surface water. These cold-water intrusion events are due to a combination of semidiurnal internal tides (Chapter 7) and the daily wind-driven oscillation (Chapter 6).

At the latitude of Huntington Beach it is only the semidiurnal tides that can generate internal tides. This semidiurnal tidal signal is strong offshore, specifically exhibiting a temperature signal at thermocline depths (Figure 9-5b) and a near-bottom cross-shore velocity signal at moorings offshore of the 10-m isobath (Figures 9-3a and 9-6). These internal tide waves can be expected to run up to depths shallower than the still thermocline, resulting in near-bottom

intrusions of cold water in the nearshore. This was observed at 10 m, but coherent run-up events are rare at 5 m. Time series of near-bottom velocities at nearshore moorings (Figure 9-6) illustrate the breakdown of the internal tide signal. At the 15-m mooring, a clear signal was observed with a cross-shore velocity signal of amplitude of about 10 cm/s, whereas at the 6.5-m mooring there is no obvious semidiurnal signal.

This demise of the semidiurnal signal is also seen in spectra for velocity (Figure 9-3a and 9-3b). Inshore of 10 m there is a rapid dissipation of cross-shore flow energy in the internal wave frequency band (Figure 9-7): an average energy density of 6.7 J/m at the 10-m isobath is reduced to only 4.2 J/m at the 6.5-m isobath.

Given the regular onshore winds in the afternoon ("sea breeze") and weaker or offshore winds after midnight ("land breeze") (Figure 9-8), one may expect a regular wind-forced onshore movement of surface water and nearshore thermocline depression during the afternoon and evening, followed by a rebound of the thermocline, onshore movement of cold bottom water, and offshore movement of surface water after midnight. As this cycle would be phase-locked to the time of day, a canonical-day pattern was calculated for temperatures, currents, and wind in the nearshore (Figure 9-8). The "canonical day", or average day, is obtained by averaging all values from the same time of the day; this 24-hour series of average values then defines the canonical, average, or typical daily pattern. The nearshore wind pattern is calculated from 2002 data, as there were no shoreline wind data for 2001 and the sea-breeze cycle should be similar from year to year (at least in phase, if not strength). Coldest water is found in the nearshore during the early morning (Figure 9-8), preceded by a period of onshore flow and onshore wind. While this cycle is statistically weak (large standard deviation), a consistent cycle is seen at all nearshore moorings, and this cycle matches the expected onshore swash of cold bottom water following the weakening and reversal of the sea breeze. Further, this cycle matches the diurnal patterns observed at offshore moorings (Chapter 6).

While the diurnal cycle in nearshore temperatures may at first appear to match daily warming and nighttime cooling, typical daytime surface heat fluxes (100-1000 W/m) are too weak to account for the strength and depth of warming, and this direct warming effect would not account for the associated diurnal pattern of currents (Figures 9-3a and 9-8). Nevertheless, in the surfzone this surface heating may drive a significant thermal cycle of amplitude of 1-2°C, as this water is shallow (assuming that water is resident in the surfzone for a few hours); given this, one cannot interpret the canonical day pattern in the surfzone as evidence of a diurnal cold-water intrusion, as one can for the nearshore outside of the surfzone. Likewise, one must interpret this signal with care at moorings near the power plant thermal discharge. There is a day-night variation in thermal discharge from the power plant which results in a diurnal cycle in near-surface stratification at mooring T5; however, this power plant effect is limited to the vicinity of the power plant outfall and the associated heat flux is too weak to effect the large-scale nearshore pattern observed. Outside of the surfzone and away from the power plant discharge, this diurnal pattern suggests a regular pathway into the nearshore, but it should be noted that the associated velocities are weak (order 2 cm/s) and the horizontal excursion is thus short (order 1 km). In other words, this diurnal swash may be able to move cold water through the nearshore, but it can

only do so if the cold water is already in the outer nearshore at the beginning of the cycle (i.e., inshore of the 15-m isobath).

Both the internal tide run-up and the wind-driven swash of cold water into the nearshore suggest that observed temperature changes in the nearshore should be explained primarily by the onshore advection of cold water from further offshore. This argument has been made by Boehm et al (2002), who found that cross-shore advection dominated the observed temperature changes at the 18-m isobath in data from the summer of 2000. However, this thermal balance breaks down in the nearshore. Ignoring a number of terms that should be of secondary importance (like mixing) and expecting vertical velocities to be zero near-bottom, one can expect a simple thermal balance: $\partial_t T + u.\partial_x T + v.\partial_y T \sim 0$, where u and v are onshore (x) and upcoast (y) velocities, T is temperature, and t is time. Consistent with Boehm et al (2002), we find that changes in temperature $\partial_t T$ correlate well with cross-shore advection $u.\partial_x T$ at the 15-m isobath (HB03 mooring). This correlation is dominated by the semidiurnal internal tide signal, which typically dissipates through the nearshore (Figures 9-3a, 9-5, 9-6, and 9-7), and the thermal balance becomes more complex. In the nearshore, the wind-driven diurnal signal dominates (Figures 9-3a and 9-5), but it is not a simple cross-shore swash. Both alongshore and cross-shore components are important in nearshore diurnal currents (Figures 9-3a and 9-6), due to a combination of wind-driven baroclinic flows and tidal barotropic flows. The result is a thermal balance in which both alongshore and cross-shore terms are important (Figure 9-9). At 10 m there is still a correlation ($r^2 = 0.4$) between $\partial_t T$ and $u.\partial_x T$, but at 6.5 m the alongshore advection $v.\partial_y T$ does a better job of explaining temperature changes $\partial_t T$, but even for this the correlation is weak and marginally significant ($r^2 = 0.2$).

But more notable than the shift from cross-shore to alongshore dominance in the nearshore thermal balance is the increase in the residual, due to the presence of temperature and velocity structures that are smaller than those resolved by the mooring array (and perhaps due to the importance of other terms neglected from the simple thermal balance). Figures 9-3a and 9-5a indicate that there are more high-frequency (and probably small-scale) features in cross-shore velocities nearshore than further offshore.

The above discussion addressed the onshore-offshore advection of cold water by internal tides and wind-driven diurnal swash. In this to-and-fro motion some cold water may remain in the nearshore so that there is a net flux of cold water to the nearshore over a tidal-diurnal cycle (e.g., this would result from mixing during an intrusion into the nearshore). However, this pumping may happen due to cross-shore motions at any frequency and it is best to explore it by calculating cross-spectra between cross-shore velocity and temperature. There is zero net flux if velocity and temperature are in quadrature, a maximum onshore flux of warm water if velocity and temperature are in phase, and a maximum onshore flux of cold water if in anti-phase. In the outer nearshore, near-bottom cross-shore velocity and temperature are typically well correlated in the diurnal and semidiurnal frequency bands, with phase differences such that velocity lags temperature by close to 90° (Figure 9-10), corresponding to cold water swashes with minimal net flux. This correlation decreases in the inner nearshore (inshore of 10 m). Similarly, near-bottom alongshore velocities are well correlated with temperature, but mostly in the diurnal frequency band. Again, the temperature-velocity phase difference is in quadrature, with minimal net flux.

These results suggest that mixing is secondary to the to-and-fro advection of cold water into the nearshore on diurnal and semidiurnal time scales.

While there are statistically significant peaks in near-bottom velocity and temperature spectra (and a canonical day pattern), these tidal-diurnal peaks are notably weak inshore of 10 m, and do not simply account for observed temperature changes through cross-shore advection of a cross-shore temperature gradient. Nevertheless, there are clear cold-water intrusion events observed in the nearshore from time to time, with some intrusions propagating through the entire nearshore and into the surfzone (Figure 9-11). The form and penetration of the cold-water intrusion into the nearshore depends on the incident feature and the conditions in the nearshore. The most striking events appear to have the form of internal bores, intruding into the nearshore with a marked thermal front and exhibiting propagation speeds (0.05-0.10 m/s) consistent with that of an internal bore (Figure 9-12). Further, the water velocity within the cold-water feature exceeds the speed of propagation of the feature, as expected within a bore. This characteristic indicates that some of these nearshore features are capable of transporting water shoreward as they propagate. Lagged correlations between near-bottom thermistors in the nearshore indicate similar propagation speeds on average (0.08 m/s between 10- and 6-m isobaths, and 0.03 m/s between 3- and 0.5-m isobaths).

The thermistors deployed in the surfzone were at 0.5 m below mean lower low water (MLLW) and remained submerged during the entire deployment period; however, they were at times under less than 0.5 m of water (low tide) and at times in as much as 3 m of water (high tide), mostly being under about 1.5 m of water. It is expected that the surfzone is mixed and close to isothermal most of the time, except when there is an active intrusion event (Smith and Largier, 1995), so this tidal variation in water level is not expected to (and does not appear to) have a major influence on the observed temperatures. In Figure 9-13, one can see a clear diurnal cycle that is also represented in canonical day calculations (Figure 9-8). During warm weather, it is reasonable to expect a day-night cycle due to diurnal surface heating with an amplitude of order 1-2°C for surfzone residence of a few hours. This appears to explain the smooth background diurnal signal in records plotted in Figure 9-13, but cannot explain the brief cooling events observed on specific days (e.g., days 228-233), when water temperatures may drop over 2°C in an hour. Examining the event on day 232 (Figure 9-11), one can see that it is associated with a cold-water intrusion that has propagated through the nearshore and into the surfzone, indicating that this cold water is advected into the surfzone. On some other days, cold-water intrusions are observed penetrating to the mooring at the 2.5-m isobath and then presumably mixing into the surfzone as the surfzone thermistors show cooling a few hours later. However, on many days there is no clear penetration of the surfzone by cold-water intrusions (e.g., days 234-236).

While there are clear examples of cold-water intrusions penetrating the surfzone, it should be noted that these "cold" temperatures are never less than 17.5^{o}C and well above the temperature of water found in the wastewater plume. Further, the horizontal excursions associated with these cold-water intrusions are short and can only import water from just beyond the nearshore itself. Nevertheless, an analysis of shoreline bacteria data is presented in Chapter 3, where an association between contamination events and cold-water events is sought.

9.3. The Possible Effects of the AES Corporation Power Plant

It has been suggested that the AES Corporation power plant may explain the observed contamination of the beach between surfzone stations 3N and 9N, because it is found in exactly this vicinity. There are three primary possibilities:

1. *A source*: The power plant is a source of bacteria, or a conduit through which contaminated runoff enters the ocean.

2. *A perturbation*: The inflow, entrainment, and outflow of cooling water from the power plant perturbs natural coastal flows in a way that enhances onshore transport of bacteria.

3. *A pathway*: The cooling water flow offers a pathway by which contaminated cold-water intrusions can be transported to the surfzone.

The power plant draws in cooling water at the 8-m isobath, cycles it through the plant for about 20 minutes, and then discharges heated water at the 6.5-m depth contour (Figure 9-4). Unfortunately, the power plant was not operated during May and June 2001, resulting in a minimal flow rate for cooling water and zero discharge of heat–i.e., the discharge was the same temperature as the intake (Figure 9-14). Once the power plant came back online in early July, the discharge was about 15°C above the ambient ocean and intake temperature. However, all through July flow rates were low (about 120 mgd) and only increased to 240 mgd in August and to 360 mgd in October, by which time the summer was over and the experiment almost complete. This precluded observations of power plant thermal effects in summer 2001. Nevertheless, a study of the power plant effects was commissioned by the California Energy Commission in 2002 (the CEC-KOMEX study). This review has focused on the source and pathway issues, and a report is due in mid-2003. Consequently, the discussion of power plant effects on beach bacteria contamination is premature here and it will be brief.

Some preliminary bacteria and salinity data collected by MBC in 2001 indicate that low-salinity water in the plant may have high levels of fecal indicator bacteria, presumably from a land runoff source. The volume, nature, and existence of a specific possible source is unknown and examining this was one of the primary aims of the CEC-KOMEX study in 2002.

The withdrawal flow of water to the intake, the entrainment of water into the discharge jet, and the enhanced stratification due to the thermal plume are thought to alter the strength and penetration of cold surges in the vicinity of the power plant. However, late summer comparison of near-bottom velocity and temperature data on 10-m moorings at HBN2 (offshore of the intake), HBN3 (2 km upcoast from HBN2), and AES3 (0.5 km downcoast from HBN2), when the power plant was operating, revealed no apparent differences in the strength of flow nor in the intensity of temperature drops between these three moorings along the 10-m isobath. Not only are the intake and discharge effects expected to be localized, but the strength of the cold-water intrusions are already weakening by the 10-m isobath and unlikely to be enhanced by a localized power plant effect.

The extent of the thermal plume is illustrated in Figure 9-15 by the distribution of average temperatures. While the power plant discharge is 15°C above the ambient, this warm water quickly mixes into the receiving waters and appears to be diluted more than ten-fold in the near-field. Near-surface temperatures at moorings nearest to the discharge are 0.5-1.0°C higher than further afield (corresponding to a weak density effect), and the spatial extent of this effect is limited to a few hundred meters.

The idea that has received most attention to date has been the possibility that the power plant can draw in sub-thermocline water as it surges up to 8 m of water depth, and then be pumped into the cooling water system and entrained into the discharge jet (a combined flow of order 5000 mgd). These waters then form a thermal plume at the surface with little obstacle to this plume moving ashore. In fact, the discharge process results in radial spreading that would impact the surfzone; further, the regular onshore sea breeze every afternoon may transport this thin surface layer into the surfzone. Clearly, colder water is found at the 8-m isobath than in the surfzone (Figure 9-2), and a thermal plume forms and may enter the surfzone easily. Thus, the transport possibility does exist, but its role in beach contamination depends on the presence of contaminated water at the intake/discharge locations. While there was one observation of contaminated water in the power plant intake and discharge during the preliminary 2001 sampling by MBC, this was not during a cool event. Intense sampling of both the intake and discharge is a primary focus of the CEC-KOMEX study in 2002; this should allow a better evaluation of this issue. However, it is worth noting that there were regular beach contamination events during May-June 2001, a period during which the power plant was not operating, indicating that this mechanism was not playing a role in those events (Chapter 3). Further, if the thermal plume is an important part of this pathway, one would expect to see maximum contamination in the late afternoon and evening, during and following the afternoon sea-breeze maximum, and after the daytime maximum plant heat discharge. Historical observations reveal a maximum in the morning (Figure 3-27).

9.4. Summary

Cold-water intrusions penetrate the outer nearshore due to the action of internal tide run-up and wind-driven diurnal swash. In the inner nearshore the internal tide appears to have dissipated and the diurnal signal dominates. At times cold-water intrusions penetrate the surfzone, although temperatures are only relatively cool (always above 17.5°C). At the same time, cold-water intrusions are entrained into the power plant thermal plume, which may easily penetrate the surfzone. Either route offers a possible pathway for near-bottom waters to enter the surfzone, and for bacterial concentrations to enter the surfzone if they are initially present immediately outside of the surfzone (i.e., where the thermocline intersects the bottom). If either of these transport pathways are a regular cause of beach contamination, one should see an association between bacteria concentrations and water temperature in the surfzone. Concurrent bacteria and temperature data are plotted in Figure 9-16, and no obvious association of high bacteria concentration with either warm water or cold water is apparent. This may be because contamination events are occasional and do not occur during most cold-water or warm-water events. The examination of individual contamination events is presented in Chapter 3.

9.5. References

Boehm, A.B., B.F. Sanders, and C.D. Winant, 2002. Cross-shelf transport at Huntington Beach; Implications for the fate of sewage discharged through an offshore ocean outfall. Environmental Science and Technology, v. 36, p. 1899-1906.

Carrillo, L., J. Largier, M. Noble, P. Hamilton, and L. Rosenfeld, 2004. Polarization of low-frequency currents and the importance of internal waves in near-coastal waters off Huntington Beach, California. To be submitted to Journal of Geophysical Research.

Smith, J.A. and J.L. Largier, 1995. Observations of nearshore circulation: rip currents. Journal of Geophysical Research, v. 100 (C6), p. 10967-10975.

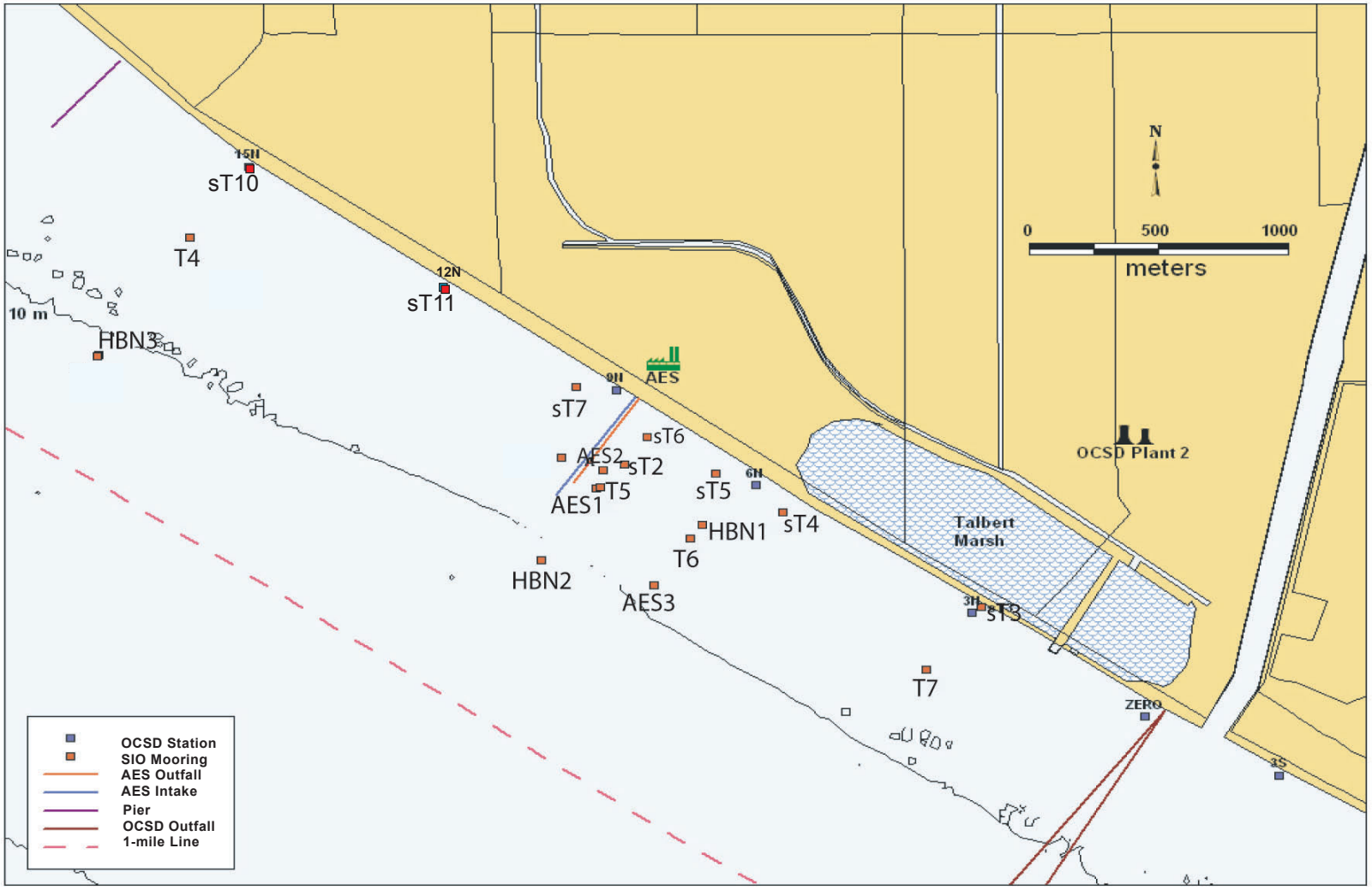

Figure 9-1. Location of nearshore moorings (red squares), beach sampling (blue squares), power plant intake (blue), and discharge (red), Talbert Marsh, and Santa Ana River.

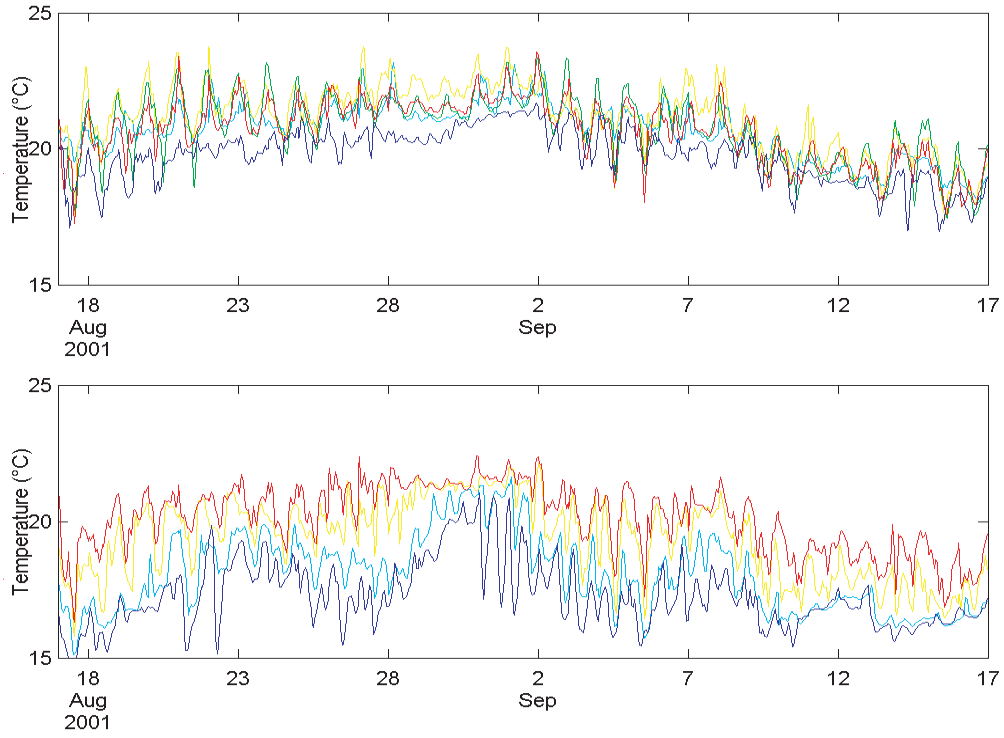

Figure 9-2. Temperature near-surface (upper panel) and near-bottom (lower panel) on moorings at 15 m (blue, HB03), 10 m (cyan, HBN2), 7.5 m (yellow, T5), 2.5 m (red, sT2), and 0.5 m (green, sT6).

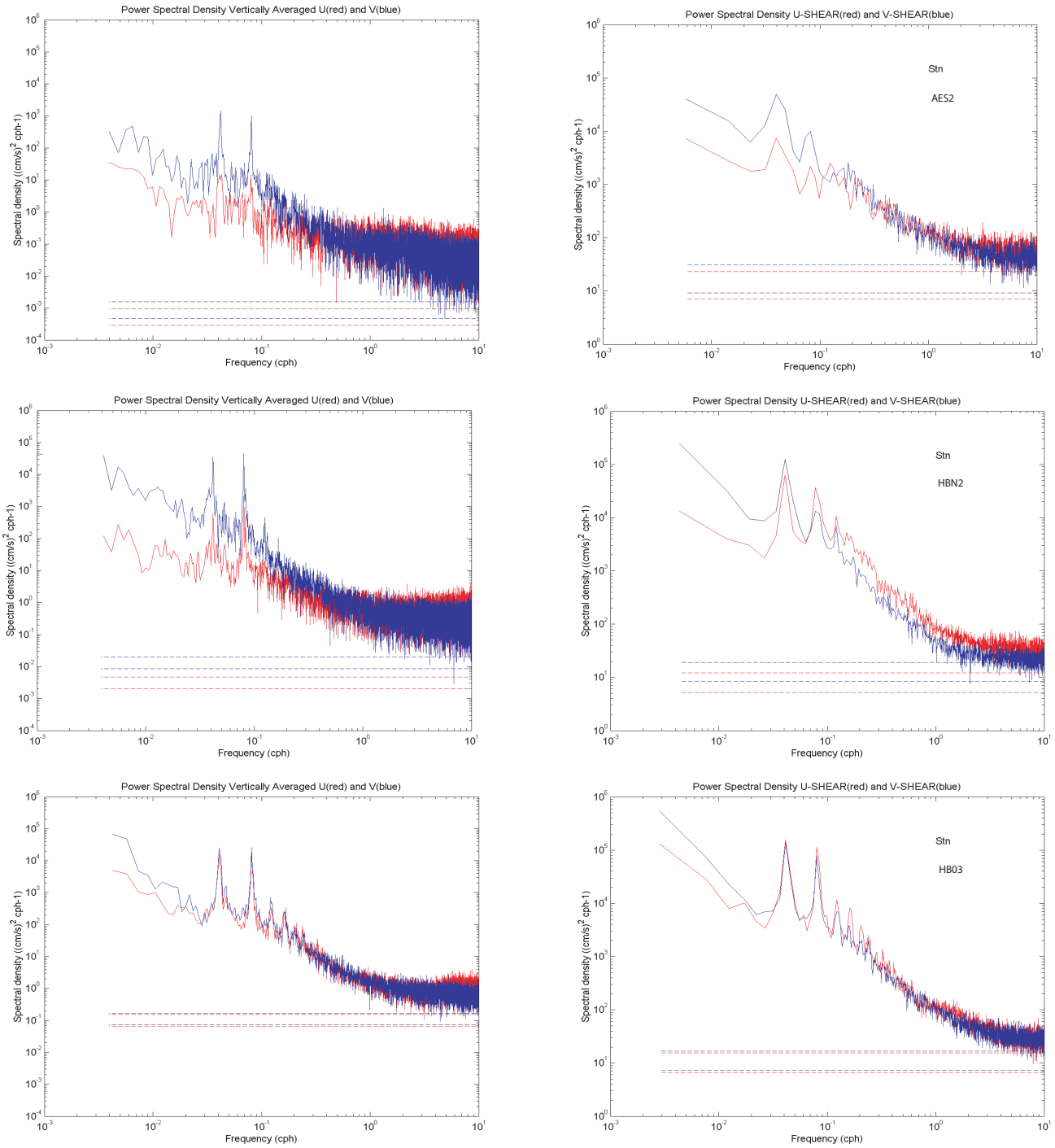

Figure 9-3a. Spectra of depth-averaged near-bottom velocities (left panels) and sheared flow (top-bottom difference, right panels) for moorings AES2 (top row), HBN2 (middle row), and HB03 (bottom row). Alongshore currents are blue, cross-shore currents are red. The 95% confidence interval is shown.

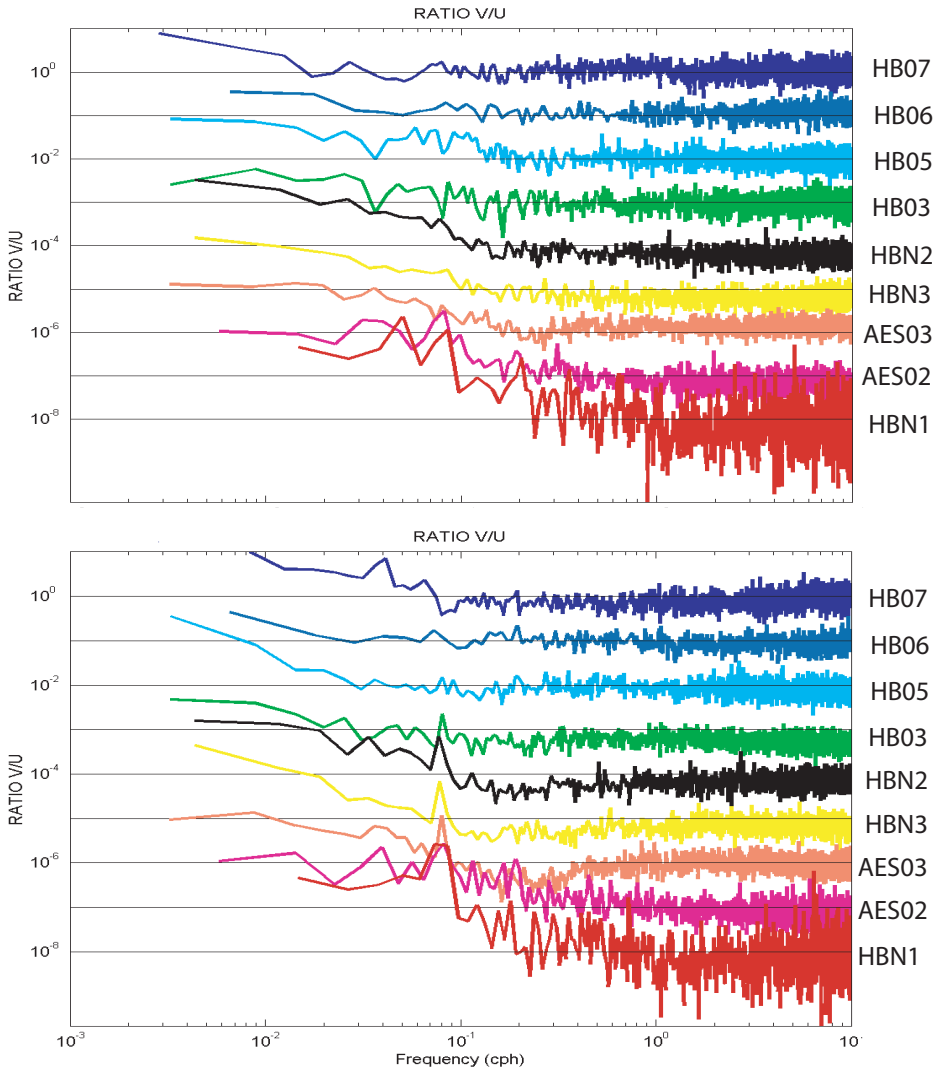

Figure 9-3b. Ratio of spectral power (along:cross) for near-surface currents (top panel) and near-bottom currents (bottom panel) at all moorings. Data are shown for both nearshore and offshore moorings. Plots are offset by an order of magnitude, so that line indicates ratio of one for each plot line.

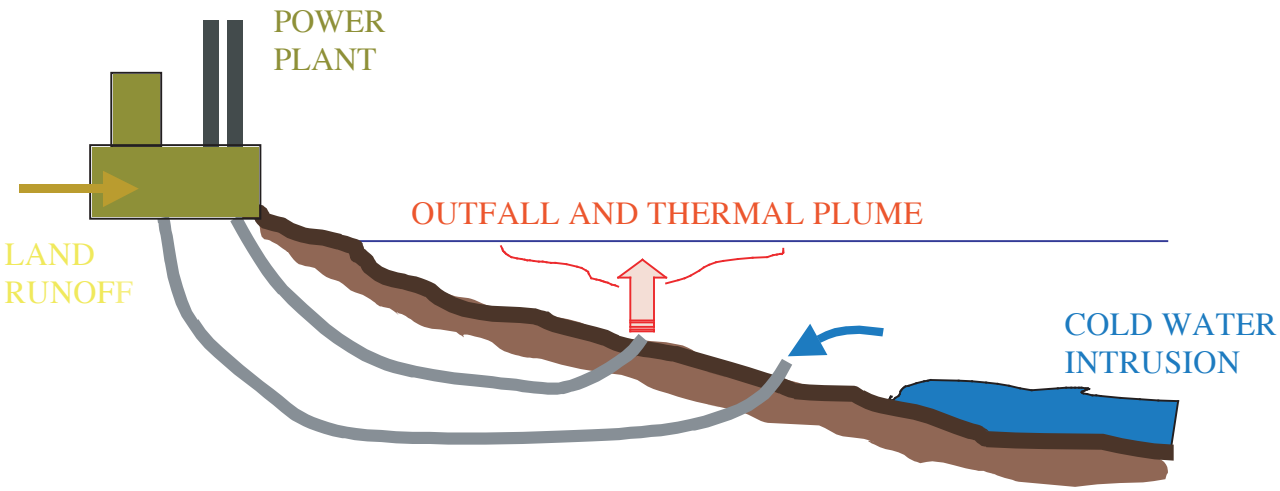

Figure 9-4. Schematic of power plant, showing thermal plume and cold-water intrusion.

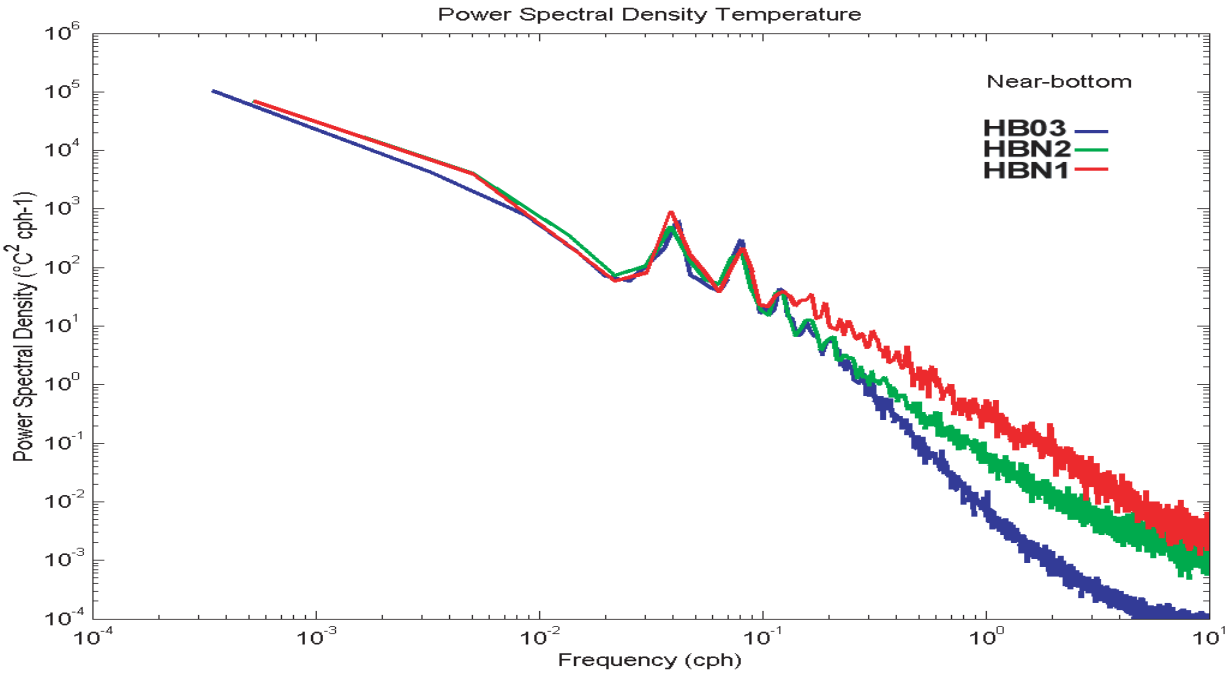

Figure 9-5a. Spectra of near-bottom temperature fluctuations on moorings HB03 (15 m, blue line), HBN2 (10 m, green line), and HBN1 (5 m, red line).

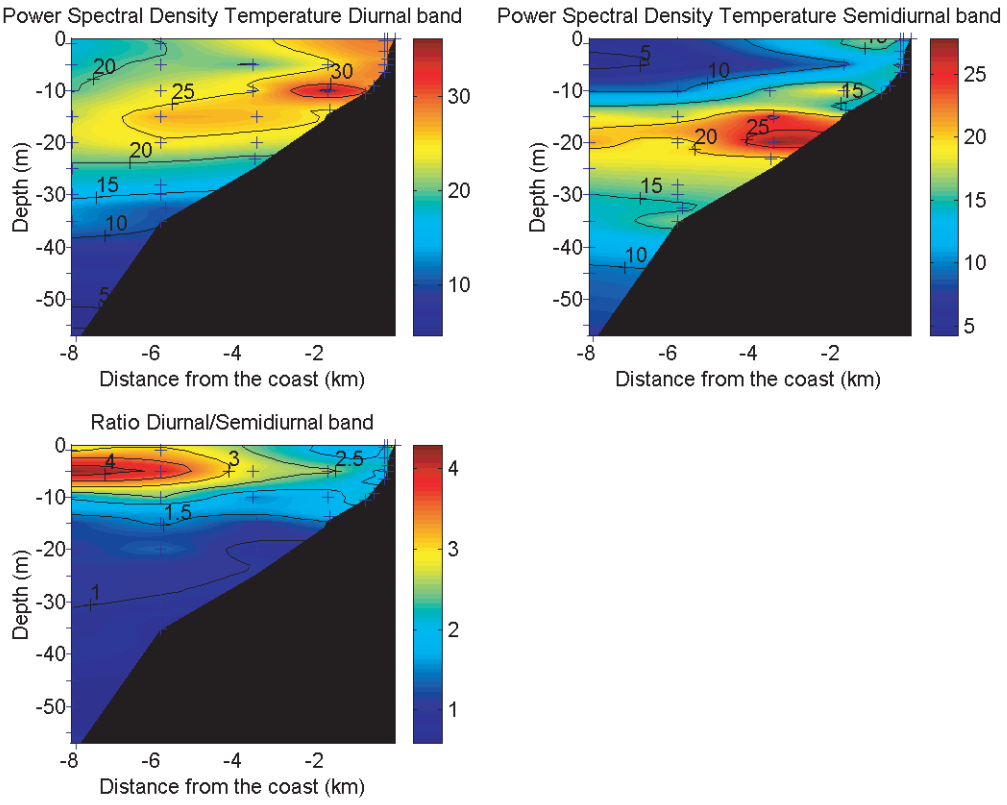

Figure 9-5b. Spatial distribution of the relative importance of diurnal (23-25-hr) and semidiurnal (11-13-hr) temperature fluctuations along the main mooring line. Attention is on the spatial pattern, rather than the absolute values, which depend on the width of the spectral band. Top left panel shows the strength of the diurnal peak, top right panel shows the strength of the semidiurnal peak, and bottom panel is the ratio of diurnal to semidiurnal–showing the importance of diurnal fluctuations in the upper 10 m and nearshore.

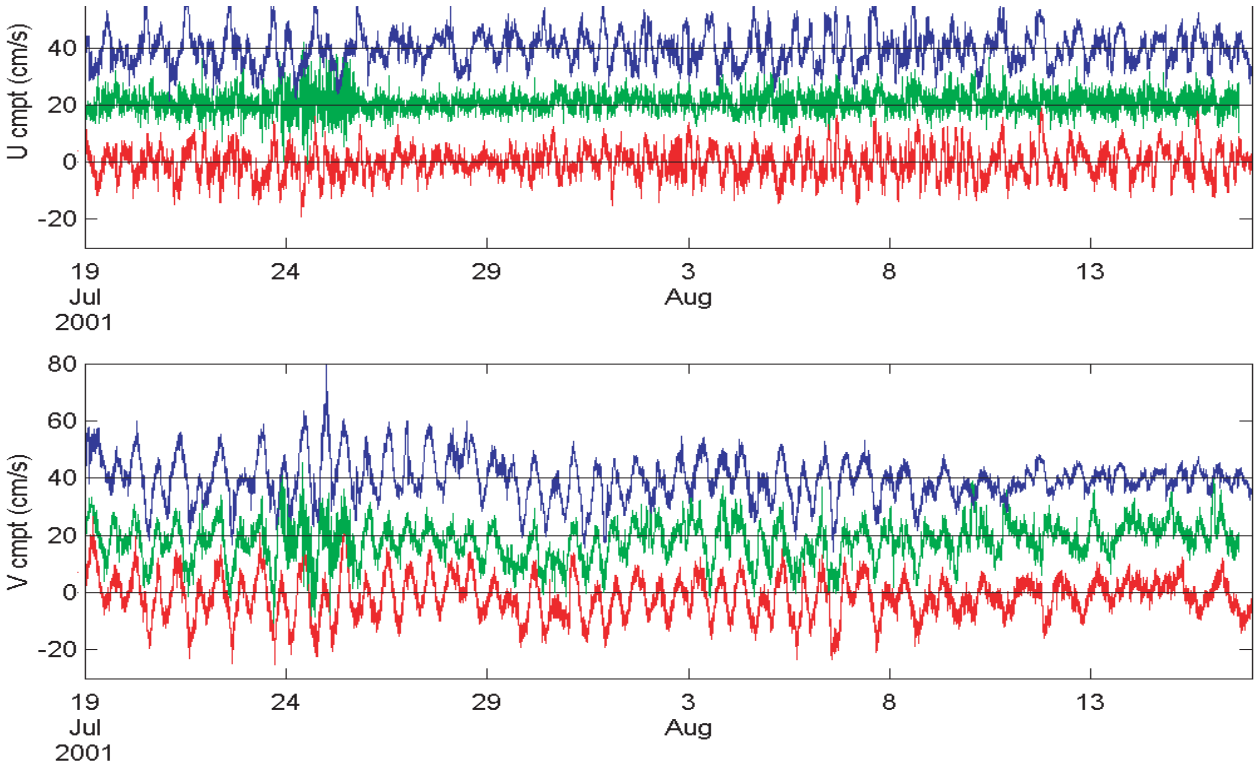

Figure 9-6. Near-bottom cross-shore velocities (upper panel) and alongshore velocities (lower panel) at HB03 (15 m, blue), HBN2 (10 m, red), and AES2 (6.5 m, green). Plots are offset 20 cm/s to separate lines–a zero line is shown for each trace. Note the decrease in both energy and coherence of cross-shore flows in the nearshore, in contrast to strong alongshore flows.

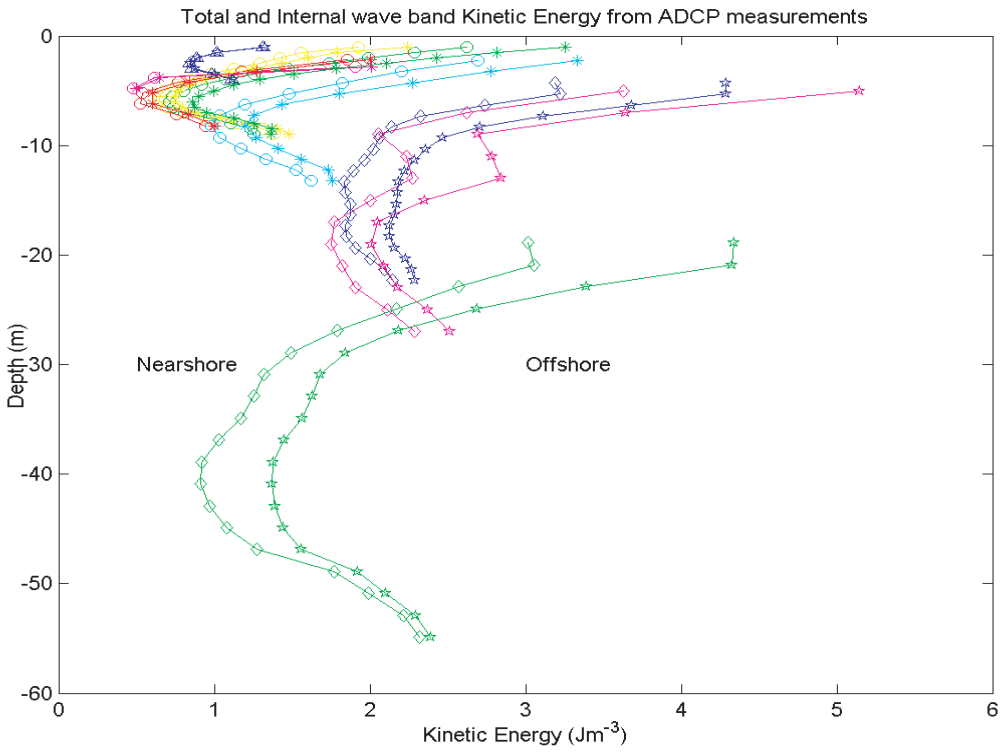

Figure 9-7. Energy density of cross-shore currents in each ADCP bin–across all frequencies (star and asterisk) and for internal wave frequencies only (open symbols). Data shown for moorings HB07 (green), HB06 (magenta), HB05 (blue), HB03 (cyan), HBN2 (yellow), AES3 (green), HBN3 (red), AES2 (magenta), and HBN1 (blue).

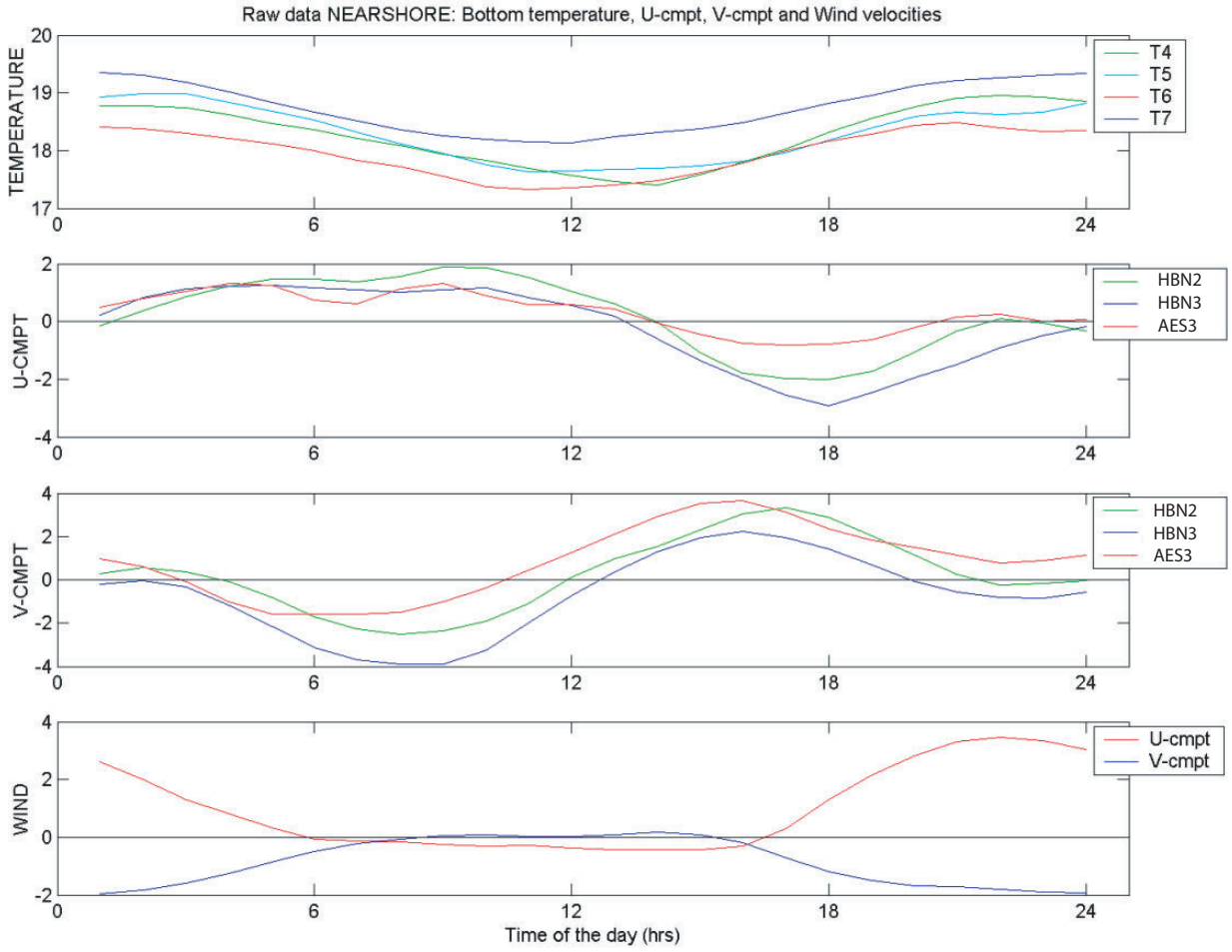

Figure 9-8. Canonical-day patterns for near-bottom temperature at four nearshore moorings on the 7.5m isobath (T4, T5, T6, T7)–top panel. Time of day is in UTC; local time is obtained by subtracting 8 hours, so that minimum temperature occurs between 0200 and 0500 local time. In parallel with temperature are canonical-day patterns for near-bottom cross-shore (u, positive onshore) and alongshore (v, positive upcoast) currents at 10-m moorings HBN2, HBN3, and AES3, and for wind at the shoreline (calculated from data collected in 2002).

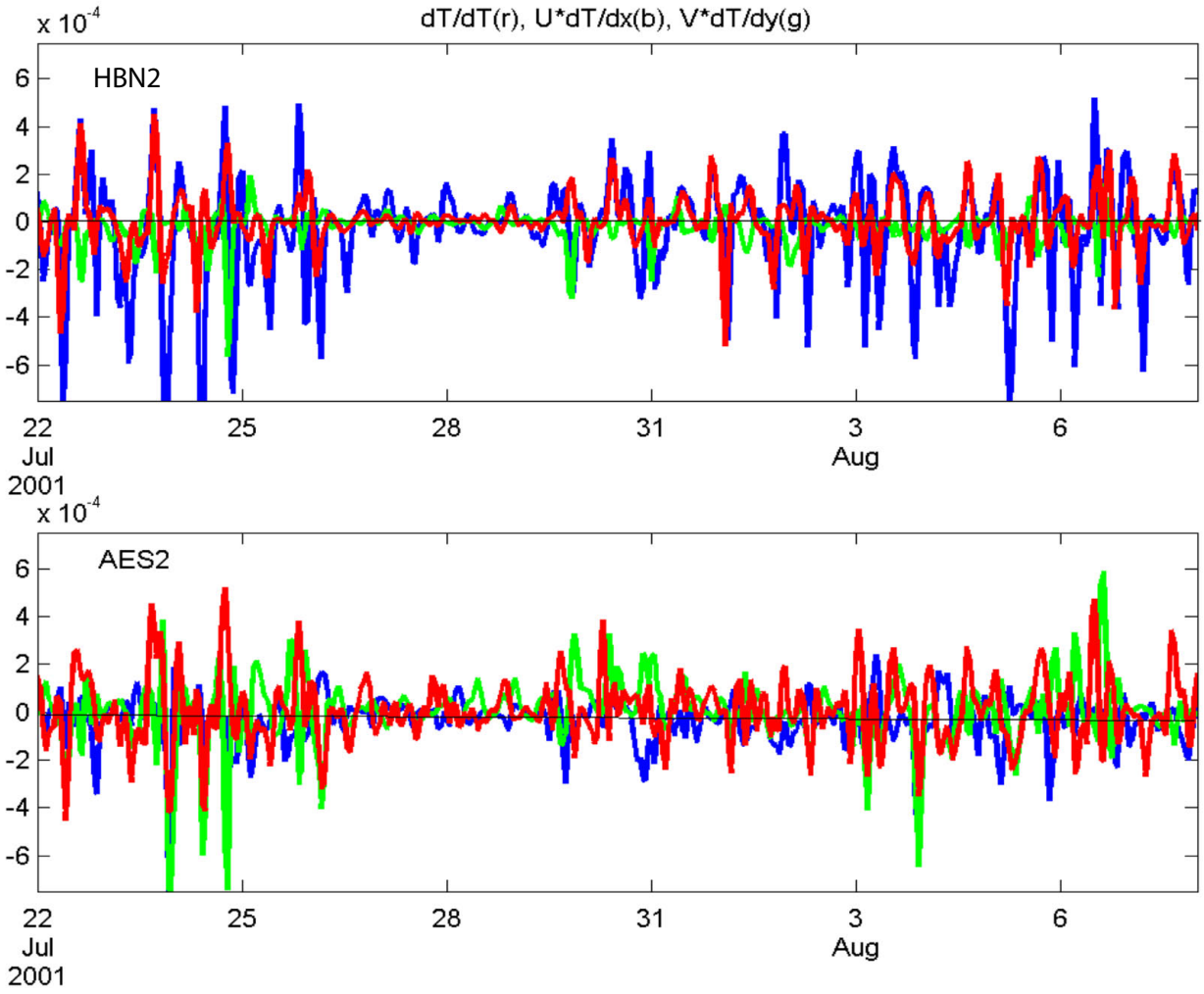

Figure 9-9. Summary of thermal balance calculations centered at HBN2 (10 m, top panel) and AES2 (6.5 m, bottom panel). The observed ∂tT is plotted in red, cross-shore advection u.∂xT in blue, and alongshore advection v.∂yT in green.

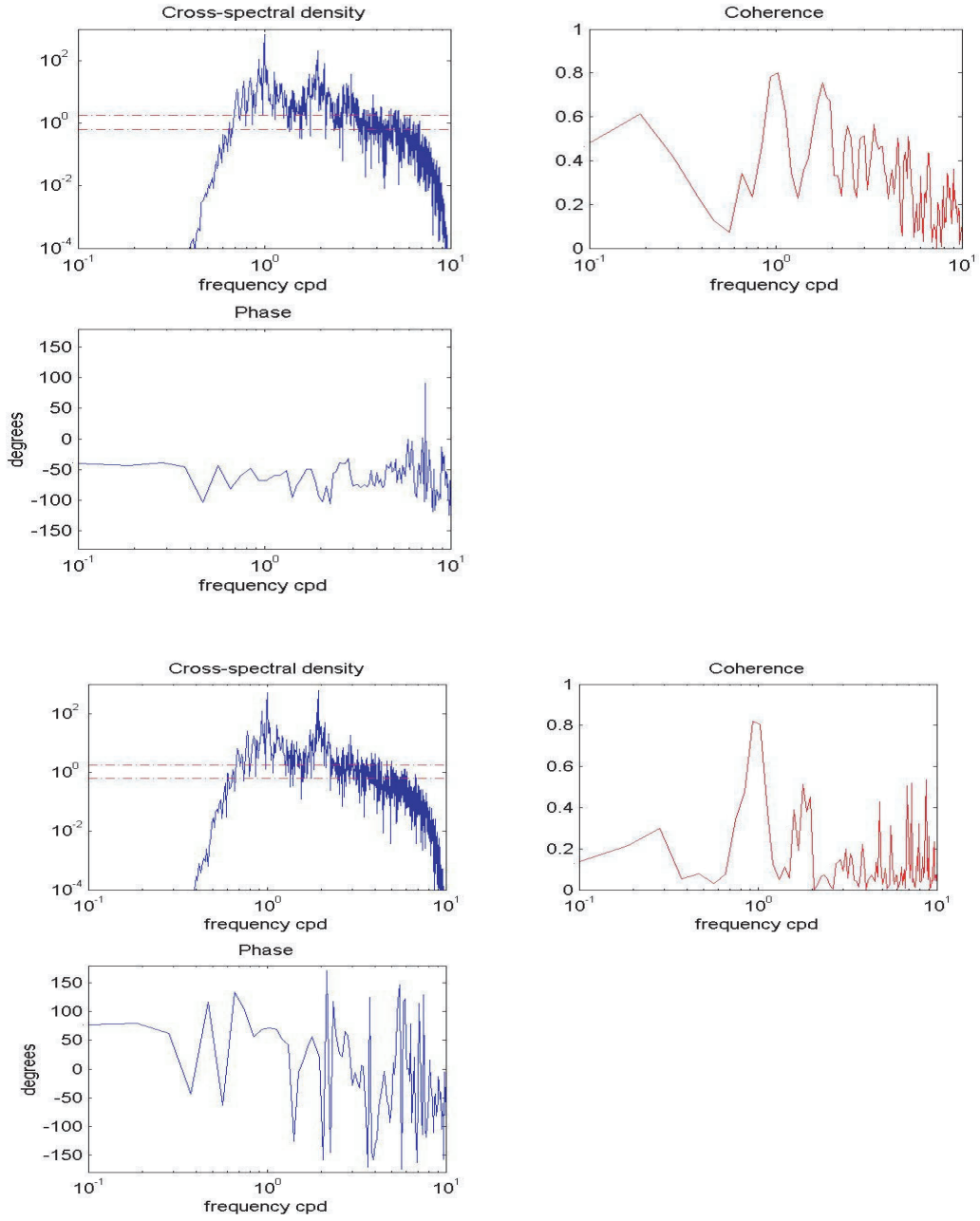

Figure 9-10. Cross-spectra, coherence, and phase for near-bottom temperature and velocity at HB03 (15-m isobath): cross-shore (upper 3 panels); alongshore (lower 3 panels).

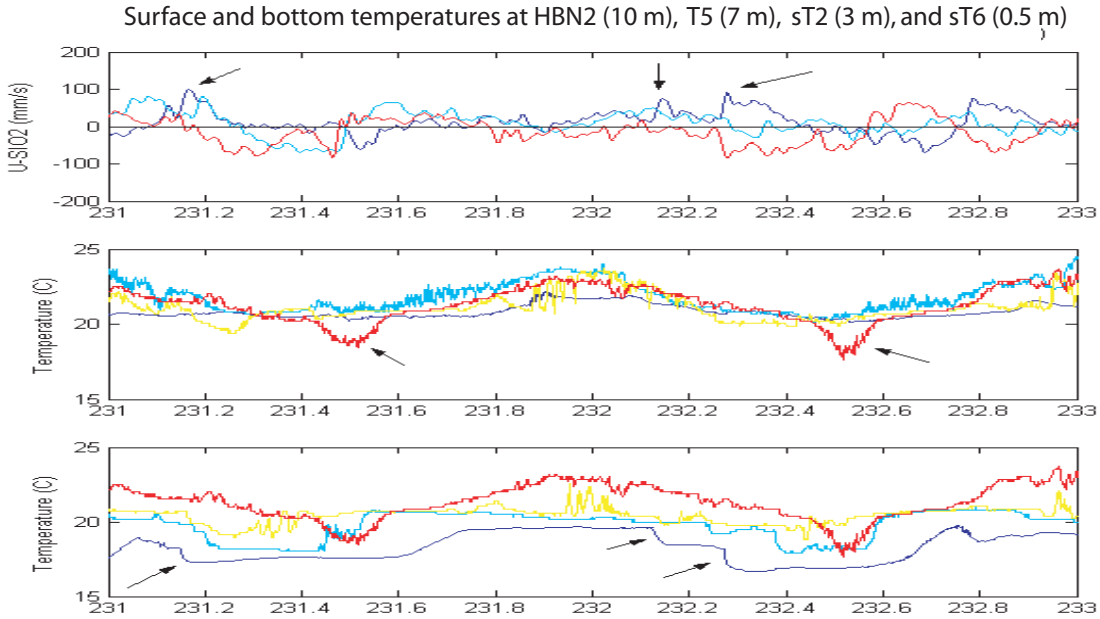

Figure 9-11. Top panel: cross-shore current at HBN2 (near-bottom red; near-surface blue). Middle and bottom panels: near-surface and near-bottom temperatures at 3002 (10 m, blue), T5 (7.5 m, cyan), sT2 (2.5 m, yellow), and sT6 (0.5 m, red).

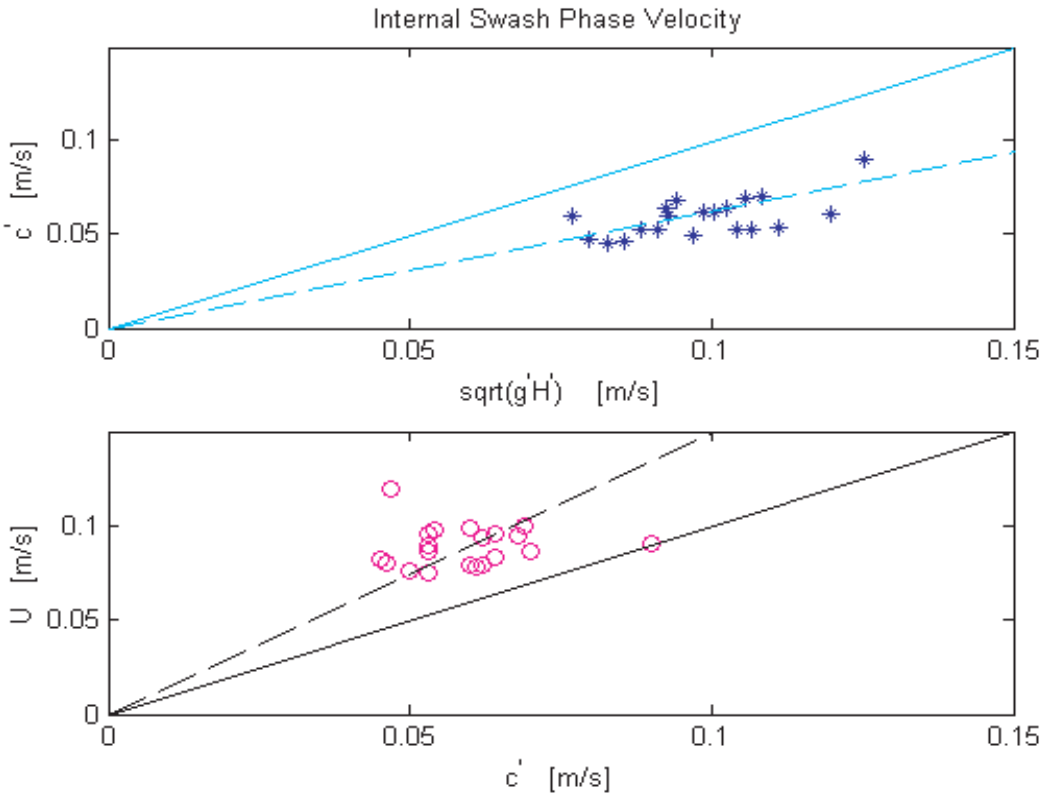

Figure 9-12. Upper panel: Observed propagation speeds c' for frontal features moving through the nearshore, compared with scale estimate sqrt(g'.H'), where $H'=H_1.H_2/H$. Observed speeds are slower than scale speeds due to viscous effects and the presence of a "headwind". Lower panel: Observed cross-shore water velocities are faster than propagation speed of feature, illustrating that water is continuously flowing toward the head of the intruding feature.

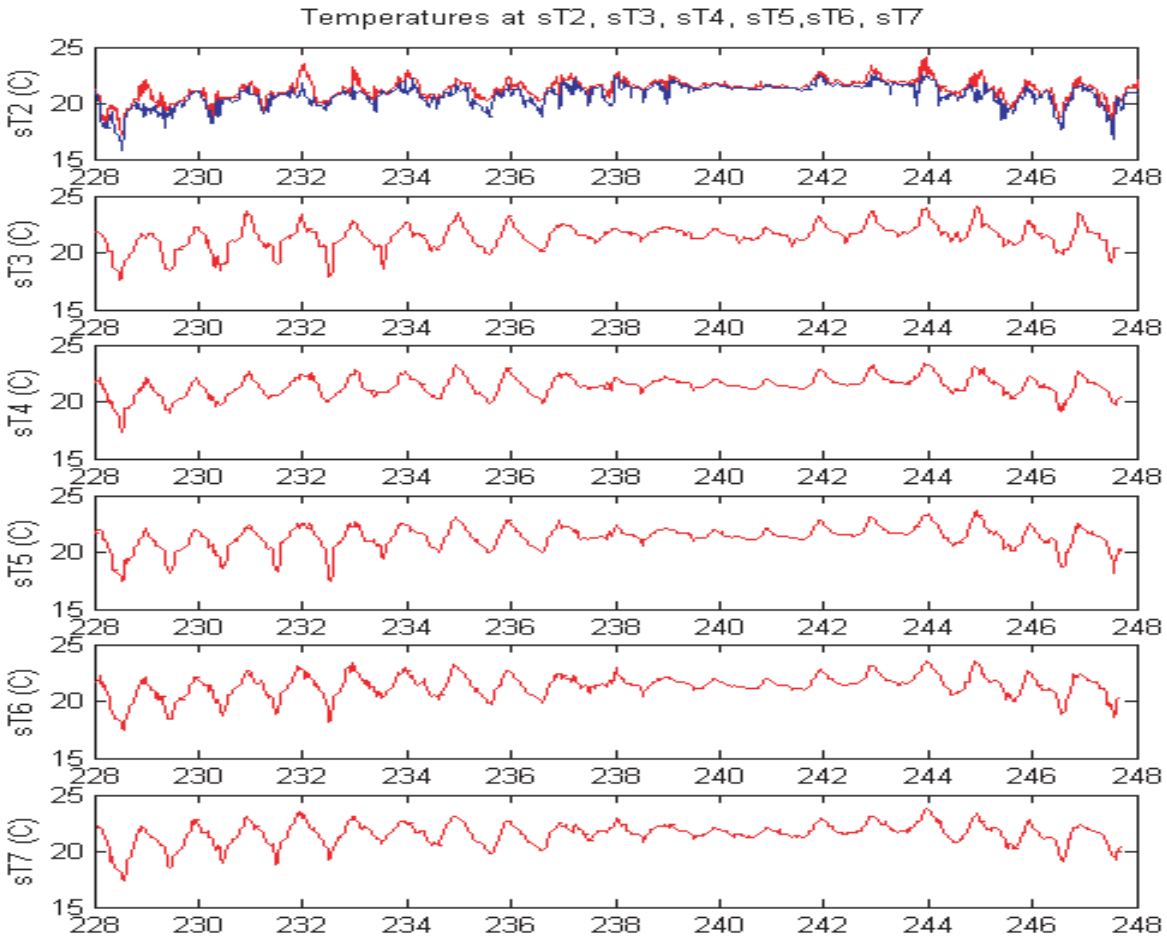

Figure 9-13. Surfzone temperature (lower 5 panels) at 5 locations alongshore, and surface and bottom temperature at sT2 (2.5-m isobath; top panel), deployed offshore of surfzone site sT6 (second bottom panel).

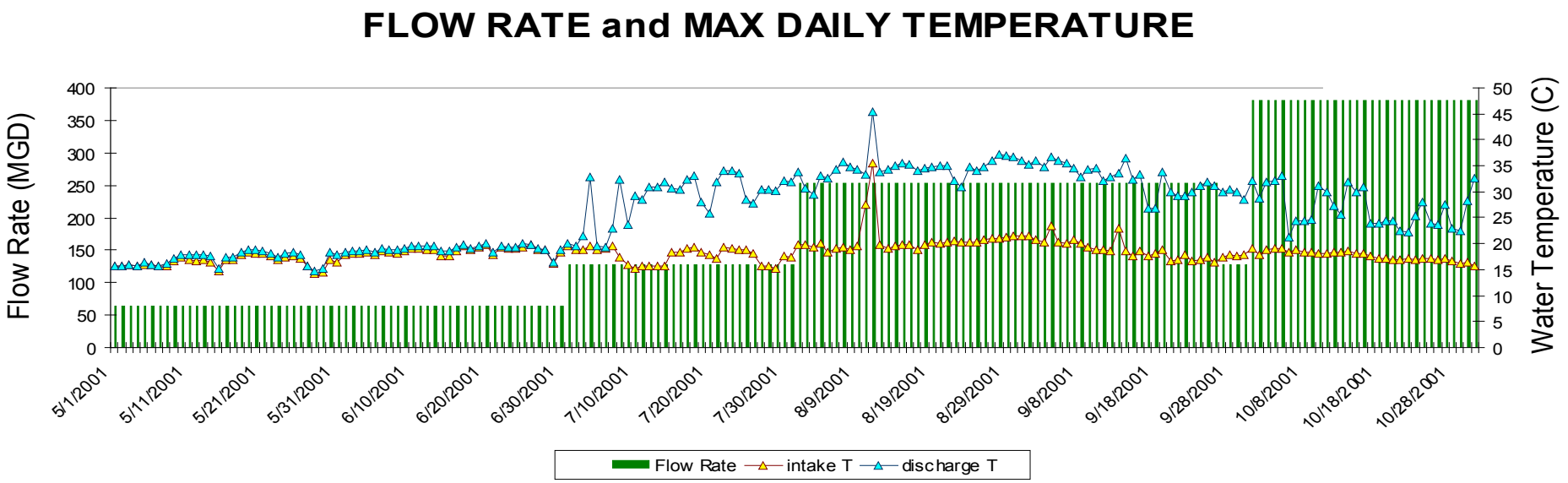

Figure 9-14. Summary of power plant operations during 2001: green bars indicate flow rate, yellow symbols indicate maximum daily intake temperature, and cyan symbols indicate maximum daily discharge temperature.

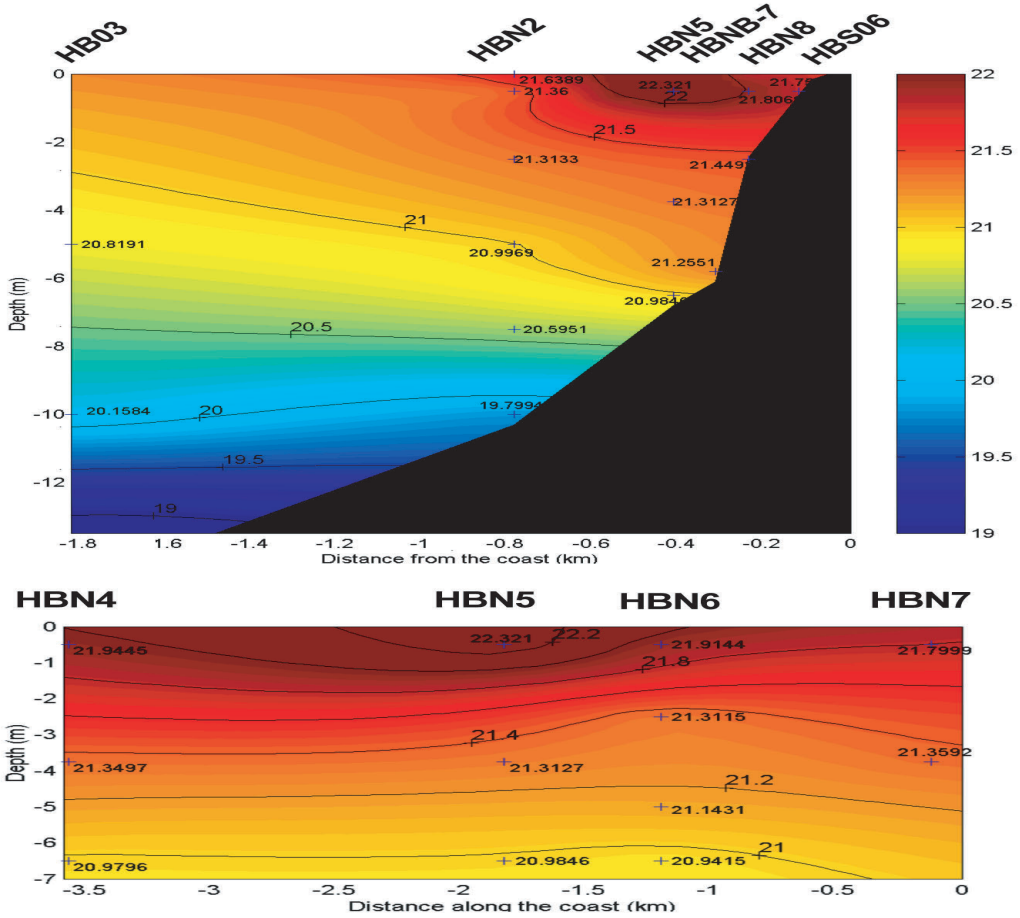

Figure 9-15. Average temperatures in the nearshore, indicating the presence of a thermal plume in the vicinity of moorings T5 and AES2. Upper panel is a cross-shore section out to mooring HB03. Bottom panel is an alongshore section, including 4 moorings on the 7.5-m isobath. Averages calculated for August 28-September 3, 2001.

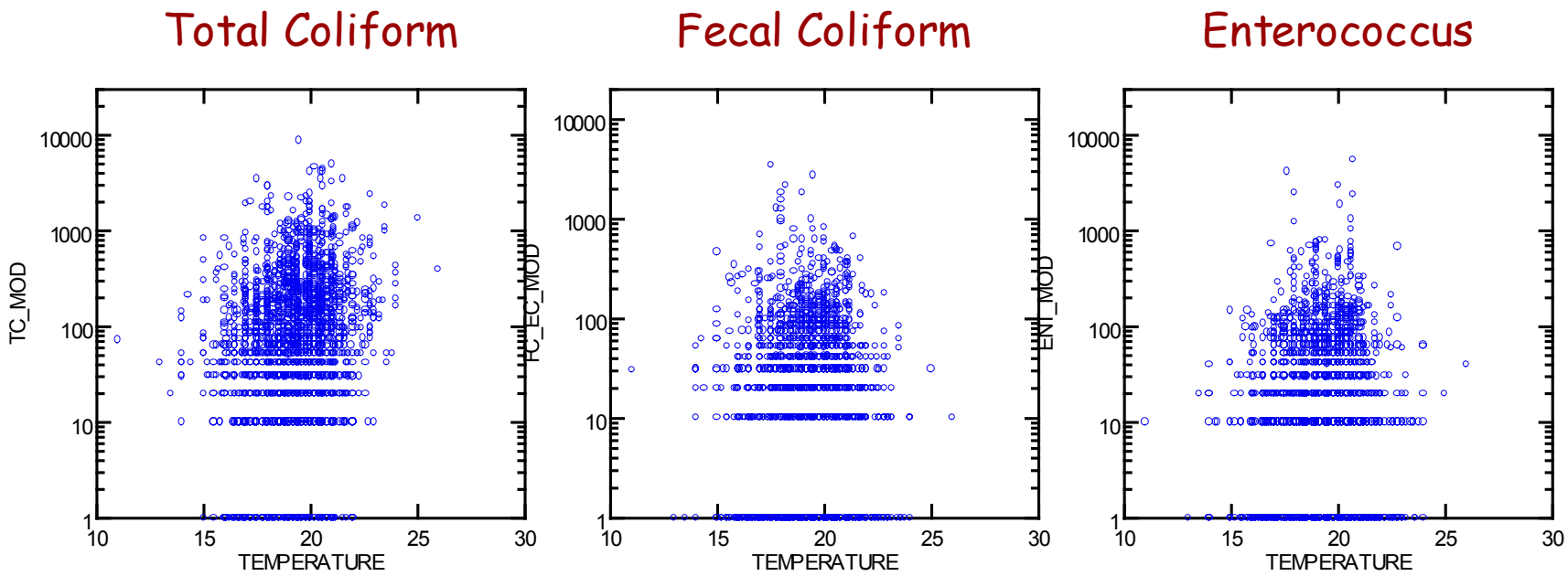

Figure 9-16. Scatter plots of the log of bacteria concentration against water temperature for the shoreline data.

CHAPTER 10. SPATIAL AND TEMPORAL PATTERNS OF PLUME TRACERS

Burton Jones

10.1. Characterization of Sampling Periods

In the summer of 2001 hydrographic surveys were conducted six times during spring tides to map the distributions of the water-column tracers of the plume (Figure 10-1). Prior research indicated that the periods of beach contamination were most common at spring tides. During each survey, the plume tracers were mapped for a continuous 48-hour period. The region between 400 m from the beach and 3.3 km offshore was mapped at 4-hour intervals with CTD profiles, resulting in 12 realizations. The region between 3.3 km and offshore was mapped with a towed undulating vehicle (TUV) each 8 hours, producing up to 6 three-dimensional maps of the region. Beach sites were sampled at hourly intervals.

Four types of flow conditions were observed during the six mapping surveys (Table 10-1):

1. Upcoast flow at plume depth,
2. Downcoast flow throughout water column,
3. Downcoast flow in upper layer and upcoast flow in lower layer, and
4. Downcoast flow in upper layer and sheared flow in lower layer.

The plume was defined by low-salinity anomalies, high fecal bacteria measurements, and elevated ammonium counts in the following manner:

1. The salinity anomaly was at least 0.005 psu less than the predicted ambient salinity. The predicted ambient salinity was calculated from the measured temperature using a set of linear equations to define the ambient temperature-salinity (T-S) relationship. The ambient T-S was determined by examining the T-S relationship for observations that were outside of the influence of the effluent plume–either offshore or upcurrent from the outfall. For the salinity anomaly, we primarily considered observations where the temperature was less than 14°C as being part of the effluent plume. Normally, there was a distinct minimum in the absolute value of the salinity anomaly above 14°C, and often a secondary feature near-surface where it is believed that runoff contributes to the low salinity signal.

2. Fecal indicator bacteria abundance was elevated, particularly for water temperatures less than 14°C, and where the salinity anomaly was at least 0.005 psu less than the predicted ambient salinity. Ammonium was used as a secondary indicator. If elevated bacteria concentrations were found, and there was no significant salinity anomaly or increase in ammonium above background, then we did not consider that bacteria to be due to the outfall.

10.2. Where Was the Plume Observed?

Corresponding to the list of flow regimes above, several examples from these periods demonstrate different characteristic distributions associated with each type of regime. In all of the cases the general pattern of the plume distribution conformed to the direction of the measured flow in that the plume extended along the coast in the direction of the measured currents (Table

10-1). The depth of the plume was generally in agreement with plume modeling results using the RSB multiport diffuser model (Roberts et al., 1989a; 1989b; 1989c).

10.2.1. Upcoast Flow

The only case when the currents appeared to be flowing upcoast was during the first survey (May 21-22, 2001). The flow direction was inferred from the plume because there was no current data available at this time. The plume remained offshore when the flow at plume depth was upcoast presumably because the flow followed bottom topography that veers away from the coast (Figure 10-2). Three indicators of the presence of the plume (salinity anomaly, ammonium concentration, and fecal coliform abundance) all showed that the plume was submerged and offshore, tending to follow the topography. Shoreward transport of the plume was not likely during upcoast flow because the isopycnals tend to tilt downward toward the coast (Chapter 4), providing a density boundary between the offshore plume and the nearshore surface layer.

10.2.2. Downcoast Flow

When the currents below 30 m were flowing downcoast, two types of plume distribution were observed: 1) the plume separated from the shelf break at the offshore end of Newport Canyon and advected downcoast; and 2) a portion of the plume followed the shelf break and entered the canyon. During the fourth cycle (from 1201 to 1706 PDT on June 20, 2001), the plume remained at the offshore end of the survey line and appeared to separate from the topography at the mouth of Newport Canyon (Figure 10-3). In contrast, during Survey 6 (September 15-17, 2001), the effluent plume was found in the canyon and near to shore at the beginning of the survey (Figure 10-4). By the end of the cruise, the plume was no longer present within the canyon, and it was more offshore, similar to the observations from Survey 2 in June.

10.2.3. Sheared Flow

During Survey 4 (July 19-21, 2001), the mean alongshore currents were vertically sheared between 24- and 44-m water depth during the 48-hour period of the survey. The depth of the shear varied with the tide phase, but in general the current was downcoast above 24 m. Below 24 m, however, the flow rotated clockwise with increasing depth until it became upcoast at 44 m. In this situation the flow affecting the plume was mostly upcoast (Figure 10-5). Although the bulk of the plume appeared to advect upcoast from the outfall, the complex vertical current structure also caused parts of the plume to move downcoast from the outfall. The downcoast portion of the effluent plume appeared to penetrate into Newport Canyon, but bacteria concentrations were low.

10.2.4. Weak Flow

An example from the third cruise (July 5-7, 2001) shows the distribution of the salinity anomaly (Figure 10-6). Like the other plume observations during the summer, the plume was submerged and remained below depths of 25 m in the offshore region. In this example, when the flow below 30 m was weak, the plume is present both upcoast and downcoast from the outfall diffuser. In the most downcoast section, it appears that the plume extended shoreward into Newport Canyon and may have shallowed some but still remained below 20-m water depth.

Although the plume shallowed nearer to shore, it generally remained below depths of about 15 m. The plume was observed at a distance of 2 km from shore on several occasions, but at 0.8 km from shore maxiumum total coliform and *E. coli* concentrations were usually low compared with offshore, nearshore, and beach concentrations (Figure 10-3 and Table 10-2). Occasionally, the bacteria concentrations within 2 km of shore were correlated with the cross-shelf currents.

10.3. Cross-shelf Transport Due to Currents

An important objective of this study was to determine whether cross-shelf currents transported the plume to the beach. Boehm et al. (2002) have speculated that cross-shelf transport due to internal tides is a likely mechanism for transporting bacteria from the OCSD outfall to the shore. Because of the intensive grid sampling in the region between 0.4 and 3.3 km offshore, it is possible to characterize the cross-shelf transport associated with the plume and cross-shelf currents. During the third cruise between July 5 and 7, 2001, the alongshore currents were relatively weak below 30-m water depth (Table 10-1). During this period there was a good relationship between the cross-shore velocities and the distribution of plume. As shown in Figure 10-7, bacteria concentrations increased on the alongshelf Lines 3 and 4 when the currents were shoreward. This close relationship between the abundance along these two lines and the cross-shelf currents was only observed during the third survey cruise when the currents at depth were relatively weak. During other cruises this relationship was not readily apparent.

Because cross-shelf currents can transport the effluent plume shoreward, we examined the cross-shelf distribution of bacteria for all of the cruises. Summaries of maximum concentrations for each alongshelf hydrographic line for each cruise are given in Table 10-2. During each survey, Line 2, 0.8 km offshore from the beach, always had lower maximum concentrations of bacteria than were observed at the beach and along Line 1. It was usually lower than Line 3 (with the exception of cruise 4), and always lower than Line 4. Even though exceedances of AB411 standards for total coliform and *E. coli* may occur offshore in the water column and along Line 1 and at the beach, exceedances did not occur along Line 2, 0.8 km from shore, during any of the five cruises from June through September. The conclusion from this is that bacteria from the plume may extend shoreward as close as 2 km from the shore, but the bacteria do not appear to cross into the region within about 1 km of the shore. Higher bacteria concentrations 0.4 km (400 m) from shore are likely to come from transport from the beach via rip currents and other cross-shore surfzone exchange processes.

10.4. Bacterial Relationships within the Plume

Fecal indicator bacteria in the effluent plume were well correlated with each other (Figure 10-8). Enterococci are often stated to remain viable for longer time periods (lower T90) than either total or fecal coliforms. However, in the submerged plume measured offshore, the ratio of total coliform:fecal coliform:enterococci is typically about 25:5:1 and is relatively conservative with distance away from the outfall discharge. This suggests that die-off rates in the plume may be relatively uniform. The relationships appear to become less clear as concentrations of a given indicator fall below 100 MPN/100 mL. If there is any difference in relative die-off of bacteria within the plume, enterococci appear to decrease more rapidly compared to total coliform bacteria (Figure 10-5) when the enterococci concentration falls below 100 MPN/100 mL and

total coliform bacteria fall below 1000 MPN/100 mL. Whether this is real, or an artifact of the error at lower concentrations, is uncertain.

In the earlier Plume Tracking SPS, high bacteria concentrations were observed at least 12.5 km downcoast from the outfall. Transit times from the outfall were estimated to be on the order of 2 days. Therefore, the die-off rates of the bacteria may be low when the plume is submerged well beneath the surface where it is below the euphotic zone and in relatively cool water.

10.5. Variability on the Beach

We examined the variability of bacteria on the beach during the six intensive sampling periods. Three trends, or modes of variability, in the beach bacteria distribution were observed. The first mode was diurnal variability of all three indicator bacteria. This was a spatially ubiquitous pattern that occurred during each of the studies. The second major pattern was during low-low tide periods in the daily cycle, which typically occurred during the night for each of our studies. Total coliform would increase first in the vicinity of the mouths of the Santa Ana River and Talbert Marsh and then propagate upcoast from the Santa Ana River and Talbert Marsh region at rates that were on the order of 0.25-0.3 cm/s (0.48-0.57 knots). These rates are consistent with the wave-induced surfzone transport that would result from southerly waves with a wave height of about 0.75 m. The third mode of variability was that single sites would have high bacterial concentrations. These were sometimes repeatable with the tidal cycle and sometimes not. In one case, it was found that there was a leaking bathroom at station 6N that accounted for high fecal-indicator bacteria at the beach (Orange County Sanitation District, 1999).

The variability observed on the beach suggests that alternative sources of bacteria can account for many of the exceedances on the beach. Because many of the beach postings and closures have resulted from enterococci, it suggests that the source of the bacteria may not be the effluent plume, especially since the concentrations of enterococci observed in the surfzone are often higher than the concentrations observed in the effluent plume. Based on the relationships observed in the effluent plume, high enterococci counts should also be associated with high total and fecal coliform counts.

10.6. Other Low-Salinity Sources

In addition to the outfall plume observed beneath the surface and offshore, a nearshore, surface, low-salinity feature was often present in the region during our hydrographic surveys. This feature was present in at least four of the six hydrographic surveys. When present this low-salinity layer could extend alongshore across the entire sampling region and extended offshore for a distance of 2-3 km. This low-salinity layer is much warmer than the plume and represents runoff from the Los Angeles and San Gabriel Rivers that has been transported downcoast by near-surface currents.

An important question with regard to this plume is whether there is evidence of elevated bacterial concentrations within the river plume that could contribute to the high bacterial concentration on the beach. For example, during the third intensive bacterial sampling event

(July 5-7, 2001) the runoff plume was very evident in the nearshore region as indicated by the three-dimensional map of the salinity anomaly (Figure 10-6). In an examination of observations within the river plume one instance of total coliform abundance greater than 24000 MPN/100 mL was observed within the water that was identified as river plume (Figure 10-9).

10.7. Summary and Conclusions

The plume was sampled under a range of conditions throughout the summer of 2001. The six survey periods provided a range of current conditions over the shelf off Huntington Beach, California. Four distinct types of flow regimes were observed during the study:

1) Upcoast flow,

2) Downcoast flow,

3) Sheared flow, and

4) Weak flow.

In each case the distribution of the plume correlated with the currents in the vicinity of the effluent plume. The most complex case was that of sheared flow when the evidence of the plume was found both upcoast and downcoast from the outfall diffuser.

When the currents are downcoast, the plume was observed in Newport Canyon. But when present in the canyon, effluent indicators were not observed above a depth of 25 m. Indication of the plume in the canyon was also observed when sheared flow resulted in a portion of the plume advecting downcoast. However, the presence of the plume in the canyon may be transient, as observed during Survey 6, when the plume was observed in the canyon at the beginning of the study, but was offshore from the canyon by the end of the 48-hour period.

Cross-shelf transport of the plume was observed. Elevated bacterial concentrations were found as close as 2.2 km from shore. This is consistent with the observations of Boehm et al. (2002). The cross-shelf oscillations coincided with internal tide variations in the cross-shelf currents (Figure 10-7); however, the elevated bacteria concentrations did not penetrate inshore of 1 km in any of the surveys. Thus, while internal tides certainly can move the plume cross-shelf, as Boehm et al. (2002) hypothesized, it does not appear that the transport routinely brings bacteria near the surfzone.

Many of the bacterial postings and closures that occur on Huntington Beach are due to exceedances of enterococci. While elevated levels of enterococci exist within the plume, it appears that they may dissipate away from the core of the plume more rapidly than the coliform bacteria. This is contrary to what is often expected. Thus, the many beach closures due to enterococci suggest that a source of bacteria other than the outfall was polluting the beach. This is particularly so when high enterococci counts are not correlated with similarly elevated levels of coliform indicator bacteria.

There is considerable variability in the location of the plume with varying flow regimes over the San Pedro shelf. However, within the context of this study, there was no direct evidence of the plume being transported sufficiently close to shore to contribute to the surfzone contamination that is frequently observed along Huntington Beach.

For an expanded summary of the entire hydrographic plume tracer study see Jones (2004).

10.8. References

Boehm, A.B., B.F. Sanders, and C.D. Winant, 2002. Cross-shelf transport at Huntington Beach. Implications for the fate of sewage discharged through an offshore ocean outfall. Environmental Science and Technology, v. 36, p. 1899-1906.

Jones, B., 2004, Huntington Beach Shoreline Contamination Investigation, Phase III: Hydrographic and plume tracer data report. In preparation.

Orange County Sanitation District, 1999. Huntington Beach Closure Investigation, Phase I: Final Report. Fountain Valley, CA.

Roberts, P.J.W., W.H. Snyder, and D.J. Baumgartner, 1989a. Ocean outfalls: 1. Submerged wastefield formation. Journal of Hydraulic Engineering-Asce, v. 115, p. 1-25.

—. 1989b. Ocean outfalls: 2. Spatial evolution of submerged wastefield. Journal of Hydraulic Engineering-Asce, v. 115, p. 26-48.

—. 1989c. Ocean outfalls: 3. Effect of diffuser design on submerged wastefield. Journal of Hydraulic Engineering-Asce, v. 115, p. 49-70.

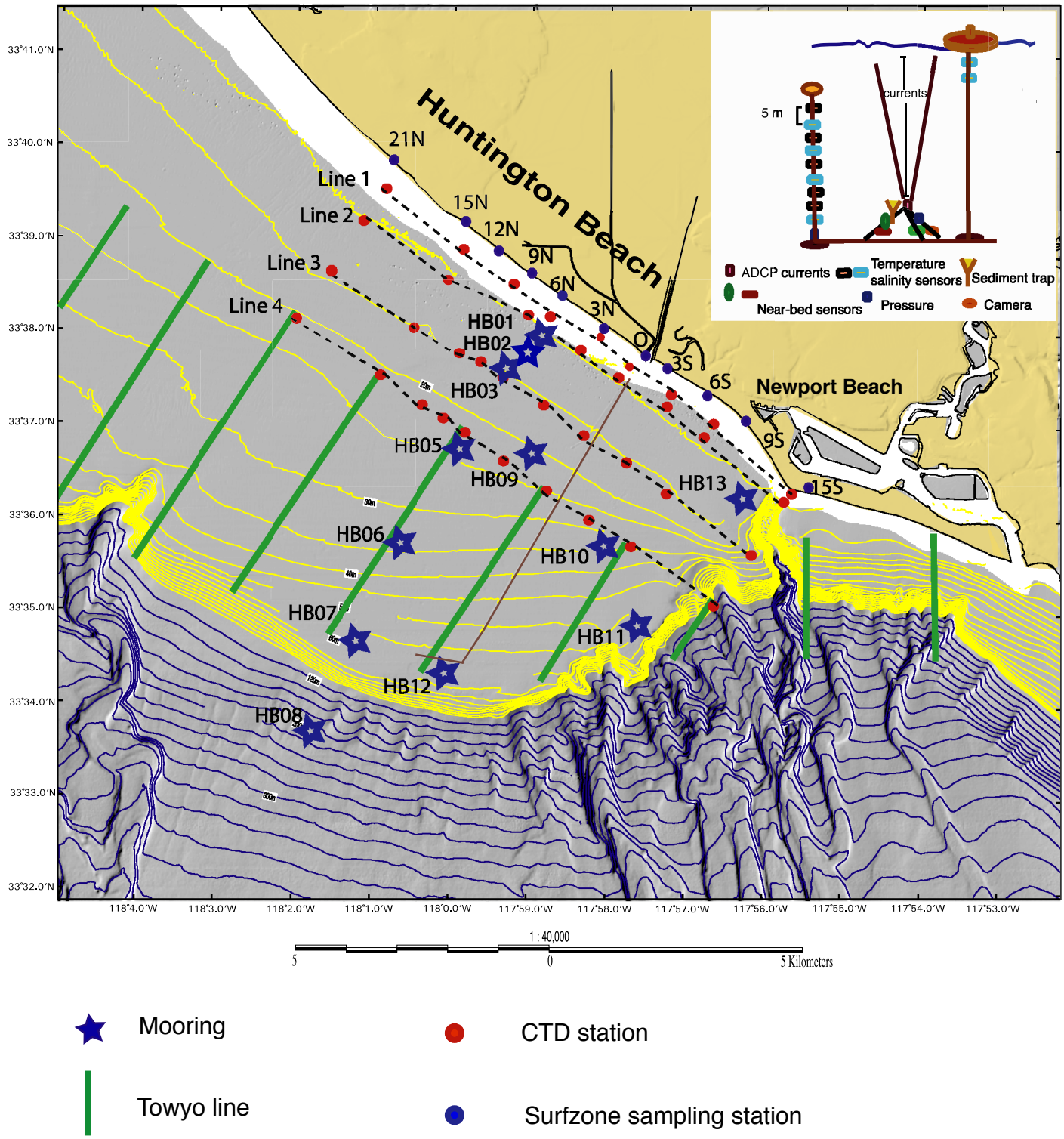

Figure 10-1. Map of the region, mooring sites, surfzone sampling stations, and instrumentations of a typical mooring (inset).

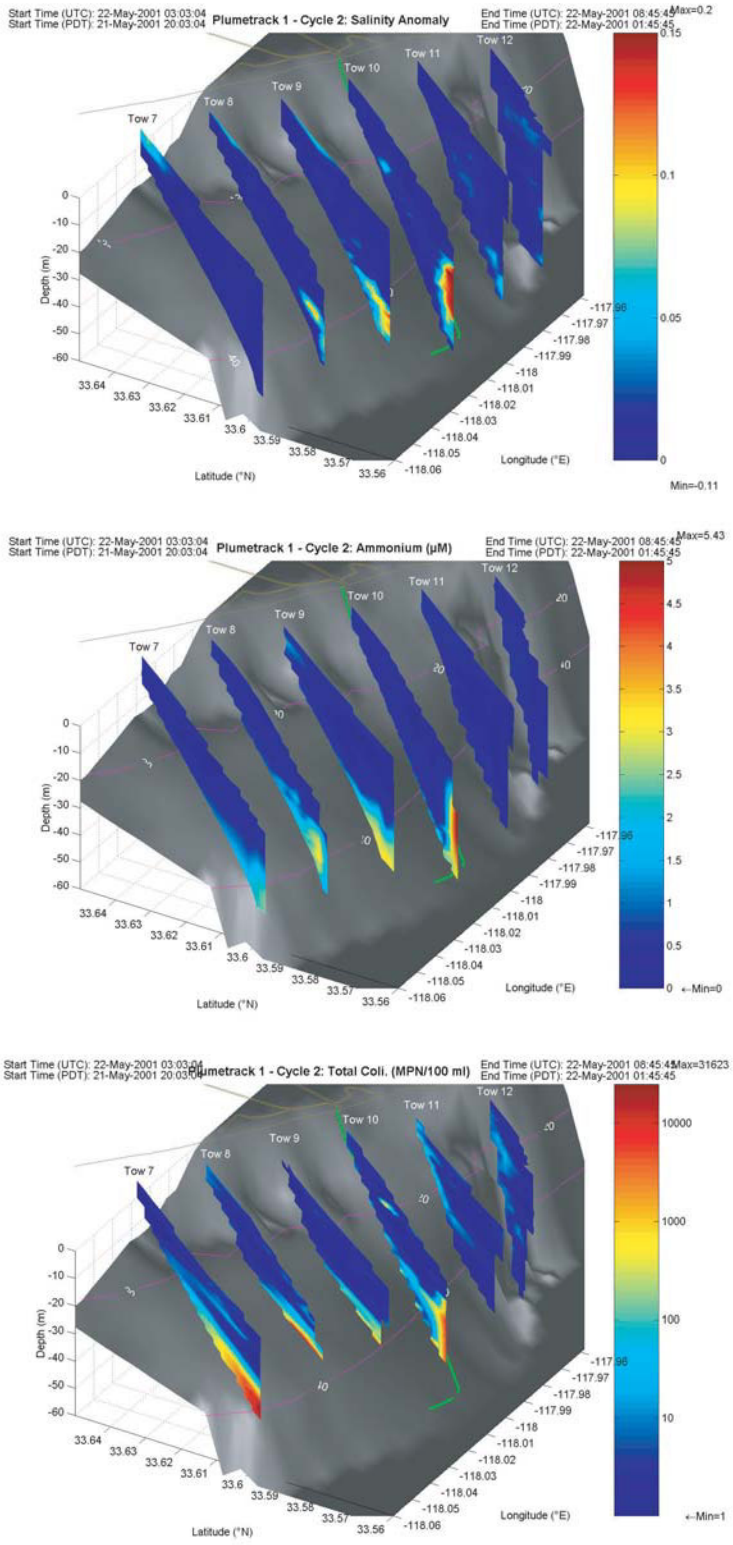

Figure 10-2. Spatial maps of salinity anomaly (top panel), ammonium (middle panel), and fecal coliform concentration (lower panel) for Survey 1, Cycle 2 (2003, May 21, to 0145, May 22, 2001).

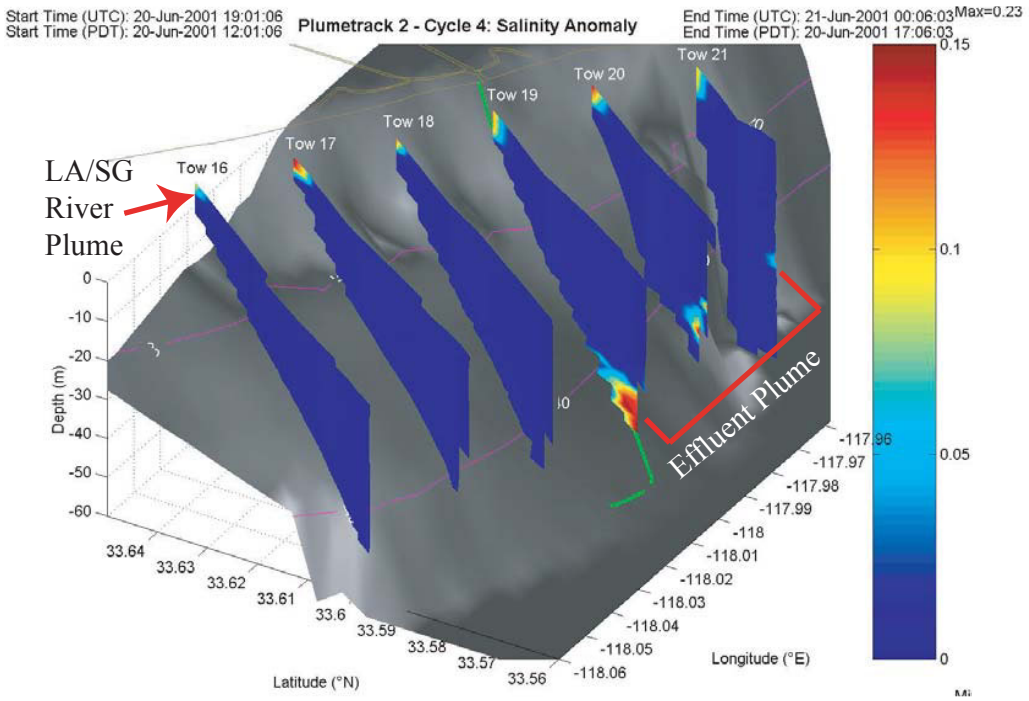

Figure 10-3. A section of the salinity anomaly from Survey 2 (June 19-21, 2001). In this example the effluent plume indicated by the salinity anomaly can be seen advecting down-coast (toward the right) and stays away from the coastal boundary. In tow 21, that coincides with Newport Canyon, the plume is located at the offshore end of the transect and shows no evidence close to shore within the canyon. This was true for all the surveys during the second cruise. A low-salinity anomaly occurs near to shore at the surface that can be seen in all of the transects. This is the signature of the Los Angeles/San Gabriel River plume that extends downcoast from Los Angeles/Long Beach Harbor.

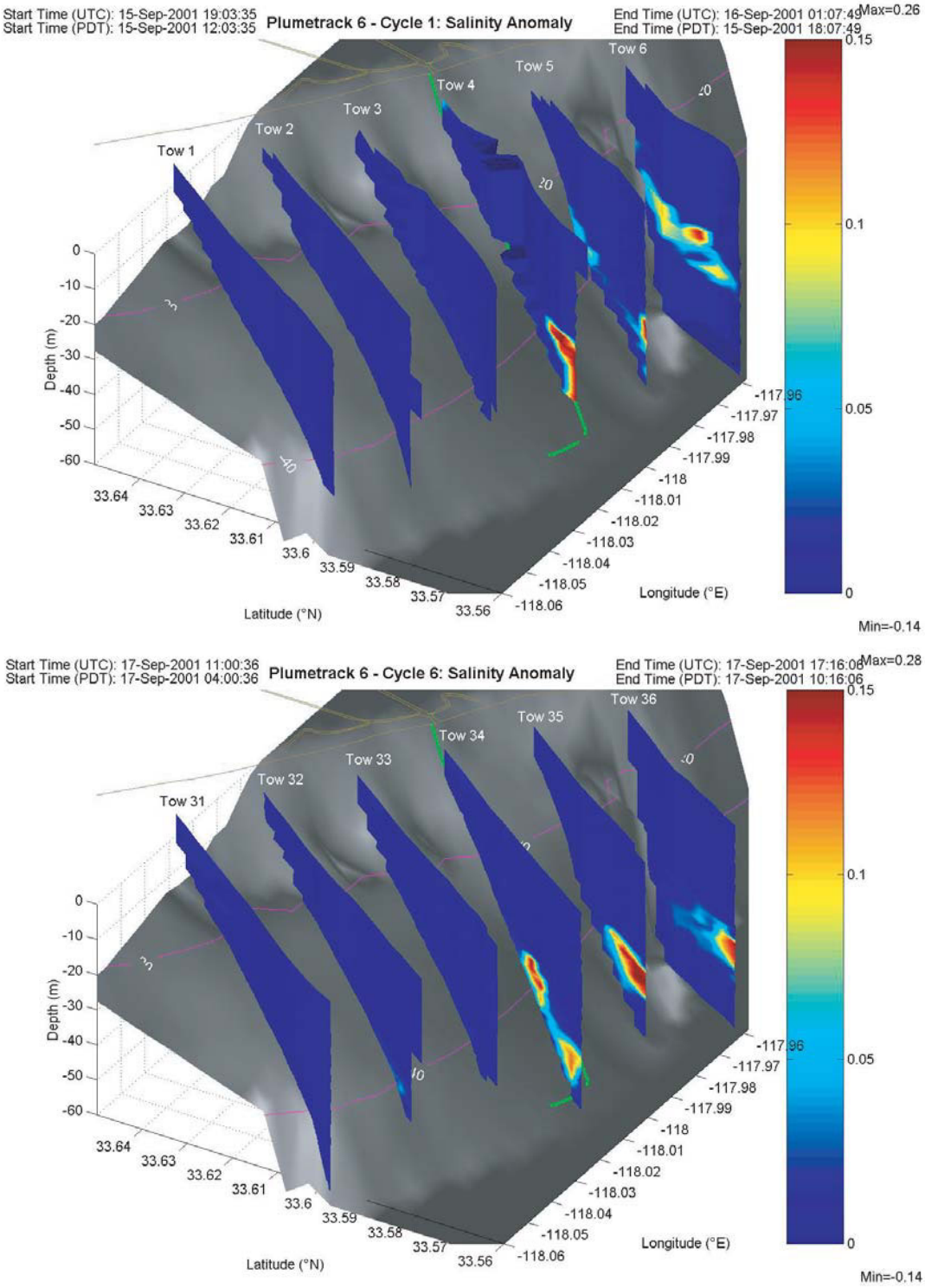

Figure 10-4. Two sections of the salinity anomaly from Survey 6. The top panel shows the salinity anomaly from the first cycle from 1203 to 1807 PDT on Sept. 15, and the bottom panel shows the salinity anomaly from 0400 to 1016 PDT on Sept. 17. In the top panel, the salinity anomaly shows the plume going into Newport Canyon (Tow 6), and in the bottom panel, the plume is not present close to shore in the canyon.

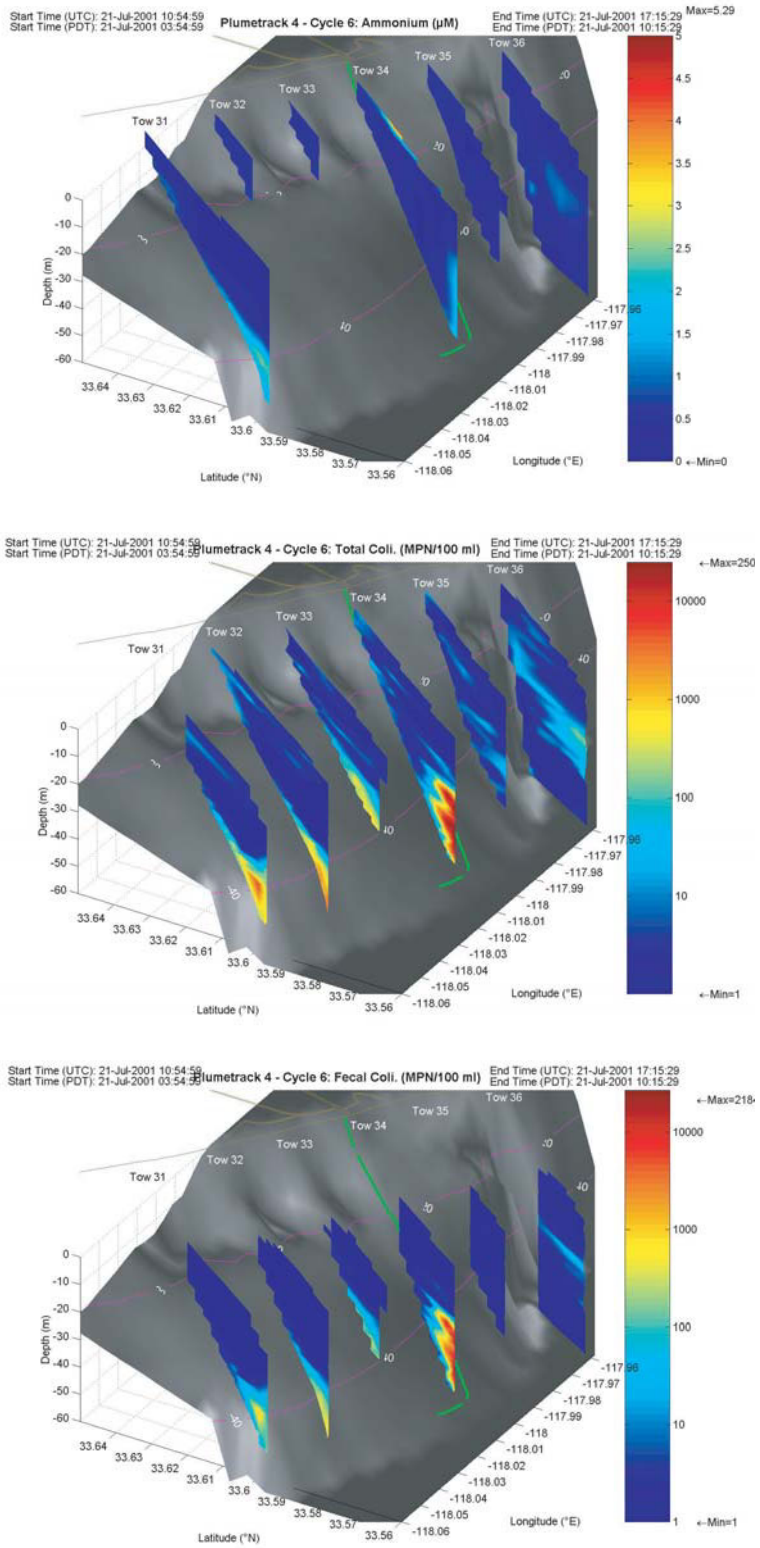

Figure 10-5. This figure shows sections of ammonium (top panel), total coliforms (middle panel), and fecal coliforms (lower panel). This figure demonstrates the plume distribution when the currents are sheared through the water column. Evidence of plume is found both upcoast and downcoast from the outfall.

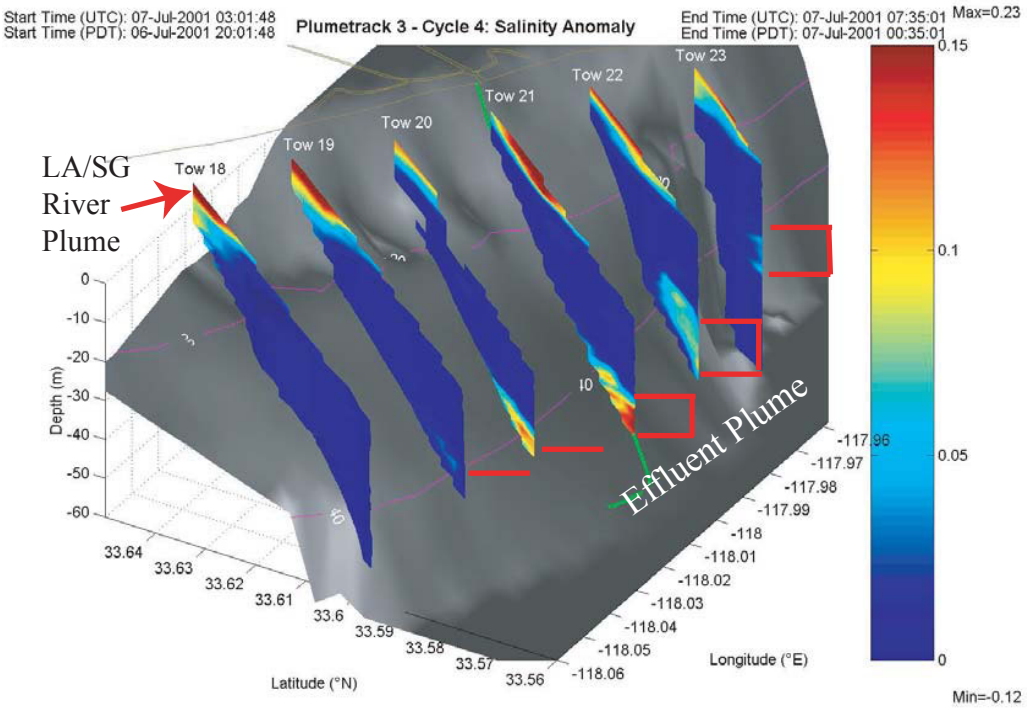

Figure 10-6. Cross-shelf section of salinity anomaly from cruise 3, cycle 4, a period of weak flow over the continental shelf off Huntington Beach. The salinity anomaly indicates that the plume is present in both alongshore directions extending away from the outfall diffuser at a depth of between 25 and 50 m. The salinity anomaly also shows the presence of the Los Angeles/San Gabriel River plume nearshore at the surface.

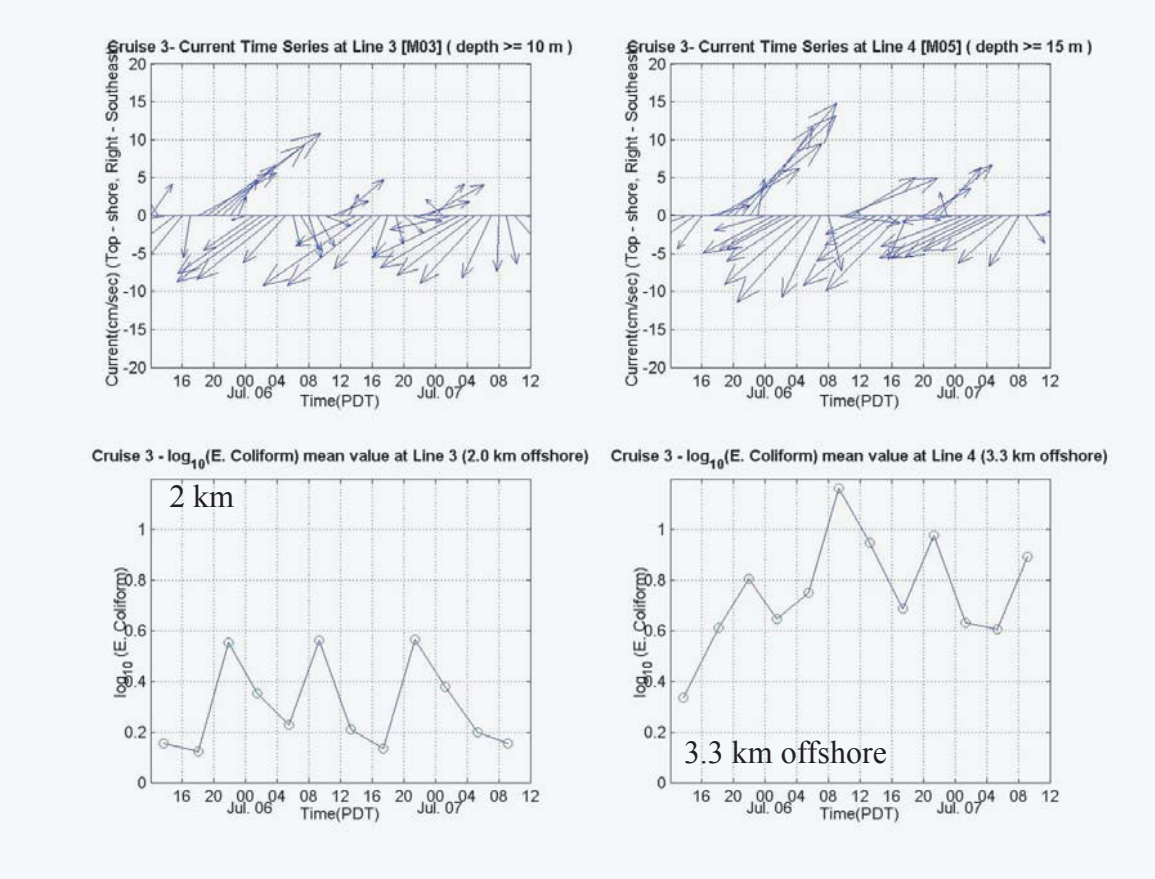

Figure 10-7. Temporal variability of cross-shelf distribution of the maximum concentration of bacteria during Survey 3, July 5-7, 2001. The top panels show the velocity vector time series and the bottom panels show the bacteria concentrations at 2 and 3.3 km offshore.

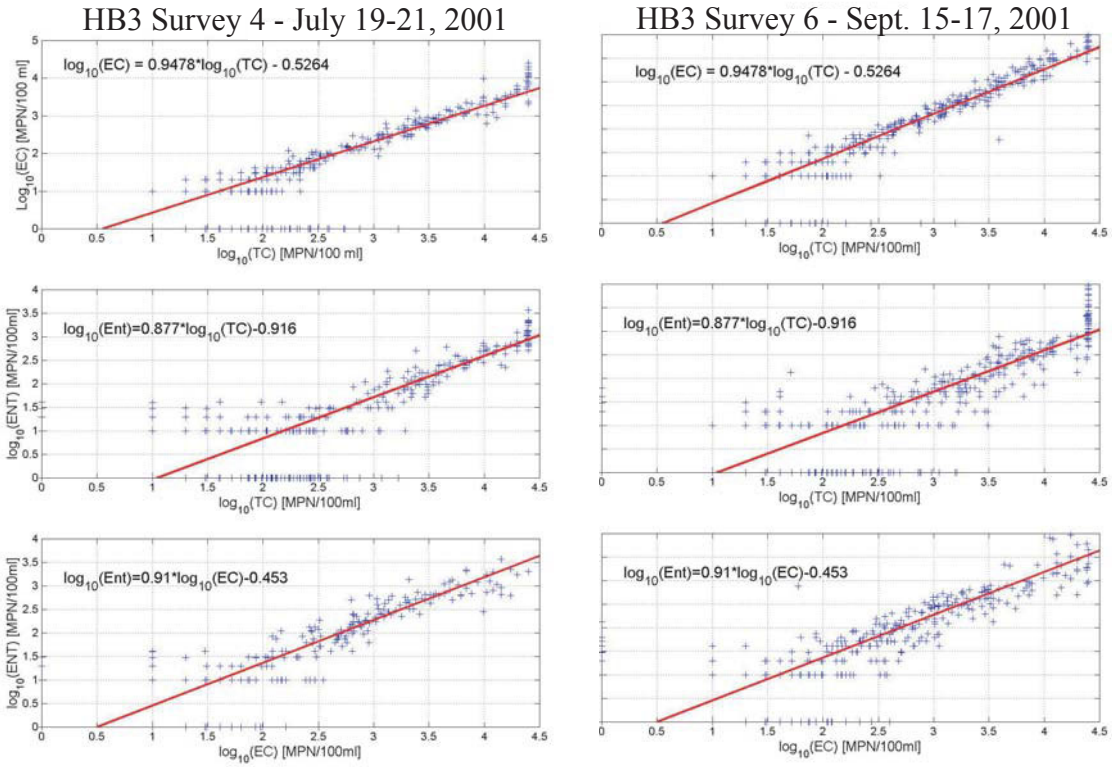

Figure 10-8. Relationships of the different fecal indicator bacteria within an entire survey period for Surveys 4 and 6. The data includes all of the fecal indicator bacteria samples within a survey. The red lines and the associated equations are subjectively drawn lines through the data set.

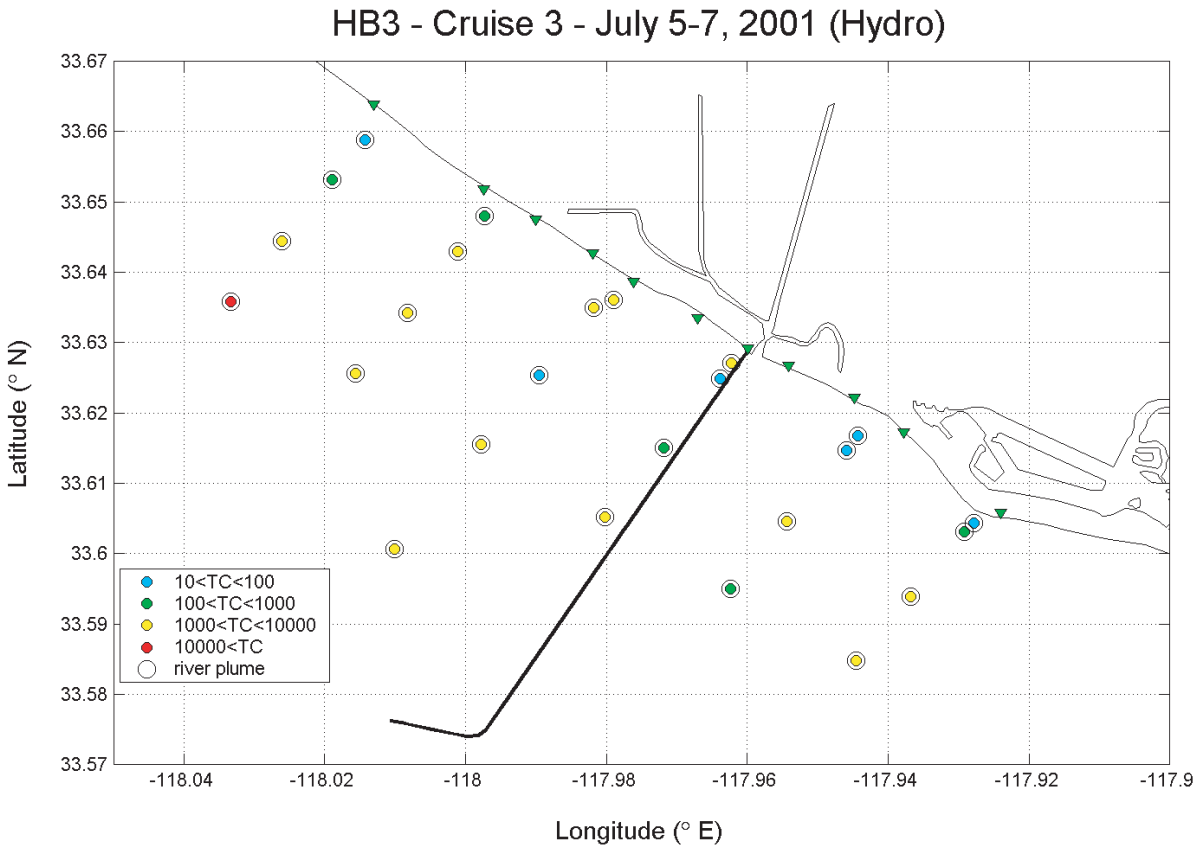

Figure 10-9. Map of the distribution of maximum total coliform bacteria abundance within the region affected by the Los Angeles/San Gabriel River plume.The plot shows the maximum concentration of total coliform bacteria at each of the nearshore hydrographic stations for the entire 48-hr period between 1200 July 5 and 1200 July 7, 2001 PDT The data that are shown fall within the region that we defined as influenced by the Los Angeles/San Gabriel River plume. The criteria for the data shown are that the depth was shallower than 15 m and the absolute value of the salinity anomaly was at least 0.02 psu. The legend indicates the concentrations corresponding to the color code. The black circles indicate where river plume was detected - all of the sites.

Table 10-1. Summary of hydrographic survey cruises of the coastal ocean off Huntington Beach during the summer of 2001. The sampling grid is shown in Figure 10-1.

Survey Number	Period of Sampling (PDT)	Overall Conditions	Plume Location
1	May 21 (1200)- May 22 (1200)	Stratified Upcoast flow (inferred from plume observations)	Upcoast from outfall and below 20 m
2	June 19 (1200)- June 21 (1200)	Stratified Downcoast flow throughout water column	Downcoast from outfall and away from coast
3	July 5 (1200)- July 7 (1200)	Stratified Slow upcoast flow below 30 m, downcoast flow above 30 m	Plume is centered over diffuser and oscillates across shelf with tides. Evidence of plume in canyon
4	July 19 (1200)- July 21 (1200)	Stratified Sheared flow below 25 m, downcoast flow above 25 m	Plume spreading upcoast below 30 m and remaining offshore
5	Aug 19 (1200)- Aug 21 (1200)	Stratified Upcoast flow below 40 m, downcoast flow above 40 m	Plume advecting downcoast and offshore
6	Sept 15 (1200)- Sept 17 (1200)	Stratified Downcoast flow throughout water column	Plume advecting downcoast. Clear evidence in all indicators of plume in Newport Canyon near its head

Table 10-2. Maximum bacteria concentrations for alongshelf line from the nearshore hydrographic sections for Cruises 2 to 6. The concentrations reported are the maximum concentration per line for each cruise. The number for each line for each cruise represents 12 iterations of that hydrographic line.

Total Coliform, Fecal Coliform, and Enterococci Maximum Bacteria Abundance per Line							
		Cruise 2	Cruise 3	Cruise 4	Cruise 5	Cruise 6	Average
Total Coliform	Beach	3750	2512	4054	2321	2760	3080
	Line 1 (0.4 km)	432	426	15531	450	448	3457
	Line 2 (0.8 km)	201	189	1450	171	272	457
	Line 3 (2.0 km)	3873	1467	624	1616	6488	2814
	Line 4 (3.3 km)	1989	24192	5172	4611	24192	12031
		Cruise 2	Cruise 3	Cruise 4	Cruise 5	Cruise 6	Average
Fecal Coliform	Beach	1268	769	2057	768	2759	1524
	Line 1 (0.4 km)	63	122	201	85	86	111
	Line 2 (0.8 km)	41	63	52	109	52	63
	Line 3 (2.0 km)	52	309	121	288	1153	385
	Line 4 (3.3 km)	305	5475	1145	1211	7270	3081
		Cruise 2	Cruise 3	Cruise 4	Cruise 5	Cruise 6	Average
Enterococci	Beach	5415	774	2931	667	1891	2336
	Line 1 (0.4 km)	146	106	169	97	135	131
	Line 2 (0.8 km)	52	2012	120	51	41	455
	Line 3 (2.0 km)	223	719	41	52	767	360
	Line 4 (3.3 km)	85	789	216	231	1850	634
Cells highlighted in salmon color indicate exceedance of California AB411 standards. For total coliform values of >1000 are highlighted corresponding to the lower standard when fecal coliform is at least 10% of total coliform abundance.							

CHAPTER 11. TEMPORAL AND SPATIAL PATTERNS FOR SURFZONE BACTERIA BEFORE AND AFTER DISINFECTION OF THE OCSD OUTFALL

Marlene Noble, Jingping Xu, George Robertson, Leslie Rosenfeld, Burton Jones, and Charles McGee

11.1. Introduction

More than 5 million people visit the beaches off Huntington Beach, California, each summer, helping to support a regional tourism industry of $80 million annually. However, large sections of these beaches were posted or closed for several months in the summer of 1999 and intermittently posted or closed in subsequent summers because bacteria levels in the surfzone exceeded beach sanitation standards in the California Health and Safety Code (Assembly Bill 411, or AB411) for extended periods. Because people stayed away from the beaches, local residents and tourists were seriously inconvenienced and the recreational and business communities in the region suffered serious economic losses. Local agencies conducted a wide variety of studies during Phase I (OCSD, 1999) and Phase II (Grant et al., 2000) of the Huntington Beach Shoreline Investigation to try to identify possible contamination pathways from upland sources, adjacent estuaries, and the coastal ocean. Unfortunately, these investigations could not determine specific sources for many of the contamination events. In particular, it was not clear whether coastal ocean processes occasionally brought bacteria-rich effluent from the Orange County Sanitation District's (OCSD) ocean outfall to the beach.

In the summer of 2001, Phase III of the Huntington Beach Shoreline Investigation was instigated to study coastal-ocean processes that may allow the transport of OCSD's outfall plume to the beach. Initial findings were reported to the OCSD board in May 2002. At that time, preliminary analysis indicated that the OCSD outfall was not responsible for the contamination events that caused beach closures. In April 2003**,** a full report on hypothetical coastal-ocean pathways that could transport a significant amount of effluent to the beach was presented to OCSD's board and interested members of the public. Further analysis of this rich data set did not change the researchers' initial conclusion that bacteria from the OCSD effluent plume were not responsible for beach closures. The data sets and analyses the scientists used to draw this conclusion are given in the first ten chapters of this Phase III final report.

Notwithstanding the above conclusion, OCSD chose not to renew its 301(h) waiver, and, further, began disinfecting their outfall in August 2002. In this chapter, we will examine the patterns in the extensive fecal indicator bacteria (FIB) data sets collected before and after disinfection of the outfall to determine whether the initial conclusion that the outfall was not the primary cause of beach closures is supported by the subsequent data sets. We will document the magnitude of reduction in FIB levels in the outfall itself and in the plume near the diffuser site (Figure 11-1). We will also look at the frequency characteristics of the FIB for the surfzone bacterial data collected at sites along the beach since 1998 (Figure 11-1). This data set includes the recent FIB measurements taken at the standard OCSD surfzone sites from stations 39N to 39S prior to disinfection of the outfall (see Chapter 3 for a discussion of the full data set) and the year of measurements that have been collected since that analysis. These additional data sets will help assess the usefulness of effluent disinfection. The information on the temporal and spatial patterns for contamination events may also suggest potential sources for the contamination that could be investigated in future studies and possibly identify other locations that could be subject to similar contamination events.

11.2. Pre- and Post-disinfection FIB Patterns at the Outfall Site

It took about two months to fully implement the procedures to disinfect the outfall. The process was finally stabilized in mid-October 2002, when the post-disinfection bacteria count measured in the last-stage bay before the effluent was piped to the ocean decreased dramatically (Figure 11-2). The median total coliform density was reduced by four orders of magnitude, from $\sim 10^7$ to $\sim 10^3$ MPN/100 mL. Reductions of similar magnitude were found in fecal coliform and enterococci. One can estimate a very conservative bacteria concentration in the coastal ocean near the diffuser by dividing the measured FIB density at the last-stage bay by 100 because the designed dilution rate at the diffuser is actually 1:200. It can be seen clearly in Figure 11-3 that the estimated FIB densities at the diffuser are usually smaller than those measured for surfzone bacteria densities at station 6N, which is located on the central portion of Huntington Beach. After October 2002, the bacterial levels near the diffuser were too low to cause contamination events at the beach, even if the probable further dilution of bacteria as they are transported in the coastal ocean is not taken into account.

The actual densities of bacteria at the outfall site before and after disinfection of the final effluent were measured during several cruises. These measurements confirm the above estimate that, after disinfection, much lower densities of bacteria are being released into the coastal ocean (Figure 11-4). Before disinfection, the measured levels of bacteria at OCSD's outfall site at the normal depths the outfall plume rises to in the coastal ocean (centered on 30-45 m) (Jones, 2004) were above AB411 standards. After disinfection, the bacterial levels were reduced considerably. Even at the core of the effluent plume, the box plots show that most bacteria samples were below AB411 standards for the periods between August 2002 and June 2003. Additional FIB measurements from a 1-km grid of stations around the outfall confirm that very small densities of bacteria are being discharged from the disinfected outfall (OCSD, 2004).

Yet, measurements of bacteria in the surfzone during this same period of time show that contamination events remained a problem (Figure 11-4). Surfzone bacteria densities still occasionally exceeded AB411 standards, especially for enterococci. Postings and closures continued to occur at Huntington and the adjacent beaches.

11.3. Frequency-Domain Characteristics and Distribution Patterns for Surfzone FIB

The surfzone FIB are usually measured five days per week, with one of the measurement days occurring on a weekend. Here, we use Lomb periodograms (Lomb, 1976) to characterize the frequency patterns in FIB time series at the 18 surfzone sampling stations because Lomb periodograms calculate the dominant frequencies in an unequally spaced data set. Lomb periodograms (hereafter periodograms) essentially use the least-squares method to fit a set of frequencies to an unevenly spaced time series. The set of frequencies fit to the data set do not necessarily have to be a complete set of basis functions or satisfy the Raleigh criteria. Here, we normalized the periodograms by the maximum value in each periodogram. Hence, the amplitudes for spectral peaks can only be compared within individual periodograms. The amplitude of a spectral peak must exceed the 95% confidence limits in order to distinguish it from random noise. The further the amplitude of a spectral peak exceeds the confidence limit, the more confident we are that the fit is not the result of random noise. The confidence limits for

the normalized periodograms were calculated according to Scargle (1982), using the modified normalization proposed by Horne and Baliunas (1986).

Periodograms of the log of the bacterial counts were computed for three time periods:

1) Five years of pre- and post-disinfection total coliform, fecal coliform, and enterococci data from March 1998-December 2003;

2) One year of pre-disinfection total coliform, fecal coliform, and enterococci data from September 2001-September 2002; and

3) One year of post-disinfection total coliform, fecal coliform, and enterococci data from October 2002-November 2003.

11.3.1. Patterns Using FIB Data from 1998-2003

The most prominent feature in the periodograms for the recent five years of total coliform data is the annual cycle (Figure 11-5a). The annual peaks overwhelm other spectral peaks at most of the surfzone sampling sites. The most dominant annual peaks are found near the Santa Ana River (Station 0) and at stations south of the river. It is interesting to note that the relative amplitude of the annual cycle in total coliform decreases sharply at stations 3N-15N and increases again at stations further to the north. This is the only region where the fortnightly cycle, which is related to the spring-neap cycle of tides, dominates the spectrum. The dominance of the fortnightly cycle is particularly strong between stations 3N and 12N, a region where contamination events on Huntington Beach have recently been centered.

The frequency patterns in the periodograms of the recent five-year fecal coliform data reflect those for total coliform data (Figure 11-5b). The patterns for the pre- and post-disinfection of fecal coliform also reflect those for total coliform. The figures are included in this chapter for completeness, but individual patterns for fecal coliform will not be discussed further.

The spatial patterns in the recent five-year enterococci data set are markedly different from those for total coliform and fecal coliform data (Figure 11-5c). The fortnightly cycle, instead of being roughly confined to a small region between stations 3N and 12N, is present at most surfzone sampling stations. It is particularly strong between stations 3N and 21N, a spatial region that encompasses the fortnightly cycle seen for total coliform, and in stations located at and south of the mouth of Newport Harbor (stations 29S, 39S). The fortnightly cycle is relatively weaker, but significant at other southern stations that bracket Newport Pier and the head of Newport Canyon. The only stations that do not have significant fortnightly cycles in enterococci are located near the mouth and south of the Santa Ana River.

The annual cycle in enterococci is dominant primarily near the mouth of the Santa Ana River and at stations to the south, similar to that seen in total coliform. However, near the mouth of Newport Harbor, the annual cycle is overwhelmed by the fortnightly cycle. North of the river, the annual cycle for enterococci is dominant only at the most northern sampling station, 39N.

11.3.2. Patterns Using Pre- and Post-disinfection FIB Data

Periodograms for total coliform and enterococci were calculated from approximately year-long data sets taken immediately prior to (Figures 11-6a-c) and after (Figures 11-7a-c) disinfection of the outfall. Because of the short time series, these periodograms could not resolve the annual cycle. However, we can still determine whether the spatial patterns in the fortnightly cycle change after disinfection.

The spatial patterns in the fortnightly cycle for the pre- and post-disinfection total coliform data sets are similar to those found for the entire five-year data set. The only significant spectral peaks are found north of the Santa Ana River. The most significant fortnightly cycles are located between stations 3N and 9N, though the range extends north of Huntington Pier (station 21N) in the year before disinfection of the outfall began. After disinfection, the fortnightly cycle is confined to a slightly smaller region between stations 3N and 12N. It is not clear if this change will be a consistent feature found in future data sets because the data sets are short. We have only one year of data collected after disinfection.

The fortnightly cycle in enterococci before and after disinfection is significant at most northern and southern stations, except for the stations near and south of the mouth of the Santa Ana River. This is similar to the spatial pattern in the entire five-year data set. Again, the significance levels of the spectral peaks are slightly higher for the pre-disinfection data, but most peaks exceed the 95% confidence level. The fortnightly cycle accounts for relatively more of the variability in each data set in the region between stations 3N and 15N, near the mouth of Newport Harbor and the stations surrounding Newport Pier for both the pre- and post-disinfection periods. This last set of stations also lies inshore of the head of Newport Canyon. The broad spatial range for enterococci is consistent with the spatial patterns found for the entire set of pre-disinfection enterococci data described in Chapter 3 (pattern type 2).

11.4. Discussion

The annual cycle in the FIB data sets is caused by local runoff from storms in the wet winter season. It is well known that runoff contaminates beaches (Reeves, et al., 2004); this entire region tends to exceed AB411 standards after large rains. The annual cycle dominates the variability in all three FIB data sets for most stations at or south of the Santa Ana River. It is also the dominant frequency in coliform bacteria for stations north of station 15N. These data suggest that local runoff is the dominant contamination source for most of the southern and some of the northern beaches in this region. The strong annual cycle at the most northern site (station 39N) for all types of bacteria, coupled with the tendency for fresher water to be found close to shore at the most northern hydrographic sites in summer (Chapter 10), does suggest that runoff from local rivers may also be important at some sites in all seasons. Possibly contaminated water from the San Gabriel or Los Angeles Rivers may enter the northern Huntington Beach region in summer.

The contamination most commonly associated with summer postings and closings on Huntington Beach occurs at the fortnightly, or spring/neap, tidal cycle (MEC, 2000; Grant et al., 2000) (Chapter 3). These data support that result; sites between stations 3N and 15N on

Huntington Beach have significant fortnightly cycles in all three FIB data sets. They are most likely to be posted or closed during spring tides. Given that these sites have relatively weak annual cycles, local runoff is not the primary cause of contamination in this limited region of the beach.

A significant fortnightly cycle in enterococci, but not for either species of coliform bacteria, is found at many other surfzone stations. It appears that an enterococci contamination source tied to the fortnightly cycle is present at many more stations than previously thought. It is disturbing to note that a relatively strong enterococci fortnightly cycle is found near and south of the entrance to Newport Harbor (stations 29S, 39S). The fortnightly cycle overwhelms the annual cycle for enterococci. This suggests not only that local runoff is not primarily responsible for the enterococci contamination, but that there may be different Newport Harbor sources for the two species of bacteria. Fortunately, the enterococci contamination levels have not yet been high enough to cause significant posting and closures at these beaches.

It is probable that the source of the fortnightly cycle in contamination events is related to the wetting and draining of the land during the large tidal excursions found during spring tides (Grant et al., 2001; Kim et al., 2004). During spring tides, seawater can: 1) wet previously dry areas of the Talbert Marsh or the banks of the Santa Ana River, 2) enhance the exchange between the flood channels that enter the Talbert Marsh and the coastal ocean, 3) enhance the exchange with Santa Ana River estuary water, and 4) reach higher on the local beaches, causing seawater and any dissolved material to drain back into the coastal ocean. These pathways deserve more investigations in future studies at Huntington Beach and at the other sites with significant fortnightly cycles in enterococci.

The extensive data set collected during the Phase III study showed that the fortnightly contamination events on Huntington Beach were not associated with the transport of bacteria from OCSD's outfall plume by internal waves during spring tides, as one early hypothesis stated (Boehm et al., 2002). These data support the original conclusion of the Phase III study as well as previous studies (OCSD, 1999; Sea Grant, 2000). Bacteria from the OCSD outfall were not the primary cause of contamination of the local beaches. Post-disinfection measurements of FIB levels at the outfall site are below levels presently found on the beach and well below AB411 standards. There is no significant difference in the spatial patterns for contamination from any species of FIB in the pre- and post-disinfection time periods. Yet, the beaches are still being posted and/or closed, despite disinfection of the outfall.

It is unclear whether low concentrations of bacteria from the outfall plume were transported to the beach before disinfection occurred. The data suggest that the relative spectral levels at the fortnightly period are a bit lower after disinfecting the effluent. However, given the changing management policies for FIB sources in the region, we expect that the beaches would be less contaminated even if the effluent plume were not disinfected. Several local storm drains that empty contaminated water onto the beach during the dry summer season have been and are continuing to be found. Water from these storm drains is being diverted from the beach into the sewage system in the critical summer months.

Pursuing a more precise quantification of possible low-level contributions of FIB to the surfzone from the outfall plume before it was disinfected is not as important as trying to find the continuing sources of the summer contamination events. Given the differing spatial and temporal patterns for the coliform bacteria and enterococci discussed above and in Chapter 3 of this report, it is possible that the enterococci contamination has a different source from that of the coliform not only at Newport Harbor, but at many beaches in the study area. The very similar spatial and temporal patterns found for total coliform and fecal coliform bacteria suggest that most coliform bacteria share a similar source.

Unfortunately, further investigations into the issue of different sources for bacteria based on differing spatial patterns for coliform and enterococci bacteria is complicated by our lack of knowledge of how different bacteria species survive in seawater. Recent work suggests that the ecology of bacteria is very complex and changes with temperature, sunlight, salinity, and possibly other environmental factors (Hurst et al., 2002; Noble et al., 2004). An even more complex task is to develop fast and inexpensive methods to determine if the high FIB concentrations on local beaches have human or animal sources. More information on these issues is necessary before one can come to definitive conclusions based on FIB spatial patterns. Hourly samples of FIB concentrations in the surfzone at selected stations during both spring and neap tidal cycles may increase our understanding of this complex process.

11.5. References

Boehm, A.B., B.F. Sanders, and C.D. Winant, 2002. Cross-shelf transport at Huntington Beach: Implications for the fate of sewage discharged through an offshore ocean outfall. Environmental Science and Technology, v. 36, p. 1899-1906.

Chamberlin, C.E. and R. Mitchell, 1993. A decay model for enteric bacteria in natural waters. Water Pollution Microbiology, John Wiley & Sons.

Grant, S.B. et al., 2000. Huntington Beach Water Quality Investigation, Phase II: An analysis of ocean, surfzone, watershed, sediment, and groundwater data collected from June 1998 through September 2000. Final Report.

Grant, S.B. et al., 2001. Generation of Enterococci bacteria in a coastal saltwater marsh and its impact on surf zone water quality. Environmental Science and Technology, v. 35, p. 2407-2416.

Horne, J.H. and S.L. Baliunas, 1986. A prescription for period analysis of unevenly sampled time series. Astrophysical Journal, v. 302, p. 757-763.

Hurst, C.J., R.L. Crawford, M.J. McInerney, G.R. Knudsen, and L.D. Stetzenbach, eds., 2002. Manual of environmental microbiology, 2nd ed. ASM Press, Washington, D.C.

Jones, B., 2004. Huntington Beach Shoreline Contamination Investigation, Phase III, v. II. In press.

Kim, J.H. and S.B. Grant, 2004. Public misnotification of coastal water quality: A probabilistic evaluation of posting errors at Huntington Beach, California. Environmental Science and Technology, in press, 8 p.

Kim, J.H. et al., 2004. Locating sources of surf zone pollution: a mass budget analysis of fecal indicator bacteria at Huntington State Beach, California. Environmental Science and Technology, submitted.

Leecaster, M.K. and S.B. Weisberg, 2001. Effect of sampling frequency on shoreline microbiology assessments. Marine Pollution Bulletin, v. 42, p. 1150-1154.

Lomb, N.R., 1976. Least-squares frequency analysis of unequally spaced data. Astrophys. Space Sci., v. 39, p. 447-462.

MEC, 2000. Huntington Beach closure: Relationships between high counts of bacteria on Huntington Beach and potential sources. Final Report.

Noble, R.T., I.M. Lee, and K.C. Schiff, 2004. Inactivation of indicator bacteria from various sources of fecal contamination in seawater and freshwater. Journal of Applied Microbiology, in press.

OCSD, 1999. Huntington Beach Closure Investigation. Phase I. December 1999, Fountain Valley, CA.

——, 2004. Receiving water microbiological data: Pre- and post-disinfection. Preliminary Report, May 2004, Fountain Valley, CA.

Reeves, R. l., S.B. Grant, R.D. Morse, C.M. Copil, Oancea, B.F. Sanders, and A.B. Boehm, 2004. Scaling and management of fecal indicator bacteria in runoff from a coastal urban watershed in Southern California. Environmental Science and Technology, in press, 12 p.

Scargle, J.D., 1982. Studies in astronomical time series analysis II: Statistical aspects of spectral analysis of unevenly spaced data. Astrophysical Journal, v. 263, p. 835-853.

Sea Grant, 2000. Huntington Beach closure investigation: technical review. Wrigley Institute for Environmental Studies, University of Southern California, Los Angeles, CA.

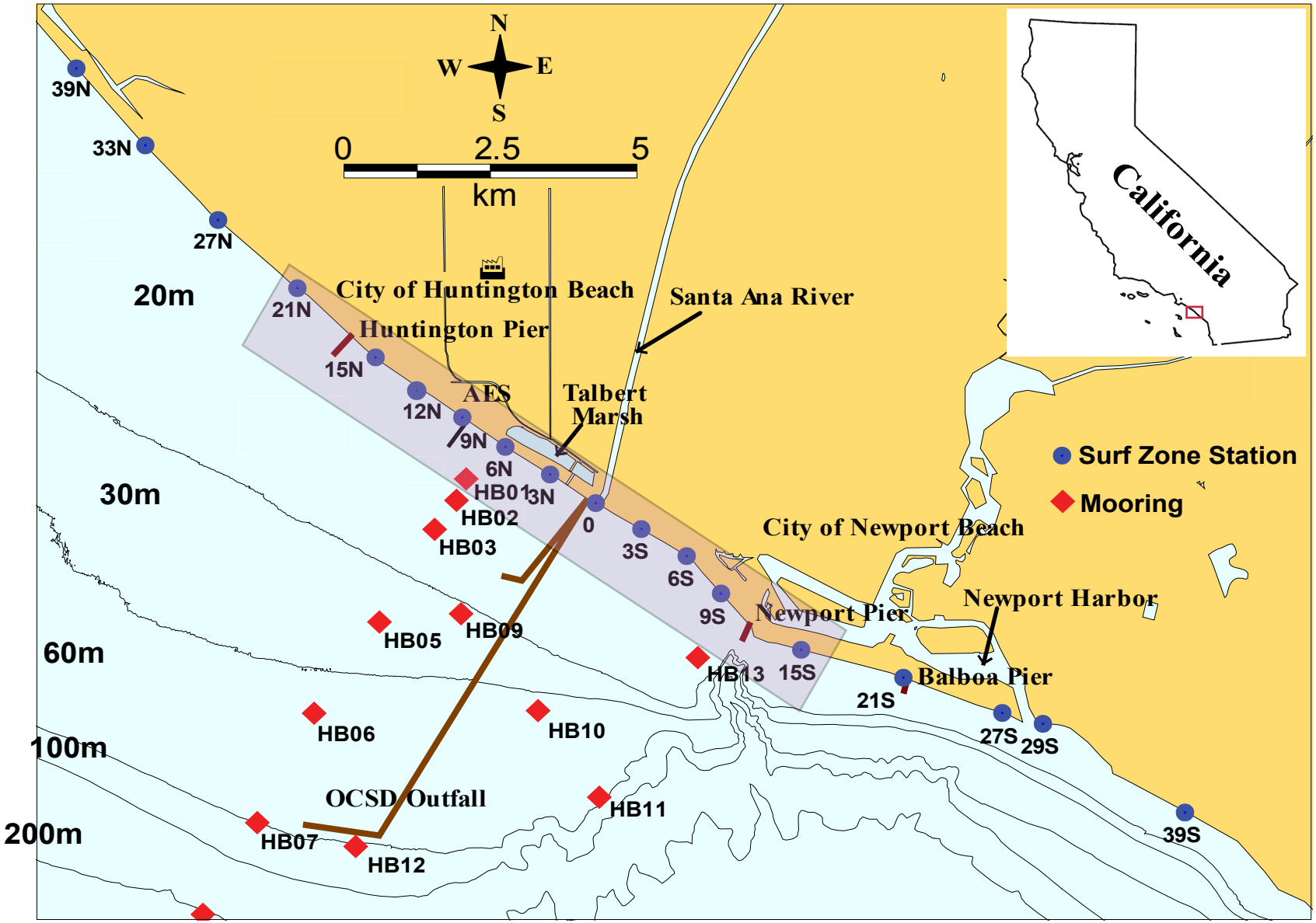

Figure 11-1. Map of the coastal zone surrounding Huntington Beach, California. The blue dots show the location of the surfzone sampling stations from 39N to 39S. The outfall is shown leaving the coast near station 0. The diffuser of the outfall is located near stations HB07 and HB12. Station 12S is located at Newport Pier.

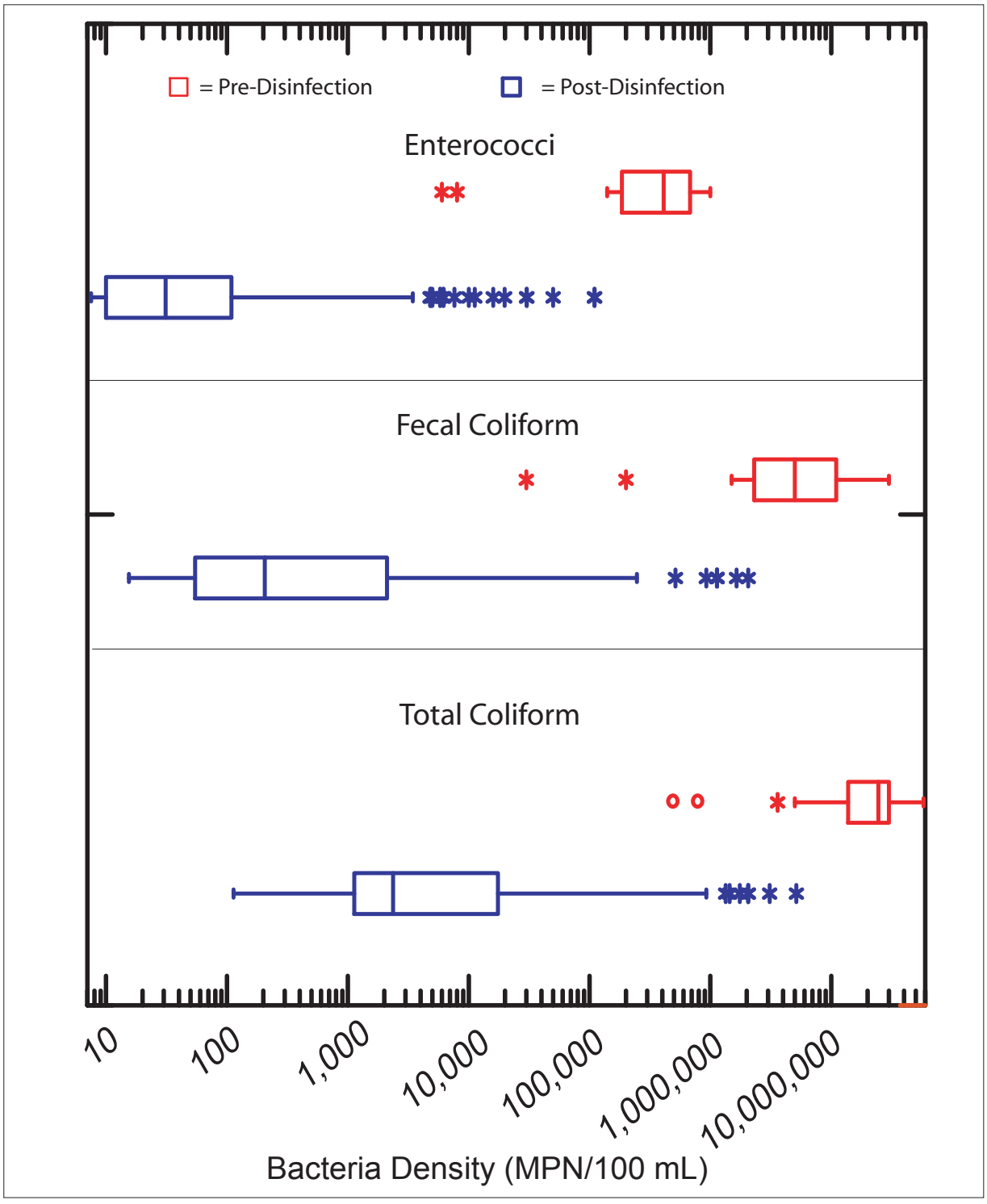

Figure 11-2. Box plots of FIB measured in the last-stage bay before the effluent was piped to the ocean before (red) and after (blue) disinfection. In a box plot, the center vertical line marks the sample median. The box length represents the range within which 50% of the values fall with the box edges equal to the first and third quartiles. The "whiskers" (lines extending from the box edges) are calculated based on the spread between the first and third quartiles (i.e., length of the box).

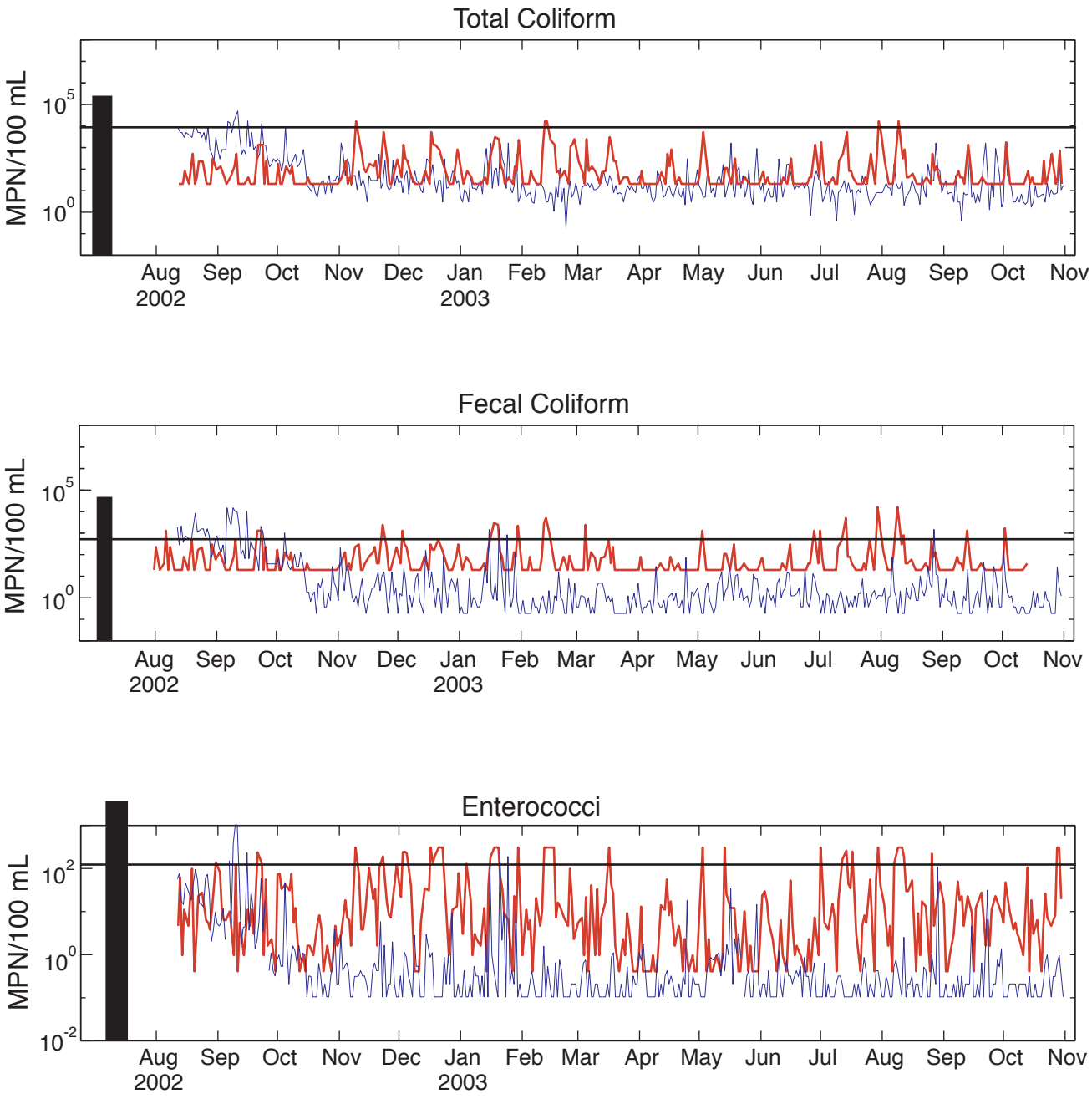

Figure 11-3. FIB bacterial levels measured at the last stage of processing in the OCSD plant after disinfection began. The levels are divided by 100 to simulate bacterial levels in the coastal ocean near the diffuser. The solid lines are the AB411 single-sample standards for each bacteria species.

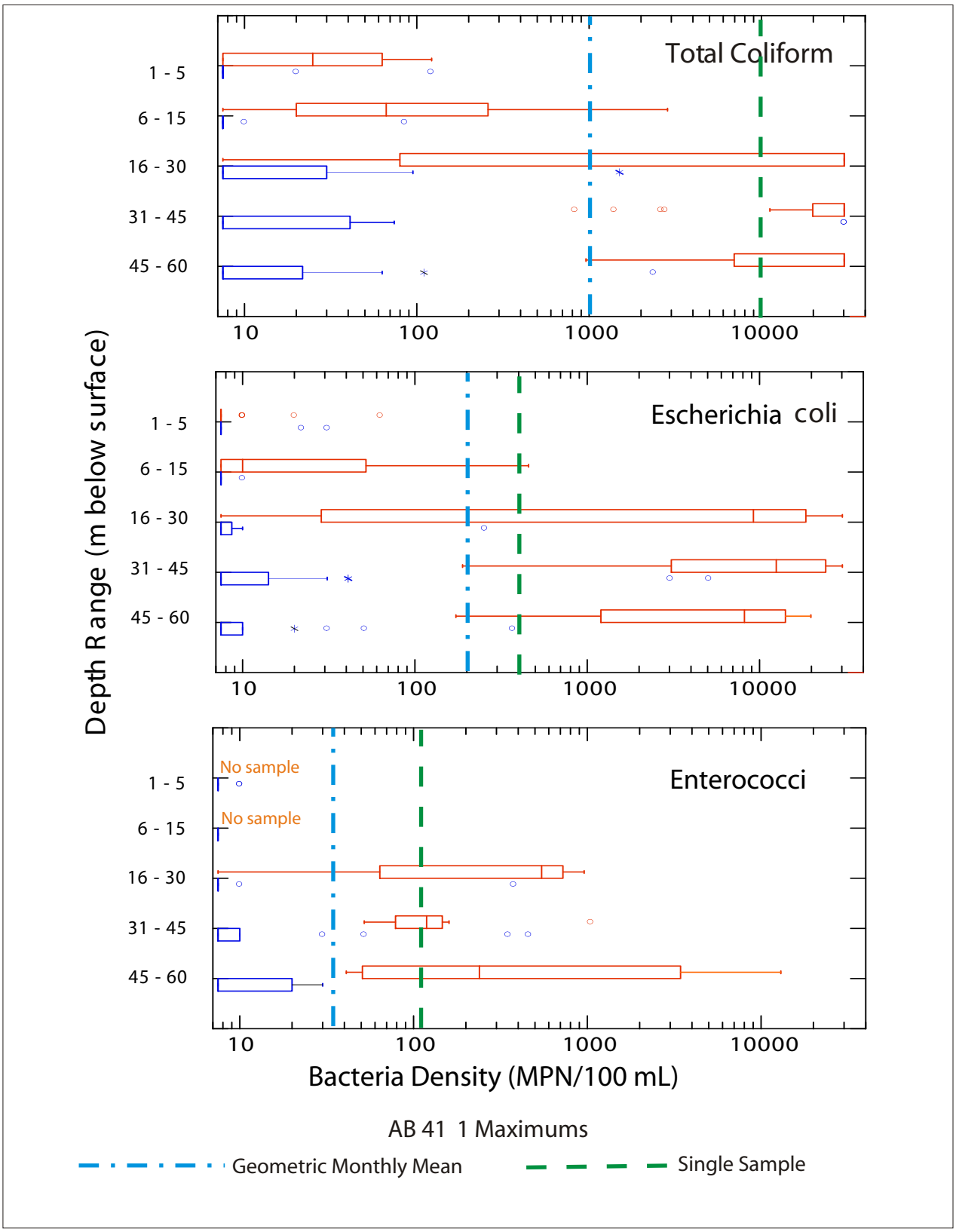

Figure 11-4. Box plots of FIB measured near OCSD's outfall before (red: 8/1/2001 to 8/11/2002) and after (blue: 8/12/2002 to 6/30/2003) disinfection of the final effluent.

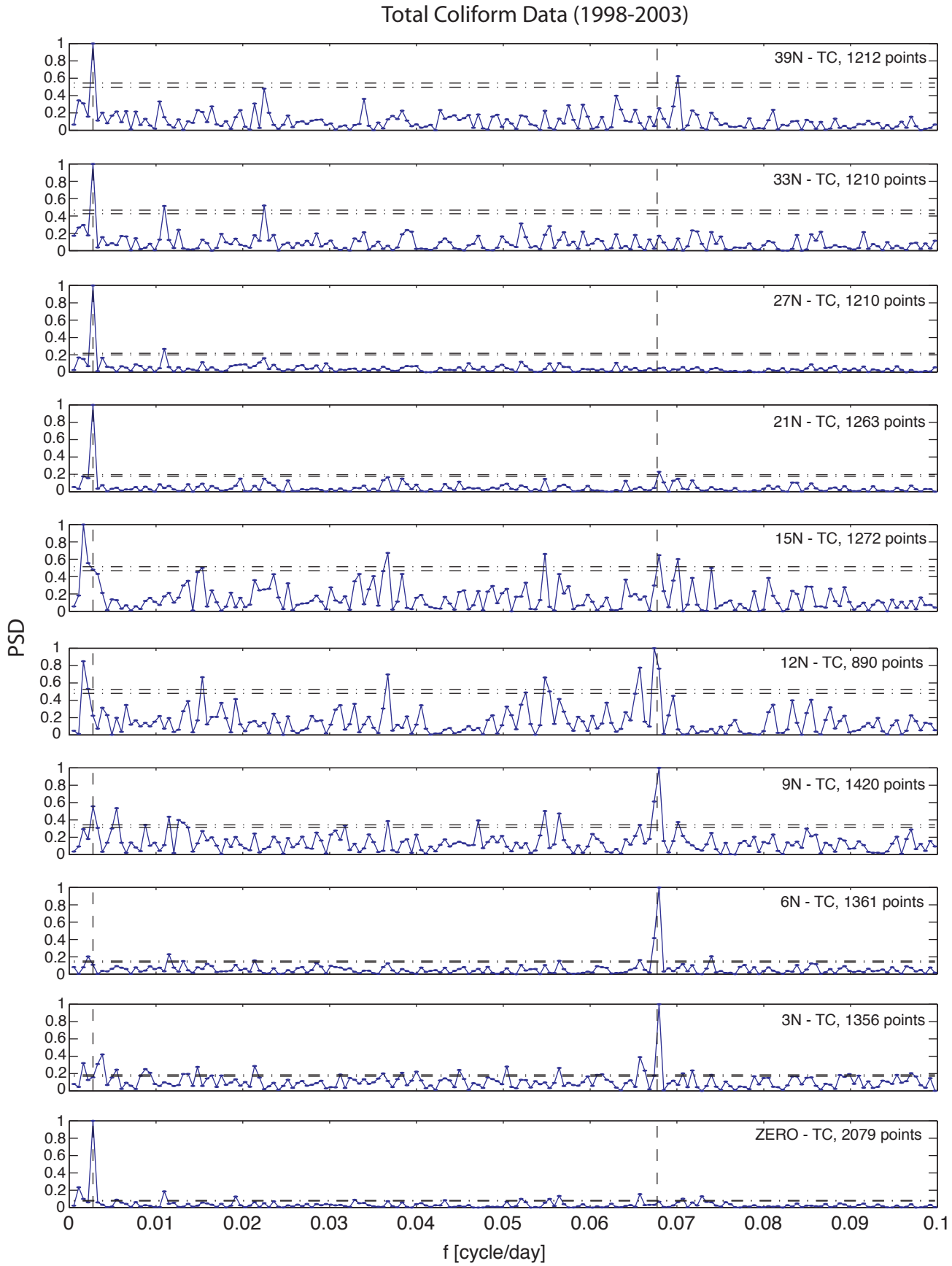

Figure 11-5a. Periodograms of the log of the bacterial counts for total coliform at the surfzone sampling stations. The periodograms have been normalized by the maximum value in each plot. The vertical dashed lines denote periods of 1 year and 14.77 days (the fortnightly cycle). A spectral peak must be above the horizontal dashed line to be significant at the 95% confidence level.

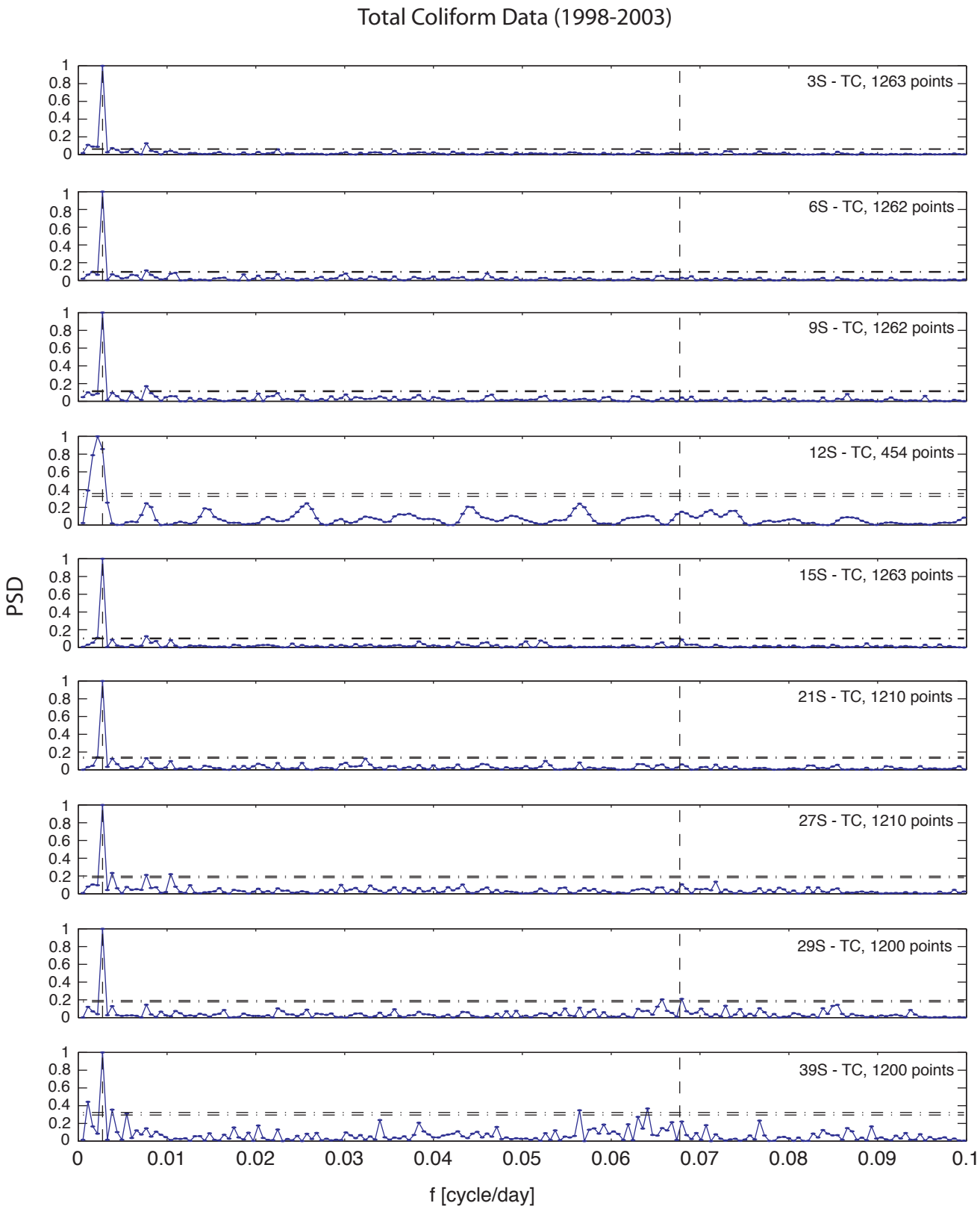

Figure 11-5a, cont. Periodograms of the log of the bacterial counts for total coliform at the surfzone sampling stations. The periodograms have been normalized by the maximum value in each plot. The vertical dashed lines denote periods of 1 year and 14.77 days (the fortnightly cycle). A spectral peak must be above the horizontal dashed line to be significant at the 95% confidence level.

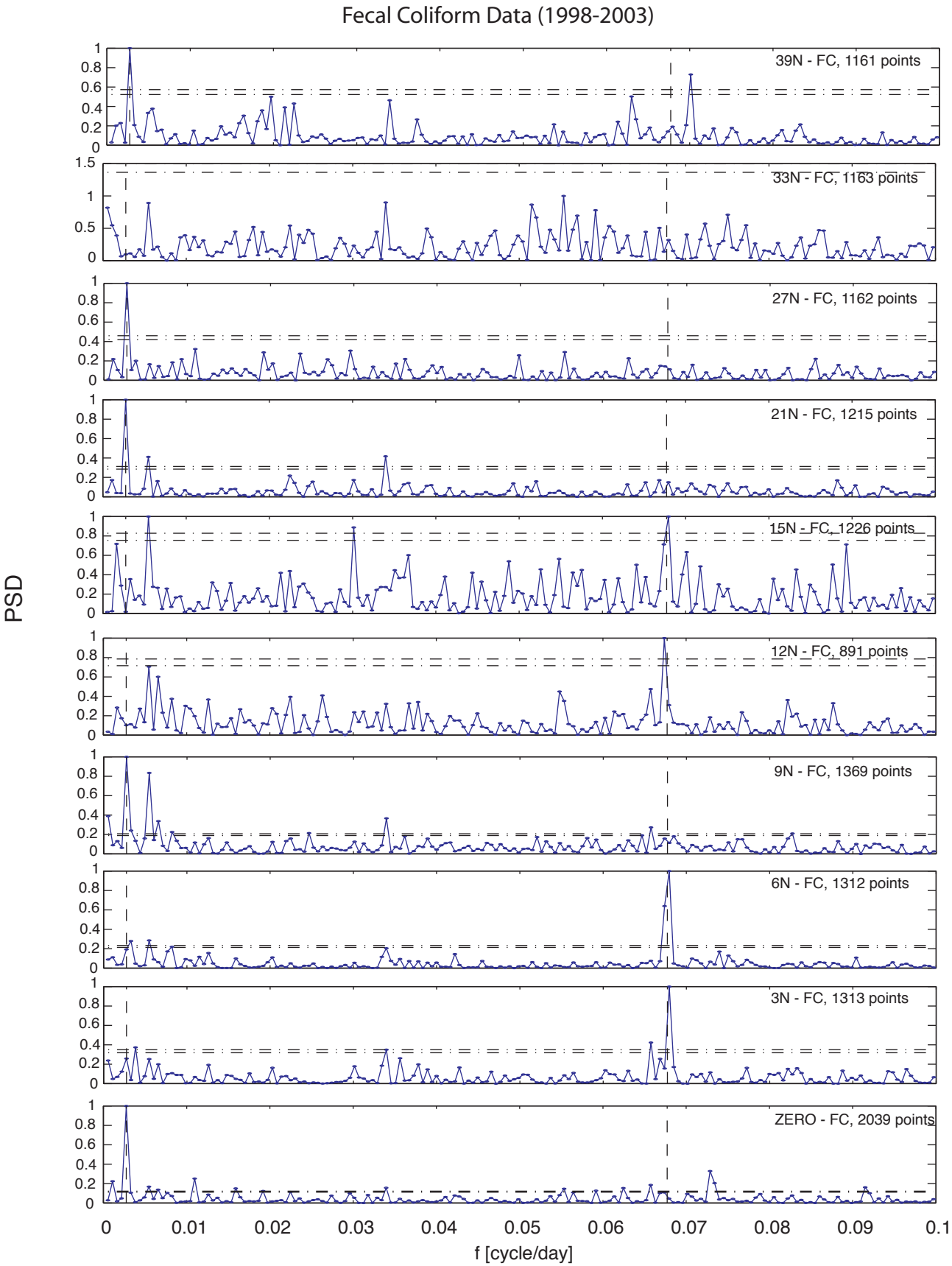

Figure 11-5b. Periodograms of the log of the bacterial counts for fecal coliform at the surfzone sampling stations. The periodograms have been normalized by the maximum value in each plot. The vertical dashed lines denote periods of 1 year and 14.77 days (the fortnightly cycle). A spectral peak must be above the horizontal dashed line to be significant at the 95% confidence level.

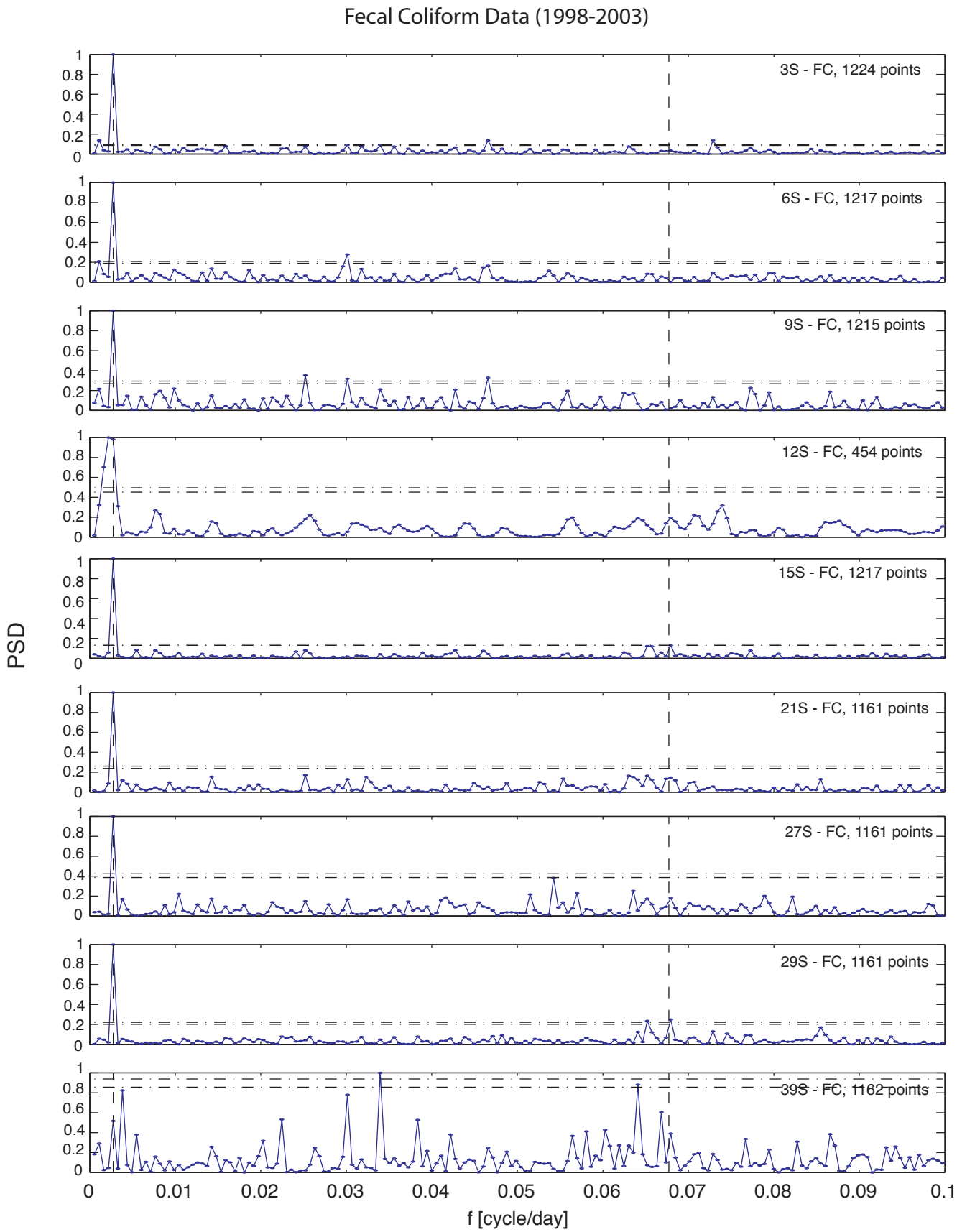

Figure 11-5b, cont. Periodograms of the log of the bacterial counts for fecal coliform at the surfzone sampling stations. The periodograms have been normalized by the maximum value in each plot. The vertical dashed lines denote periods of 1 year and 14.77 days (the fortnightly cycle). A spectral peak must be above the horizontal dashed line to be significant at the 95% confidence level.

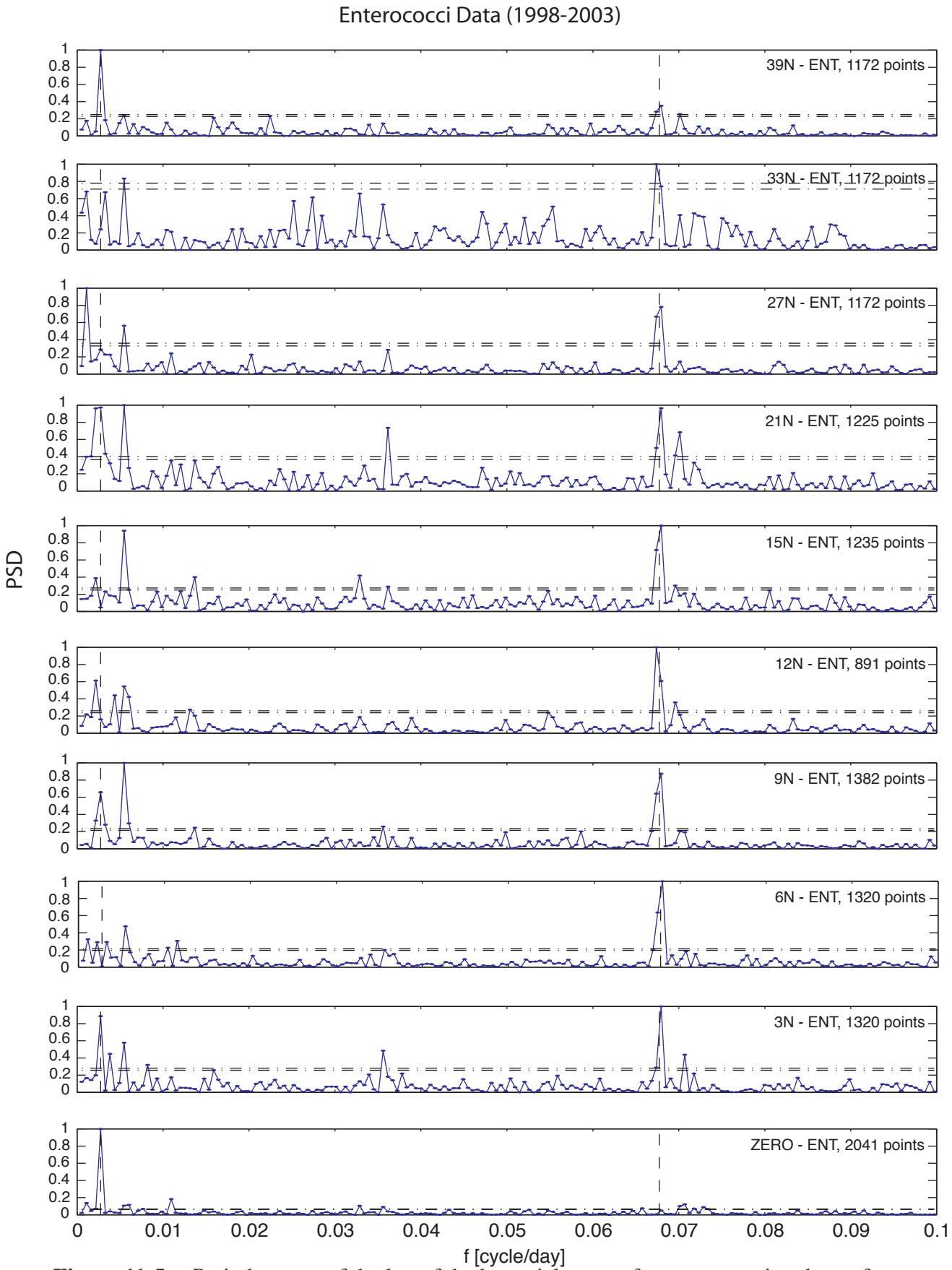

Figure 11-5c. Periodograms of the log of the bacterial counts for enterococci at the surfzone sampling stations. The periodograms have been normalized by the maximum value in each plot. The vertical dashed lines denote periods of 1 year and 14.77 days (the fortnightly cycle). A spectral peak must be above the horizontal dashed line to be significant at the 95% confidence level.

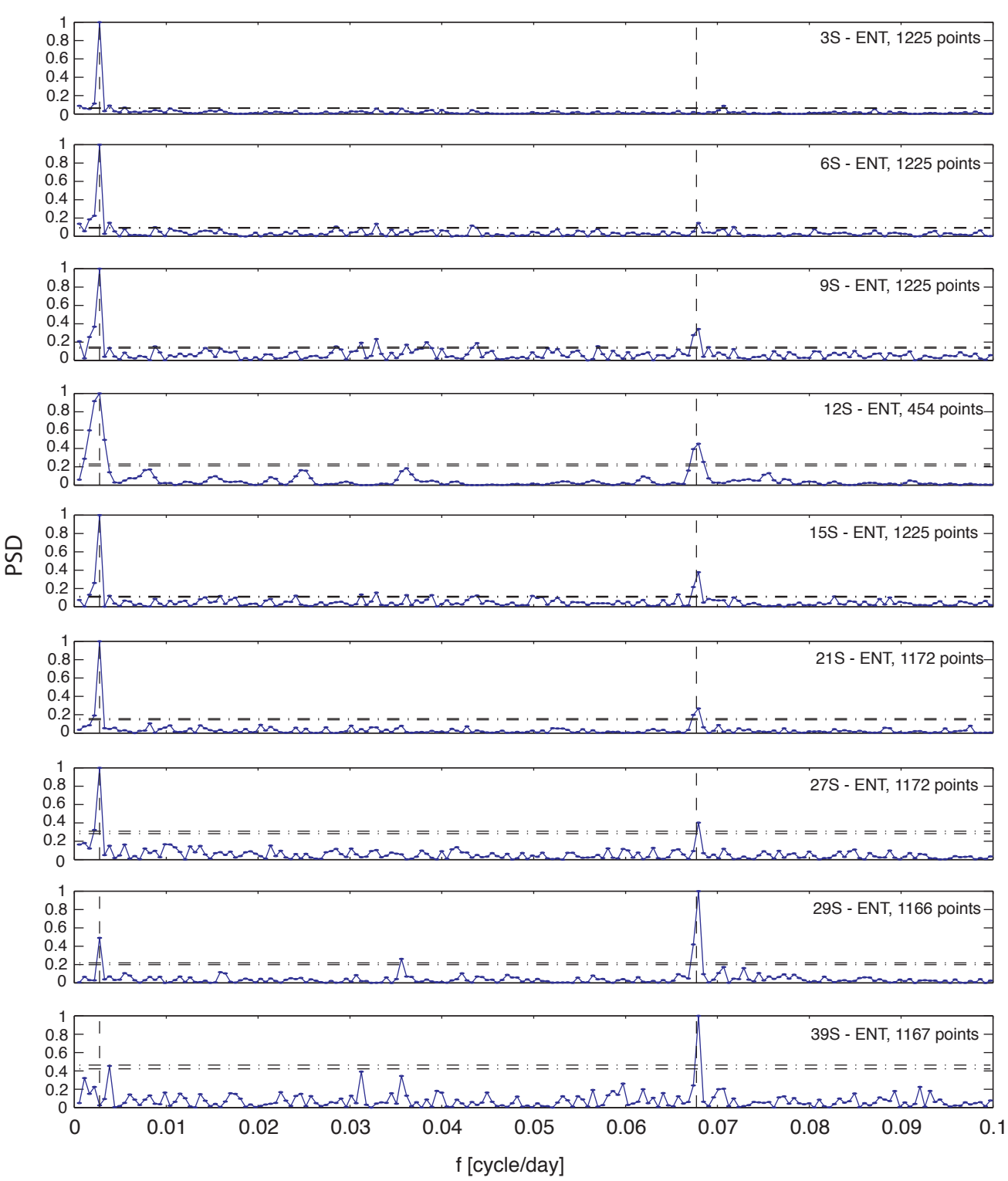

Figure 11-5c, cont. Periodograms of the log of the bacterial counts for enterococci at the surfzone sampling stations. The periodograms have been normalized by the maximum value in each plot. The vertical dashed lines denote periods of 1 year and 14.77 days (the fortnightly cycle). A spectral peak must be above the horizontal dashed line to be significant at the 95% confidence level.

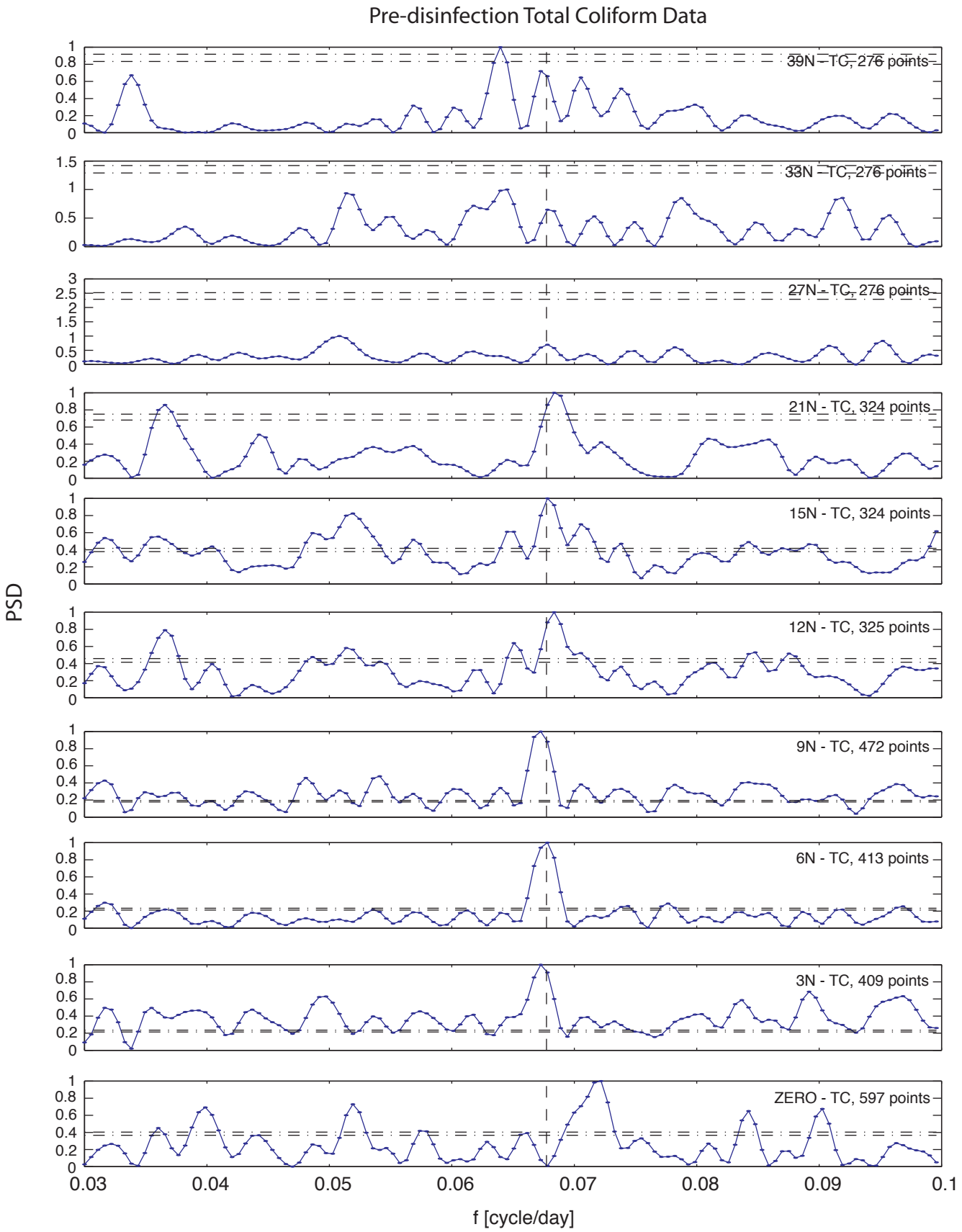

Figure 11-6a. Periodograms of the log of the bacterial counts for total coliform before disinfection of the OCSD effluent. The periodograms have been normalized by the maximum value in each plot. The vertical dashed lines denote periods of 14.77 days (fortnightly cycle). A spectral peak must be above the horizontal dashed line to be significant at the 95% confidence level.

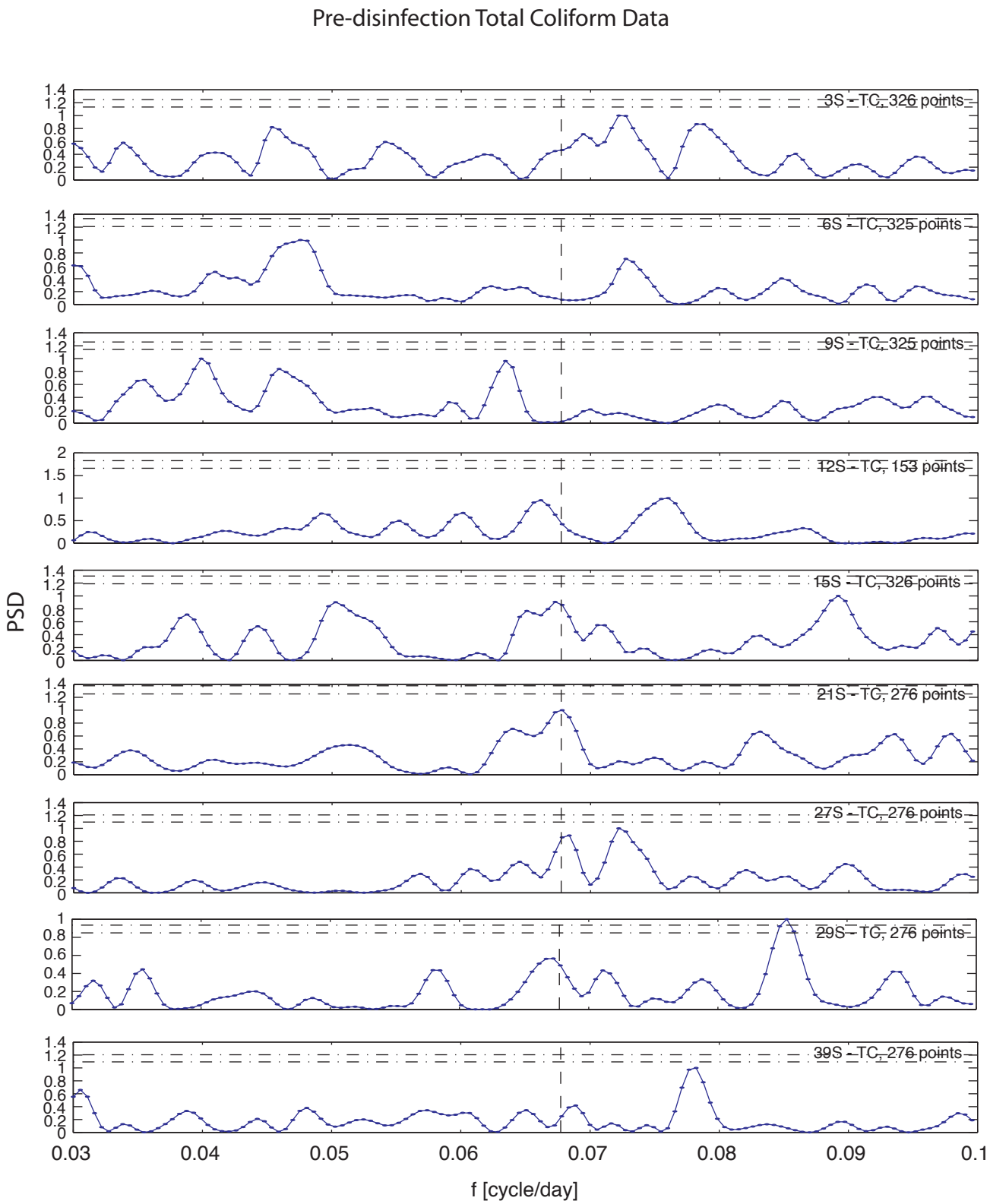

Figure 11-6a, cont. Periodograms of the log of the bacterial counts for total coliform before disinfection of the OCSD effluent. The periodograms have been normalized by the maximum value in each plot. The vertical dashed lines denote periods of 14.77 days (fortnightly cycle). A spectral peak must be above the horizontal dashed line to be significant at the 95% confidence level.

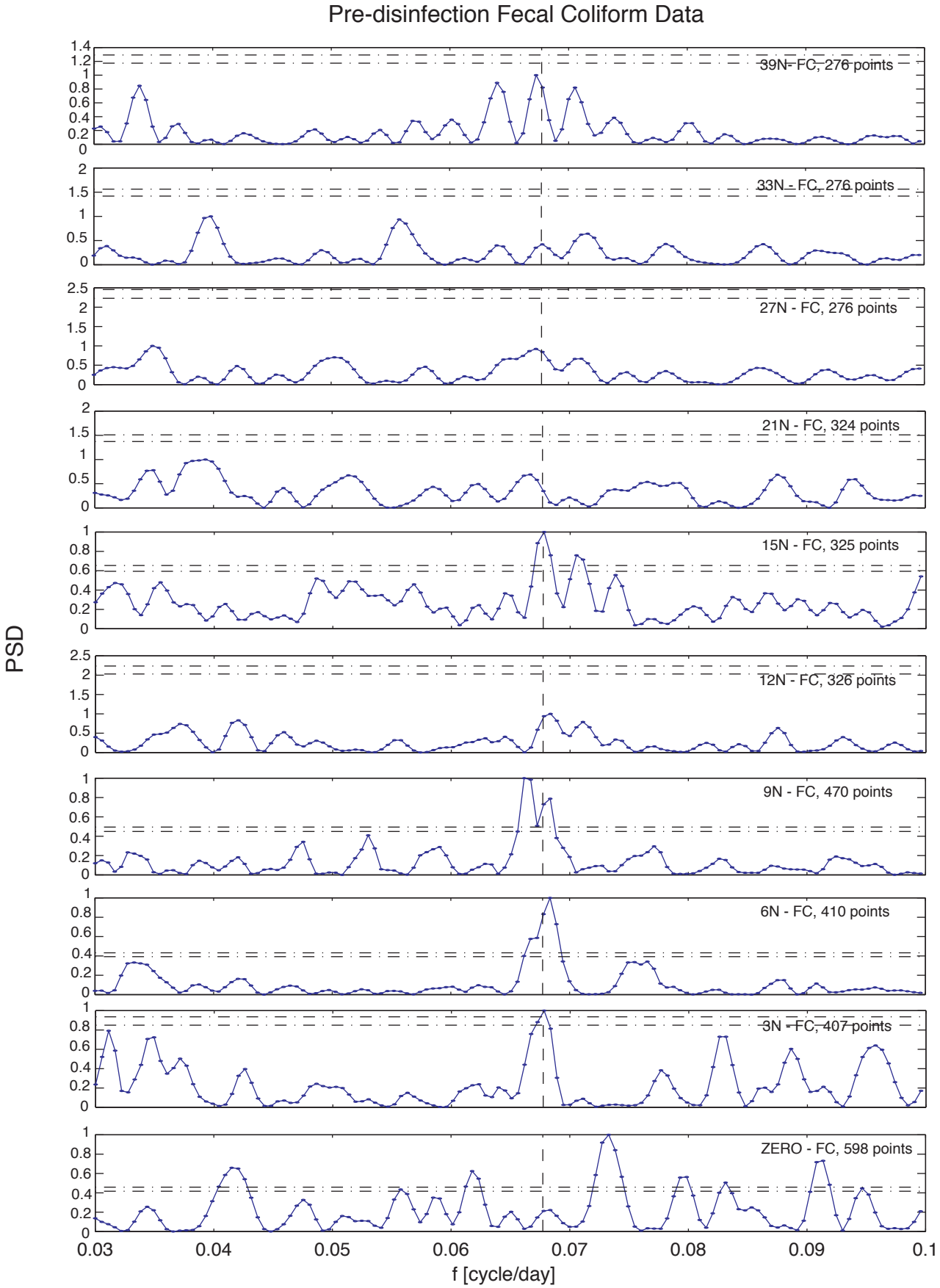

Figure 11-6b. Periodograms of the log of the bacterial counts for fecal coliform before disinfection of the OCSD effluent. The periodograms have been normalized by the maximum value in each plot. The vertical dashed lines denote periods of 14.77 days (fortnightly cycle). A spectral peak must be above the horizontal dashed line to be significant at the 95% confidence level.

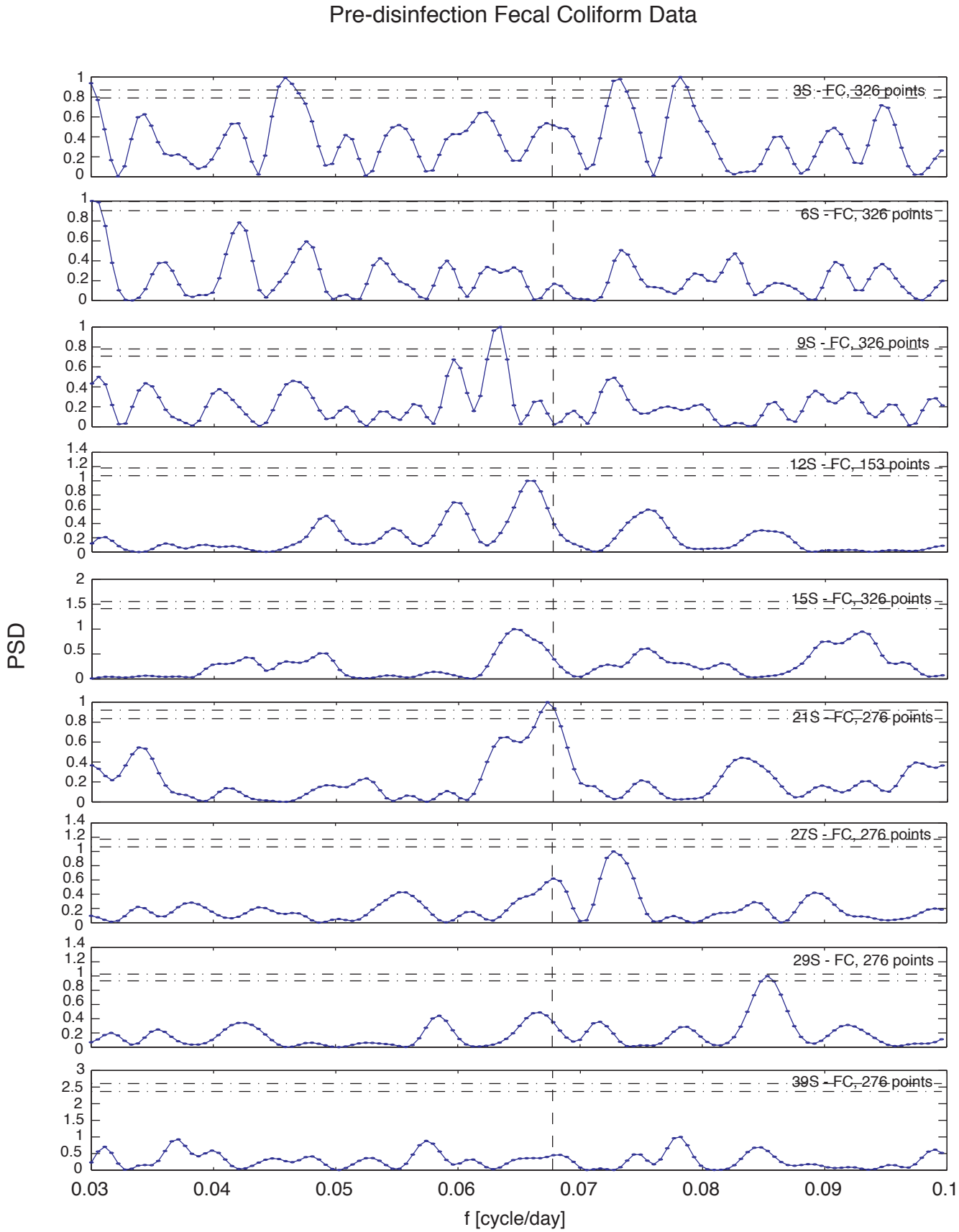

Figure 11-6b, cont. Periodograms of the log of the bacterial counts for fecal coliform before disinfection of the OCSD effluent. The periodograms have been normalized by the maximum value in each plot. The vertical dashed lines denote periods of 14.77 days (fortnightly cycle). A spectral peak must be above the horizontal dashed line to be significant at the 95% confidence level.

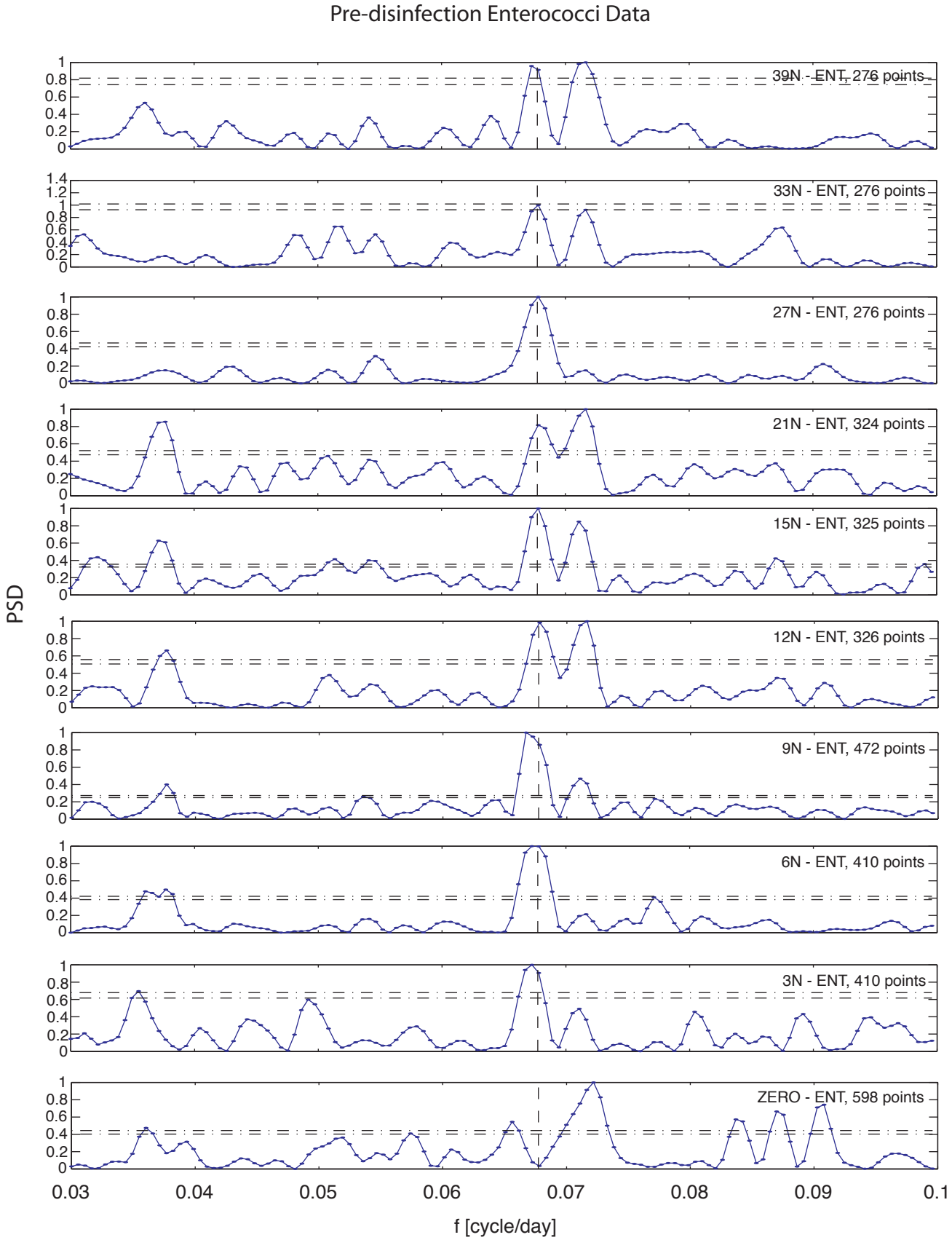

Figure 11-6c. Periodograms of the log of the bacterial counts for enterococci before disinfection of the OCSD effluent. The periodograms have been normalized by the maximum value in each plot. The vertical dashed lines denote periods of 14.77 days (fortnightly cycle). A spectral peak must be above the horizontal dashed line to be significant at the 95% confidence level.

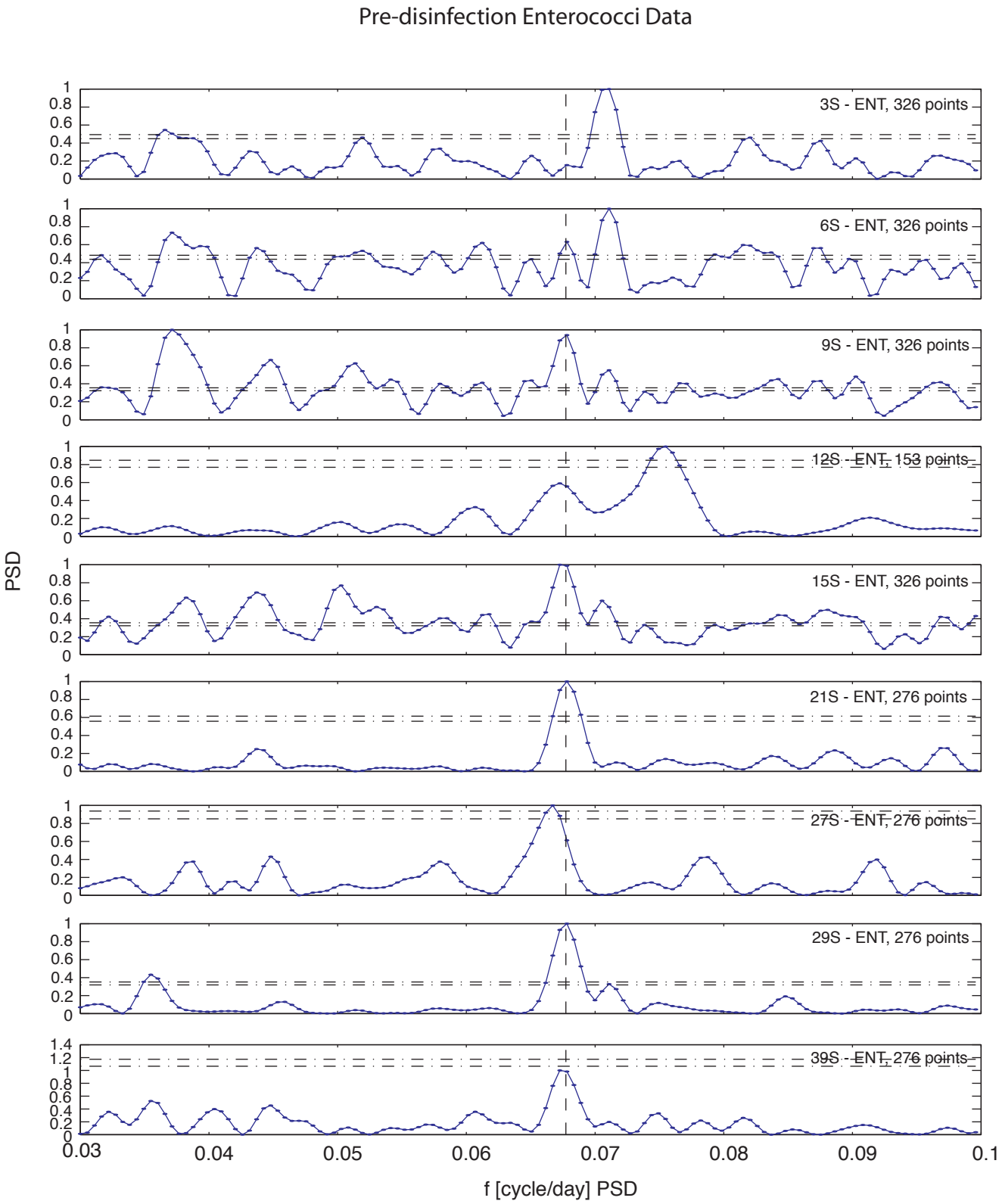

Figure 11-6c, cont. Periodograms of the log of the bacterial counts for enterococci before disinfection of the OCSD effluent. The periodograms have been normalized by the maximum value in each plot. The vertical dashed lines denote periods of 14.77 days (fortnightly cycle). A spectral peak must be above the horizontal dashed line to be significant at the 95% confidence level.

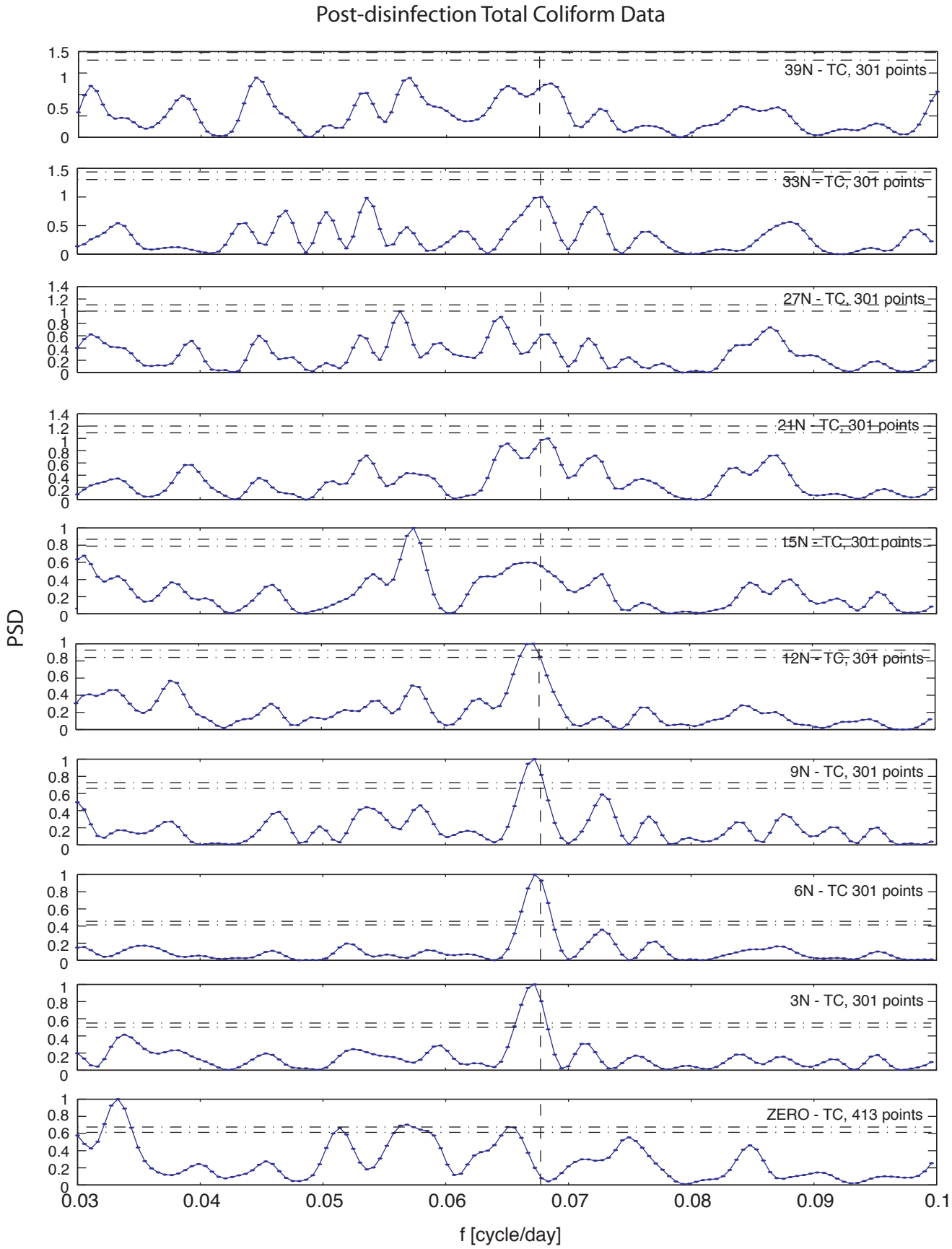

Figure 11-7a. Periodograms of the log of the bacterial counts for total coliform after disinfection of the OCSD effluent. The periodograms have been normalized by the maximum value in each plot. The vertical dashed lines denote periods of 14.77 days (fortnightly cycle). A spectral peak must be above the horizontal dashed line to be significant at the 95% confidence level.

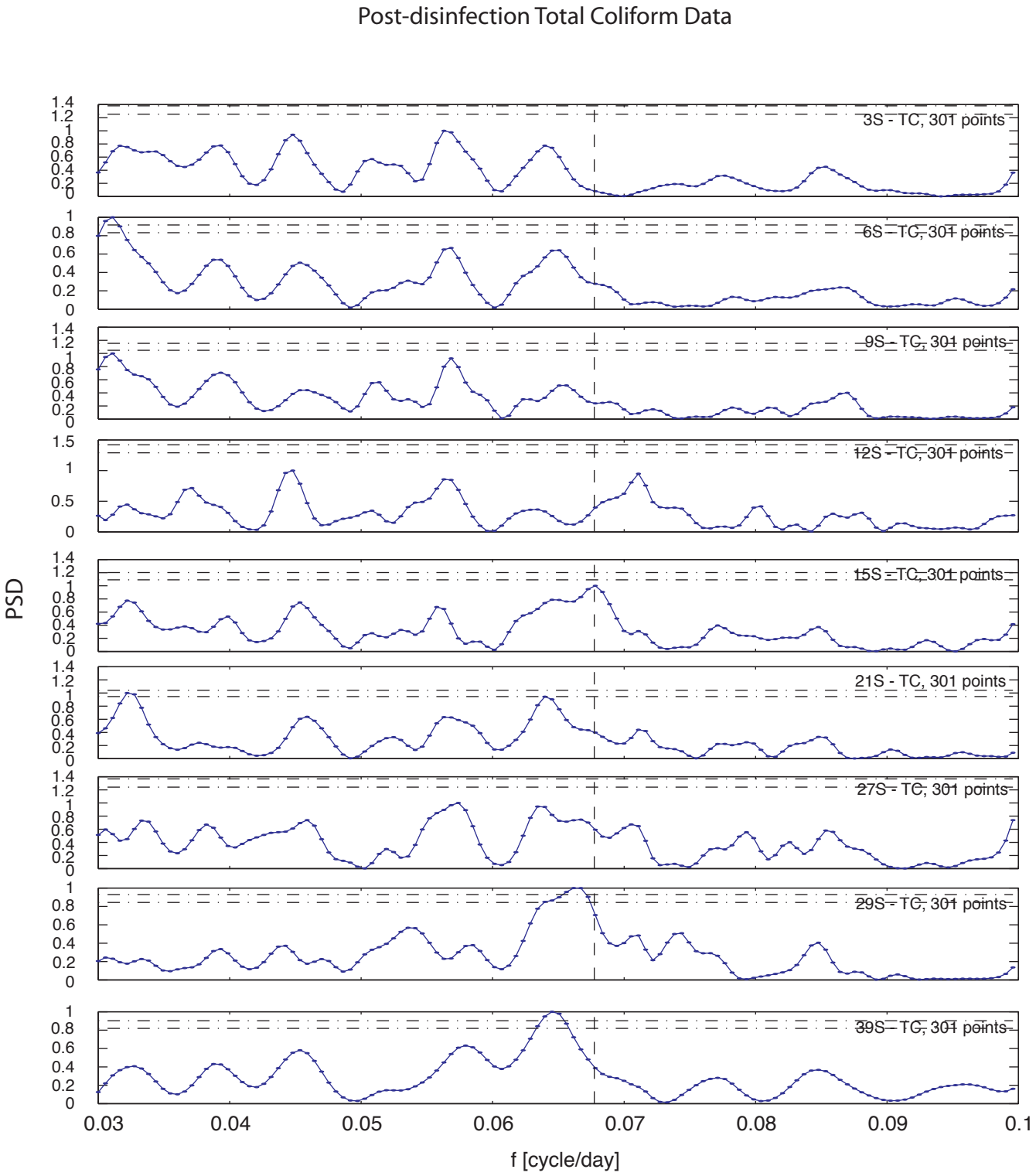

Figure 11-7a, cont. Periodograms of the log of the bacterial counts for total coliform after disinfection of the OCSD effluent. The periodograms have been normalized by the maximum value in each plot. The vertical dashed lines denote periods of 14.77 days (fortnightly cycle). A spectral peak must be above the horizontal dashed line to be significant at the 95% confidence level.

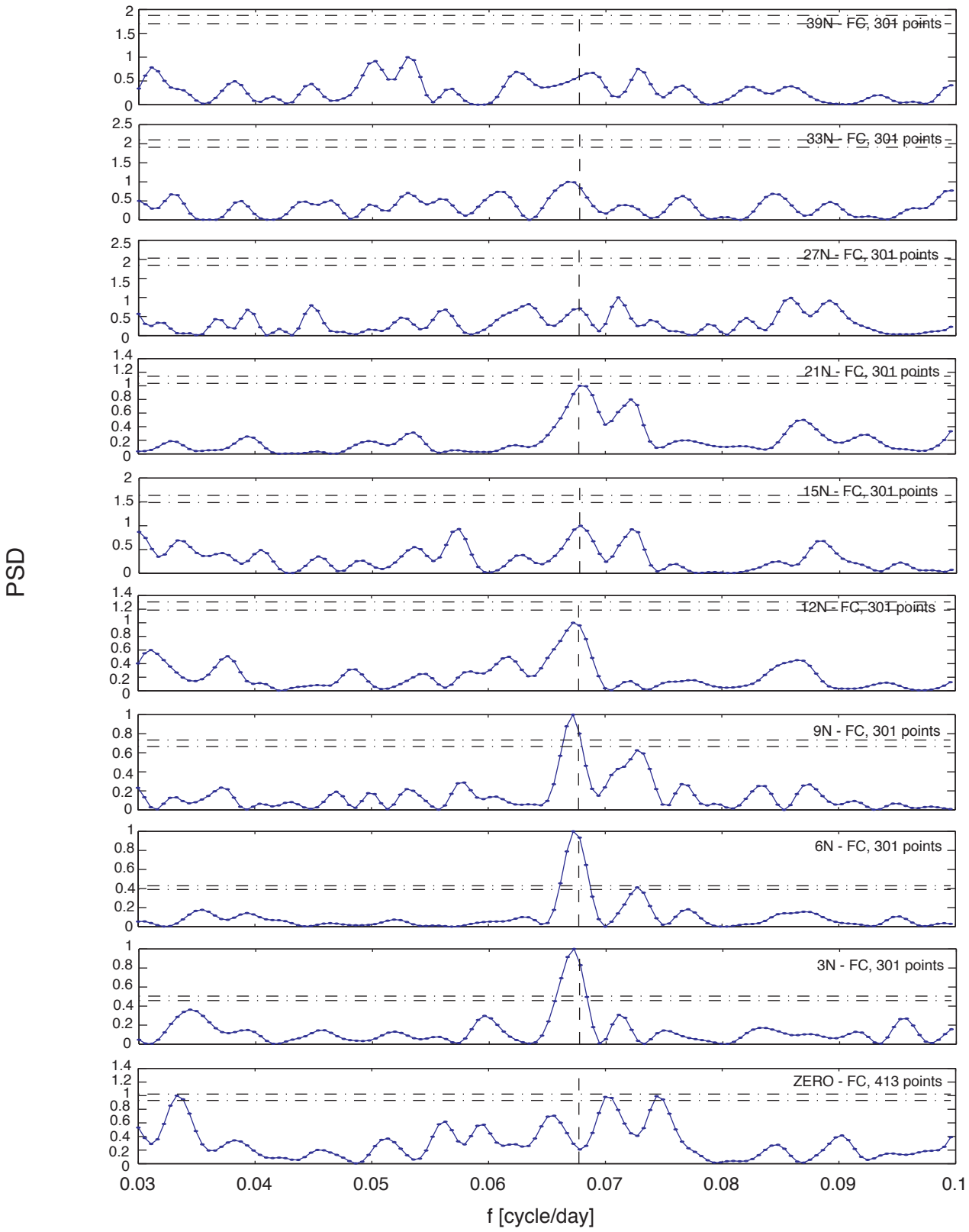

Figure 11-7b. Periodograms of the log of the bacterial counts for fecal coliform after disinfection of the OCSD effluent. The periodograms have been normalized by the maximum value in each plot. The vertical dashed lines denote periods of 14.77 days (fortnightly cycle). A spectral peak must be above the horizontal dashed line to be significant at the 95% confidence level.

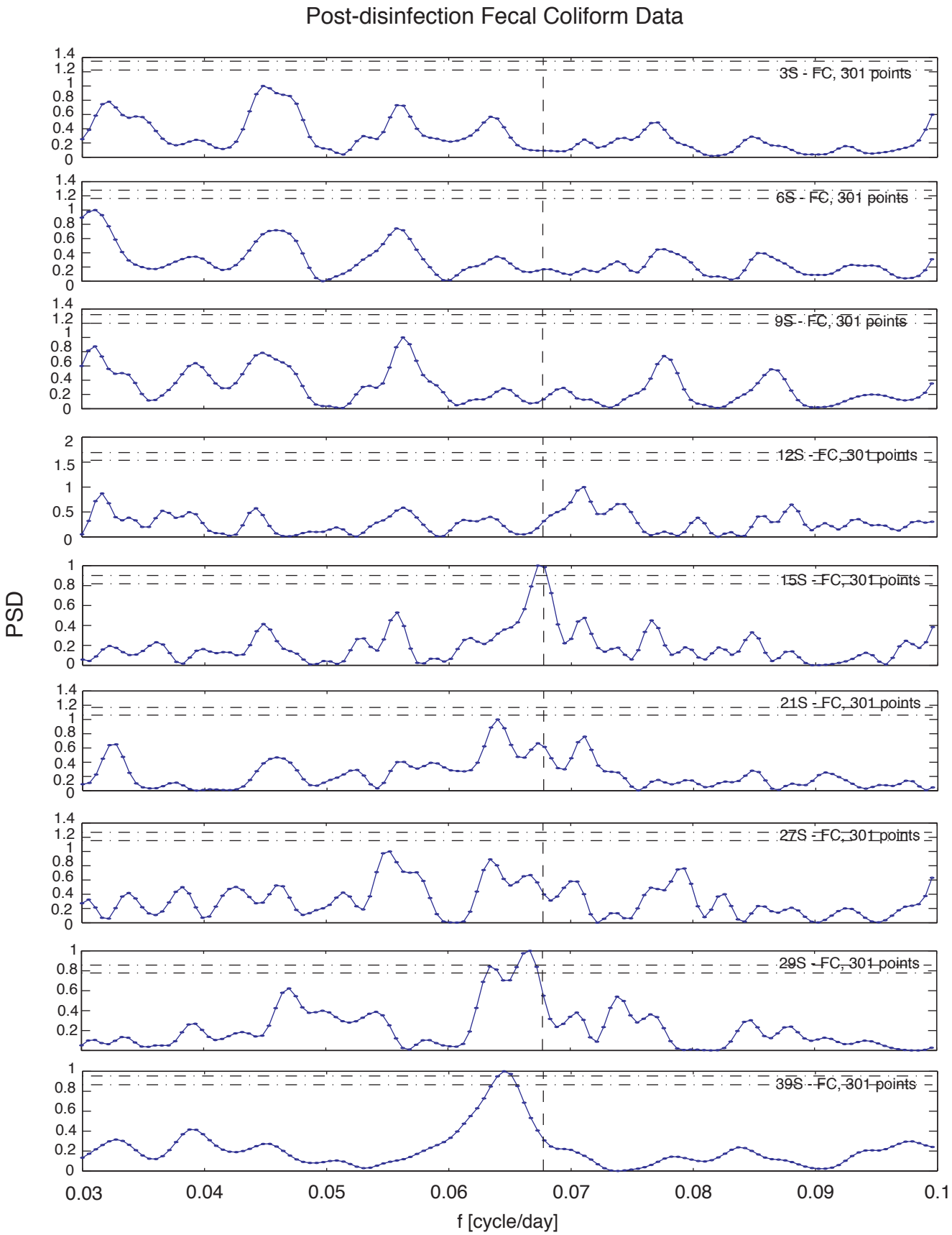

Figure 11-7b, cont. Periodograms of the log of the bacterial counts for fecal coliform after disinfection of the OCSD effluent. The periodograms have been normalized by the maximum value in each plot. The vertical dashed lines denote periods of 14.77 days (fortnightly cycle). A spectral peak must be above the horizontal dashed line to be significant at the 95% confidence level.

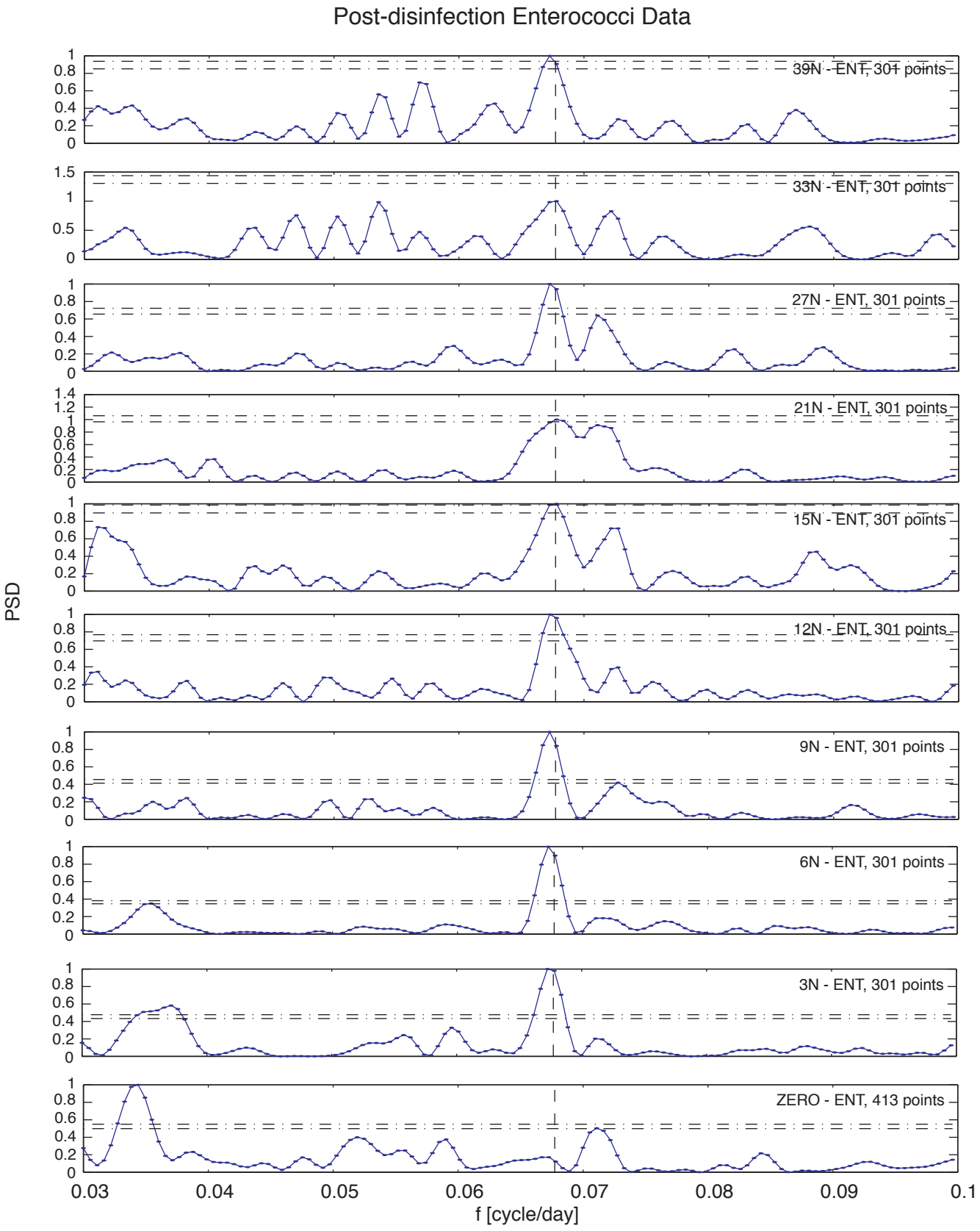

Figure 11-7c. Periodograms of the log of the bacterial counts for enterococci after disinfection of the OCSD effluent. The periodograms have been normalized by the maximum value in each plot. The vertical dashed lines denote periods of 14.77 days (fortnightly cycle). A spectral peak must be above the horizontal dashed line to be significant at the 95% confidence level.

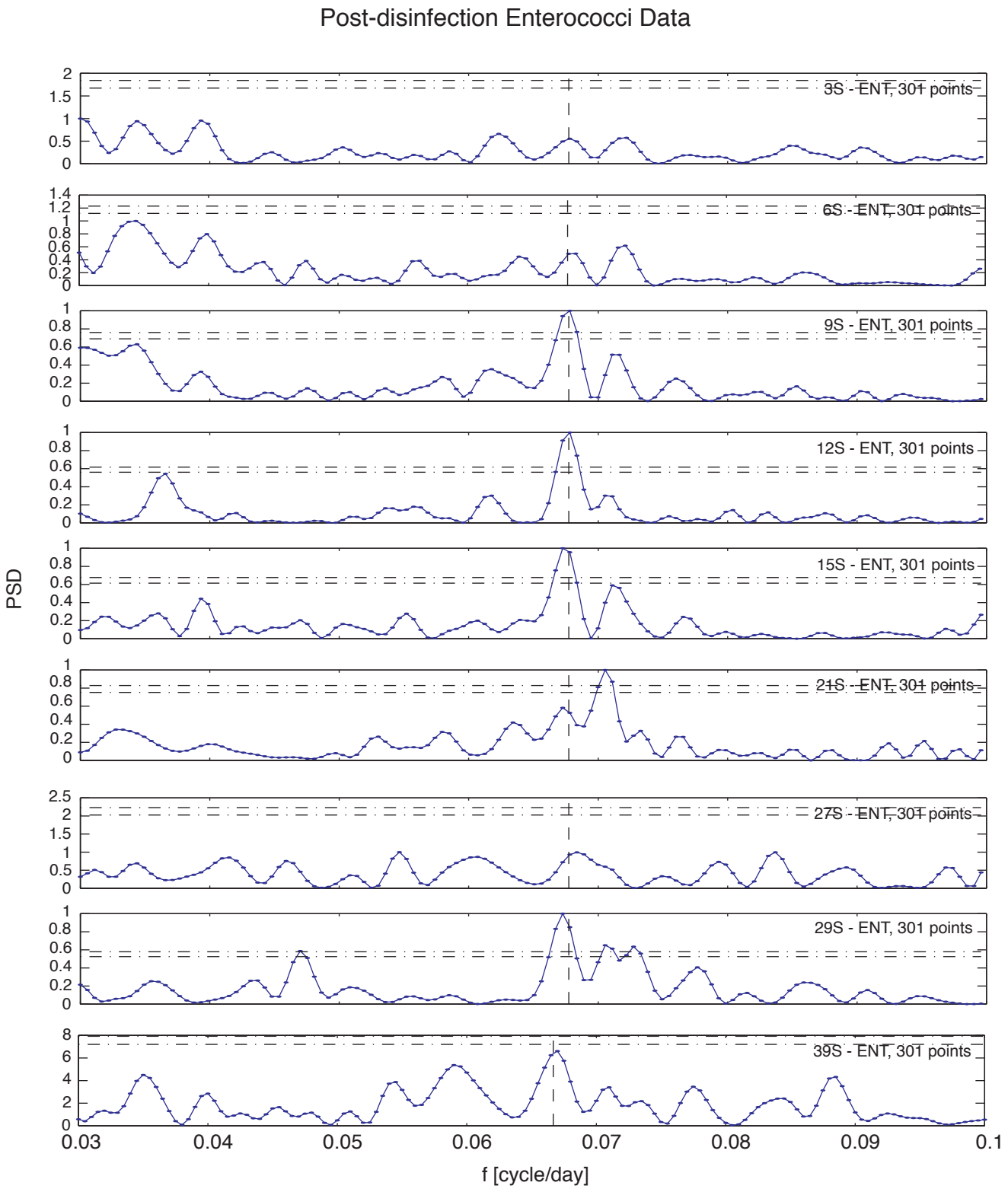

Figure 11-7c, cont. Periodograms of the log of the bacterial counts for enterococci after disinfection of the OCSD effluent. The periodograms have been normalized by the maximum value in each plot. The vertical dashed lines denote periods of 14.77 days (fortnightly cycle). A spectral peak must be above the horizontal dashed line to be significant at the 95% confidence level.